



**Università  
degli Studi  
di Ferrara**



**Uniwersytet  
Wrocławski**

**DOCTORAL COURSE IN  
"CHEMISTRY"**

CYCLE 34

**International Joint Doctoral Study Programme in Chemistry  
with University of Wrocław (Wrocław, Poland)**

**COORDINATOR prof. Alberto Cavazzini**

**IRIDIUM(III) COMPLEXES WITH PHOSPHINE-FLUOROQUINOLONE  
CONJUGATES - DESIGN, SYNTHESIS, BIOACTIVITY AND NANOFORMULATION  
AS A POTENTIAL PLATFORM FOR DRUG DELIVERY**

Scientific/Disciplinary Sector (SDS) CHIM/03

**Candidate**

Dott. Sandra Amanda Koziel

(signature)

**Supervisor**

Prof. Alina Bieńko

(signature)

**Supervisor**

Prof. Stefano Caramori

Years 2018/2021



**Università  
degli Studi  
di Ferrara**



**Uniwersytet  
Wrocławski**

**Department of Chemistry, University of Wrocław**

**The Department of Chemical, Pharmaceutical and Agricultural Sciences,  
University of Ferrara**

**Sandra Koziel**

**Iridium(III) complexes with phosphine-fluoroquinolone  
conjugates - design, synthesis, bioactivity and  
nanoformulation as a potential platform for drug delivery.**

**Supervisor: Dr. Alina Bieńko, prof. UWr (University of Wrocław)**

**Supervisor: prof. Stefano Caramori (University of Ferrara)**

**Auxiliary supervisor: Dr. Urszula Komarnicka (University of Wrocław)**

**Wrocław, 2022**



## Acknowledgements

*I would like to sincerely thank everyone who made the research included in this doctoral thesis not only possible but also a pleasure for the fulfillment of my professional dreams and plans.*

*First of all, I would like to express my gratitude to my supervisor **Dr. Alina Bieńko, prof. UWr** for giving me the opportunity to undertake a PhD study and her supervision of my work. The kindness, support, and trust that she has placed in me will always be remembered, and will always be a role model for the Perfect Boss. I was very lucky in my life that I could pursue my professional career under the supervision of such a wonderful specialist as the Professor, but most of all, that I was able to work with such a Professor.*

*I would like to express my heartfelt thanks to my second supervisor, **prof. Stefano Caramori** for the invaluable help provided during the preparation of the doctoral dissertation, patience and understanding, and motivation to take a critical look at research issues. I would also like to thank you for looking after me during my stay in Ferrara, where I also studied and did the research for my doctoral dissertation.*

### **Auxiliary Supervisor of Dr. Urszula Komarnicka**

*Thank you for fueling the fire of my love of chemistry. Our cooperation was not afraid of exchanging messages late at night and tight schedules. I did not realize that at first, a stranger can devote so much time selflessly to helping another person.*

***Dr. Miłosz Siczek and Dr. Agnieszka Skórska-Stania** for help with crystal structures.*

*Thank you **Alessandro Niorettini** for your help with cyclic voltammetry measurements and the enjoyable time I spent during my internship in Ferrara.*

*I thank **Dr. Dariusz Bieńko and Dr. inż. Edyta Dyguda-Kazimierowicz** for performing DFT calculations for my compounds which results in a joined publication.*

***Prof. Dr. Grażyna Stochel** for enabling research in her laboratories.*

### **Dr. Agnieszka Kyziół, prof. UJ**

*Thank you for the opportunity to carry out the biological research contained in this doctoral dissertation.*

### **Dr. Barbara Pucelik**

*Thank you for your irreplaceable help in planning experiments and your creative approach to finding solutions to biological problems.*

### **Daria Wojtala**

*For help in carrying out the experiments and for the amazing time spent together at night in the office room.*

*I would like to sincerely thank **my parents**. First of all, for their support throughout my educational path, from the hard beginnings in primary school until today, when I submit my doctoral dissertation. Additionally, for showing me the beauty of the world and the desire to understand that led me to study chemistry.*

*I would also like to acknowledge the funding support, which assisted the research from the financial side:*



*National Science Centre Poland for the PRELUDIUM grant (no. 2020/37/N/ST4/02698)*

## Streszczenie

Na całym świecie, choroby nowotworowe powodują kilka milionów zgonów rocznie. Przewiduje się, że przed końcem 2023 roku pojawi się więcej niż dwadzieścia dwa miliony nowych przypadków chorób nowotworowych. Wiele leków przeciwnowotworowych jest obecnie stosowanych w leczeniu klinicznym, ale ponad 50% z nich to leki oparte na bazie jonów platyny. Ich skuteczność nadal utrudniają problemy kliniczne, w tym nabyta lub wrodzona oporność, ograniczone spektrum działania oraz wysoka toksyczność prowadząca do działań niepożądanych. Jedną ze strategii przyjętych w celu przewyciężenia tych ograniczeń jest opracowanie nowych alternatywnych środków przeciwnowotworowych na bazie jonów metali przejściowych (np. Cu, Ru, Pd i Au).

Obecnie spośród badanych kompleksów metali przejściowych to związki irydu są prawdopodobnie najbardziej obiecującą grupą potencjalnych leków przeciwnowotworowych. W porównaniu do związków platyny charakteryzują się one zredukowanym stopniem toksyczności w stosunku do komórek zdrowych, a zatem wyższą selektywnością działania na komórki zmienione nowotworowo. Ponadto wykazują właściwości przeciwnowotworowe poprzez indukcję apoptozy oraz interakcje z DNA lub kinazami białkowymi.

Fluorochinolony to antybiotyki o szerokim spektrum działania stosowane w leczeniu infekcji bakteryjnych nie tylko u ludzi, ale także u zwierząt. Oprócz silnego działania przeciwdrobnoustrojowego antybiotyki te wykazują również działanie immunomodulujące i przeciwnowotworowe. Dlatego też, połączenie fluorochinolonów poprzez ugrupowanie fosfinowe z kompleksami irydu(III) może dodatkowo zmniejszyć ogólną toksyczność i umożliwić selektywne dostarczanie do komórek nowotworowych.

Celem nadrzędnym moich badań było opracowanie metod syntezy kompleksów irydu(III) z fosfinowymi pochodnymi fluorochinolonów, a następnie ich charakterystyka fizykochemiczna oraz biologiczna. W kolejnym kroku dla związków o najwyższej aktywności przeciwnowotworowej zaprojektowano metody ich selektywnego dostarczania poprzez enkapsulację w nanoformulacjach.

W ramach pracy doktorskiej zsyntetyzowałem trzy związki koordynacyjne irydu(III) zawierające fosfinowe pochodne fluorochinolonów. W celu porównania wpływu antybiotyków, zsyntetyzowano również jeden kompleks irydu(III) bez antybiotyku. Otrzymane związki koordynacyjne scharakteryzowano z wykorzystaniem analizy elementarnej, spektrometrii mas (ESI-MS) oraz wybranych metod spektroskopowych (np. IR, NMR, UV-Vis

oraz fluorescencyjnej). Co warto podkreślić, w przypadku wszystkich kompleksów, udało się otrzymać monokryształy odpowiednie do badań krystalograficznych. Kompleksy zawierają jon Ir(III), do którego koordynuje ligand aromatyczny (cyklopentadienyl), oraz dwa ligandy chlorkowe i jedna cząsteczka fosfiny – wykazując geometrię pseudooktaedryczną typu „half-sandwich”. Kompleksy homojądrowe Ir(III) zawierające motyw fluorochinolonowy są stabilne w roztworze wodnym, w porównaniu do kompleksu bez tego motywu. Kompleks ten hydrolyzował w roztworze wodnym, co zostało udowodnione za pomocą  $^1\text{H}$  NMR przy różnych stężeniach roztworu NaCl.

Aktywność przeciwnowotworową *in vitro* zsyntezowanych kompleksów i cisplatyny przebadano wobec pięciu linii komórek nowotworowych: MCF7 (ludzki gruczolakorak piersi), A549 (ludzki gruczolakorak płucny), PANC-1 (ludzki rak przewodowy trzustki) oraz DU-145 (ludzki rak prostaty), WM2664 (ludzki rak skóry) a także wobec pierwotnej linii embrionalnych ludzkich komórek nerek (HEK293T). Badane kompleksy wykazywały obiecującą cytotoksyczność *in vitro* z wartościami  $\text{IC}_{50}$  znacznie niższymi niż dla cisplatyny. Co warto podkreślić, wprowadzenie motywu fluorochinolonowego do kompleksów znacząco zwiększyło cytotoksyczność przeciwnowotworową finalnych związków wobec linii komórkowej płuc, piersi i czerniaka. Badanie to umożliwiło wyselekcjonowanie z puli wszystkich zsyntetyzowanych związków, kompleksu o najlepszym działaniu przeciwnowotworowym (**IrPCp**), a następnie podjęcie próby określenia mechanizmu działania cytotoksycznego. Wstępne badania skoncentrowane na wyjaśnieniu sposobu działania pozwoliły na sformułowanie następujących wniosków: **(i)** kompleksy irydu(III) akumulują się w komórce zarówno w jądrze, jak i w cytoplazmie, **(ii)** na podstawie analizy cytometrycznej wykazano, że w komórce zachodzi głównie apoptoza (programowana śmierć komórki), **(iii)** aktywacja kaspazy-3/7 wraz ze spadkiem potencjału błony mitochondrialnej również potwierdziła apoptotyczną śmierć komórki, **(iv)** kompleksy irydu(III) mogą indukować zmiany w cyklu komórkowym prowadzące do fazy G2/M **(v)** potwierdzono generację reaktywnych form tlenu (z udziałem rodnika hydroksylowego, tlenu singletowego i anionorodnika ponadtlenkowego) jako prawdopodobnego szlaku odpowiedzialnego za cytotoksyczność, **(vi)** wykazano skuteczne działanie przeciwnowotworowe na trójwymiarowych wielokomórkowych zespołach sferoidalnych guza (3D), **(vii)** związki irydu(III) wykazują multimodalną interakcję DNA z przewagą wiązania do małego rowka, **(viii)** ponadto wiążą się z resztami tryptofanu HSA w miejscu I (subdomena II A) oraz wiążą się do apo-Tf.

W celu przezwyciężenia słabej rozpuszczalności, poważnych skutków ubocznych związanych z ogólnoustrojową cytotoksycznością kompleksów i nabyciem oporności komórek rakowych, powstałe kompleksy irydu(III) zamknięto w nanoemulsjach i micelach. Zamknięcie związków w micelach (**IrPCp\_M**) poprawiło skuteczną akumulację leków w ludzkim gruczolakoraku płuc i ludzkim raku prostaty oraz zwiększyło ich cytotoksyczność.

## Summary

Cancer is a group of diseases classified as one of the most life-threatening worldwide. Many anti-cancer medicines are currently used in clinical treatment, but more than 50% of them are platinum-based drugs. Their effectiveness is still hampered by clinical problems, including acquired or congenital resistance, a limited spectrum of action, and high toxicity leading to adverse effects. One strategy adopted to overcome these limitations is the development of new alternative transition metal (*e.g.* Cu, Ru, Pd, and Au) anti-cancer agents.

Nowadays, transition metal complexes and iridium compounds are probably the most promising group of potential medicine. They appear to be an attractive alternative to their platinum counterparts, mainly because they are less toxic and exhibit anticancer properties through the induction of apoptosis and interactions with DNA or protein kinases.

Fluoroquinolones are broad-spectrum antibiotics used to treat bacterial infections not only in humans but also in animals. In addition, to their strong antimicrobial activity, these antibiotics have also shown immunomodulatory and antitumor effects. Consequently, the linking of fluoroquinolones *via* phosphine moiety to iridium(III) complexes may decrease the overall toxicity and may enable selective delivery to neoplastic cells.

The main aim of my work was to design and synthesis organometallic iridium(III) complexes with phosphines derived from fluoroquinolone antibiotics possessing anticancer potential. In the next step, for the compounds with the highest antitumor activity, methods for their selective delivery using encapsulation in nanoformulations were designed.

During my work, I prepared four iridium(III) complexes containing phosphine ligands with/without a fluoroquinolone motif. The physicochemical properties in both solution and solid-state of each obtained complex were investigated using elemental analysis, mass spectrometry, cyclic voltamperometry, and spectroscopic methods (NMR, IR, UV-Vis, fluorescence). The crystal structures of every synthesized complex were obtained using the X-ray single-crystal diffraction method. The mononuclear iridium(III) complexes adopt half-sandwich pseudo-octahedral “three-leg piano-stool” geometry with an  $\eta^5$ -coordinated cyclopentadienyl and three additional sites of ligation occupied by one phosphine ligand and two chloride ligands. Homonuclear Ir(III) complexes containing the fluoroquinolone motif are stable in an aqueous solution. In the case of the complex without the fluoroquinolone motif, hydrolysis was observed in an aqueous solution, which was monitored in the presence of various concentrations of NaCl (mimicking the most important environment in the body).

The cytotoxicity of all compounds was tested *in vitro* against the five most common cancer cell lines: MCF7 (human breast adenocarcinoma), A549 (human lung adenocarcinoma), PANC-1 (human pancreatic/duct carcinoma), WM2664 (metastatic human melanoma) and DU-145 (human prostate carcinoma) as well as one normal, human embryonic kidney (HEK293T). Based on these results, examined complexes exhibited promising cytotoxicity *in vitro* with IC<sub>50</sub> values significantly lower than that of the cisplatin. It is worth emphasizing that the introduction of the fluoroquinolone motif in complexes significantly increased the antitumor cytotoxicity of the final compounds against the lung, breast, and melanoma cell line. This study made it possible to select from a pool of all compounds with the best effect (**IrPCp**) and to make an attempt to determine their mechanism of cytotoxic action. Furthermore, preliminary investigation focused on elucidation of the mode of action allowed to formulate the following conclusions: **(i)** iridium(III) complexes are accumulated in both nucleus and cytoplasm, **(ii)** cytometric analysis showed clear evidence for predominance of apoptosis in the induced cell death, **(iii)** the activation of caspase-3/7 along with the decrease of mitochondrial membrane potential also confirmed the apoptotic cell death, **(iv)** iridium(III) complexes may induce the changes in cell cycle leading to G2/M phase arrest, **(v)** ROS generation (involving hydroxyl radical, singlet oxygen and superoxide anion radical) as plausible pathway responsible for the cytotoxicity **(vi)** efficient anticancer action on 3D multicellular tumor spheroids assemblies was demonstrated, **(vii)** inorganic compounds exhibited multimodal DNA interaction with predominance of minor groove binding, **(viii)** and they bind to HSA tryptophan residues at site I (subdomain II A) and bind to all four possible apo-Tf binding sites containing tyrosine or tryptophan residues.

To overcome poor solubility, serious side effects related to the systemic cytotoxicity of the complexes, and the acquisition of cancer cell resistance, the resulting homonuclear complexes were encapsulated in nanoemulsions and Pluronic-123 micelles. The enclosure of compounds in micelles (**IrPCp\_M**) improved the effective accumulation of drugs in human lung adenocarcinoma and human prostate cancer and increased their cytotoxicity by an order of magnitude.



# Table of Contents

List of abbreviations.....	10
<b>1. Introduction .....</b>	<b>13</b>
1.1. Iridium compounds as anticancer agents.....	14
1.2. Aminomethylphosphines derived from fluoroquinolone .....	19
1.2.1. Fluoroquinolones.....	19
1.2.2. Phosphinesdervied from fluoroquinolones .....	22
1.3. Towards increased anticancer selectivity .....	23
<b>2. Aims of this Work.....</b>	<b>26</b>
<b>3. Experimental section .....</b>	<b>27</b>
<b>4. Results and discussion.....</b>	<b>30</b>
4.1. Synthesis and physicochemical characteristics of mononuclear Ir(III) complexes .....	30
4.1.1. Synthesis of mononuclear Ir(III) complexes.....	31
4.1.2. Analysis of structures in solution.....	32
4.1.3. Analysis of structures in solid state .....	37
4.2. Biological properties analysis .....	39
<b>5. Concluding Remarks.....</b>	<b>47</b>
<b>6. The most important achievements.....</b>	<b>49</b>
<b>7. Perspectives .....</b>	<b>50</b>
7.1. Modification of biological activity and characteristic of heteronuclear Ir(III)/Cu(II) complexes .....	51
7.2. Magnetic drug targeting – <i>nanof ormulation</i> .....	57
<b>8. References .....</b>	<b>60</b>

## List of abbreviations

$\chi_M$	magnetic susceptibility
$\cdot\text{OH}$	hydroxyl radical
$^1\text{O}_2$	singlet oxygen
A2780	ovarian cancer cell line
A549	human lung adenocarcinoma cell line
acac	acetylacetonato
apo-tf	apo-transferrin
Arg	arginine residue
Asp	aspartate residue
$B_0$	magnetic induction
CDDP	cisplatin
cod	1,5-cyclooctadiene
Cp*	pentamethylcyclopentadienyl
CT DNA	circulating tumor DNA
CT26	mouse colon carcinoma cell line
CV	cyclic voltammetry
DACHPt	Dichloro(1,2-Diaminocyclohexane)Platinum(II)
DAPI	4',6-diamidino-2-phenylindole
DCFH <sub>2</sub> -DA	2'-7'-dichlorofluorescein diacetate
DMEM	Dulbecco's Modified Eagle Medium
DMF	dimethylformamide
DMSO	dimethyl sulfoxide
DNA	deoxyribonucleic acid
DOX	doxorubicin
DU145	human prostate carcinoma
EB	ethidium bromide
EMU	the units of magnetization
EPR	electron paramagnetic resonance
ESI-MS	electrospray ionization mass spectrometry
Fe <sub>3</sub> O <sub>4</sub>	Iron(II, III) oxide
H	magnetic field strength
HCp	ciprofloxacin
HDVV	Heisenberg-Dirac-Van Vleck
HEK293T	human embryonic kidney
HeLa	immortal cell line
HepG2	hepatocellular carcinoma cell line
HFQ	fluoroquinolones
His	histidine residue
HLm	lomefloxacin
HNr	norfloxacin
HSA	human serum albumin

I	intensity
$I_0$	intensity in the absence of dye
IC <sub>50</sub>	a quantitative measure that indicates how much of a particular inhibitory substance ( <i>e.g.</i> drug) is needed to inhibit, <i>in vitro</i> , a given biological process or biological component by 50%
ICP-MS	inductively coupled plasma mass spectrometry
ImM	imidazole
IR	infrared spectroscopy
IrPCp	Ir( $\eta^5$ -Cp*)Cl <sub>2</sub> PCp, figure 14
IrPCp_M	IrPCp encapsulated in Pluronic P-123
IrPCpCu	Ir( $\eta^5$ -Cp*)Cl <sub>2</sub> PCp-Cu(phen), figure 30
IrPCpCu_L	IrPCpCu encapsulated in liposome
IrPLm	Ir( $\eta^5$ -Cp*)Cl <sub>2</sub> PLm, figure 14
IrPLmCu	Ir( $\eta^5$ -Cp*)Cl <sub>2</sub> PLm-Cu(phen), figure 30
IrPNr	Ir( $\eta^5$ -Cp*)Cl <sub>2</sub> PNr, figure 14
IrPNrCu	Ir( $\eta^5$ -Cp*)Cl <sub>2</sub> PNr-Cu(phen), figure 30
IrPOH	Ir( $\eta^5$ -Cp*)Cl <sub>2</sub> PPh <sub>2</sub> CH <sub>2</sub> OH, figure 14
K	kelvin
LC	ligand-centered transitions
Lys	lysine residue
M	magnetization
MCF7	human breast adenocarcinoma cell line
Me	metal
MG	green methyl
MLCT	metal-ligand charge transfer
MMP	mitochondrial membrane potential
MNPs	magnetic nanoparticles
MRI	magnetic resonance imaging
MTT	3-[4,5-dimethylthiazole-2-yl]-2,5-diphenyltetrazolium bromide
NAD <sup>+</sup>	the oxidised form of nicotinamide adenine dinucleotide
NADH	1,4-Dihydronicotinamide adenine dinucleotide
NAMI-A	imidazolium-trans-tetrachloro(dimethylsulfoxide)imidazoliruthenium(III)
NaN <sub>3</sub>	sodium azide
NMR	nuclear magnetic resonance spectroscopy
O <sub>2</sub> <sup>•-</sup>	superoxide radical anion
Oe	oersted
PANC-1	human pancreatic/duct carcinoma cell line
PCp	PPh <sub>2</sub> CH <sub>2</sub> Cp, figure 11
Ph <sub>2</sub> PCH <sub>2</sub> OH	diphenyl(hydroxymethyl)phosphine
phen	phenantroline
PHI	computer program designed for the calculation of the magnetic properties of paramagnetic coordination complexes
PLm	PPh <sub>2</sub> CH <sub>2</sub> Lm, figure 11
PNr	PPh <sub>2</sub> CH <sub>2</sub> Nr, figure 11

POH	Ph <sub>2</sub> PCH <sub>2</sub> OH
PPOA	phosphine phosphonic amide ligand
ROS	reactive oxygen species
S	spin
SIM	Single Ion Magnet
SMM	Single Molecule Magnet
SOD	superoxide dismutase
SQUID	superconducting quantum interference device
T	tesla
TBAP	tetrabutyl ammonium perchlorate
TEM	transmission electron microscopes
Tyr	tyrosine residue
UV-Vis	ultraviolet–visible spectroscopy
$\mu$	magnetic moment
WHO	World Health Organization
WM2664	human melanoma cell line

## 1. Introduction

Cancer has been one of the biggest global issues facing humankind in recent decades. It is estimated that in 2020 they caused approximately 10.0 million deaths worldwide [1]. Currently, only cardiovascular disease is responsible for the greater number of deaths. However, it is predicted that in the coming years the mortality caused by neoplastic diseases will increase significantly, thus distancing the death caused by cardiovascular diseases in this respect [2]. Despite many years of intensive research on the introduction of new active inorganic anticancer drugs, there is still only one group of transition metal complexes currently used in cancer chemotherapy – cisplatin and its derivatives (carboplatin, oxaliplatin, nedaplatin and lobaplatin) (**Fig. 1**). Cisplatin was introduced into clinical treatment in the late 1970s, mainly thanks to Rosenberg's discovery [3].

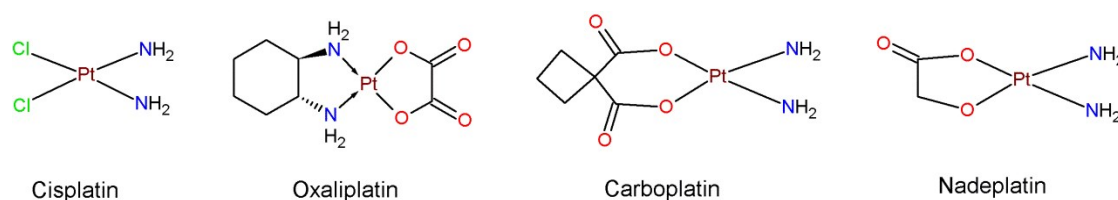


**Figure 1** Overview of approved or clinically investigated drugs based on platinum ions.

Today, this inorganic compound is still used as one of the best chemotherapeutics agents for many types of cancers. Unfortunately, the use of platinum-based drugs has many limitations. The disadvantage of chemotherapy is the ability of neoplastic cells to become resistant to the action of platinum therapeutics, and also the significant toxicity of these complexes toward healthy cells [4-7]. Therefore, it is necessary to search for new chemical compounds that could replace the platinum ones in the future. Such compounds are sought from among metal complexes due to their broad and diverse structural types and distinct ligand binding modes, which may lead to the improvement of their biological properties (*e.g.* antitumor activity) [8-11]. Currently, the scientific attention focuses on iridium compounds, which seem to be the most promising future antitumor compounds [10, 12-14]. The effectiveness of the therapeutics is also determined by the way it is delivered to the body [15].

The conventional approach is mostly often based on the oral ingestion or direct injection into the blood of the appropriate dose of the drug to obtain the desired effect in the affected area [16,17]. Unfortunately, as it is difficult to control the distribution of the drug in the body, the drug substance "incidentally" also reaches other places. It can lead to the side effects of such kind of treatment and also the patients being forced to take higher doses of medication to be

sure that the desired therapeutic effect will be achieved. There are also problems with the kinetics of drug release. The standard approach initially releases the drug in high concentration very rapidly, after which the dosage of the drug becomes approximately sinusoidal [5-7]. These data show the necessity to search for new, effective solutions in the fight against cancer, in particular drugs with a high selectivity profile.

One effective means of delivering drugs to a target in the body is through the use of nanostructures. From a pharmacological point of view, there is a noticeable better potential for improving drug bioavailability, spreading drug circulation time, regulatory drug release, and targeting neoplastic cells [18-22]. Smart systems (*e.g.* micelles, liposomes, *etc.*) characteristic feature is the ability to change their properties in a controlled manner in response to environmental stimuli, such as oxidative stress [23], pH [24], ultrasound [25], temperature [26], magnetism [27] or glucose level [28]. However, among the aforementioned nanoparticles (*e.g.* polymers, liposomes, micelles, *etc.*), magnetic nanoparticles (MNPs) are among the most used in biomedical applications [29-31]. Compared to others, magnetic nanoparticles can be easily transported through the magnetic field even after drug administration [27].

## 1.1. Iridium compounds as anticancer agents

Over the past decades, many iridium complexes have been synthesized and have attracted much attention in many fields, especially catalysis, *e.g.* Crabtree's hydrogenation catalyst [32,33]. However, the relatively unexplored chemistry of organo-iridium compounds differs from others due to their highly tunable properties making them suitable for use as potential anticancer drugs. First off, iridium exhibits potential redox properties by adopting various degrees (most common oxidation states are +3 and +4) of oxidation and kinetic stability in a biological environment. Thus, complexes with iridium ions can generate reactive oxygen species (ROS), leading to cell apoptosis induction by reducing mitochondrial membrane potential [13,34]. They are well soluble in water - therefore, they have higher cellular absorption efficiency [12]. Furthermore, they are characterized by long emission lifetimes, large Stokes shifts, and non-linear absorption, which makes them used as bio-imaging and bio-detection agents [35]. Octahedral cyclometalated Ir<sup>III</sup> complexes not only serve as cell imaging agents but can also inhibit tumor necrosis factor  $\alpha$ , promote DNA oxidation, and exhibit good anticancer activity *in vivo/vitro*. The above-described scientific findings indicate that iridium compounds

have a different mechanism of action than cisplatin and could break cancer cell resistance [34,36-38].

Initial studies of anticancer activity of iridium complexes focused on square-planar Ir<sup>I</sup> complexes because of their structural and electronic similarity to Pt<sup>II</sup> anticancer complexes such as cisplatin, *e.g.* [Ir(acac)(cod)] [39] and binuclear [IrCl(cod)]<sub>2</sub> [40] (**Fig. 2**). Both compounds had antitumor activity comparable to cisplatin and inhibited the growth of lung cancer [39,40].

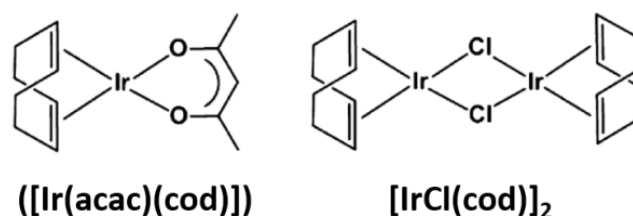


**Figure 2** Example of structure of iridium(I) complexes with square-planar geometry [39,40].

Recently, the half-sandwich Ir<sup>III</sup> complexes have attracted continuous research interest [12], because of their higher anticancer activity than Ir<sup>I</sup> compounds. The name reflects the pseudo-octahedral structure they resemble a stool, where the "top of the stool" is a six-electron aromatic ligand (pentamethylcyclopentadienyl (Cp\*) or its derivatives) while the last three coordination sites belong to halides (or other labile groups), nitrogen-, oxygen-, sulfur- or phosphorous-donor ligands (monodentate or chelating) forming "legs" (**Fig. 3**). However, the most frequent complexes are those possessing all three monodentate ligands or one monodentate and one chelating ligand [12,41].

Every component of a half-sandwich iridium complex allows adjusting its biological properties. The  $\pi$ -bound negatively charged pentamethylcyclopentadienyl or its derivatives stabilize the entire structure by modifying the electronic behavior of the remaining ligands. Additionally, the presence of Cp\* can cause fine-tuning of the electronic properties of the iridium center, which may increase the complex binding to biomolecules [14]. Usually, only inside the cell, one of the ligands is labile (Cl<sup>-</sup>, Br<sup>-</sup>, I<sup>-</sup>, SCN<sup>-</sup>) allowing interaction of iridium compound with biomolecules, as cisplatin does. Moreover, this aromatic ring facilitates iridium complex penetration through the membranes, which enhances cellular uptake, and may play a role in interactions with the target, incl. through DNA and affects the rate of hydrolysis [12, 14].



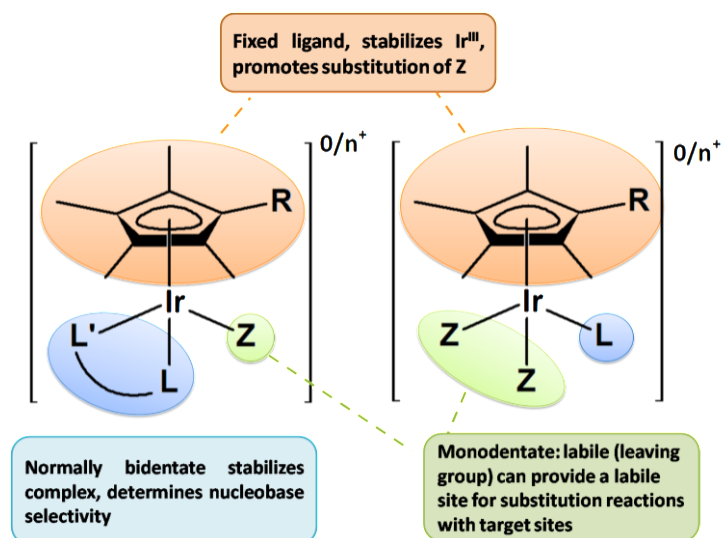


**Figure 3** Iridium half-sandwich structure-activity relationships.

The above-described scientific findings clearly indicate possible various mechanisms of cellular response (biological activity) dependent on the type of the ligand, or spatial structure of complexes (geometry) [12,42].

P. Sadler group reported a series of half-sandwich iridium(III) complexes [12], with the formula  $[(\eta^5\text{-Cp}^*)\text{Ir}(\text{L}^{\wedge}\text{L}')\text{Cl}]^{0/+}$  containing  $\text{N}^{\wedge}\text{N}$ - (e.g. 1,10-phenanthroline (phen)) and modified the  $\text{Cp}^*$  ring by introducing of a phenyl ( $\text{Cp}^{\text{xph}}$ ; orange circle) or biphenyl ( $\text{Cp}^{\text{xbiph}}$ ; purple circle) substituent (**Fig. 4**). These studies have shown that organometallic compounds undergo rapid hydrolysis, which activates the  $\text{Me-Cl}$  ( $\text{Me}$ : metal) bond. This process distinguishes these compounds from cisplatin, which contains two labile  $\text{Pt-Cl}$  bonds. Cytotoxic activity toward human ovarian cancer cells (A2780) increases with phenyl substitution on pentamethylcyclopentadienyl moiety:  $3 > 2 > 1$  (**Fig. 4**). This increase in cytotoxic activity corresponds to an increase in DNA binding and hydrophobicity, which increases the accumulation in cells [12].

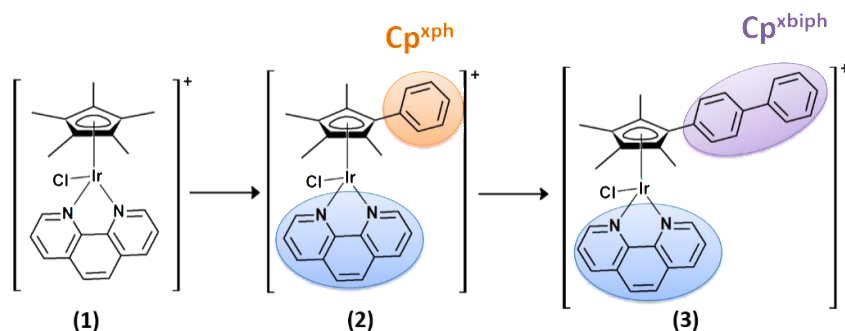


**Figure 4** Structures of Iridium (III) complexes with general formula  $[(\eta^5\text{-Cp}^{\text{x}})\text{Ir}(\text{N}^{\wedge}\text{N})\text{Cl}]^+$ .

The same group also showed that the anticancer activity of Ir(III) complexes can also be achieved by changing the chelating ligand. They modified complexes **1** and **3** by replacing the neutral N, N-chelating ligand (**Fig. 4**, blue circle) with the negatively charged C, N-chelating ligand, resulting in the formation of complexes **4** and **5** (**Fig. 5**, green circle) [43,44]. This resulted in a change in binding to nucleobases and increased hydrophobicity leading to higher cellular uptake and consequently increased cytotoxicity to A2780 cancer cells. For example, complex **2** showed good cytotoxicity with an IC<sub>50</sub> of 10.5 mM toward human ovarian cancer cells (A2780), whereas complex **1** was inactive. Cytotoxicity activity trend was found to be in the order: **5** > **3** > **4** > **1** [12,43,44]. Results show that these complexes induce apoptosis through ROS-dependent mitochondrial pathway and protein synthesis disruption [43,44].

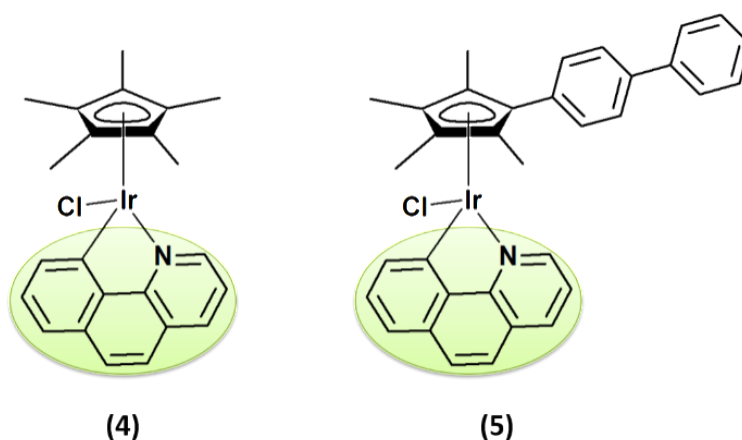


**Figure 5** Structures of iridium(III) complexes with general formula  $[(\eta^5\text{-Cp}^x)\text{Ir}(\text{C}^{\wedge}\text{N})\text{Cl}]$ .

Yanjing Yang and co-workers synthesized and characterized half sandwich zwitter ionic iridium(III) complexes containing different substituent's in the Cp\* rings (**Fig. 6**) [45]. These researchers similarly to the group of prof. Sadler [12] investigated the effect of Cp\* ring elongation on the biological activity of cationic iridium(III) half-sandwich complexes [45]. It was found that the presence of fluorine substituents significantly increased the hydrophobicity of the obtained complexes. As it has been mentioned earlier, this causes a significant increase in the accumulation of complexes in cells and an increased antitumor activity [45].

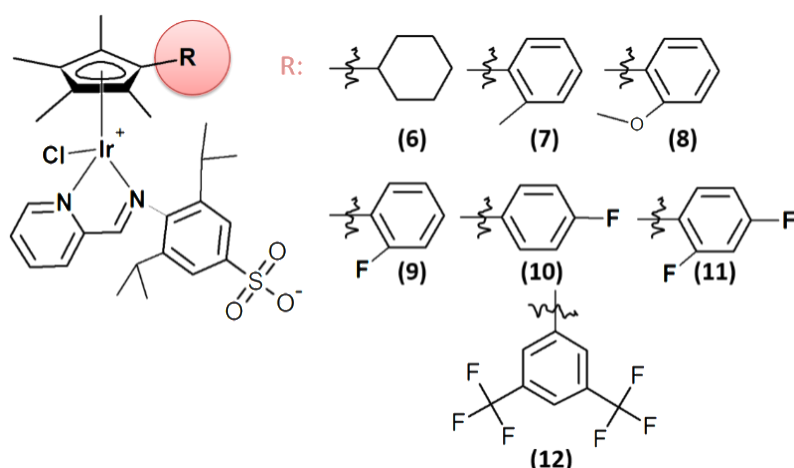


**Figure 6** Structures of iridium(III) complexes with general formula  $[(\eta^5\text{-C}_5\text{Me}_5)\text{Ir}(\text{XY})\text{Cl}]^{0/+}$ .

The cytotoxicity of these complexes (**6-12**, **Fig. 6**) was tested against hepatoma (HepG2), lung (A549), and immortal (HeLa) cell lines. Complexes **9-12** (**Fig. 6**) showed significant antitumor activity, in contrast to complexes **6-8** (**Fig. 6**) which were inactive. Inorganic compounds **9-12** can convert NADH to NAD<sup>+</sup>, exhibit fluorescence emission and induce intercellular ROS. It had been proven that complex **9** successfully entered lung cells *via* an energy-dependent pathway. In addition, it may induce cell death *via* the disruption of lysosomes [45].

Zhe Liu and co-workers synthesized a series of half sandwiched iridium(III) complexes containing P-O- chelating ligand (phosphine phosphonic amide ligand (PPOA)) (**Fig.7**) [46]. Compared to the previously discussed complexes (**1-12**) [12,43-45], the presence of elongated phenyl rings in this resulting Ir system only slightly changed the antitumor activity of the obtained complexes.

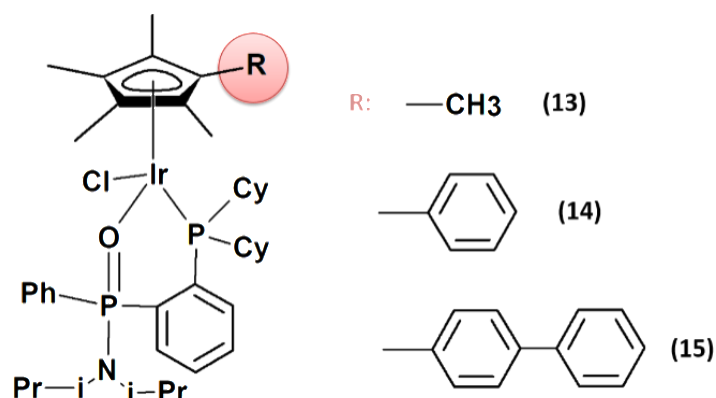


**Figure 7** Structure of iridium complexes  $[(\text{Cp}^x)\text{Ir}(\text{P}^{\wedge}\text{O})\text{Cl}]\text{PF}_6$  with phosphine phosphonic amide ligand.

The cytotoxicity of **13-15** complexes (**Fig. 7**) was tested on immortal (HeLa) and lung (A549) cells with average IC<sub>50</sub> values 1 μM and 4.4 μM, respectively. These results were comparatively better than the IC<sub>50</sub> values calculated for cisplatin against a lung cancer cell line. The **13-15** complexes were able to generate ROS by converting NADH to NAD<sup>+</sup> by catalytic hydride transfer from NADH coenzyme to oxygen. Studies on the mechanism of action of these complexes showed that they induce oxidative stress through cell cycle perturbation at S and G2/M phase, and apoptosis in HeLa cancer cells [46].

## 1.2. Aminomethylphosphines derived from fluoroquinolone

The goal of science is to design a therapeutic agent whose mechanism of action will be different from that of all drugs obtained so far. However, the design and synthesis of new therapeutic substances are very time-consuming and expensive. It takes at least 10 years to bring a new drug to market and costs up to millions of dollars. To paraphrase Confucius saying "When it is obvious that the goals cannot be reached, don't adjust the goals, adjust the action steps", to achieve goals, instead of looking for new classes of therapeutic compounds, it is better to modify the structure of a drug currently used in medicine [47,48]. This can be done by attaching to it another structural motif responsible for selective transport or changing biological properties. It is noted that the most common modification is the secondary nitrogen atom that is part of the piperazine ring of the fluoroquinolone antibiotic [49-58].

### 1.2.1. Fluoroquinolones

In 1962, George Leshner accidentally discovered the first quinolone antibiotic, nalidixic acid, which was a by-product of the reaction of the antimalarial chloroquine. This discovery led to extensive research on many thousands of compounds based on the quinolone skeleton (**Fig. 8A**), of which over two dozen have found clinical application. Since the 1960s, quinolone antibiotics have been one of the most frequently used antibiotics, especially in urinary tract infections, but also in the treatment of malaria or with immunomodulatory and anticancer effects [59,60].

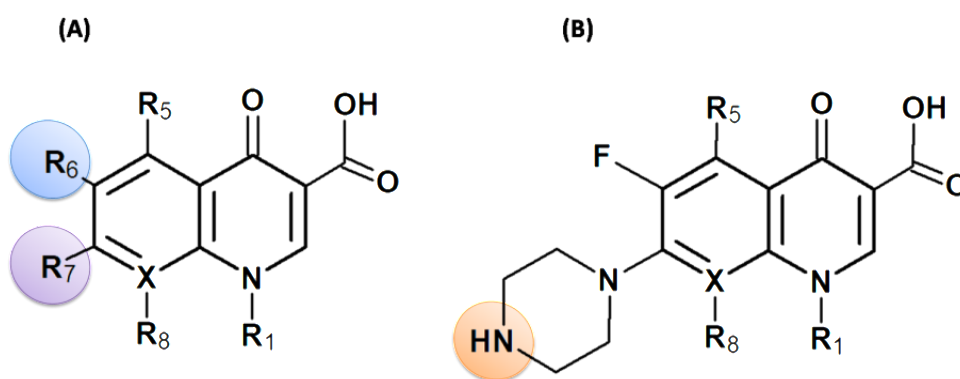


**Figure 8** (A) The core structure of quinolone antibiotics with important positions for modifications to improve the activity of the drug. (B) The core structure of fluoroquinolones with positions for modifications. R<sub>1</sub>, R<sub>5</sub>, R<sub>6</sub>, R<sub>7</sub>, R<sub>8</sub>, and X are drug modification positions that improve their biological properties.

One of the first modifications was the introduction of a fluorine atom in the 6-position (R<sub>6</sub>, **fig. 8A**, blue circle, **8B**) of the quinolone ring as well as the piperazine ring in the 7-position ((R<sub>7</sub>, **fig. 8A**, purple circle, **8B**). These changes resulted in a significant increase in the activity of the antibiotics against microorganisms. Quinolones containing a fluorine atom or atoms are called fluoroquinolones (HFQ) (*e.g.* ciprofloxacin, norfloxacin, lomefloxacin **Fig. 9**). The action mode of quinolone antibiotics inhibits the bacterial activity of enzymes (topoisomerase II (DNA gyrase) and topoisomerase IV) by causing the breakage of bacterial chromosomes. As a result of these processes, the activity of enzymes is blocked leading to inhibition of replication, transcription, repair, and recombination of DNA, which results in the death of the bacterial cell [59,61,62].

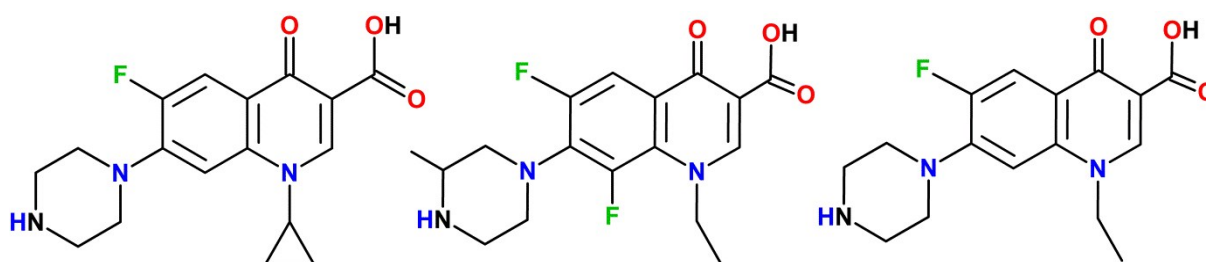


**Figure 9** Structure of the molecule of ciprofloxacin, lomefloxacin, and norfloxacin (on the left).

Due to the quinolones' ability to inhibit topoisomerase II - and thus the DNA repair activity - their antitumor activity in recent years has been thoroughly investigated [59,61]. Many complexes obtained by coordinating quinolones with metal ions have been characterized by

their ability to interact with DNA. This fact makes them promising in terms of anticancer properties [58, 62]. Unfortunately, the widespread and frequent use of antibiotics has led to a significant increase in bacterial resistance to antimicrobial agents [63]. Bacteria have developed a variety of resistance systems which are making antibiotic therapy slowly ineffective [64,65]. That is why nowadays scientists put great attention to modifying structures of these antibiotics that can lead to the breakdown bacterial resistance but also strengthen and increase their bacterial but also anticancer action [63,66].

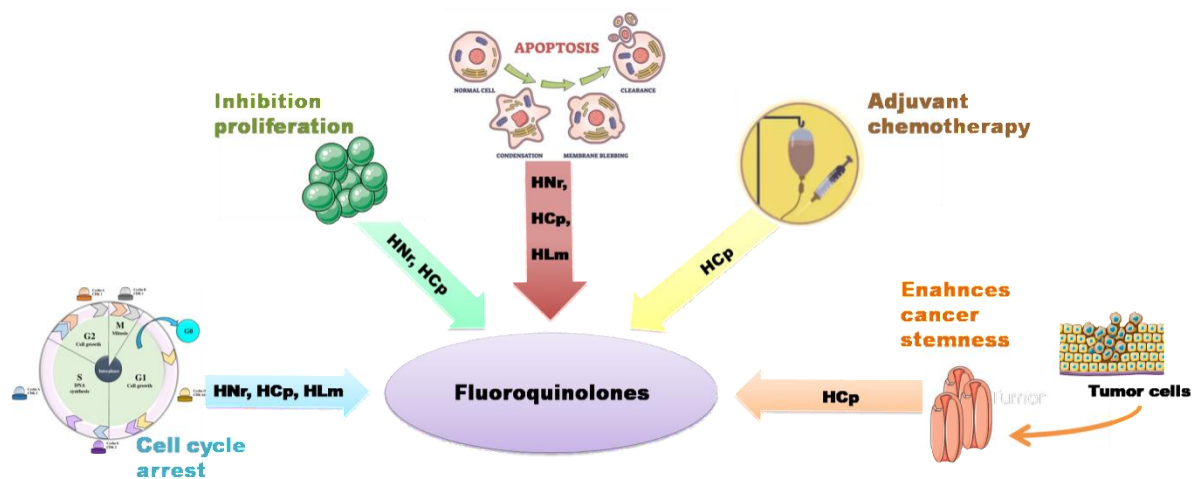


**Figure 10** Anticancer activities of fluoroquinolones antibiotics: HNr - norfloxacin, HCp - ciprofloxacin, HLm – lomefloxacin.

The subject of the research undertaken in this work is second-generation antibiotics: ciprofloxacin, lomefloxacin, and norfloxacin (**Fig. 9**). For example, ciprofloxacin is the antibiotic most commonly used in respiratory and urinary tract infections but has also been shown to have anticancer properties against melanoma [67], breast [68], colorectal [69], pancreatic [70], and human prostate [71] cancer cell lines. Studies have shown that ciprofloxacin induced apoptosis by mitochondrial-dependent pathways or S/G2 [72] and G2/M phase arrest [67,68,73]. Other studies have shown a similar S/G2 phase for the antibiotic lomefloxacin in human epithelial tumor cells [74]. The third antibiotic I chose is norfloxacin, which can inhibit cytokine synthesis even at lower concentrations. Additionally, like lomefloxacin, it can also induce apoptosis by decreasing the level of cellular reduced glutathione, increasing mitochondrial dysfunction and oxidative stress in cancer cells [72] (**Fig. 10**).

### 1.2.2. Phosphinesderived from fluoroquinolones

The purpose of introducing various structural modifications to quinolone molecules is not only to avoid the phenomenon of drug resistance but also to increase their biological activity. An example of such modification can be an attachment of a phosphine motif - one of the strongest electron-pair donors – to a fluoroquinolone drug. Phosphine ligands, in general, can be easily functionalized, in particular, aminomethylphosphanes derived from aminoacids [75-78] or prepared from the highly water-soluble aliphatic secondary amines [79, 80]. It has been already proven that aminomethylphosphanes derived from fluoroquinolones (**Fig. 11**) can be characterized by better antibacterial properties than parent drugs but also possess new anticancer activity [54, 55, 56, 57, 73, 81]. Those phosphines derived from ciprofloxacin, norfloxacin, and lomefloxacin (**Fig. 11**) were found nontoxic toward healthy cells but at the same time have weak biological activity, especially anticancer [81].

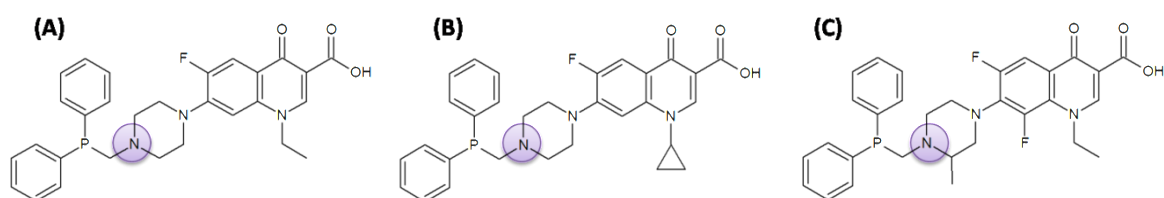


**Figure 11** Structures of aminomethylphosphanes derived from fluoroquinolones: (A) norfloxacin, (B) ciprofloxacin, (C) lomefloxacin.

However, coordination compounds of such aminomethylphosphanes with ions: Cu(I), Cu(II), Se(II), and Ru(II) significantly increased their antimicrobial and anticancer *in vitro* activity. Such complexes are in most cases, air-stable, and importantly, more cytotoxic *in vitro* against cancer cells than cisplatin. Studies have shown that the cytotoxicity of complexes with phosphines derived from antibiotics against tumor cell lines is much higher than all starting ligands, antibiotics, and cisplatin [55, 57, 58, 81-83]. For example,  $IC_{50}$  values for structures depicted below on (investigated by U.Komarnicka *et al.* [58]) are 30 times higher than for cisplatin against human lung adenocarcinoma and mouse colon carcinoma cell lines. It was proved that they penetrate the tumor cells which generate ROS and intercalate with DNA, consequently, causing its degradation. Moreover, treatment of tumor cells with compounds has shown that these compounds cause apoptosis in the induced cell death along with a reduction in the potential of the mitochondrial membrane [58]. The above facts were the reason for my decision to continue work on increasing the biological activity of those phosphines by coordinating them to Ir(III).



### 1.3. Towards increased anticancer selectivity

One way to enhance the therapeutic effect of drugs is to develop carriers that enable their delivery in the appropriate concentration to pathologically changed tissues, but without affecting normal cells [84]. For this purpose, nanomaterials can be used, which can be categorized into four types (i) inorganic, (ii) carbon, (iii) organic, and (iv) composite [85]. Among nanomaterials we can include polymer nanoparticles, liposomes, polymeric micelles, dendrimers, and nanotubes. In my dissertation, it has been used polymeric micelles and liposomes, therefore I will focus only on discussing these two structures (**Fig. 12**).

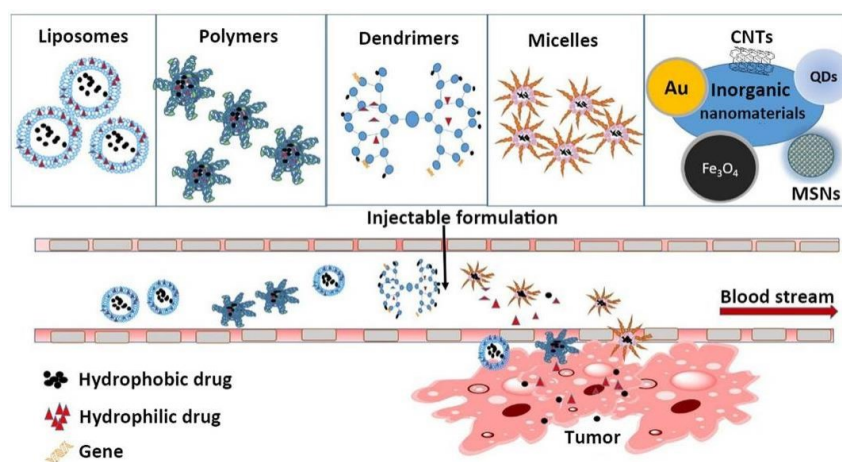


**Figure 12** Nanomaterials used as drug carriers for cancer therapy [86].

Polymer micelles consist of a hydrophobic inner part - a core - and a hydrophilic outer part - a shell. Therefore, compounds with poor water solubility can accumulate in the hydrophobic part. In addition, polymer micelles can be functionalized with targeted ligands to increase accumulation within the tumor [87]. Depending on the composition, the polymer micelles are internalized by the neoplastic cells and then induce the action of the drug in an organelle-specific manner. Thus, polymer micelles potentially avoid drug efflux or intracellular uptake mechanisms, overcoming drug resistance in neoplastic cells. Consequently, these micelles have found wide application as drug delivery systems in anti-cancer therapy due to their excellent physicochemical and biological properties [84, 87-89]. Examples of drugs encapsulated inside micelles that have entered clinical trials are CDDP (cisplatin) and DACHPt loading micelles (active oxaliplatin complex), which are in phase III and I clinical trials, respectively. Following systemic administration, micelles have been shown to achieve remarkable *in vivo* antitumor efficacy with reduced side effects on healthy cells due to prolonged circulation and efficient tumor accumulation [90, 91].

Another modified version of the lipid bilayer nanocarriers, liposomes, as a drug delivery platform is also gaining increasing importance in cancer therapy. Briefly, this is because of its excellent biocompatibility and the ability to select particle size and surface modification to overcome biological barriers and reach destinations [92]. Currently, there are many products available on the market and in the clinical development phase for use as drug carriers with anti-cancer properties. Pegylated liposomal doxorubicin is one such example used in epithelial ovarian cancer. The encapsulated doxorubicin significantly improved drug accumulation in tumor tissues, minimizing many side effects, *e.g.* it reduced the cardiotoxicity caused by non-liposomal doxorubicin [93]. Interestingly, the combination of magnetic inorganic nanoparticles (MNPs) with liposomes offers many advantages. As a result of this connection, the magnetic surfaces of the nanoparticles are modified, which increases their solubility in the aqueous environment and increases the intracellular uptake [94]. On the other hand, because the phospholipids in liposomes are biocompatible, the loading of MNPs in the liposomes will not cause any adverse toxicity, and will additionally assist them in targeted anticancer therapy using a magnetic field [95]. For example, H. Nobuto and co-workers have developed novel multifunctional magnetic liposomes containing doxorubicin (magnetic DOX liposomes) that treat osteosarcoma-bearing hamsters. To maximize the DOX concentration in the neoplastic tissue, the authors used a DC dipole magnet applying a magnetic field strength of 0.4 T for 1 h. It should be emphasized that this therapy inhibited tumor growth for two weeks and significantly suppressed metastasis for three weeks after treatment [96].

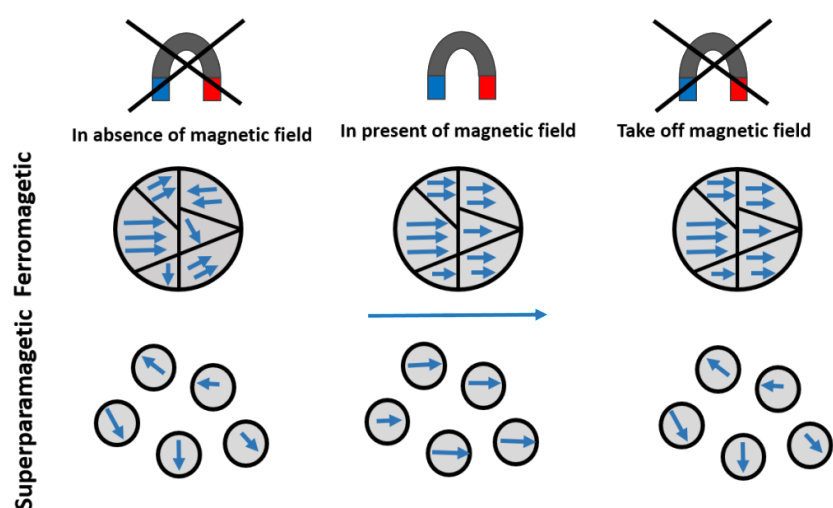


**Figure 13** Behavior of magnetic domains in ferromagnets and magnetic moments in superparamagnetic nanoparticles in relation to an external magnetic field.

In the last 20 years, MNPs (Magnetic Nanomaterials) have already been used in modern medicine as (i) biosensors - to detect a specific type of biomolecules [97, 98], (ii) drug carriers

[99, 100], (iii) tumor biomarkers in photodynamic therapy [101, 102] (iv) an important element of hyperthermia [103,104] or as (v) contrast agents in computed tomography and MRI imaging [105].

Typically, MNPs are considered to exhibit ferrimagnetic, ferromagnetic, or superparamagnetic properties, however, from a medical point of view, the use of superparamagnetic particles is the preferred approach (**Fig. 13**) [106]. The majority of nanoparticles used in these applications are superparamagnetic iron oxides magnetite  $\text{Fe}_3\text{O}_4$  or maghemite  $\text{Fe}_2\text{O}_3$ , because due to their known metabolic pathways and low overall toxicity [99, 106].

## 2. Aims of this Work

*The principal aim of this desideration was to design and synthesize organometallic iridium(III) complexes with phosphines derived from fluoroquinolone antibiotics possessing anticancer potential.*

*In the next step, for the compounds with the highest antitumor activity, methods for their selective delivery using encapsulation in nanoformulations were designed.*

Successfully obtained materials will be good candidates for the next stage of *in vivo* research and in the future may be considered as medicines.

*To achieve the main goal of the work, it was necessary to develop many intermediate steps:*

- Synthesis diphenyl(hydroxymethyl)phosphine ( $\text{Ph}_2\text{PCH}_2\text{OH}$ ) and three phosphine ligands derived from fluoroquinolones (e.g. lomefloxacin, ciprofloxacin and lomefloxacin);
- Synthesis new mononuclear Ir(III) with phosphine-fluoroquinolone conjugate. A hydrophobic phosphine unit ( $\text{Ph}_2\text{PCH}_2\text{OH}$ ) will be used as the linker between the cytotoxic metal complex and the fluoroquinolone carrier;
- Physicochemical characterization of the synthesized complexes in the solid-state as well as in solution (X-ray, elemental analysis, MS spectrometry, NMR, UV-Vis, luminescence, IR spectroscopies);
- Determination of the stability of the complexes in water solution and the air;
- Description of the properties of luminescent complexes;
- Description of electrochemical properties;
- Encapsulation of the resulting Ir(III) complexes in micelle and liposome structure;
- Examine biological activity *in vitro* against several tumor and normal cell lines for all obtained compounds;
- Determination of cell viability in a 3D model of cell culturing (spheroids)
- Establish the mechanism of cancer cell death induced by the tested compounds:
  - ♣ Type of cell death characterization of initiator and effector caspase expressions in cancer cell;
  - ♣ Analysis of the cell cycle;
  - ♣ ROS production inside the cancer cell and mitochondrial damages;
  - ♣ Analysis of DNA interaction with complexes;
  - ♣ Investigation of interaction of complexes with human protein such as album and transferrin.

## Publications constituting the basis of the doctoral dissertation

The research results obtained for the above-mentioned goals have been described in the form of three published scientific articles.

[S1] Synthesis, physicochemical characterization and preliminary *in vitro* antitumor activity of phosphine Ru(II) and Ir(III) complexes, *Dalton Transactions*, advanced article, 2022, DOI: 10.1039/D2DT01055K; **back cover**

[S2] Anticancer potency of novel organometallic Ir(III) complexes with phosphine derivatives of fluoroquinolones encapsulated in polymeric micelles; *Inorganic Chemistry Frontiers*, 2020, 7, 3386-3401; DOI:10.1039/d0qi00538j

[S3] Interaction between DNA, albumin and apo-transferrin and iridium(III) complexes with phosphines derived from fluoroquinolones as a potent anticancer drug; *Pharmaceuticals*, 2021, 14, 685/1-685/25; DOI:10.3390/ph14070685

In addition, some unpublished results will be presented also in this report to show the applicative nature of the Ir(III)-phosphine complexes.

It is worth mentioning, that presented in this paper data have been obtained thanks to NCN grant prelude "Homo- and heterometallic phosphine ruthenium and iridium complexes - design, synthesis, bioactivity, and magnetic-nanof ormulation as a potential platform for dual-targeted drug delivery", which I am the leader.

[S4] Liposomal formulation of magnetic iridium-copper complexes with phosphine derived from fluoroquinolones for human prostate carcinoma treatment; *Inorganic Chemistry Frontiers*, submitted

## 3. Experimental section

Several organic and inorganic compounds have been synthesized using Schlenk techniques. In the next step, the obtained compounds have been characterized in detail using many physicochemical methods.

The conditions of the conducted experiments were described in detail in the articles that will be the basis of the scientific achievement. Only the most important data are presented below.

- ✚ All synthetic works with the use of aminomethylphosphines and mononuclear iridium(III) compounds were carried out using the Schlenk technique in an inert gas (nitrogen) atmosphere to avoid oxidation of any of the reactants in the presence of atmospheric oxygen. The solvents used for the synthesis were each time deaerated.
- ✚ All synthesized mononuclear complexes were subjected to detailed NMR analysis taking into account the phosphorus, proton, and carbon spectra. In problematic situations, two-dimensional measurements were also used.
- ✚ The structure of all compounds was confirmed by electrospray ionization mass spectrometry (ESI-MS), and the purity of the compounds was each time checked by elemental analysis.
- ✚ In justified cases, additional measurements were used with the methods of IR or UV-Vis spectroscopy. In addition, using spectroscopic methods, I also determined the stability of compounds in an aqueous solution (UV-Vis, NMR), and characterized their fluorescent properties as well as their electrochemical potential (CV).
- ✚ The fluorescent properties of the complexes can provide useful information on the distribution, accumulation, and uptake of anti-cancer drugs in living cells or organisms.
- ✚ All synthesized compounds were obtained in the form of single crystals, which made it possible to perform X-ray diffraction measurements and solve the crystal structure. These measurements were carried out in cooperation with Dr. Agnieszka Skórska-Stania from the Faculty of Chemistry of the Jagiellonian University.
- ✚ To overcome poor solubility, serious side effects related to the systemic cytotoxicity of the complexes, and the acquisition of cancer cell resistance, the resulting mononuclear complexes were encapsulated in nanoemulsions and polymer micelles.
- ✚ Determination of the cytotoxicity of compounds as well as an attempt to explain the mechanism of action was carried out at the Faculty of Chemistry of the Jagiellonian University (in the team of Prof. Grażyna Stochel) and in cooperation with the Małopolska Biotechnology Center with Dr. Barbara Pucelik: **(i)** determination of cytotoxicity against healthy and cancer cells (determination of IC<sub>50</sub> using the MTT test): human breast adenocarcinoma (MCF7), human lung adenocarcinoma (A549), mouse colon carcinoma (CT26), human pancreatic/duct carcinoma (PANC-1), (human prostate carcinoma (DU145), metastatic human melanoma (WM2664), human embryonic kidney (HEK293T); **(ii)** use of a fluorescence microscope to visualize and confirm the results on tumor cells stained with propidium iodide and fluorescein diacetate; **(iii)** metal uptake and intracellular localization (ICP-MS, confocal microscopy, commercially used

tests); **(iv)** determination of the type of cell death (flow cytometer, commercially used kits); **(v)** characterization of initiator and effector caspase expressions in cancer cell; **(vi)** analysis of the cell cycle **(vii)** and apoptosis-related proteins e.g. caspase -3/7; **(viii)** study of level of mitochondrial membrane; **(ix)** drug cytotoxicity analysis on 3D tumor spheroids.

- ✚ The ability to interact with selected iridium complexes with blood plasma proteins: albumin and transferrin was also determined. These proteins may have a key influence on the transport and metabolism of synthesized iridium compounds in the body. The analysis was performed by quenching the characteristic fluorescence of both proteins due to their mixing with iridium complexes. In addition, several selected compounds were tested for their ability to interact with DNA using the spectrometry of the disappearance of the characteristic fluorescence of the ethidium bromide (EB; intercalation), 4',6-diamidino-2-phenylindole (DAPI; binding to a minor groove), and methyl green (MG; binding to a major groove) complex with calf thymus DNA (CT DNA).
- ✚ Gel electrophoresis of the pBR322 plasmid was used to determine the ability of the compounds to induce single- and/or double-strand damage of the DNA and to confirm the generation of particular types of ROS involved in plasmid degradation.

The author independently conducted all chemical tests and took an active part in biological research with the use of cell cultures. This is evidenced by research internships in the above-mentioned centers.



## 4. Results and discussion

Using synthetic strategies to achieve the aim of the dissertation, a new coordination framework was obtained which was fully characterized in the papers **S1 - S3**. For this reason, my report will present the most important achievements and results.

This guide is divided into two parts. The first one presents the synthesis and physicochemical characteristics of mononuclear iridium(III) complexes, while the second one presents their biological properties together with an attempt to explain the mechanism of their action.

### 4.1. Synthesis and physicochemical characteristics of mononuclear Ir(III) complexes

In the first step of my work, four phosphines were synthesized  $\text{Ph}_2\text{PCH}_2\text{Nr}(\text{PNr})$  [55],  $\text{Ph}_2\text{PCH}_2\text{Cp}$  (**PCp**) [54],  $\text{Ph}_2\text{PCH}_2\text{Lm}$  [57] (**PLm**) (**Fig. 11**, page 22),  $\text{Ph}_2\text{PCH}_2\text{OH}$  (**POH**) [58]. These starting ligands were used to obtain three mononuclear iridium(III) complexes:  $\text{Ir}(\eta^5\text{-Cp}^*)\text{Cl}_2\text{PNr}$  (**IrPNr**),  $\text{Ir}(\eta^5\text{-Cp}^*)\text{Cl}_2\text{PCp}$  (**IrPCp**),  $[\text{Ir}(\eta^5\text{-Cp}^*)\text{Cl}_2\text{PLm}]$  (**IrPLm**) (**Fig. 14**). In order to understand the biological role of antibiotics in the resulting complexes, a phosphine-iridium(III) compound was also synthesized without fluoroquinolones:  $\text{Ir}(\eta^5\text{-Cp}^*)\text{Cl}_2\text{PPh}_2\text{CH}_2\text{OH}$  (**IrPOH**, **Fig. 14**).

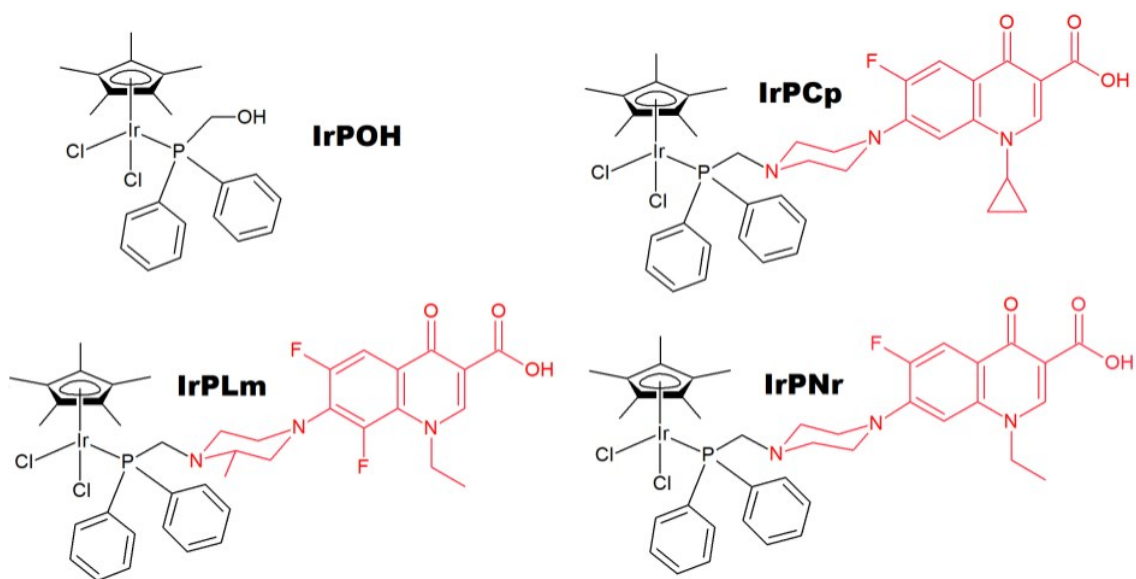
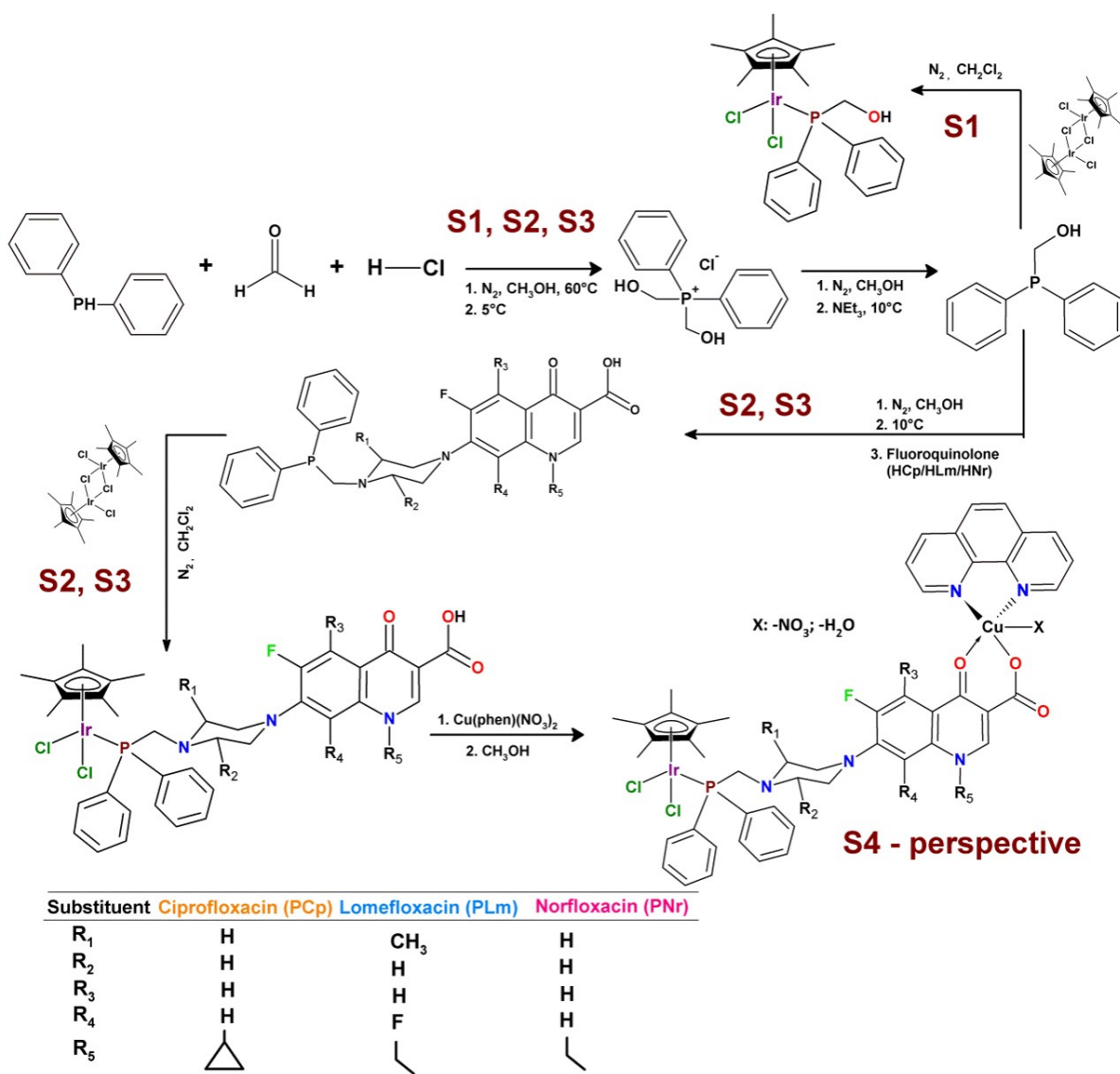


**Figure 14** Coordination scheme of iridium(III) ion with pentamethylcyclopentadiene and phosphine ligand.

#### 4.1.1. Synthesis of mononuclear Ir(III) complexes [S1,S2, S3]

All syntheses were carried out under a nitrogen environment using Schlenk techniques. The complexes and phosphines derived from fluoroquinolones are soluble in dimethyl sulfoxide, chloroform, and dichloromethane. Additionally, the iridium(III) complexes are insoluble in water but become highly water-soluble when a small amount of DMSO (1-2%) is added. The synthesized homonuclear Ir(III) complexes are stable in the solid-state.



**Scheme 1** Schematic view of the compounds and synthetic routes.

#### 4.1.2. Analysis of structures in solution [S1, S2]

The techniques such as NMR, UV-Vis and mass spectrometry allowed us to confirm the mononuclear structure of the discussed Ir(III) complexes in solution under the atmospheric oxygen.

A characteristic signal from the phosphorus atom was observed on all the  $^{31}\text{P}\{^1\text{H}\}$  NMR spectra of the examined compounds **IrPOH**, **IrPNr**, **IrPLm** and **IrPCp** (Fig. 15). The lack of other signals in the phosphorus spectrum proves that the obtained systems are free of phosphine derivatives (*e.g.* phosphine oxides).

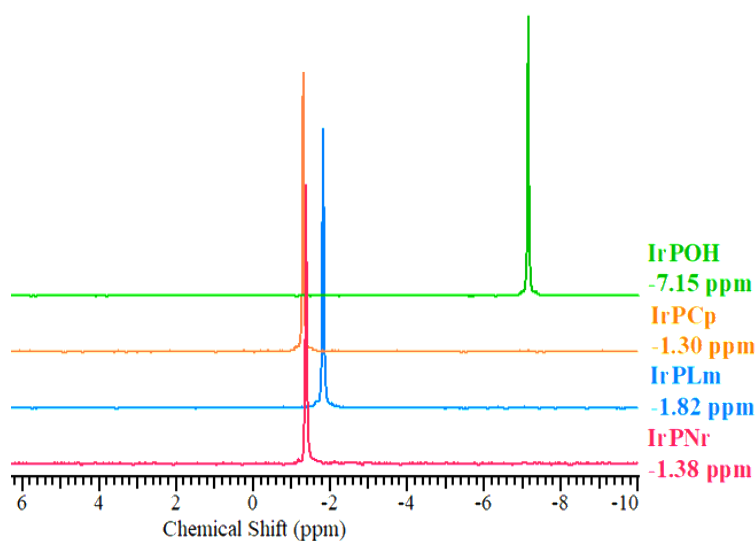


**Figure 15** Comparison of  $^{31}\text{P}\{^1\text{H}\}$  NMR spectra for mononuclear Ir(III) complexes.

Literature and experimental data indicate that the signal of the uncoordinated aminomethylphosphane is in the negative part of the spectrum (**POH**: -11.46 ppm; **PCp**: -27.4 ppm; **PLm**: -27.4 ppm; **PNr**: -27.5 ppm) [54, 55, 57, 58]. Coordination of phosphine to iridium(III) ion caused a downfield shift of the signal originating from the phosphorus atom (**IrPOH**: -7.15; **IrPCp**: -1.30 ppm; **IrPLm**: -1.82 ppm; **IrPNr**: -1.38 ppm, (Fig. 15). Most likely, this may be due to an increase in the screening effect (known as the Shielding effect) resulting from the formation of iridium(III) inorganic compounds. It is also noted that the singlet characteristic for **IrPOH** at -7.15 ppm is shifted by about 5.5 ppm towards the higher fields, after the addition of a fluoroquinolone molecule to the  $\text{PPh}_2\text{CH}_2$ - motif, which is undoubtedly related to the change of the substituent in the vicinity of the phosphorus atom. The coordination process also initiates changes in the  $^{13}\text{C}\{^1\text{H}\}$  spectra as well as in the  $^1\text{H}$  spectra. The data obtained from the  $^{13}\text{C}\{^1\text{H}\}$  and  $^1\text{H}$  NMR spectra indicate that the biggest changes are observed for atoms close to the coordination. Namely, the  $\text{H}^1$  proton of the

Ph<sub>2</sub>PCH<sub>2</sub>- group is undergoing an upfield shift regardless of the type of substituent attached to the piperazine ring.

The ESI(+)MS spectra (recorded in the positive ion modality) show the corresponding peaks of molecular ions [M+H]<sup>+</sup> by the neutral character of these compounds only for complexes with phosphine derivatives from fluoroquinolones. Fewer peaks corresponding to [M-Cl]<sup>+</sup> and [M-2Cl]<sup>+</sup> ions were also recorded, indicating that chloride groups were easily displaced under the appropriate conditions. In the case of the **IrPOH** complex, abundant [M+Na]<sup>+</sup> sodiated ions were detected at m/z 637, however [M - Cl]<sup>+</sup> ions dominated at m/z 579. In the ESI(+)MS spectra no peaks corresponding to the loss of the phosphine ligands and the arene ring were observed. These results indicate strong metal-ligand and metal-arene bonds.

As the Me-Cl (Me: metal) bond in this type of complex is often subject to hydrolysis, it was decided to measure their stability using UV-Vis spectroscopy. The electronic spectra (recorded over 72 hours) of all mononuclear iridium(III) complexes were measured in a cellular medium (DMEM with 2% DMSO), due to the poor solubility of these complexes. During the 72-hour incubation, significant changes in the intensity and shape of the characteristic absorption band (MLCT) were observed only for **IrPOH**. The attachment of the fluoroquinolone motif to the starting phosphine ligands (PPh<sub>2</sub>CH<sub>2</sub>-) changed the electronic nature of the final complexes and most importantly increased their stability in solution. These complexes did not dissociate or decompose under the model conditions. The stability of complexes with phosphines derived from fluoroquinolones was also confirmed by <sup>1</sup>H NMR (**Fig. 16** shows a selected **IrPCp** complex). As in the case of the UV-Vis spectra, no additional peaks were found in the NMR spectra during the 48 h incubation with the compounds.

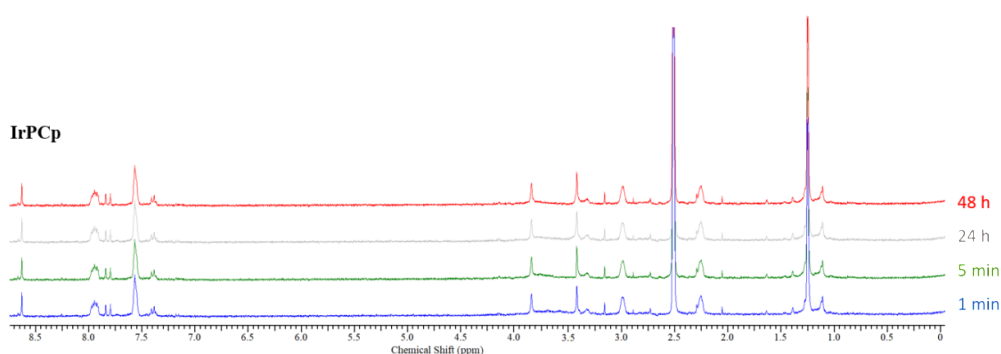


**Figure 16** Time-dependent <sup>1</sup>H NMR spectroscopic stability study for **IrPCp** in the mixed of 80% DMSO-d<sub>6</sub> and 20% D<sub>2</sub>O for 48 h of the experiment.

Therefore, in order to confirm the hydrolysis of the **IrPOH** complex, experiments have been performed using  $^1\text{H}$  NMR spectroscopy in the presence of NaCl in different concentrations ( $C_{\text{NaCl}} = 4, 23$  and  $104$  mM), which reflect the chloride concentrations in the cell nucleus, cytoplasm and blood plasma, respectively. Along with NaCl concentrations increased, the decrease of aqua complex ( $\text{Ir-OD}_2/\text{OD}$ ) simultaneously with the increase of chloro-complex ( $\text{Ir-Cl}_2$ ) was observed (**Fig. 17**).

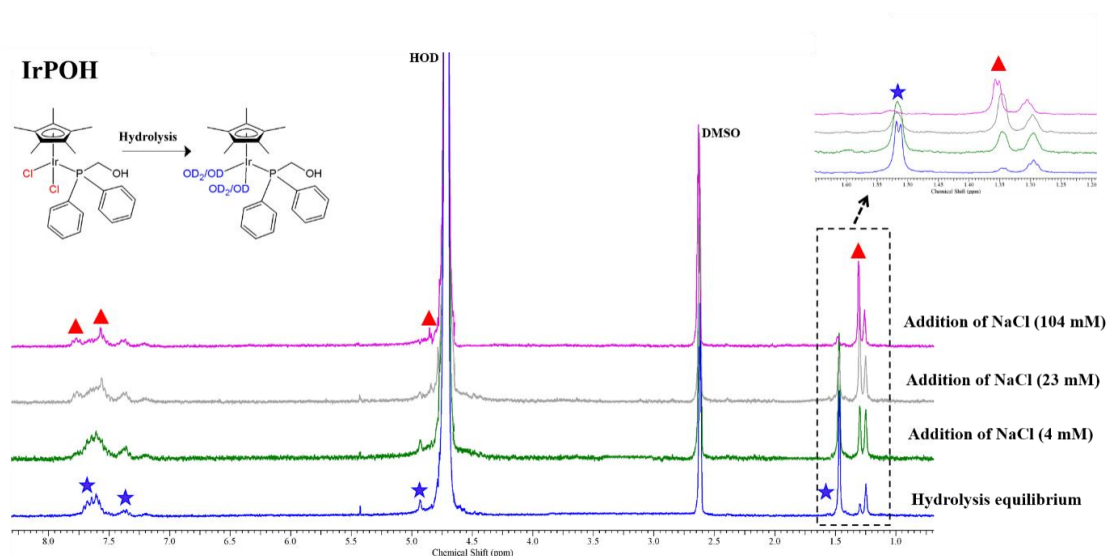


**Figure 17** Confirmation of hydrolysis of **IrPOH**. From the bottom:  $^1\text{H}$  NMR spectrum of an equilibrium solution of **IrPOH** (1 mM) in a mixture of 20% DMSO- $d_6$  and 80%  $\text{D}_2\text{O}$  (v/v) at 298 K. The spectra were measured 10 min after the addition of: 4 mM NaCl; 23 mM NaCl; 104 Mm NaCl to the equilibrium solution of **IrPOH**.

The analysis of the NMR spectra showed that at a concentration of 104 mM  $[\text{Cl}^-]$  there was still a small amount (approx. 10%) of the aqueous form. These results illustrate that  $\text{Ir}^{\text{III}}$  complex at biologically relevant chloride concentrations exists as aqua form ( $\text{Ir-OH}_2$ ) [107]. Hydrolysis is a common mechanism of metal drug activation by displacing weakly bound  $\sigma$ -donor ligands by water molecules [108]. However, inside cells, where chloride ion concentration is lower, hydrolysis can be inhibited. On the other hand, metal complexes can also interact with many targets inside the cell, which can also be reflected in their hydrolysis. One of the reasons may be the interaction of metal complexes by direct substitution of chloride by nucleobases (DNA) [44, 108, 109].

As rapid hydrolysis complexes sometimes lead to decrease cytotoxic activity due to rapid inactivation by side reactions before achieving the intended goals. The complexes formed during hydrolysis containing water molecules in an aqueous solution in their structure ( $\text{Ir-OH}_2$ )

react more easily with nucleobases than chloride complexes (Ir-Cl). So, it has been also decided to investigate the hydrolysis rate of the **IrPOH** complex using UV-Vis spectroscopy (**Fig. 18**).

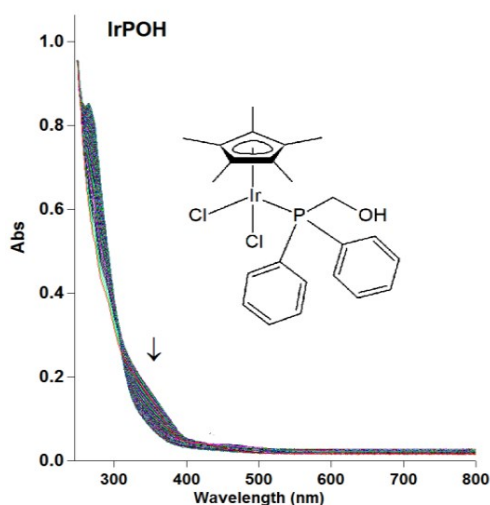


**Figure 18** UV/Vis spectra of **IrPOH** in 20 % DMSO/80% H<sub>2</sub>O (v/v) solution over 24 h.

The spectral characteristics of mononuclear iridium(III) complexes indicate the presence of an absorption band at high energies (<300 nm) in the UV-Vis spectra. These absorption bands are attributed to the ligand-centered (LC)  $^1\pi-\pi^*$  transitions of both the phosphine ligands (POH and FQ). In the range of 300 to 400 nm, metal-to-ligand charge transfer (MLCT) transitions are observed [110]. Changes in the band intensity were noted within 24 h of the experiment (**Fig. 18**). The dependence on the time of Ir-OH<sub>2</sub> formation for the **IrPOH** complex was fitted to the pseudo-first-order kinetics. The value of the hydrolysis rate constant was  $4.57 \cdot 10^{-4} \text{ min}^{-1}$ , and the half-lives of hydrolysis were 1515.2 min. Comparing the half-lives of the **IrPOH** complex with other complexes containing the iridium ion, it can be concluded that hydrolysis occurs relatively quickly (in minutes) [14, 111]. For example, this value for the compound  $[\text{Ir}(\text{H}_2\text{O})_6]^{3+}$  was over 300 years [112], while *trans*- $[\text{IrCl}_4(\text{DMSO})(\text{Im})]$  [ImH] (DMSO=dimethylsulfoxide, ImH=imidazole) compound was neutral to hydrolysis and showed no anti-tumor activity (NAMI-A iridium analog) [113].

Additionally, it is worth mentioning that complexes with phosphine conjugates of fluoroquinolones show intense fluorescence in solution in contrast to **IrPOH**. The fluorescent properties of the complexes (**IrPCp**, **IrPNr**, **IrPLm**) can provide useful information on the distribution, accumulation, and uptake of anti-cancer drugs in living cells or organisms. The maximum emission band for the second generation antibiotics (**PCp**, **PNr** and **PLm**) is around 420 nm, and it is in agreement with literature data [54, 55, 57]. After coordinating the phosphine ligands of fluoroquinolones to the iridium(III) ions, a redshift was observed in the emission spectra, showing purple emission at a maximum wavelength of around 440 nm (**Fig. 19**).

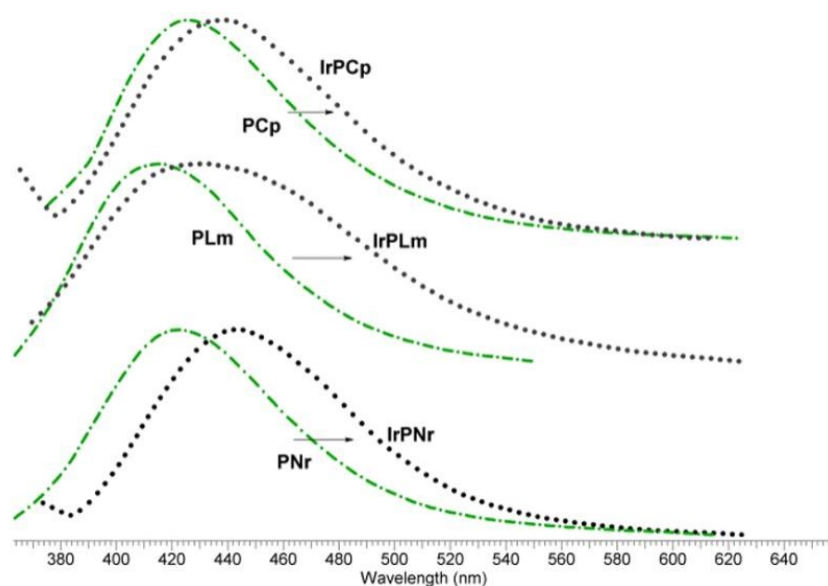


**Figure 19** Normalized emission spectra for Ir(III) complexes and the corresponding phosphine ligands;  $\lambda_{ex} = 340$  nm, 298 K.

To obtain qualitative information about the course of the electrochemical reaction, cyclic voltammetry (CV) was performed for all examined complexes. It will also allow us to understand the redox activity of the studied complexes through the production of reactive oxygen species in cancer cells. This fact is due to the reduction or oxidation of metal centers or the ligands surrounding them, or by their interaction with various biomolecules in the redox pathways [108].

Cyclic voltammograms for the **IrPOH** complex showed one irreversible oxidation peak at 1.5-1.7 V attributed to the phosphine ligand. In the case of complexes containing the fluoroquinolone motif (**IrPCp**, **IrPLm**, **IrPNr**) two irreversible oxidation peaks at about 1.0 V and 1.25 V are observed, which are attributable to the phosphine ligand and the iridium(III) ion. Moreover, for all investigated complexes, one quasi-reversible reduction peak of about -0.55 V is observed, which is attributed to the phosphine ligand (**Fig. 20**). In addition, both the cathode peak and the anode peak were shifted only slightly as the scan speed increased. This shows that the redox process occurs through controlled diffusion. Using cyclic voltammetry in conjunction with absorption spectroscopy, we can determine the electron transfer reactions that occur without changes in the stereochemistry of the complexes. The production of ROS in the examined systems is related to the oxidation of iridium(III) ions to iridium(IV) ions.



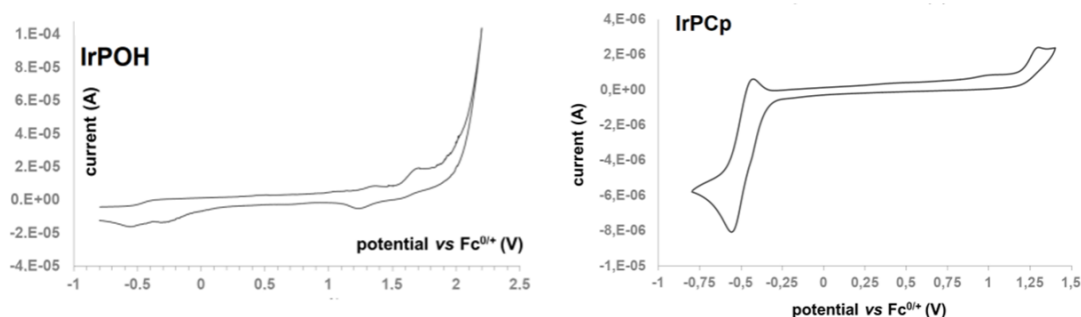


**Figure 20** Cyclic voltammograms of **IrPOH** and **IrPCp** (1 mM), recorded with 0.1 M tetrabutyl ammonium perchlorate (TBAP) as supporting electrolyte in DMF solution. Scan rates ( $10 \text{ mVs}^{-1}$ ). The potentials were referenced to the  $\text{Fc}^{0/+}$  redox couple.

#### 4.1.3. Analysis of structures in solid state [S1, S2]

In the process of crystallization by slow solvent evaporation, single crystals of all four coordination compounds were obtained (**Fig. 21**). All the complexes were structurally identified by single-crystal X-ray diffraction analysis. Details concerning crystal data and refinement are given in publications **S1** and **S2**. Despite similar molecular structures, the presented derivatives crystallize in different space groups, additionally, in each case, there is only one molecule in the asymmetric unit.

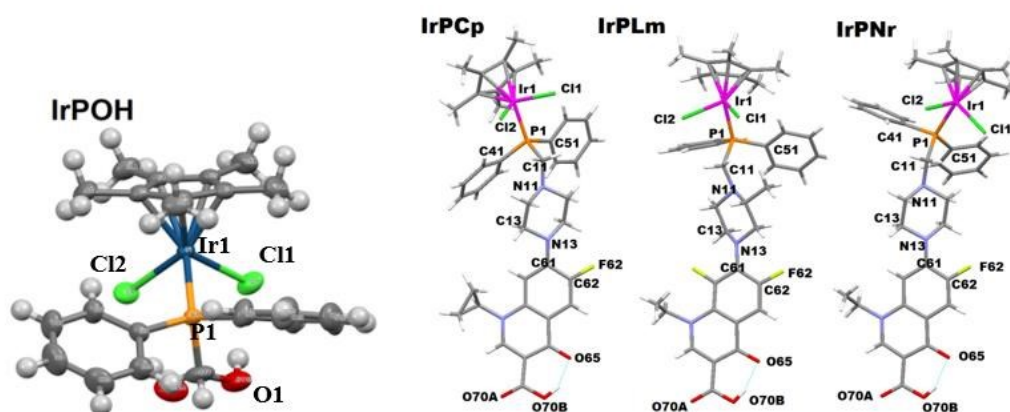


**Figure 21** The monocrystal structures of the complex molecules **IrPOH**, **IrPCp**, **IrPLm** and **IrPNr**. The solvent molecules are omitted for clarity.

Interpretation of the crystallographic data obtained for the complexes confirms (similarly to the studies of the complex solutions) that the central iridium(III) ion is coordinated by the cyclopentadienyl moiety, phosphorous atoms from ligands and two terminal chloride anions.



The mononuclear iridium(III) complexes adopt half-sandwich pseudo-octahedral “three-leg piano-stool” geometry. The bond lengths and angles are within the range typical of iridium(III) complex compounds with cyclopentadienyl moiety and phosphine ligands. The bond lengths P1-Ir1 in all structures were found to be on an average value of 2.3 Å, whereas distances between P1-C11 are in the range of 1.810-1.865 Å.

In the case of the complex without the fluoroquinolone motif (**IrPOH**), the strongest hydrogen bond form between the hydroxyl group (-OH) acting as a donor and the chlorine atom (-Cl) acting as an acceptor. This intramolecular interaction gives rise to the  $S_1^1$  motif (6).

The arrangement of molecules in complexes containing fluoroquinolone derivatives in the crystal structure of the discussed compounds is determined by the orientation of the piperazine ring and fluoroquinolone moiety. In each examined molecule, intramolecular hydrogen bonds between hydroxyl groups (O70B–H70B) and oxygen atoms from carbonyl groups (O65=C65) are observed. Among all the obtained single crystals, only in one crystal structure - **IrPCp·CHCl<sub>3</sub>**, the intermolecular  $\pi$ -ring stacking in the unit cell is observed. A fragment of the heterocyclic moiety of fluoroquinolone (*i.e.* 6-membered rings) is involved in a strong  $\pi$ - $\pi$  interaction with symmetry related to the other fragment of the fluoroquinolone moiety a neighboring ligand in the unit cell. The arrangement of  $\pi$  -  $\pi$  in the structure of this complex is a face to face pattern, with a centroid (N67 - C67 - C66 - C65 - C64 - C68) - centroid (C69 - C68 - C64- C63 - C62 - C61) a distance of value 3.652 Å. Moreover, the chloroform molecule represented in the **IrPCp** structure is located in the peripheral part of the examined molecule. Such an arrangement allows the  $\pi$  -  $\pi$  interactions in the **IrPCp** molecule (**Fig. 22**).

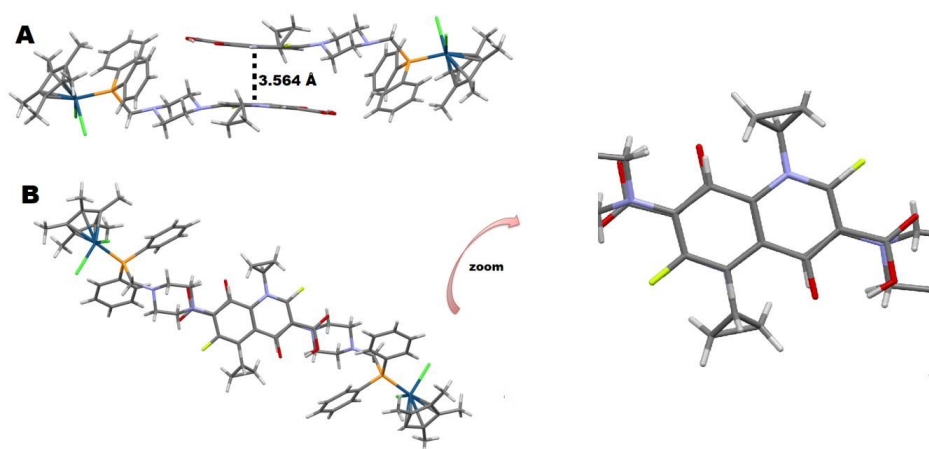


**Figure 22** The packing in the crystal **IrPCp·CHCl<sub>3</sub>** showing  $\pi$ -stacking interaction between the fluoroquinolone rings (**A**) and face-to-face pattern of the  $\pi$ - $\pi$  stacking in this complex (**B**).

The conformation of the fluoroquinolone motif of examined compounds can be defined in terms of torsion angle, defining the orientation of the piperazine ring and antibiotics moiety (**IrPCp**: C13 – N13 – C61 – C62 –165.92°; **IrPLm**: C13 – N13 – C61 – C62 117.48° **IrPNr**: C14 – N13 – C61 – C62 –165.97°). The comparative analysis of the data obtained for the **IrPLm** complex with the data for the **IrPCp** and **IrPNr** complexes showed that the values of the torsion angle described above are significantly different. As in the **IrPCp** and **IrPNr** complexes, the solvent molecules are placed differently positioned in the molecule and the fluorine atoms do not interact with them. The situation is different in the case of the **IrPLm** complex, where weak interaction of the fluorine atom with the solvent molecule was observed.

#### 4.2. Biological properties analysis [S1, S2, S3]

In order to characterize the biological properties of the obtained compounds, *in vitro* cytotoxic activity was determined towards five selected cancer cell lines: metastatic human melanoma (WM2664), human lung adenocarcinoma (A549), human breast adenocarcinoma (MCF7), human pancreatic/duct carcinoma (PANC-1), human prostate carcinoma (DU-145) and one normal which was human embryonic kidney (HEK293T) cell line. Moreover, in order to increase the cellular accumulation of metal complexes and to control their uptake only to neoplastic cells as compared to normal cells, which would further reduce the systemic toxicity of the complexes, the synthesized compounds were encapsulated in micelles. Mechanistic studies were performed for the most active compounds. Additionally, *in vitro* cytotoxicity assays within multicellular tumor spheroids (3D) has been also performed. Cytotoxicity was assessed on the basis of the IC<sub>50</sub> value (drug concentration required to inhibit the growth of 50% of cells). As the table shows (**Tab. 1**), the studies were carried out in two different approaches - after 24 h and 24 h + 48 h of incubation of compounds with cancer cells. Cell lines were also treated with cisplatin (reference drug) in the same concentration range as the synthesized complexes. This approach not only provides more accurate information on their cytotoxicity, but also allows the rate of their entry into the cell to be estimated.

**Table 1** Values of IC<sub>50</sub> [μM] (concentration of a drug required to inhibit the growth of 50 % of the cells) for WM2661, A549, MCF7, PANC-1, DU-145, HEK293T cells after 24 h and 24 h + 48 h treatment with the studied compounds and cisplatin as reference

IC <sub>50</sub> [μM] ± SD; 24h						
	A549	MCF7	PANC-1	DU-145	WM2664	HEK293T
<b>IrPOH</b>	45.8± 1.6	>1000	35.5±1.1	31.5±0.4	>1000	754.2±10.1
<b>IrPCp</b>	68.8±1.7	65.7±2.8	43.0±1.3	11.8±1.1	*	42.1±2.1
<b>IrPLm</b>	69.7±4.1	64.5±2.2	48.1±4.3	11.3±0.9	*	46.0±1.6
<b>IrPNr</b>	71.4±1.6	68.8±5.3	42.6±8.1	12.9±2.1	*	41.8±1.7
<b>cisplatin</b>	>100	51.9±4.6	>100	>100	2.63±0.6	21.0±1.8
IC <sub>50</sub> [μM] ± SD; 72h (24h + 48h)						
<b>IrPOH</b>	22.5±1.3	>1000	139.1±2.	52.4 ± 0.9	>1000	834.2±11.8
<b>IrPCp</b>	29.5±0.7	35.0±0.9	8.7±0.3	4.8±0.1	*	28.5±1.5
<b>IrPLm</b>	27.4±1.7	33.7±3.8	8.1±1.1	5.1±0.4	*	28.0±1.7
<b>IrPNr</b>	29.1±1.2	31.7±0.3	8.3±1.3	5.5±0.2	*	21.4±1.2
<b>cisplatin</b>	71.7±3.7	17.7±8.6	74.5±2.3	65.5±3.6	8.29±0.4	10.3±2.1

\* no available data

The organometallic Ir(III) complexes showed significant and differentiated cytotoxic activity against all the tested cell lines. Comparing these data with the literature data, it is worth noting that all complexes were characterized by higher cytotoxicity than phosphine ligands without and with fluoroquinolone motifs (**POH**, **PCp**, **PNr**, **PLm**), regardless of the cell type or incubation time [54, 55, 57, 58]. The activity of Ir(III) complexes for all tested cell lines was much better after 24 h of incubation time and 48 h of regeneration time (24 h + 48 h) than after 24 h of the experiment (without recovery time – extra 48 h without complexes). This is a very good result because the cytotoxic changes initiated in the cells during the 24-hour incubation cannot be repaired by the cells. Most likely, their repair systems to minimize toxicity are not sufficient, which may result in resistance breakdown. What is worth emphasizing, the introduction of the fluoroquinolone motif in complexes significantly increased the antitumor cytotoxicity of the final compounds against the lung, breast and melanoma cell line. Several recent reports suggest that fluoroquinolones have the potential to be anticancer agents [61, 62, 72], which is consistent with our results. Moreover, it can be observed that prostate cancer (DU-145) and pancreatic/duct carcinoma (PANC-1) cells were the most sensitive cell line to the mononuclear iridium(III) complexes even with both experimental approaches. Among all tested Ir(III) complexes, the **IrPCp** complex showed the most significant antitumor activity *in vitro* with an IC<sub>50</sub> value of 4.8 μM for DU-145 in 24 h + 48 h approach.

Drug encapsulation has revolutionized drug delivery research, especially in the treatment of cancer. This is because nano-systems promote drug retention in tissues, protect against

chemical and biological degradation, reduce non-specific side effects and toxicity of the encapsulated drug, and increase cellular uptake. Encapsulation also eliminates the need to dissolve a lipophilic drug in organic solvents such as DMSO, which can be toxic to human health. For this purpose, we also encapsulated metal compounds into micelles (**Fig. 23**). Detailed characteristics of the prepared nanoformulations can be found in the manuscript of publications **S2**.

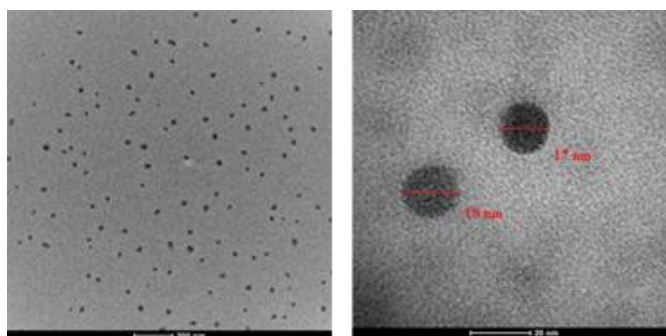


**Figure 23** TEM images of Pluronic P-123 formulation with encapsulated **IrPCp** complex (**IrPCp\_M**).

It is worth noting that the obtained  $IC_{50}$  values for the complex encapsulated inside micelles (**IrPCp\_M**) are an order of magnitude lower than for the corresponding complexes in case A549 cells (line most resistant to non-encapsulated Ir(III) compounds). In addition, in the case of the most sensitive line - prostate cancer (DU-145) – the anticancer effect was about 3 times higher for **IrPCp\_M** (**Tab. 2**). From these data, it is concluded that the encapsulation of compounds in micelle increased drug accumulation in the tumor.

*Therefore, IrPCp was selected as the one with the best activity for further mechanistic studies.*

**Table 2**  $IC_{50}$  ( $\mu$ M) values of the investigated compounds toward

	$IC_{50}$ [ $\mu$ M] $\pm$ SD; 24h	
	A549	DU-145
<b>IrPCp</b>	$68.8 \pm 1.7$	$11.8 \pm 1.1$
<b>IrPCp_M</b>	$8.9 \pm 0.7$	$4.1 \pm 0.6$
<b>Cisplatin</b>	>100	>100

Since conventional 2D cell cultures cannot mimic the complexity and heterogeneity of clinical tumors, three-dimensional (3D) spheroids where prospered. Compared to classic adherent culture, spheroids can provide a microenvironment that more closely mimics the cellular interactions observed in tumor tissues *e.g.* cell-cell or a cell-intercellular substance [114]. The therapeutic potential of Ir(III) complex **IrPCp\_M** towards 3D A549 and DU-145

spheroidal culture was detected by fluorescence staining of live and dead cells (**Fig. 24**). As illustrated, mainly live cells (green) and a relatively small number of dead cells (red) were observed in the control spheroids (without studied complex). In contrast, a high percentage of dead cells, especially in the inner core, were observed in spheroids treated with the compound **IrPCp\_M**. When DU-145 spheroids were treated with **IrPCp\_M**, the structural integrity of spheroids was even destroyed at the increased concentration of the studied compound. It means that complex is highly cytotoxic.

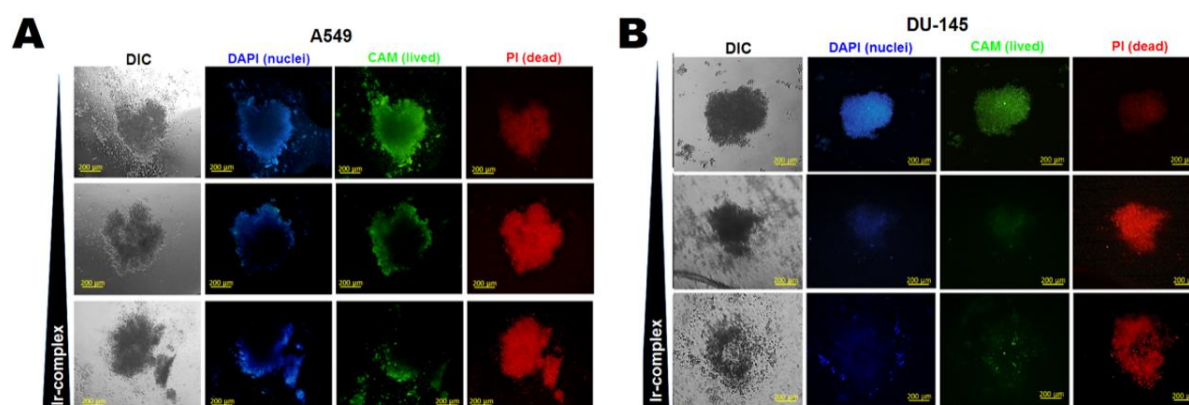


**Figure 24 (A)** A549 and **(B)** DU-145 spheroids after treatment with increasing concentration of **IrPCp\_M** complex. DAPI: 4',6-diamidino-2-phenylindole, CAM: calcein AM, PI: propidium iodide, Hoechst 33342.

Since many aspects of the inhibitory effects of iridium complexes on cancer are still unknown, attempts have also been made to approximate their mode of action. For precise determination of the mode of observed cell death, flow cytometry was applied. Data analysis proved that treatment of the cancer breast and lung cells with **IrPCp** complex resulted in the vast majority of the population of apoptotic cells appearing, opposite to necrotic ones. It is worth mentioning that inducing apoptosis has become very important in cancer drug research and is a more desirable process of cell death than necrosis [115, 116]. This is because it does not lead to the inflammatory process that accompanies necrosis [117].

Additionally, it was proven that **IrPCp** complex probably induced G2/M phase arrest. However, in the case of line A549, the G0/G1 phase population was still observed. Many metal complex cytotoxic agents inhibit the proliferation of cancer cells, causing the G0-, S-, or G2/M-phase arrest cell cycle. The G2 checkpoint ensures the propagation of error-free copies of the genome to each daughter cell by preventing cells from entering mitosis in the event of DNA damage. Whereas, the S phase of the cell division cycle represents the period during which cells

replicate their DNA. The arrest of the cell cycle by the compounds in this phase could result in an inhibition of DNA replication [118].

Moreover, a study of the mitochondrial membrane potential was performed along with the determination of caspase 3/7 activation. Mitochondria play a key role in apoptotic cell death, and a reduction in their membrane potential (MMP) usually triggers a cascade of executive caspases [81]. After 24 hours of incubation with **IrPCp** in lung cells (A549) it was observed that the investigated complex significantly decreased the mitochondrial membrane potential. In addition, the study clearly showed that this complex activated caspase-7 and caspase-3 simultaneously. In contrast, in prostate cells (DU145), caspase-3/7 activation decreased, possibly indicating activation of necrotic cell death instead of apoptosis.

Localization studies revealed that Ir(III) complexes can be accumulated inside the whole cancer cells (**Fig. 25**), so it has been decided to check if the complex can interact with DNA. Several well-known DNA-binding dyes [ethidium bromide (EB; intercalation), 4',6-diamidino-2-phenylindole (DAPI; binding to a minor groove), and methyl green (MG; binding to a major groove)] were used to study the mode of drug-DNA interactions.

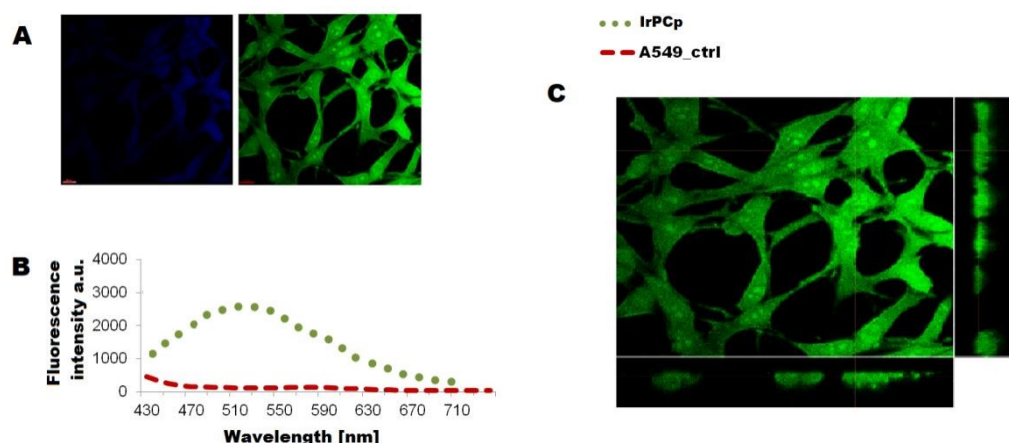


**Figure 25** Selected images of A549 cells obtained by confocal microscopy (magnification 60.00 $\times$ , ex = 358 nm) after treatment with **IrPCp** ( $c = 1 \mu\text{M}$ ) for 4 h (**A, C**). Emission spectra of cells after treatment with **IrPCp** together with the reference spectra of control untreated (**B**).

It was found that our complexes exhibited multimodal DNA interaction with predominance of minor groove binding (**Fig. 26**). It is worth noting that the trend in the ability to interact with CT DNA was different than in the case of previously reported complexes based on identical phosphine ligands [57, 82]. Previously reported compounds interacted with CT DNA mainly true by intercalation. This tendency suggests that the type of metal ions



influences the type and intensity of intercalation with DNA. Additionally, circular dichroism (CD) was used to confirm how the complex interacts with CT DNA. After titration of CT DNA with the studied **IrPCp**, the signals in the 250-300 nm range changed slightly. This means that the compound prefers to bind in a minor groove, consistent with the results obtained above. This slight change also means that the **IrPCp** did not affect the DNA helix.

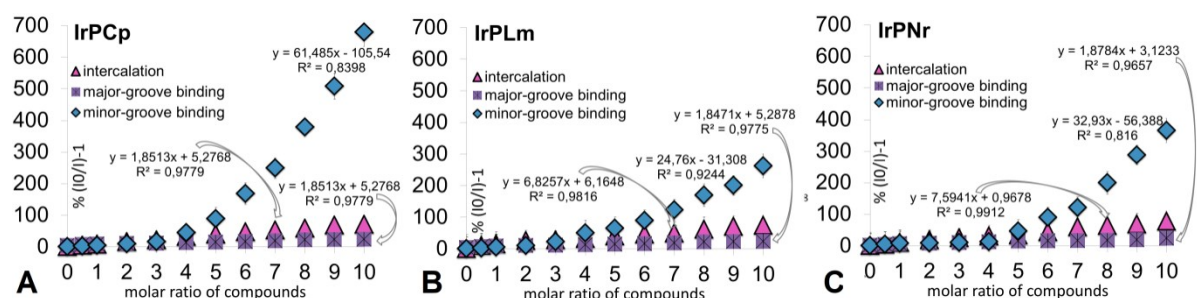


**Figure 26** Stern–Volmer plots of the CT DNA-EB, CT DNA-DAPI and CT DNA-MG system quenched by examined complex: (A) **IrPCp**; (B) **IrPLm**; (C) **IrPNr** (on the left) (I0 and I-intensity of CT DNA-EB or DAPI or MG in the absence and the presence of increasing concentration [mM] of the compounds.

What is important and worth to emphasize **IrPCp** did not cause a double-strand cleavage of DNA even at very high concentrations (**Fig. 27**). This experimental evidence suggests a different mechanism of action than targeting DNA - a mechanism typical of Pt(II) drugs, mainly based on damage to nucleic acids, e.g. intercalation. This hypothesis is also confirmed by the results obtained by fluorescence spectroscopy and circular dichroism.

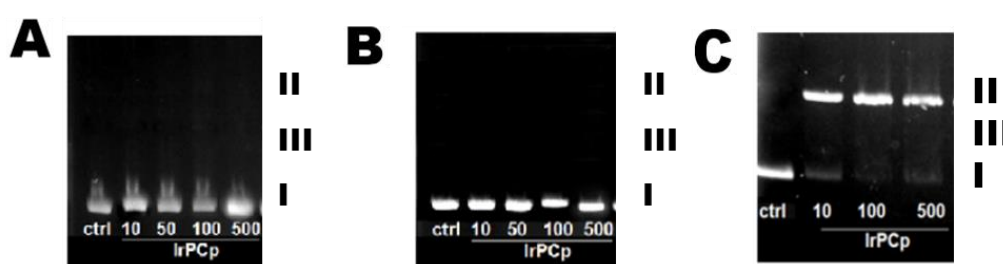


**Figure 27** Agarose gel electrophoresis of pBR322 plasmid cleavage by different concentration (10-500uM) of **IrPCp** in the 10 % DMF solution, ctrl: plasmid—control. (A) 1 h of incubation; (B) 4 h of incubation; (C) 24 h of incubation. Forms of plasmid DNA:superhelical (form I); relaxed/nicked (form II) and linear (form III) forms.

The level of intracellular reactive oxygen species generated by the test compound was measured. The formation of reactive oxygen species (ROS) was monitored using fluorescence

spectroscopy and a non-fluorescent 2',7'-dichlorodihydrofluorescein diacetate (DCFH<sub>2</sub>-DA) probe as a detector. The complex with the ciprofloxacin derivative showed the ability to induce ROS production in DU-145 tumor cells at a much higher level than the ligand alone and the positive control. Moreover, even after 72 hours, increased production of ROS was observed.

To confirm the type of reactive oxygen species involved in the degradation of the plasmid, an experiment was carried out with hydrogen peroxide and with the use of DMSO (effective scavenger of hydroxyl radical:  $\cdot\text{OH}$ ), SOD (effective scavenger of superoxide radical anion:  $\text{O}_2^{\cdot-}$ ), and  $\text{NaN}_3$  (effective scavenger of singlet oxygen:  $^1\text{O}_2$ ). The **IrPCp** complex in the presence of  $\text{H}_2\text{O}_2$  caused marked changes in the structure of the plasmid, resulting in increased amounts of form II (relaxed/nicked form). After the addition of a radical inhibitor (DMSO), a clear inhibition of DNA damage was observed, suggesting the participation of the  $\cdot\text{OH}$  in the cleavage process. Moreover, also, a slight inhibition of DNA cleavage was observed in other cases, *i.e.*  $\text{NaN}_3$  and SOD, confirming the presence of  $^1\text{O}_2$ ,  $\text{O}_2^{\cdot-}$  respectively.

Using cyclic voltammetry in conjunction with absorption spectroscopy, it can be stated that ROS generation in the studied systems is related to the oxidation of iridium(III) ions to iridium(VI). The analysis of my research allowed me to hypothesize that ROS are involved in the mechanism of cytotoxic action. It was also proven that the studied iridium(III) complex (**IrPCp**) is responsible for DNA damage through a ROS-dependent mechanism involving hydroxyl radical, singlet oxygen and superoxide anion radical.

Another factor extremely important for understanding the activity of the examined compound is knowledge about the transport processes of the studied compound into the cell. The binding of biologically active substances to these proteins may lead to the loss or increase in their activity or may allow the transport of the compound in the body [119]. For example, albumin tends to accumulate in cancer tissue and inflamed tissues [120]. The expression of transferrin is significantly increased in neoplastic cells and often correlates with the tumor stage which makes it an attractive natural carrier for anti-cancer chemotherapeutic agents [121]. Therefore, it was also decided to determine the ability of the complex to bind human albumin serum (HSA) and apo-Transferrin (apo-Tf) using spectroscopic methods combined with theoretical calculations such as molecular docking. For all the complexes containing the fluoroquinolone motif, it was noticed that with increasing concentrations, the intensity of the emission band of human albumin (HSA) at a wavelength of 342 nm gradually decreased. At the same time, an additional fluorescence band appeared with an emission maximum at 425 nm, which is due to the fluorescence from the starting complexes or the new system of HSA-Ir(III) complex. These changes indicate a strong interaction of complexes with albumin,



additionally increased polarization in the area surrounding the Trp residue and/or energy transfer between the investigated complexes and human albumin. The binding strength to albumin can be represented in the following order: **IrPLm** > **IrPCp** > **IrPNr**. This phenomenon may be related to the presence of additional fluorine atoms in the quinolone moiety and the methyl group attached to the piperazine ring. Additionally, the studied compound was found to bind to HSA tryptophan residues at the site I (subdomain II A) (**Fig. 28**). Molecular docking confirmed that the investigated complexes bind to HSA, where the Ir(III) core is located at the entrance to the binding pocket and the fluoroquinolone motif is buried deep in the binding site. In addition, hydrogen bond formation was observed between the fluoroquinolone motif and the residue Arg218. Other hydrogen bonds have also been found which may exist between the complex carboxylate group and the His242 residue in the case of the **IrPNr** and **IrPLm** complexes or Arg257 in **IrPCp**.

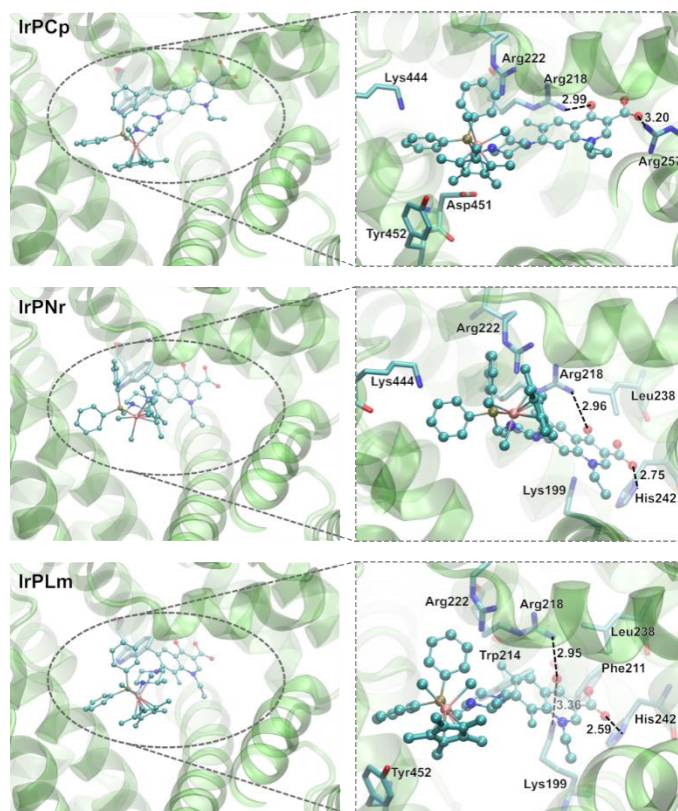


**Figure 28** Binding mode of HSA-phosphino iridium(III) complexes.

When investigating the interaction of the synthesized compounds with apo-transferrin a decrease in the fluorescence intensity was also noticed (at 343 nm). This suggests that these compounds may bind to apo-transferrin and disturb the tryptophan microenvironment. The strength of apo-Tf fluorescence quenching by compounds can be presented in the following order: **IrPCp** > **IrPNr** > **IrPLm**. However, the binding strength of the complexes with

transferrin was lower than with albumin. This suggests that different moieties in the structure of the complexes and different interactions are responsible for the quenching of the emissions of these two proteins. Molecular docking shows that all complexes bind to all four possible apo-Tf binding sites containing tyrosine or tryptophan residues and they are located between the residues Tyr317 and Tyr647 in the apo-transferrin molecule (**Fig. 29**). The **IrPCp** and **IrPLm** complexes form three hydrogen bonds with the residues Tyr317, Arg677 and Asp240. The **IrPNr** complex exhibits a separate binding mode and binds to the Lys401 residue *via* a hydrogen bond mediated by an oxygen-containing fluoroquinolone moiety.

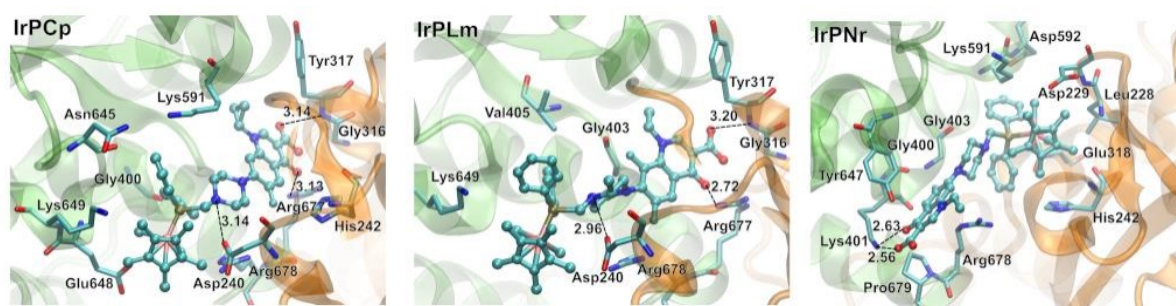


**Figure 29** Binding mode of apo-Tf-complexes within the #2 binding pocket.

## 5. Concluding Remarks

The aim of the studies presented in this thesis was to design and synthesize monometallic iridium(III) complexes with phosphine ligands derived from fluoroquinolone antibiotics possessing potential anticancer activity.

To achieve the assumed research goals of this work, three iridium(III) complexes with aminomethyl(diphenyl)phosphines derived from fluoroquinolones (ciprofloxacin: PCp (PPh<sub>2</sub>CH<sub>2</sub>Cp), lomefloxacin: PLm (PPh<sub>2</sub>CH<sub>2</sub>Lm), and norfloxacin: PNr (PPh<sub>2</sub>CH<sub>2</sub>Nr)) were synthesized (**IrPCp**, **IrPLm** and **IrPNr**) as well as with phosphine without antibiotic motif (**IrPOH**). Physicochemical properties of these obtained compounds in solution and solid-state were determined using elemental analysis, mass spectrometry, cyclic voltamperometry, and spectroscopic methods (NMR, IR, UV-Vis, fluorescence). These studies allowed us to obtain information about the fluorescent properties, structure, purity, and stability of the Ir(III) complexes in aqueous solutions as well as in the presence of atmospheric oxygen. For all systems, crystal structures were determined using X-ray diffraction. In these complexes, the central iridium(III) ion is coordinated by a cyclopentadienyl moiety, phosphorus atoms from the ligands and two terminal chloride ligands.

To determine their anticancer properties and the initial mechanism of their action a series of biological tests were also carried out. The *in vitro* cytotoxic activity of all synthesized compounds was determined against healthy and cancer cells (determination of IC<sub>50</sub> using the MTT test): human breast adenocarcinoma (MCF7), human lung adenocarcinoma (A549), mouse colon carcinoma (CT26), human pancreatic/duct carcinoma (PANC-1), (human prostate carcinoma (DU145), metastatic human melanoma (WM2664), human embryonic kidney (HEK293T). This study allowed selecting the compound with the best effect and attempting to determine its mechanism of cytotoxic action. For this purpose: **(i)** metal uptake and intracellular localization were determined using ICP-MS, confocal microscopy, and commercially used tests; **(ii)** the type of cell death using flow cytometry and commercially used kits; **(iii)** the cell cycle and apoptosis-related proteins e.g. caspase-3/7; **(iv)** mitochondrial membrane potential; **(v)** cellular ROS generation us; **(vi)** interaction complexes with DNA and serum proteins by gel electrophoresis, fluorescence spectroscopy, circular dichroism; **(vii)** drug cytotoxicity analysis on 3D tumor spheroids.

***The results of these studies allowed for the formulation of a number of conclusions:***

- Homonuclear Ir(III) complexes containing the fluoroquinolone motif are stable in an aqueous solution.
- The **IrPOH** complex hydrolyzes in an aqueous solution. This property is biologically important, as M–OH<sub>2</sub> water complexes are often more reactive than the corresponding complexes
- In the case of all complexes, two bands are observed in the UV-Vis spectra: the first being the result of MLCT transitions and the second is attributed to the spin allowed ligand centered (LC) <sup>1</sup>π-π\* transitions of both the phosphine ligands.
- In all complexes, irrespective of the type of phosphine ligand, the iridium(III) ion adopts the half-sandwich pseudo-octahedral “three-leg piano-stool” geometry.
- In the aqueous solutions of the complexes containing the fluoroquinolone motif, intense luminescence is observed as a result of the transitions inside the quinolone fragment.
- Prostate carcinoma cancer cells (DU-145) and human pancreatic/duct carcinoma were the most sensitive cell lines to Ir<sup>III</sup> complexes.
- Introduction of the fluoroquinolone motif in complexes significantly increased the antitumor cytotoxicity of the final compounds against the lung, breast, and melanoma cell line.

- Of all the synthesized compounds, the **IrPCp** complex showed the best anticancer properties.
- ICP-MS analysis revealed efficient iridium accumulation with increasing time, which was assessed to be the highest in the case of prostate cells.
- The investigated complexes presumably induce G2/M phase arrest, along with caspase-3/7 activation accompanied by a decrease in mitochondrial membrane potential.
- Precise cytometric analysis provided clear evidence for the predominance of apoptosis in the induced cell death.
- Inorganic compounds exhibited multimodal DNA interaction with a predominance of minor groove binding.
- Investigated iridium(III) complexes are responsible for DNA damage *via* a ROS-dependent mechanism involving hydroxyl radical, singlet oxygen and superoxide anion radical.
- Additionally, the test compound was found to bind to HSA tryptophan residues at site I (subdomain II A) and bind to all four possible apo-Tf binding sites containing tyrosine or tryptophan residues.
- Enclosure of compounds in micelles (**IrPCp\_M**) improved the effective accumulation of drugs in human lung adenocarcinoma and human prostate cancer.
- In addition, it also increased the cytotoxicity of the A548 and DU-145 tumor cells by an order of magnitude.

## 6. The most important achievements

- Synthesis of four new iridium(III) complexes containing phosphine ligands with/without a fluoroquinolone motif.
- Characterization of the physicochemical properties of all compounds in a solid as well as in a solution: (i) complexes structure and their geometry, (ii) the stability of compounds in aqueous solutions in the presence of oxygen, (iii) the ability to hydrolyze in aqua solutions (iv) luminescent properties, (v) electrochemical potential.
- The cytotoxicity of all compounds was tested *in vitro* against the five most common cancer cell lines: lung, prostate, pancreatic, breast, and skin as well as one normal, human embryonic kidney. Based on these results, **IrPCp** complex was characterized by much higher cytotoxicity than cisplatin simultaneously being less toxic to healthy cells.
- The mode of cytotoxic action of homonuclear Ir(III) complexes has been proposed.

- Encapsulation of inorganic compounds in Pluronic P-123 micelles to overcome low solubility, severe side effects associated with the systemic cytotoxicity, and acquired cancer cell resistance.

The chosen method of modifying the structure of antibiotics by phosphine motif attachment allowed obtaining complexes with unique anticancer properties, where the mechanism of action was initially proposed in this work. In the era of constant and frightening reports (WHO 2020 "WHO Cancer Report 2020") on the number of cases and deaths caused by neoplastic diseases. In addition, the currently used anticancer drugs are not sufficiently selective. They cause a number of side effects such as diarrhea, anemia, hair loss, damage to the heart, kidneys, bladder, lungs, and nervous system, and many more. All of these facts show how important it is to develop a system that selectively kills cancer.

## 7. Perspectives [S4]

Data describing physicochemical and biological properties of Ir(III)-Cu(II) complexes ( $\text{Ir}(\eta^5\text{-Cp}^*)\text{Cl}_2\text{PCp-Cu(phen)}$  – **IrPCpCu**;  $\text{Ir}(\eta^5\text{-Cp}^*)\text{Cl}_2\text{PLm-Cu(phen)}$  – **IrPLmCu**;  $\text{Ir}(\eta^5\text{-Cp}^*)\text{Cl}_2\text{PCp-Cu(phen)}$  – **IrPNrCu**) have been presented here to demonstrate possible use and evolution of Ir(III) complexes with phosphines derived from fluoroquinolones (**Fig. 30**). In addition, a potential platform for dual drug delivery using magnetic nanoparticle systems has been proposed.

These issues are carried out by me as part of a NCN research project, PRELUDIUM which I am the leader.

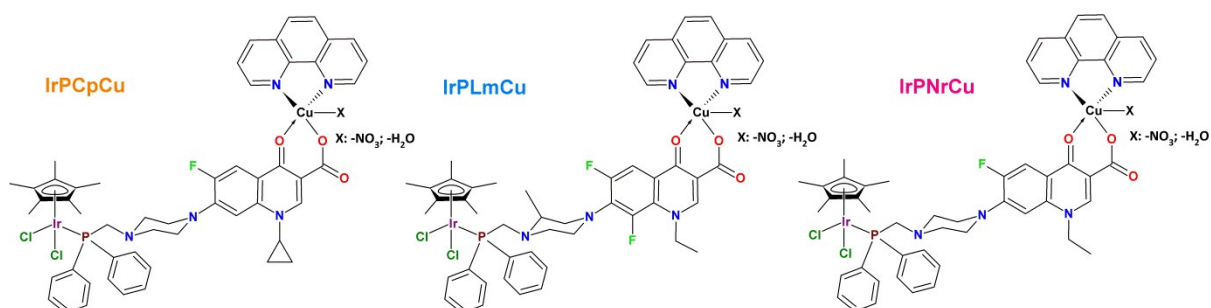


**Figure 30** Structure of heteronuclear iridium(III)-copper(II) complexes.

## 7.1. Modification of biological activity and characteristic of heteronuclear Ir(III) / Cu(II) complexes

To increase the selectivity towards neoplastic cells and to reduce the toxicity leading to side effects, further modifications of the obtained complexes were performed. One of the strategies adopted to overcome these limitations, scientists to find inspiration in the activity of novel heteronuclear complexes [122 -124]. The presence of two different metals in one molecule can improve their activity as anti-cancer agents due to interactions between different metals with multiple biological targets or through improved chemical-physical properties of the resulting compound [124]. Therefore, it was decided to attach a copper(II) ion to the homonuclear complexes (IrPCp, IrPNr, IrPLm). It was proved that through many processes, such as DNA damage or generation of ROS, Cu(II) complexes could effectively induce cancer cells death [83, 125]. In addition, the superiority of these substances is also represented by the fact that Cu(II) ions are already present in the human body limiting the possibility of excessive immunological system response is low [125]. Most importantly, the introduction of a transition metal, such as copper(II), can also give the obtained complexes unique magnetic properties [126].

### *Analysis of structures in solution*

All heteronuclear Ir(III)/Cu(II) complexes were characterized by mass spectrometry recorded in the positive ion modality and infrared spectroscopy. For the **IrPNrCu** and **IrPLmCu** complexes, the corresponding molecular ion was detected, consistent with the expected isotopic distribution for  $[M]^+$  or  $[M+H]^+$ . Only the complex with ciprofloxacin (**IrPCpCu**) did not show the corresponding  $[M]^+$  molecular ion peaks. The analysis of MS spectra showed that in all the types of complexes mentioned, chloride groups were easily displaced. As a result, adducts with solvent molecules, e.g. H<sub>2</sub>O or CH<sub>3</sub>OH, were observed.

In the IR spectra of fluoroquinolones, very strong bands around 1720 cm<sup>-1</sup> were observed, corresponding to the stretching vibrations of the C=O group of the carboxyl group (-COOH), while in the case of complexes they were very weak or not observed in the ATR spectra. Additionally, in the FT-IR spectra of heteronuclear Ir<sup>III</sup>/Cu<sup>II</sup> complexes, two characteristic bands were observed around 1630 and 1335 cm<sup>-1</sup>, corresponding to antisymmetric stretching vibrations ( $\nu\text{COO}^-$ ) which may be a marker of the coordination model. A model for the binding



of phosphine fluoroquinolone ligands to the  $\text{Cu}^{2+}$  ion was also determined by the difference in the  $\nu\text{COO}^-$  bands described above, which is in the range  $285\text{-}339\text{ cm}^{-1}$ .

Coordination of  $\text{Cu(II)}$  ions to  $\text{Ir(III)}$  complexes leads to a bathochromic shift of the maximum wavelength of the peak emission (**Fig. 31**). At room temperature, a structureless emission curve can be identified with a maximum centered at  $450\text{ nm}$  relating to all the solutions of  $\text{Ir(III)/Cu(II)}$  complexes. These emission patterns were obtained upon photoexcitation at a specific wavelength of  $340\text{ nm}$ .

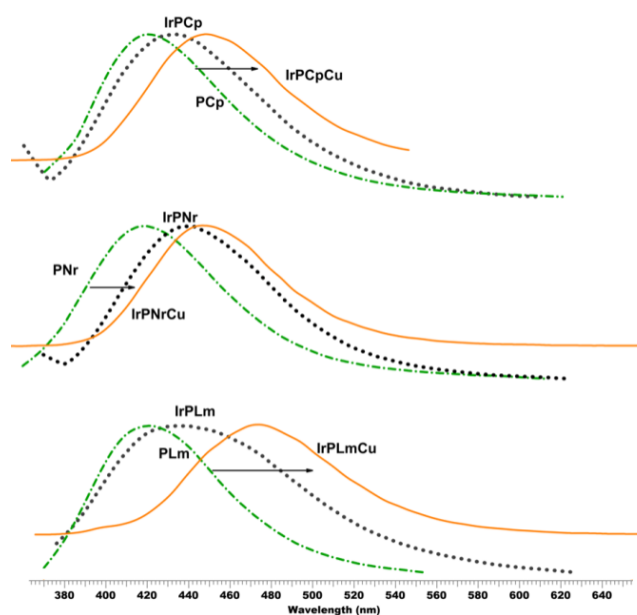


**Figure 31** Normalized emission spectra for heteronuclear  $\text{Ir(III)/Cu(II)}$  complexes, homonuclear  $\text{Ir(III)}$  complexes and the corresponding phosphine ligands;  $\lambda_{\text{exc}} = 340\text{ nm}$ ,  $298\text{ K}$ .

In addition, cyclic voltammetry (CV) was performed to thoroughly understand the redox activity of the investigated heteronuclear  $\text{Ir(III)/Cu(II)}$  complexes. The cyclic voltammograms of the complexes exhibit two irreversible oxidation peaks at around  $-1.6\text{ V}$  and  $-1.1\text{ V}$  which are assigned to the phosphine ligands and iridium(III) ion. One quasi-reversible reduction peak with  $E_{1/2}$  of ca.  $0\text{ V}$  is observed for all complexes and refers to the  $\text{Cu(II)/(I)}$  redox process.

### *Analysis of structures in solid*

The coordination geometry of the iridium(III) ion in all heteronuclear complexes is the same as that of the  $\text{Ir(III)}$  heteronuclear complexes. The complexes  $\text{IrPNrCu}\cdot(\text{NO}_3)\cdot 1.75(\text{CH}_4\text{O})\cdot 0.75(\text{H}_2\text{O})$  and  $\text{IrPCpCu}\cdot(\text{NO}_3)\cdot 2.75(\text{H}_2\text{O})$  crystallize in the triclinic crystal system, in the  $P1$  space group. Whereas,  $\text{IrPLmCu}\cdot(\text{NO}_3)\cdot 1.3(\text{H}_2\text{O})\cdot 1.95(\text{CH}_4\text{O})$  crystallizes in the  $Pbcn$  space group (orthorhombic system) and contains the 1D metal-organic polymer assembled from copper(II) centers, iridium(III) complex linkers, phenanthroline molecule and  $\text{OH}^-$  ligands (**Fig. 32**).

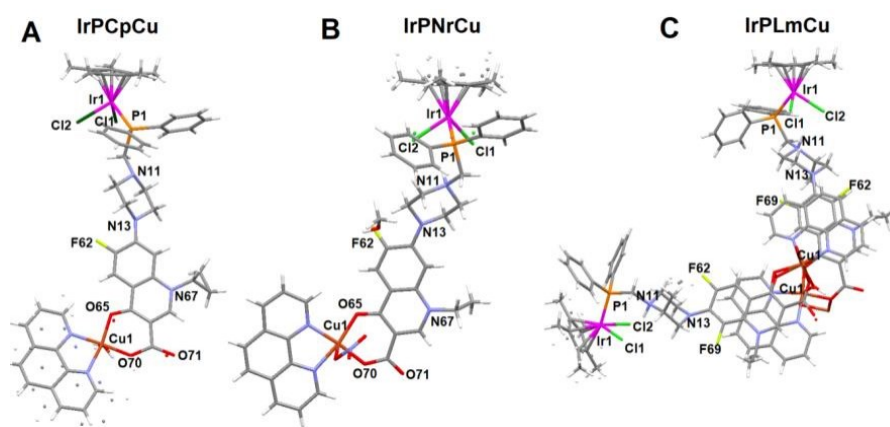


**Figure 32** The monocrystal structures of the complex molecules **IrPCpCu**, **IrPLmCu** and **IrPNrCu**. The solvent molecules are omitted for clarity.

In the **IrPCpCu** and **IrPNrCu** complexes Cu(II) ion adopt a distorted square-pyramidal coordination geometry, where the copper ion is coordinated *via* two nitrogen atoms (from phenanthroline ligand) and IrPNr or IrPCp complex *via* deprotonated carboxylate and pyridone oxygen atoms. In the case of **IrPLmCu**, the packing analysis showed that the Cu(II) ion adopts an octahedral distorted geometry, and is coordinated by four oxygen atoms (two carboxylates, one pyridine oxygen, and one from hydroxy group) and two nitrogen atoms from phenanthroline ligand (**Fig. 33**).

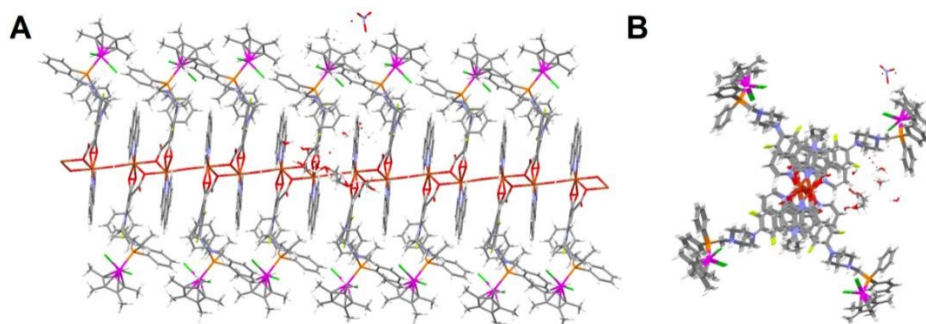


**Figure 33** A perspective view (**A** and **B**) of the 1D polymer chain in the crystal structure of **IrPLmCu**.

The presence of copper(II) ion in Cu(II) – Ir(III) heterometallic complex was also confirmed by magnetic measurement and EPR spectroscopy. Magnetic data were acquired with the help of the SQUID magnetometer (MPMS, Quantum Design) at the applied field of  $B_0 = 0.5$  T and, after correction to the underlying diamagnetism, transformed to the temperature dependence of the  $\chi_{MT}$  product (or effective magnetic moment, (**Figures 34** – left). The field dependence of the magnetization per formula unit  $M = M_{\text{mol}}/N_A\mu_B$  at the constant temperature is shown in figure 34 – right.



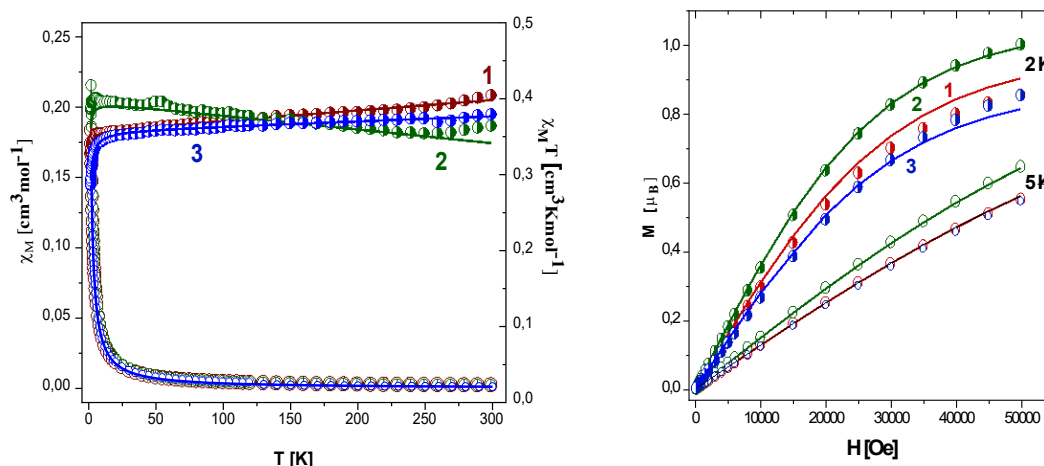


**Figure 34** Left - thermal dependencies of  $\chi_M T$  (half-open circles) and  $\chi_M$  (open circles) for **1 - IrPCpCu**, **2 - IrPNrCu**, **3 -IrPLmCu**; right - magnetization as a function of magnetic field at 2.00 K (half-open circles) and 5.00 K (open circles) for **1 - IrPCpCu**, **2 - IrPNrCu**, **3 - IrPLmCu**. The solid lines (on all graphs) are calculated using the HDVV spin Hamiltonian and PHI programme.

All examine complexes magnetically behave as a mononuclear unit with  $S_{Cu} = 1/2$  because Ir(III) ions are diamagnetic.  $\chi_M T$  vs T graph indicates the antiferromagnetic nature of exchange interaction for complex **IrPCpCu** and **IrPLmCu** and weak ferromagnetic coupling in compounds **IrPNrCu**. The magnetization data at  $T = 2.0$  and  $BDC = 5.0$  T saturates to  $M = M_{mol}/(N_A \mu_B) = 0.86 \mu_B$  (**IrPCpCu**, **IrPLmCu**) and  $1.00$  (**IrPNrCu**). Theoretical calculation of these magnetic data using the proper Hamiltonian (for an alternating Ising chain for polymeric complex **IrPLmCu** or Heisenberg-Dirac-Van Vleck for **IrPCpCu** and **IrPNrCu**) confirm the nature and strength of observed magnetic interaction.

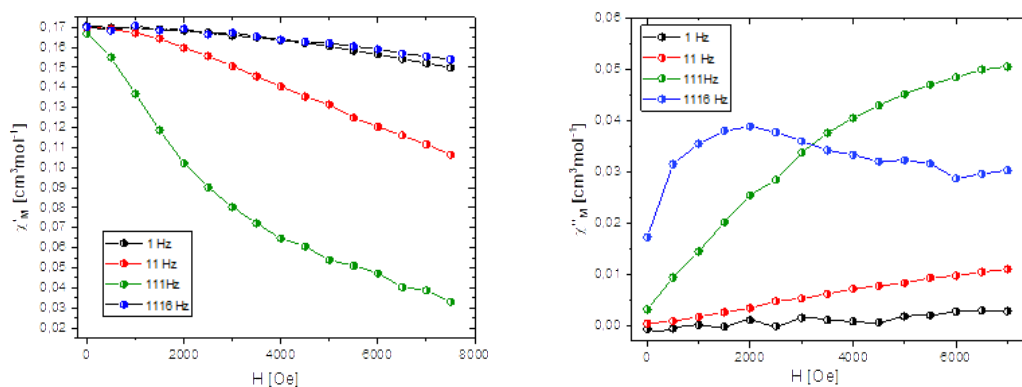


**Figure 35** Field dependencies of the AC susceptibility components for **2** at  $T = 2.0$  K for a set of frequencies of the AC field. Lines are a guide for the eye.

New information was obtained from the AC susceptibility measurements. The in-phase ( $\chi M'$ ) and out-of-phase ( $\chi M''$ ) components (**Fig. 35**) exhibit small frequency dependences with the application of an external field of 0.2 T, indicative of the possibility of slow relaxation of magnetization, although the maxima in  $\chi''$  are missing. Using this data we cannot suggest SMM or SIM behavior. However, the relaxation process for Cu(II) ions is very rare due to the absence of a barrier to spin reversal: the axial zero-field splitting parameter D is undefined. The presence of a relaxation process in complex **IrPNrCu** can be a result of geometry around Cu(II) ions. Though the D parameter cannot be assigned to mononuclear copper(II) complexes, these are well-known as anisotropic systems showing at least two distinct  $g_z \neq g_x$  values well seen in the EPR spectra of an axial type. Thus, even in the absence of the zero-field splitting, there exists a magnetic anisotropy. The results of magnetic studies in the alternating field (AC) indicate a significant role and usefulness of phosphine ligands in the functionalization of organic ligands leading to modification of the geometry of the metal coordination sphere and, consequently, the magnitude of anisotropy. This fact may mark an important path toward obtaining multifunctional materials.

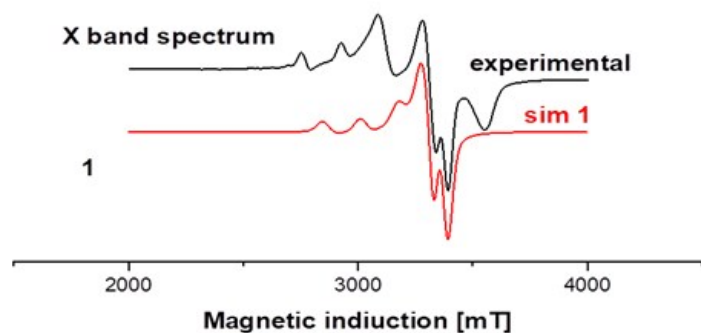


**Figure 36** EPR frozen solution spectra (at 77 K) of **IrPCpCu** in DMSO solvent together with the theoretical spectrum calculated.

The polycrystalline EPR spectra of the magnetically concentrated samples and also in the frozen solution confirm the axial symmetry with  $d_{x^2-y^2}$  ground state, where the geometry can correspond to an elongated octahedral, a square pyramidal or a square planar (**Fig. 36** – an exemplary spectrum for one of the examined complexes). The frozen solution EPR spectra exhibit a well-defined resolution of hyperfine splitting of parallel orientation resulting from the interaction of an unpaired electron with copper nuclei ( $I = 3/2$ ). The spin Hamiltonian parameters are obtained by computer simulation of the experimental spectra with  $g_x = g_y = g_{\perp} = 2.065$ ,  $g_z = g_k = 2.211$  and  $A_k = 164$  G for **IrPCpCu**,  $g_x = 2.069$ ,  $g_y = 2.073$ ,  $g_z = g_k = 2.215$  and  $A_k = 113$  G for **IrPNrCu**,  $g_x = g_y = g_{\perp} = 2.098$ ,  $g_z = g_k = 2.289$  and  $A_k = 163$  G for **IrPLmCu**.

### Biological properties

The comparison of the IC<sub>50</sub> values determined for homo- and heteronuclear complexes (**Tab. 3**) showed that the presence of the second metal caused a significant increase in cytotoxic activity against MCF7 and A549 cell lines, and most importantly a reduction in toxicity against normal cell lines (HEK293T). Additionally, what was remarkable, despite the addition of a second metal with phenanthroline - which is known to be toxic - there was a significant reduction in toxicity to normal cell lines by more than 40 times than cisplatin. This suggests that the introduction of a second metal is an effective method of minimizing toxicity to healthy cells and may bring into play different properties of the resulting compound. Interestingly, human lung adenocarcinoma (A549) was the most sensitive cell line to heteronuclear Ir<sup>III</sup>/Cu<sup>II</sup> complexes even in the case of both experimental approaches (24 h and 24 h + 48 h treatment with the examined compounds). *In vitro* cytotoxicity assays were also carried out within multicellular tumor spheroids and efficient anticancer action on these 3D assemblies was demonstrated.

**Table 3** Values of IC<sub>50</sub> [μM] (concentration of a drug required to inhibit the growth of 50% of the cells) for WM2661, A549, MCF7, PANC-1, DU-145, HEK293T cells after 24 h and 24 h + 48 h treatment with the studied compounds and cisplatin as reference

IC <sub>50</sub> [μM] ± SD; 24 h					
	A549	MCF7	DU-145	WM2664	HEK293T
<b>IrPCpCu</b>	35.5 ± 5.6E-03	35.3 ± 6.5	12.8 ± 2.7E-07	12.8 ± 2.7E-07	786.8 ± 11.2
<b>IrPLmCu</b>	31.6 ± 7.6E-03	24.2 ± 7.22	14.2 ± 2.4E-03	10.1 ± 2.2E-03	775.8 ± 15.7
<b>IrPNrCu</b>	11.2 ± 7.8E-03	29.97 ± 0.67	10.8 ± 1.9E-04	9.9 ± 3.8E-03	756.8 ± 5.7
<b>cisplatin</b>	>100	51.9 ± 4.6	>100	2.63 ± 0.6	21.0 ± 1.8
IC <sub>50</sub> [μM] ± SD; 72 h (24 h + 48 h)					
<b>IrPCpCu</b>	42.4 ± 7.3E-05	>1000	125.7 ± 3.4	137.1 ± 2.2	886.8 ± 12.7
<b>IrPLmCu</b>	36.0 ± 2.2E-02	>1000	126.2 ± 4.4	229.3 ± 25.9	822.8 ± 12.3
<b>IrPNrCu</b>	36.6 ± 2.8E-03	>1000	122.7 ± 5.4	155.1 ± 3.2	856.8 ± 15.9
<b>cisplatin</b>	71.7 ± 3.7	17.7 ± 8.6	65.5 ± 3.6	8.29 ± 0.4	10.3 ± 2.1

In order to increase the cellular accumulation of heteronuclear complexes and to control their uptake only to neoplastic cells, bypassing healthy cells - as was the case with homonuclear complexes - we encapsulated compounds in liposomes. In the case of DU145 line, it can be observed as a 10-fold decrease in cytotoxicity (**Tab. 4**).

<b>Table 4</b> IC <sub>50</sub> (µg/ml and µM) values of the investigated compounds toward the selected cancer cell lines for 24 h.			
	HaCaT	A549	DU145
<b>L</b>	180.47±0.108 µg/mL	21,18±0,1430 µg/mL	12,56 ± 0,1746 µg/mL
<b>IrPCpCu</b>	200.68±2.081 µM	9.47±0.261 µM	1.34±0.051 µM
<b>cisplatin</b>	32.20±0.881 µM	>100	>100

In addition, the accumulation of liposome compounds was confirmed by ICP-MS and a confocal microscope. For all tumor cell lines, a significant increase in iridium accumulation was detected after incubation with compounds as compared to normal control cells. Furthermore, analyses of the cross-sectional images, nuclei specific probe Hoechst33342 (blue) and intensity of the emission bands of the cancer cells proved clearly that the compounds penetrate into the tumor cells. This analysis proves that the heteronuclear complexes accumulate in the nucleus. A precise cytometric analysis revealed a predominance of apoptosis over the other types of cell death. Furthermore, the investigated nanoformulation may induce changes in the cell cycle leading to S phase arrest in a dose-dependent manner.

## 7.2. Magnetic drug targeting – nanoformulation

A promising approach to drug delivery is to target drugs magnetically, *e.g.* with an applied magnetic field, taking advantage of the fact that the drug delivery vehicle has a strong magnetic moment. For this purpose, it was decided to use the well-known magnetic properties of magnetite (Fe<sub>3</sub>O<sub>4</sub>) particles, which, after being minimized to nanometric structures, are characterized by the phenomenon of superparamagnetism. In practice, this phenomenon consists in imparting magnetic properties to nanomaterials after applying an external magnetic field and their extinction after removing the source of the magnetic field. The fragmentation of the material causes the separation of magnetic domains, which significantly reduces the value of the coercivity and makes them applicable in the human body. The reason for the use of iron oxides as magnetic nano molecules in biological applications is the fact that iron oxide nanoparticles show low cytotoxicity, unlike other ferromagnetic materials. Moreover, they have an easily functionalized material surface, which allows for high biocompatibility with biological material. Nevertheless, the magnet geometry and the tumor-magnet distance are critical to the efficient delivery of magnetic compounds.

In the first stage, it was chosen one complex **IrPOH** ( $\text{Ir}(\eta^5\text{-Cp}^*)\text{Cl}_2\text{PPh}_2\text{CH}_2\text{OH}$ ), which presents high cytotoxicity to the A549 human lung adenocarcinoma. This compound was surrounded by a polymeric micelle doped with a properly selected amount of  $\text{Fe}_3\text{O}_4$  particles with a grain size of 10 nm. The presence of magnetite nanoparticles in examine material was confirmed by magnetic measurements (DC) using a superconducting quantum interference device (SQUID) within a magnetic field of 0 – 5 T (**Fig. 37**) at 2 and 300 K. The results clearly show the superparamagnetic behavior of nanoparticles. The magnetization vs magnetic field curve indicates a nonlinear variation at all measuring temperature; 2, 5, and 300K (**Fig. 37**).

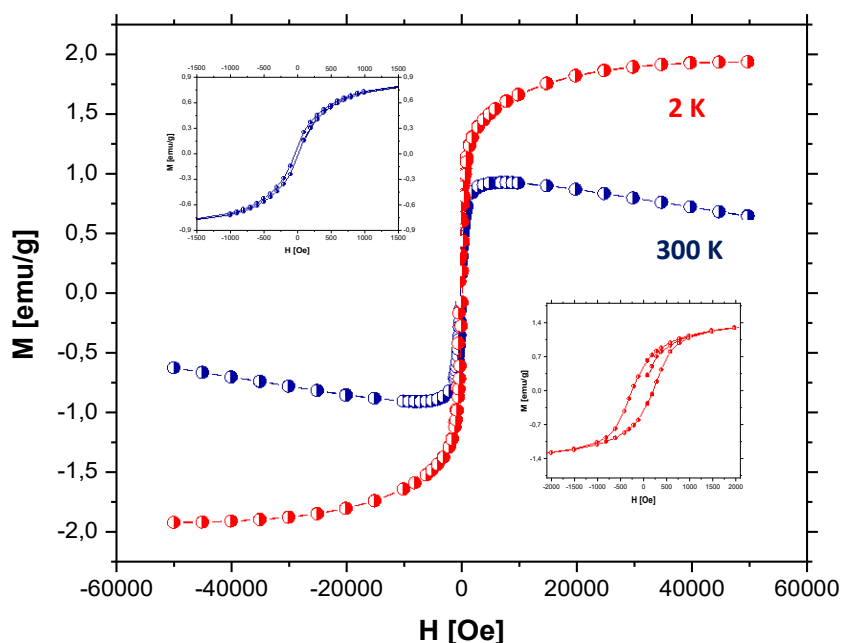


**Figure 37** Field H dependence of magnetization M of **IrPOH** - M at 2 K (red circle) and 300 K (blue circle).

This sample is saturated at the low magnetic field with the  $M_s$  saturation magnetization value (obtained as an extrapolation to the zero-field from the high field area in  $M(H)$ ) of 2.1 EMU/g (at 2 K) and 1.2 EMU/g (at 300 K). The former is significantly lower than the saturation magnetization of bulk magnetite ( $M_s \text{ bulk} = 98 \text{ EMU/g}$ ) [127] which may be the result of the final particle size effect and high surface area to volume ratio, the spin deflection effect at the grain boundary or the presence of other materials in the examined species that may lead to a reduction of the effective magnetic moment [128]. At 300 K, the coercivity (28.3 Oe) and remanence values (0.2 EMU/g) are not discernible, indicating a superparamagnetic

behavior while at 2 K the value of coercivity (251 Oe) and remanence (1.9 EMU/g) showing a ferrimagnetic behavior.

*The obtained core/shell structures are the starting point for further modifications aimed at giving the magnetic nanoparticles appropriate functions and properties. Moreover, such intelligent materials can deliver drugs directly to the diseased tissue thanks to the magnetic field - thanks to this solution; we can avoid systemic toxicity as the drug will be delivered only to the diseased area.*

## 8. References

- [1] H. Sung, J. Ferlay, R.I. Siegel, M. Laversanne, I. Soerjomataram, A. Jemal, F. Bray, Global Cancer Statistics 2020: GLOBOCAN Estimates of Incidence and Mortality Worldwide for 36 Cancers in 185 Countries, *CA Cancer J Clin.*, 2021, **3**, 209-249
- [2] H.K. Weir, R.N. Anderson, S.M. Coleman King, A. Soman, T.D. Thompson, Y. Hong, B. Moller, S. Leadbetter, Heart Disease and Cancer Deaths - Trends and Projections in the United States, 1969-2020. *Prev Chronic Dis.*, 2016, **13**, E157
- [3] N.J. Wheate, S. Walker, G.E. Craig, R. Oun, The status of platinum anticancer drugs in the clinic and in clinical trials, *Dalton Trans.*, 2010, **35**, 8113-8127
- [4] S. Dasari, P.B. Tchounwou, Cisplatin in cancer therapy: molecular mechanisms of action. *Eur J Pharmacol.*, 2014, **740**, 364-378
- [5] A. Brown, S. Kumar, P.B. Tchounwou, Cisplatin-Based Chemotherapy of Human Cancers, *J Cancer Sci Ther.* 2019, **11**, 94-95
- [6] D. Hanahan, R.A. Weinberg, The hallmarks of cancer, *Cell.*, 2000, **100**, 57-70
- [7] E. Espinosa, P. Zamora, J. Feliu, M. González Barón, Classification of anticancer drugs--a new system based on therapeutic targets, *Cancer Treat Rev.*, 2003, **29**, 515-523
- [8] U. Ndagi, N. Mhlongo, M.E. Soliman, Metal complexes in cancer therapy - an update from drug design perspective, *Drug Des Devel Ther.*, 2017, **11**, 599-616
- [9] P. Pedrosa, A. Carvalho, P. V. Baptista, and A. R. Fernandes, Inorganic Coordination Chemistry: Where We Stand in Cancer Treatment?, in *Basic Concepts Viewed from Frontier in Inorganic Coordination Chemistry.*, London, United Kingdom: IntechOpen, 2018
- [10] Q. Du, Y. Yang, L. Guo, M. Tian, X. Ge, Z. Tian, L. Zhao, Z. Xu, J. Li, Z. Liu, Fluorescent half-sandwich phosphine-sulfonate iridium(III) and ruthenium(II) complexes as potential lysosome-targeted anticancer agents, *Dyes Pigm.*, 2019, **162**, 821-830
- [11] R.H Crabtree. The organometallic chemistry of the transition metals, Inc., Hoboken, New Jersey; 2005
- [12] Z. Liu, A. Habtemariam, A.M. Pizarro, S.A. Fletcher, A. Kisova, O. Vrana, L. Salassa, P.C. Bruijninx, G.J. Clarkson, V. Brabec, P.J. Sadler, Organometallic half-sandwich iridium anticancer complexes, *J Med Chem.*, 2011, **54**, 3011-3026
- [13] S. Ajay Sharma, P. Sudhindra, R. Nilmadhab, P. Priyankar, Advances in novel iridium (III) based complexes for anticancer applications: A review, *Inorg. Chim. Acta*, 2020, **513**, 119925
- [14] Z. Liu, P.J. Sadle, Organoiridium complexes: anticancer agents and catalysts. *Acc Chem Res.*, 2014, **47**, 1174-1185
- [15] C. Liao, D. Xu, X. Liu, Y. Fang, J. Yi, X. Li, B. Guo, Iridium (III) complex-loaded liposomes as a drug delivery system for lung cancer through mitochondrial dysfunction, *Int J Nanomedicine*, 2018, **13**, 4417- 4431
- [16] J. Kim, O. De Jesus, Medication Routes of Administration, In: StatPearls, 2022

- [17] A. Baldi, M. Chaudhary, S. Sethi, Abhiav, R. Chandra, J. Madan, Armamentarium of nanoscaled lipid drug delivery systems customized for oral administration: In silico docking patronage, absorption phenomenon, preclinical status, clinical status and future prospects, *Colloids Surf B Biointerfaces*, 2018, **170**, 637-647
- [18] J.Y.C. Edgar, H. Wang, Introduction for Design of Nanoparticle Based Drug Delivery Systems, *Curr Pharm Des.*, 2017, **23**, 2108-2112
- [19] H. Jahangirian, E.G. Lemraski, T.J. Webster, R. Rafiee-Moghaddam, Y. Abdollahi, A review of drug delivery systems based on nanotechnology and green chemistry: green nanomedicine, *Int. J. Nanomed.*, 2017, **12**, 2957-2978
- [20] A. Kermanizadeh, L.G. Powell, V. Stone, P. Møller, Nanodelivery systems and stabilized solid-drug nanoparticles for orally administered medicine: current landscape, *Int. J. Nanomed.*, 2018, **13**, 7575-7605
- [21] X. Tan, X. Liu, Y. Zhang, H. Zhang, X. Lin, C. Pu, J. Gou, H. He, T. Yin, Y. Zhang, X. Tang, Silica nanoparticles on the oral delivery of insulin, *Expert Opin. Drug Deliv.*, 2018, **15**, 805-820
- [22] Y. Yun, Y.W. Cho, K. Park, Nanoparticles for oral delivery: targeted nanoparticles with peptidic ligands for oral protein delivery, *Adv. Drug Deliv. Rev.*, 2013, **65**, 822-832
- [23] A. Manke, L. Wang, Y. Rojanasakul, Mechanisms of nanoparticle-induced oxidative stress and toxicity, *Biomed Res Int.*, 2013, **2013**, 942916
- [24] M. Motornov, Y. Roiter, I. Tokarev, S. Minko, Stimuli-responsive nanoparticles, nanogels and capsules for integrated multifunctional intelligent systems, *Prog Polym Sci.*, 2010, **35**, 174-211
- [25] P. Tharkar, R. Varanasi, W.S.F. Wong, C.T. Jin, W. Chrzanowski, Nano-Enhanced Drug Delivery and Therapeutic Ultrasound for Cancer Treatment and Beyond, *Front Bioeng Biotechnol.*, 2019, **7**, 324
- [26] M. Creixell, A.C. Bohórquez, M. Torres-Lugo, C. Rinaldi, EGFR-Targeted Magnetic Nanoparticle Heaters Kill Cancer Cells without a Perceptible Temperature Rise, *ACS Nano*, 2011, **9**, 7124–7129
- [27] P. Pradhan, J. Giri, R. Banerjee, J. Bellare, D. Bahadur, Preparation and characterization of manganese ferrite-based magnetic liposomes for hyperthermia treatment of cancer, *J Magn Magn Mater.*, 2007, **311**, 208-215
- [28] S.A. Torres-Pérez, C.E. Torres-Pérez, M. Pedraza-Escalona, S.M. Pérez-Tapia, E. Ramón-Gallegos Glycosylated Nanoparticles for Cancer-Targeted Drug Delivery, *Front Oncol.*, 2020, **10**: 605037
- [29] X. Li, Wei J, K.E. Aifantis, Y. Fan, Q. Feng, F.Z. Cui, F. Watari, Current investigations into magnetic nanoparticles for biomedical applications, *J Biomed Mater Res A.*, 2016, **104**, 1285-1296
- [30] L. Mohammed, H.G. Gomaa, D. Ragab, J. Zhu, Magnetic nanoparticles for environmental and biomedical applications: A review, *Particuology*, 2017, **30**, 1-14
- [31] L.H. Reddy, J.L. Arias, J. Nicolas, P. Couvreur, Magnetic nanoparticles: design and characterization, toxicity and biocompatibility, pharmaceutical and biomedical applications, *Chem. Rev.* 2012, **112**, 5818–5878



- [32] R. Crabtree, Iridium compounds in catalysis, *Acc. Chem. Res.*, 1979, **12**, 331–337
- [33] J. Schneekönig, W. Liu, T. Leischner, K. Junge, C. Schotes, C. Beier, M. Beller, Application of Crabtree/Pfaltz-Type Iridium Complexes for the Catalyzed Asymmetric Hydrogenation of an Agrochemical Building Block, *Org. Process Res. Dev.*, 2020, **24**, 443–447
- [34] W.Y. Zhang, F. Du, M. He, L. Bai, Y.Y. Gu, L.L. Yang, Y.J. Liu. Studies of anticancer activity in vitro and in vivo of iridium(III) polypyridyl complexes-loaded liposomes as drug delivery system, *Eur J Med Chem.*, 2019, **178**, 390-400
- [35] J.-B. Liu, K. Vellaisamy, G. Li, C. Yang, S.-Y. Wong, C.-H. Leung, S.-Z. Pu, D.-L. Ma, A long-lifetime iridium(III) complex for lysosome tracking with high specificity and a large Stokes shift, *J. Mater. Chem. B*, 2018, **6**, 3855-3858
- [36] L. He, K. Xiong, L. Wang, R. Guan, Y. Chen, L. Ji, H. Chao, Iridium(III) complexes as mitochondrial topoisomerase inhibitors against cisplatin-resistant cancer cells, *Chem. Commun.*, 2021, **57**, 8308-8311
- [37] J.-Q. Wang, X.-J. Hou, H.-B. Bo, Q.-z. Chen, A cyclometalated iridium(III) complex that induces apoptosis in cisplatin-resistant cancer cells, *Inorg. Chem. Commun.*, 2015, **61**, 31-34
- [38] Q. Xiao, Z. Zhao, K. Lina, J. Wang, A phosphorescent cyclometalated iridium(III) complex as mitochondria-targeted theranostic anticancer agent, *Inorg. Chem. Commun.*, 2019, **94**, 75-79
- [39] T. Giraldi, G. Sava, G. Mestroni, G., Zassinovich, D. Stofa, Antitumour Action of Rhodium (I) and Iridium (I) Complexes, *Chem.-Biol. Interact.*, 1978, **22**, 231–238
- [40] G. Sava, S. Zorzet, L. Perissin, G. Mestroni, Zassinovich G.; Bontempi A. Coordination Metal Complexes of Rh(I), Ir(I) and Ru(II): Recent Advances on Antimetastatic Activity on Solid Mouse Tumors. *Inorg. Chim. Acta* 1987, **137**, 69–71
- [41] A. De Palo, D. Draca, M.G. Murrari, S. Zacchini, G. Pampaloni, S. Mijatovic, D. Maksimovic-Ivanic, F. Marchetti, A Comparative Analysis of the In Vitro Anticancer Activity of Iridium(III)  $\{\eta^5\text{-C}_5\text{Me}_4\text{R}\}$  Complexes with Variable R Groups., *Int J Mol Sci.*, 2021, **22**, 7422
- [42] E. Armingol, A. Officer, O. Harismendy, N.E. Lewis, Deciphering cell–cell interactions and communication from gene expression. *Nat Rev Genet.*, 2021, **22**, 71–88
- [43] J.M. Hearn, I. Romero-Canelón, B. Qamar, Z. Liu, I. Hands-Portman, P.J. Sadler, Organometallic Iridium(III) Anticancer Complexes with New Mechanisms of Action: NCI-60 Screening, Mitochondrial Targeting, and Apoptosis, *ACS Chem. Biol.*, 2013, **8**, 1335–1343
- [44] Z. Liu, A. Habtemariam, A.M. Pizarro, G.J. Clarkson, P.J. Sadler, Organometallic Iridium(III) Cyclopentadienyl Anticancer Complexes Containing C,N-Chelating Ligand, *Organometallics*, 2011, **30**, 4702–4710
- [45] Y. Yang, L. Guo, X. Ge, T. Zhu, W. Chen, H. Zhou, L. Zhao, Z. Liu, The Fluorine Effect in Zwitterionic Half-Sandwich Iridium(III) Anticancer Complexes, *Inorg. Chem.*, 2020, **59**, 748–758
- [46] Z. Liu, I. Romero-Canelón, A. Habtemariam, G.J. Clarkson, P.J. Sadler, Potent Half-Sandwich Iridium(III) Anticancer Complexes Containing C,N-Chelated and Pyridine Ligands, *Organometallics*, 2018, **37**, 2880–2889
- [47] G.A. Van Norman, Drugs, Devices, and the FDA: Part 1: An Overview of Approval Processes for Drugs, *JACC Basic Transl Sci.*, 2016, **1**, 170-179

- [48] Institute of Medicine (US) Committee on Accelerating Rare Diseases Research and Orphan Product Development; Field MJ, Boat TF, editors. Rare Diseases and Orphan Products: Accelerating Research and Development. Washington (DC): National Academies Press (US); 2010. 5, Development of New Therapeutic Drugs and Biologics for Rare Diseases. Available from: <https://www.ncbi.nlm.nih.gov/books/NBK56179/>
- [49] K. Chauhan, P. Singh, V. Kumar, P.K. Shukla, M.I. Siddiqi, P.M. Chauhan, Investigation of Ugi-4CC derived 1H-tetrazol-5-yl-(aryl) methyl piperazinyl-6-fluoro-4-oxo-1,4-dihydroquinoline-3-carboxylic acid: synthesis, biology and 3D-QSAR analysis, *Eur J Med Chem.*, 2014, **78**, 442-54
- [50] A. Foroumadi, S. Ghodsi, S. Emami, S. Najjari, N. Samadi, M.A. Faramarzi, L. Beikmohammadi, F.H. Shirazi, A. Shafiee, Synthesis and antibacterial activity of new fluoroquinolones containing a substituted N-(phenethyl)piperazine moiety, *Bioorg Med Chem Lett.*, 2006, **16**, 3499-503
- [51] A. Foroumadi, S. Emami, S. Mansouri, A. Javidnia, N. Saeid-Adeli, F.H. Shirazi, A. Shafiee, Synthesis and antibacterial activity of levofloxacin derivatives with certain bulky residues on piperazine ring, *J. Med. Chem.*, 2007, **42**, 985–992
- [52] Y.-L. Zhao, Y.-L. Chen, J.-Y. Sheu, I.-L. Chen, T.-C. Wang, C.-C. Tzeng, Synthesis and antimycobacterial evaluation of certain fluoroquinolone derivatives, *Bioorg. Med. Chem.*, 2005, **13**, 3921–3926
- [53] S. Jazayeri, M.H. Moshafi, L. Firoozpour, S. Emami, S. Rajabalian, M. Haddad, F. Pahlavanzadeh, M. Esnaashari, A. Shafiee, A. Foroumadi, Synthesis and antibacterial activity of nitroaryl thiadiazole–gatifloxacin hybrids, *Eur. J. Med. Chem.*, 2009, **44**, 1205–1209
- [54] A. Bykowska, R. Starosta, A. Brzuszkiewicz, B. Bażanów, M. Florek, N. Jackulak, J. Król, J. Grzesiak, K. Kaliński, M. Jeżowska-Bojczuk, Synthesis, properties and biological activity of a novel phosphines ligand derived from ciprofloxacin, *Polyhedron*, 2013, **60**, 23-29
- [55] A. Bykowska, R. Starosta, U. K. Komarnicka, Z. Ciunik, A. Kyzioł, K. Guz-Regner, G. Bugła-Płoskońska, M. Jeżowska-Bojczuk, Phosphine derivatives of ciprofloxacin and norfloxacin, a new class of potential therapeutic agents, *New J. Chem.*, 2014, **38**, 1062-1071
- [56] U.K. Komarnicka, R. Starosta, K. Guz-Regner, G. Bugła-Płoskońska, A. Kyzioł, M. Jeżowska-Bojczuk, Phosphine derivatives of sparfloxacin – Synthesis, structures and in vitro activity, *J. Mol. Struct.*, 2015, **1096**, 55-63
- [57] U.K. Komarnicka, R. Starosta, A. Kyzioł, M. Płotek, M. Puchalska, M. Jeżowska-Bojczuk, New copper(I) complexes bearing lomefloxacin motif: Spectroscopic properties, in vitro cytotoxicity and interactions with DNA and human serum albumin, *J Inorg. Bio.*, 2016, **165**, 25-35
- [58] U.K. Komarnicka, R. Starosta, A. Kyzioł, M. Jeżowska-Bojczuk, Copper(i) complexes with phosphine derived from sparfloxacin. Part I – structures, spectroscopic properties and cytotoxicity, *Dalton Trans.*, 2015, **44**, 12688-12699
- [59] V.T. Andriole, The quinolones: past, present, and future, *Clin Infect Dis.*, 2005, **41**, 113-119
- [60] T.D.M. Pham, Z.M. Ziora, M.A.T. Blaskovich, Quinolone antibiotics, *Med chem. comm.*, 2019, **10**, 1719-1739

- [61] G.A.R.Y. Suaifan, A.A.M. Mohammed, Fluoroquinolones structural and medicinal developments (2013-2018): Where are we now?, *Bioorg Med Chem.*, 2019, **27**, 3005-3060
- [62] V. Yadav, P. Talwar, Repositioning of fluoroquinolones from antibiotic to anti-cancer agents: An underestimated truth, *Biomed Pharmacother.*, 2019, **111**, 934-946
- [63] R.J. Fair, Y. Tor, Antibiotics and bacterial resistance in the 21st century, *Perspect Medicin Chem.*, 2014, **6**, 25-64
- [64] G.A. Jacoby, Mechanisms of resistance to quinolones, *Clin Infect Dis.*, 2005, **41**, 120-126
- [65] D.C. Hooper, Mechanisms of fluoroquinolone resistance, *Drug Resist Updat.*, 1999, **2**, 38-55
- [66] C.T. Walsh, T.A. Wenczewicz, Prospects for new antibiotics: a molecule-centered perspective, *J Antibiot (Tokyo)*, 2014, **67**, 7-22
- [67] A. Beberok, D. Wrześniok, A. Minecka, J. Rok, M. Delijewski, Z. Rzepka, M. Respondek, E. Buszman, Ciprofloxacin-mediated induction of S-phase cell cycle arrest and apoptosis in COLO829 melanoma cells, *Pharmacol Rep.*, 2018, **70**, 6-13
- [68] A. Beberok, D. Wrześniok, J. Rok, Z. Rzepka, M. Respondek, E. Buszman, Ciprofloxacin triggers the apoptosis of human triple-negative breast cancer MDA-MB-231 cells via the p53/Bax/Bcl-2 signaling pathway, *Int J Oncol.*, 2018, **52**, 1727-1737
- [69] C. Herold, M. Ocker, M. Ganslmayer, H. Gerauer, E.G. Hahn, D. Schuppan, Ciprofloxacin induces apoptosis and inhibits proliferation of human colorectal carcinoma cells, *Br J Cancer.*, 2002, **86**, 443-448
- [70] V. Yadav, P. Varshney, S. Sultana, J. Yadav, N. Saini, Moxifloxacin and ciprofloxacin induces S-phase arrest and augments apoptotic effects of cisplatin in human pancreatic cancer cells via ERK activation, *BMC Cancer.*, 2015, **15**, 581
- [71] O. Aranha, R. Grignon, N. Fernandes, T.J. McDonnell, D.P. Wood Jr, F.H. Sarkar, Suppression of human prostate cancer cell growth by ciprofloxacin is associated with cell cycle arrest and apoptosis, *Int J Oncol.*, 2003, **22**, 787-794
- [72] P. Perucca, M. Savio, O. Cazzalini, R. Mocchi, C. Maccario, S. Sommatitis, D. Ferraro, R. Pizzala, L. Pretali, E. Fasani, A. Albini, L.A. Stivala, Structure-activity relationship and role of oxygen in the potential antitumour activity of fluoroquinolones in human epithelial cancer cells, *J. Photochem. Photobiol. B*, 2014, **140**, 57-68
- [73] H.H.H. Mohammed, A.A. Abd El-Hafeez, S.H. Abbas, E-S.M.N. Abdelhafez, GE.-DA. Abuo-Rahma, New antiproliferative 7-(4-(N-substituted carbamoylmethyl)piperazin-1-yl) derivatives of ciprofloxacin induce cell cycle arrest at G2/M phase. *Bioorg Med Chem.* 2016, **24**, 4636-46
- [74] A. Beberok, D. Wrześniok, M. Szlachta, J. Rok, Z. Rzepka, M. Respondek, E. Buszman, Lomefloxacin Induces Oxidative Stress and Apoptosis in COLO829 Melanoma Cells. *Int J Mol Sci.*, 2017, **18**, 2194
- [75] C. Abu-Gnim, I. Amer, Phosphine oxides as ligands in the hydroformylation reaction, *J. Organomet. Chem.*, 1996, **516**, 235-243
- [76] P. Smoleński, F.P. Pruchnik, Aminoalkylphosphines, the Water Soluble Chiral Phosphines, *Pol. J. Chem.* 2007, **81**, 1771-1776

- [77] K. Raghuraman, K.K. Katti, L.J. Barbour, N. Pillarsetty, C.L. Barnes, K.V. Katti, Characterization of supramolecular (H<sub>2</sub>O)<sub>18</sub> water morphology and water-methanol (H<sub>2</sub>O)<sub>15</sub>(CH<sub>3</sub>OH)<sub>3</sub> clusters in a novel phosphorus functionalized trimeric amino acid host, *J Am Chem Soc.*, 2003, **125**, 6955-61
- [78] D.E. Berning, K.V. Katti, C.L. Barnes, W.A. Volkert, Chemical and Biomedical Motifs of the Reactions of Hydroxymethylphosphines with Amines, Amino Acids, and Model Peptides, *J. Am. Chem. Soc.*, 1999, **121**, 1658–1664
- [79] S. Deshayes, M.C. Morris, G. Divita, F. Heitz, Cell-penetrating peptides: tools for intracellular delivery of therapeutics, *Cell Mol Life Sci.*, 2005, **62**, 1839-1849
- [80] M.C. Garnett, Targeted drug conjugates: principles and progress, *Adv Drug Deliv Rev.*, 2001, **53**, 171-216
- [81] A. Kyzioł, A. Cierniak, J. Gubernator, A. Markowski, M. Jeżowska-Bojczuk, U. K. Komarnicka, Copper(i) complexes with phosphine derived from sparfloxacin. Part III: multifaceted cell death and preliminary study of liposomal formulation of selected copper(i) complexes, *Dalton Trans.*, 2018, **47**, 1981-1992
- [82] P. Kołoczek, A. Skórska-Stania, A. Cierniak, V. Sebastian, U.K. Komarnicka, M. Płotek, A. Kyzioł, Polymeric micelle-mediated delivery of half-sandwich ruthenium(II) complexes with phosphanes derived from fluoroloquinolones for lung adenocarcinoma treatment, *Eur J Pharm Biopharm.*, 2018, 128:69-81
- [83] A. Bykowska, U.K. Komarnicka, M. Jeżowska-Bojczuk, A. Kyzioł, CuI and CuII complexes with phosphine derivatives of fluoroquinolone antibiotics - A comparative study on the cytotoxic mode of action, *J Inorg Biochem.*, 2018, **181**, 1-10
- [84] S. Gavas, S. Quazi, T.M., Karpiński Nanoparticles for Cancer Therapy: Current Progress and Challenges, *Nanoscale Res Lett.*, 2021, **16**, 173
- [85] N. Baig, I. Kammakakam, W. Falathabe, Nanomaterials: a review of synthesis methods, properties, recent progress, and challenges, *Mater. Adv.*, 2021, **2**, 1821-1871
- [86] Z. Li, S. Tan, S. Li, Q. Shen, K. Wang, Cancer drug delivery in the nano era: An overview and perspectives (Review), *Oncol Rep.*, 2017, **38**, 611-624
- [87] J. Wang, S. Li, Y. Han, J. Guan, S. Chung, C. Wang, D. Li, Poly(Ethylene Glycol)-Polylactide Micelles for Cancer Therapy, *Front Pharmacol.*, 2018, **9**, 202
- [88] Z. Hussain, S. Khan, M. Imran, M. Sohail, S.W.A. Shah, M. de Matas, PEGylation: a promising strategy to overcome challenges to cancer-targeted nanomedicines: a review of challenges to clinical transition and promising resolution, *Drug Deliv Transl Res.*, 2019, **9**, 721-734
- [89] Y. Li, T. Zhang, Q. Liu, J. He, PEG-Derivatized Dual-Functional Nanomicelles for Improved Cancer Therapy, *Front Pharmacol.*, 2019, **10**, 808
- [90] Y. Matsumura, K. Kataoka, Preclinical and clinical studies of anticancer agent-incorporating polymer micelles, *Cancer Sci.*, 2009, **100**, 572-579
- [91] K. Miyata, N. Nishiyama, K. Kataoka, Rational design of smart supramolecular assemblies for gene delivery: chemical challenges in the creation of artificial viruses, *Chem. Soc. Rev.*, 2012, **41**, 2562-2574

- [92] H. Pandey, R. Rani, V. Agarwal, Liposome and Their Applications in Cancer Therapy, *Braz. arch. biol. technol.*, 2016, **59**
- [93] E. Beltrán-Gracia, A. López-Camacho, I. Higuera-Ciapara, J.B. Velázquez-Fernández, A.A. Vallejo-Cardona, Nanomedicine review: clinical developments in liposomal applications, *Cancer Nano.*, 2019, **10**, 11
- [94] S. Salatin, A.Y. Khosroushahi, Overviews on the cellular uptake mechanism of polysaccharide colloidal nanoparticles, *J Cell Mol Med.*, 2017, **21**, 1668-1686
- [95] M. Musielak, J. Potoczny, A. Boś-Liedke, M. Kozak, The Combination of Liposomes and Metallic Nanoparticles as Multifunctional Nanostructures in the Therapy and Medical Imaging- A Review, *Int J Mol Sci.*, 2021, **22**, 6229
- [96] H. Nobuto, T. Sugita, T. Kubo, S. Shimose, Y. Yasunaga, T. Murakami, M. Ochi, Evaluation of systemic chemotherapy with magnetic liposomal doxorubicin and a dipole external electromagnet, *Int J Cancer.*, 2004, **109**, 627-635
- [97] T.A.P. Rocha-Santos, Sensors and biosensors based on magnetic nanoparticles, *Trends Anal. Chem.*, 2014, **62**, 28-36
- [98] K.M.Koo, N. Soda. M.J.A.Shiddiky, Magnetic nanomaterial-based electrochemical biosensors for the detection of diverse circulating cancer biomarkers, *Curr. Opin.Electrochem.*, 2021, **25**, 100645
- [99] K.El-Boubbou, Magnetic iron oxide nanoparticles as drug carriers: clinical relevance, *Nanomedicine*, 2018, **13**
- [100] P.M. Price, W.E. Mahmoud, A.A. Al-Ghamdi, L.M..Bronstein, Magnetic Drug Delivery: Where the Field Is Going, *Front Chem.*, 2018, **6**, 619
- [101] K.H. Choi, K.C. Nam, U.H. Kim, G. Cho, J.S. Jung, B.J.Park, Optimized Photodynamic Therapy with Multifunctional Cobalt Magnetic Nanoparticles, *Nanomaterials(Basel).*, 2017, **7**, 144.
- [102] H. Hou, X. Huang, G. Wei, F. Xu, Y. Wang, S. Zhou, Fenton Reaction-Assisted Photodynamic Therapy for Cancer with Multifunctional Magnetic Nanoparticles, *ACS Appl. Mater. Interfaces*, 2019, **11**, 29579–29592
- [103] C.S.S.R.Kumar, F. Mohammada, Magnetic nanomaterials for hyperthermia-based therapy and controlled drug delivery, *Adv. Drug Deliv. Rev.*, 2011, **63**, 789-808
- [104] M. Kalubowilage, K.Janik, S.H. Bossmann, Magnetic Nanomaterials for Magnetically-Aided Drug Delivery and Hyperthermia, *Appl. Sci.*, 2019, **9**, 2927
- [105] A. Avasthi, C. Caro, E. Pozo-Torres, M.P. Leal, M.L.García-Martín, Magnetic Nanoparticles as MRI Contrast Agents, *Top Curr Chem (Cham).*, 2020, **378**, 40
- [106] M. Ferreira, J. Sousa, A. Pais, C.Vitorino, The Role of Magnetic Nanoparticles in Cancer Nanotheranostics, *Materials (Basel).*, 2020, **13**, 266
- [107] E. Pereira-Maia, A. Garnier-Suillerot, Impaired hydrolysis of cisplatin derivatives to aquated species prevents energy-dependent uptake in GLC4 cells resistant to cisplatin, *J. Biol. Inorg. Chem.*, 2003, **8**, 626-634
- [108] E.J. Anthony, E.M. Bolitho, H.E. Bridgewater, O.W.L. Carter, J.M. Donnelly, C. Imberti, E.C. Lant, F. Lermyte, R.J. Needham, M. Palau, P.J. Sadler, H. Shi, F.X. Wang, W.Y. Zhang,

Z.Zhang, Metallodrugs are unique: opportunities and challenges of discovery and development, *Chem Sci.*, 2020, **11**, 12888-12917

[109] F. Wang, H. Chen, S. Parsons, I.D. Oswald, J.E. Davidson, P.J.Sadler, Kinetics of aquation and anation of ruthenium(II) arene anticancer complexes, acidity and X-ray structures of aqua adducts, *Chemistry.*, 2003, **9**, 5810-5820

[110] C. Wu, Q. Li, X. Zhang, C. Shi, G. Li, M. Wang, K. Li, A. Yuan, Tuning the Photophysical and Excited State Properties of Phosphorescent Iridium(III) Complexes by Polycyclic Unit Substitution. *ChemistryOpen.*, 2019, **8**, 339-343

[111] X. Liu, M. Shao, C. Liang, J. Guo, G. Wang, X.A. Yuan, Z. Jing, L. Tian, Z. Liu, Preparation and Bioactivity of Iridium(III) Phenanthroline Complexes with Halide Ions and Pyridine Leaving Groups. *Chembiochem.*, 2021, **22**, 557-564

[112] L.Helm, A.E.Merbach, Water exchange on metal ions: experiments and simulations, *Coord. Chem. Rev.*, 1999, **187**, 151-181

[113] G.Sava, S.Pacor, G.Mestroni, E.Alessio, Na[trans-RuCl<sub>4</sub>(DMSO)Im], a metal complex of ruthenium with antimetastatic properties, *Clin. Exp. Metastasis*, 1992, **10**, 273– 280

[114] S. J. Han, S. Kwon, K. S. Kim, Challenges of applying multicellular tumor spheroids in preclinical phase, *Cancer Cell International*, 2021, **21**, 152

[115] R. Gerl, D. L. Vaux, Apoptosis in the development and treatment of cancer, *Carcinogenesis*, 2005, **26**, 263-270

[116] W.R. Sellers, D.E.Fisher, Apoptosis and cancer drug targeting, *J Clin Invest.*, 1999, **104**, 1655-1661

[117] N.R. Jog, R.Caricchio, The role of necrotic cell death in the pathogenesis of immune mediated nephropathies, *Clin Immunol.*, 2014, **153**, 243-253

[118] X. Xu, F. Hamhouyia, S.D. Thomas, T.J. Burke, A.C. Girvan, W.G. McGregor, J.O. Trent, D.M. Miller, P.J.Bates Inhibition of DNA replication and induction of S phase cell cycle arrest by G-rich oligonucleotides, *J Biol Chem.*, 2001, **276**, 43221-43230

[118] P. Živec, F. Perdih, I. Turel, G. Giester, G.Psomas, Different types of copper complexes with the quinolone antimicrobial drugs ofloxacin and norfloxacin: structure, DNA- and albumin-binding, *J Inorg Biochem.*, 2012, **117**, 35-47

[120] P.Zhao, Y. Wang, A. Wu, Y.Rao, Y.bHuang, Roles of Albumin-Binding Proteins in Cancer Progression and Biomimetic Targeted Drug Delivery, *ChemBioChem.*, 2018, **19**, 179

[121] J. Wang, S. Tian, R.A. Petros, M.E. Napier, J.M. DeSimone, The Complex Role of Multivalency in Nanoparticles Targeting the Transferrin Receptor for Cancer Therapies, *J. Am. Chem. Soc.*, 2010, **132**, 11306–11313

[122] A. van Niekerk, P. Chellan, S.F. Mapolie, Heterometallic Multinuclear Complexes as Anti-Cancer Agents-An Overview of Recent Developments, *Eur J Inorg Chem.*, 2019, **30**, 3432-3455

[123] N. Mirzadeh, T. S. Reddy, S.H. Privér, S.K. Bhargava, Synthesis, anti-proliferative and apoptosis-inducing studies of palladacycles containing a diphosphine and a Sn,As-based chelate ligand, *Dalton Trans.*, 2019, **48**, 5183-5192

- [124] M. Wenzel, E. Bigaeva, P. Richard, P. Le Gendre, M. Picquet, A. Casini, E. Bodio, New heteronuclear gold(I)-platinum(II) complexes with cytotoxic properties: are two metals better than one?, *J Inorg Biochem.*, 2014, **141**, 10-16
- [125] M. Wehbe, A. W. Y. Leung, M. J. Abrams, C. Orvig, M. B. Bally, A Perspective – can copper complexes be developed as a novel class of therapeutics?, *Dalton Trans.*, 2017, **46**, 10758-10773
- [126] K. Verma, A. Kumar, D. Varshney, Effect of Zn and Mg doping on structural, dielectric and magnetic properties of tetragonal  $\text{CuFe}_2\text{O}_4$ , *Current Appl. Phys.*, 2013, **13**, 467-473
- [127] P. Saravanan, S. Alam, G.N. Mathur, Comparative study on the synthesis of  $\gamma\text{-Fe}_2\text{O}_3$  and  $\text{Fe}_3\text{O}_4$  nanocrystals using high-temperature solution-phase technique, *J. Mater. Sci. Lett.*, 2003, **22**, 1283-1285
- [128] A.N. Yadav, A.K. Singh, P. Kumar, K. Singh, Graphene-Induced Room Temperature Ferromagnetism in Cobalt Nanoparticles Decorated Graphene Nanohybrid, *Nanoscale Res Lett.*, 2020, **15**, 166

# Curriculum Vitae

## Education

---

- **2018 – present:** Ph.D. student (4<sup>th</sup> year) Faculty of Chemistry, University of Wrocław, Poland
- **2018 – present:** Ph.D. student (4<sup>th</sup> year) Department of Chemical and Pharmaceutical Sciences at the University of Ferrara, Italy
- **2016-2018:** University of Wrocław, Faculty of Chemistry: Research Group of Structural Applications of Electron Paramagnetic Resonance Spectroscopy, **MA Environmental Chemistry; Title of master thesis:** "Because it takes three to tango..." drug-linker-carrier. Synthesis and physicochemical and biological properties study of phosphine P(p-OCH<sub>3</sub>Ph)<sub>2</sub>CH<sub>2</sub>OH and its Cu(I) complex
- **2012-2016** Wrocław University of Science and Technology, Faculty of Chemistry: Department of Analytical Chemistry and Chemical Metallurgy, **Chemistry BEng; Title of engineer's thesis:** Non-chromatographic approach to the arsenic speciation - application of the HG technique

## Publication

---

**Total publications: 9**

**Total IF: 45.98**

**Average IF: 5.11**

### **Publications constituting the basis of this doctoral dissertation (Total impact factor: 16.822)**

1. Urszula K. Komarnicka<sup>a</sup>, **Sandra Koziel**<sup>a</sup>, Agnieszka Skórska-Stania, Agnieszka Kyziół, Francesco Tisato, Synthesis, physicochemical characterization and preliminary *in vitro* antitumor activity of phosphino Ru(II) and Ir(III) complexes, ***Dalton Transactions***, 2022, DOI: 10.1039/D2DT01055K; IF: 4.39; **back cover**, a – first author
2. **Koziel Sandra**, Komarnicka Urszula K., Ziółkowska Aleksandra, Skórska-Stania Agnieszka, Pucelik Barbara, Płotek Michał, Sebastian Victor, Bieńko Alina, Stochel Grażyna, Kyziół Agnieszka, Anticancer potency of novel organometallic Ir(III) complexes with phosphine derivatives of fluoroquinolones encapsulated in polymeric



micelles; *Inorganic Chemistry Frontiers*, 2020, 7, 3386-3401; IF: 6.569; DOI:10.1039/d0qi00538j

3. **Koziel Sandra\***, Lesiów Monika Katarzyna, Wojtala Daria, Dyguda-Kazimierowicz Edyta, Bieńko Dariusz, Komarnicka Urszula Katarzyna, Interaction between DNA, albumin and apo-transferrin and iridium(III) complexes with phosphines derived from fluoroquinolones as a potent anticancer drug; *Pharmaceuticals*, 2021, 14, 685/1-685/25; IF: 5.863; DOI:10.3390/ph14070685, \* - corresponding author
4. Liposome-mediated delivery of magnetic iridium-copper complexes with phosphine derived from fluoroquinolones for prostate carcinoma treatment, *Inorganic Chemistry Frontiers*, submitted

#### *Others publications (Total impact factor:29.152)*

1. Komarnicka Urszula K., Niorettini Alessandro, **Koziel Sandra**, Pucelik Barbara, Barzowska Agata, Wojtala Daria, Ziółkowska Aleksandra, Lesiów Monika, Kyzioł Agnieszka, Caramori Stefano, Porchia Marina, Bieńko Alina, Two out of Three Musketeers Fight against Cancer: Synthesis, Physicochemical, and Biological Properties of Phosphino Cu<sup>I</sup>, Ru<sup>II</sup>, Ir<sup>III</sup> Complexes, *Pharmaceuticals*, 2022, 15, 169/1-169/22, IF: 5.863; DOI: 10.3390/ph15020169,
2. Wojciechowska Agnieszka, Bregier-Jarzębowska Romualda, Komarnicka Urszula K., **Koziel Sandra**, Szuster-Ciesielska Agnieszka, Sztandera-Tymoczek Monika, Jarząb Anna, Staszak Zbigniew, Witkowska Danuta, Bojarska-Junak Agnieszka, Jezierska Julia, Isothiocyanate L-argininato copper(II) complexes : solution structure, DNA interaction, anticancer and antimicrobial activity, *Chemico-Biological Interactions*, 2021, 348, 109636/1-109636/12, IF: 5.192; DOI: 10.1016/j.cbi.2021.109636
3. Świtlicka Anna, Machura Barbara, Bieńko Alina, **Koziel Sandra**, Bieńko Dariusz C., Rajnák Cyril, Boča Roman, Ozarowski Andrew, Ozerov Mykhaylo, Non-traditional thermal behavior of Co(II) coordination networks showing slow magnetic relaxation. *Inorganic Chemistry Frontiers*, 2021, 8, 4356-4366, IF: 6.569; DOI: 10.1039/d1qi00667c,
4. Guz-Regner Katarzyna, Komarnicka Urszula Katarzyna, Futoma-Kołoch Bożena, Wernecki Maciej, Cal Magdalena, **Koziel Sandra**, Ziółkowska Aleksandra, Bugła-Płoskońska Gabriela, Antibacterial activity and action mode of Cu(I) and Cu(II) complexes with phosphines derived from fluoroquinolone against clinical and

multidrug-resistant bacterial strains, *Journal of Inorganic Biochemistry*, 2020, 210, 111124/1-111124/11, IF: 4.155; DOI: 10.1016/j.jinorgbio.2020.111124

5. Komarnicka Urszula K., **Kozieł Sandra**, Zabierowski Piotr, Kruszyński Rafał, Lesiów Monika K., Tisato Francesco, Porchia Marina, Kyzioł Agnieszka, Copper(I) complexes with phosphines P(p-OCH<sub>3</sub>-Ph)<sub>2</sub>CH<sub>2</sub>OH and P(p-OCH<sub>3</sub>-Ph)<sub>2</sub>CH<sub>2</sub>SarGly: synthesis, multimodal DNA interactions, and prooxidative and in vitro antiproliferative activity, *Journal of Inorganic Biochemistry*, 2020, 203, 110926/1-110926/14, IF: 4.155; DOI: 10.1016/j.jinorgbio.2019.110926
6. Komarnicka Urszula K., **Kozieł Sandra**, Starosta Radosław, Kyzioł Agnieszka, Selective Cu(I) complex with phosphine-peptide (SarGly) conjugate contra breast cancer: synthesis, spectroscopic characterization and insight into cytotoxic action, *Journal of Inorganic Biochemistry*, 2018, 186, 162-175, IF: 3.224; DOI: 10.1016/j.jinorgbio.2018.06.009

### *Lider in research project*

---

- **14.01.2021 – 13.01.2024 Preludium 19 NCN (2020/37/N/ST4/02698):** Homo- and heterometallic phosphine ruthenium and iridium complexes - design, synthesis, bioactivity and magnetic-nanoformulation as a potential platform for dual-targeted drug delivery. **Amount: 195 600 PLN**
- **19.11.2018 – 30.10.2019 MNiSW(nr decyzji 4478/E-344/M/2018):** Przeprowadzanie badań dotyczących fosfinowych kompleksów rutenu(II) i irydu(III) jako potencjalnych leków przeciwnowotworowych. **Amount: 14 000 PLN**

### *Co-investigator in research project*

---

- **1.11.2018 – 7.11.2021 SONATA 12 NCN (2016/23/D/ST5/00269):** Do copper(I) complexes with conjugates of phosphine-peptide carriers can cause selective cancer cells death? Synthesis, physicochemical and biological properties (start: 2017-07-12). **Amount: 452 800 PLN**

### *Conference contributions (posters)*

---

- *Poster:* **Sandra Koziel**, Agnieszka Skórska-Stania, Barbara Pucelik, Victor Sebastiane, Alina Bieńko, Grażyna Stochel, Agnieszka Kyzioł, Urszula K. Komarnicka „Aktywność przeciwnowotworowa nowych kompleksów irydu(III) zawierających fosfinowe pochodne fluorochinolonów zamkniętych w polimerowych micelach” IV Ogólnopolskie Forum Chemii Nieorganicznej, Wydział Chemii Uniwersytetu Mikołaja Kopernika w Toruniu, 7-9.09.2021
- *Oral presentation:* **Sandra Koziel**, Agnieszka Skórska-Stania, Barbara Pucelik, Victor Sebastiane, Alina Bieńko, Grażyna Stochel, Agnieszka Kyzioł, Urszula K. Komarnicka: „Anticancer potency of novel organometallic Ir(III) complexes with phosphines derived from fluoroquinolones encapsulated in polymeric micelles”. International Symposium on Thermodynamics of Metal Complexes ISMEC 2021, Białystok, Polska, 16-18.06.2021
- *Flash talk and poster:* **Sandra Koziel**, Agnieszka Kyzioł, Alina Bieńko, Urszula K. Komarnicka "Novel piano-stool Ru(II) and Ir(III) complexes containing aminomethylphosphanes based on fluoroquinolones". ISABC 2019 – 15th International Symposium on Applied Bioinorganic Chemistry; 2-5 June 2019, Nara, Japan
- *Oral presentation:* **Sandra Koziel** "Kompleksy miedzi(I) z fosfinowym koniugatem dipeptydu Sar-Gly-OH zawierającym motyw(p-OCH<sub>3</sub>Ph)<sub>2</sub>CH<sub>2</sub>OH. Multimodalne interakcje DNA, aktywność prooksydacyjna i cytotoksyczna". Young scientists conference. Analysis of the issue, analysis of results - presentation of a young scientist; 21 May 2019, Rzeszów, Poland
- *Poster:* **Sandra Koziel**, Agnieszka Kyzioł, Alina Bieńko, Urszula K. Komarnicka "Nowe kompleksy Ru(II) i Ir(III) z aminometylofosfinowymi pochodnymi fluorochinolonów". Young scientists conference. Analysis of the issue, analysis of results - presentation of a young scientist; 21 May 2019, Rzeszów, Poland
- *Poster:* **Sandra Koziel**, Radosław Starosta, Agnieszka Kyzioł, Urszula K. Komarnicka "Kompleksy miedzi(I) z fosfinowym koniugatem dipeptydu (SarGlyOH) w walce z rakiem piersi - charakterystyka fizykochemiczna i biologiczna". 61. Zjazd Naukowy Polskiego Towarzystwa Chemicznego, 17-21 September 2018, Krakow, Poland

### *Awards and Fellowships*

---

- Finalist in the "Young Talent" competition in the category of scientific success, organized by "Dolnośląski Klub Kaptiału" (2022, Wrocław, Poland)
- Jan Mozrzykmas scholarship in the field of interdisciplinary research conducted by the Wrocław Academic Center and the city of Wrocław (2021/2022)
- Award for a distinction in a poster session: „Aktywność przeciwnowotworowa nowych kompleksów irydu(III) zawierających fosfinowe pochodne fluorochinolonów zamkniętych w polimerowych micelach” IV Ogólnopolskie Forum Chemii Nieorganicznej, Wydział Chemii Uniwersytetu Mikołaja Kopernika w Toruniu, 7-9.09.2021
- Nomination for the award: Scientist of the Future 2021 in the category: Science for a better life in the future (2021, Wrocław, Poland)
- Scholarship of the Rector of the University of Wrocław for the best PhD students (2018-2022)
- Scholarships of Ministry of Higher Education and Science for the best PhD students (pro-quality scholarship, 2018-2022)
- Piotr Ludwik Sosabowski Scientific Scholarship (2019/2020)

## *Internship*

---

- **2018 - 2022** Italy, doctoral studies at the University of Ferrara, Department of Chemical, Pharmaceutical and Agricultural Sciences (collaboration with Professor Stefano Caramori)
- **2018 - 2022** Poland, Jagiellonian University, Krakow; Department of Inorganic Chemistry (total 9 months, collaboration with Professor Grażyna Stochel and Dr Agnieszka Kyzioł)
- **2021 - 2022** Poland, University of Wrocław, Poland; Institute of Genetics and Microbiology, Department of Microbiology (total 2 months, collaboration with Professor Gabriela Bugła-Płoskońska and Dr Katarzyna Guz-Regner)
- **1 April – 31 October, 2020** Poland, internship at Colgate-Palmolive Services (Poland) sp.z o.o. in Świdnica
- **7 November – 5 December 2018** Italy, Institute of Condensed Matter Chemistry and Technologies for Energy (ICMATE) in Padua (collaboration with Marina Porchia and Francesco Tisato)

## *Training*

---

- **09 - 18 April 2018** Poland, Wrocław University of Science and Technology European standardization of cosmetic products.
- **15 - 20 January 2018** Poland, Wrocław University of Science and Technology Participation in team projects of biological chemistry conducted by Professor Marcin Drąg
- **12 - 13 October 2017** Poland, Wrocław Technology Park Accreditation of analytical laboratories using alternative determination methods
- **26 June - 08 July 2017** Poland, Wrocław University of Science and Technology Gas chromatography

## *Organizational activities*

---

- **2020 – present:** Chemistry teacher in Dialogue Of Culture Primary School Etz Chaim
- **2019 – present:** An active member of the „Stowarzyszenie Nauczycieli Przedmiotów Przyrodniczych (PSNPP)”
- **2019 – present:** Laboratory classes for elementary school and high school students at the University of Wrocław
- **2020 – present:** Co-managementsocial media of the Faculty of Chemistry, University of Wrocław (instagram, facebook, website)
- **2021 – 2022** Organizing an auction for the Great Orchestra of Christmas Aid (WOŚP): "a day in the life of a mad chemist"
- **2019-2020:** Assistance in organizing the “Dolnośląski Festiwal Nauki” at the Faculty of Chemistry and at the Faculty of Law, Administration and Economics of the University of Wrocław
- **1.10.2019 - 30.09.2020:** Chairwoman of the council of doctoral students at the Faculty of Chemistry, University of Wrocław.
- **2015 - 2020:** Member of the Students' Scientific Circle of Forensics at the Department of Forensics at the Faculty of Law, Administration and Economics of the University of Wrocław.

# Dyplom



LOWER SILESIA CAPITAL CLUB

KAPITUŁA KONKURSU MŁODE TALENTY  
NOMINUJE DO NAGRODY



MŁODE TALENTY

PANIĄ

# Sandrę Koziel

ZA WYBITNY SUKCES  
NAUKOWY

KAPITUŁA VI EDYCJI KONKURSU MŁODE TALENTY  
• WROCŁAW 2022 •

*prof. dr hab. Waldemar Banasiak, prof. dr hab. Marek Bojarski, prof. dr hab. inż. Jarosław Bosy, Piotr Chęciński, Marcin Chłudziński,  
dr Janusz Cymanek, prof. dr hab. Szymon Dragan, prof. dr hab. Bogusław Fiedor, dr Stanisław Han, Rafał Holanowski,  
prof. dr hab. Andrzej Kaleta, prof. dr hab. Krystian Kiełb, prof. dr hab. Roman Kołacz, Tomasz Kurzewski,  
prof. dr hab. inż. Cezary Madryas, Andrzej Panas, plk dr hab. Piotr Płonka, Roman Potocki, Cezary Przybylski, Andrzej Przybyło,  
prof. dr hab. Wojciech Pukocz, prof. dr hab. Andrzej Rokita, Janusz Rybak, Jacek Sutryk, prof. dr hab. Tadeusz Szulc,  
Robert Ślawski, prof. dr hab. inż. Tadeusz Trziszka, prof. dr hab. inż. Arkadiusz Wójs*



Prezydent  
Dolnośląskiego Klubu Kapitału

Janusz Rybak

Przewodniczący  
Kapituły Konkursu Młode Talenty

prof. dr hab. Bogusław Fiedor





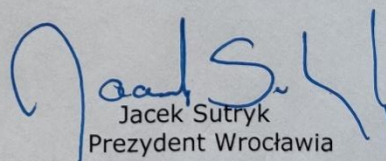
## STUDENCKI PROGRAM STYPENDIALNY

Prezydent Wrocławia na podstawie rekomendacji Komisji  
działającej w ramach Studenckiego Programu Stypendialnego

przyznaje **pani Sandrze Koziel**  
doktorantce pani dr hab. Aliny Bieńko

stypendium im. Jana Mozrzymasa  
za osiągnięcia w dziedzinie badań interdyscyplinarnych  
w wysokości 2000 zł miesięcznie

Wrocław, 15 listopada 2021 r.

  
Jacek Sutryk  
Prezydent Wrocławia

# PUBLICATION S1

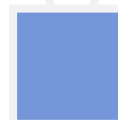
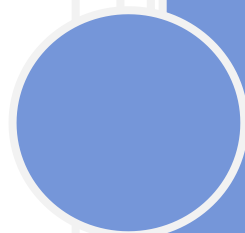
Komarnicka Urszula K., Kozieł Sandra, Skórska-Stania Agnieszka,  
Kyzioł Agnieszka, Tisato Francesco

*Synthesis, physicochemical characterization and antiproliferative activity of phosphino Ru(II) and Ir(III) complexes.*

Dalton Transactions, 2022, 51, 8605-8617

DOI: [10.1039/D2DT01055K](https://doi.org/10.1039/D2DT01055K)

This paper has been chosen for a back cover











As featured in:



See Urszula K. Komarnicka et al.,  
*Dalton Trans.*, 2022, 51, 8605.

Cite this: Dalton Trans., 2022, 51,  
8605Synthesis, physicochemical characterization and  
antiproliferative activity of phosphino Ru(II) and  
Ir(III) complexes†Urszula K. Komarnicka, \*‡<sup>a</sup> Sandra Kozieł, ‡<sup>a</sup> Agnieszka Skórska-Stania, <sup>b</sup>  
Agnieszka Kyzioł <sup>b</sup> and Francesco Tisato<sup>c</sup>

Herein, we present the synthesis of new complexes based on ruthenium(II) (Ru( $\eta^6$ -p-cymene)Cl<sub>2</sub>PPh<sub>2</sub>CH<sub>2</sub>OH (RuPOH) and Ru( $\eta^6$ -p-cymene)Cl<sub>2</sub>P(p-OCH<sub>3</sub>Ph)<sub>2</sub>CH<sub>2</sub>OH (RuMPOH)) and iridium(III) (Ir( $\eta^5$ -Cp\*)Cl<sub>2</sub>P(p-OCH<sub>3</sub>Ph)<sub>2</sub>CH<sub>2</sub>OH (IrMPOH) and Ir( $\eta^5$ -Cp\*)Cl<sub>2</sub>PPh<sub>2</sub>CH<sub>2</sub>OH (IrPOH)) containing phosphine ligands with/without methoxy motifs on phenyl rings (P(p-OCH<sub>3</sub>Ph)<sub>2</sub>CH<sub>2</sub>OH (MPOH) and PPh<sub>2</sub>CH<sub>2</sub>OH (POH)). The complexes were characterized by mass spectrometry, NMR spectroscopy (1D: <sup>1</sup>H, <sup>13</sup>C{<sup>1</sup>H}, and <sup>31</sup>P{<sup>1</sup>H} and 2D: HMQC, HMBC, and COSY NMR) and elemental analysis. All the complexes were structurally identified by single-crystal X-ray diffraction analysis. The Ru(II) and Ir(III) complexes have a typical piano-stool geometry with an  $\eta^6$ -coordinated arene (Ru<sup>II</sup> complexes) or  $\eta^5$ -coordinated (Ir<sup>III</sup> compounds) and three additional sites of ligation occupied by two chloride ligands and the phosphine ligand. Oxidation of NADH to NAD<sup>+</sup> with high efficiency was catalyzed by complexes containing P(p-OCH<sub>3</sub>Ph)<sub>2</sub>CH<sub>2</sub>OH (IrMPOH and RuMPOH). The catalytic property might have important future applications in biological and medical fields like production of reactive oxygen species (ROS). Furthermore, the redox activity of the complexes was confirmed by cyclic voltamperometry. Biochemical assays demonstrated the ability of Ir(III) and Ru(II) complexes to induce significant cytotoxicity in various cancer cell lines. Furthermore, we found that RuPOH and RuMPOH selectively inhibit the proliferation of skin cancer cells (WM266-4; IC<sub>50</sub>, after 24 h: av. 48.3  $\mu$ M; after 72 h: av. 10.2  $\mu$ M) while Ir(III) complexes were found to be moderate against prostate cancer cells (DU145).

Received 5th April 2022,  
Accepted 12th May 2022

DOI: 10.1039/d2dt01055k

rsc.li/dalton

## Introduction

Methods of identifying and treating cancer are currently undergoing significant changes because of the application of nanotechnologies or nanomedicine.<sup>1</sup> However, one of the significant methods of cancer disease treatment is still chemotherapy.<sup>2–4</sup> Unfortunately, this kind of treatment causes many side effects that are the result of off-target effects on healthy tissues. Since cisplatin became one of the most widely used anticancer drugs,<sup>5</sup> the development of new metal-based antitumor drugs has significantly increased; for instance,

ruthenium, gold, and iridium compounds have been receiving much attention in recent years in biology and medicine.<sup>6–8</sup> In biocatalysis, organometallic complexes have been mostly responsible for the conversion of coenzyme NAD<sup>+</sup><sup>9,10</sup> to its reduced form NADH.<sup>8,11–15</sup> Such organometallic compounds including Ir<sup>III</sup>, Rh<sup>III</sup>, and Ru<sup>II</sup> complexes can drive enzymatic reactions relying on NADH as a cofactor.<sup>8,12–17</sup> In vivo, both NAD<sup>+</sup> and NADH take part as cofactors in many biocatalyzed processes (e.g. energy transfer, oxidative stress, or cell death).<sup>8</sup>

Furthermore, it has been shown that organometallic half-sandwich Ru(II) and Ir(III) complexes exhibit excellent in vitro and in vivo anticancer properties, but still need to be explored in detail.<sup>17–21</sup> Hence, ruthenium-based antitumor complexes represent a promising alternative to platinum drugs, a number of them being already in clinical trials.<sup>22,23</sup> Ruthenium has a large range of available oxidation states under physiological conditions.<sup>24</sup> Although the mechanism of action of ruthenium-based drugs is still unclear, it is believed that the ability of ruthenium to mimic iron in binding to biological molecules (such as transferrin or albumin) is an important feature. This property is mainly reflected in less toxic compounds compared

<sup>a</sup>Faculty of Chemistry, University of Wrocław, Joliot-Curie 14, 50-383 Wrocław, Poland. E-mail: urszula.komarnicka@chem.uni.wroc.pl<sup>b</sup>Faculty of Chemistry, Jagiellonian University in Krakow, Gronostajowa 2, 30-387 Krakow, Poland<sup>c</sup>ICMATECNR, Corso Stati Uniti 4, 35127 Padova, Italy†Electronic supplementary information (ESI) available. CCDC 2087020, 2087023, 2087025 and 2087026. For ESI and crystallographic data in CIF or other electronic format see DOI: <https://doi.org/10.1039/d2dt01055k>

‡First author.

to their platinum counterparts,<sup>25</sup> resulting from a more efficient delivery to cancer cells. The mechanism of action seems to be different from that of the platinum compounds. Therefore, ruthenium compounds have great potential as anticancer agents,<sup>26,42</sup> and different approaches of investigation have been reviewed recently.<sup>27</sup>

Whereas the medicinal properties of ruthenium compounds are well established,<sup>28–30</sup> the development of anticancer iridium compounds is a relatively new scientific field.<sup>31,32</sup> Ir<sup>III</sup> complexes are often considered to be relatively inert, which is a common characteristic of low-spin d<sup>6</sup> metal ions and especially third-row transition metals.<sup>32</sup> However, iridium compounds have not only displayed potent anticancer reactivity,<sup>33,34</sup> but their mechanism of action (MoA) and spectrum of sensitivity to tumours are unlike those of the conventional platinum-based drugs.<sup>35,36</sup> Half-sandwich iridium(III) complexes have drawn particular attention owing to their particular anticancer mechanisms, which include catalyzing the intracellular redox reaction and inhibition of proteins (VEGF R3, Bcl-2, etc.). These results can lead to the accumulation of intracellular reactive oxygen species (ROS, <sup>1</sup>O<sub>2</sub>) and lead to cell death.<sup>37–39</sup>

One rational approach to improve the efficacy of metal complexes consists of incorporating different chelating ligands with complementary biological activity to enhance the physiological targets of the metallodrug.<sup>40</sup> In this context, P-donor ligands represent an unquestioned tool in bioinorganic medicinal chemistry for improving the anticancer activity of metal complexes.<sup>41–45</sup> Thus, the use of phosphines (PR<sub>3</sub>-R = H, alkyl, aryl, etc.) as auxiliary ligands has been accompanied by the synthesis of various ruthenium and iridium complexes. Phosphines are σ-donor and π-acceptor ligands and stabilize mainly the low oxidation states of soft metals, and are one of the few ligands whose electronic properties can be widely modified in a systematic way by changing the R groups.<sup>3</sup> Besides, they confer a lipophilic character to the compounds

facilitating cellular uptake, which is essential for improving the overall biological response.<sup>42,43</sup> For example, RAPTA-C exhibited preclinical antimetastatic and antiangiogenic behaviour in vivo, and it was able to reduce the growth of certain primary tumours.<sup>46</sup> This also encouraged us to introduce phosphine ligands into the half-sandwich of ruthenium/iridium complexes.

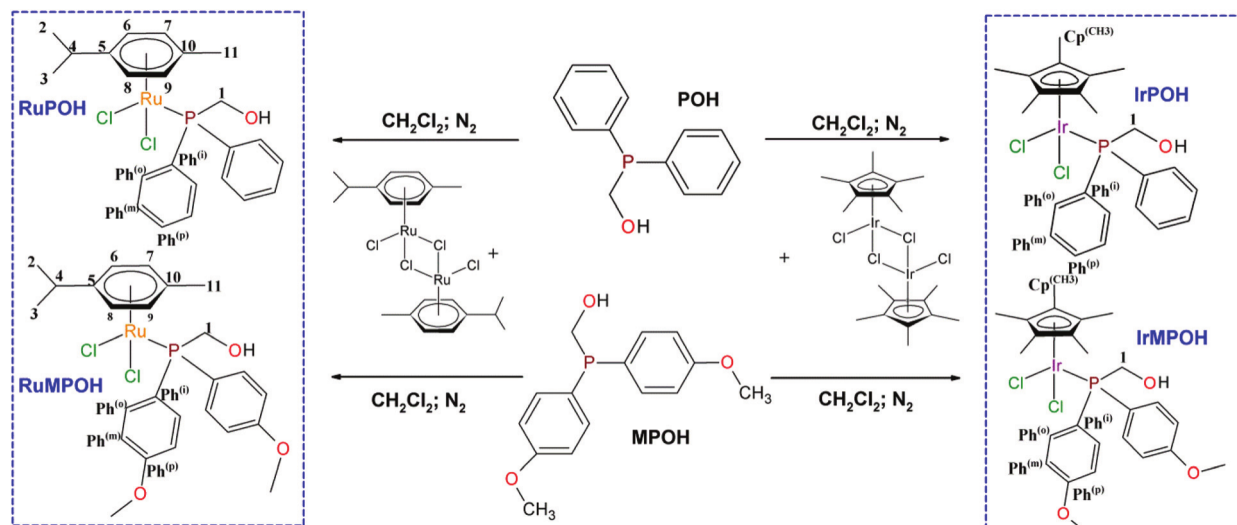
In this paper, we report on the syntheses, physicochemical characterization, and biological study of the in vitro anticancer activity of two novel piano-stool ruthenium(II) complexes Ru(η<sup>6</sup>-p-cymene)Cl<sub>2</sub>PPh<sub>2</sub>CH<sub>2</sub>OH (RuPOH) and Ru(η<sup>6</sup>-p-cymene)Cl<sub>2</sub>P(p-OCH<sub>3</sub>Ph)<sub>2</sub>CH<sub>2</sub>OH (RuMPOH) and two half-sandwich Ir(III) complexes Ir(η<sup>5</sup>-Cp\*)Cl<sub>2</sub>P(p-OCH<sub>3</sub>Ph)<sub>2</sub>CH<sub>2</sub>OH (IrMPOH) and Ir(η<sup>5</sup>-Cp\*)Cl<sub>2</sub>PPh<sub>2</sub>CH<sub>2</sub>OH (IrPOH) with two phosphine ligands with/without methoxy motifs on phenyl rings, PPh<sub>2</sub>CH<sub>2</sub>OH (POH) and P(p-OCH<sub>3</sub>Ph)<sub>2</sub>CH<sub>2</sub>OH (MPOH) (Scheme 1).

## Results and discussion

### Synthetic procedures

All syntheses were carried out under an atmosphere of dry oxygen-free dinitrogen using standard Schlenk techniques or a glove box. The ligands Ph<sub>2</sub>P(CH<sub>2</sub>OH)<sub>2</sub>Cl (POHC),<sup>47</sup> Ph<sub>2</sub>PCH<sub>2</sub>OH (POH),<sup>48</sup> (p-OCH<sub>3</sub>Ph)<sub>2</sub>P(CH<sub>2</sub>OH)<sub>2</sub>Cl (MPOHC),<sup>49</sup> and (p-OCH<sub>3</sub>Ph)<sub>2</sub>PCH<sub>2</sub>OH (MPOH)<sup>49</sup> were prepared using previously described methods. The synthetic routes of iridium(III) complexes IrPOH Ir(η<sup>5</sup>-Cp\*)Cl<sub>2</sub>PPh<sub>2</sub>CH<sub>2</sub>OH and IrMPOH Ir(η<sup>5</sup>-Cp\*)Cl<sub>2</sub>P(p-OCH<sub>3</sub>Ph)<sub>2</sub>CH<sub>2</sub>OH and ruthenium(II) complexes RuPOH Ru(η<sup>6</sup>-p-cymene)Cl<sub>2</sub>PPh<sub>2</sub>CH<sub>2</sub>OH and RuMPOH Ru(η<sup>6</sup>-p-cymene)Cl<sub>2</sub>P(p-OCH<sub>3</sub>Ph)<sub>2</sub>CH<sub>2</sub>OH are presented in Scheme 1.

The complexes were found to be air stable and soluble in polar solvents such as dichloromethane and acetone but insoluble in non-polar solvents such as pentane and hexane. The analytical data of all the ruthenium(II) and iridium(III) com-



Scheme 1 Schematic view of the compounds and synthetic routes.

plexes are in good agreement with the molecular formula proposed. The target complexes were characterized by 1D and 2D NMR spectra, ESI-MS and elemental analysis. These analytical and spectral data confirmed the stoichiometry of new complexes. In addition, the molecular structures of all complexes have been authenticated by single crystal X-ray crystallography.

### Structural analysis

The crystal data and the details of data collection and structure refinement of Ru(II) and Ir(III) complexes are given in Tables 1 and S1 and S2 in the ESI† The Ru(II) complexes, RuPOH and RuMPOH, have a typical piano-stool geometry with an  $\eta^6$ -coordinated arene and three additional sites of ligation occupied by two chloride ligands and the phosphine ligand (Fig. 1). The structure of RuPOH differs from that of RuMPOH only by the phosphine ligand. In RuMPOH, two phenyl rings have additional methoxy groups in the para-positions. The phosphorus atom is also bonded to the CH<sub>2</sub>-OH group.

The conformations of both molecules of RuPOH and RuMPOH are very similar as shown in Fig. 2. The Ir(III) complexes, IrPOH and IrMPOH, have a typical piano-stool geometry with an  $\eta^5$ -coordinated arene and three additional sites of ligation occupied by two chloride ligands and the phosphine ligand (Fig. 1).

Analogically, IrPOH and IrMPOH differ from each other only by para-substituents in the two phenyl groups bonded to the phosphorus atom (P1). The third connection of the P1 atom in both Ir(III) complexes is also a CH<sub>2</sub>-OH group. The hydroxyl group in IrPOH is disordered with occupancy factors ranging from 72% for O11B to 28% for O11A. The most significant bond lengths and bond angles involving atom Ru1 for RuPOH and RuMPOH and involving atom Ir1 for IrPOH and IrMPOH, respectively, are given in Table 1.

The bond lengths of P1-C for all structures are in the range of 1.810–1.865 Å and the C-P-C angles range from 98.63° to 105.60°. The strongest hydrogen bonds in the structures RuPOH, IrPOH and IrMPOH are intramolecular O-H⋯Cl. The strongest hydrogen bond in all structures is an O-H⋯Cl inter-

action between the hydroxyl group as a donor and chlorine atom as an acceptor (Fig. 3 and Table S2 ESI†). In complexes RuPOH, IrPOH and IrMPOH, this interaction is intramolecular forming S<sub>1</sub>(6), whereas in complex RuMPOH it forms the intramolecular motif R<sub>2</sub>(12).<sup>51</sup>

### Characterization of organometallic Ru(II) and Ir(III) complexes

All complexes IrPOH, IrMPOH, RuPOH and RuMPOH were precisely characterized by 1D NMR techniques (<sup>1</sup>H, <sup>13</sup>C{<sup>1</sup>H} and <sup>31</sup>P{<sup>1</sup>H} NMR) and 2D NMR (COSY, HMQC and HMBC) (Fig. 4 and 5; Fig. S1–S10, ESI†) and mass spectrometry (Fig. S11–S19, ESI†). The application of these techniques allowed the determination of the structures of the complexes in solution under atmospheric oxygen.

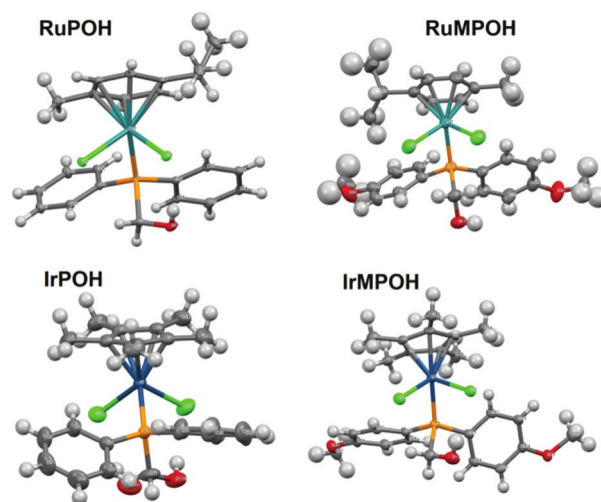


Fig. 1 Asymmetric units of Ru( $\eta^6$ -p-cymene)Cl<sub>2</sub>PPh<sub>2</sub>CH<sub>2</sub>OH (RuPOH), Ru( $\eta^6$ -p-cymene)Cl<sub>2</sub>P(p-OCH<sub>3</sub>Ph)<sub>2</sub>CH<sub>2</sub>OH (RuMPOH) and two half-sandwich Ir(III) complexes Ir( $\eta^5$ -Cp\*)Cl<sub>2</sub>P(p-OCH<sub>3</sub>Ph)<sub>2</sub>CH<sub>2</sub>OH (IrMPOH) and Ir( $\eta^5$ -Cp\*)Cl<sub>2</sub>PPh<sub>2</sub>CH<sub>2</sub>OH (IrPOH). Displacement ellipsoids are drawn at the 50% probability level (using Mercury 2020.1<sup>50</sup>).

Table 1 Comparison of the bond lengths and angles around Ir atoms for IrPOH and IrMPOH and around Ru atoms for RuPOH and RuMPOH, respectively

Bonds	IrPOH [Å]	IrMPOH [Å]	Bonds	RuPOH [Å]	RuMPOH [Å]
P1–Ir1	2.3026(7)	2.3141(13)	P1–Ru1	2.3313(9)	2.3511(5)
Cl1–Ir1	2.4251(7)	2.3993(14)	Cl1–Ru1	2.4366(9)	2.4262(6)
Cl2–Ir1	2.4076(7)	2.4097(13)	Cl2–Ru1	2.4051(9)	2.4108(6)
Cg1–Ir1	1.8264(12)	1.827(2)	Cg2–Ru1	1.7023(15)	1.7042(9)
Angles	[°]	[°]	Angles	[°]	[°]
P1–Ir1–Cl2	88.85(3)	89.10(5)	P1–Ru1–Cl2	84.79(3)	82.64(2)
P1–Ir1–Cl1	89.05(2)	87.26(5)	P1–Ru1–Cl1	89.29(3)	87.74(2)
Cl2–Ir1–Cl1	88.41(3)	85.26(5)	Cl2–Ru1–Cl1	85.77(3)	87.57(2)
Cg1–Ir1–Cl1	121.71	123.91	Cg2–Ir1–Cl1	126.38	125.24
Cg1–Ir1–Cl2	124.06	124.59	Cg2–Ir1–Cl2	128.43	127.62
Cg1–Ir1–P1	132.20	132.55	Cg2–Ir1–P1	127.91	131.45
5-Membered ring Cg1 = C1–C2–C3–C4–C5			6-Membered ring Cg2 = C4–C5–C6–C7–C8–C9		



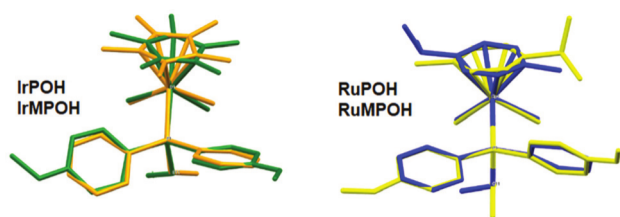


Fig. 2 Structure overlay diagrams (using Mercury 2020.1<sup>43</sup>) of the two molecules IrPOH—orange and IrMPOH—green and RuPOH—blue and RuMPOH—yellow, respectively.

The  $^{31}\text{P}\{^1\text{H}\}$  NMR analysis, a very useful method for the preliminary determination of sample purity, was applied to verify if the product of the synthesis is the desired one (Fig. 4 and Fig. S1–S8, ESI<sup>†</sup>). First of all, the signal of uncoordinated phosphines is situated in the negative part of the spectrum (POH:  $-9.33$  ppm; MPOH:  $-13.60$  ppm) and undergoes a downfield shift as a result of phosphine coordination (RuPOH:  $16.74$  ppm; RuMPOH:  $15.07$  ppm; IrPOH:  $-7.15$  ppm and IrMPOH:  $-9.18$  ppm). The absence of other signals in the spectrum confirms that the coordination compound is the only product of synthesis, free from phosphine derivatives (e.g., phosphine oxides; Fig. 4 and Fig. S1–S8, ESI<sup>†</sup>).

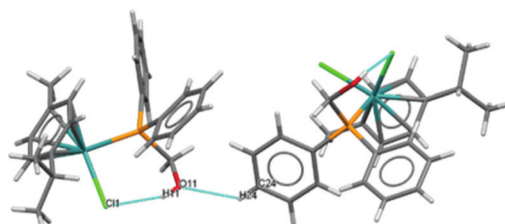
As expected, the biggest changes in the  $^1\text{H}$  and  $^{13}\text{C}\{^1\text{H}\}$  NMR spectra (Fig. 4 and Fig. S1–S8, ESI<sup>†</sup>) upon the complexa-

tion process were observed for the atoms neighbouring the coordination metal ions: Ru(II) and Ir(III). Almost all protons undergo an upfield shift independent of the type of metal ion (Ir(III) and Ru(II)) and phosphine ligand (POH or MPOH). This might be related to the electron density increase around the ligands caused by the formation of complex compounds. However, the signals of H(–OCH<sub>3</sub>) on the phenyl ring in the phosphine ligand (MPOH), H(Cp\*CH<sub>3</sub>) on the methyl group of the cyclopentadienyl (Ir(III) complexes) and H1 of all complexes undergo a downfield shift.

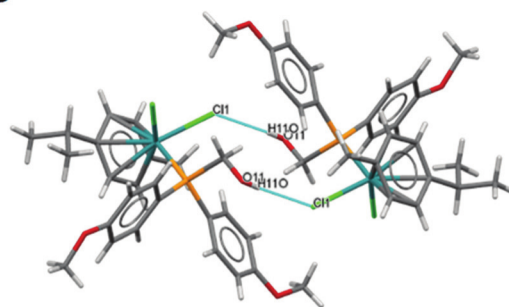
It is worth mentioning that after complexations, the chemical shifts of the H1 (PPh<sub>2</sub>CH<sub>2</sub>-) signals of Ir complexes are bigger than those of Ru compounds. This means that both phosphine ligands are bound via a phosphorus atom much stronger than the iridium ion compared to the ruthenium complex.

For phosphine ligands, analogous to the  $^1\text{H}$  NMR spectra, the largest changes in the  $^{13}\text{C}\{^1\text{H}\}$  NMR spectra were observed for the C1 atom. After phosphine complexation, the signals (C1) for all the complexes studied here (RuPOH, RuMPOH, IrPOH and IrMPOH) shifted strongly towards lower fields. The C1 signal is a feature strongly distinguishing all inorganic compounds, where doublets of  $1J(\text{C}-\text{P}) = \text{ca. } 40$  Hz for RuMPOH and IrMPOH as well as  $1J(\text{C}-\text{P}) = \text{ca. } 31$  Hz for RuPOH and IrPOH coupling constants were observed.

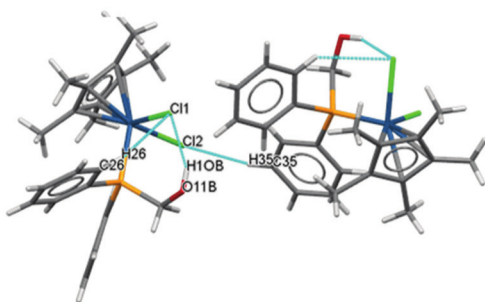
**A** RuPOH - O11-H11...C11  $S_1^1(6)$



**B** RuMPOH - R<sub>2</sub><sup>2</sup>(12)



**C** IrPOH - O11B-H11B...C11  $S_1^1(6)$



**D** IrMPOH - O11-H11...C12  $S_1^1(6)$

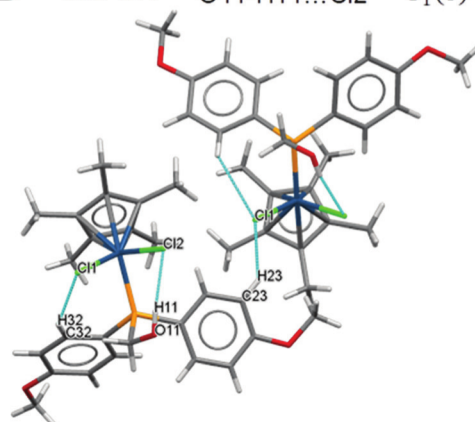


Fig. 3 The strongest hydrogen bonds of (A) RuPOH, (B) RuMPOH, (C) IrPOH and (D) IrMPOH.

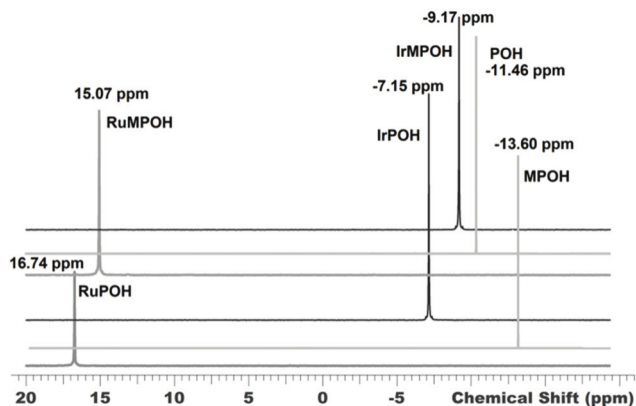


Fig. 4  $^{31}\text{P}\{^1\text{H}\}$  NMR spectra (298 K, DMSO) of the ligands (MPOHC, POHC, MPOH, and POH) and complexes (IrPOH, IrMPOH, RuPOH, and RuMPOH). MPOHC and POHC are not reported.

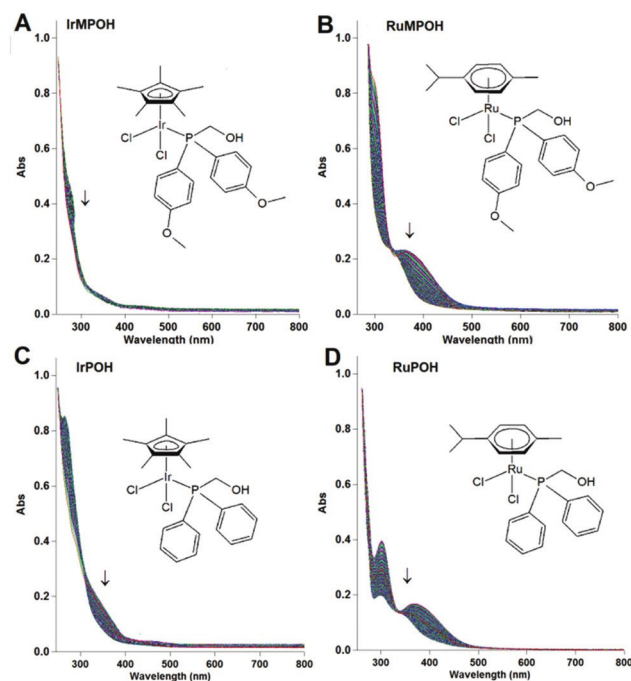


Fig. 5 The UV/vis spectra of (A) IrMPOH, (B) RuMPOH, (C) IrPOH, and (D) RuPOH in 20% DMSO/80%  $\text{H}_2\text{O}$  (v/v) solution at 298 K over 24 h; the arrows show the change over time.

### Hydrolysis studies

Hydrolysis of the Ir(III)-Z and Ru(II)-Z (Z is the leaving group in both types of complexes) bonds represents an activation step of organometallic anticancer complexes. M-OH<sub>2</sub> aqua complexes are often more reactive than the corresponding complexes.<sup>37</sup>

The hydrolysis characteristics of IrMPOH, RuMPOH, IrPOH and RuPOH were measured by UV-vis absorption spectroscopy (Fig. 5 and Table 2), and the presence of DMSO ensured the solubility of these complexes. As shown, the UV-vis spectra of all complexes displayed some changes over time, which indi-

Table 2 The values of the hydrolysis rate constants [ $\text{min}^{-1}$ ] and the half-life [min] calculated for IrPOH, IrMPOH, RuPOH, and RuMPOH

	$k'$ [ $\text{min}^{-1}$ ]	$t_{1/2}$ [min]
IrPOH	$4.57 \times 10^{-4} \pm 4.6 \times 10^{-6}$	1515.2
RuPOH	$7.53 \times 10^{-4} \pm 1.3 \times 10^{-6}$	920.4
IrMPOH	$8.40 \times 10^{-5} \pm 4.1 \times 10^{-7}$	8255.8
RuMPOH	$8.49 \times 10^{-4} \pm 0.5 \times 10^{-6}$	816.5

cated the slow hydrolysis process. The time dependence of the formation of the aqua adducts of complexes was fitted to the pseudo-first-order kinetics (Fig. 5 and Table 2). The values of the hydrolysis rate constants were  $4.57 \times 10^{-4} \pm 4.6 \times 10^{-6}$ ,  $7.53 \times 10^{-4} \pm 1.3 \times 10^{-6}$ ,  $8.40 \times 10^{-5} \pm 4.1 \times 10^{-7}$ , and  $8.49 \times 10^{-4} \pm 0.5 \times 10^{-6} \text{ min}^{-1}$  and the values of the half-life of hydrolysis were 1515.2 min, 920.4 min, 8255.8 min and 816.5 min for IrPOH, RuPOH, IrMPOH, and RuMPOH, respectively. The values of the hydrolytic half-life of ruthenium complexes were lower than those of iridium compounds.

The hydrolysis of all compounds IrPOH, IrMPOH, RuPOH, and RuMPOH in 20% DMSO- $d_6$ /80%  $\text{D}_2\text{O}$  (v/v) was additionally monitored by  $^1\text{H}$  NMR in the presence of 4.0 mM, 23.0 mM, or 103.0 mM NaCl (mimicking the chloride concentrations in the blood plasma, cell cytoplasm, and cell nucleus, respectively)<sup>34</sup> (Fig. 6 and Fig. S9 and S10, ESI<sup>+</sup>). DMSO was required to ensure the solubility of the complexes in aqueous solution and it is also a widely used solvent in preparing metal complex stock solutions for therapeutic studies.

Hydrolysis was confirmed by the sequential addition of NaCl (after 15 min) to the equilibrium solution. The intensity of the aqua complex peaks associated with Ir-OD<sub>2</sub>/OD or Ru-OD<sub>2</sub>/OD decreased with the increase in the peaks associated with the Ir-Cl<sub>2</sub> or Ru-Cl<sub>2</sub> species as the NaCl concentration increased (Fig. 6 and Fig. S9 and S10, ESI<sup>+</sup>). This would imply that at biologically relevant chloride concentrations (i.e., in the nucleus), the complexes would exist as Ir(Ru)-Cl rather than the aqua species. A similar trend can be observed for different organometallic Ir(III) and Ru(II) complexes.<sup>34,52</sup> On the basis of the  $^1\text{H}$  NMR data, the reaction of aqua complexes was almost complete in 104 mM  $[\text{Cl}^-]$ , and ca. 10% of the aqua complexes were observed at this concentration after 15 min with no further change after 24 h. Extracellularly, when the chloride ion concentration is >100 mM, hydrolysis of the complexes may be suppressed. However, inside cells where the concentration is lower (approx. 23 mM in the cytoplasm and 4 mM in the nucleus), the complexes can be activated. However, metal complexes can interact with many targets inside the cell, which may also be reflected in their hydrolysis. For example, the complexes can react by directly substituting chloride for nucleobases (DNA).<sup>53–55</sup>

### Mass spectrometry

The ESI(+)-MS spectra (recorded in the positive ion modality) of the two IrPOH and IrMPOH complexes did not show the corresponding  $[\text{M}]^+$  molecular ion peaks according to the

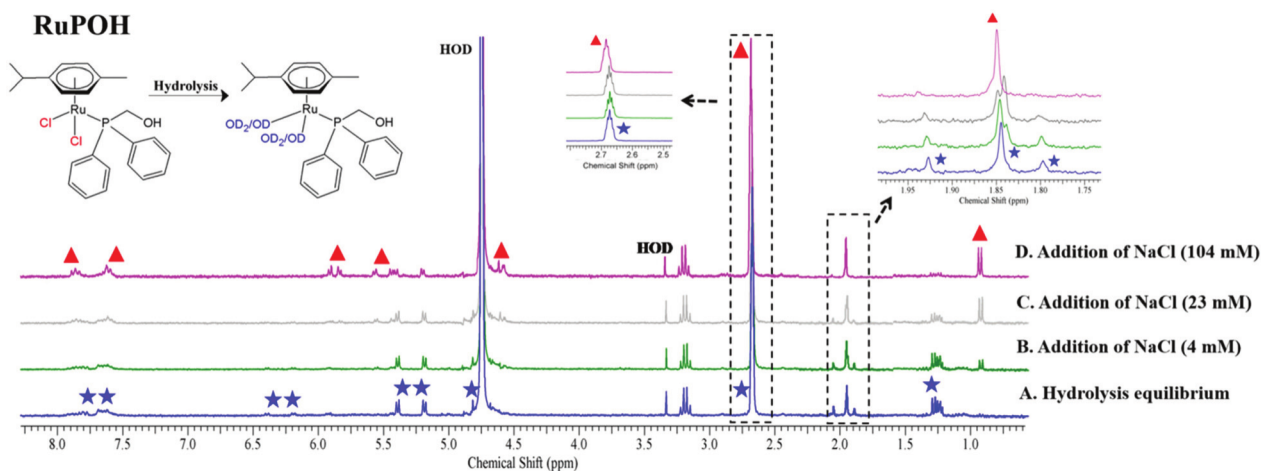


Fig. 6 Confirmation of the hydrolysis of (A) RuPOH (1 mM) by  $^1\text{H}$  NMR in 20% DMSO- $d_6$ /80%  $\text{D}_2\text{O}$  (v/v) at 298 K. The peaks for the aqua complex are marked in blue and the peaks for the chlorido complex are marked in red. The peaks for the chlorido complex RuPOH increased (red triangle) in intensity while the peaks for the aqua complex decreased (blue star). (B) IrPOH (1 mM) by  $^1\text{H}$  NMR in 20% DMSO- $d_6$ /80%  $\text{D}_2\text{O}$  (v/v) at 298 K. The peaks for the chlorido complex IrPOH increased (red triangle) in intensity while the peaks for the aqua complex decreased (blue star).

neutral character of these compounds, but low abundant  $[\text{M} + \text{Na}]^+$  sodiated ions were detected at  $m/z$  637 (Fig. S11 and S12, ESI $^+$ ) and at  $m/z$  697 (Fig. S13 and S14, ESI $^+$ ) for IrPOH and IrMPOH, respectively. The ESI(+)-MS spectra were dominated by  $[\text{M} - \text{Cl}]^+$  ions at  $m/z$  579 (Fig. S11, ESI $^+$ ) and  $m/z$  639 (Fig. S13, ESI $^+$ ) for IrPOH and IrMPOH, respectively. Less abundant peaks corresponding to  $[\text{M} - \text{Cl} - \text{HCl}]^+$  and  $[\text{M} - \text{Cl} - \text{HCl} - \text{H}_2\text{CO}]^+$  ions were also recorded indicating that chloride groups and the hydroxymethyl pendant arm of the phosphine ligand were easily displaced.

As illustrated in Fig. S12 and S14 ESI $^+$ , the cluster peaks arising from the experimental traces compared with those calculated for the pertinent species indicate excellent superimposition. The ESI(+)-MS spectra of similar Ru complexes showed comparable results. They did not show the  $[\text{M}]^+$  molecular ion peaks, but low abundant  $[\text{M} + \text{Na}]^+$  sodiated ions were detected at  $m/z$  545 (Fig. S15, ESI $^+$ ) and  $m/z$  605 (Fig. S18, ESI $^+$ ) for RuPOH and RuMPOH, respectively.

Analogously to what was observed in Ir complexes, these ESI(+)-MS spectra were dominated by  $[\text{M} - \text{Cl}]^+$  ions at  $m/z$  487 (Fig. S15, ESI $^+$ ) and 547 (Fig. S17, ESI $^+$ ) for RuPOH and RuMPOH, respectively. Additional low abundant peaks corresponding to  $[\text{M} - \text{Cl} - \text{HCl}]^+$  and  $[\text{M} - \text{Cl} - \text{HCl} - \text{H}_2\text{CO}]^+$  ions were also measured. As illustrated in Fig. S16, ESI $^+$  for RuPOH, the experimental cluster profile of the  $[\text{M} + \text{Na}]^+$  ion at  $m/z$  545 is in close agreement with the calculated cluster. The ESI(-) MS spectra of the Ru complexes displayed the chlorinated  $[\text{M} + \text{Cl}]^-$  molecular ion peak at  $m/z$  559 (Fig. S17, ESI $^+$ ) and 619 (Fig. S19, ESI $^+$ ) for RuPOH and RuMPOH, respectively.

#### Voltamperometry cyclic

Cyclic voltammetry (CV) was performed to precisely understand the redox activity of the studied complexes (i.e., cellular ROS production, *vide supra*). The redox potentials for all complexes, the corresponding phosphine ligands, and ferrocene

were determined by cyclic voltammetry in DMF solution using 0.1 M tetrabutylammonium perchlorate (TBAP) as the supporting electrolyte in the selected potential window from  $-1.0$  V to  $2.0$  V vs.  $\text{Ag}/\text{Ag}^+$  at different scan rates (from 1 to  $20$   $\text{mV s}^{-1}$ ). The cyclic voltammograms (CVs) of all studied compounds are presented in (Fig. 7 and Fig. S20 and S21, ESI $^+$ ). The cyclic voltammograms of all complexes exhibited one irreversible oxidation peak at around  $1.5$ – $1.7$  V which is assigned to phosphine ligand oxidation. One quasi-reversible reduction peak around  $-0.55$  V is observed for all complexes (around  $\Delta E = 0.98$  V for all complexes) and it can also be assigned to the phosphine ligand.

Replacement of the anionic chloro ligands by the neutral solvent molecules as in all complexes studied here produces positively charged species (*vide supra*), which could be expected to be more difficult to oxidize.<sup>56</sup> However, the cyclic voltamperograms of all complexes (IrPOH, IrMPOH, RuPOH, and RuMPOH) displayed one electrochemically reversible redox wave. As shown in Fig. 6A, compounds IrPOH and IrMPOH show reversible oxidation waves in the region of  $1.2$ – $1.5$  V, which can be attributed to the metal-centered Ir(III)/Ir(IV) oxidation. The determined oxidation potentials for the studied iridium(III) complexes, referring to the Ir(III)/Ir(IV) redox process, are in agreement with the literature data for other organometallic Ir(III) compounds with various ligands.<sup>17,57–60</sup> The position of the cathodic peak was slightly shifted towards the negative potential, while the anodic peak was shifted a little towards positive potentials simultaneously with the scan rate increase. These observations suggest a diffusion controlled redox process.<sup>61</sup> An electrochemical investigation of Ru(II) complexes (RuPOH and RuMPOH) revealed a quasi-reversible one-electron Ru(II)/Ru(III) oxidation process in the region of  $1.1$ – $1.3$  V, which is in agreement with the literature data.<sup>7,19</sup> Thus, even though it is stated that Ru(II) arene “piano-stool” complexes are normally unable to change their +II oxidation



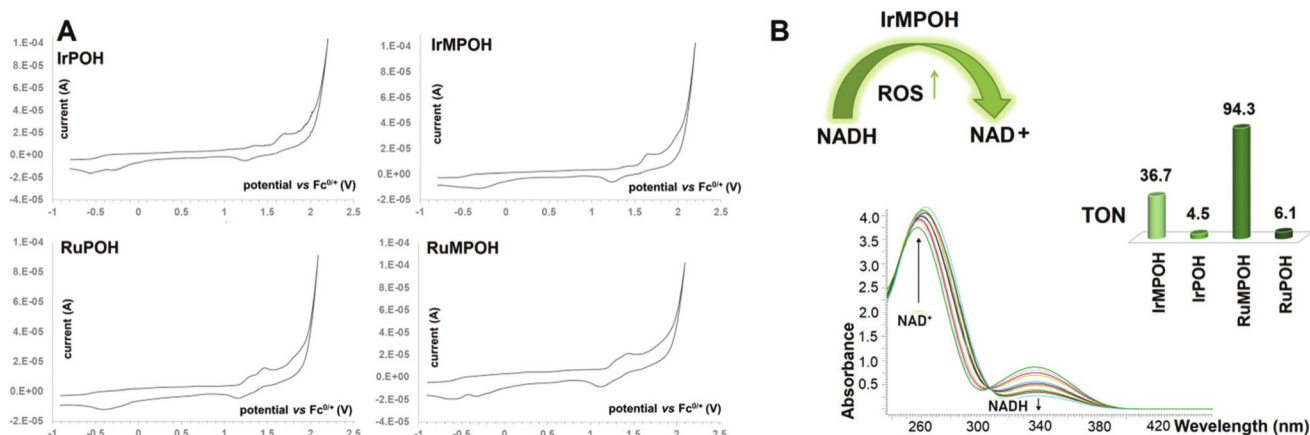


Fig. 7 (A) Cyclic voltammograms of iridium(III) complexes (1 mM), recorded with 0.1 M tetrabutyl ammonium perchlorate (TBAP) as the supporting electrolyte in DMF solution. Scan rates (10 mV s<sup>-1</sup>). The potentials were referenced to the Fc<sup>0/+</sup> redox couple. (B) The UV/vis spectra of NADH (100 μM) were determined after incubation with IrMPOH (1 μM) in CH<sub>3</sub>OH/H<sub>2</sub>O (1 : 9, v/v) at 298 K for 8 h. The arrows show the absorbance change over time. The histogram of TONs for complex RuPOH, RuMPOH, IrPOH and IrMPOH.

state due to stabilization by the  $\pi$ -bonded arene ligands,<sup>19</sup> the studied organometallic complexes with aminomethyl(diphenyl)phosphines are prone to undergo electrochemical processes.

#### Catalysis of NADH oxidation

The coenzyme, nicotinamide adenine dinucleotide (NADH), plays a vital role in the biocatalysis process. NAD<sup>+</sup> is a ubiquitous cofactor utilized by more than 300 dehydrogenase enzymes. The nicotinamide region is the site of reversible redox processes in living cells.<sup>6,17</sup> Literature data indicated that Ir(III) and Ru(II) complexes are able to catalyse the conversion of NADH to NAD<sup>+</sup> and induce the production of reactive oxygen species (ROS), which provide a pathway for the mechanism of oxidation.<sup>5,8,62</sup> Therefore, the reactions between synthesized metal complexes and NADH were investigated (Fig. 7B and Fig. S22, ESI<sup>†</sup>). A slight decrease in the absorption band at 339 nm and its increase at 259 nm (the absorbance of NADH and NAD<sup>+</sup>, respectively) revealed the catalytic activity of all investigated complexes. The turnover numbers (TONs) of NADH are shown in Fig. 7B. The changes in metal ions led to little variations in the catalytic activity of the complexes. However, the substituent effect of the chelating ligands on the catalytic activities of the Ir(III) and Ru(II) complexes showed a similar trend as follows: RuMPOH (94.3) > IrMPOH (36.7) > RuPOH (6.1) > IrPOH (4.5). This fact leads to the assumption that the catalytic activity of the hydride transfer reaction in this system is mainly determined by the ligands. Comparing two metal ions employed in our research (Ru(II) and Ir(III)), we can conclude that complexes with ruthenium ions showed slightly better catalytic activity.

#### Anticancer activity in vitro

The cytotoxicity of the complexes (IrPOH, IrMPOH, RuPOH and RuMPOH) was tested in vitro against various cancer cell lines: human lung adenocarcinoma (A549), human breast

adenocarcinoma (MCF7), metastatic human melanoma (WM2664); human malignant glioma cell line (LN18); human prostate carcinoma (DU-145), human pancreatic/duct carcinoma (PANC-1), as well as towards two immortalized human embryonic kidney (HEK293T), the primary line of human pulmonary fibroblasts (MCR-5) and human keratinocyte (HaCat) cell lines. The IC<sub>50</sub> values (concentration of a drug required to inhibit the growth of 50% of the cells) were assessed using two different approaches—after 24 h or 24 h + 48 h using the 3-(4,5-dimethylthiazole)-2,5-diphenyltetrazoliumbromide (MTT) method. In addition, the cells were also treated with cisplatin at the same concentration range as our complexes and considered as a control (Table 3).

The IC<sub>50</sub> values were determined from the plots of cell viability at various concentrations of each compound by matching appropriate dose–response curves and are presented in Table 2. The ligands (POH and MPOH) were inactive against all cell lines tested with IC<sub>50</sub> values >100 μM, regardless of the incubation time. The lack of activity of the ligands indicates that the activity is solely attributed to the metal–ligand complexes. Starting metal complexes [Ru( $\eta^6$ -p-cymene)Cl<sub>2</sub>]<sub>2</sub> and [Ir( $\eta^5$ -Cp\*)Cl<sub>2</sub>]<sub>2</sub> were inactive towards the A549, MCF7, LN-18, M266-4 and PANC-1 cancer cell lines in contrast to the Du145 cancer cell line against which they showed a moderate cytotoxic effect. Complementary studies show that the IC<sub>50</sub> values of all investigated phosphine Ru(II) and Ir(III) complexes are >100 μM against MCF7 and LN-18 cells and thus are deemed inactive. Tumor cell selectivity was achieved only for human lung adenocarcinoma (A549), human prostate carcinoma (DU-145), metastatic human melanoma (WM2664) and human pancreatic/duct carcinoma (PANC-1) cells. At the same time, all complexes are significantly less cytotoxic towards normal human embryonic kidney (HEK293T), human keratinocyte (HaCat) and human pulmonary fibroblast (MCR-5) cell lines after 24 h and 72 h of incubation time when compared to cancer cell lines. For a compound to be a successful anticancer



Table 3 The values of IC<sub>50</sub> [μM] (concentration of a drug required to inhibit the growth of 50% of the cells) for cancer and normal cells after 24 h and 24 h + 48 h treatment with the studied compounds and cisplatin as reference. IC<sub>50</sub> [μM] ± SD

	A549	Du145	WM266-4	MCF7	LN-18	PANC-1	MRC5	HEK293T	HaCat
24 h									
RuPOH	89.5 ± 5.8	>100	47.2 ± 2.1	>100	>100	85.5 ± 3.8	285.1 ± 5.1	674.5 ± 12.4	375.5 ± 9.4
IrPOH	45.8 ± 1.6	31.5 ± 0.4	>100	>100	>100	35.3 ± 1.1	245.2 ± 3.6	754.2 ± 10.1	251.2 ± 0.9
RuMPOH	95.5 ± 5.8	>100	48.8 ± 5.1	>100	>100	90.2 ± 5.1	299.1 ± 2.1	711.4 ± 9.3	321.4 ± 6.3
IrMPOH	47.6 ± 2.6	34.3 ± 4.7	>100	>100	>100	40.1 ± 1.2	247.3 ± 7.4	792.2 ± 12.1	252.9 ± 7.9
[Ru(η <sup>6</sup> -p-cymene)Cl <sub>2</sub> ] <sub>2</sub>	>100	74.3 ± 2.7	>100	>100	>100	>100	22.9 ± 3.9	62.9 ± 1.2	225.9 ± 1.9
[Ir(η <sup>5</sup> -Cp*)Cl <sub>2</sub> ] <sub>2</sub>	>100	98.3 ± 5.1	>100	>100	>100	>100	42.1 ± 1.2	84.1 ± 5.2	341.1 ± 5.2
POH	>100	>100	>100	>100	>100	>100	>1000	>1000	>1000
MPOH	>100	>100	>100	>100	>100	>100	>1000	>1000	>1000
cisplatin	81.3 ± 3.5	73.5 ± 2.1	2.63 ± 0.6	50.9 ± 7.6	56.8 ± 5.3	12.4 ± 1.3	31.5 ± 4.1	23.6 ± 2.3	26.4 ± 2.7
72 h (24 h + 48 h recovery time)									
RuPOH	63.1 ± 2.4	>100	11.7 ± 1.5	>100	>100	>100	274.1 ± 3.1	875.5 ± 10.1	395.5 ± 2.7
IrPOH	22.5 ± 1.3	52.4 ± 0.9	>100	>100	>100	>100	215.1 ± 9.1	834.2 ± 11.8	181.8 ± 1.9
RuMPOH	65.2 ± 5.2	>100	8.8 ± 5.1	>100	>100	>100	275.6 ± 4.3	887.5 ± 3.6	321.4 ± 2.3
IrMPOH	27.6 ± 2.3	85.8 ± 1.06	>100	>100	>100	>100	232.3 ± 4.4	892.3 ± 11.6	195.9 ± 3.7
[Ru(η <sup>6</sup> -p-cymene)Cl <sub>2</sub> ] <sub>2</sub>	>100	84.3 ± 6.1	>100	>100	>100	>100	52.9 ± 6.2	112.3 ± 3.2	292.9 ± 2.5
[Ir(η <sup>5</sup> -Cp*)Cl <sub>2</sub> ] <sub>2</sub>	>100	>100	>100	>100	>100	>100	82.1 ± 3.1	164.1 ± 3.2	391.1 ± 1.2
POH	>100	>100	>100	>100	>100	>100	>1000	>1000	>1000
MPOH	>100	>100	>100	>100	>100	>100	>1000	>1000	>1000
Cisplatin	84.3 ± 4.5	78.5 ± 5.1	8.29 ± 0.4	34.9 ± 7.1	49.1 ± 2.1	25.75 ± 0.02	21.48 ± 4.1	15.56 ± 2.3	60.34 ± 2.5

drug aspirant, it is expected to efficiently inhibit the proliferation of cancer cells and cause apoptosis, but at the same time spare the normal cells from its action, contributing to lesser or negligible side-effects.<sup>63</sup>

Based on our observations, the type of metal ions in the compounds has a major influence on the anticancer activity of the compounds. Our results indicated that compounds IrPOH and IrMPOH which carry an iridium ion, have the highest cytotoxicity against the A549, DU-145 and PANC-1 cancer cell lines.

The iridium complexes were found to be moderately active against the DU145 cancer cell line with IC<sub>50</sub> values in the range of 31.5–34.13 μM and 52.43–85.58 μM, respectively, for 24 h and 24 h + 48 h recovery time. It can be hypothesized that the activation of cellular repair mechanisms is responsible for this increase in IC<sub>50</sub> value after 72 h. Furthermore, we found that RuPOH and RuMPOH based on Ru ions selectively inhibit the proliferation of WM266-4 skin cancer cells (after 24 h: IC<sub>50</sub> = 47.2 ± 2.1 and 48.8 ± 5.1; after 72 h: IC<sub>50</sub> = 11.7 ± 1.5 and 8.8 ± 5.1), while Ir(III) complexes showed no cytotoxic activity (IC<sub>50</sub> > 100 μM).

In recent years, iridium based complexes have been widely studied as anticancer agents. For instance, Li and co-workers synthesized iridium(III) complexes bearing P<sup>+</sup>P-chelating ligand and all these complexes had better potent anticancer activity than cisplatin towards A549 and HeLa cells. The studies indicate that they can cause lysosomal damage and the release of cathepsin B from lysosomes.<sup>64</sup>

Literature iridium half sandwiched complexes with α-picolinic acid frameworks were evaluated for their anticancer properties against lung tumor cells. These complexes could be transferred by serum albumin and could also catalyze the conversion of NADH to NAD<sup>+</sup>. They successfully entered tumor cells by energy dependent mechanisms targeting lysosomes and then mitochondria which induced apoptosis.<sup>17</sup> Our results also indi-

cated that complexes (IrPOH, IrMPOH, RuPOH, and RuMPOH) can convert NADH to NAD<sup>+</sup> and the catalytic performance may provide the potential pathway to induce ROS and enhance the killing of cancer cells by an oxidant mechanism of action. Qing Du and co-workers have synthesized, characterized and evaluated the anticancer activities of some neutral fluorescent Ir(III) and Ru(II) half-sandwich organometallic complexes containing phosphine-sulfonate ligands. Most of these complexes display promising anticancer activities toward HeLa and A549 cancer cells comparable to, and for some complexes, even higher than the clinical cisplatin. However, like in our research, the ruthenium(II) complexes in this system display a lower potency than iridium(III) complexes, which can be attributed to the combinatorial action of the metal and phosphine ligand. These complexes can also convert NADH to NAD<sup>+</sup> and the catalytic performance may provide the potential pathway to induce ROS and enhance the killing of cancer cells by an oxidant mechanism of action.<sup>17</sup> The cytotoxic potential of half-sandwich organometallic Ru(II) complexes towards skin cancer was also described by Ruilin Guan and co-workers.<sup>58</sup> They synthesized, characterized and tested the anticancer potential of two novel arene ruthenium(II) complexes with bis-phosphino amine ligand on A375 malignant melanoma and non-malignant HEK293 cell line. The Ru(II) complexes displayed a highly selective anticancer profile as they hindered cellular proliferation in malignant melanoma cells and did not cause toxicity towards non-malignant cells.<sup>65</sup>

## Experimental section

### Reagents

All syntheses and operations were carried out under an atmosphere of dry oxygen-free dinitrogen, using standard Schlenk

techniques.  $\text{PPh}_2\text{CH}_2\text{OH}$  (POH)<sup>48</sup> and  $\text{P}(\text{p-OCH}_3\text{Ph})_2\text{CH}_2\text{OH}$  (MPOH)<sup>49</sup> were synthesized according to the literature procedures.  $[\text{Ir}(\eta^5\text{-Cp}^*)\text{Cl}_2]_2$  (>96%) was purchased from ACROS organics (Fisher Scientific).  $[\text{Ru}(\eta^6\text{-p-cymene})\text{Cl}_2]_2$  (1) (>98%) and other small reagents and solvents were purchased from Sigma Aldrich.

## Methods

The NMR spectra were recorded using a Bruker Avance III spectrometer (at 298 K; 500 MHz for  $^1\text{H}$  NMR, 125 MHz for  $^{13}\text{C}$  NMR and 202 MHz for  $^{31}\text{P}$ ) with traces of protonated solvent as an internal reference for  $^1\text{H}$  ( $\text{CDCl}_3$ : 7.26 ppm) and  $^{13}\text{C}\{^1\text{H}\}$  spectra ( $\text{CDCl}_3$ : 77.36 ppm) and 85%  $\text{H}_3\text{PO}_4$  in  $\text{H}_2\text{O}$  as an external standard for  $^{31}\text{P}\{^1\text{H}\}$ . The signals in the spectra are defined as: s = singlet (\* – strongly broadened signal), d = doublet, dd = doublet of doublets, t = triplet and m = multiplet. The chemical shifts are reported in ppm and the coupling constants are reported in Hz. Elemental analysis was carried out using a Vario EL3 CHN analyzer for C and H, and they were within 0.3% of the theoretical values. The absorption spectra were recorded using a Cary 50 Bio spectrophotometer (Varian Inc., Palo Alto, CA) in the 800–200 nm range. Mass spectra were collected using an LCQ Fleet ion trap mass spectrometer (Thermo-Scientific) equipped with an ESI source operating in the positive ion mode. Metal complexes were dissolved in chloroform giving ca.  $2 \times 10^{-3}$  M stock solutions. These solutions were subsequently diluted in methanol to obtain ca.  $2 \times 10^{-5}$  M solutions which were directly infused into the ESI source via a syringe pump at a flow rate of  $10 \mu\text{L min}^{-1}$ . The ions were produced using a spray voltage of 3.5 kV and the entrance capillary temperature was kept at 280 °C. Other instrumental parameters were automatically adjusted to optimize the signal-to-noise ratio.

## Synthesis

Preparation of  $\text{Ru}(\eta^6\text{-p-cymene})\text{Cl}_2\text{PPh}_2\text{CH}_2\text{OH}$  (RuPOH). The binuclear ruthenium complex of  $[\text{Ru}(\eta^6\text{-p-cymene})\text{Cl}_2]_2$  (0.3045 g, 0.497 mmol) was added to a solution of  $\text{PPh}_2\text{CH}_2\text{OH}$  (0.2150 g, 0.994 mmol) in dichloromethane (15 mL). After few minutes, the cloudy solution became clean and brown. The mixture was stirred for 24 h and then the solvent was removed under vacuum. RuPOH is well soluble in  $\text{CHCl}_3$ ,  $\text{CH}_2\text{Cl}_2$ , methanol, DMSO and a mixture of  $\text{H}_2\text{O}$ : DMSO (100 : 1).

Yield: 88%, molar mass: 522.41  $\text{g mol}^{-1}$ .

Anal. calcd for  $\text{RuCl}_2\text{PC}_{23}\text{H}_{27}\text{O}$ : C, 52.88; H, 5.21%. Found: C, 52.84; H, 5.22%.

NMR (298 K,  $\text{CDCl}_3$ ):  $^{31}\text{P}\{^1\text{H}\}$ : 16.74 ppm;  $^1\text{H}$ :  $\text{H}^{2,3}$ : 0.93 d (J = 7.00);  $\text{H}^{11}$ : 1.91 s;  $\text{H}^4$ : 2.56 spt (J = 7.00);  $\text{H}^1$ : 4.64 s;  $\text{H}^{6,7-9}$ : 5.27 dd (J = 19.60; 6.20);  $\text{H}^{\text{Ph(m)}}$ ,  $\text{Ph(p)}$ : 7.41–7.58 m;  $\text{H}^{\text{Ph(o)}}$ : 7.79–7.93 m;  $^{13}\text{C}\{^1\text{H}\}$ :  $\text{C}^1$ : 63.28 d;  $\text{C}^{11}$ : 17.70 s;  $\text{C}^{2,3}$ : 21.73 s;  $\text{C}^4$ : 30.34 s;  $\text{C}^{6,8}$ : 86.42 d (J = 5.4);  $\text{C}^{7,9}$ : 89.74 d (J = 3.6);  $\text{C}^{10}$ : 95.60 s;  $\text{C}^5$ : 108.84 s;  $\text{C}^{\text{Ph(m)}}$ : 128.55 d (J = 9.1);  $\text{C}^{\text{Ph(p)}}$ : 131.17 s;  $\text{C}^{\text{Ph(i)}}$ : 132.49 d (J = 47.23);  $\text{C}^{\text{Ph(o)}}$ : 133.61 d (J = 9.1).

ESI(+)-MS in  $\text{CHCl}_3/\text{MeOH}$ , m/z (%): 545 (15)  $[\text{Ru}(\text{p-Cym})(\text{Cl})_2(\text{Ph}_2\text{PCH}_2\text{OH}) + \text{Na}]^+$  or  $[\text{M} + \text{Na}]^+$ ; 487 (100)  $[\text{Ru}(\text{p-Cym})(\text{Cl})(\text{Ph}_2\text{PCH}_2\text{OH})]^+$  or  $[\text{M} - \text{Cl}]^+$ ; 451 (15)  $[\text{Ru}(\text{p-Cym})$

$(\text{Ph}_2\text{PCH}_2\text{O})]^+$  or  $[\text{M} - \text{Cl} - \text{HCl}]^+$ ; 421 (20)  $[\text{Ru}(\text{p-Cym})(\text{Ph}_2\text{PH})]^+$  or  $[\text{M} - \text{Cl} - \text{HCl} - \text{H}_2\text{CO}]^+$ .

ESI(-)-MS in  $\text{CHCl}_3/\text{MeOH}$ , m/z (%): 559 (100)  $[\text{Ru}(\text{p-Cym})(\text{Cl})_3(\text{Ph}_2\text{PCH}_2\text{OH})]^-$  or  $[\text{M} + \text{Cl}]^-$ .

Preparation of  $\text{Ru}(\eta^6\text{-p-cymene})\text{Cl}_2\text{P}(\text{p-OCH}_3\text{Ph})_2\text{CH}_2\text{OH}$  (RuMPOH). Following the method presented for RuPOH, binuclear ruthenium complex (0.3126 g, 0.510 mmol) and  $\text{P}(\text{p-OCH}_3\text{Ph})_2\text{CH}_2\text{OH}$  (0.3103 g, 1.123 mmol) gave a brown precipitate. RuMPOH is well soluble in  $\text{CHCl}_3$ ,  $\text{CH}_2\text{Cl}_2$ , methanol, DMSO and a mixture of  $\text{H}_2\text{O}$ : DMSO (100 : 1).

Yield: 73%, molar mass: 582.46  $\text{g mol}^{-1}$ .

Anal. calc. for  $\text{RuCl}_2\text{PC}_{25}\text{H}_{31}\text{O}_3$ : C, 51.55; H, 5.36%. Anal. found: C, 51.53; H, 5.37%.

NMR (298 K,  $\text{CDCl}_3$ ):  $^{31}\text{P}\{^1\text{H}\}$ : 15.07 ppm;  $^1\text{H}$ :  $\text{H}^{2,3}$ : 0.97 d (J = 6.98);  $\text{H}^9$ : 1.89 s;  $\text{H}^4$ : 2.61 spt (J = 7.00);  $\text{H}^{\text{OCH}_3}$ : 3.86 s;  $\text{H}^1$ : 4.54 s;  $\text{H}^{6,7-9}$ : 5.25 s;  $\text{H}^{\text{Ph(o)}}$ : 6.98 dd (J = 8.66; 1.40);  $\text{H}^{\text{Ph(m)}}$ : 7.77 t (J = 9.07);  $^{13}\text{C}\{^1\text{H}\}$ :  $\text{C}^{11}$ : 17.57 s;  $\text{C}^{2,3}$ : 21.60 s;  $\text{C}^4$ : 30.18 s;  $\text{C}^{\text{OCH}_3}$ : 55.39 s;  $\text{C}^1$ : 63.51 d (J = 31.79);  $\text{C}^{6,8}$ : 86.19 d (J = 5.4);  $\text{C}^{7,9}$ : 89.31 s;  $\text{C}^{10}$ : 95.14 s;  $\text{C}^5$ : 108.76 s;  $\text{C}^{\text{Ph(o)}}$ : 114.15 s;  $\text{C}^{\text{Ph(i)}}$ : 123.14 d (J = 47.23);  $\text{C}^{\text{Ph(m)}}$ : 135.02 s;  $\text{C}^{\text{Ph(p)}}$ : 161.68 s.

ESI(+)-MS in  $\text{CHCl}_3/\text{MeOH}$ , m/z (%): 605 (15)  $[\text{Ru}(\text{p-Cym})(\text{Cl})_2(\text{p-OMe-Ph}_2\text{PCH}_2\text{OH}) + \text{Na}]^+$  or  $[\text{M} + \text{Na}]^+$ ; 547 (100)  $[\text{Ru}(\text{p-Cym})(\text{Cl})(\text{p-OMe-Ph}_2\text{PCH}_2\text{OH})]^+$  or  $[\text{M} - \text{Cl}]^+$ ; 511 (20)  $[\text{Ru}(\text{p-Cym})(\text{p-OMe-Ph}_2\text{PCH}_2\text{O})]^+$  or  $[\text{M} - \text{Cl} - \text{HCl}]^+$ ; 481 (25)  $[\text{Ru}(\text{p-Cym})(\text{p-OMe-Ph}_2\text{PH})]^+$  or  $[\text{M} - \text{Cl} - \text{HCl} - \text{H}_2\text{CO}]^+$ .

ESI(-)-MS in  $\text{CHCl}_3/\text{MeOH}$ , m/z (%): 619 (100)  $[\text{Ru}(\text{p-Cym})(\text{Cl})_3(\text{p-OMe-Ph}_2\text{PCH}_2\text{OH})]^-$  or  $[\text{M} + \text{Cl}]^-$ .

Preparation of  $\text{Ir}(\eta^5\text{-Cp}^*)\text{Cl}_2\text{PPh}_2\text{CH}_2\text{OH}$  (IrPOH). The binuclear iridium complex of  $[\text{Ir}(\eta^5\text{-Cp}^*)\text{Cl}_2]_2$  (0.3163 g, 0.397 mmol) was added to a solution of  $\text{PPh}_2\text{CH}_2\text{OH}$  (0.1717 g, 0.794 mmol) in dichloromethane (15 mL). After few minutes, the cloudy solution became clean and orange. The mixture was stirred for 24 h and then the solvent was removed under vacuum. IrPOH is well soluble in  $\text{CHCl}_3$ ,  $\text{CH}_2\text{Cl}_2$ , methanol, DMSO and a mixture of  $\text{H}_2\text{O}$ : DMSO (100 : 1).

Yield: 78%, molar mass: 614.56  $\text{g mol}^{-1}$ .

Anal. calc. for  $\text{IrCl}_2\text{PC}_{23}\text{H}_{28}\text{O}$ : C, 44.95; H, 4.59%. Anal. found: C, 44.92; H, 4.60%.

NMR (298 K,  $\text{CDCl}_3$ ):  $^{31}\text{P}\{^1\text{H}\}$ : -7.15 ppm;  $^1\text{H}$ :  $\text{H}^{\text{Cp}(\text{CH}_3)}$ : 1.40 d (J = 2.19);  $\text{H}^1$ : 4.96 d (J = 6.64);  $\text{H}^{\text{Ph(m)}}$ ,  $\text{Ph(p)}$ : 7.41–7.54 m;  $\text{H}^{\text{Ph(o)}}$ : 7.72–7.84 m;  $^{13}\text{C}\{^1\text{H}\}$ :  $\text{C}^1$ : 64.25 d;  $\text{C}^{\text{Cp}(\text{CH}_3)}$ : 8.08 s;  $\text{C}^{\text{Cp}}$ : 92.28 d (J = 2.2);  $\text{C}^{\text{Ph(m)}}$ : 128.15 d (J = 9.9);  $\text{C}^{\text{Ph(p)}}$ : 130.92 s;  $\text{C}^{\text{Ph(o)}}$ : 133.8 d (J = 9.9).

ESI(+)-MS in  $\text{CHCl}_3/\text{MeOH}$ , m/z (%): 637 (10)  $[\text{Ir}(\text{Me}_5\text{Cp})(\text{Cl})_2(\text{Ph}_2\text{PCH}_2\text{OH}) + \text{Na}]^+$  or  $[\text{M} + \text{Na}]^+$ ; 607 (15)  $[\text{Ir}(\text{Me}_5\text{Cp})(\text{Cl})_2(\text{Ph}_2\text{PH}) + \text{Na}]^+$  or  $[\text{M} - \text{H}_2\text{CO} + \text{Na}]^+$ ; 579 (100)  $[\text{Ir}(\text{Me}_5\text{Cp})(\text{Cl})(\text{Ph}_2\text{PCH}_2\text{OH})]^+$  or  $[\text{M} - \text{Cl}]^+$ ; 543 (65)  $[\text{Ir}(\text{Me}_5\text{Cp})(\text{Ph}_2\text{PCH}_2\text{O})]^+$  or  $[\text{M} - \text{Cl} - \text{HCl}]^+$ ; 513 (15)  $[\text{Ir}(\text{Me}_5\text{Cp})(\text{Ph}_2\text{PH})]^+$  or  $[\text{M} - \text{Cl} - \text{HCl} - \text{CH}_2\text{O}]^+$ .

Preparation of  $\text{Ir}(\eta^5\text{-Cp}^*)\text{Cl}_2\text{P}(\text{p-OCH}_3\text{Ph})_2\text{CH}_2\text{OH}$  (IrMPOH). Following the method presented for IrPOH, binuclear iridium complex (0.3022 g, 0.379 mmol) and  $\text{P}(\text{p-OCH}_3\text{Ph})_2\text{CH}_2\text{OH}$  (0.2305 g, 0.834 mmol) gave orange precipitate. IrMPOH is well soluble in  $\text{CHCl}_3$ ,  $\text{CH}_2\text{Cl}_2$ , methanol, DMSO and a mixture of  $\text{H}_2\text{O}$ : DMSO (100 : 1).

Yield: 84%, molar mass: 674.62  $\text{g mol}^{-1}$ .

Anal. calcd for  $\text{IrCl}_2\text{PCl}_2\text{C}_{25}\text{H}_{32}\text{O}_3$ : C, 44.51; H, 4.78%. Anal. found: C, 44.49; H, 4.79%.

NMR (298 K,  $\text{CDCl}_3$ ):  $^{31}\text{P}\{^1\text{H}\}$ : -9.18 ppm;  $^1\text{H}$ :  $\text{H}^{\text{Cp}(\text{CH}_3)}$ : 1.40 d ( $J = 2.19$ );  $\text{H}^{\text{OCH}_3}$ : 3.85 s;  $\text{H}^1$ : 4.96 s;  $\text{H}^{\text{Ph}(\text{o})}$ : 9.98 dd ( $J = 8.80$ ; 1.50);  $\text{H}^{\text{Ph}(\text{m})}$ : 7.70 t ( $J = 9.34$ );  $^{13}\text{C}\{^1\text{H}\}$ :  $\text{C}^{\text{Cp}(\text{CH}_3)}$ : 8.35 s;  $\text{C}^{\text{OCH}_3}$ : 55.35 s;  $\text{C}^1$ : 64.87 d ( $J = 39.06$ );  $\text{C}^{\text{Cp}}$ : 92.34 d ( $J = 2.72$ );  $\text{C}^{\text{Ph}(\text{o})}$ : 113.93 d ( $J = 10.9$ );  $\text{C}^{\text{Ph}(\text{i})}$ : 118.82 d ( $J = 55.4$ );  $\text{C}^{\text{Ph}(\text{m})}$ : 135.57 d ( $J = 10.9$ );  $\text{C}^{\text{Ph}(\text{p})}$ : 161.83 s.

ESI(+)-MS in  $\text{CHCl}_3/\text{MeOH}$ ,  $m/z$  (%): 697 (10)  $[\text{Ir}(\text{Me}_5\text{Cp})(\text{Cl})_2(\text{p-OMe-Ph}_2\text{PCH}_2\text{O}) + \text{Na}]^+$  or  $[\text{M} + \text{Na}]^+$ ; 667 (10)  $[\text{Ir}(\text{Me}_5\text{Cp})(\text{Cl})_2(\text{p-OMe-Ph}_2\text{PH}) + \text{Na}]^+$  or  $[\text{M} - \text{H}_2\text{CO} + \text{Na}]^+$ ; 639 (100)  $[\text{Ir}(\text{Me}_5\text{Cp})(\text{Cl})(\text{p-OMe-Ph}_2\text{PCH}_2\text{OH})]^+$  or  $[\text{M} - \text{Cl}]^+$ ; 603 (40)  $[\text{Ir}(\text{Me}_5\text{Cp})(\text{p-OMe-Ph}_2\text{PCH}_2\text{O})]^+$  or  $[\text{M} - \text{Cl} - \text{HCl}]^+$ ; 573 (8)  $[\text{Ir}(\text{Me}_5\text{Cp})(\text{p-OMe-Ph}_2\text{P})]^+$  or  $[\text{M} - \text{Cl} - \text{HCl} - \text{CH}_2\text{O}]^+$ .

### Single crystal X-ray diffraction

Crystals of RuPOH, RuMPOH, IrPOH and IrMPOH suitable for X-ray analysis were obtained under refrigeration by slow evaporation of a dichloromethane/methanol (1 : 1, v/v) solution under normal oxygen conditions. The crystal data and details of data collection and structure refinement of RuPOH, IrPOH, RuMPOH and IrMPOH are given in Table S1, ESI.† The aromatic and aliphatic H atoms of all structures were included at idealized positions and refined using a riding model, with  $\text{C-H} = 0.95 \text{ \AA}$  for aromatic,  $0.99 \text{ \AA}$  for methylene and  $0.98 \text{ \AA}$  for methyl H atoms, and with  $U_{\text{iso}}(\text{H}) = 1.5U_{\text{eq}}(\text{C})$  for methyl H atoms and  $1.2U_{\text{eq}}(\text{C})$  otherwise. The positions of the H atoms of OH were also refined using the riding model. In the IrPOH structure, the hydroxyl groups are disordered and hence they are refined in two positions with occupancy.

### Hydrolysis studies

The hydrolysis characteristics of IrMPOH, RuMPOH, IrPOH and RuPOH in 20% DMSO/80%  $\text{H}_2\text{O}$  (v/v) solution at 298 K over 24 h were measured by UV-vis absorption spectroscopy, and the presence of DMSO ensured the solubility of these complexes.

The aquation of complexes IrPOH, IrMPOH, RuPOH, and RuMPOH (each 1 mM) in 20% DMSO- $d_6$ /80%  $\text{D}_2\text{O}$  (v/v) was monitored by  $^1\text{H}$  NMR in the presence of 4.0 mM, 23.0 mM, or 103.0 mM NaCl (10 min after addition of NaCl). DMSO was required to ensure the solubility of the complexes in aqueous solution and also its widely used solvent in preparing metal complex stock solutions for therapeutic studies. Hydrolysis was confirmed by the sequential addition of NaCl (after 15 min) to the equilibrium solution. NaCl was added to aid the assignment of species to either the Ir(Ru)- $\text{OD}_2$  or Ir(Ru)-Cl adducts. The percentages of each adduct were calculated based on the  $^1\text{H}$  NMR peak integrations.

### Catalytic oxidation of NADH to $\text{NAD}^+$

The complexes were evaluated for the catalytic oxidation of NADH to  $\text{NAD}^+$  by UV-visible spectroscopy over a 24 h period in 0.5% MeOH/99.5%  $\text{H}_2\text{O}$  at 310 K in 5 mM  $\text{Na}_2\text{HPO}_4/\text{NaH}_2\text{PO}_4$  buffer at pH 7.5. The complex concentration remained fixed at 2.5  $\mu\text{M}$  with varying NADH concentrations of

69, 103, 127, and 146  $\mu\text{M}$ . The conversion of NADH to  $\text{NAD}^+$  was followed by absorption at 339 nm ( $\epsilon_{\text{NADH}} = 6220 \text{ cm}^{-1} \text{ M}^{-1}$ ) to allow the evaluation of kinetic data. The reaction between complex 2 (250  $\mu\text{M}$ ) and NADH (750  $\mu\text{M}$ ) in 50% MeOH/50%  $\text{H}_2\text{O}$  at 310 K at pH 7.4 was monitored by  $^1\text{H}$ NMR spectroscopy.

### Electrochemical measurements

Cyclic voltammetry (CV) for 1 mM iridium(III) and ruthenium(II) complexes was carried out on the electrochemical analyzer (Bio-Logic, SP-150). Three-electrode glass cell with a working electrode – graphite disk electrode (2 mm diameter), a counter electrode – Pt wire, and a pseudo-reference electrode – Ag wire ( $\text{Ag}/\text{Ag}^+$ , 0.01 M  $\text{AgNO}_3$ , 0.1 M tetrabutyl ammonium perchlorate ( $\text{Bu}_4\text{NClO}_4$ ). All measurements were done in dimethylformamide (DMF) with 0.05 M  $\text{Bu}_4\text{NClO}_4$  as a supporting electrolyte at room temperature with a scan rate of  $10 \text{ mV s}^{-1}$  in the potential range from -0.5 to 1.2 V vs.  $\text{Ag}/\text{Ag}^+$ . Scans start at 0 V vs.  $\text{Ag}/\text{Ag}^+$  in the positive potential direction. All reported potentials were converted vs. the ferrocene/ferrocenium redox couple ( $\text{Fc}^{0/+}$ ).<sup>66</sup>

### Cell cultures

The MCF7 cell line (human breast adenocarcinoma, morphology: epithelial-like, ATCC: HTB-22), PANC-1 cell line (human pancreatic/duct carcinoma, morphology: epithelial, ATCC: CRL-1469), A549 cell line (human lung adenocarcinoma, morphology: epithelial, ATCC: CCL-185), and LN-18 cell line (brain; cerebrum; right temporal lobe, morphology: epithelial, ATCC: CRL-2610) were cultured in Dulbecco's Modified Eagle's Medium (DMEM, Corning) with phenol red, supplemented with 10% fetal bovine serum (FBS) and 1% streptomycin/penicillin. The WM266-4 cell line (human skin (metastasis), morphology: epithelial, ATCC CRL-1676) was cultured in EMEM (EBSS) + 2 mM glutamine + 1% Non-Essential Amino Acids (NEAA) + 1% sodium pyruvate (NaP) + 10% Foetal Bovine Serum (FBS). The DU-145 cell line (human prostate carcinoma derived from the metastatic site brain), the MCR-5 cell line (primary line of human pulmonary fibroblasts, ATCC: CCL-171) and the HEK293T cell line (human embryonic kidney) were cultured in a minimum essential medium (MEM, Corning) with only 10% fetal bovine serum (FBS). The cultures were incubated at 37 °C under a humidified atmosphere containing 5%  $\text{CO}_2$ . The cells were passed using a solution containing 0.05% trypsin and 0.5 mM EDTA. All media and other ingredients were purchased from ALAB, Poland.

### Cytotoxic activity

Since most of the studied compounds are insoluble in aqueous media, they needed to be pre-dissolved in DMSO for biological tests. Cytotoxicity was assessed by MTT assay performed according to the protocols described previously.<sup>67</sup> In brief,  $1 \times 10^4$  cells per well, seeded in a 96-well flat bottom microtiter plate, were incubated with the tested complexes (RuPOH, RuMPOH, IrPOH, and IrMPOH) at various concen-

trations for 24 h. After that time, the solutions of compounds were washed out, the cells were washed three times with PBS and a fresh medium was applied. Each compound concentration was tested in five replicates and repeated at least three times. The determined values of IC<sub>50</sub> (concentration of a drug required to inhibit the growth of 50% of the cells) are given as mean + S.D. (Standard Deviation). Furthermore, the post-treatment survival assessment of the treated cells was analyzed under a fluorescence inverted microscope (Olympus IC51, Japan) with an excitation filter of 470/20 nm. For this, the cells were stained with two versatile fluorescence dyes: fluorescein diacetate (FDA, 5 mg mL<sup>-1</sup>) and propidium iodide (PI, 5 mg mL<sup>-1</sup>) under standard conditions in the dark for 20 min. Before visualization the dyes were removed and the cells were washed with PBS twice. The IC<sub>50</sub> values were determined after 72 h from the plots of cell viability in the presence of various concentrations of each compound by matching the dose-response curves and using the Hill equation (Origin 9.0)<sup>68</sup> with regard to the untreated cells (control), where  $y_0$  denotes untreated cell control (which was set to 100% viability),  $y_{100}$  denotes lysis control (where the cells treated with 0.5% Triton X-100 were set to 0% viability, which was found to be sufficient to induce 100% cell death), IC<sub>50</sub> denotes the concentration [c] at which the viability of the cells reaches 50%, and H denotes the Hill coefficient:

$$y = \frac{y_0 + y_{100} \frac{c^H}{IC_{50}^H + c^H}}{1 + \frac{c^H}{IC_{50}^H}}$$

## Conclusions

The present article demonstrates the synthesis, physico-chemical characterization, and biological study of the in vitro anticancer activity of two novel piano-stool ruthenium(II) complexes Ru( $\eta^6$ -p-cymene)Cl<sub>2</sub>PPh<sub>2</sub>CH<sub>2</sub>OH (RuPOH) and Ru( $\eta^6$ -p-cymene)Cl<sub>2</sub>P(p-OCH<sub>3</sub>Ph)<sub>2</sub>CH<sub>2</sub>OH (RuMPOH) and two half-sandwich Ir(III) complexes Ir( $\eta^5$ -Cp\*)Cl<sub>2</sub>P(p-OCH<sub>3</sub>Ph)<sub>2</sub>CH<sub>2</sub>OH (IrMPOH) and Ir( $\eta^5$ -Cp\*)Cl<sub>2</sub>PPh<sub>2</sub>CH<sub>2</sub>OH (IrPOH). The complexes were characterized by mass spectrometry, NMR spectroscopy and elemental analysis. All the complexes were structurally identified by single-crystal X-ray diffraction analysis. The Ru(II) and Ir(III) complexes have a typical piano-stool geometry with an  $\eta^6$ -coordinated arene (Ru(II) complexes) or  $\eta^5$ -coordinated arene (Ir(III) complexes) and three additional sites of ligation occupied by two chloride ligands and the phosphine ligand. NMR spectra analysis revealed that both phosphine ligands are bound via a phosphorus atom much stronger than the iridium ion in contrast to the ruthenium ion.

Furthermore, investigation of the elucidation of the behavior of the Ru(II) and Ir(III) compounds allowed us to formulate the following general conclusions: (i) all complexes undergo slow hydrolysis. However, in the presence of a high concentration of chloride ions (i.e., in the nucleus), the following forms are created: Ir(III)-Cl<sub>2</sub> or Ru(II)-Cl<sub>2</sub>; (ii) all Ir(III) and Ru(II) inorganic compounds catalyse the oxidation of NADH to

NAD<sup>+</sup>. The type of metal ions used is not relevant in contrast to the type of the phosphine ligand. The complexes (IrMPOH and RuMPOH) containing phosphine with the methoxy group on the phenyl rings P(p-OCH<sub>3</sub>Ph)<sub>2</sub>CH<sub>2</sub>OH catalyse the oxidation of NADH to NAD<sup>+</sup> with high efficiency; and (iii) the redox activity of all complexes was confirmed by cyclic voltamperometry.

The above-described observation can have an important influence on understanding the cytotoxicity of the investigated complexes. Our results indicated that compounds IrPOH and IrMPOH have the highest cytotoxicity against the A549, DU-145 and PANC-1 cancer cell lines. The iridium complexes were found to be moderately active against the DU145 cancer cell line with IC<sub>50</sub> values in the range of 31.5–34.13  $\mu$ M and 52.43–85.58  $\mu$ M, respectively, for a 24 h and 72 h recovery time. It can be hypothesized that the activation of cellular repair mechanisms is responsible for this increase in the IC<sub>50</sub> value after 72 h. Furthermore, it was found that RuPOH and RuMPOH based on Ru ions selectively inhibit the proliferation of WM266-4 skin cancer cells (after 24 h: IC<sub>50</sub> = 47.2  $\pm$  2.1 and 48.8  $\pm$  5.1; after 72 h: IC<sub>50</sub> = 11.7  $\pm$  1.5 and 8.8  $\pm$  5.1). These results turned out to be very interesting and need more precise and detailed biological investigations to understand the mode of action of the Ir(III) and Ru(II) complexes.

## Author contributions

U. K. designed the scientific rationale; U. K. and S. K. performed the synthesis, purification, crystallization and characterisation (NMR, elemental analysis) of phosphines and complexes; designed and performed the experiments related to hydrolysis, NADH to NAD<sup>+</sup> oxidation, and cytotoxic activity; and performed the data analysis; U. K. designed and performed the experiments related to cyclic voltamperometry with data analysis and description and prepared all graphics; A. S.-S. performed the crystal structure description; F. T. performed the MS measurement with description of the result; U. K. and S. K. wrote the manuscript; and A. K. corrected the manuscript. The manuscript was reviewed by all authors prior to submission.

## Conflicts of interest

There are no conflicts to declare.

## Acknowledgements

The authors gratefully acknowledge financial support from the Polish National Science Centre (grant number 2020/37/N/ST4/02698). The authors would like to thank Marina Porchia and Alina Bieńko for their helpful advice and comments. We also extend a word of thanks to Rimon Mikhail for language editing of our manuscript.



## Notes and references

- M. Ebadi, K. Buskaran, S. Bullo, M. Z. Hussein, S. Fakurazi and G. Pastorin, *Alexandria Eng. J.*, 2021, **60**, 733–747.
- R. Abou-Jawde, T. Choueiri, C. Alemany and T. Mekhail, *Clin. Ther.*, 2003, **25**, 2121–2137.
- C. Fitzmaurice, C. Allen, R. M. Barber, L. Barregard, Z. A. Bhutta, H. Brenner, D. J. Dicker, O. Chimed-Orchir, R. Dandona and L. Dandona, *JAMA Oncol.*, 2017, **3**, 524–548.
- M. R. Noori-Dalooi and N. Ebadi, *Med. Sci. J. Islamic Azad Univ. Tehran Med. Branch*, 2015, **25**, 1–15.
- H. Hao, X. Liu, X. Ge, Y. Z. Xu, T. T. Ren, Y. Wang, C. Zhao and Z. Liu, *J. Inorg. Biochem.*, 2019, **192**, 52–61.
- J. J. Li, L. Guo, Z. Tian, M. Tian, S. Zhang, K. Xu, Y. Qiana and Z. Liu, *Dalton Trans.*, 2017, **46**, 15520–15534.
- J. Grau, V. Noe, C. Ciudad, M. J. Prieto, M. Font-Bardia, T. Calvet and V. Moreno, *J. Inorg. Biochem.*, 2012, **109**, 72–81.
- S. Betanzos-Lara, Z. Liu, A. Habtemariam, A. M. Pizarro, B. Qamar and P. J. Sadler, *Angew. Chem., Int. Ed.*, 2012, **51**, 3897–3900.
- R. T. Hembre and S. McQueen, *J. Am. Chem. Soc.*, 1994, **116**, 2141–2142.
- J. P. Collman, P. S. Wagenknecht and N. S. Lewis, *J. Am. Chem. Soc.*, 1992, **114**, 5665–5673.
- J. P. Collman, *Nat. Struct. Biol.*, 1996, **3**, 213–217.
- Y. Yan, M. Melchart, A. Habtemariam, A. Peacock and P. Sadler, *J. Biol. Inorg. Chem.*, 2006, **11**, 483–488.
- J. Canivet, G. Süß-Fink and P. Štěpnička, *Eur. J. Inorg. Chem.*, 2007, **30**, 4736–4742.
- H. C. Lo, O. Buriez, J. B. Kerr and R. H. Fish, *Angew. Chem.*, 1999, **111**, 1524–1527.
- P. Haquette, B. Talbi, L. Barilleau, N. Madern, C. Fosse and M. Salmain, *Org. Biomol. Chem.*, 2011, **9**, 5720–5727.
- J. J. Soldevila-Barreda, A. Habtemariam, I. Romero-Canelón and P. J. Sadler, *J. Inorg. Biochem.*, 2015, **153**, 322–333.
- Q. Du, L. Guo, M. Tian, X. Ge, Y. Yang, X. Jian, Z. Xu, Z. Tian and Z. Liu, *Organometallics*, 2018, **37**, 2880–2889.
- R. K. Gupta, R. Pandey, G. Sharma, R. Prasad, B. Koch, S. Srikrishna, P.-Z. Li, Q. Xu and D. S. Pandey, *Inorg. Chem.*, 2013, **52**, 3687–3698.
- P. Kołoczek, A. Skórska-Stania, A. Cierniak, V. Sebastian, U. K. Komarnicka, M. Płotek and A. Kyzioł, *Eur. J. Pharm. Biopharm.*, 2018, **128**, 69–81.
- M. Płotek, R. Starosta, U. K. Komarnicka, A. Skórska-Stania, P. Kołoczek and A. Kyzioł, *J. Inorg. Biochem.*, 2017, **170**, 178–187.
- U. K. Komarnicka, A. Niorettini, S. Kozieł, B. Pucelik, A. Barzowska, D. Wojtala, A. Ziółkowska, M. Lesiów, A. Kyzioł, S. Caramori, M. Porchia and A. Bieńko, *Pharmaceuticals*, 2022, **15**, 169.
- C. G. Hartinger, S. Zorbas-Seifried, M. A. Jakupc, B. Kynast, H. Zorbas and B. K. Keppler, *J. Inorg. Biochem.*, 2006, **100**, 891–904.
- J. M. Rademaker-Lakhai, D. van den Bongard, D. Pluim, J. H. Beijnen and J. H. Schellens, *Clin. Cancer Res.*, 2004, **10**, 3717–3727.
- C. S. Allardyce, A. Dorcier, C. Scolaro and P. J. Dyson, *Appl. Organomet. Chem.*, 2005, **19**, 1–10.
- P. J. Dyson and G. Sava, *Dalton Trans.*, 2006, **16**, 1929–1933.
- A. H. Velders, H. Kooijman, A. L. Spek, J. G. Haasnoot, D. de Vos and J. Reedijk, *Inorg. Chem.*, 2000, **39**, 2966–2967.
- W. H. Ang and P. J. Dyson, *Eur. J. Inorg. Chem.*, 2006, **2006**, 3993–3993.
- Z. Zhu, Z. Wang, Y. Hao, C. Zhu, Y. Jiao, H. Chen, Y.-M. Wang, J. Yan, Z. Guo and X. Wang, *Chem. Sci.*, 2016, **7**, 2864–2869.
- S. Dilruba and G. V. Kalayda, *Cancer Chemother. Pharmacol.*, 2016, **77**, 1103–1124.
- T. C. Johnstone, K. Suntharalingam and S. J. Lippard, *Chem. Rev.*, 2016, **116**, 3436–3486.
- C. G. Hartinger, N. Metzler-Nolte and P. J. Dyson, *Organometallics*, 2012, **31**, 5677–5685.
- Z. Liu, I. Romero-Canelón, B. Qamar, J. M. Hearn, A. Habtemariam, N. P. Barry, A. M. Pizarro, G. J. Clarkson and P. J. Sadler, *Angew. Chem., Int. Ed.*, 2014, **53**, 3941–3946.
- Y. Li, C. P. Tan, W. Zhang, L. He, L. N. Ji and Z. W. Mao, *Biomaterials*, 2015, **39**, 95–104.
- Z. Liu, A. Habtemariam, A. M. Pizarro, S. A. Fletcher, A. Kisova, O. Vrana, L. Salassa, P. C. A. Bruijninx, G. J. Clarkson, V. Brabec and P. J. Sadler, *J. Med. Chem.*, 2011, **54**, 3011–3026.
- L. Tabrizi and H. Chiniforoshan, *Dalton Trans.*, 2017, **46**, 2339–2349.
- C. Wang, J. Liu, Z. Tian, M. Tian, L. Tian, W. Zhao and Z. Liu, *Dalton Trans.*, 2017, **46**, 6870–6883.
- X. Liu, M. Shao, C. Liang, J. Guo, G. Wang, X.-A. Yuan, Z. Jing, L. Tian and Z. Liu, *ChemBioChem*, 2020, **21**, 1–9.
- L. He, Y. Li, C. P. Tan, R. R. Ye, M. H. Chen, J. J. Cao, L. N. Ji and Z. W. Mao, *Chem. Sci.*, 2015, **6**, 5409–5418.
- S. J. Chen, X. C. Liu, X. X. Ge, Q. H. Wang, Y. Q. Xie, Y. Y. Hao, Y. Zhang, L. Zhang, W. J. Shang and Z. Liu, *Inorg. Chem. Front.*, 2020, **7**, 91–100.
- K. D. Mjos and C. Orvig, *Chem. Rev.*, 2014, **114**(8), 4540–4563.
- J. J. Li, Z. Tian, S. Zhang, Z. Xu, X. Mao, Y. Zhou and Z. Liu, *Appl. Organomet. Chem.*, 2019, **33**, e4685.
- G. Y. S. Delgado, D. P. Marcon, A. L. de Oliveira and H. F. Dos Santos, *J. Inorg. Biochem.*, 2019, **200**, 110804.
- A. K. Renfrew, A. E. Eggera, R. Scopelliti, C. G. Hartinger and P. J. Dyson, *C. R. Chim.*, 2010, **13**, 1144–1150.
- Q. Du, Y. Yang, L. Guo, M. Tian, X. Ge, Z. Tian, L. Zhao, Z. Xu, J. Li and Z. Liu, *Dyes Pigm.*, 2019, **162**, 821–830.
- C. Icsel, V. T. Yilmaz, M. Aygun and E. Ulukaya, *ACS Med. Chem. Lett.*, 2020, **30**, 127077.
- A. Weiss, R. H. Berndsen, M. Dubois, C. Müller, R. Schibli, A. W. Griffioen, P. J. Dyson and P. Nowak-Sliwinska, *Chem. Sci.*, 2014, **5**, 4742–4748.

- 47 J. Fawcett, P. A. T. Hoye, R. D. W. Kemmitt, D. J. Law and D. R. Russell, *J. Chem. Soc., Dalton Trans.*, 1993, 2563–2568.
- 48 U. K. Komarnicka, R. Starosta, A. Kyzioł and M. Jeżowska-Bojczuk, *Dalton Trans.*, 2015, 44, 12688–12699.
- 49 U. K. Komarnicka, S. Kozioł, P. Zabierowski, R. Kruszyński, M. K. Lesiów, F. Tisato, M. Porchia and A. Kyzioł, *J. Inorg. Biochem.*, 2020, 203, 110926.
- 50 C. F. Macrae, I. Sovago, S. J. Cottrell, P. T. A. Galek, P. McCabe, E. Pidcock, M. Platings, G. P. Shields, J. S. Stevens, M. Towler and P. A. Wood, *Mercury* 2020.1, *J. Appl. Crystallogr.*, 2020, 53, 226–235.
- 51 M. C. Etter, J. C. MacDonald and J. Bernstein, *Acta Crystallogr., Sect. B: Struct. Sci.*, 1990, 46, 256–262.
- 52 A. M. Pizarro, A. Habtemariam and P. J. Sadler, *Medicinal Organometallic Chemistry*, in *Topics in Organometallic Chemistry*, ed. G. Jaouen and N. Metzler-Nolte, Springer-Verlag, Heidelberg, Germany, 1st edn, 2010, vol. 32, pp. 21–56.
- 53 E. J. Anthony, E. M. Bolitho, H. E. Bridgewater, O. W. L. Carter, J. M. Donnelly, C. Imberti, E. C. Lant, F. Lermite, R. J. Needham, M. Palau, P. J. Sadler, H. Shi, F. Wang, W.-Y. Zhang and Z. Zhang, *Chem. Sci.*, 2020, 11, 12888–12917.
- 54 Z. Liu, A. Habtemariam, A. M. Pizarro, G. J. Clarkson and P. J. Sadler, *Organometallics*, 2011, 30(17), 4702–4710.
- 55 F. Wang, H. Chen, S. Parsons, I. D. H. Oswald, J. E. Davidson and P. J. Sadler, *Chem. – Eur. J.*, 2003, 9, 5810.
- 56 J. Tauchman, B. Therrien, G. Süß-Fink and P. Štěpniček, *Organometallics*, 2012, 31, 3985–3994.
- 57 D. Zeng, X.-A. Yuan, J.-C. Liu, L. Li, L.-P. Wang, M.-F. Qin, S.-S. Bao, J. Ma and L.-M. Zheng, *ACS Omega*, 2019, 4, 16543–16550.
- 58 R. Guan, Y. Chen, L. Zeng, T. W. Rees, C. Jin, J. Huang, Z.-S. Chen, L. Jia and H. Chao, *Chem. Sci.*, 2018, 9, 5183–5190.
- 59 S. Kozioł Sandra, U. K. Komarnicka, A. Ziółkowska, A. Skórska-Stania, B. Pucelik, M. Płotek, V. Sebastian, A. Bieńko, G. Stochel and A. Kyzioł, *Inorg. Chem. Front.*, 2020, 7, 3386–3401.
- 60 K. Hasan, A. K. Bansal, I. D. W. Samuel, C. Roldán-Carmona, H. J. Bolink and E. Zysman-Colman, *Sci. Rep.*, 2015, 5, 12325.
- 61 M.-A. Tehfe, M. Lepeltier, F. Dumur, D. Gigmès, J.-P. Fouassier and J. Lalevée, *Macromol. Chem. Phys.*, 2017, 218, 170019.
- 62 Z. Liu, R. J. Deeth, J. S. Butler, A. Habtemariam, M. E. Newton and P. J. Sadler, *Angew. Chem., Int. Ed.*, 2013, 52, 4194–4197.
- 63 G. Gupta, A. Das, N. B. Ghate, T. Kim, J. Y. Ryu, J. Lee, N. Mandal and C. Y. Lee, *Chem. Commun.*, 2016, 52, 4274–4277.
- 64 J. Li, Z. Tian, Z. Xu, S. Zhang, Y. Feng, L. Zhang and Z. Liu, *Dalton Trans.*, 2018, 47, 15772–15782.
- 65 Z. Engelbrecht, K. E. Roberts, A. Hussan, G. Amenuvor, M. J. Cronjé, J. Darkwa, B. C. E. Makhubela and L. Sitole, *Bioorg. Med. Chem. Lett.*, 2020, 30, 127492.
- 66 C. Santini, M. Pellei, V. Gandin, M. Porchia, F. Tisato and C. Marzano, *Chem. Rev.*, 2014, 114, 815–862.
- 67 M. L. Circu and T. Y. Aw, *Free Radicals Biol. Med.*, 2010, 48, 749–776.
- 68 J. Weyermann, D. Lochmann and A. Zimmer, *Int. J. Pharm.*, 2005, 288, 369–376.

# Synthesis, physicochemical characterization and antiproliferative activity of phosphino Ru(II) and Ir(III) complexes.

Urszula K. Komarnicka,<sup>a†\*</sup> Sandra Kozieł,<sup>a†</sup> Agnieszka Skórska-Stania,<sup>b</sup> Agnieszka Kyzioł,<sup>b</sup> Francesco Tisato<sup>c</sup>

<sup>a</sup>Faculty of Chemistry, University of Wrocław, Joliot-Curie 14, 50-383 Wrocław, Poland

<sup>b</sup>Faculty of Chemistry, Jagiellonian University in Krakow, Gronostajowa 2, 30-387 Krakow, Poland

<sup>c</sup>ICMATECNR, Corso Stati Uniti 4, 35127 Padova, Italy

<sup>†</sup> First Author, <sup>\*</sup>corresponding Author: [urszula.komarnicka@chem.uni.wroc.pl](mailto:urszula.komarnicka@chem.uni.wroc.pl)

Herein we present the synthesis of new complexes based on ruthenium(II) (Ru( $\eta^6$ -*p*-cymene)Cl<sub>2</sub>PPh<sub>2</sub>CH<sub>2</sub>OH (RuPOH), Ru( $\eta^6$ -*p*-cymene)Cl<sub>2</sub>P(*p*-OCH<sub>3</sub>Ph)<sub>2</sub>CH<sub>2</sub>OH (RuMPOH)) and iridium(III) (Ir( $\eta^5$ -Cp\*)Cl<sub>2</sub>P(*p*-OCH<sub>3</sub>Ph)<sub>2</sub>CH<sub>2</sub>OH (IrMPOH), Ir( $\eta^5$ -Cp\*)Cl<sub>2</sub>PPh<sub>2</sub>CH<sub>2</sub>OH (IrPOH) containing phosphine ligands with/without methoxy motif on phenyl rings (P(*p*-OCH<sub>3</sub>Ph)<sub>2</sub>CH<sub>2</sub>OH (MPOH) and PPh<sub>2</sub>CH<sub>2</sub>OH (POH)). The complexes were characterized by mass spectrometry, NMR spectroscopy (1D: <sup>1</sup>H, <sup>13</sup>C{<sup>1</sup>H}, <sup>31</sup>P{<sup>1</sup>H}, 2D: HMQC, HMBC, COSY NMR) and elemental analysis. All the complexes were structurally identified by single-crystal X-ray diffraction analysis. The Ru(II) and Ir(III) complexes have typical piano-stool geometry with a  $\eta^6$ -coordinated arene (Ru<sup>II</sup> complexes) or  $\eta^5$ -coordinated (Ir<sup>III</sup> compounds) and three additional sites of ligation occupied by two chloride ligands and the phosphine ligand. Oxidation of NADH to NAD<sup>+</sup> with high efficiency was catalyzed by complexes containing P(*p*-OCH<sub>3</sub>Ph)<sub>2</sub>CH<sub>2</sub>OH (IrMPOH and RuMPOH). The catalytic property might have important future applications in biological and medical fields like production of reactive oxygen species (ROS). Furthermore redox activity of complexes was confirmed by cyclic voltamperometry. Biochemical assays demonstrated the ability of Ir(III) and Ru(II) complexes to induce significant cytotoxicity in various cancerous cell lines. Furthermore we found that RuPOH and RuMPOH selectively inhibit proliferation of skin cancer cells (WM266-4; IC<sub>50</sub>, after 24h: *av.*48.3  $\mu$ M; after 72h: *av.*10.2  $\mu$ M) while Ir(III) complexes were found to be moderately active against prostate cancer cells (DU145).

# Graphical Abstract

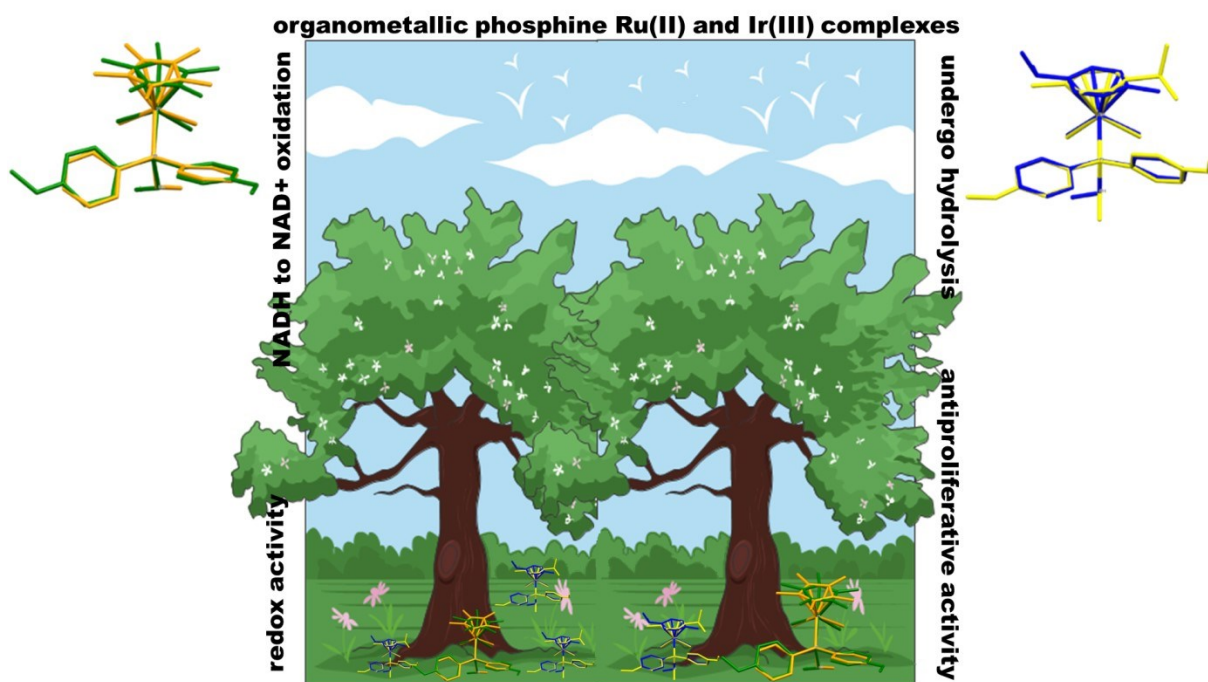




**Table S1.** Crystallographic experimental details.

Identification code	RuPOH	IrPOH	RuMPOH	IrMPOH
<b>Crystal data</b>				
Empirical formula	C <sub>23</sub> H <sub>27</sub> Cl <sub>2</sub> O <sub>2</sub> PRu	C <sub>23</sub> H <sub>28</sub> Cl <sub>2</sub> IrOP	C <sub>25</sub> H <sub>31</sub> Cl <sub>2</sub> O <sub>3</sub> PRu	C <sub>25</sub> H <sub>32</sub> Cl <sub>2</sub> IrO <sub>3</sub> P
Formula weight	522.38	614.52	582.44	674.57
Temperature [K]	100(2)	293(2)	293(2)	100(2)
Wavelength [Å]	1.54184	0.71073	0.71073	1.54184
Crystal system, space group	Monoclinic, P 2 <sub>1</sub>	Monoclinic, P 2 <sub>1</sub> /n	Monoclinic, P 2 <sub>1</sub> /n	Monoclinic, P 2 <sub>1</sub> /n
a, b, c [Å]	7.6065(1), 13.8332(1), 10.7154(1)	10.5605(1), 17.1832(2), 12.7618(1)	9.6600(1), 11.1867(1), 23.5077(3)	8.5562(2), 20.6545(6), 13.9418(2)
β [°]	105.490(1)	93.613(1)	92.598(1)	92.251(2)
V [Å <sup>3</sup> ]	1086.54(2)	2311.19(4)	2537.71(5)	2461.95(10)
Z	2	4	4	4
Radiation type	Cu K <sub>α</sub>	Mo K <sub>α</sub>	Mo K <sub>α</sub>	Cu K <sub>α</sub>
μ [mm <sup>-1</sup> ]	8.881	6.089	0.916	13.313
Crystal size [mm]	0.40 x 0.25 x 0.10	0.20 x 0.20 x 0.20	0.50 x 0.30 x 0.20	0.10 x 0.05 x 0.01
<b>Data collection</b>				
Diffractometer	Rigaku (Cu) XtaLAB Synergy-DW VHF with a HyPix-Arc 150 detector	Rigaku OD SuperNova Dual source with an Atlas detector	Rigaku OD SuperNova Dual source with an Atlas detector	Rigaku (Cu) XtaLAB Synergy-DW VHF with a HyPix-Arc 150 detector
Absorption correction	Multi-scan ( <i>CrysAlisPRO</i> ; Rigaku OD, 2020)	Multi-scan ( <i>CrysAlisPRO</i> ; Rigaku OD, 2015)	Multi-scan ( <i>CrysAlisPRO</i> ; Rigaku OD, 2015)	Multi-scan ( <i>CrysAlisPRO</i> ; Rigaku OD, 2020)
No. of measured, independent and observed [I > 2σ(I)] reflections	9002/8981/3776	35098/6202/5185	37574/6823/5422	27876/5031/4572
R(int)	0.0360	0.0397	0.0388	0.0482
Completeness	99.7 %	99.6 %	99.8 %	99.6 %
<b>Refinement</b>				
Data / restraints / parameters	9002 / 1 / 261	6201 / 0 / 270	6823 / 0 / 297	5031 / 0 / 297
R[F <sup>2</sup> > 2σ(F <sup>2</sup> )], wR(F <sup>2</sup> ), S	0.0191, 0.0497, 1.201	0.0220, 0.0411, 1.075	0.0305, 0.0626, 1.069	0.0394, 0.1008, 1.095
Δρ <sub>max</sub> , Δρ <sub>min</sub> (e Å <sup>-3</sup> )	0.376 and -0.427	0.850 and -0.614	0.350 and -0.470	1.426 and -2.097

Rigaku OD (2015). *CrysAlis PRO*. Rigaku Oxford Diffraction Ltd, Yarnton, Oxfordshire, England.

Rigaku OD (2020). *CrysAlis PRO*. Rigaku Oxford Diffraction, Yarnton, England.

Sheldrick, G. M. (2015a). *Acta Cryst.* **A71**, 3–8

**Table S2.** Hydrogen-bond geometry (Å, °)

D-H...A	d(D-H)	d(H...A)	d(D...A)	<(DHA)
<b>RuPOH</b>				
C11-H11A...Cl2	0.99	2.89	3.487(4)	120.0
O11-H11...Cl1	0.80(6)	2.30(6)	3.059(3)	159(5)
<b>IrPOH</b>				
C26-H26...Cl1	0.93	2.87	3.640(3)	140.5
C32-H32...Cl2	0.93	2.96	3.606(3)	127.6
O11B_a-H10B_a...Cl1	0.82	2.20	2.957(3)	153.0
O11A_b-H10A_b...Cl2	0.82	2.32	3.099(9)	159.7
<b>RuMPOH</b>				
C11-H11A...Cl1	0.97	2.76	3.336(2)	118.6
C11-H11B...Cl2	0.97	2.78	3.355(2)	118.4
C25-H25...O34_#1	0.93	2.47	3.313(3)	150.8
C27-H27C...Cl2_#2	0.96	2.97	3.870(3)	157.5
C33-H33...Cl2_#3	0.93	2.83	3.426(2)	122.6
O11-H11O...Cl1_#2	0.77(3)	2.50(3)	3.259(2)	171(3)
Symmetry transformations used to generate equivalent atoms: #1 -x-1/2, y+1/2, -z+3/2 #2 -x, -y, -z+1 #3 -x+1/2, y+1/2, -z+3/2				
<b>IrMPOH</b>				
C23-H23...Cl1#1	0.95	2.72	3.444(6)	133.5
C32-H32...Cl1	0.95	2.84	3.667(6)	145.4
C33-H33...Cl2#2	0.95	2.99	3.590(6)	122.6
O11-H11...Cl2	0.84	2.39	3.186(5)	157.2
Symmetry transformations used to generate equivalent atoms: #1 x-1/2, -y+1/2, z+1/2 #2 x-1/2, -y+1/2, z-1/2				

**Table S3.** Cumulative NMR data (298 K,  $\delta$  [ppm], J [Hz]) for ligands (in CDCl<sub>3</sub>) and iridium-complexes (in CD<sub>2</sub>Cl<sub>2</sub>).

	POHC <sup>40</sup>	MPOHC <sup>42</sup>	POH <sup>41</sup>	MPOH <sup>42</sup>	[Ir( $\eta^5$ -Cp*)Cl <sub>2</sub> ] <sub>2</sub> <sup>a</sup>	[Ru( $\eta^6$ -p-cymene)Cl <sub>2</sub> ] <sub>2</sub>	IrPOH	IrMPOH	RuPOH	RuMPOH
<sup>31</sup> P	<b>-11.46</b>	<b>15.23</b>	<b>-9.33</b>	<b>-13.60</b>			<b>-7.15</b>	<b>-9.18</b>	<b>16.74</b>	<b>15.07</b>
H <sup>Ph(m)</sup>	7.52-7.21	7.25-7.82	7.60-7.31	7.25-7.82			7.41-7.54 m	7.70 t (9.34)	7.41-7.58 m	7.77 t (9.07)
H <sup>Ph(o)</sup>							7.72-7.84 m	6.98 dd (8.80; 1.50)	7.79-7.93 m	6.98 dd (8.66; 1.40)
H <sup>1</sup>	4.32 d (7.7)	5.03 s	4.42 d (8.39)	4.27 d (9.01)			4.97 d (6.6)	4.86 s	4.64 s	4.54 s
H <sup>-OH</sup>		not observed	1.80 m	not observed			not observed	not observed	not observed	not observed
H <sup>-OCH3</sup>		3.87 s		3.74 s				3.85 s		3.86 s
C <sup>Ph(i)</sup>	135.65 d (12.0)	106.89 d (84.47)	135.65 d (12.0)	126.28 d (9.08)				118.82 d (55.4)	132.49 d (15.2)	123.14 d (47.23)
C <sup>Ph(o)</sup>	132.91 d (17.6)	115.63 d (7.54)	132.91 d (17.6)	114.41 d (7.27)			133.80 d (9.9)	113.93 d (10.9)	133.61 d (9.1)	114.15 s
C <sup>Ph(m)</sup>	128.39 d (5.6)	135.61 d (9.99)	128.39 d (5.6)	134.58 d (19.07)			128.15 d (9.9)	135.57 d (10.9)	128.55 d (9.1)	135.02 s
C <sup>Ph(p)</sup>	128.64 s	164.03 s	128.64 s	160.42 s			130.92 s	161.83 s	131.17 s	161.68 s
C <sup>1</sup>	62.46 d (13.0)	53.31 d (59.04)	62.46 d (13.0)	62.94 d (14.53)			64.25 d (39.1)	64.87 d (31.06)	63.28 d (40.1)	63.51 d (31.79)
C <sup>-OCH3</sup>		55.86 s		55.23 s				55.35 s		55.39 s
H <sup>Cp*(CH3)</sup>					0.96 s		1.40 d (2.19)	1.40 d (2.19)		
H <sup>2,3</sup>						1.29 d (6.9)			0.93 d (7.0)	0.97 d (6.98)
H <sup>4</sup>						2.93 spt (7.0)			2.56 spt (7.0)	2.61 spt (7.00)
H <sup>6,7,8,9</sup>						5.42 dd (19.2; 6.0)			5.27 dd (19.6; 6.2)	5.25 s
H <sup>11</sup>						2.16 s			1.91 s	1.89 s
C <sup>Cp*(CH3)</sup>					9.38 s		8.08 s	8.35 s		
C <sup>Cp*</sup>					86.28 s		92.28 d (2.2)	92.34 d (2.72)		
C <sup>2,3</sup>						22.12 s			21.73 s	21.60 s
C <sup>4</sup>						30.63 s			30.34 s	30.18 s
C <sup>5</sup>						101.22 s			108.84 s	108.76 s
C <sup>6,8</sup>						80.54 s			86.42 d (5.4)	86.19 s
C <sup>7,9</sup>						81.32 s			89.74 d (3.6)	89.31 s
C <sup>10</sup>						96.75 s			95.60 s	95.14 s
C <sup>11</sup>						18.89 s			17.70 s	17.57 s

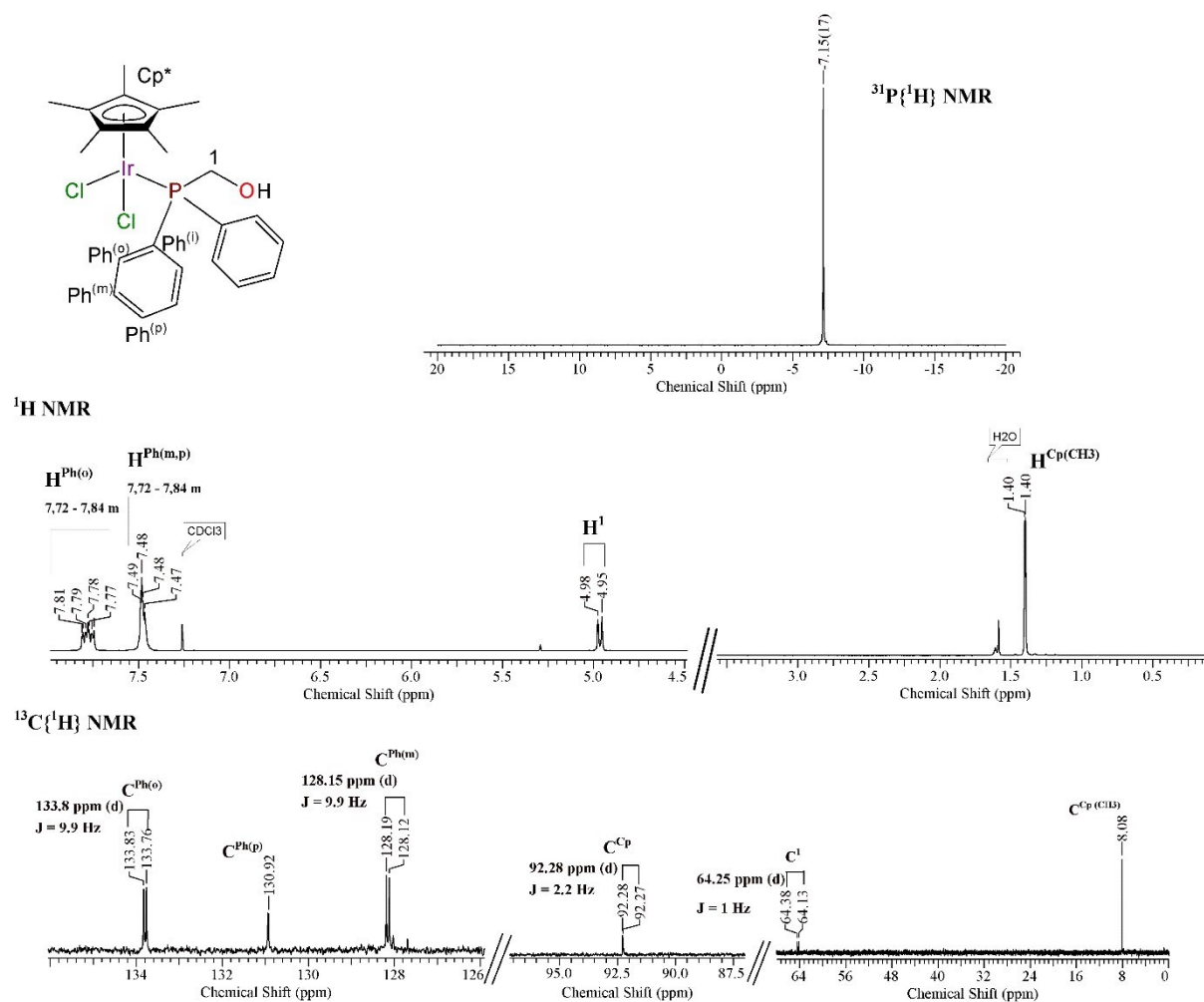


**Figure S1.**  $^1\text{H}$ ,  $^{13}\text{C}\{^1\text{H}\}$  and  $^{31}\text{P}\{^1\text{H}\}$  NMR spectra for IrPOH (298 K,  $\text{CDCl}_3$ ).

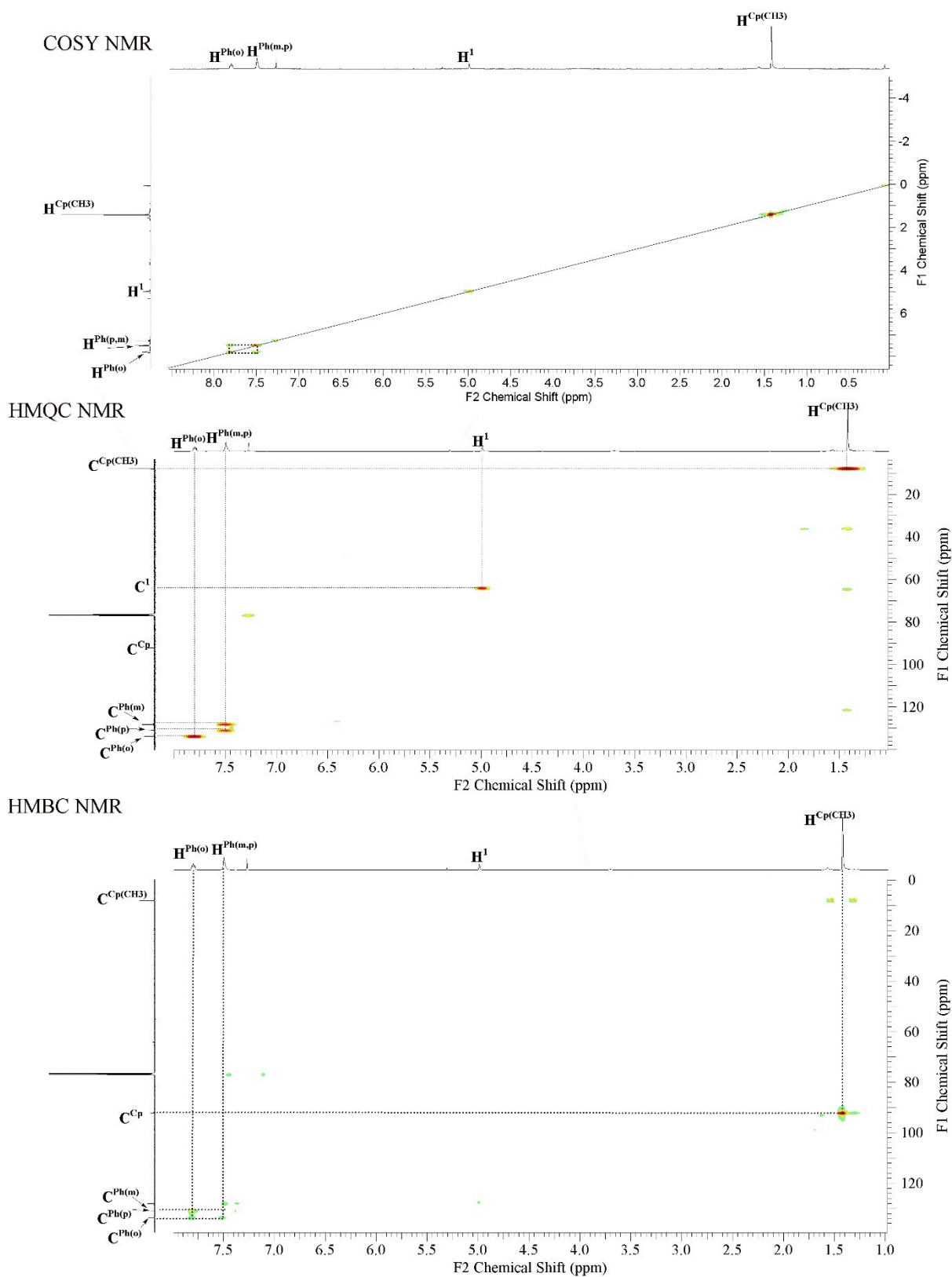
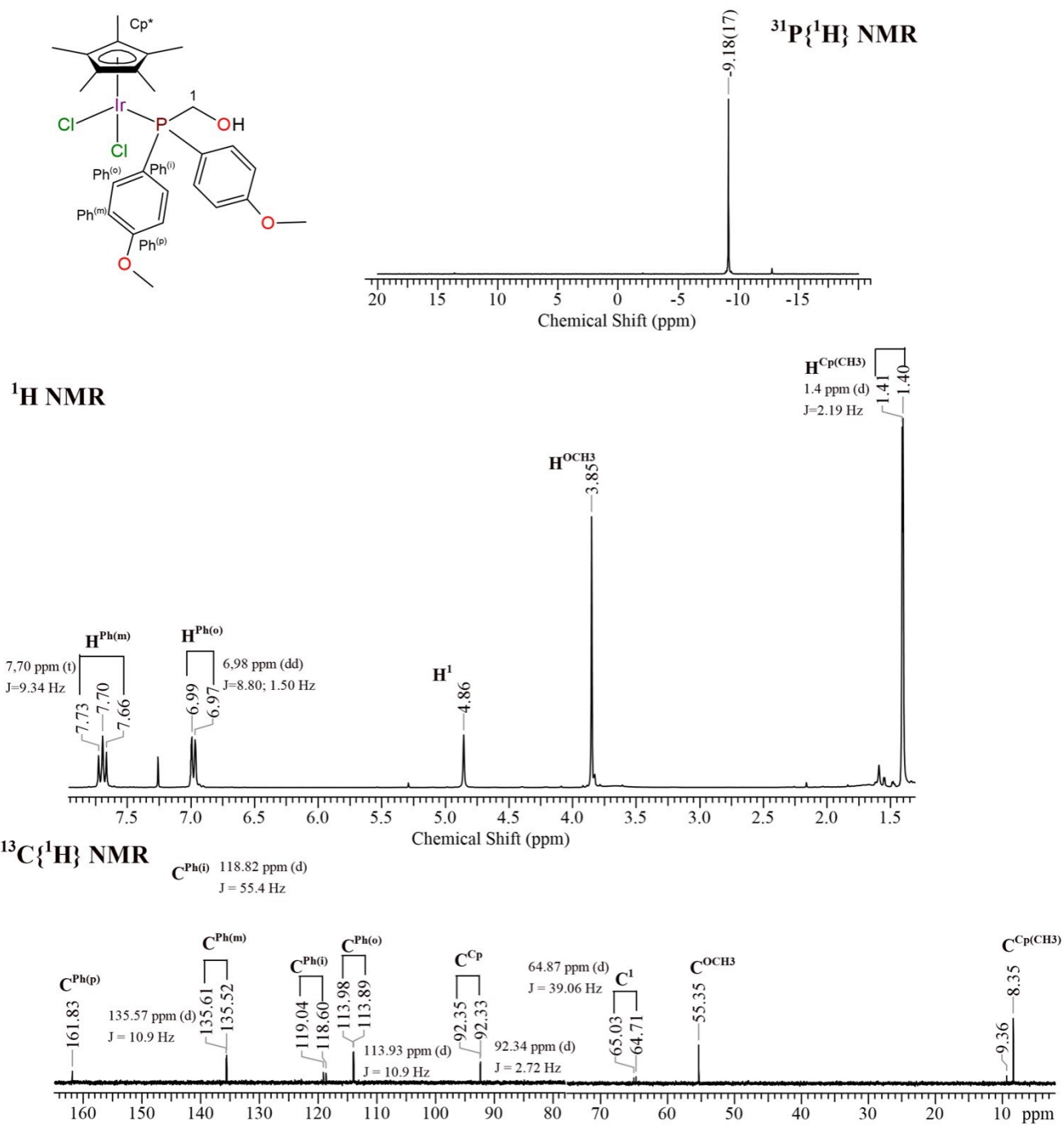
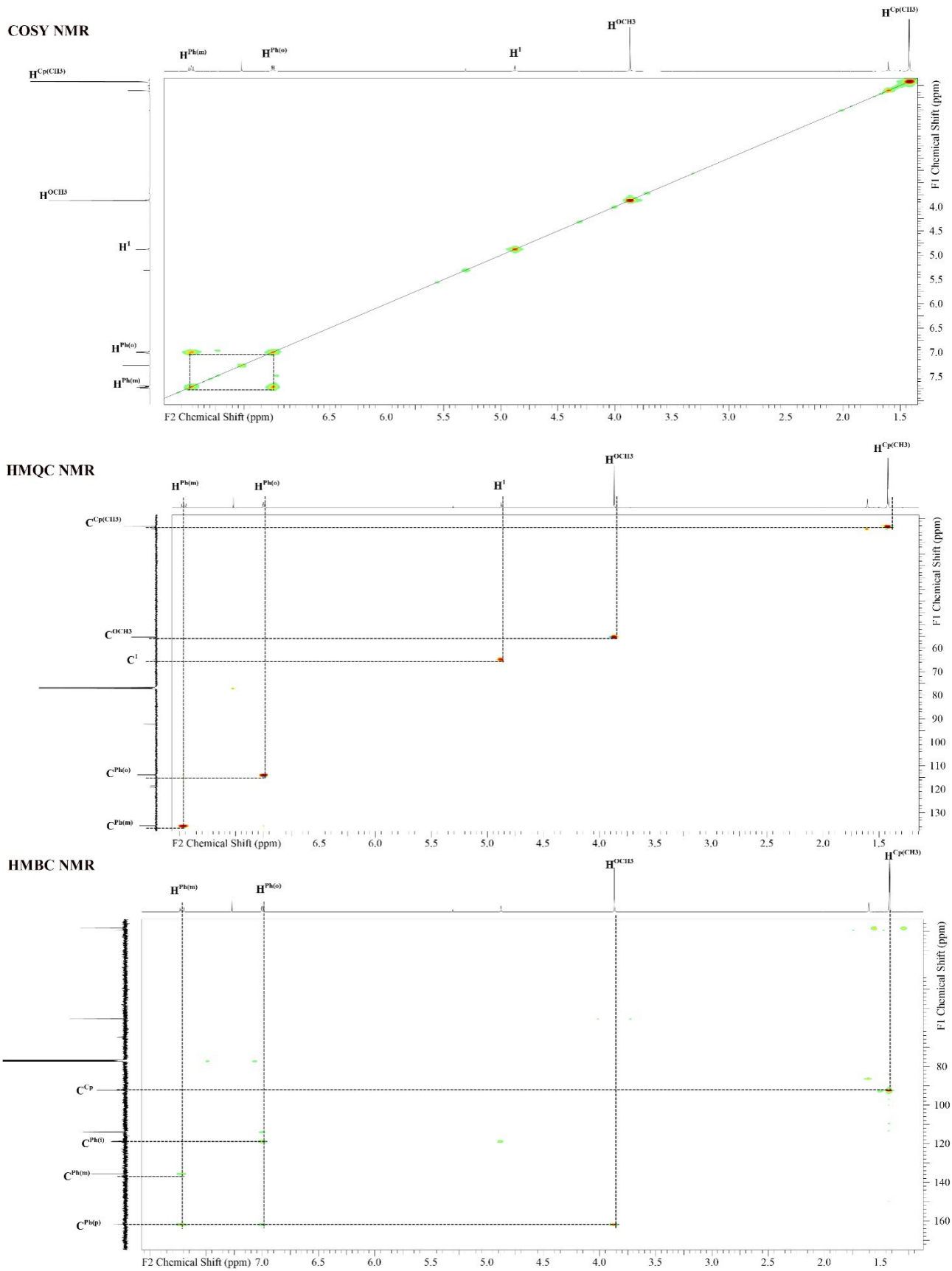


Figure S2. HMQC, HMBC, COSY NMR spectra for IrPOH (298 K, CDCl<sub>3</sub>).



**Figure S3.**  $^1\text{H}$ ,  $^{13}\text{C}\{^1\text{H}\}$  and  $^{31}\text{P}\{^1\text{H}\}$  NMR spectra for IrMPOH (298 K,  $\text{CDCl}_3$ ).



**Figure S4.** HMQC, HMBC, COSY NMR spectra for **IrMPOH** (298 K,  $\text{CDCl}_3$ ).

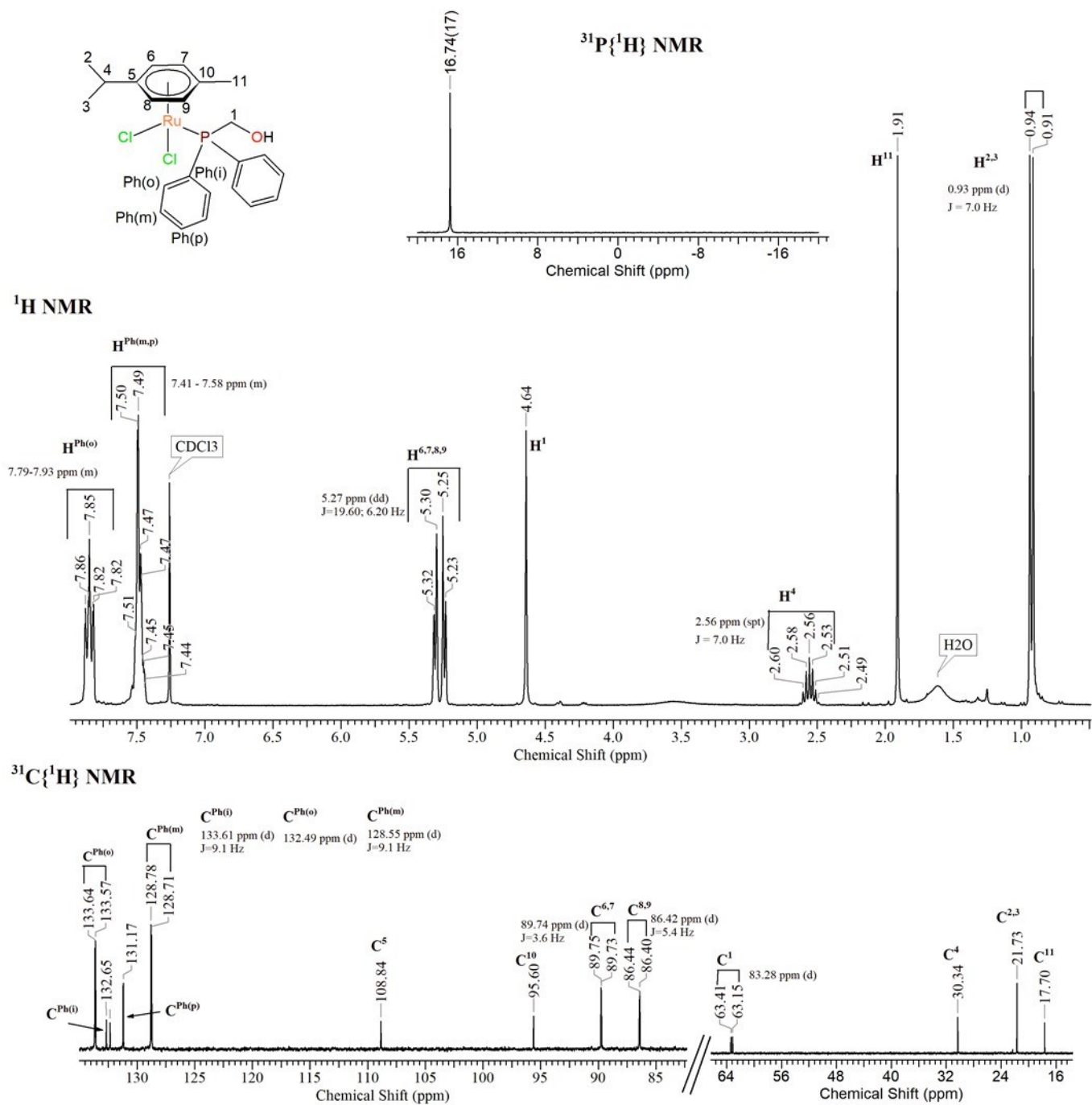


**Figure S5.**  $^1\text{H}$ ,  $^{13}\text{C}\{^1\text{H}\}$  and  $^{31}\text{P}\{^1\text{H}\}$  NMR spectra for **RuPOH** (298 K,  $\text{CDCl}_3$ ).



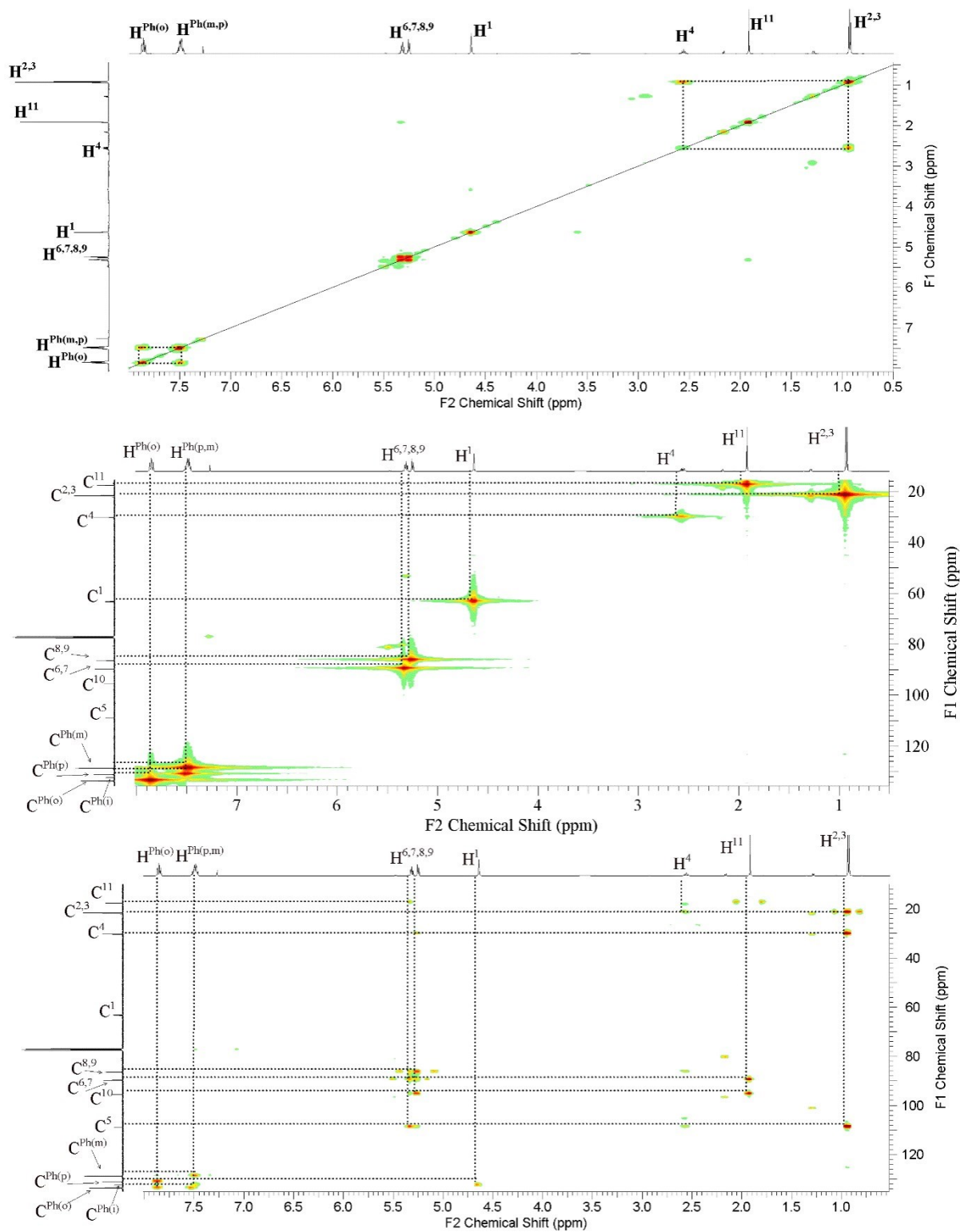


**Figure S6.** HMQC, HMBC, COSY NMR spectra for **RuPOH** (298 K, CDCl<sub>3</sub>).

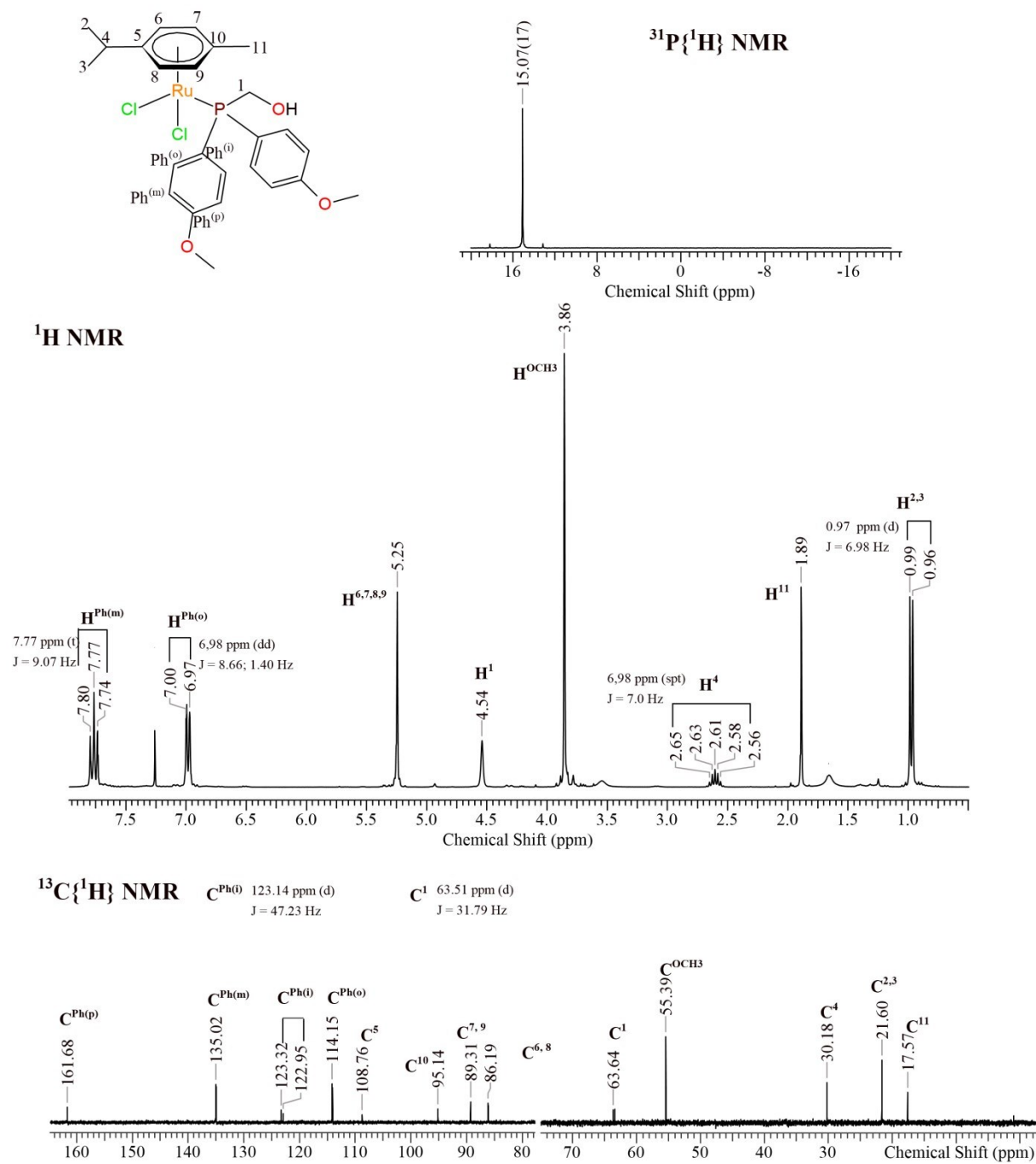


**Figure S7.**  $^1\text{H}$ ,  $^{13}\text{C}\{^1\text{H}\}$  and  $^{31}\text{P}\{^1\text{H}\}$  NMR spectra for **RuMPOH** (298 K,  $\text{CDCl}_3$ ).

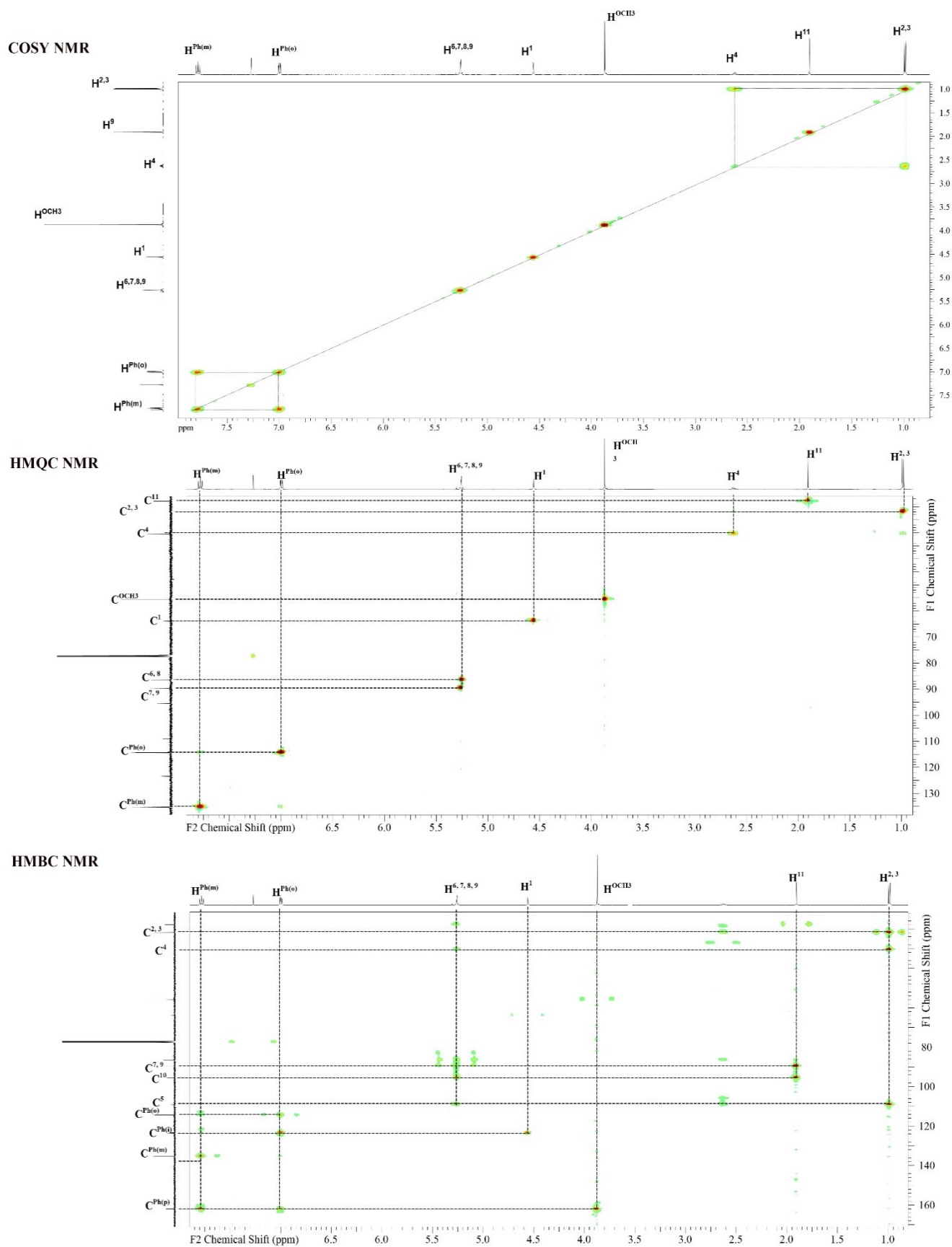


**Figure S8.** HMQC, HMBC, COSY NMR spectra for **RuMPOH** (298 K,  $\text{CDCl}_3$ ).

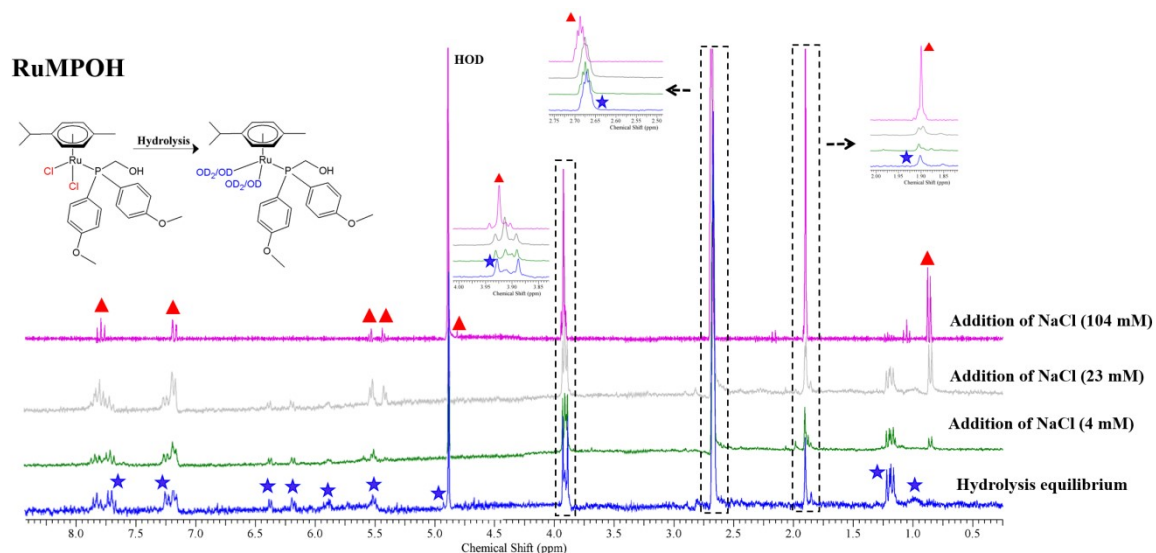


**Figure S9.** Confirmation of hydrolysis of **RuMPOH** by  $^1\text{H}$  NMR in 20%  $\text{DMSO-d}_6/80\%$   $\text{D}_2\text{O}$  (v/v) at 298 K. From bottom to top:  $^1\text{H}$  NMR spectrum of an equilibrium solution of **RuMPOH** (1 mM); spectrum recorded 10 min after addition of NaCl (final concentration, 4 mM) to the equilibrium solution of **RuMPOH**; final concentration of NaCl, 23mM; final concentration of NaCl, 104mM – respectively. The peaks for the chlorido complex **RuMPOH** (red triangle) increased in intensity while peaks for the aqua complex decreased (blue star).

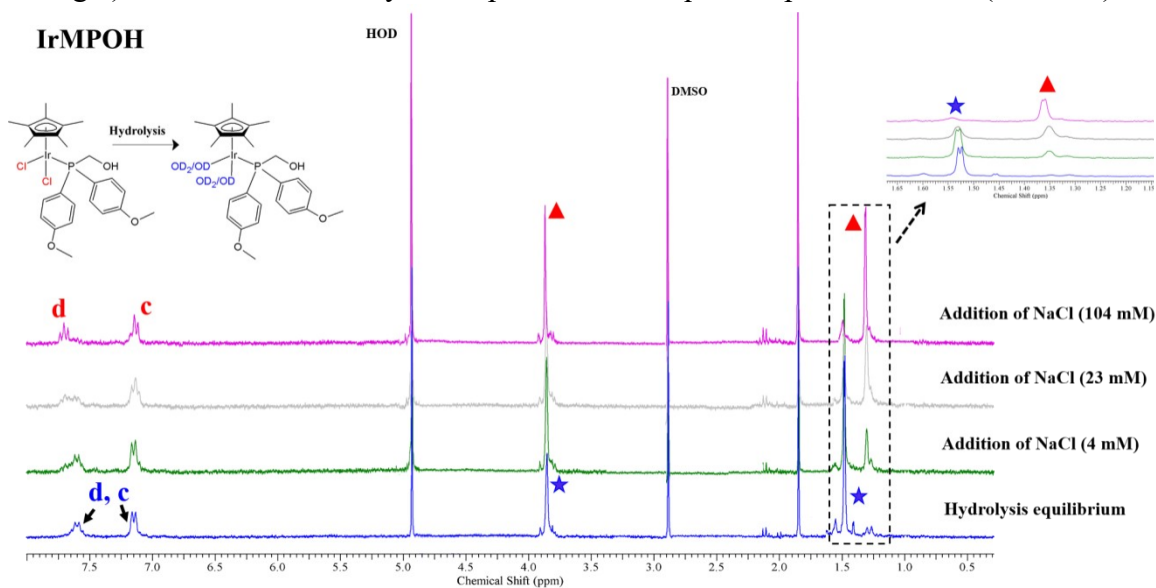


**Figure S10.** Confirmation of hydrolysis of **IrMPOH** by  $^1\text{H}$  NMR in 20%  $\text{DMSO-d}_6/80\%$   $\text{D}_2\text{O}$  (v/v) at 298 K. From bottom to top:  $^1\text{H}$  NMR spectrum of an equilibrium solution of **IrMPOH** (1 mM); spectrum recorded 10 min after addition of NaCl (final concentration, 4 mM) to the equilibrium solution of **IrMPOH**; final concentration of NaCl, 23mM; final concentration of NaCl, 104mM – respectively. The peaks for the chlorido complex **IrMPOH** (red triangle) increased in intensity while peaks for the aqua complex decreased (blue star).

Ir PK010 CHCl3 MeOH bis Z 637\_181116110705 #1 RT: 0,00 AV: 1 NL: 4,15E4  
T: ITMS + c ESI Full ms [155,00-1500,00]

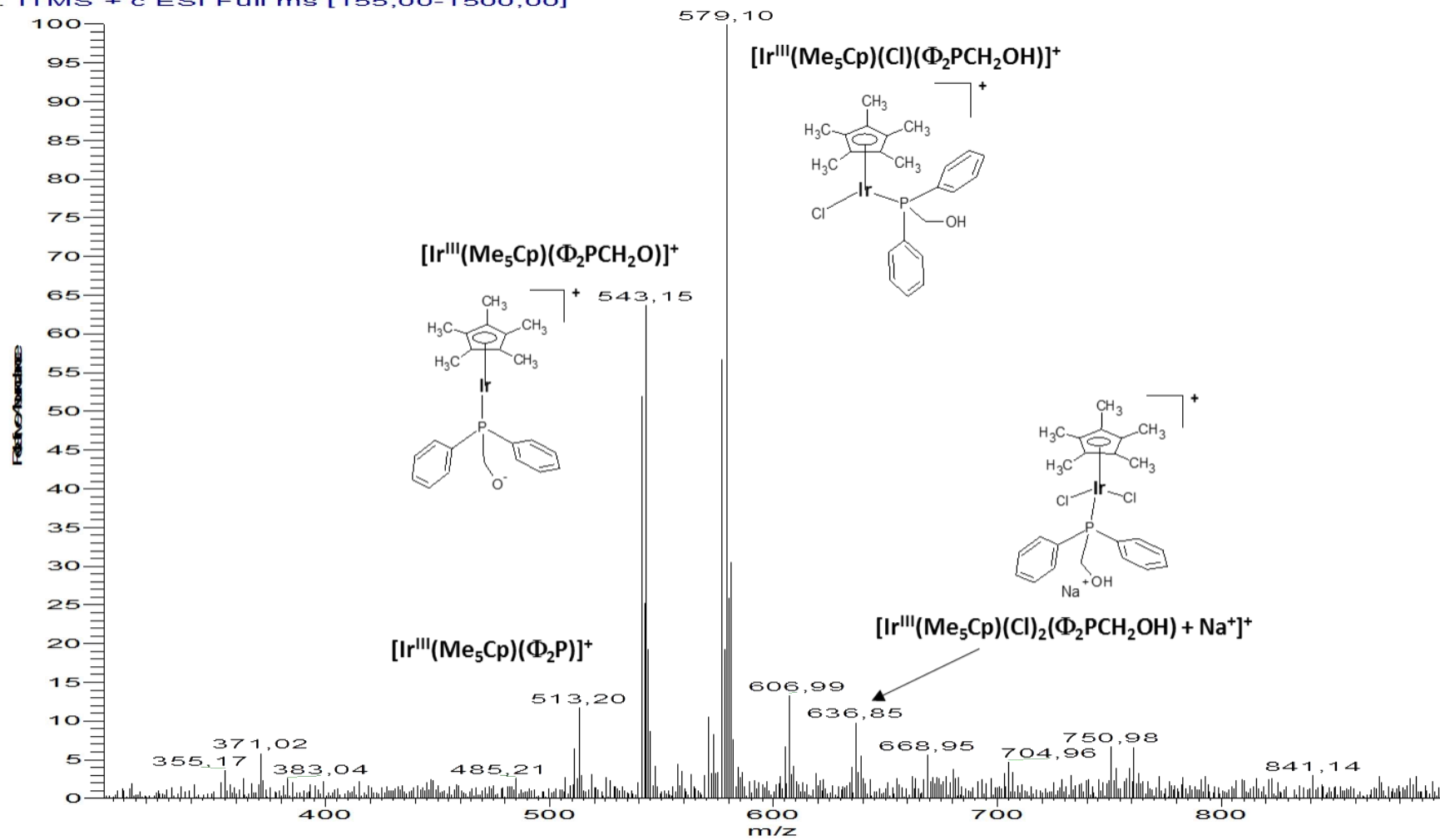
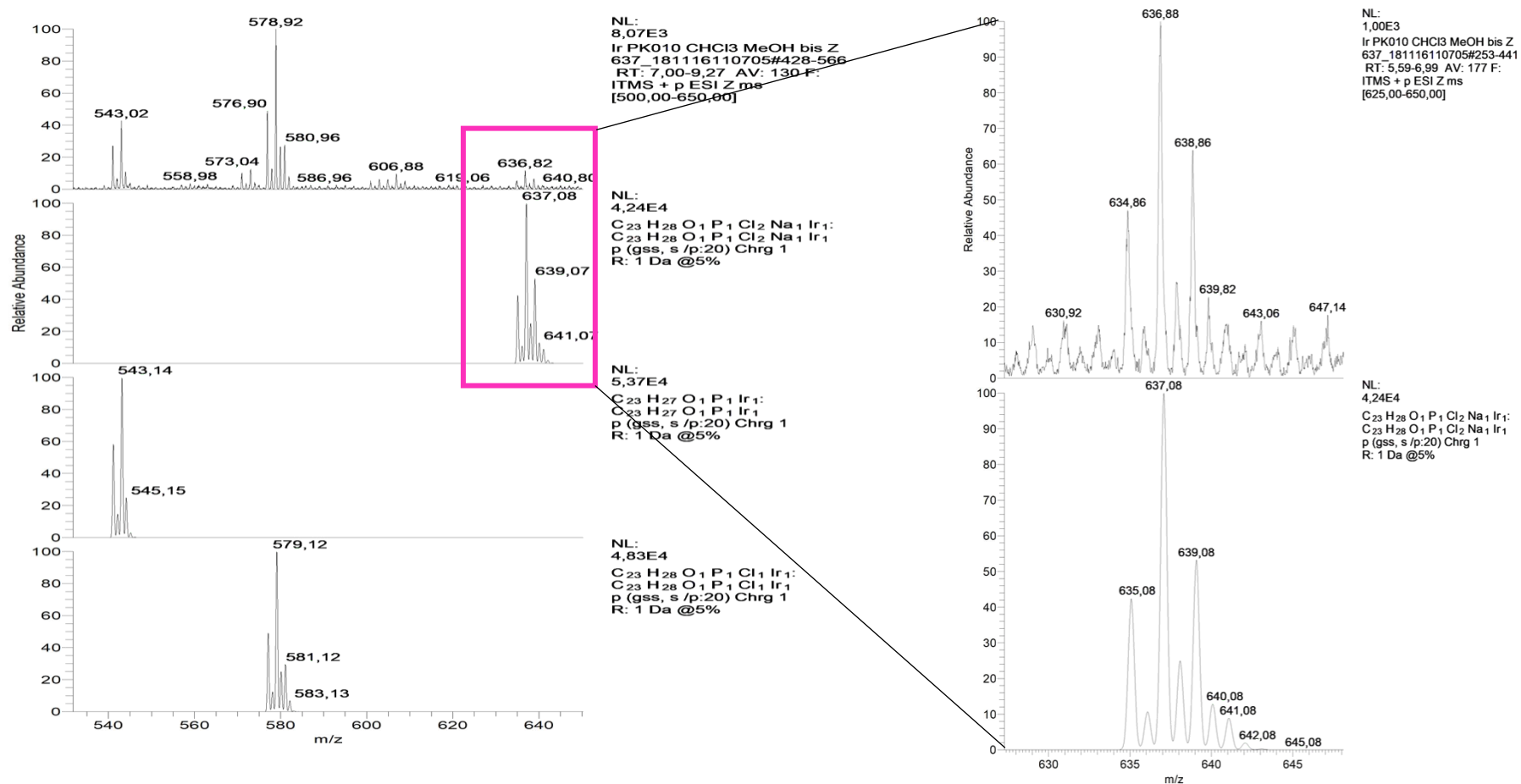


Figure S11. Full ESI(+)-MS spectrum of IrPOH



**Figure S12.** Comparison of ion peaks (experimental (top traces) vs calculated (bottom traces)) in the 630 – 650 m/z region of **IrPOH**. Note the different profile of the cluster centred at m/z 637 ( $[\text{Ir}(\text{Me}_5\text{-Cp})(\text{Cl})_2(\text{Ph}_2\text{PCH}_2\text{OH}) + \text{Na}]^+$ , containing the  $\text{IrCl}_2$  moiety) with respect to that centred at m/z 579 ( $[\text{Ir}(\text{Me}_5\text{-Cp})(\text{Cl})(\text{Ph}_2\text{PCH}_2\text{OH})]^+$ , containing the  $\text{IrCl}$  moiety), and to that centred at m/z 543 ( $[\text{Ir}(\text{Me}_5\text{-Cp})(\text{Ph}_2\text{PCH}_2\text{O})]^+$ , containing the  $\text{Ir}$  ion only).

Ir PK012 CHCl3 MeOH bis Z 697\_181116110705 #1 RT: 0,00 AV: 1 NL: 8,45E4  
T: ITMS + c ESI Full ms [50,00-2000,00]

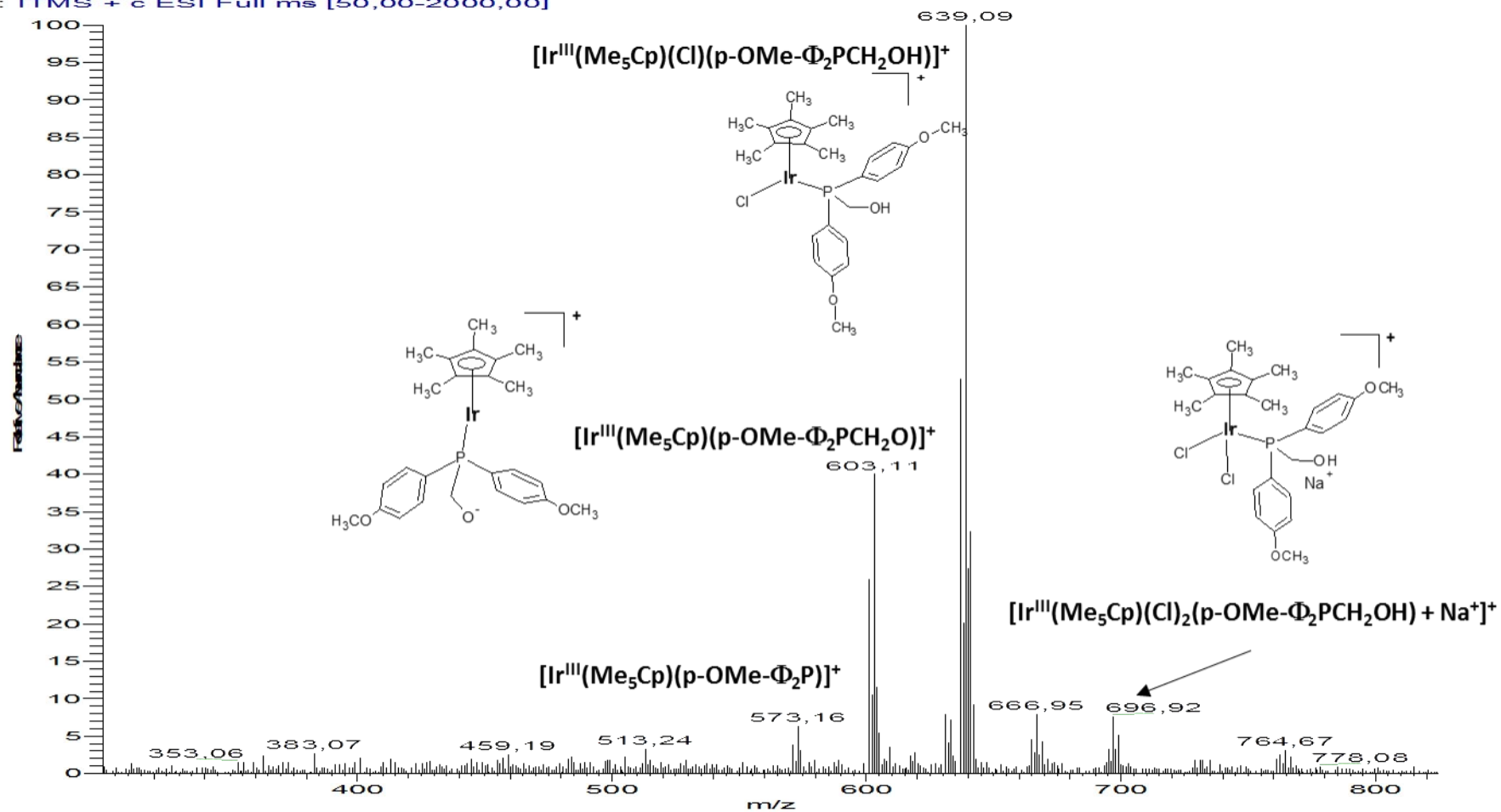
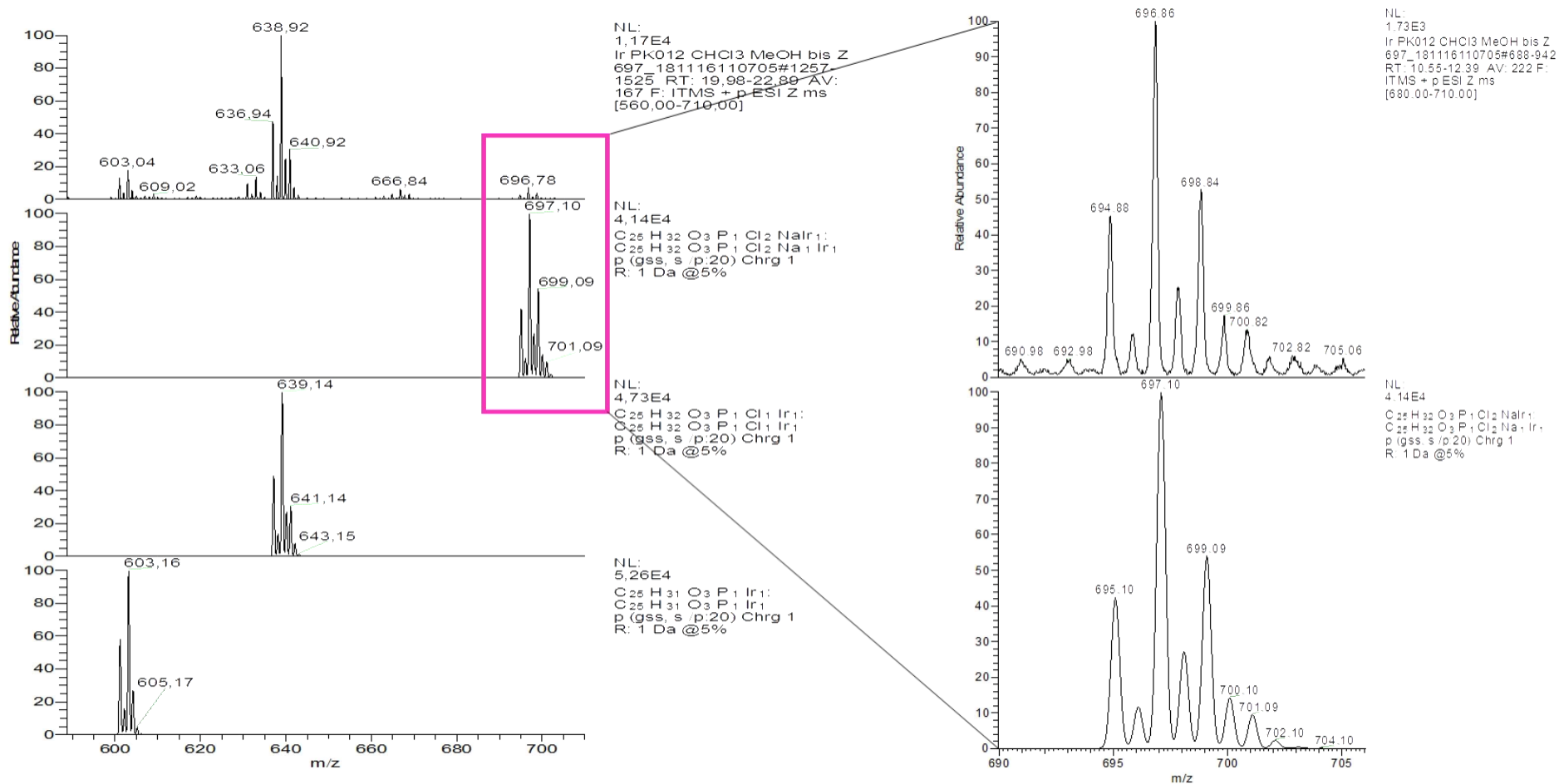


Figure S13. Full ESI(+)-MS spectrum of IrMPOH.





**Figure S14** Comparison of high abundant cluster ion peaks (experimental vs calculated) in the 690 – 710 m/z region of IrMPOH. Note the different profile of the cluster centered at m/z 639 (containing the IrCl moiety) with respect to the other two profiles centered at m/z 603 and 573 (containing Ir only).



Ru PK009 CHCl3 MeOH bis Z 545\_181116110705 #939 RT: 11,16 AV: 1 NL: 1,17E5  
T: ITMS + c ESI Full ms [110,00-1000,00]

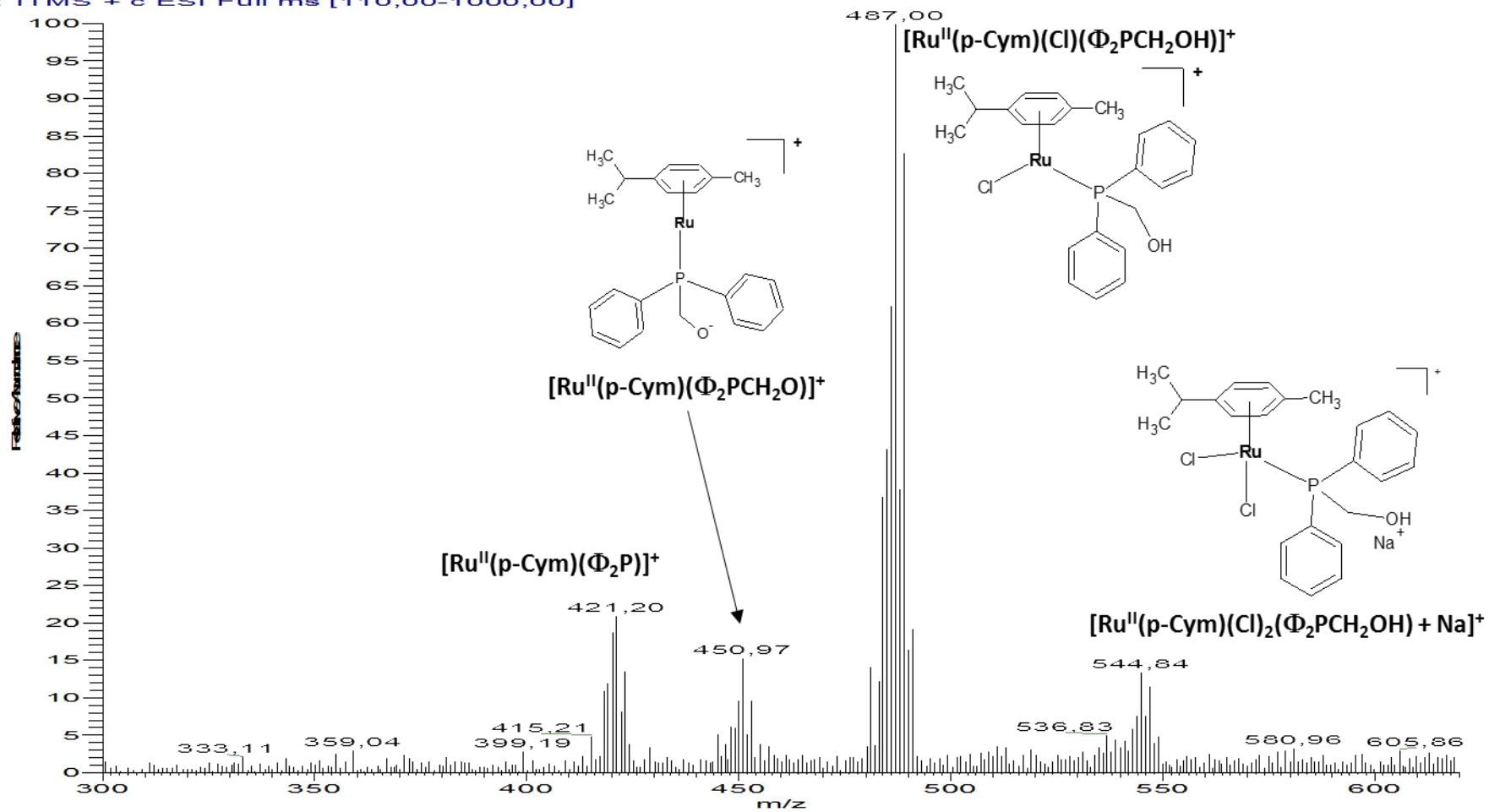
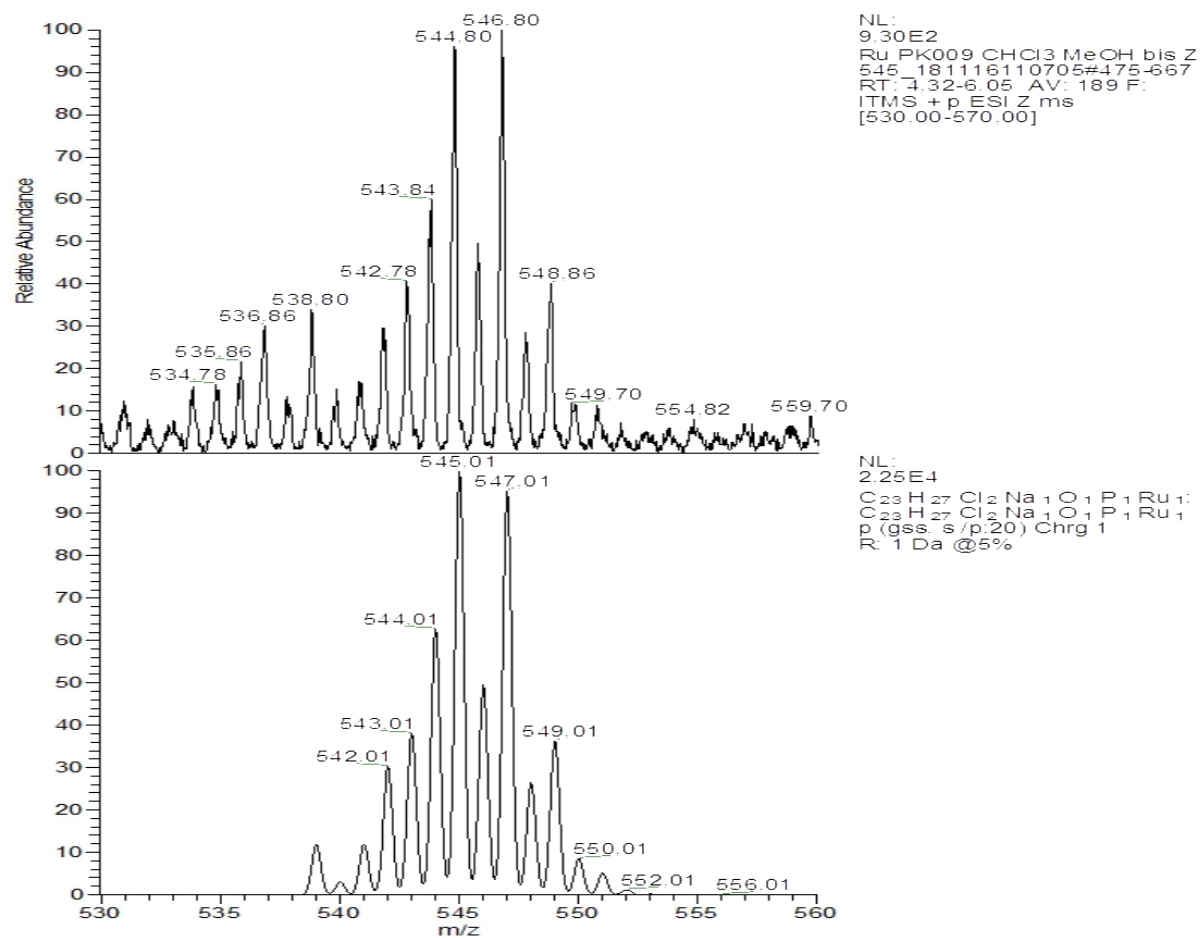


Figure S15. Full ESI(+)-MS spectrum of RuPOH.



**Figure S16.** Comparison of the cluster ion peak of **RuPOH** centered at  $m/z$  545 (experimental (top) vs calculated (bottom)) corresponding to the sodiated  $[M + Na]^+$  ion.

Ru PK009 CHCl3 MeOH #1156-1582 RT: 7,02-10,35 AV: 73 NL: 1,36E3  
F: ITMS - c ESI Full ms [50,00-1400,00]

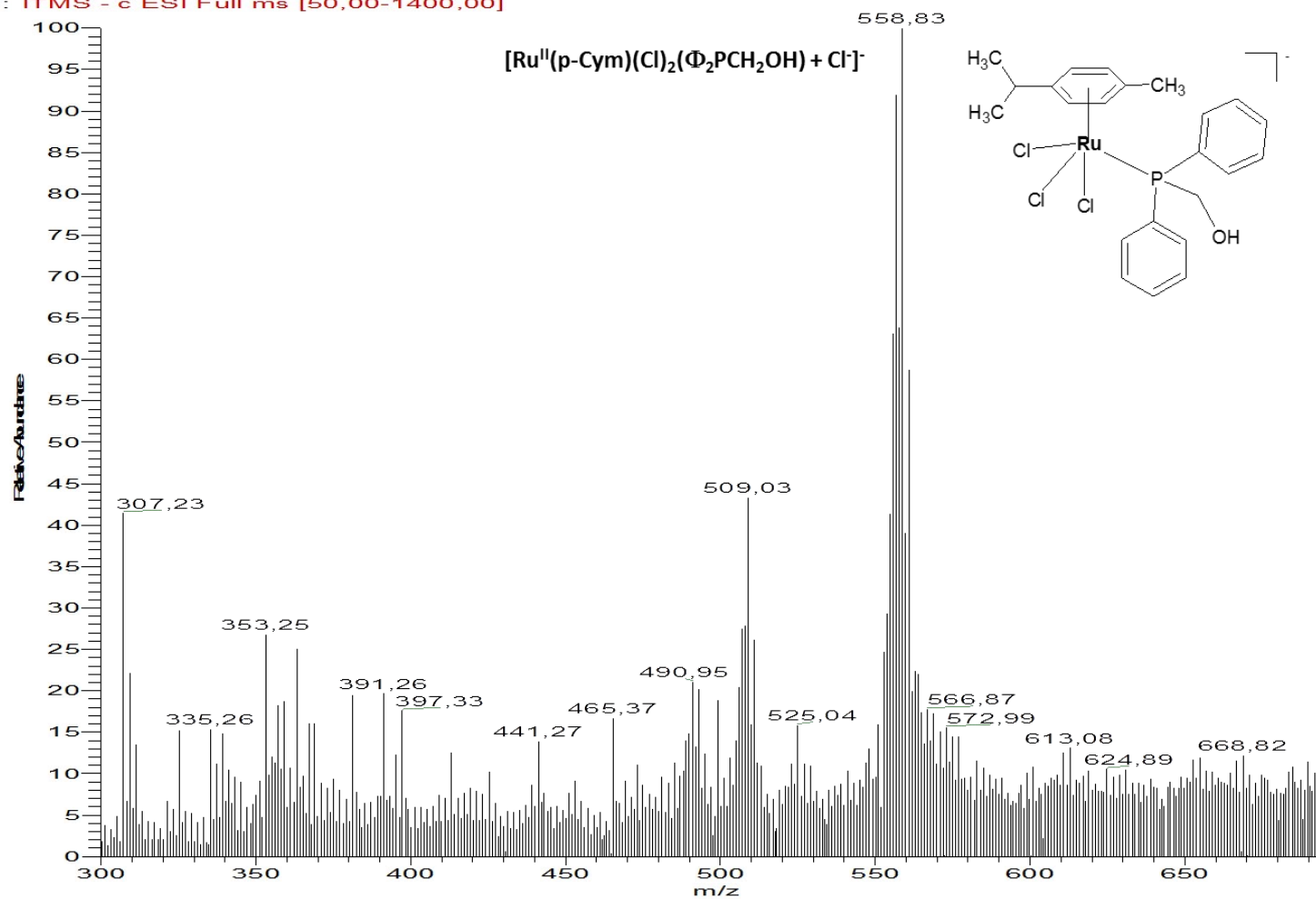


Figure S17. Full ESI(+)-MS spectrum of RuPOH.

Ru PK011 CHCl3 MeOH bis Z 605 181116110705 #610 RT: 6,92 AV: 1 NL: 3,86E4  
T: ITMS + c ESI Full ms [130,00-1000,00]

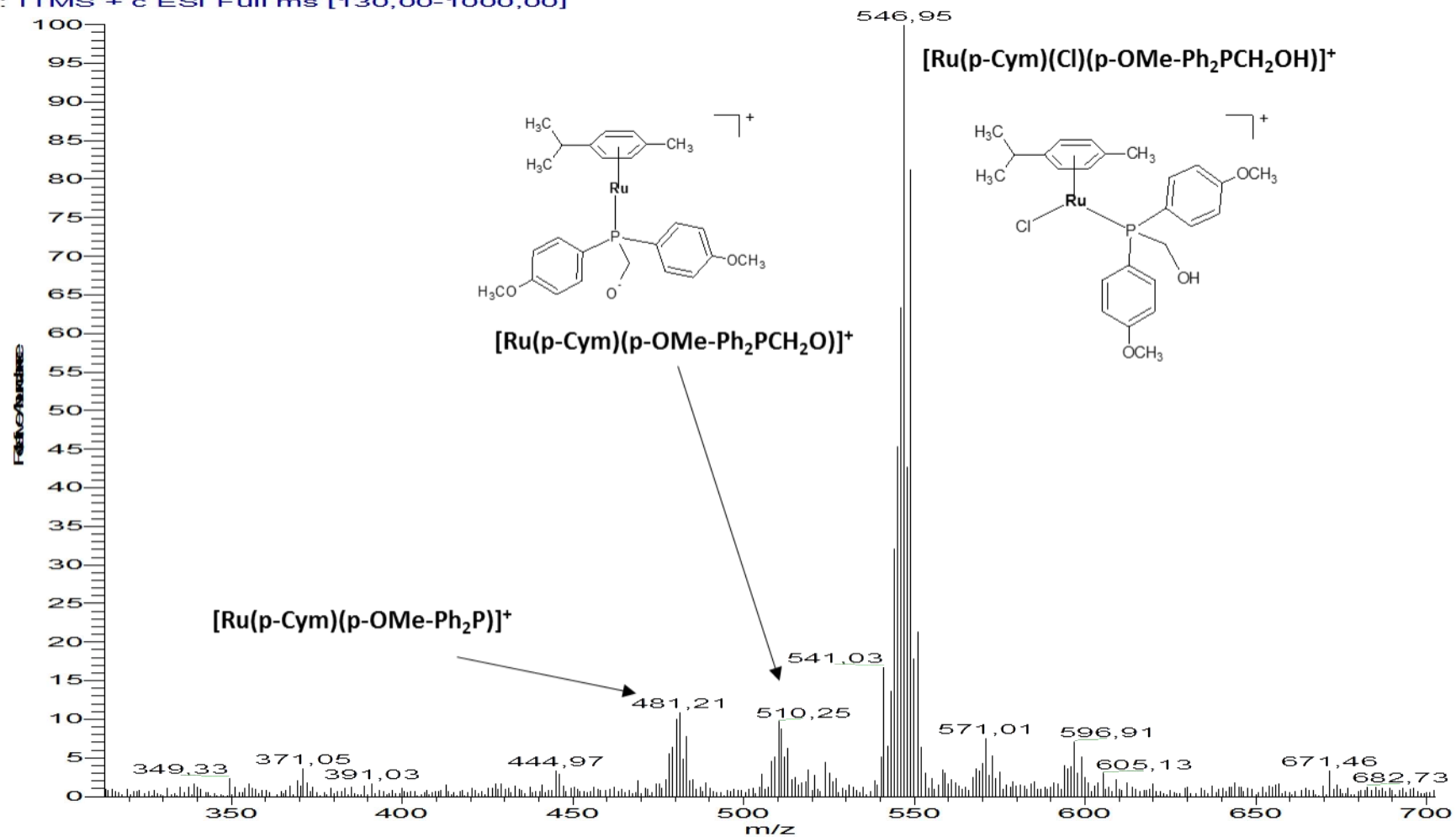


Figure S18. Full ESI(-)MS spectrum of RuMPOH.

Ru PK011 CHCl3 MeOH #498-534 RT: 8,82-9,27 AV: 29 NL: 8,27E2  
F: ITMS - c ESI Full ms [70,00-1300,00]

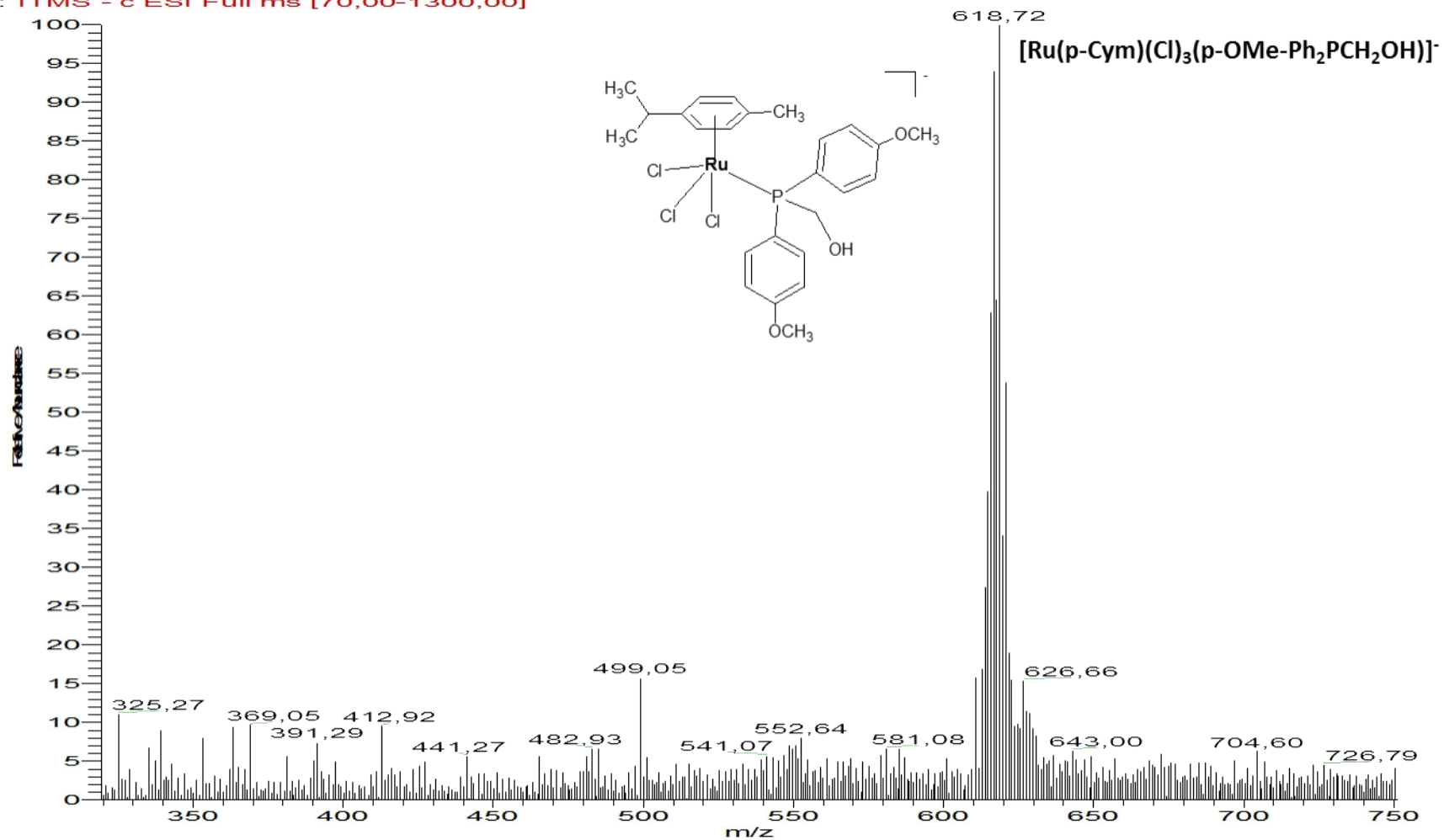
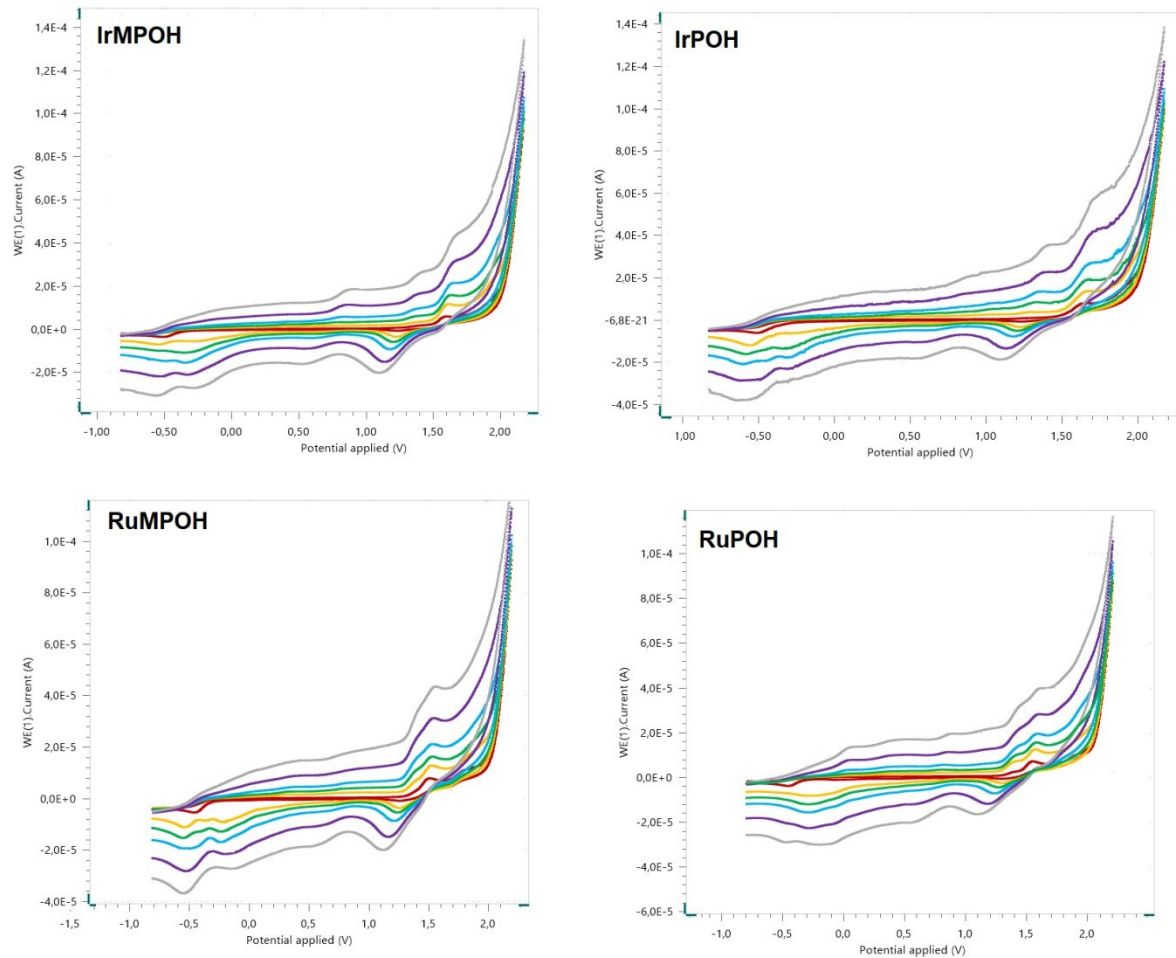
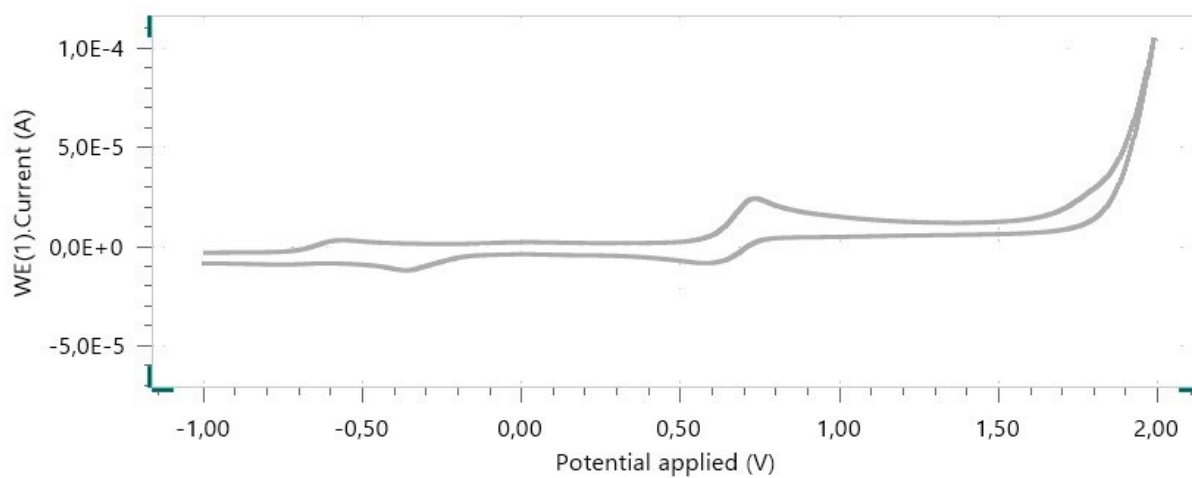


Figure S19. Full ESI(-)MS spectrum of RuMPOH.



**Figure S20.** Cyclic voltammetric trace of **RuPOH**, **RuMPOH**, **IrPOH** and **IrMPOH** (1 mM) as a function of scan rate, recorded with recorded with 0.1 M tetrabutyl ammonium perchlorate (TBAP) as supporting electrolyte in DMF solution. Scan rates 1 – 100 (mV s<sup>-1</sup>). Potential (V) versus Fc<sup>0/+</sup>.



**Figure S21.** CV voltammograms for ferrocene in DMF in the range of potentials from -01 V to 1.2 V. Scan rate: 10 mV s<sup>-1</sup>.

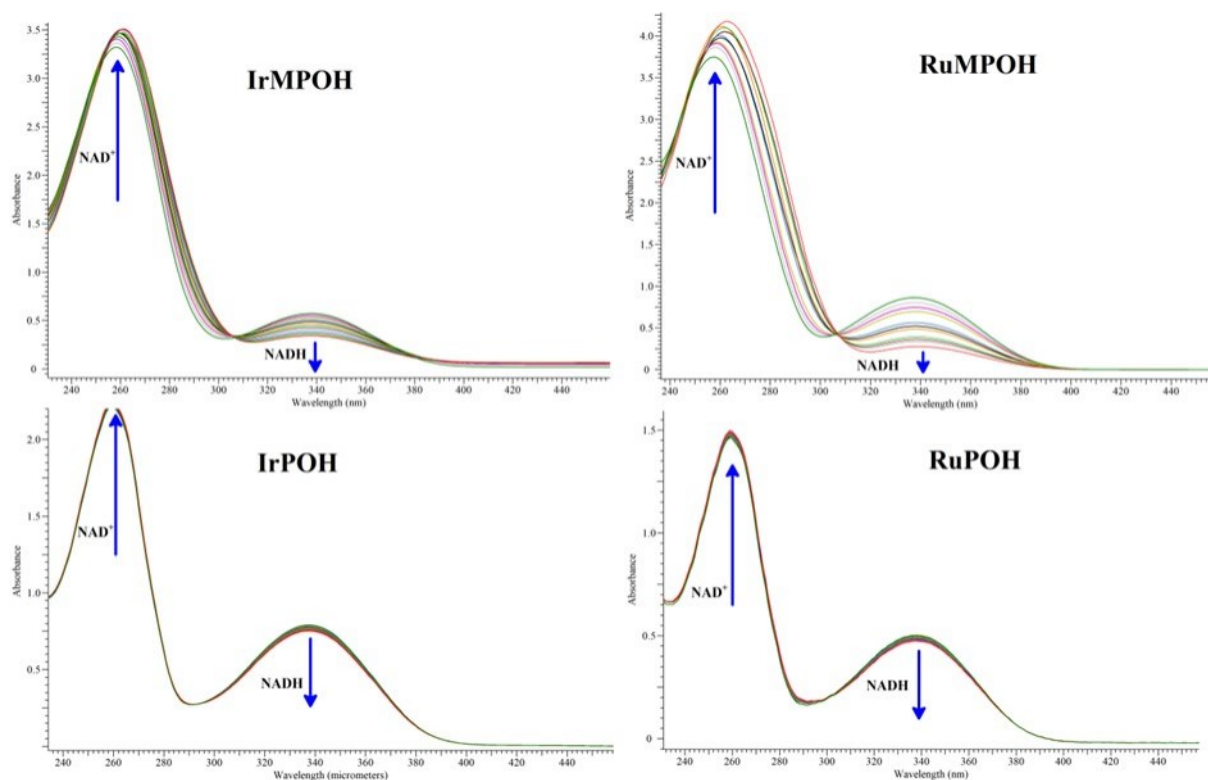


**Figure S22.** UV/Vis spectra of NADH (100  $\mu$ M) were determined after incubated with RuPOH, RuMPOH, IrPOH, IrMPOH (1  $\mu$ M) in CH<sub>3</sub>OH/H<sub>2</sub>O (1 : 9, v/v) at 298 K for 8 h. The arrows show the absorbance change over time.



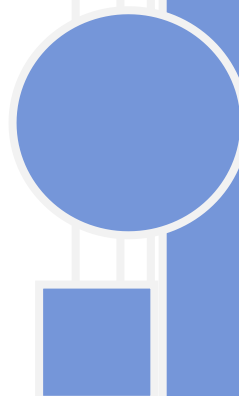
# PUBLICATION S2

Koziel Sandra, Komarnicka Urszula K., Ziolkowska Aleksandra, Skórska-Stania Agnieszka, Pucelik Barbara, Płotek Michał, Sebastian Victor, Bieńko Alina, Stochel Grażyna, Kyzioł Agnieszka

*Anticancer potency of novel organometallic Ir(III) complexes with phosphine derivatives of fluoroquinolones encapsulated in polymeric micelles.*

Inorganic Chemistry Frontiers, 2020, 7, 3386-3401








DOI: 10.1039/d0qi00538j





Cite this: *Inorg. Chem. Front.*, 2020, 7, 3386

# Anticancer potency of novel organometallic Ir(III) complexes with phosphine derivatives of fluoroquinolones encapsulated in polymeric micelles†

Sandra Kozieł, <sup>a</sup> Urszula K. Komarnicka, <sup>\*a</sup> Aleksandra Ziótkowska,<sup>a</sup> Agnieszka Skórska-Stania, <sup>b</sup> Barbara Pucelik, <sup>c</sup> Michał Płotek,<sup>b,d</sup> Victor Sebastian, <sup>e,f</sup> Alina Bieńko, <sup>a</sup> Grażyna Stochel<sup>b</sup> and Agnieszka Kyzioł <sup>\*b</sup>

Novel half-sandwich iridium(III) complexes with aminomethyl(diphenyl)phosphine derived from fluoroloquinolones (IrPCp, IrPSf, IrPLm, IrPNr) were studied as possible anticancer chemotherapeutics and showed higher potency than other well-known metal-based agents i.e., Pt(II) drugs. All compounds were characterized by elemental analysis, selected spectroscopic methods (i.e., absorption and fluorescence spectroscopy, NMR), ESI-MS spectrometry, X-ray diffraction, and electrochemical techniques. The studied complexes exhibited promising cytotoxicity in vitro with IC<sub>50</sub> values significantly lower than that of the reference drug – cisplatin. The insight into the mode of action revealed the uniform distribution of the Ir(III) complexes in both the nucleus and cytoplasm (Pearson's co-localization coefficient of 0.63). Precise cytometric analysis provided clear evidence for the predominance of apoptosis in the induced cell death. The activation of caspase-3/7 along with the decrease of mitochondrial membrane potential also confirmed the apoptotic cell death. The investigated Ir(III) complexes may induce changes in the cell cycle leading to G2/M phase arrest. ROS generation as a plausible pathway responsible for the cytotoxicity was confirmed by determination of redox potentials enabling efficient ROS production. Furthermore, Pluronic P-123 micelles loaded with selected Ir(III) complexes were proposed to overcome low solubility and to minimize serious systemic side effects by administering the complex in a controlled manner. The resulting nanoformulations (IrPCp\_M, IrPNr\_M) facilitated efficient drug accumulation for human lung adenocarcinoma and human prostate carcinoma (A549 and DU-145 cell lines), as demonstrated by confocal microscopy and ICP-MS analysis. In vitro cytotoxicity assays were also carried out within multicellular tumor spheroids and efficient anticancer action on these 3D assemblies was demonstrated.

Received 7th May 2020,  
Accepted 20th July 2020

DOI: 10.1039/d0qi00538j

rsc.li/frontiers-inorganic

<sup>a</sup>Faculty of Chemistry, University of Wrocław, Joliot-Curie 14, 50-383 Wrocław, Poland. E-mail: urszula.komarnicka@chem.uni.wroc.pl

<sup>b</sup>Faculty of Chemistry, Jagiellonian University in Krakow, Gronostajowa 2, 30-387 Krakow, Poland. E-mail: kyziol@chemia.uj.edu.pl

<sup>c</sup>Małopolska Centre of Biotechnology, Jagiellonian University, Gronostajowa 7A, 30-387 Kraków, Poland

<sup>d</sup>Faculty of Conservation and Restoration of Works of Art, Jan Matejko Academy of Fine Arts in Krakow, Lea 27-29, 30-052 Krakow, Poland

<sup>e</sup>Department of Chemical Engineering, Aragon Institute of Nanoscience (INA), The Aragón Materials Science Institute (ICMA), University of Zaragoza, Campus Río Ebro-Edificio I+D, Mariano Esquillor S/N, 50018 Zaragoza, Spain

<sup>f</sup>Networking Research Center on Bioengineering, Biomaterials and Nanomedicine, CIBER-BBN, 28-029 Madrid, Spain

†Electronic supplementary information (ESI) available. CCDC 1996074, 1996071 and 1996073. For ESI and crystallographic data in CIF or other electronic format see DOI: 10.1039/d0qi00538j

## Introduction

Cancer has been considered one of the most threatening diseases for humanity in recent decades. It is estimated that there will be more than 22 million new cancer cases every year by 2030.<sup>1</sup> Lots of anticancer drugs are currently being used in clinical treatment, but over 50% of metallodrugs are platinum-based anticancer medicines that cause severe side effects (e.g., hair loss, nausea and vomiting, kidney/liver damage etc.), and many types of cancer acquired resistance to these drugs.<sup>2,3</sup> The abovementioned disadvantages have provided encouragement to develop new alternative transition metal-based antitumor agents. A variety of metal complexes with ions such as Cu, Pd, Au and Ru have been currently proposed as new anticancer agents. Many of them are now under extensive investigations for potential clinical applications.<sup>4,5</sup> Until now there have been only a limited number of papers on the anticancer activity of

iridium(III) complexes.<sup>6–12</sup> Ir(III) complexes have been recently reported to exert anticancer efficacy through the induction of apoptosis and through interactions with DNA<sup>7,13</sup> or protein kinases.<sup>7,14</sup> In general, there are two main types of iridium(III) complexes: half-sandwich and cyclometalated.<sup>15</sup> Organometallic complexes exhibit unusual characteristics, such as versatile redox features, universal structure, and a wide range of ligand substitution rates that can be used to produce novel diagnostic agents and drugs with new modes of action.<sup>11</sup> In turn, carbon-bound cyclopentadienyl ligands provide control over the balance between the hydrophilicity and hydrophobicity of the coordination complex – an important parameter determining efficient cell targeting and uptake.<sup>16–18</sup> Octahedral cyclometalated Ir(III) complexes show anti-tumor activity by inducing apoptosis,<sup>7,19</sup> perturbing the cell cycle and increasing the intracellular ROS level,<sup>19</sup> and exhibit good anticancer activity.<sup>20–23</sup> Moreover, due to their large Stokes shifts, good photostability, and long-lived and environment-sensitive emission, iridium(III) complexes have also been widely explored as luminescent probes for studying various molecular pathways of cytotoxicity occurring during chemotherapy.<sup>18,21</sup>

The research on organometallic Ir(III) compounds described herein is a continuation of our project in which phosphines bearing fluoroquinolones: sparfloxacin (PSf),<sup>24–28</sup> ciprofloxacin (PCp),<sup>27,29,30</sup> lomefloxacin (PLm),<sup>31</sup> and norfloxacin (PNr)<sup>28</sup> were coordinated to various metal centers: Cu(I), Cu(II), Ru(II), Ru(III), Ir(III). In addition to persistent research on anticancer activity of the resulting complexes,<sup>24–31</sup> we have also proved that the introduction of the Ph<sub>2</sub>PCH<sub>2</sub>– moiety to fluoroquinolones enhances their antibacterial properties. This moiety may generate additional interactions, so it could have an influence on biological activity, bioavailability and toxicity of the original drug.<sup>24–31</sup> Thus, motivation for the current research was the significant activity of previously studied complexes and the reasonability of possible future structure–activity analysis. Novel synthesized complexes with fluoroquinolone-based phosphines, most of all copper(I) and ruthenium(II) ones, exhibited considerable anti-proliferative activity and were more active than the parent antibiotics, causing apoptotic cancer cell death via the caspase-dependent mitochondrial pathway.<sup>24–27</sup> On the other hand, as reported in the recent literature the excellent properties as both phosphorescent probes and anticancer agents make Ir(III) complexes perfect potential candidates for the future development of theranostics.<sup>12,19,32–34</sup> Hence, four half-sandwich complexes (IrPCp, IrPSf, IrPNr, IrPLm) with different phosphino-fluoroquinolone ligands were synthesized and their physicochemical properties were determined using elemental analysis, 1D NMR, UV–Vis spectroscopy and mass spectrometry (ESI-MS). In addition, complexes were examined by means of structural X-ray analysis. To reduce the systemic toxicity of these complexes, they were encapsulated into polymeric micelles. In vitro cytotoxic activity of all studied compounds was evaluated against five cancer cell lines: mouse colon carcinoma (CT26), human lung adenocarcinoma (A549), human breast adenocarcinoma (MCF7), human prostate carcinoma (DU-145),

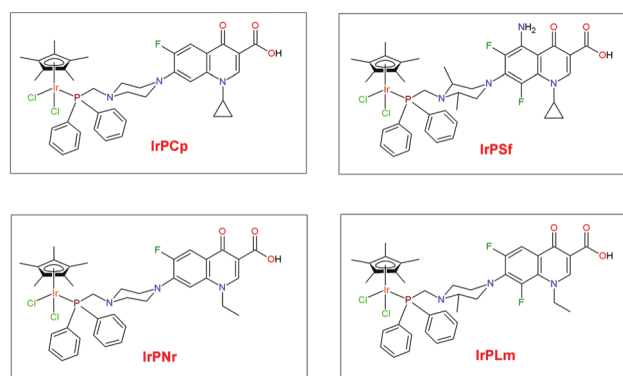
human pancreatic/duct carcinoma (PANC-1) and one healthy cell line of human embryonic kidney (HEK293T). The cytotoxic effect of the selected Ir(III) complex with ciprofloxacin conjugated to a phosphine ligand was also examined on preformed A549 and DU-145 spheroids. As many aspects of the cancer-inhibiting action displayed by iridium complexes are still unknown, we also tried to approach their mode of action. Since it is supposed that reactive oxygen species (ROS) may significantly contribute to the general cytotoxicity of metal complexes, we examined the ability of the novel Ir(III) synthesized complexes to generate ROS by cyclic voltamperometry. Finally, the intracellular uptake of the tested complexes was studied by ICP-MS spectroscopy and confocal microscopy.

## Results and discussion

### Synthesis

The half-sandwich Ir(III) complexes presented herein with aminomethyl(diphenyl)phosphines derived from fluoroquinolones (PSf (PPh<sub>2</sub>CH<sub>2</sub>Sf), PCp (PPh<sub>2</sub>CH<sub>2</sub>Cp), PLm (PPh<sub>2</sub>CH<sub>2</sub>Lm), and PNr (PPh<sub>2</sub>CH<sub>2</sub>Nr)) were synthesized for the first time – IrPCp, IrPSf, IrPLm, and IrPNr, while the aminomethyl(diphenyl) phosphines: PSf,<sup>24</sup> PCp,<sup>29</sup> PLm,<sup>31</sup> and PNr<sup>29</sup> were synthesized according to the literature procedure described by our group in previous publications. All syntheses were carried out under a nitrogen environment using Schlenk techniques. Chemical structures of studied Ir(III) complexes are presented in Scheme 1.

Phosphines derived from fluoroquinolones are soluble in DMSO, CHCl<sub>3</sub>, and CH<sub>2</sub>Cl<sub>2</sub>, and poorly soluble in water, whereas, iridium(III) complexes are insoluble in water, but they become well soluble in water by the addition of 2% DMSO. All synthesized complexes are stable in the solid state and under aerobic conditions, except for phosphine ligands that are sensitive to oxidation. Encapsulation of the resulting iridium(III) compounds into polymeric micelles drastically increased their water solubility and presumably will improve bioavailability in vivo.



Scheme 1 Schematic view of the investigated iridium(III) complexes with phosphanes derived from fluoroquinolones.

## Characterization of organometallic Ir(III) complexes

All complexes IrPCp, IrPSf, IrPLm, and IrPNr were precisely characterized by  $^1\text{H}$  NMR,  $^{31}\text{P}$  NMR, UV-Vis spectroscopy and mass spectrometry. Application of these techniques allowed for determining the structures of the complexes in solution under atmospheric oxygen.

In all  $^{31}\text{P}\{^1\text{H}\}$  NMR spectra of the synthesized compounds (IrPCp, IrPNr, IrPSf, IrPLm), one characteristic peak was observed indicating only one product of synthesis (Fig. 1).

The signal of uncoordinated aminomethylphosphane is situated in the negative part of the spectrum (PCp:  $-27.4$  ppm; PSf:  $-35.9$  ppm; PLm:  $-27.4$  ppm; PNr:  $-27.5$  ppm)<sup>24,29,31</sup> and undergoes a downfield shift to the more positive part of the spectrum as a result of phosphine coordination (IrPCp:  $-1.30$  ppm; IrPSf:  $-3.06$  ppm; IrPLm  $-1.82$  ppm; IrPNr:  $-1.38$  ppm). This can be related to the increase of the shielding effect resulting from the formation of coordination complexes. As expected, the biggest changes in the  $^1\text{H}$  NMR spectra (ESI, Table S3 and Fig. S2–S5<sup>†</sup>) upon the complexation process were observed for the atoms neighboring the coordination metal. Namely,  $\text{H}^1\text{--H}^{17}$  undergoes an upfield shift independently of the type of substituent bonded to the piperazine ring. However, the signals of the atoms on the phenyl ring in the phosphine ligand ( $\text{H}^{41}\text{--H}^{43}$ ) undergo a downfield shift. This might be related to the increase in electron density around the phosphine ligand caused by the formation of a complex compound. The values of the chemical shifts of other atoms (in the fluoroquinolone part) are not significantly changed.

In general, M–Cl bonds in these types of complexes often undergo hydrolysis. Thus, the aqueous stability of IrPCp, IrPNr, IrPSf, and IrPLm was monitored in 80% DMSO- $d_6$ /20% D $_2$ O (v/v) and 70% DMSO- $d_6$ /20% D $_2$ O by  $^1\text{H}$  NMR (Fig. S6–S12<sup>†</sup>). After incubation for 48 h, no additional peaks were found in the  $^1\text{H}$  NMR spectra for all complexes, suggesting that these complexes did not suffer from ligand dissociation or decomposition under the investigated model conditions.

The presence of DMSO ensured the solubility of the complexes. Long-term stability monitoring was also performed

using UV-Vis spectroscopy in DMEM (Dulbecco's Modified Eagle's Medium) with 2% DMSO (Fig. S13<sup>†</sup>). During 72 h of incubation no significant changes in the intensity and shape of the characteristic absorption band (MLCT) were observed. In general, the study suggests that all of the Ir(III) complexes in the investigated system have sufficient stability for further investigation of biological activity and chemical reactivity. These results are comparable to the stability observed for other reported metal complexes.<sup>19,35–38</sup>

Spectral characterization of the iridium(III) complexes indicates the intense absorption bands at high energies ( $<300$  nm) which can be assigned to the spin-allowed  $^1\pi\text{--}\pi^*$  electronic ligand-centered (LC) transitions arising from phosphine derived from fluoroquinolones.<sup>39</sup>

Furthermore, according to the neutral character of all iridium(III) complexes, ESI-MS analysis confirmed the molecular ion peaks  $[\text{M} + \text{H}]^+$  in the positive ion modality. Less abundant peaks corresponding to  $[\text{M} - \text{Cl}]^+$  and  $[\text{M} - 2\text{Cl}]^+$  ions were also recorded indicating that chloride groups of the cyclopentadienyl ligand were easily displaced. The peaks corresponding to the loss of the phosphine ligands and the arene ring are not observed which indicates the strong metal to ligand and metal to arene bond (ESI, Fig. S14–S21<sup>†</sup>).

## Structural analysis

The products of all syntheses were recrystallized in order to obtain pure complexes. Their purity was confirmed using elemental analysis, while the single crystals were analysed by the X-ray diffraction technique (Fig. 2, Tables S1 and S2<sup>†</sup>). All obtained iridium(III) complexes crystallized in different space groups and there is only one molecule in the asymmetric unit in each case. Every structure contains also chloroform molecules (disordered in the case of IrPLm, and IrPNr).

The complexes adopt the expected half-sandwich pseudo-octahedral “three-leg piano-stool” geometry, where the cyclopentadienyl moiety served as the top of the stool and the three leg sites were occupied by phosphorous atoms from ligands

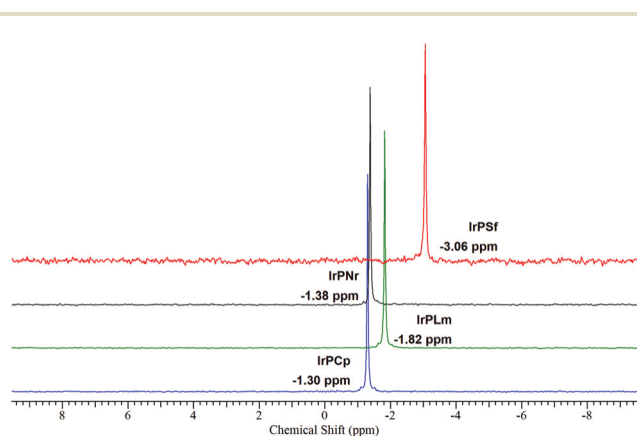


Fig. 1  $^{31}\text{P}\{^1\text{H}\}$  NMR spectra (298 K, DMSO) of IrPCp, IrPSf, IrPLm, and IrPNr.

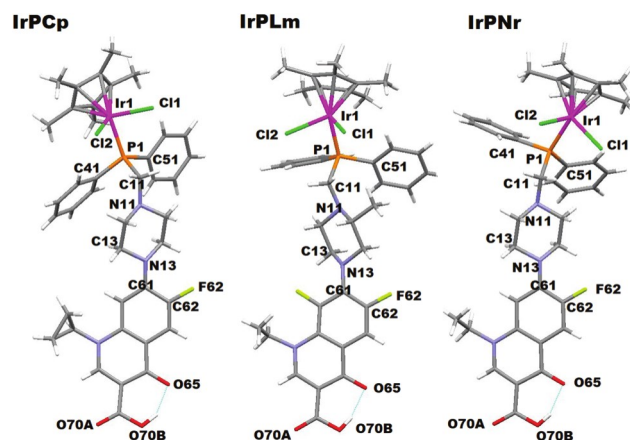


Fig. 2 The crystal structures of the complex molecules IrPCp, IrPLm and IrPNr. The solvent molecules are omitted for clarity. Blue dashed lines represent the intramolecular hydrogen bond.

and two terminal chloride anions.<sup>40–42</sup> The bond angle values P–Ir–Cl and Cl–Ir–Cl are found to be in the range of 86.04–90.45° thus suggesting the pseudo-octahedral arrangement of atoms around the metal center.<sup>42</sup> The bond distances between iridium atoms and phosphorus atoms of complexes IrPCp, IrPLm and IrPNr were found to be on an average 2.3 Å, whereas the Ir–Cl1 and Ir–Cl2 bond distances of complexes IrPCp, IrPLm and IrPNr were found to be on an average 2.4 Å and are comparable with earlier reported complexes.<sup>40,41</sup>

The conformation of the antibiotic fragment of complexes can be defined in terms of torsion angle, defining the orientation of the piperazinium ring and fluoroquinolone moiety (IrPCp: C13–N13–C61–C62 –165.92°; IrPLm: C13–N13–C61–C62 117.48° IrPNr: C14–N13–C61–C62 –165.97°). The different value of this angle for IrPLm is a result of weak interactions of the fluorine atom, F62, with the chloroform molecule. In the case of IrPCp and IrPNr, solvent molecules are differently positioned relative to the complex molecule, so fluorine atoms do not interact with them. Another interesting feature of all structures is the presence of intramolecular hydrogen bonds between hydroxyl groups O70B–H70B and oxygen atoms from carbonyl groups O65vC65.

Intermolecular  $\pi$ -ring stacking in the unit cell is observed only in one crystal structures – IrPCp·CHCl<sub>3</sub> (Fig. 3). A fragment of the heterocyclic moiety of fluoroquinolone (i.e. 6-membered rings) is involved in a strong  $\pi$ - $\pi$  interaction with a symmetry related to the other fragment of the fluoroquinolone moiety a neighbouring ligand in the unit cell (Fig. 3A).<sup>43</sup> As observed in the single crystal structure, the  $\pi$ - $\pi$  stacking in complex IrPCp is a face-to-face pattern, with a centroid (N67–C67–C66–C65–C64–C68)–centroid (C69–C68–C64–C63–C62–C61) distance of 3.652 Å (Fig. 3B). It is worth mentioning that the solvent molecule presented in the IrPCp structure is located in the peripheral part of the complex molecule (i.e. near the cyclopentadienyl anion) allowing  $\pi$ - $\pi$  stacking interactions in the IrPCp complex.

### Luminescence properties

Fluoroquinolone antibiotics (HCp, Hsf, HLM, HNR) and their phosphine derivatives (PCp, PSf, PLm, PNr) are characterized by intense luminescence in PBS (phosphate buffered saline) with the addition of DMSO (<2% (v/v)). In general, the maximum of the emission band for PCp, PNr, and PLm is located around 420 nm, while that for PSf is located at 540 nm upon excitation at 340 nm.<sup>25,29–31</sup> The emission spectra for all resulting Ir(III) complexes with phosphine ligands were obtained at 298 K and are presented in Fig. 4, whereas the corresponding excitation spectra are shown in Fig. S22.†

After the coordination of PCp, PLm, and PNr to iridium(III) ions a redshift in the emission spectra for resulting complexes was observed. Only in the case of IrPSf the blue-shift was noticed. Under ambient conditions, all complexes displayed a purple emission with the maximum wavelength at 440 nm for IrPCp, IrPNr, and IrPLm and at 475 nm for IrPSf.

Thus, the ligand structure appears to have an influence on the emission wavelength of the studied Ir(III) complexes. This

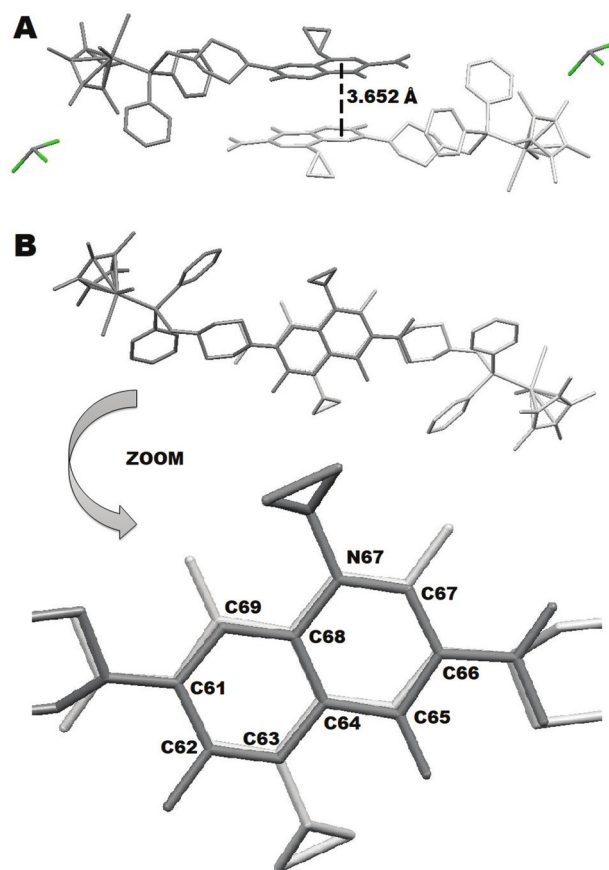


Fig. 3 Packing diagram of complex IrPCp·CHCl<sub>3</sub> showing (A)  $\pi$ -stacking interaction between the fluoroquinolone rings (B) face-to-face pattern of the  $\pi$ - $\pi$  stacking in complex IrPCp.

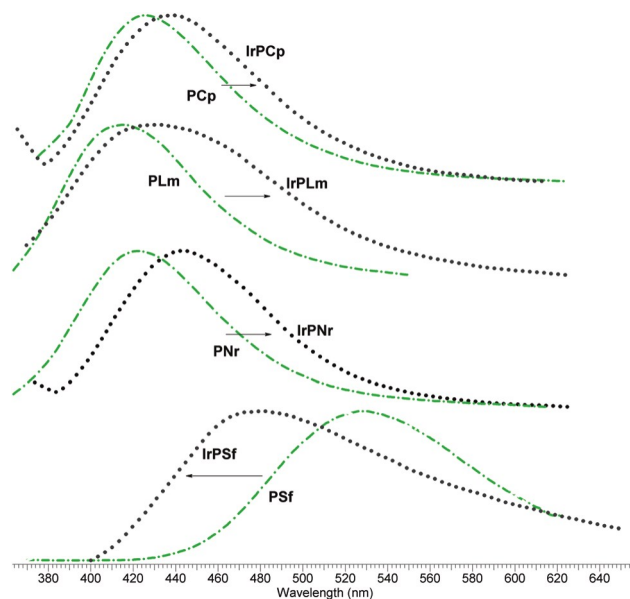


Fig. 4 Normalized emission spectra for Ir(III) complexes and the corresponding phosphine ligands;  $\lambda_{\text{ex}} = 340$  nm, 298 K.



is in agreement with previous observations made for the Cu(I) and Ru(II) complexes. The complexes with the ligand bearing sparfloxacin, the third generation fluoroquinolone, are characterized by the maximum of emission significantly shifted towards shorter wavelengths. This is probably due to the most extensively developed and substituted chemical structure for this antibiotic affecting the electronic properties of the entire complex.

#### Cytotoxic study in vitro

The cytotoxicity of the four novel organometallic Ir(III) complexes was evaluated against five selected cancer cell lines: CT26, A549, MCF7, PANC-1, DU-145 and one normal HEK293T cell line. IC<sub>50</sub> values (concentration of a drug required to inhibit the growth of 50% of the cells) were assessed in two different approaches – after 24 h or 24 h + 48 h using the 3-(4,5-dimethylthiazole)-2,5-diphenyltetraazolium bromide (MTT) method.<sup>6,44–46</sup> Cells were also treated with cisplatin in the same concentration range as Ir(III) complexes and considered as a control. IC<sub>50</sub> values were determined from the plots of cell viability at various concentrations of each compound by matching appropriate dose–response curves and are presented in Table S4.† The investigated complexes IrPCp, IrPSf, IrPLm, and IrPNr exhibited significant and diversified cytotoxic activity against all studied cell lines. Of note, all Ir(III) complexes were characterized by a higher cytotoxicity than the ligands (PCp, PSf, PLm, PNr), regardless of the cell type or the incubation time. A similar observation was made in the case of complexes of other metals such as copper or ruthenium studied by our group with these types of phosphine ligands.<sup>24–27,29,31</sup>

Notably, all the half-sandwich Ir(III) complexes displayed higher cytotoxicity than cisplatin against all cell lines except for the MCF7 cell line after 24 h incubation. Presumably, Ir(III) complexes exhibited a different cross-resistance profile from cisplatin. The activity of these complexes for all studied cell lines was higher after 24 h of incubation with compounds and 48 h of recovery time (24 h + 48 h), when compared with the experimental approach in which cytotoxicity was determined just after 24 hours. This indicates that the cytotoxic changes initiated in the cells during 24 h incubation cannot be repaired by cells and their repair systems minimizing toxicity are not sufficient, which may result in overcoming the resistance. Of note, the cytotoxicity of Ir(III) complexes was also evaluated against non-tumor cells (HEK293T). The results indicate similar or slightly lower toxicity profiles toward a normal cell line than that determined for cisplatin.

Interestingly, prostate carcinoma cancer cells (DU-145) were the most sensitive cell line to iridium(III) complexes even in the case of both experimental approaches. Among all tested complexes, the IrPSf complex showed the most significant antitumor activity in vitro with an IC<sub>50</sub> value of 3.5 μM and 4.1 μM for DU-145 and CT26, respectively (in 24 h + 48 h approach). In both cases SI (selectivity index – IC<sub>50</sub> (normal cell line)/IC<sub>50</sub> (cancer cell line)) was determined to be ca. 6 related to the HEK293T cell line. In general, the cytotoxic

activity of Ir(III) complexes with phosphine conjugated with sparfloxacin (IrPSf) exhibited the most prominent activity in vitro towards all tested tumor cell lines. It is evident that the combination of two or even more new structural elements brings into play different properties of the resulting compound. This, in turn, may result in improving the spectrum of biological activity, novel mechanisms of action or modification of the pharmacokinetic profile of the drug.<sup>21</sup> Thus, the highest activity of IrPSf can be explained by the modified activity of the resulting new complex involving two modes of action – associated with the metal center and ligand. Importantly, HSf apart from exhibiting significant antimicrobial activity also inhibits the human ether-a-go-go-related gene (hERG) potassium channels, which are overexpressed in a wide range of tumors.<sup>24–26</sup>

In addition, human pancreatic/duct carcinoma (PANC-1) was also found to be a sensitive cell line, when recovery time was applied. To confirm the determined cytotoxicity, viable and dead cells were survival stained with fluorescein diacetate (FDA) and propidium iodide (PI) after treatment and the effect was visualized under a fluorescence microscope (Fig. 5). FDA was used as a versatile fluorescent dye in the form of a cell-permeant esterase substrate. Only in viable cells with suitable enzymatic activity fluorescein is intracellularly generated and serves as a viability probe, while PI was applied as a red-fluorescent cell viability dye, which is excluded from live cells with intact membranes, but penetrates dead or damaged cells and binds to DNA and RNA by intercalating between the bases.

Cytotoxicity in vitro was also precisely analyzed by flow cytometry allowing the determination of the mode of cell death. Cell staining with Annexin-V and 7-AAD (7-Aminoactinomycin D) after treatment enables quantitative evaluation of apoptosis and/or necrosis induction by the investigated compounds (IrPCp, IrPSf, IrPLm, IrPNr). The percentage of viable, early/late apoptotic and necrotic cells upon treatment with the compounds for the two selected cell lines (A549, DU-145) is presented in Fig. S23.† By extension, analysis of cell death of A549 and Du-145 cells after exposure to IrPCp, IrPSf, IrPLm, IrPNr complexes at 100 μM for 24 h + 48 h revealed that proportions of late apoptotic cells after treatment with IrPCp, IrPSf, IrPLm, IrPNr were 28.53%, 37.56%, 46.17%, and 5.17%, respectively in the case of D-145 cells. This corresponds to 99.07%, 96.10%, 98.77%, and 95.26% of the overall toxicity (early and late apoptosis, necrosis), respectively. Of note, most of the appearing dead cells are the population of early or late apoptotic cells.

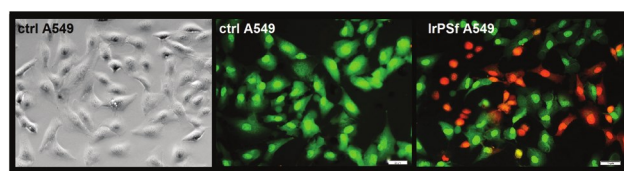


Fig. 5 Selected images of A549 cells treated with IrPSf in IC<sub>50</sub> (magnification 20.00×, bar 50 μm). The green cells with normal morphology are viable ones (fluorescein diacetate, FDA), while round red cells are dead (propidium iodide, PI).

## Cellular uptake

It has been recently demonstrated that organometallic Ir(III) complexes are capable of entering cells in either an energy-dependent or an energy-independent mode. For instance, induction of apoptosis in cancer cells may be realized by targeting lysosomes, mitochondria or the endoplasmic reticulum and causing lysosomal damage, serious changes in mitochondrial membrane potential, and endoplasmic reticulum stress.<sup>47,48</sup> However, to cause all these changes which result in cell death, efficient and selective accumulation inside cancer cells over normal cells is firstly necessary. Both the chemical structure and the relatively high hydrophobicity can promote efficient accumulation inside cancer cells. In addition, appropriate pharmaceutical nanoformulations can be prepared to ensure selective drug delivery to the interior of the cell and to provide biological effects only at the target site (vide infra).

Cellular accumulation of iridium(III) compounds after treatment of the tested cells was determined by the ICP-MS technique. Time-dependent cellular uptake of IrPCp, IrPSf, IrPLm, and IrPNr complexes is given in Fig. S24.† ICP-MS analysis revealed efficient iridium accumulation with increasing time, which was assessed to be the highest in the case of DU-145 cells (ca. 900 and 1300 ng mg<sup>-1</sup> protein for 24 h and 24 h + 48 h, respectively) among all tested Ir(III) compounds. On the other hand, the uptake was at the lowest level for A549 cells after 24 hours of incubation with Ir(III) complexes. Nonetheless, the A549 cells were chosen for confocal analysis since they do not exhibit auto fluorescence which would render the analysis impossible. Thus, these results, together with confocal analysis enabling the calculation of Pearson's co-localization coefficient (PCC) (Fig. 6) and determination of hydrophobic/hydrophilic properties (Table 1, vide infra), clearly support an efficient pattern of cellular uptake into tumor cells of the studied organometallic iridium(III) complexes.

Uniform distribution of IrPSf inside A549 cells clearly confirms the sufficient uptake of the metal complex and its observed cytotoxicity *in vitro*. The cross-sectional analysis of images and emission spectra of the tested compound revealed consistency in intensity emission visible inside the whole cell. This indicates the uniform distribution of the Ir(III) complex throughout the cells and no favorable accumulation in any cellular compartments or organelles.

Furthermore, to confirm the co-localization of IrPSf (green signal) with the nuclei-specific probe (Hoechst 33342, blue signal) more clearly, the spectral profiles for these components were defined. The obtained profiles are presented in Fig. 6D, while the detailed co-localization study, performed with ImageJ plugin, is presented in Fig. S25.† The analysis allowed for calculating Pearson's co-localization coefficient (PCC) which was found to be 0.63. The resulting value presumably means a high agreement of IrPSf co-localization between the nucleus and cytoplasm. Accordingly, this suggests that a significant part of the IrPSf complex reaches the cell nucleus.

The pharmacological activity of many substances correlates with their lipophilicity (hydrophobicity); thus this physico-

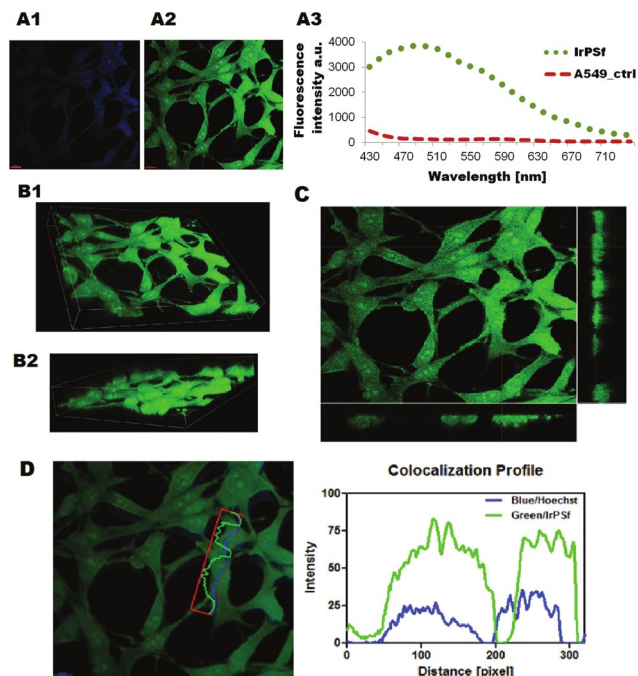


Fig. 6 Selected images of A549 cells obtained by confocal microscopy (magnification 60.00 $\times$ , ex = 358 nm) after treatment with IrPSf ( $c = 1 \mu\text{M}$ ) for 4 h (A1, A2, B1, B2). In addition, emission spectra of cells after treatment with IrPSf together with the reference spectra of control untreated (A3), cross-sectional images (C), and colocalization of IrPSf (green) and nuclei specific probe Hoechst33342 (blue) determined along with quantification analysis by Zen software (Zeiss, Jena, Germany) (D).

Table 1 Calculated log P values for ligands (PCp, PSf, PLm, PNr) using program ACD/log P<sup>49</sup> and complexes (IrPCp, IrPSf, IrPLm, IrPNr) using program ALOGPS 2.1<sup>50</sup>

Ligands		Complexes	
PCp	5.81	IrPCp	7.73
PSf	6.35	IrPSf	7.44
PLm	6.86	IrPLm	7.51
PNr	5.97	IrPNr	7.26

chemical parameter is helpful for both design of new metal compounds and explanation of correlation between the biological activity and chemical structure. The octanol–water partition coefficient (log P) value provides information about hydrophobicity that is usually a factor relevant for efficient cell uptake and the resulting biological activity.<sup>48</sup> log P values for IrPCp, IrPSf, IrPLm, and IrPNr complexes and the corresponding ligands were determined and are presented in Table 1.

For the investigated Ir(III) complexes, the determined log P values are significantly higher than those for their parent ligands. The performed calculations clearly indicate the strong hydrophobic character of the investigated compounds. These supplementary theoretical data confirm effective penetration into cancer cells, however, despite the high log P values



because of poor solubility of the studied iridium(III) complexes in water we decided to encapsulate them into polymeric micelles (*vide infra*). As expected, the successful and efficient uptake of poorly soluble half-sandwich Ir(III) complexes will be enhanced by the relevant unique features of Pluronic P-123. This hydrophobic copolymer is capable of interacting with cell membranes resulting in decreased microviscosity, pore formation on the membrane, and thus accelerated transmembrane drug translocation.<sup>27</sup>

#### Analysis of the cell cycle and apoptosis-related proteins

The cell cycle analysis along with the determination of caspases 3/7 activation has been performed. First, to understand the impact of the selected Ir(III) complexes (IrPCp, IrPSf) on cell growth, the A549 and DU145 cell cycles after treatment were evaluated by flow cytometry (Fig. 7). The analysis revealed that the tested compounds probably induced G2/M phase arrest. In the case of DU145 cells the interruption of chromatin synthesis may occur (less cells are in the G0/G1 phase and the number of cells in S phase are increased). On the other hand, for A549 the G0/G1 phase population is still observed. Our results are in agreement with other authors concluding that the metal center plays a key role in the cell cycle arrest.<sup>51</sup> Many cytotoxic agents based on metal complexes inhibit tumor cell proliferation by causing cell cycle G0-, S-, or G2/M-phase arrest. The G2 checkpoint prevents cells from entering mitosis when DNA is damaged and ensures the propagation of error-free copies of the genome to each daughter cell. The Cdk1/cyclin B1 complex controls the cell cycle progression from the G2 phase to the M phase by regulating the phosphorylation or dephosphorylation of

proteins. In addition, actin remodeling in coordination can ensure proper execution of G2/M checkpoint arrest and is crucial for entry into mitosis.<sup>9,52–57</sup>

Secondly, the activation of caspases 3 and 7 (cysteine proteases involved in both the initiation and execution phases of apoptosis) was studied (Fig. 7). Indeed, activation of these executioner caspases is usually taken as a hallmark of apoptosis after cytochrome c leaks out from mitochondria during the intrinsic pathway of apoptosis.<sup>51,52</sup> After 24 hours of incubation with IrPCp and IrPSf complexes in the case of A459 cells the activation of both caspases increases with the increased concentration of complexes, whereas, in the case of DU145 cells at higher concentrations of Ir(III) complexes the caspase-3/7 activation decreases. This probably indicates the activation of necrotic cell death instead of apoptosis in the case of these the most sensitive cells for treatment with the studied compounds.

#### Polymeric micelles

To enhance the cellular accumulation of metal complexes and to control their uptake only into tumor cells over normal ones, we encapsulated metal compounds into Pluronic P-123 micelles (Fig. 8, *vide infra*). Detailed characterization of prepared nanoformulations, including hydrodynamic diameter, zeta potential, drug loading content (LC), and encapsulation efficiency (EE), is shown in Table S5.† The determined LC and EE values proved the effective loading of the Ir(III) complexes inside the Pluronic P-123 micelles. The mean micelle size of IrPCp\_M and IrPNr\_M was less than 30 nm, while zeta potential of stable micelles was ca. -1.5 mV (pH = 7.4). The latter value can be explained by the slightly negative potential of Pluronic P-123 comprising the uncharged PEO (polyethylene oxide) amphiphilic blocks.<sup>27</sup> The spherical morphology and homogeneous particle size distribution were also confirmed by transmission electron microscopy (Fig. 8). These physical characteristics meet all the necessary requirements to ensure efficient delivery of the resulting nanoformulations into the pathological tumor microenvironment and to facilitate efficient release of metal complexes due to micelle aggregation at the lower pH of tumor cells.

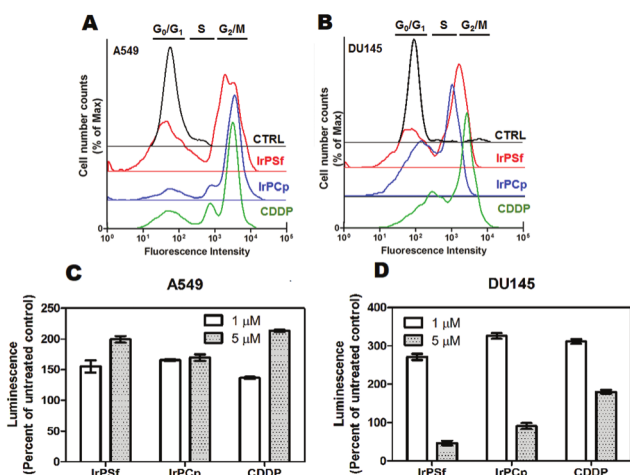


Fig. 7 Cell cycle analysis of A549 (A) and DU145 (B) cells after the treatment with investigated compounds (IrPSf, IrPCp) and cisplatin (CDDP, reference). Caspase activation after treatment with IrPSf, IrPCp and cisplatin (CDDP, reference compound). Analyses were performed using the caspase-Glo® 3/7 assay. A549 (C) and DU145 (D) cells were incubated with or without each compound for 24 h. The results are expressed as the ratio of the mean relative light units (RLU) obtained with treatment to the mean RLU obtained without treatment.

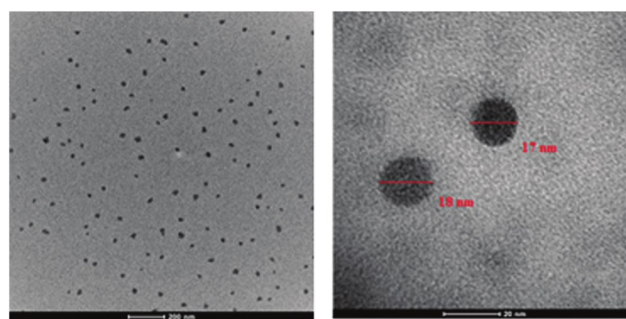


Fig. 8 TEM images of Pluronic P-123 formulation with the encapsulated IrPCp complex (IrPCp\_M).

Table 2 Values of  $IC_{50}$  [ $\mu M$ ] for A549 and DU-145 cells after 24 h treatment with IrPCp, IrPNr, IrPCp\_M, and IrPNr\_M

$IC_{50}$ [ $\mu M$ ] $\pm$ SD; 24 h		
	A549	DU-145
IrPCp	$68.8 \pm 1.7$	$11.8 \pm 1.1$
IrPCp_M	$8.9 \pm 0.7$	$4.1 \pm 0.6$
IrPNr	$71.4 \pm 1.6$	$12.9 \pm 2.1$
IrPNr_M	$10.1 \pm 0.4$	$3.1 \pm 0.5$

For the *in vitro* study we selected two polymeric nanoformulations of Ir(III) complexes (IrPCp\_M, IrPNr\_M), that exhibited the lowest cytotoxicity in the form of free compounds (IrPCp, IrPNr) to prove the rationality and sense of encapsulation. Cytotoxicity *in vitro* was determined for the least and the most sensitive cell lines according to the above-described studies – A549 and DU-145, respectively (Table S4<sup>†</sup>).  $IC_{50}$  values for both complexes in solution and the corresponding nanoformulations are presented in Table 2.

Of note, the determined  $IC_{50}$  values for IrPCp\_M and IrPNr\_M are one order of magnitude lower than those in the case of the corresponding complexes studied in solution for A549 cells (the most resistant line towards not encapsulated Ir(III) compounds), while, in the case of the most sensitive line (DU-145), this activity was about 3 times lower. Thus, prepared FDA-proved Pluronic P-123 nanoformulations with encapsulated organometallic Ir(III) complexes presumably will guarantee biocompatibility with improved pharmacokinetics and pharmacodynamics.

### Spheroid assembly

Having established the optimal conditions for spheroid formation, the effect of the selected Ir(III) complex with ciprofloxacin conjugated to the phosphine ligand (IrPCp\_M) was examined on preformed A549 and DU-145 spheroids. Of note, in the monolayer culture, these cell lines displayed a marked difference in sensitivity to the Ir(III) complexes (Table S4<sup>†</sup>), while, the selected complex exhibited the highest increase of cytotoxicity when encapsulated, as demonstrated by  $IC_{50}$  values (Table 2, *vide supra*).

Therefore, these conclusions were drawn after analysing the results of both studied systems: solution and polymeric nanoformulation of this particular Ir(III) complex. The results of live/dead assay employing fluorescence images are shown in Fig. 9. As illustrated, a relatively small number of dead cells were observed in control spheroids. The low-intensity signal of PI may be attributed to the intratumoral-like necrotic area in the tumour. In contrast, a high percentage of red fluorescent cells was observed in the compound-treated spheroids. In the more IrPCp\_M-sensitive DU-145 spheroids, the earlier onset of cytotoxicity manifested due to an increase in red and a decrease in green fluorescence (after treatment with increasing concentration of nanoformulation). In this case, the major outcome of IrPCp\_M treatment of DU-145 spheroids was spheroid disruption (Fig. 9, bottom right corner).<sup>53</sup>

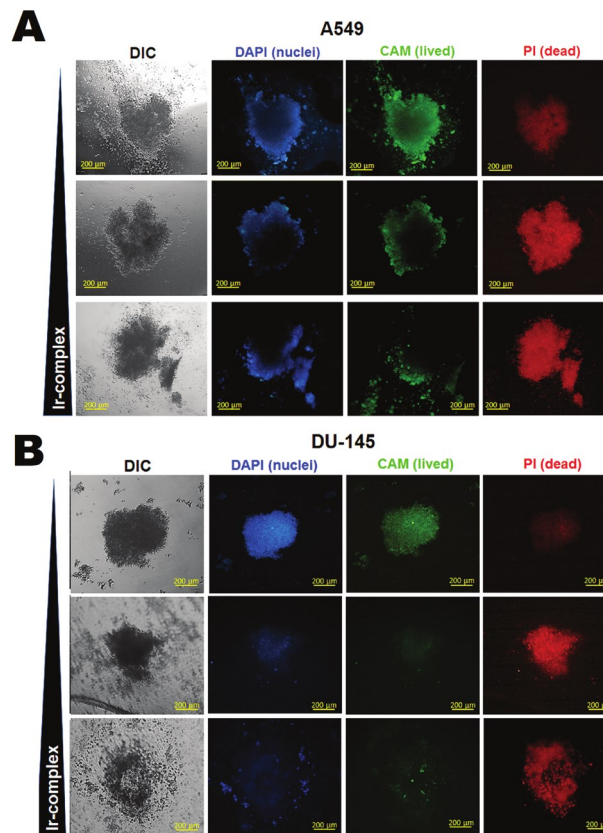


Fig. 9 Labelled (A) A549 and (B) DU-145 spheroids treated with the Pluronic P-123 Ir(III) complex (IrPCp\_M) after treatment with increasing concentration of complex  $0.1 \times IC_{50}$ ,  $IC_{50}$ , and  $10 \times IC_{50}$  for 48 h. Z-projections of stack registered with a fluorescence microscope. Ir-Complex dose indicated by a triangle at the left. DAPI: 4',6-diamidino-2-phenylindole, CAM: calcein AM, PI: propidium iodide.

### Cellular ROS generation and mitochondrial damage

For the first time, to give insights into the possible mode of action of the studied novel organometallic iridium(III) complexes the ability of complexes (IrPCp, IrPSf, IrPLm, IrPNr) and their corresponding ligands (PCp, PSf, PLm, PNr) to generate reactive oxygen species (ROS) was studied. It is well documented that metal-based agents that target altered biochemical pathways in cancer cells are powerful candidates as new chemotherapeutics, especially if more than one pathway is targeted simultaneously. Any drug that is able to cause global cellular effects, for instance by disrupting the redox balance in cells, may be advantageous, given the heterogeneous nature of solid tumours. In general, cancer cells are more active than normal cells with regard to reactive oxygen species generation which is directly associated with the behavior of mitochondria.<sup>54,58</sup> In particular, any oxidative damage of mitochondrial respiratory chain components, caused indirectly or directly by the metal ions, can lead to disturbances in the mitochondrial respiration process.<sup>56–63</sup>

Herein, we investigated novel half-sandwich organometallic Ir(III) cyclopentadienyl complexes as potent cytotoxic anti-cancer agents, and their mode of action can be based, among

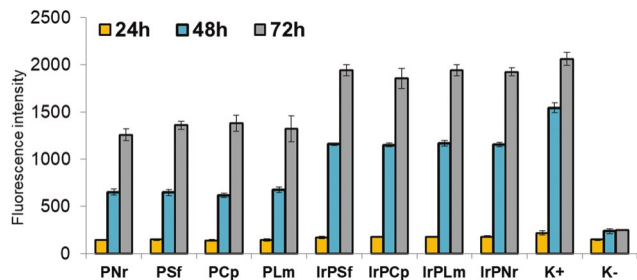


Fig. 10 The ROS generation monitored by H<sub>2</sub>DCF-DA assay in DU-145 cells during steady incubation with complexes (IrPCp, IrPSf, IrPLm, IrPNr) and their corresponding ligands (PCp, PSf, PLm, PNr) for 24, 48 and 72 h in  $c = 1 \mu\text{M}$ . K(+): H<sub>2</sub>O<sub>2</sub> as positive control and K(-): negative control, cell without compound.

others, on the generation of reactive oxygen species. ROS generation was detected with the application of a nonfluorescent 2',7'-dichlorodihydrofluorescein diacetate (DCFH<sub>2</sub>-DA) probe as a ROS detector and monitored by fluorescence spectroscopy. The obtained results, presented in Fig. 10, were related to the fluorescence intensity of positive control cells (K+); in the presence of extra H<sub>2</sub>O<sub>2</sub>) and negative control (K-); control untreated cells).

All investigated phosphine derivatives of the antibiotics (PCp, PSf, PLm, PNr) and their Ir(III) complexes (IrPCp, IrPSf, IrPLm, IrPNr) displayed the ability to induce ROS generation in DU-145 tumor cells at a level much higher than the positive control. Of note, the studied complexes induced ROS generation at a significantly higher level (about two times higher) than their uncoordinated ligands. In addition, the increased ROS production by the investigated Ir(III) compounds was noticed over all studied time periods.

It is well-known that around 90% intracellular ROS is generated in mitochondria – which are the major source of superoxide radicals (precursor of most ROS species). Furthermore, excessive amounts of reactive oxygen species can damage lipids, proteins and DNA, which is obviously associated with changes of mitochondrial functions.<sup>64</sup> Herein, to designate the significance of mitochondrial disorder in ROS production and finally cancer cell death induced by Ir(III) complexes, the variation in the mitochondrial membrane potential (MMP) was monitored using the JC-10 probe (Fig. S26<sup>†</sup>). Gentamicin, which causes an increase in MMP and ciprofloxacin with its opposite effect on MMP were used as a positive and a negative control, respectively.<sup>26</sup>

As clearly seen in Fig. S26,<sup>†</sup> the studied Ir(III) complexes caused a significantly higher MMP decrease, when compared with the corresponding organic ligands and control drug (ciprofloxacin). This means that cell treatment with the investigated Ir(III) inorganic compounds resulted in the increase of permeability of the mitochondrial membrane. Decrease in MMP leads to the release of cytochrome c into the cytoplasm. Then, cytochrome c, in the presence of ATP, interacts with the Apaf-1 factor and activates the initiator caspase 9. This interaction usually triggers a cascade of executive caspases

(especially caspase 3 responsible for apoptotic cell death).<sup>26</sup> Thus, these results support the assumption that the mitochondrial pathway leads to the induction of the observed apoptosis (vide supra).

Presumably, the generated ROS can be involved in cytotoxic action and the resulting type of cell death. This is in agreement with other authors, who showed that Ir(III) complexes, both organometallic and cyclometalated, are highly potent chemotherapeutics with the mode of action largely based on ROS generation. For instance, the half-sandwich tetraphenylethylene Ir(III) complexes were reported as powerful antineoplastic agents effectively catalyzing the conversion of NADH to NAD<sup>+</sup> and inducing ROS accumulation inside cells. Thus, this points to an oxidation-based anticancer mechanism of these organometallic complexes that could as well specifically accumulate in lysosomes, resulting in lysosomal damage, and eventually induce apoptosis.<sup>48</sup> Likewise, Liu et al. demonstrated that novel cyclometalated iridium(III) phosphine-imine (P<sup>^</sup>N) complexes can induce apoptosis by depolarization of the mitochondrial membrane potential, ROS overproduction and ROS-mediated DNA damage.<sup>34</sup>

#### Electrochemical characterization

Furthermore, cyclic voltammetry (CV) was performed to precisely understand the redox activity of the studied complexes (i.e., cellular ROS production, vide supra). The redox potentials for all Ir(III) complexes, the corresponding phosphine ligands, and ferrocene were determined by cyclic voltammetry in DMF solution using 0.1 M tetrabutyl ammonium perchlorate (TBAP) as the supporting electrolyte in the selected potential window from -1.0 V to 1.0 V vs. Ag/Ag<sup>+</sup> at different scan rates (from 1 to 20 mV s<sup>-1</sup>). The cyclic voltammograms (CVs) of all studied compounds are presented in Fig. S27–S32.<sup>†</sup> The cyclic voltammograms of the complexes exhibit two irreversible oxidation peaks at around 1.0 V and 1.25 V which are assigned to the phosphine ligands and the iridium ion, respectively. The determined oxidation potentials for the studied iridium(III) complexes, referring to the Ir(III)/Ir(IV) redox process, are in agreement with literature data for other organometallic Ir(III) compounds with various ligands.<sup>52,65,66</sup> The additional peak (around 1.0 V) can be safely associated with irreversible oxidation processes within the ligand moiety on comparing with the electrochemical data of ligands alone.<sup>27</sup> One quasi-reversible reduction peak around -0.55 V is observed for all complexes (around  $\Delta E = 0.98$  V for all complexes) and it can also be assigned to the phosphine ligand.

The position of the cathodic peak was slightly shifted towards the negative potential, while the anodic peak was shifted a little towards positive potentials simultaneously with the scan rate increase. These observations suggest a diffusion controlled redox process.<sup>67</sup> However, it can be presumed that the electron transfer reactions take place without changes in the stereochemistry of the complexes that can be monitored by UV-vis spectroscopy. In the UV-vis spectra no significant changes were observed, indicating the formation of completely new chemical compounds, as only a decrease



in absorption was detected after the electrochemical study (data not shown).

Regrettably, cancer cells can acquire resistance towards anticancer compounds, in particular the ones that are designed to activate apoptosis, for instance metal compounds. This is mainly by up-regulation of pro-survival factors, involving inhibitors of apoptosis proteins (IAPs) that in turn block caspases required to activate the apoptosis cascade. However, in the case of Ir(III) complexes studied herein, cytotoxicity may be based on other possible actions such as ROS generation (vide supra), affecting mitochondria or interactions with DNA (vide infra). In such a case, other pathways leading to cell death are possible such as energy deficiency or distortion of the DNA structure as key consequences, respectively. Thus, even if the caspase cascade is blocked successfully, cell growth can still be halted through ATP deficiency or tackling of DNA synthesis, giving rise to cataplasia or resulting in dramatic increase in cytotoxicity.<sup>39,58</sup>

## Conclusions

Iridium-based anticancer agents, including organometallic iridium(III) complexes, have currently attracted attention as promising anticancer agents with potency higher than Pt(II) drugs in the clinic. Herein, we present for the first time four novel half-sandwich Ir(III) complexes with phosphines conjugated with fluoroquinolones as ligands (IrPCp, IrPSf, IrPLm, IrPNr). All complexes were precisely characterized by elemental analysis, selected spectroscopic methods (i.e., absorption and fluorescence spectroscopy, NMR), ESI-MS, X-ray diffraction, and electrochemical techniques. In addition, we have studied their cytotoxic effects in vitro towards selected cancer cell lines: CT26, A549, MCF7, PANC-1, and DU-145, and the normal HEK293T cell line. We demonstrated in vitro that the studied complexes are characterized by lower IC<sub>50</sub> values than that of cisplatin, exhibit the ability to induce apoptotic cell death in predominance, and possess a high selectivity index. Furthermore, preliminary investigation on the elucidation of action of the selected Ir(III) compounds allowed us to formulate the following general conclusions: (i) Pearson's co-localization coefficient of 0.63 indicates uniform distribution of complexes in both nucleus and cytoplasm, (ii) the tested compounds presumably induce G2/M phase arrest, (iii) both the activation of caspase-3/7 and the decrease of mitochondrial membrane potential confirm the apoptotic pathway of cell death, and (iv) redox potentials enable efficient ROS generation. Also, we continued herein investigations on the potential of Pluronic P-123 micelles as suitable nanocarriers of metal complexes overcoming low solubility, serious side effects connected with systemic cytotoxicity of metal complexes, and preventing acquisition of resistance. The resulting nanoformulations (IrPCp\_M, IrPNr\_M) enabled efficient drug accumulation inside A549 and DU-145 tumor cell lines and allowed more efficient cytotoxic action, when compared with the corresponding solutions of complexes. Finally, the 3D model of cell culturing (spheroids),

imitating three-dimensionality and the complexity of tumour structure, was explored and the anticancer potential of the selected novel organometallic Ir(III) complex (IrPCp\_M) encapsulated in Pluronic P-123 micelles was clearly proved.

## Experimental

### Reagents

All starting materials, including 2<sup>nd</sup> (HCp, HNr, HLM) and 3<sup>rd</sup> (HSf) generation fluoroquinolones (>98%), [Ir( $\eta^5$ -Cp\*)Cl<sub>2</sub>]<sub>2</sub> (>96%), Pluronic P-123 and other small chemicals and solvents were purchased from Sigma Aldrich and used without further purifications. All syntheses were performed using standard Schlenk techniques, under an atmosphere of dry oxygen-free dinitrogen. All solvents were deaerated prior to use.

### Characterization of organometallic iridium(III) complexes

Single crystals of IrPCp·CHCl<sub>3</sub>, IrPLm·1.5CHCl<sub>3</sub> and IrPNr·2CHCl<sub>3</sub> were collected on a SuperNova diffractometer using graphite monochromatic MoK $\alpha$  radiation at 293 K, 100 K or 293 K, respectively. Data processing was undertaken with CrysAlisPRO.<sup>68</sup> The structures were solved using direct methods and for refinement the non-H atoms were treated anisotropically. The main calculations were performed with SHELXL<sup>69</sup> and figures were plotted with MERCURY.<sup>70</sup> The crystal data, experimental details and refinement results are summarized in Tables S1 and S2.† Crystallographic data of the structures have been deposited at the Cambridge Crystallographic Data Centre with CCDC reference numbers 1996074 (IrPCp·CHCl<sub>3</sub>), 1996071 (IrPLm·1.5CHCl<sub>3</sub>) and 1996073 (IrPNr·2CHCl<sub>3</sub>).†

Elemental analyses (C, H and N) were carried out with a Vario Micro Cube – Elementar. NMR spectra were recorded using a Bruker Avance II 300 MHz spectrometer in CDCl<sub>3</sub> with traces of CHCl<sub>3</sub> as an internal reference for <sup>1</sup>H and 85% H<sub>3</sub>PO<sub>4</sub> in H<sub>2</sub>O as an external standard for <sup>31</sup>P{<sup>1</sup>H}. Mass spectra were recorded with a Bruker MicrOTOF-Q II spectrometer with an ESI ion source under the following conditions: nebulizer pressure: 0.4 bar, dry gas: 4.0 l min<sup>-1</sup> heated to 180 °C. Data were recorded in the positive ion mode, while profile spectra were recorded in the mass range 50–3000 m/z; end plate offset –500 V; capillary voltage 4500 V; mass resolving power of the instrument – over 18 000. Mass calibration was done using the cluster method with a mixture of 10 mM sodium formate and isopropanol (1 : 1, v/v) before the run. In order to record the spectra the compounds were dissolved in chloroform. Excitation and emission spectra were recorded at 298 K using a Cary Eclipse fluorescence spectrophotometer.

### Synthesis of organometallic iridium(III) compounds

IrPCp – [Ir( $\eta^5$ -Cp\*)Cl<sub>2</sub>PCp]. Binuclear iridium complex 1 (0.100 g, 0.126 mmol) was added to solution of PCp (0.146 g, 0.276 mmol) in dichloromethane (10 ml). The resulting mixture was stirred for 24 h. After that, it was evaporated to dryness giving a solid orange residue of the product. IrPCp is well soluble in CHCl<sub>3</sub>, CH<sub>2</sub>Cl<sub>2</sub> and DMSO.

Yield: 80%. Anal. found: C, 47.01; H, 4.32; N, 4.00%. Anal. calc. for  $C_{40}H_{44}Cl_2F_{1r}N_3O_3P \cdot CHCl_3$  ( $C_{41}H_{45}Cl_3F_{1r}N_3O_3P$ ): C, 47.02; H, 4.33; N, 4.01%.

NMR (298 K,  $CDCl_3$ ):  $^{31}P\{^1H\}$ : -1.30 ( $P^1$ , s);  $^1H$ : 1.11–1.33 ( $H^{72,73}$ , m, 4-H), 1.35 ( $H^1$ , d, 2.2 Hz, 15-H), 2.39 ( $H^{13,14}$ , bt, 4.8 Hz, 4-H), 2.99 ( $H^{12,15}$ , bt, 4.8 Hz, 4-H), 3.47 ( $H^{71}$ , m, 1-H), 4.07 ( $H^{11}$ , s, 2-H), 7.16 ( $H^{69}$ , d, 7.1 Hz, 1-H), 7.44–7.53 ( $H^{43,44}$ , m, 6-H), 7.92 ( $H^{63}$ , d, 13.3 Hz, 1-H), 8.00–8.11 ( $H^{42}$ , m, 4-H), 8.72 ( $H^{67}$ , s, 1-H), 15.02 ( $H^{70}$ , s, 1-H).

$^+ESI-MS$  ( $CHCl_3/H_2O$ , m/z): 928.21 [ $M + H$ ] $^+$ , 892.23 [ $M - Cl$ ] $^+$ , 888.28 [ $M - 2Cl + CH_3OH$ ] $^+$ , 856.26 [ $M - 2Cl$ ] $^+$ .

Crystals of  $IrPCp \cdot CHCl_3$  suitable for X-ray analysis were obtained under refrigeration by slow diffusion of hexane into a solution of the complex in chloroform under normal oxygen conditions. Crystal data:  $C_{41}H_{45}Cl_3F_{1r}N_3O_3P$ ,  $M = 1047.22 \text{ g mol}^{-1}$ , crystal size:  $0.20 \times 0.20 \times 0.02 \text{ mm}$ , crystal system: triclinic, space group:  $P\bar{1}$ ,  $a = 9.0544(4) \text{ \AA}$ ,  $b = 11.8197(5) \text{ \AA}$ ,  $c = 20.8951(8) \text{ \AA}$ ,  $\alpha = 85.841(3)^\circ$ ,  $\beta = 86.837(3)^\circ$ ,  $\gamma = 67.930(4)^\circ$ ,  $V = 2065.94(16) \text{ \AA}^3$ ,  $D_{\text{calc}} (Z = 2) = 1.683 \text{ g cm}^{-3}$ ,  $\theta$  range for data collection:  $4.042$  to  $71.700^\circ$ , Mo  $K\alpha$  radiation ( $\lambda = 1.54184 \text{ \AA}$ ),  $\mu_{\text{Mo}} = 9.983 \text{ mm}^{-1}$ , reflections collected/unique: 28 428/7969, [ $R_{\text{int}} = 0.0886$ ], completeness to  $\theta$  full = 99.9%, final R indices [ $I > 2\sigma(I)$ ]:  $R_1 = 0.0440$ ,  $wR_2 = 0.1081$ , R indices (all data):  $R_1 = 0.0544$ ,  $wR_2 = 0.1169$ , GOF = 1.026, largest diff. peak and hole: 1.919 and  $-1.931 \text{ e \AA}^{-3}$ , data/restraints/parameters: 7969/0/504,  $T = 293 \text{ K}$ .

$IrPSf - [Ir(\eta^5-Cp^*)Cl_2PSf]$ . Following the method presented for  $IrPCp$ , **1** (0.101 g, 0.126 mmol) and  $PSf$  (0.164 g, 0.278 mmol) gave a brown precipitate.  $IrPSf$  is well soluble in  $CH_2Cl_2$ , DMF and DMSO.

Yield: 80%. Anal. found: C, 50.97; H, 4.87; N, 5.65%. Anal. calc. for  $C_{42}H_{48}Cl_2F_2IrN_4O_3P$ : C, 51.01; H, 4.89; N, 5.67%.

NMR (298 K,  $CDCl_3$ ):  $^{31}P\{^1H\}$ : -3.06 ( $P^1$ , s);  $^1H$ : 0.72 ( $H^{16,17}$ , d, 6.4 Hz, 6-H), 1.04–1.20 ( $H^{72,73}$ , m, 4-H), 1.33 ( $H^1$ , d, 2.2 Hz, 15-H), 2.45 ( $H^{12,15}$ , m, 2-H), 2.80 ( $H^{13,14}$ , m, 2-H), 3.07 ( $H^{13,14}$ , m, 2-H), 3.87 ( $H^{71}$ , m, 1-H), 4.25 ( $H^{11}$ , s, 2-H), 6.41 ( $H^{63}$ , bs, 2-H), 7.43–7.51 ( $H^{43,44}$ , m, 6-H), 7.98–8.13 ( $H^{42}$ , m, 4-H), 8.61 ( $H^{67}$ , s, 1-H), 14.65 ( $H^{70}$ , bs, 1-H).

$^+ESI-MS$  ( $CHCl_3/H_2O$ , m/z): 989.25 [ $M + H$ ] $^+$ , 949.32 [ $M - 2Cl + CH_3OH$ ] $^+$ , 919.32 [ $M - 2Cl$ ] $^+$ .

$IrPLm - [Ir(\eta^5-Cp^*)Cl_2PLm]$ . Following the method presented for  $IrPCp$ , **1** (0.101 g, 0.126 mmol) and  $PLm$  (0.153 g, 0.278 mmol) gave an orange precipitate.  $IrPLm$  is well soluble in  $CHCl_3$ ,  $CH_2Cl_2$  and DMSO.

Yield: 80%. Anal. found: C, 44.20; H, 4.15; N, 3.72%. Anal. calc. for  $C_{40}H_{45}Cl_2F_2IrN_3O_3P \cdot 1.5CHCl_3$  ( $C_{41.5}H_{46.5}Cl_{6.5}F_2IrN_3O_3P$ ): C, 44.23; H, 4.16; N, 3.73%.

NMR (298 K,  $CDCl_3$ ):  $^{31}P\{^1H\}$ : -1.82 ( $P^1$ , s);  $^1H$ : 0.62 ( $H^{16}$ , d, 6.3 Hz, 3-H), 1.34 ( $H^1$ , d, 2.2 Hz, 15-H), 1.50 ( $H^{72}$ , t, 7.0 Hz, 3-H), 2.14–3.14 ( $H^{12,13,14,15}$ , m, 7-H), 4.15 ( $H^{11}$ , dd,  $J_1 = 40 \text{ Hz}$ ,  $J_2 = 16 \text{ Hz}$ , 2-H), 4.40 ( $H^{71}$ , qd,  $J_1 = 7.2 \text{ Hz}$ ,  $J_2 = 3.3 \text{ Hz}$ , 2-H), 7.39–7.56 ( $H^{43,44}$ , m, 6-H), 7.87 ( $H^{63}$ , dd,  $J_1 = 12.0 \text{ Hz}$ ,  $J_2 = 1.7 \text{ Hz}$ , 1-H), 7.99–8.15 ( $H^{42}$ , m, 4-H), 8.55 ( $H^{67}$ , s, 1-H), 14.68 ( $H^{70}$ , s, 1-H).

$^+ESI-MS$  ( $CHCl_3/H_2O$ , m/z): 948.22 [ $M + H$ ] $^+$ , 914.26 [ $M - Cl$ ] $^+$ , 906.28 [ $M - 2Cl + CH_3OH$ ] $^+$ , 878.28 [ $M - 2Cl$ ] $^+$ .

Crystals of  $IrPLm \cdot 1.5CHCl_3$  suitable for X-ray analysis were obtained under refrigeration by slow evaporation of chloroform/methanol (1 : 1, v/v) solution under normal oxygen conditions. Crystal data:  $C_{41.5}H_{46.5}Cl_{6.5}F_2IrN_3O_3P$ ,  $M = 1126.91 \text{ g mol}^{-1}$ , crystal size:  $0.100 \times 0.100 \times 0.050 \text{ mm}$ , crystal system: monoclinic, space group:  $I2/a$ ,  $a = 24.6249(3) \text{ \AA}$ ,  $b = 8.35470(1) \text{ \AA}$ ,  $c = 44.3459(6) \text{ \AA}$ ,  $\alpha = 90^\circ$ ,  $\beta = 104.3440(10)^\circ$ ,  $\gamma = 90^\circ$ ,  $V = 8839.03 (18) \text{ \AA}^3$ ,  $D_{\text{calc}} (Z = 8) = 1.694 \text{ g cm}^{-3}$ ,  $\theta$  range for data collection:  $2.215$  to  $31.772^\circ$ , Mo  $K\alpha$  radiation ( $\lambda = 0.71073 \text{ \AA}$ ),  $\mu_{\text{Mo}} = 3.501 \text{ mm}^{-1}$ , reflections collected/unique: 154 041/13 616, [ $R_{\text{int}} = 0.0395$ ], completeness to  $\theta$  full = 99.9%, final R indices [ $I > 2\sigma(I)$ ]:  $R_1 = 0.0321$ ,  $wR_2 = 0.0716$ , R indices (all data):  $R_1 = 0.00394$ ,  $wR_2 = 0.0734$ , GOF = 1.059, largest diff. peak and hole: 3.325 and  $-0.922 \text{ e \AA}^{-3}$ , data/restraints/parameters: 13 616/3/541,  $T = 100 \text{ K}$ .

$IrPNr - [Ir(\eta^5-Cp^*)Cl_2PNr]$ . Following the method presented for  $IrPCp$ , **1** (0.100 g, 0.126 mmol) and  $PNr$  (0.144 g, 0.278 mmol) gave an orange precipitate.  $IrPNr$  is well soluble in  $CHCl_3$  and  $CH_2Cl_2$ .

Yield: 80%. Anal. found: C, 42.60; H, 4.01; N, 3.63%. Anal. calc. for  $C_{39}H_{44}Cl_2F_{1r}N_3O_3P \cdot 2CHCl_3$  ( $C_{41}H_{46}Cl_8F_{1r}N_3O_3P$ ): C, 42.65; H, 4.02; N, 3.64%.

NMR (298 K,  $CDCl_3$ ):  $^{31}P\{^1H\}$ : -1.38 ( $P^1$ , s);  $^1H$ : 1.35 ( $H^1$ , d, 2.2 Hz, 15-H), 1.54 ( $H^{72}$ , t, 7.3 Hz, 3-H), 2.39 ( $H^{13,14}$ , bt, 4.6 Hz, 4-H), 2.97 ( $H^{12,15}$ , bt, 4.6 Hz, 4-H), 4.07 ( $H^{11}$ , s, 2-H), 4.25 ( $H^{71}$ , q, 7.2 Hz, 2-H), 6.64 ( $H^{69}$ , d, 6.9 Hz, 1-H), 7.42–7.54 ( $H^{43,44}$ , m, 6-H), 7.96 ( $H^{63}$ , d, 13.2 Hz, 1-H), 8.00–8.11 ( $H^{42}$ , m, 4-H), 8.62 ( $H^{67}$ , s, 1-H), 15.09 ( $H^{70}$ , s, 1-H).

$^+ESI-MS$  ( $CHCl_3/H_2O$ , m/z): 916.21 [ $M + H$ ] $^+$ , 980.24 [ $M - Cl$ ] $^+$ , 876.29 [ $M - 2Cl + CH_3OH$ ] $^+$ , 844.27 [ $M - 2Cl$ ] $^+$ .

Crystals of  $IrPNr \cdot 2CHCl_3$  suitable for X-ray analysis were obtained under refrigeration by slow evaporation of chloroform/acetone (1 : 1, v/v) solution under normal oxygen conditions. Crystal data:  $C_{41}H_{46}Cl_8F_{1r}N_3O_3P$ ,  $M = 1154.58 \text{ g mol}^{-1}$ , crystal size:  $0.300 \times 0.300 \times 0.200 \text{ mm}$ , crystal system: monoclinic, space group:  $P2_1/n$ ,  $a = 10.1356(2) \text{ \AA}$ ,  $b = 17.3727(3) \text{ \AA}$ ,  $c = 25.6237(4) \text{ \AA}$ ,  $\alpha = 90^\circ$ ,  $\beta = 93.137(1)^\circ$ ,  $\gamma = 90^\circ$ ,  $V = 4505.13(14) \text{ \AA}^3$ ,  $D_{\text{calc}} (Z = 4) = 1.702 \text{ g cm}^{-3}$ ,  $\theta$  range for data collection:  $3.075$  to  $71.674^\circ$ , Mo  $K\alpha$  radiation ( $\lambda = 1.54184 \text{ \AA}$ ),  $\mu_{\text{Mo}} = 10.818 \text{ mm}^{-1}$ , reflections collected/unique: 69 550/8730, [ $R_{\text{int}} = 0.1085$ ], completeness to  $\theta$  full = 99.8%, final R indices [ $I > 2\sigma(I)$ ]:  $R_1 = 0.0642$ ,  $wR_2 = 0.1514$ , R indices (all data):  $R_1 = 0.00710$ ,  $wR_2 = 0.1560$ , GOF = 1.108, largest diff. peak and hole: 2.658 and  $-2.947 \text{ e \AA}^{-3}$ , data/restraints/parameters: 8730/0/533,  $T = 293 \text{ K}$ .

### Preparation of micelles

Polymeric micelles with encapsulated  $Ir(III)$  compounds were prepared by the thin-film hydration method adopted by us previously.<sup>27</sup> In brief, Pluronic P-123 (PEO-PPO-PEO triblock copolymer) was dissolved in  $CHCl_3$  under reflux, while a metal complex was added to the hot solution. The solvent was slowly evaporated resulting in a thin film that was dried under reduced pressure. Then, a small volume of PBS was added under sonication leading to the formation of micelles with encapsulated  $Ir(III)$  complexes. The concentration of the non-

encapsulated Ir(III) complex was determined by the ICP-MS technique (PerkinElmer ELAN 6100), whereas, drug loading content (LC) and encapsulation efficiency (EE) were calculated according to previously defined equations.<sup>27</sup> In addition, the size and zeta potential were examined by the dynamic light scattering technique (DLS, Zetasizer Nano ZS, Malvern Instruments). Micelle morphology was also examined by transmission electron microscopy (FEI™ Tecnai G2 T20). Micelles were dropped in a carbon coated copper grid, dried at room temperature and stained with a negative staining agent (phosphotungstic acid) following a reported procedure.<sup>71</sup> The size distribution was determined from the enlarged TEM micrographs, using ImageJ software, counting at least 200 particles in different images.

### Cell lines

The MCF7 cell line (human breast adenocarcinoma, morphology: epithelial-like, ATCC: HTB-22), A549 cell line (human lung adenocarcinoma, morphology: epithelial, ATCC: CCL-185), CT26 cell line (mouse colon carcinoma, morphology: fibroblast, ATCC: CRL-2638), and PANC-1 cell line (human pancreatic/duct carcinoma, morphology: epithelial, ATCC: CRL-1469) were cultured in Dulbecco's Modified Eagle's Medium (DMEM, Corning) with phenol red, supplemented with 10% fetal bovine serum (FBS) and 1% streptomycin/penicillin. The DU-145 cell line (human prostate carcinoma), derived from the metastatic site, and brain and HEK293T cell lines (human embryonic kidney) were cultured in minimum essential medium (MEM, Corning) with only 10% fetal bovine serum (FBS). Cultures were incubated at 37 °C under a humidified atmosphere containing 5% CO<sub>2</sub>. Cells were passaged using a solution containing 0.05% trypsin and 0.5 mM EDTA. All media and other ingredients were purchased from ALAB, Poland.

### Cytotoxic study in vitro

Since most of the studied compounds are insoluble in aqueous media, therefore they needed to be pre-dissolved in DMSO for biological tests. Cytotoxicity was assessed by MTT assay performed according to the protocols described previously.<sup>62</sup> In brief,  $1 \times 10^4$  cells per well were seeded in a 96-well flat bottom microtiter plate in 0.2 mL of culture medium. Cells were incubated with the IrPCp, IrPNr, IrPSf, IrPLm complexes at various ranges of concentrations (0.01–1 mM) for 24 hours. In the first approach after that time, solutions of compounds were washed out, and cells were washed three times with PBS and IC<sub>50</sub> values were assessed at once (24 h). While, in the second approach after 24 h incubation with compounds, drug-containing medium was replaced with a fresh one and cells were left to recover for additional 48 hours (24 h + 48 h). Each compound concentration was tested in five replicates and repeated at least three times. Determined values of IC<sub>50</sub> (concentration of a drug required to inhibit the growth of 50% of the cells) are given as mean + S.D. (Standard Deviation). Furthermore, post-treatment survival assessment of the treated cells was analyzed under a

fluorescence inverted microscope (Olympus IC51, Japan) with an excitation filter 470/20 nm. For this, cells were stained with two versatile fluorescence dyes: fluorescein diacetate (FDA, 5 mg mL<sup>-1</sup>) and propidium iodide (PI, 5 mg mL<sup>-1</sup>) under standard conditions in the dark for 20 min. Before visualization dyes were removed and cells were washed with PBS twice.

### Cellular uptake

A549 and Du-145 cells at a density of  $2 \times 10^6$  cells per 2 mL were seeded on 6-well plates and were incubated with IrPCp, IrPNr, IrPSf, and IrPLm complexes (1 μM) for 24 h or 24 h + 48 h at standard conditions (37 °C, 5% CO<sub>2</sub>). Additional wells were incubated with medium alone as a negative control. Then, compound solutions were removed; the cells were washed twice with PBS buffer, and trypsinized. Measurement of the concentration of iridium ions was carried out using a mass spectrometer (ELAN 6100 PerkinElmer) with an inductively coupled plasma (ICP-MS). For analysis, the collected cells were mineralized in 1 mL of 65% HNO<sub>3</sub> at 60 °C for 1 h. The iridium content under each condition is expressed as ng mg<sup>-1</sup> protein. The protein content was assessed with Bradford Protein Assay (Thermo Scientific™).<sup>72</sup> The experiment was repeated at least 3 times and results are presented as mean value + S.D.

### Confocal microscopy visualization

Confocal laser scanning microscopy (CLSM Nikon) was used to visualize the intracellular accumulation of the selected polymeric formulation of the Ir(III) complex (IrPSf) into A549 cells. In brief, A549 cells at a density of  $5 \times 10^5$  cells per mL were seeded on coverslips in 6-well plates and incubated for 24 h allowing proper adhesion. Then, the growth medium was replaced with a medium containing 1 μM IrPSf and incubated for 4 h at 37 °C in a humidified atmosphere containing 5% CO<sub>2</sub>. After this time, the cells were washed twice with PBS buffer and fixed by treating firstly with 2.5% glutaraldehyde in PBS and secondly with an increasing concentration gradient of ethanol (20, 40, 60, 80 and 99%). Samples were directly imaged under a Nikon A1 confocal laser scanning system (CM) attached to an inverted microscope Nikon Ti (Japan). A 1009 objective lens (Nikon Plan Apo VC/1.40 oil) was used. The samples were excited with diode lasers (405 and 488 nm). Fluorescence spectra were recorded using a 32-channel spectral detector. Colocalization analysis performed with ImageJ plugin.

### Three-dimensional culturing in vitro

For hanging drop formation, the lid from a tissue culture dish was removed and  $5 \times 10^5$  A549 or DU-145 cells in 10 μL drops were placed on the bottom of the lid. In each case, the cell suspension was homogeneous and did not contain aggregates, since it determines the size and uniformity of spheroids. Then, the lid was inverted onto the PBS-filled bottom chamber and incubated at 37 °C/5% CO<sub>2</sub>/95% humidity. The sphere growth was monitored daily and incubates until either cell sheets or aggregates were formed. Once sheets were formed,



they were transferred to 96-well plates coated with Geltrex matrix and incubated with completed growth medium until spheroids were created. Using optimal growth conditions, a period of 4–7 days was found to be optimal for spheroid assembly. The direct effect of drug toxicity was examined on spheroids derived from both A549 and DU-145 cell lines. For cytotoxicity assessment, spheroids were grown and were monitored for 5–7 days. After this time, the spheres were treated with the tested Pluronic P-123 formulation of IrPCp (IrPCp\_M) at increasing doses ( $0.1 \times IC_{50}$ ,  $IC_{50}$ , and  $10 \times IC_{50}$ ,  $IC_{50}$  determined for the corresponding Pluronic P-123 nanoformulations), and the plates were further incubated at 37 °C. Forty-eight hours after treatment, the spheroids were stained with 4',6-diamidino-2-phenylindole (DAPI), calcein AM (CAM), and propidium iodide (PI) to estimate the live/dead cells population for one hour, washed and visualized using a fluorescent microscope. For manual acquisition, the images from each well were recorded using an inverted microscope (Olympus). A 10 $\times$  objective was primarily used, switching to a 4 $\times$  objective when an object area was too large. To analyse the images taken on standard and video microscopes, Fiji software was used.<sup>53</sup>

#### Cell cycle analysis

The cells (A549, DU-145) were seeded at the density of  $5 \times 10^4$ . To quantify the cell cycle phase distribution, the cells were treated with IrPSf, IrPCp and CDDP at 5  $\mu$ M concentrations for 24 h and stained with Vybrant® DyeCycle™ Ruby stain (Invitrogen) followed by flow cytometry using BD FACSCalibur™ (BD Bioscience).

#### Caspase activation

Caspase activation was determined using the caspase-Glo 3/7 assay (Promega) according to the manufacturer's instructions. Cells ( $2 \times 10^4$  cells per well) were seeded in black-walled 96-well plates and treated for 24 h with 1  $\mu$ M or 5  $\mu$ M IrPSf, IrPCp and CDDP and incubated for 1 h at room temperature. Luminescence was measured with a Tecan infinite M200Pro plate reader (Tecan).

#### Generation of reactive oxygen species

Cellular production of reactive oxygen species (ROS) was determined by photometric tests using Cyto-ID®Hypoxia/Oxidative Stress Detection Kit (Thermo Fisher) and was carried out as described previously.<sup>73</sup> The assay was performed in 96-well plates, where the cells were seeded at a density of  $10^5$  cells per 0.2 mL of medium. The experiments were performed in darkness.

#### Detection of mitochondrial membrane potential ( $\psi$ )

Mitochondrial membrane potential (MMP) depletion was determined by JC-10 Assay (Life Technologies, USA). DU-145 cells were seeded on 96-well plates at  $1 \times 10^4$  cells per 0.2 mL. After 24 h, the medium was replaced with solutions of organic and inorganic compounds at  $IC_{50}$  concentration as well as gentamicin ( $0.5 \text{ mg mL}^{-1}$ ) and ciprofloxacin ( $10 \text{ }\mu\text{g mL}^{-1}$ ) as positive and negative control, respectively. After that, cells were

incubated for 24 h under standard conditions (37 °C, 5% CO<sub>2</sub>). Then, they were washed twice with PBS buffer and incubated with JC-10 for 1 hour. Afterwards, emission was measured at two different excitation wavelengths ( $\lambda_{\text{ex}} = 540 \text{ nm}$ ,  $\lambda_{\text{em}} = 570 \text{ nm}$  and  $\lambda_{\text{ex}} = 485 \text{ nm}$ ,  $\lambda_{\text{em}} = 530 \text{ nm}$ ). The results are presented as the intensity ratio of red to green emission (mean + S.D.).

#### Electrochemical characterization

Cyclic voltammetry (CV) for 1 mM iridium(III) complexes was carried out on an electrochemical analyzer (Bio-Logic, SP-150). A three-electrode glass cell with a working electrode – graphite disk electrode (2 mm diameter), a counter electrode – Pt wire, and a pseudo-reference electrode – Ag wire (Ag/Ag<sup>+</sup>, 0.01 M AgNO<sub>3</sub>, 0.1 M tetrabutyl ammonium perchlorate (Bu<sub>4</sub>NClO<sub>4</sub>) was used. All measurements were performed in dimethylformamide (DMF) with 0.05 M Bu<sub>4</sub>NClO<sub>4</sub> as the supporting electrolyte at room temperature with scan rate 10 mV s<sup>-1</sup> in the potential range from -0.5 to 1.2 V vs. Ag/Ag<sup>+</sup>. Scans start at 0 V vs. Ag/Ag<sup>+</sup> in the positive potential direction. All reported potentials were converted vs. the ferrocene/ferrocenium redox couple (Fc<sup>0/+</sup>).<sup>73</sup>

## Conflicts of interest

There are no conflicts to declare.

## Acknowledgements

The UV-Vis and cyclic voltamperometry measurements were carried out with the equipment purchased thanks to the financial support of the Polish National Science Centre (Grant 2016/23/D/ST5/00269). We thank Przemysław Kołoczek and Bartosz Dziubaty for assistance with the synthesis of Ir(III) complexes and X-ray analysis, respectively. We are also grateful to Gabriela Dudek for her help in the preparation of micelles encapsulated with Ir(III) complexes.

## Notes and references

- 1 R. G. Abbott, S. Forrest and K. J. Pienta, Simulating the hallmarks of cancer, *Artif. Life*, 2006, 12, 617–634.
- 2 M. A. Fuertes, C. Alonso and J. M. Pérez, Biochemical Modulation of Cisplatin Mechanisms of Action: Enhancement of Antitumor Activity and Circumvention of Drug Resistance, *Chem. Rev.*, 2003, 103, 645–662.
- 3 C. A. Rabik and M. E. Dolan, Molecular mechanisms of resistance and toxicity associated with platinating agents, *Cancer Treat. Rev.*, 2007, 33, 9–23.
- 4 P. J. Dyson and G. Sava, Metal-based antitumour drugs in the post genomic era, *Dalton Trans.*, 2006, 16, 1929–1933.
- 5 M. A. Jakupiec, M. Galanski, V. B. Arion, C. G. Hartinger and B. K. Keppler, Antitumour metal compounds: more than theme and variations, *Dalton Trans.*, 2008, 2, 183–194.



- 6 Z. Liu, L. Salassa, A. Habtemariam, A. M. Pizarro, G. J. Clarkson and P. J. Sadler, Contrasting Reactivity and Cancer Cell Cytotoxicity of Isoelectronic Organometallic Iridium(III) Complexes, *Inorg. Chem.*, 2011, 50, 5777–5783.
- 7 B. Tang, D. Wan, Y. J. Wang, Q. Y. Yi, B. H. Guo and Y. J. Liu, An iridium(III) complex as potent anticancer agent induces apoptosis and autophagy in B16 cells through inhibition of the AKT/mTOR pathway, *Eur. J. Med. Chem.*, 2018, 145, 302–314.
- 8 J. Li, Z. Tian, X. Ge, Z. Xu, Y. Feng and Z. Liu, Design, synthesis, and evaluation of fluorine and Naphthyridine-Based half-sandwich organoiridium/ruthenium complexes with bioimaging and anticancer activity, *Eur. J. Med. Chem.*, 2019, 163, 830–839.
- 9 J. Li, M. Tian, Z. Tian, S. Zhang, C. Yan, C. Shao and Z. Liu, Half-Sandwich Iridium(III) and Ruthenium(II) Complexes Containing P<sup>^</sup>P-Chelating Ligands: A New Class of Potent Anticancer Agents with Unusual Redox Features, *Inorg. Chem.*, 2018, 57, 1705–1716.
- 10 G. Gupta, A. Das, N. B. Ghate, T. Kim, J. Y. Ryu, J. Lee, N. Mandal and C. Y. Lee, Novel BODIPY-based Ru(II) and Ir(III) metalla-rectangles: cellular localization of compounds and their antiproliferative activities, *Chem. Commun.*, 2016, 52, 4274–4277.
- 11 Z. Liu and P. J. Sadler, Organoiridium Complexes: Anticancer Agents and Catalysts, *Acc. Chem. Res.*, 2014, 47, 1174–1185.
- 12 J. Li, H. Chen, L. Zeng, T. W. Rees, K. Xiong, Y. Chen, L. Ji and H. Chao, Mitochondria-targeting cyclometalated iridium(III) complexes for tumor hypoxic imaging and therapy, *Inorg. Chem. Front.*, 2019, 6, 1003–1010.
- 13 D.-L. Ma, C. Wu, K.-J. Wu and C.-H. Leung, Iridium(III) Complexes Targeting Apoptotic Cell Death in Cancer Cells, *Molecules*, 2019, 24, 2739.
- 14 A. Wilbuer, D. H. Vlecken, D. J. Schmitz, K. Kräling, K. Harms, C. P. Bagowski and E. Meggers, Iridium complex with antiangiogenic properties, *Angew. Chem., Int. Ed.*, 2010, 49, 3839–3842.
- 15 Z. Liu, A. Habtemariam, A. M. Pizarro, S. A. Fletcher, A. Kisova, O. Vrana, L. Salassa, P. C. Bruijninx, J. Clarkson, V. Brabec and P. J. Sadler, Organometallic sandwich iridium anticancer complexes, *J. Med. Chem.*, 2011, 54, 3011–3026.
- 16 W. Wang, K. Vellaisamy, G. Li, C. Wu, C.-N. Ko, C.-H. Leung and D.-L. Ma, Development of a Long-Lived Luminescence Probe for Visualizing  $\beta$ -Galactosidase in Ovarian Carcinoma Cells, *Anal. Chem.*, 2017, 89, 11679–11684.
- 17 D. L. Ma, W. L. Wong, W. H. Chung, F. Y. Chan, P. K. So, T. S. Lai, Z. Y. Zhou, Y. C. Leung and K. Y. Wong, A highly selective luminescent switch-on probe for histidine/histidine-rich proteins and its application in protein staining, *Angew. Chem., Int. Ed.*, 2008, 47, 3735–3739.
- 18 Q. Zhao, M. Yu, L. Shi, S. Liu, C. Li, M. Shi, Z. Zhou, C. Huang and F. Li, Cationic Iridium(III) Complexes with Tunable Emission Color as Phosphorescent Dyes for Live Cell Imaging, *Organometallics*, 2010, 29, 1085–1091.
- 19 Q. Du, Y. Yang, L. Guo, M. Tian, X. Ge, Z. Tian, L. Zhao, Z. Xu, J. Li and Z. Liu, Fluorescent half-sandwich phosphine-sulfonate iridium(III) and ruthenium(II) complexes as potential lysosome-targeted anticancer agents, *Dyes Pigm.*, 2019, 162, 821–830.
- 20 Y. Geldmacher, M. Oleszak and W. S. Sheldrick, Rhodium(III) and iridium(III) complexes as anticancer agents, *Inorg. Chim. Acta*, 2012, 393, 84–102.
- 21 U. Ndagi, N. Mhlongo and M. E. Soliman, Metal complexes in cancer therapy - an update from drug design perspective, *Drug Des., Dev. Ther.*, 2017, 11, 599–616.
- 22 S. Gary and M. Aam, Fluoroquinolones structural and medicinal developments (2013-2018): Where are we now?, *Bioorg. Med. Chem.*, 2019, 27, 3005–3060.
- 23 V. Yadav and P. Talwar, Repositioning of fluoroquinolones from antibiotic to anti-cancer agents: An underestimated truth, *Biomed. Pharmacother.*, 2019, 111, 934–946.
- 24 U. K. Komarnicka, R. Starosta, A. Kyzioł and M. Jeżowska-Bojczuk, Copper(I) complexes with phosphine derived from sparfloxacin. Part I – structures, spectroscopic properties and cytotoxicity, *Dalton Trans.*, 2015, 44, 12688–12699.
- 25 U. K. Komarnicka, R. Starosta, M. Płotek, R. F. M. de Almeida, M. Jeżowska-Bojczuk and A. Kyzioł, Copper(I) complexes with phosphine derived from sparfloxacin. Part II: a first insight into the cytotoxic action mode, *Dalton Trans.*, 2016, 45, 5052–5063.
- 26 A. Kyzioł, A. Cierniak, J. Gubernator, A. Markowski, M. Jeżowska-Bojczuk and U. K. Komarnicka, Copper(I) complexes with phosphine derived from sparfloxacin. Part III: multifaceted cell death and preliminary study of liposomal formulation of selected copper(I) complex, *Dalton Trans.*, 2018, 47, 1981–1992.
- 27 P. Kołoczek, A. Skórska-Stania, A. Cierniak, V. Sebastian, U. K. Komarnicka, M. Płotek and A. Kyzioł, Polymeric micelle-mediated delivery of half-sandwich ruthenium(II) complexes with phosphanes derived from fluoroloquinolones for lung adenocarcinoma treatment, *Eur. J. Pharm. Biopharm.*, 2018, 128, 69–81.
- 28 U. K. Komarnicka, R. Starosta, K. Guz-Regner, G. Bugla-G. Płoskońska, A. Kyzioł and M. Jeżowska-Bojczuk, Phosphine half-derivatives of sparfloxacin- synthesis, structures and Chem., in vitro activity, *J. Mol. Struct.*, 2015, 1096, 55–63.
- 29 A. Bykowska, R. Starosta, U. K. Komarnicka, Z. Ciunik, A. Kyzioł, K. Guz-Regner, G. Bugla-Płoskońska and M. Jeżowska-Bojczuk, Phosphine derivatives of ciprofloxacin and norfloxacin, a new class of potential therapeutic agents, *New J. Chem.*, 2014, 38, 1062–1071.
- 30 A. Bykowska, R. Starosta, A. Brzuszkiewicz, B. Bażanów, M. Florek, N. Jackulak, J. Król, J. Grzesiak, K. Kaliński and M. Jeżowska-Bojczuk, Synthesis, properties and biological activity of a novel phosphines ligand derived from ciprofloxacin, *Polyhedron*, 2013, 60, 23–29.
- 31 U. K. Komarnicka, R. Starosta, A. Kyzioł, M. Płotek, M. Puchalska and M. Jeżowska-Bojczuk, New copper(I)

- complexes bearing lomefloxacin motif : spectroscopic properties, in vitro cytotoxicity and interactions with DNA and human serum albumin, *J. Inorg. Biochem.*, 2016, 165, 25–35.
- 32 P. Zhang, C. K. C. Chiu, H. Huang, Y. P. Y. Lam, A. Habtemariam, T. Malcomson, M. J. Paterson, G. J. Clarkson, P. B. O'Connor, H. Chao and P. J. Sadler, Organoiridium Photosensitizers Induce Specific Oxidative Attack on Proteins within Cancer Cells, *Angew. Chem., Int. Ed.*, 2017, 56, 14898–14902.
- 33 V. Novohradsky, G. Viguera, J. Pracharova, N. Cutillas, C. Janiak, H. Kostrhunova, V. Brabec, J. Ruiz and J. Kasparkova, Molecular superoxide radical photogeneration in cancer cells by dipyridophenazine iridium(III) complexes, *Inorg. Chem. Front.*, 2019, 6, 2500–2513.
- 34 Z. Xu, Y. Yang, X. Jia, L. Guo, X. Ge, G. Zhong, S. Chen and Z. Liu, Novel cyclometalated iridium(III) phosphine-imine (P<sup>^</sup>N) complexes: highly efficient anticancer and anti-lung metastasis agents in vivo, *Inorg. Chem. Front.*, 2020, 7, 1273–1283.
- 35 Q. Du, Y. Yang, L. Guo, M. Tian, X. Ge, Z. Tian, L. Zhao, Z. Xu, J. Li and Z. Liu, Fluorescent half-sandwich phosphine-sulfonate iridium(III) and ruthenium(II) complexes as potential lysosome-targeted anticancer agents, *Dyes Pigm.*, 2019, 162, 821–830.
- 36 J. Ruiz, C. Vicente, C. de Haro and D. Bautista, Novel C,N-chelate rhodium(III) and iridium(III) antitumor complexes incorporating a lipophilic steroidal conjugate and their interaction with DNA, *Inorg. Chem.*, 2013, 52, 974–982.
- 37 Q. Du, L. Guo, X. Ge, L. Zhao, Z. Tian, X. Liu, F. Zhang and Z. Liu, Serendipitous Synthesis of Five-Coordinated Half-Sandwich Aminoimine Iridium(III) and Ruthenium(II) Complexes and Their Application as Potent Anticancer Agents, *Inorg. Chem.*, 2019, 58, 5956–5965.
- 38 Q. Du, L. Guo, M. Tian, X. Ge, Y. Yang, X. Jian, Z. Xu, Z. Tian and Z. Liu, Potent Half-Sandwich Iridium(III) and Ruthenium(II) Anticancer Complexes Containing a P<sup>^</sup>O-Chelated Ligand, *Organometallics*, 2018, 37, 2880–2889.
- 39 C. Wu, Q. Li, X. Zhang, C. Shi, G. Li, M. Wang, K. Li and A. Yuan, Tuning the Photophysical and Excited State Properties of Phosphorescent Iridium(III) Complexes by Polycyclic Unit Substitution, *ChemistryOpen*, 2019, 8, 339–343.
- 40 W. Su, X. Wang, X. Lei, Q. Xiao, S. Huang and P. Li, Synthesis, characterization, cytotoxic activity of half-sandwich rhodium(III), and iridium(III) complexes with curcuminoids, *J. Organomet. Chem.*, 2017, 833, 54–60.
- 41 A. J. Millett, A. Habtemariam, I. Romero-Canelón, G. J. Clarkson and P. J. Sadler, Contrasting Anticancer Activity of Half-Sandwich Iridium(III) Complexes Bearing Functionally Diverse 2-Phenylpyridine Ligands, *Organometallics*, 2015, 34, 2683–2694.
- 42 A. Lapasam, O. Hussain, R. M. Phillips, W. r. Kaminsky and M. R. Kollipara, Synthesis, Characterization and Chemosensitivity Studies of Half-Sandwich Ruthenium, Rhodium and Iridium Complexes Containing  $\kappa^1$  (S) and  $\kappa^2$  (N,S) Aroylthiourea Ligands, *J. Organomet. Chem.*, 2018, 883, 272–280.
- 43 L. He, D. Ma, L. Duan, Y. Wei, J. Qiao, D. Zhang, G. Dong, L. Wang and Y. Qiu, Control of intramolecular  $\pi$ - $\pi$  stacking interaction in cationic iridium complexes via fluorination of pendant phenyl rings, *Inorg. Chem.*, 2012, 51, 4502–4510.
- 44 V. Fernández-Moreira, F. L. Thorp-Greenwood and M. P. Coogan, Application of d6 transition metal complexes in fluorescence cell imaging, *Chem. Commun.*, 2010, 46, 186–202.
- 45 K. Strohfeldt and M. Tacke, Bioorganometallicfulvene-derived titanocene anti-cancer drugs, *Chem. Soc. Rev.*, 2008, 37, 1174–1187.
- 46 J. Weyermann, D. Lochmann and A. Zimmer, A practical note on the use of cytotoxicity assays, *Int. J. Pharm.*, 2005, 288, 369–376.
- 47 X. Liu, X. He, X. Zhang, Y. Wang, J. Liu, X. Hao, Y. Zhang, X. A. Yuan, L. Tian and Z. Liu, New Organometallic Tetraphenylethylene-Iridium(III) Complexes with Antineoplastic Activity, *ChemBioChem*, 2019, 20, 2767–2776.
- 48 M. R. Reithofer, A. K. Bytzeck, S. M. Valiahdi, C. R. Kowol, M. Groessl, C. G. Hartinger, M. A. Jakupec, M. Galanski and B. K. Keppler, Tuning of lipophilicity and cytotoxic potency by structural variation of anticancer platinum(IV) complexes, *J. Inorg. Biochem.*, 2011, 105, 46–51.
- 49 A. A. Petrauskas and E. Kolovanov, ACD/Log P method description, *Perspect. Drug Discovery Des.*, 2000, 19, 99–116.
- 50 (a) V. Tetko, J. Gasteiger, R. Todeschini, A. Mauri, D. Livingstone, P. Ertl, V. A. Palyulin, E. V. Radchenko, N. S. Zefirov, A. S. Makarenko, V. Y. Tanchuk and V. V. Prokopenko, *J. Comput.-Aided Mol. Des.*, 2005, 19, 453; (b) VCCLAB, Virtual Computational Chemistry Laboratory – Design and Description, Virtual Computational Chemistry Laboratory, <http://www.vcclab.org>, 2005.
- 51 C.-P. Tan, Y.-Y. Lu, L.-N. Jia and Z.-W. Mao, Metallomics insights into the programmed cell death induced by metal-based anticancer compounds, *Metallomics*, 2014, 6, 978–995.
- 52 R. Guan, Y. Chen, L. Zeng, T. W. Rees, C. Jin, J. Huang, Z.-S. Chen, L. Jia and H. Chao, Oncosis-inducing cyclometalated iridium(III) complexes, *Chem. Sci.*, 2018, 9, 5183–5190.
- 53 B. Pucelik, L. G. Arnaut, G. Stochel and J. M. Dabrowski, Design of Pluronic-based formulation for enhanced redaporfin-photodynamic therapy against pigmented melanoma, *ACS Appl. Mater. Interfaces*, 2016, 8, 22039–22055.
- 54 J. M. Hearn, I. Romero-Canelón, B. Qamar, Z. Liu, I. Hands-Portman and P. J. Sadler, Organometallic Iridium (III) anticancer complexes with new mechanisms of action: NCI-60 screening, mitochondrial targeting, and apoptosis, *ACS Chem. Biol.*, 2013, 8, 1335–1343.
- 55 G. R. Stark and W. R. Taylor, Analyzing the G2/M Checkpoint, *Methods Mol. Biol.*, 2004, 280, 51–82.

- 56 C.-H. Shu, W. K. Yang, Y.-L. Shih, M.-L. Kuo and T.-S. Huang, Cell cycle G2/M arrest and activation of cyclin-dependent kinases associated with low-dose paclitaxel-induced sub-G1 apoptosis, *Apoptosis*, 1997, 2, 463–470.
- 57 R. Visconti, R. D. Monica and D. Grieco, Cell cycle checkpoint in cancer: a therapeutically targetable double-edged sword, *J. Exp. Clin. Cancer Res.*, 2016, 35, 153.
- 58 Z. Liu, A. Habtemariam, A. M. Pizarro, G. J. Clarkson and P. J. Sadler, Organometallic Iridium(III) Cyclopentadienyl Anticancer Complexes Containing C,N-Chelating Ligands, *Organometallics*, 2011, 30, 4702–4710.
- 59 B. Halliwell and J. M. Gutteridge, The antioxidants of human extracellular fluids, *Arch. Biochem. Biophys.*, 1990, 280, 1–8.
- 60 J. M. Matés and F. M. Sánchez-Jiménez, Role of reactive oxygen species in apoptosis: implications for cancer therapy, *Int. J. Biochem. Cell Biol.*, 2000, 32, 157–170.
- 61 U. Simon, A. Haj-Yehia and F. Levi-Schaffer, Role of reactive oxygen species (ROS) in apoptosis induction, *Apoptosis*, 2000, 5, 415–418.
- 62 M. L. Circu and T. Y. Aw, Reactive oxygen species, cellular redox systems, and apoptosis, *Free Radicals Biol. Med.*, 2010, 48, 749–762.
- 63 C. Martin-Cordero, A. J. Leon-Gonzalez, J. M. Calderon-Montano, E. Burgos-Moron and M. LopezLazaro, Prooxidant natural products as anticancer agents, *Curr. Drug Targets*, 2012, 13, 1006–1028.
- 64 W. Zhang, X. Hu and Q. Shen, Mitochondria-specific drug release and reactive oxygen species burst induced by poly-prodrug nanoreactors can enhance chemotherapy, *Nat. Commun.*, 2019, 10, 1704.
- 65 T. U. Connell, J. M. White, T. A. Smith and P. S. Donnelly, Luminescent Iridium(III) Cyclometalated Complexes with 1,2,3-Triazole “Click” Ligands, *Inorg. Chem.*, 2016, 55, 2776–2790.
- 66 K. Hasan, A. K. Bansal, I. D. W. Samuel, C. Roldán-Carmona, H. J. Bolink and E. Zysman-Colman, Tuning the Emission of Cationic Iridium(III) Complexes Towards the Red Through Methoxy Substitution of the Cyclometalating Ligand, *Sci. Rep.*, 2015, 5, 12325.
- 67 M.-A. Tehfe, M. Lepeltier, F. Dumur, D. Gigmès, J.-P. Fouassier and J. Lalevée, Structural Effects in the Iridium Complex Series: Photoredox Catalysis and Photoinitiation of Polymerization Reactions under Visible Lights, *Macromol. Chem. Phys.*, 2017, 218, 1700192.
- 68 Agilent, CrysAlis PRO, Agilent Technologies Ltd., Yarnton, Oxfordshire, England, 2015.
- 69 G. M. Sheldrick, Crystal structure refinement with SHELXL, *Acta Crystallogr., Sect. C: Struct. Chem.*, 2015, 71, 3–8.
- 70 Mercury 3.9.
- 71 A. Larrea, A. Clemente, E. Luque-Michel and V. Sebastian, Efficient production of hybrid bio-nanomaterials by continuous microchannel emulsification: Dye-doped SiO<sub>2</sub> and Au-PLGA nanoparticles, *Chem. Eng. J.*, 2017, 316, 663–672.
- 72 S. Tardito, A. Barilli, I. Bassanetti, M. Tegoni, O. Bussolati, R. Franchi-Gazzola, C. Mucchino and L. Marchiò, Copper-dependent, cytotoxicity of 8-hydroxyquinoline derivatives correlates with their hydrophobicity and does not require caspase activation, *J. Med. Chem.*, 2012, 55, 10448–10459.
- 73 C. Santini, M. Pellei, V. Gandin, M. Porchia, F. Tisato and C. Marzano, Advances in copper complexes as anticancer agents, *Chem. Rev.*, 2014, 114, 815–862.



## Anticancer potency of novel organometallic Ir(III) complexes with phosphines derived from fluoroquinolones encapsulated in polymeric micelles

Sandra Kozieł,<sup>a</sup> Urszula K. Komarnicka,<sup>\*a</sup> Aleksandra Ziółkowska,<sup>a</sup> Agnieszka Skórska-Stania,<sup>b</sup> Barbara Pucelik,<sup>c</sup> Michał Płotek,<sup>b,d</sup> Victor Sebastian<sup>e,f</sup>, Alina Bieńko,<sup>a</sup> Grażyna Stochel,<sup>b</sup> and Agnieszka Kyzioł<sup>\*b</sup>

<sup>a</sup>Faculty of Chemistry, University of Wrocław, Joliot-Curie 14, 50-383 Wrocław, Poland

<sup>b</sup>Faculty of Chemistry, Jagiellonian University in Krakow, Gronostajowa 2, 30-387 Krakow, Poland

<sup>c</sup>Małopolska Centre of Biotechnology, Jagiellonian University, Gronostajowa 7A, 30-387, Kraków, Poland.

<sup>d</sup>Faculty of Conservation and Restoration of Works of Art, Jan Matejko Academy of Fine Arts in Krakow, Lea 27-29, 30-052 Krakow, Poland

<sup>e</sup>Department of Chemical Engineering, Aragon Institute of Nanoscience (INA), The Aragón Materials Science Institute (ICMA), University of Zaragoza, Campus Río Ebro-Edificio I+D, Mariano Esquillor S/N, 50018 Zaragoza, Spain

<sup>f</sup>Networking Research Center on Bioengineering, Biomaterials and Nanomedicine, CIBER-BBN, 28-029 Madrid, Spain

Corresponding author e-mail address: [urszula.komarnicka@chem.uni.wroc.pl](mailto:urszula.komarnicka@chem.uni.wroc.pl), [kyziol@chemia.uj.edu.pl](mailto:kyziol@chemia.uj.edu.pl)

### Graphical abstract

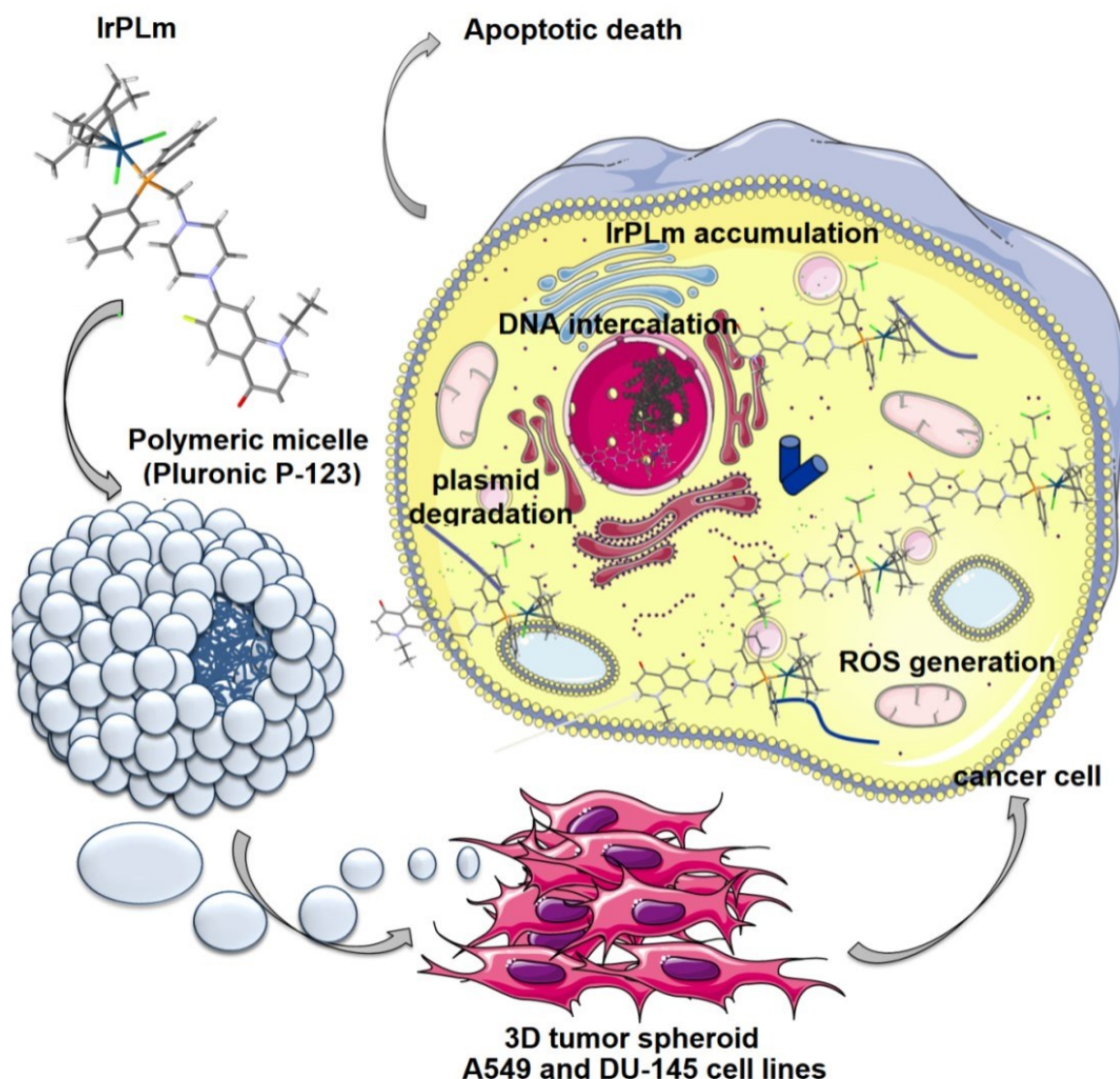


**Table S1.** Crystallographic experimental details.

Parameters	<b>IrPCp</b> ·CHCl <sub>3</sub>	<b>IrPLm</b> ·1.5CHCl <sub>3</sub>	<b>IrPNr</b> ·2CHCl <sub>3</sub>
Moiety formula	IrCl <sub>5</sub> PN <sub>3</sub> O <sub>3</sub> C <sub>41</sub> H <sub>45</sub>	IrCl <sub>6.5</sub> PN <sub>3</sub> O <sub>3</sub> C <sub>41.5</sub> H <sub>46.5</sub>	IrCl <sub>8</sub> PN <sub>3</sub> O <sub>3</sub> C <sub>41</sub> H <sub>46</sub>
Formula weight (g·mol <sup>-1</sup> )	1047.22	1126.91	1154.58
Crystal description	yellow plate	light orange plate	yellow prism
Crystal size (mm)	0.20 x 0.20 x 0.02	0.10 x 0.10 x 0.05	0.30 x 0.30 x 0.20
Temperature (K)	130	100	130
Type of radiation	Cu K $\alpha$	Mo K $\alpha$	Cu K $\alpha$
Crystal system	Triclinic	Monoclinic	Monoclinic
Space group	P1	I 2/a	P 2 <sub>1</sub> /n
a (Å)	9.0544(4)	24.6249(3)	10.1356(2)
b (Å)	11.8197(5)	8.35470(1)	17.3727(3)
c (Å)	20.8951(8)	44.3459(5)	25.6237(4)
$\alpha$ (°)	85.841(3)	90	90
$\beta$ (°)	86.837(3)	104.3440(1)	93.1370(1)°
$\gamma$ (°)	67.930(4)	90	90
Volume (Å <sup>3</sup> )	2065.94(16)	8839.03(18)	4505.13(14)
Z	2	8	4
Density calc. (g/cm <sup>3</sup> )	1.683	1.694	1.702
Absorption coeff. (mm <sup>-1</sup> )	9.983	3.501	10.818
F(000)	1044	4488	2296
$\theta_{\min} - \theta_{\max}$ (°)	4.042 to 71.700	2.215 to 31.772	3.075 to 71.574
hkl range	-11 $\leftarrow$ h $\leftarrow$ 11 -14 $\leftarrow$ k $\leftarrow$ 14 -25 $\leftarrow$ l $\leftarrow$ 25	-32 $\leftarrow$ h $\leftarrow$ 35 -11 $\leftarrow$ k $\leftarrow$ 11 -63 $\leftarrow$ l $\leftarrow$ 64	-12 $\leftarrow$ h $\leftarrow$ 12 -21 $\leftarrow$ k $\leftarrow$ 21 -31 $\leftarrow$ l $\leftarrow$ 31
Reflections collected	28428	154041	69550
Independent reflections	7969	13616	8730
R <sub>int</sub>	0.0886	0.0395	0.1085
Completeness to $\theta_{\text{full}}$ (%)	99.9	99.9	99.8
Absorption correction type	multi-scan	multi-scan	multi-scan
T <sub>max</sub> and T <sub>min</sub>	1.000 and 0.219	1.000 and 0.871	1.000 and 0.158
Data/restraints/parameters	7969 / 0 / 504	13616 / 3 / 541	8730 / 0 / 533
Goodness of fit F <sup>2</sup>	1.026	1.059	1.108
R <sub>1</sub> , wR <sub>2</sub> [I > 2 $\sigma$ (I)]	0.0440, 0.1081	0.0321, 0.0716	0.0642, 0.1514
R <sub>1</sub> , wR <sub>2</sub> (all data)	0.0544, 0.1169	0.0394, 0.0734	0.0710, 0.1560
Largest diff. peak and hole (e Å <sup>-3</sup> )	1.919 -1.931	3.325, -0.922	2.658, -2.947

**Table S2.** Selected bond lengths (Å) and angles (°) for crystallized complexes.

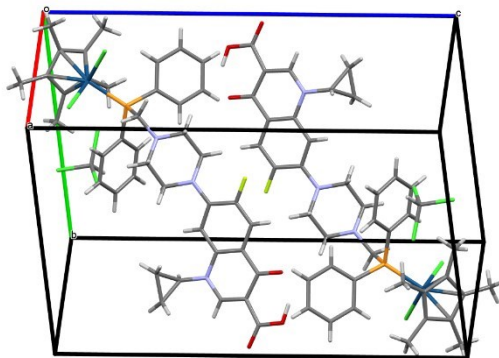
	<b>IrPCp·CHCl<sub>3</sub></b>	<b>IrPLm·1.5CHCl<sub>3</sub></b>	<b>IrPNr·2CHCl<sub>3</sub></b>
C <sup>1</sup> -C <sup>5</sup>	1.428(8)	1.403(5)	1.447(12)
C <sup>1</sup> -C <sup>2</sup>	1.432(8)	1.450(5)	1.420(13)
C <sup>2</sup> -C <sup>3</sup>	1.455(8)	1.431(4)	1.422(14)
C <sup>3</sup> -C <sup>4</sup>	1.410(8)	1.429(4)	1.439(13)
C <sup>4</sup> -C <sup>5</sup>	1.457(8)	1.454(4)	1.434(12)
C(Cp*ring)-C(Cp*CH <sub>3</sub> )	0.9600	1.495(8)	0.9600
Ir <sup>1</sup> -C <sup>1</sup>	2.159(5)	2.226(3)	2.226(8)
Ir <sup>1</sup> -C <sup>2</sup>	2.153(5)	2.169(3)	2.219(8)
Ir <sup>1</sup> -C <sup>3</sup>	2.251(5)	2.172(3)	2.158(9)
Ir <sup>1</sup> -C <sup>4</sup>	2.236(5)	2.149(3)	2.179(8)
Ir <sup>1</sup> -C <sup>5</sup>	2.177(5)	2.235(3)	2.139(8)
Ir <sup>1</sup> -CCp*(average)	2.219(5)	2.190(2)	2.184(2)
Ir <sup>1</sup> -Ccentroid	1.824	1.820	1.814
Ir <sup>1</sup> -P <sup>1</sup>	2.2919(1)	2.308(6)	2.310(6)
Ir <sup>1</sup> -Cl <sup>1</sup>	2.4195(1)	2.418(6)	2.411(6)
Ir <sup>1</sup> -Cl <sup>2</sup>	2.4114(1)	2.408(6)	2.416(2)
P <sup>1</sup> -C <sup>11</sup>	1.863(5)	1.854(3)	1.864(8)
P <sup>1</sup> -C <sup>41</sup>	1.827(5)	1.814(3)	1.817(8)
P <sup>1</sup> -C <sup>51</sup>	1.823(5)	1.826(3)	1.835(8)
P <sup>1</sup> -Ir <sup>1</sup> -Cl <sup>1</sup>	90.45(5)	90.18(2)	89.43(7)
P <sup>1</sup> -Ir <sup>1</sup> -Cl <sup>2</sup>	90.03(4)	86.75(2)	86.77(7)
Cl <sup>1</sup> -Ir <sup>1</sup> -Cl <sup>2</sup>	86.04(4)	87.52(2)	89.45(8)
Ccentroid-Ir <sup>1</sup> -P <sup>1</sup>	129.78	132.99	132.93
Ccentroid-Ir <sup>1</sup> -Cl <sup>1</sup>	124.56	123.04	132.93
Ccentroid-Ir <sup>1</sup> -Cl <sup>2</sup>	123.42	123.13	132.93
Ir <sup>1</sup> -P <sup>1</sup> -C <sup>11</sup>	116.34(17)	111.27(9)	112.1(2)
Ir <sup>1</sup> -P <sup>1</sup> -C <sup>41</sup>	111.59(18)	116.09(9)	116.4(3)
Ir <sup>1</sup> -P <sup>1</sup> -C <sup>51</sup>	115.83(18)	106.68(12)	111.0(3)
C <sup>11</sup> -P <sup>1</sup> -C <sup>41</sup>	100.4(2)	103.49(12)	107.1(4)
C <sup>11</sup> -P <sup>1</sup> -C <sup>51</sup>	101.2(2)	103.49(12)	104.8(4)
C <sup>41</sup> -P <sup>1</sup> -C <sup>51</sup>	110.1(2)	106.10(12)	104.6(4)

Ccentroid – center of gravity of cyclopentadienyl anion;

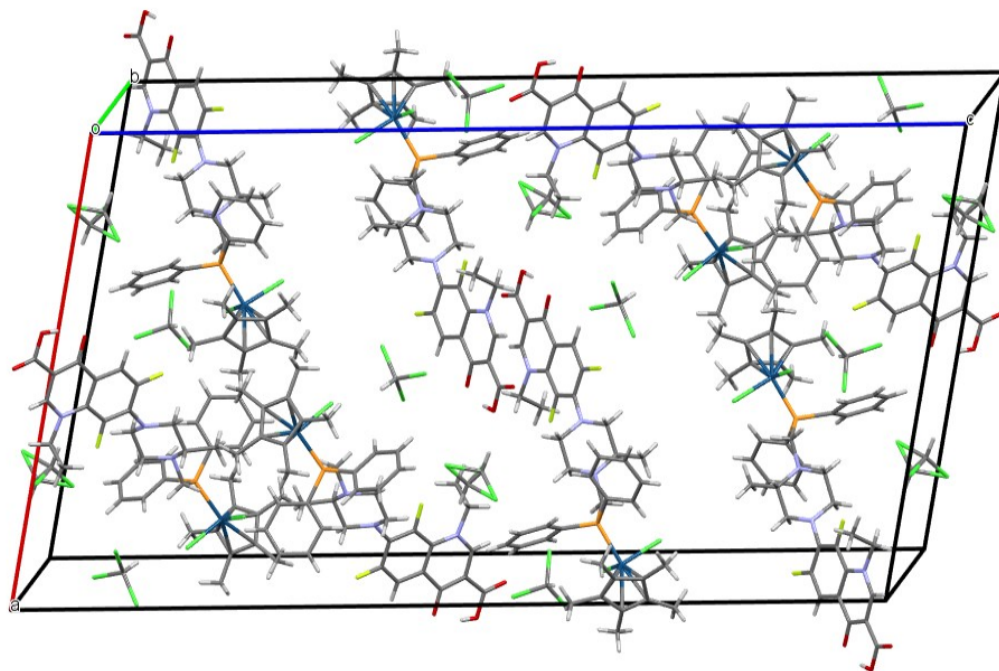
Ir<sup>1</sup>-CCp\* (average) – average calculated from: Ir<sup>1</sup>-C<sup>1</sup>, Ir<sup>1</sup>-C<sup>2</sup>, Ir<sup>1</sup>-C<sup>3</sup>, Ir<sup>1</sup>-C<sup>4</sup>, Ir<sup>1</sup>-C<sup>5</sup>C(Cp\*ring)-C(Cp\*CH<sub>3</sub>) – average calculated from: C<sup>1</sup>-C<sup>1A</sup>, C<sup>2</sup>-C<sup>2A</sup>, C<sup>3</sup>-C<sup>3A</sup>, C<sup>4</sup>-C<sup>4A</sup>, C<sup>5</sup>-C<sup>5A</sup>



**IrPCp·CHCl<sub>3</sub>**



**IrPLm·1.5CHCl<sub>3</sub>**



**IrPNr·2CHCl<sub>3</sub>**

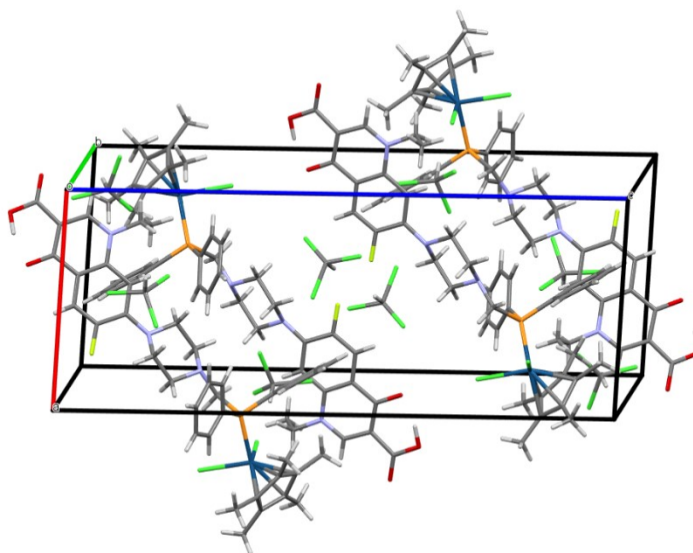


**Fig. S1.** The best view of crystal cells of **IrPCp·CHCl<sub>3</sub>**, **IrPLm·1.5CHCl<sub>3</sub>** and **IrPNr·2CHCl<sub>3</sub>**, respectively.

**Table S3.** Cumulative NMR data for ligands and iridium-complexes.

	<b>Dimer Ir</b>	<b>PCp [1]</b>	<b>PSf [2]</b>	<b>PLm [3]</b>	<b>PNr [4]</b>	<b>IrPCp</b>	<b>IrPSf</b>	<b>IrPLm</b>	<b>IrPNr</b>
<b>P<sup>I</sup></b>		<b>-27.4</b>	<b>-35.9</b>	<b>-28.8</b>	<b>-27.5</b>	<b>-1.30</b>	<b>-3.06</b>	<b>-1.82</b>	<b>-1.38</b>
H <sup>1</sup>	1.69 s					1.35 d (2.2)	1.33 d (2.2)	1.34 d (2.2)	1.35 d (2.2)
H <sup>11</sup>		3.29 d (2.9)	3.93 bs	2.80 bs	3.29 d (2.8)	4.07 s	4.25 s	4.15 dd (40.0;16.0)	4.07 s
H <sup>12, 15</sup>		3.37	3.20 m	2.95-3.45	3.36 m	2.99 bt (4.8)	2.45 m	2.14-3.14 m	2.97 bt (4.6)
H <sup>13, 14</sup>		2.90	3.93 m		2.89 m	2.39 bt (4.8)	2.80-3.07 m		2.39 bt (4.6)
H <sup>16</sup>			0.94 d (5.9)	0.97 d (5.7)			0.72 d (6.4)	0.62 d (6.3)	
H <sup>17</sup>									
H <sup>42</sup>		7.34-7.47	7.29-7.65	7.03-7.60	7.33-7.46	8.00-8.11 m	7.98-8.13 m	7.99-8.15 m	8.00-8.11 m
H <sup>43, 44</sup>						7.44-7.53 m	7.43-7.51 m	7.39-7.56 m	7.42-7.54 m
H <sup>63</sup>		7.95 d (13.8)	6.46 bs	7.84 d (11.4)	7.95 d (13.0)	7.92 d (13.3)	6.41 bd	7.87 dd (12.0; 1.7)	7.96 d (13.2)
H <sup>67</sup>		8.71 s	8.62 s	8.52 s	8.63 s	8.72 s	8.61 s	8.55 s	8.62 s
H <sup>69</sup>		7.34-7.47			6.82 d (6.8)	7.16 d (7.1)			6.64 d (6.9)
H <sup>70</sup>		15.01 s	14.54 bs	14.65 bs	15.13 bs	15.02 s	14.65 bs	14.68 s	15.09 s
H <sup>71</sup>		3.53 m	3.93 bs	4.39 d (3.6)	4.31 m	3.47 m	3.87 m	4.40 qd (7.2; 3.3)	4.25 q (7/2)
H <sup>72</sup>		1.18 m	1.07-1.21 m	1.48 t (3.7)	1.56 m	1.11-1.33 m	1.04-1.20 m	1.50 t (7.0)	1.54 t (7.3)
H <sup>73</sup>									

- [1] A. Bykowska, R. Starosta, A. Brzuszkiewicz, B. Bażanów, M. Florek, N. Jackulak, J. Król, J. Grzesiak, K. Kaliński, M. Jeżowska-Bojczuk, *Polyhedron*, 2013, **60**, 23-29.
- [2] U. K. Komarnicka, R. Starosta, K. Guz-Regner, G. Bugła-Płoskońska, A. Kyzioł, M. Jeżowska-Bojczuk, *J. Mol. Struct.*, 2015, **1096**, 55-63.
- [3] U. K. Komarnicka, R. Starosta, A. Kyzioł, M. Płotek, M. Puchalska, M. Jeżowska-Bojczuk, *J. Inorg. Biochem.*, 2016, **165**, 25-35.
- [4] A. Bykowska, R. Starosta, U. K. Komarnicka, Z. Ciunik, A. Kyzioł, K. Guz-Regner, G. Bugła-Płoskońska, M. Jeżowska-Bojczuk, *New J. Chem.*, 2014, **38**, 1062-1071.

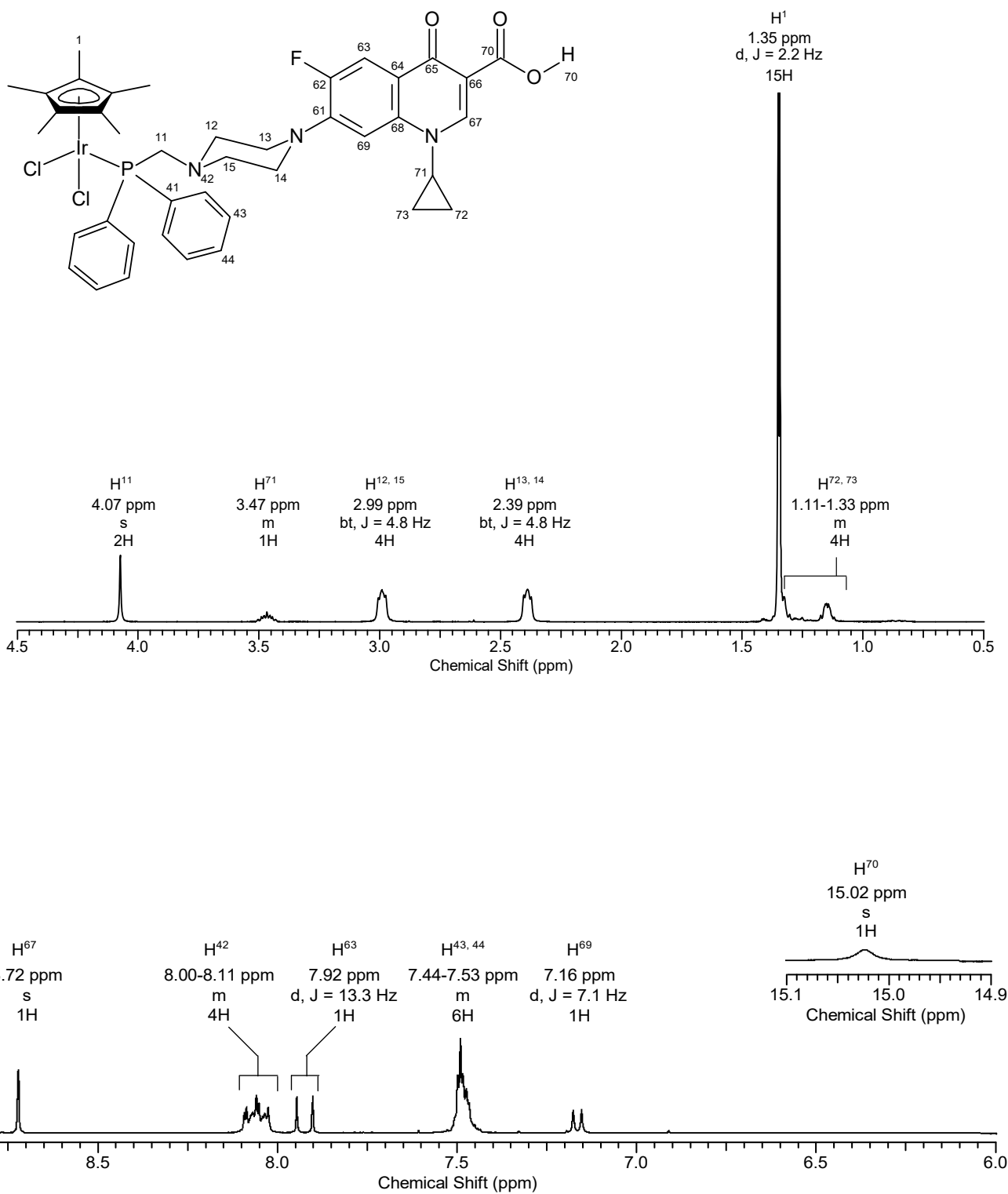


**Fig. S2.** <sup>1</sup>H NMR spectra for IrPCp (298 K, CHCl<sub>3</sub>-d)

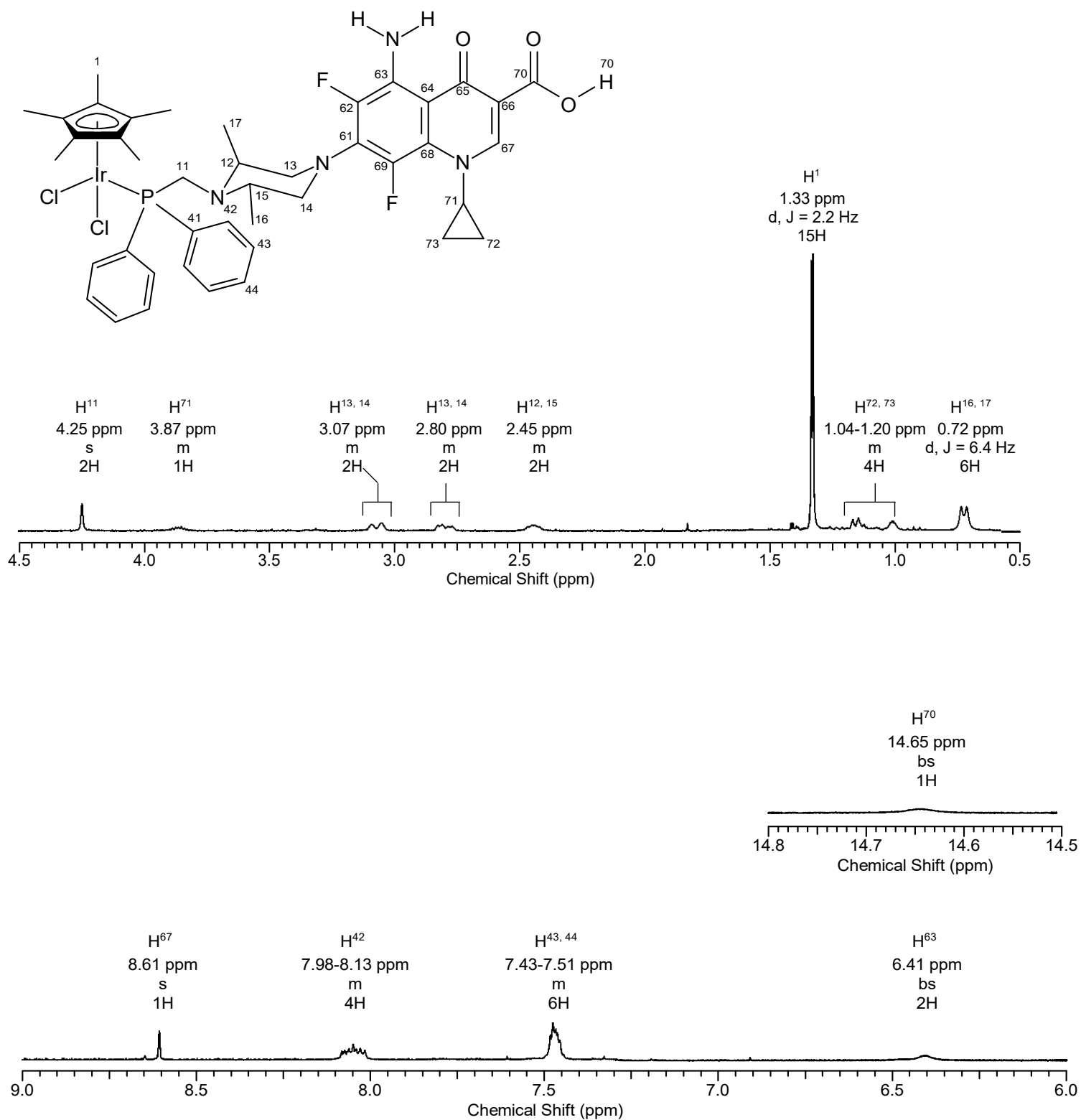


**Fig. S3.** <sup>1</sup>H NMR spectra for **IrPSf** (298 K, CHCl<sub>3</sub>-d)

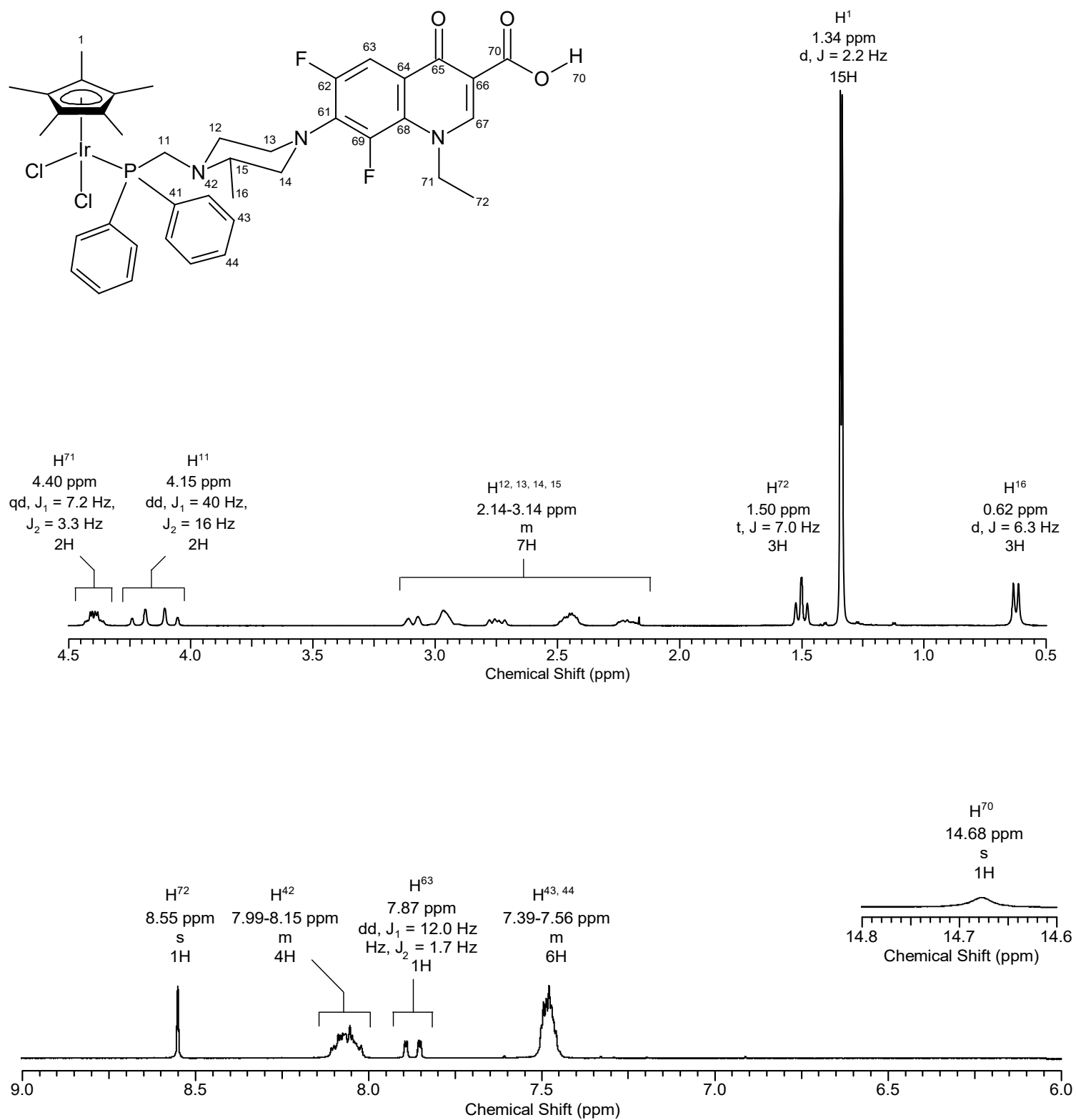


**Fig. S4.** <sup>1</sup>H NMR spectra for IrPLm (298 K, CHCl<sub>3</sub>-d).

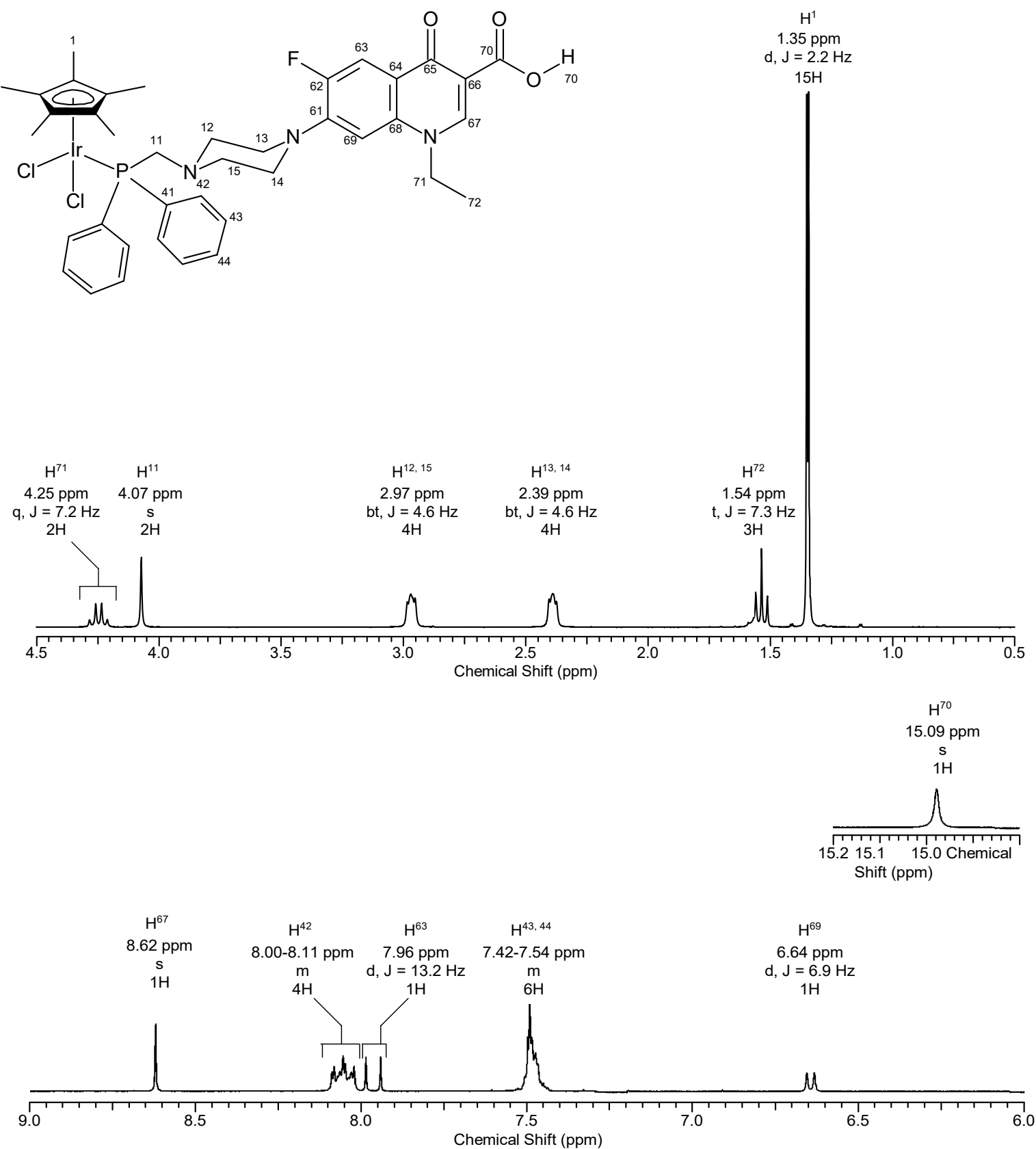


**Fig. S5.** <sup>1</sup>H NMR spectra for IrPLm (298 K, CHCl<sub>3</sub>-d).



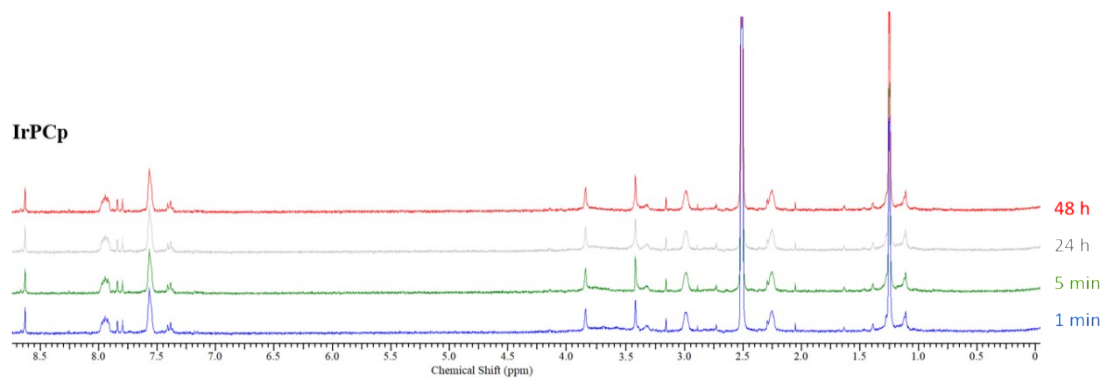


Fig S6. Time-dependent <sup>1</sup>H NMR spectroscopic stability study for **IrPCp** in 80% DMSO-d<sub>6</sub>/20% D<sub>2</sub>O over 48 h.

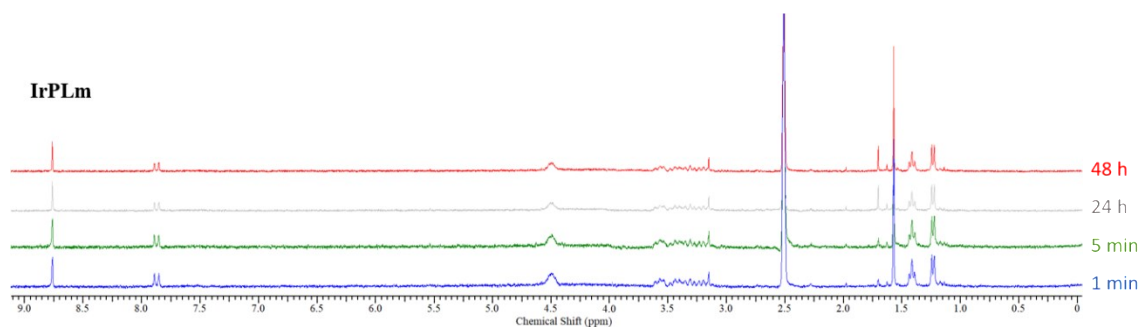


Fig. S7. Time-dependent <sup>1</sup>H NMR spectroscopic stability study for **IrPLm** in 70% DMSO-d<sub>6</sub>/30% D<sub>2</sub>O over 48 h.

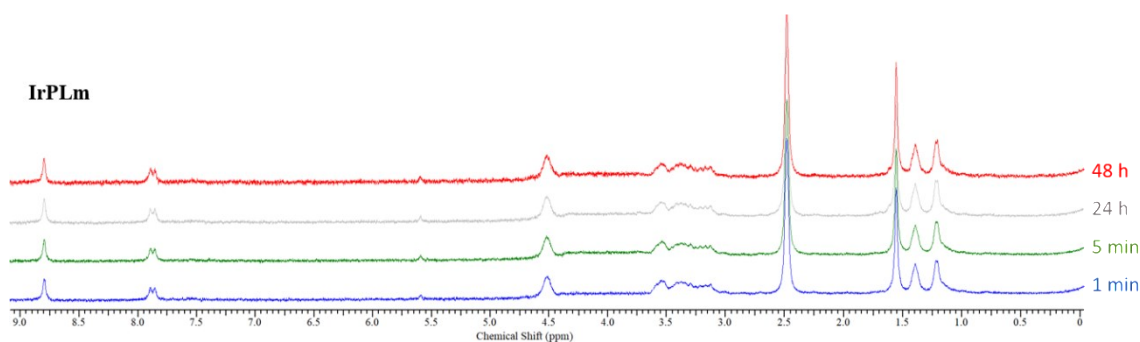


Fig. S8. Time-dependent <sup>1</sup>H NMR spectroscopic stability study for **IrPLm** in 80% DMSO-d<sub>6</sub>/20% D<sub>2</sub>O over 48 h.

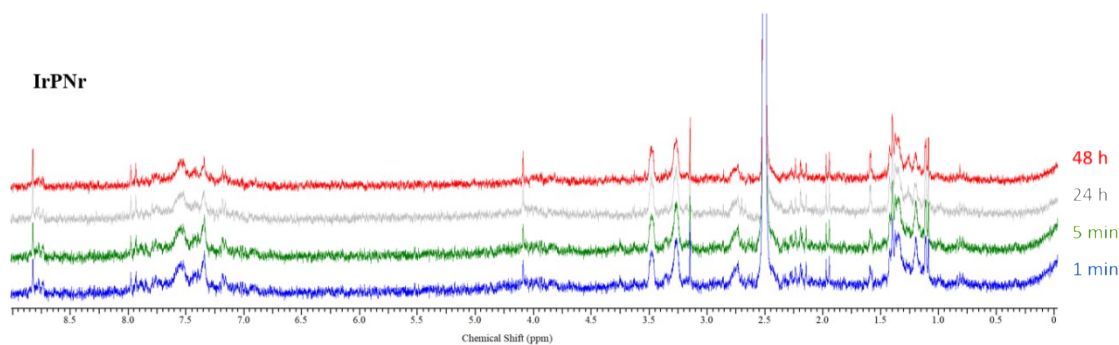


Fig. S9. Time-dependent <sup>1</sup>H NMR spectroscopic stability study for **IrPNr** in 70% DMSO-d<sub>6</sub>/30% D<sub>2</sub>O over 48 h.

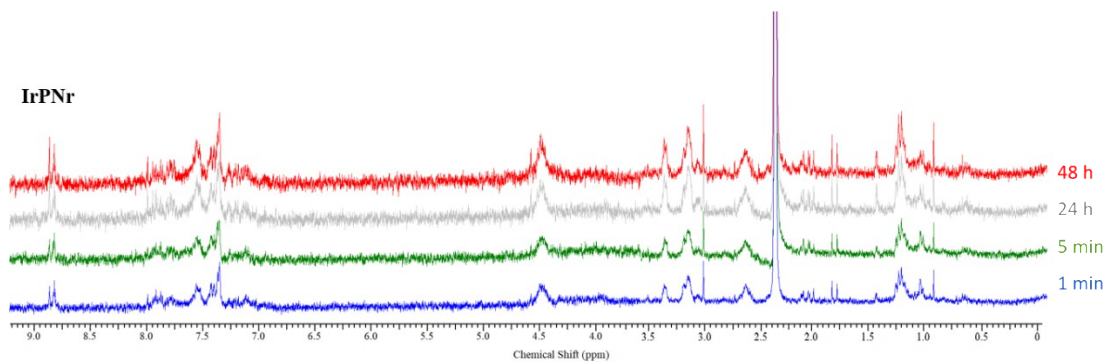


Fig. S10. Time-dependent <sup>1</sup>H NMR spectroscopic stability study for **IrPNr** in 80% DMSO-d<sub>6</sub>/20% D<sub>2</sub>O over 48 h.

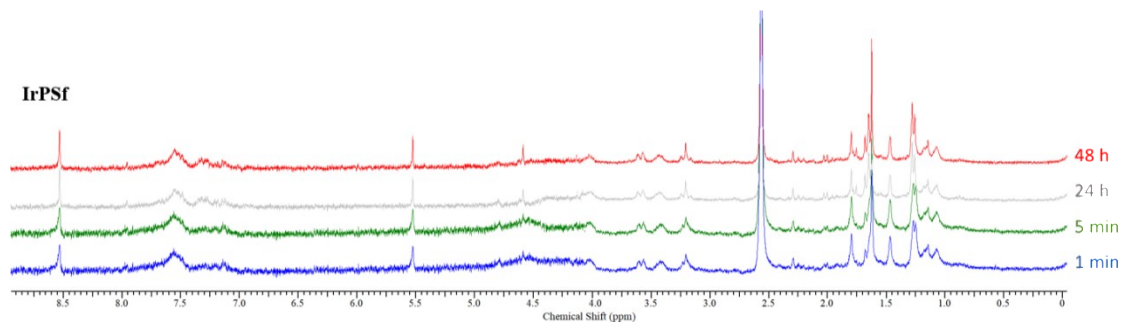


Fig. S11. Time-dependent <sup>1</sup>H NMR spectroscopic stability study for **IrPSf** in 70% DMSO-d<sub>6</sub>/30% D<sub>2</sub>O over 48 h.

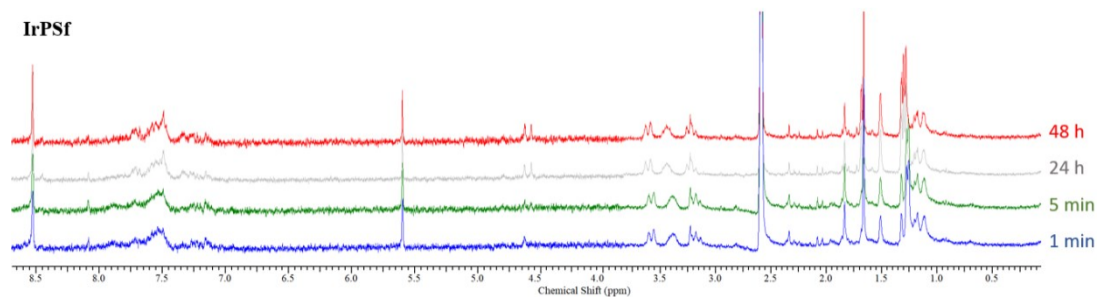
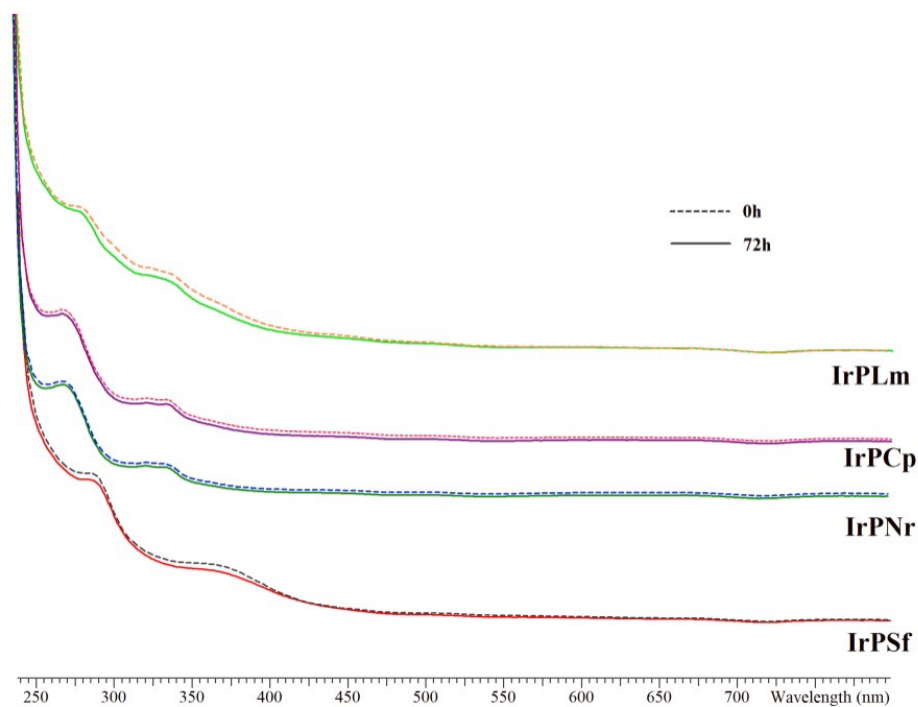
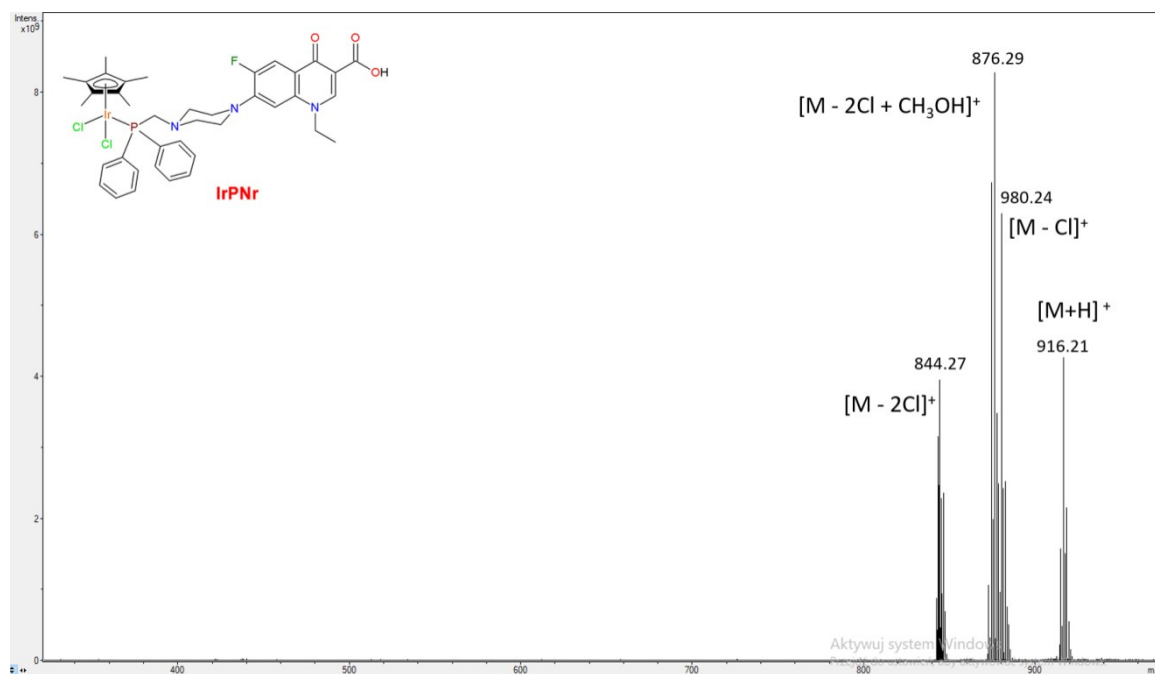


Fig. S12. Time-dependent <sup>1</sup>H NMR spectroscopic stability study for **IrPSf** in 80% DMSO-d<sub>6</sub>/20% D<sub>2</sub>O over 48 h.



**Fig. S13.** Stability of the all complexes (**IrPNr**, **IrPLm**, **IrPCp**, **IrPSf**) in cellular medium (DMEM with 2% DMSO; during 72h experiments).



**Fig. S14.** Full ESI(+)-MS spectrum of **IrPNr**.

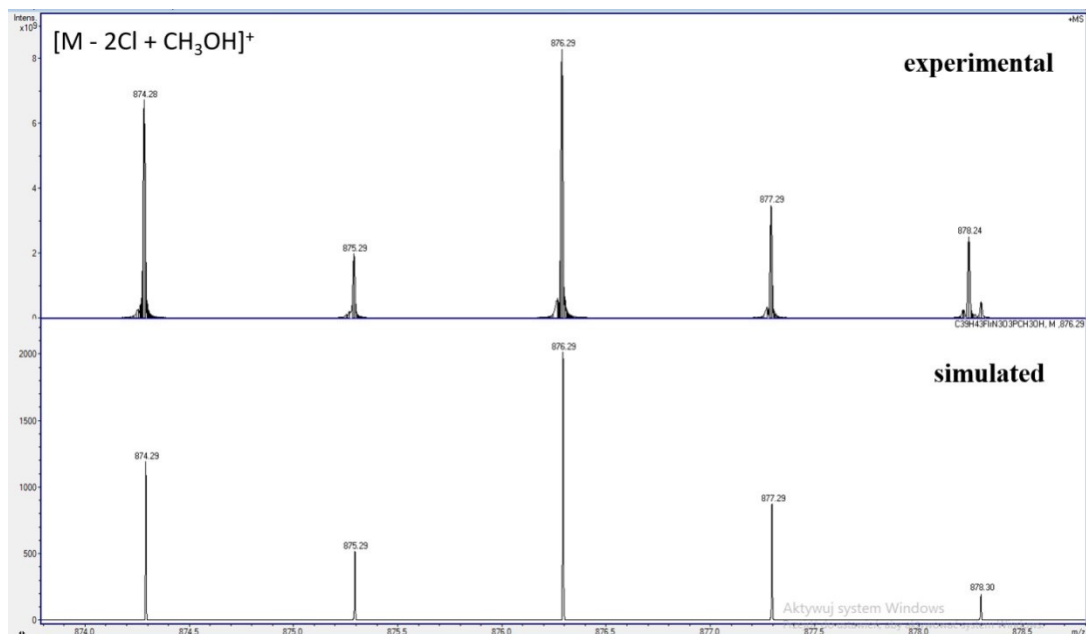


Fig. S15. Experimental and simulated spectra of  $[\text{Ir}(\eta^5\text{-Cp}^*)\text{PNr} + \text{CH}_3\text{OH}]^+$

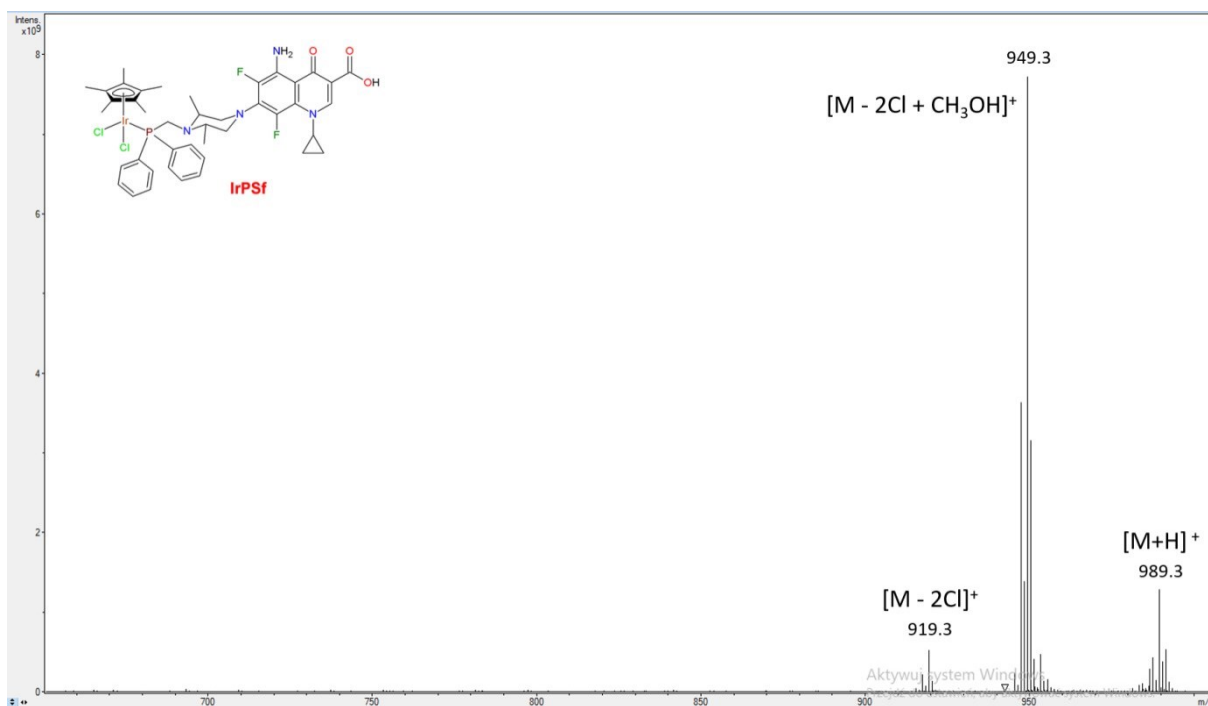


Fig. S16. Full ESI(+)-MS spectrum of IrPSf.

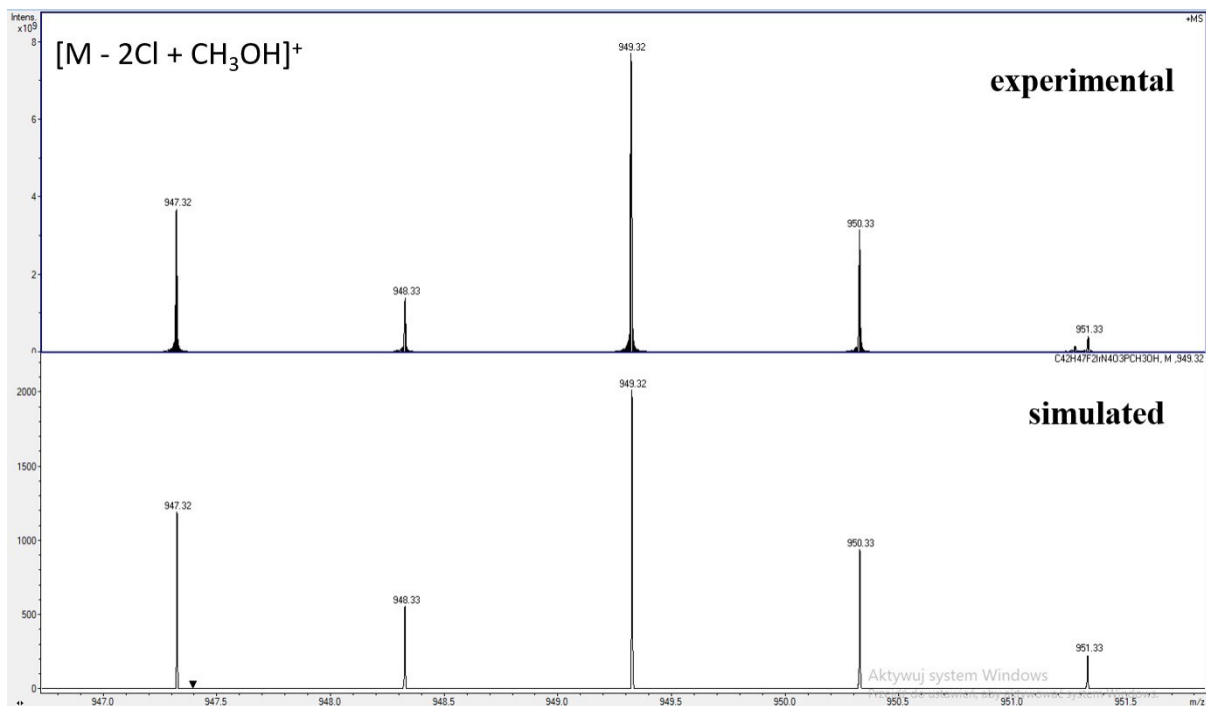


Fig. S17. Experimental and simulated spectra of  $[\text{Ir}(\eta^5\text{-Cp}^*)\text{PSf} + \text{CH}_3\text{OH}]^+$

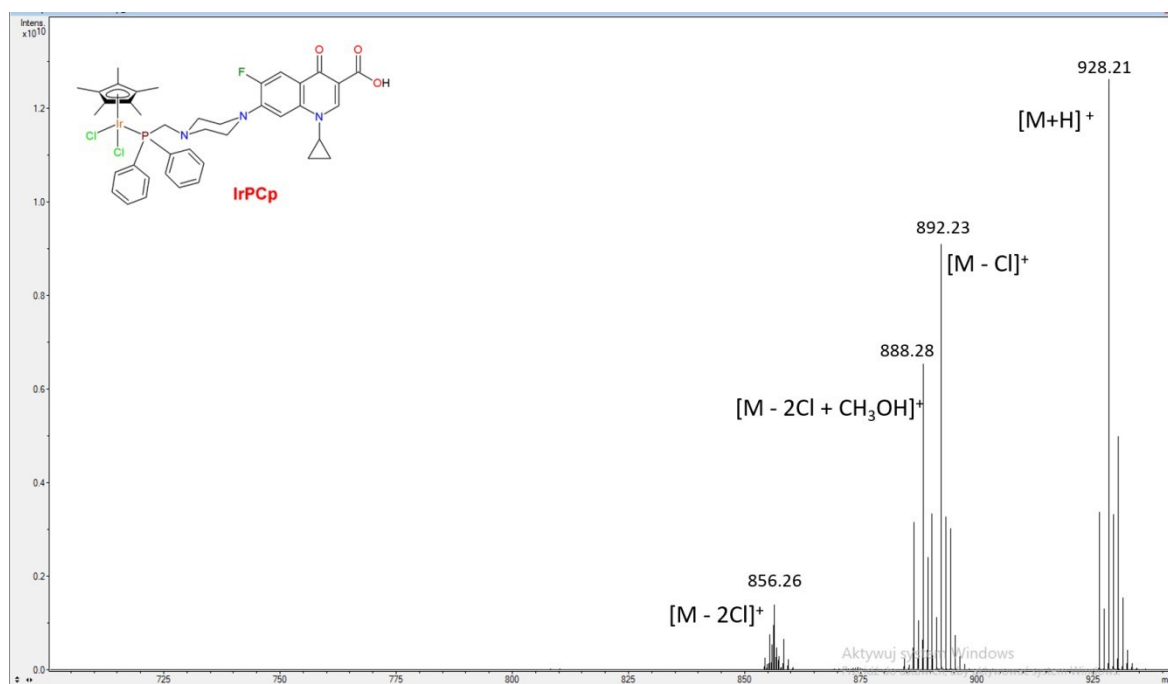


Fig. S18. Full ESI(+)-MS spectrum of IrPCp.

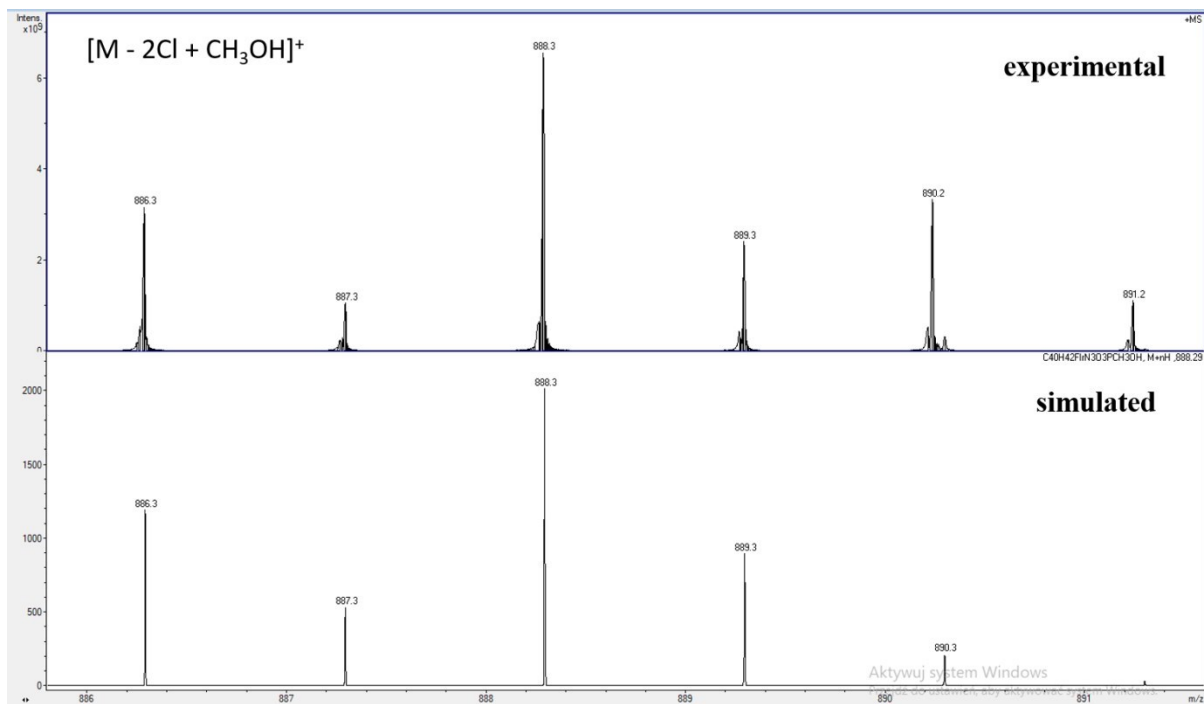


Fig. S19. Experimental and simulated spectra of  $[\text{Ir}(\eta^5\text{-Cp}^*)\text{PCp} + \text{CH}_3\text{OH}]^+$

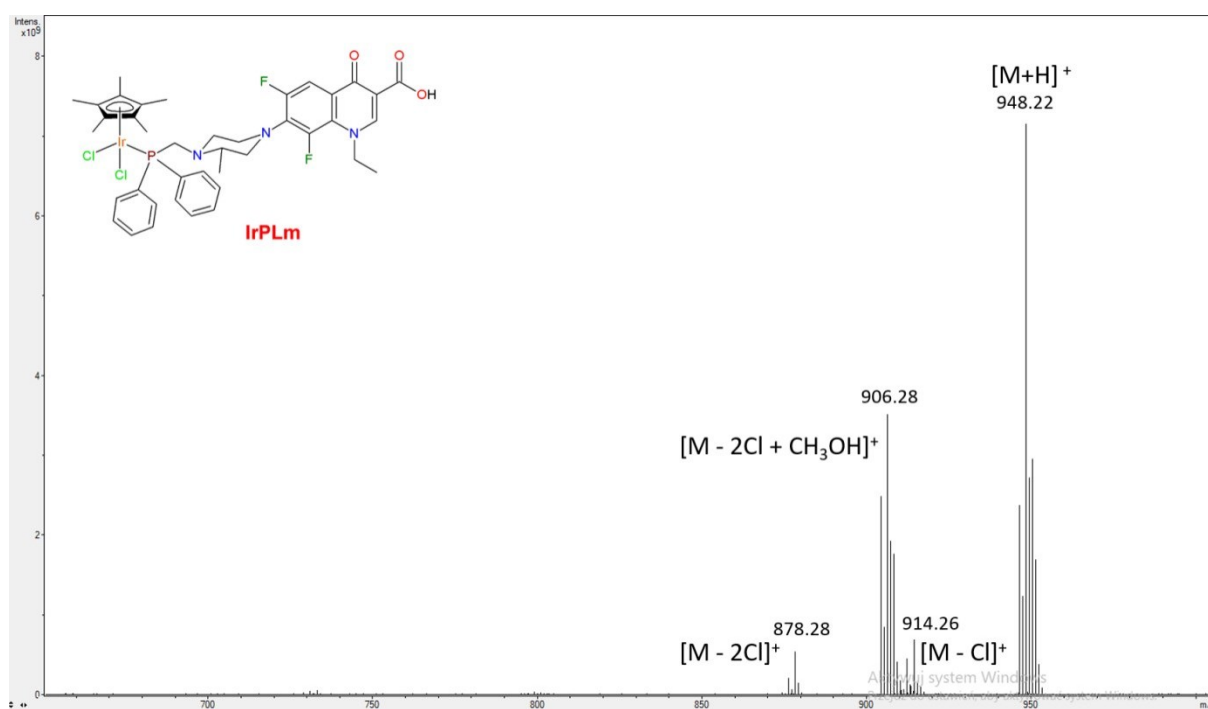


Fig. S20. Full ESI(+)MS spectrum of **IrPLm**.

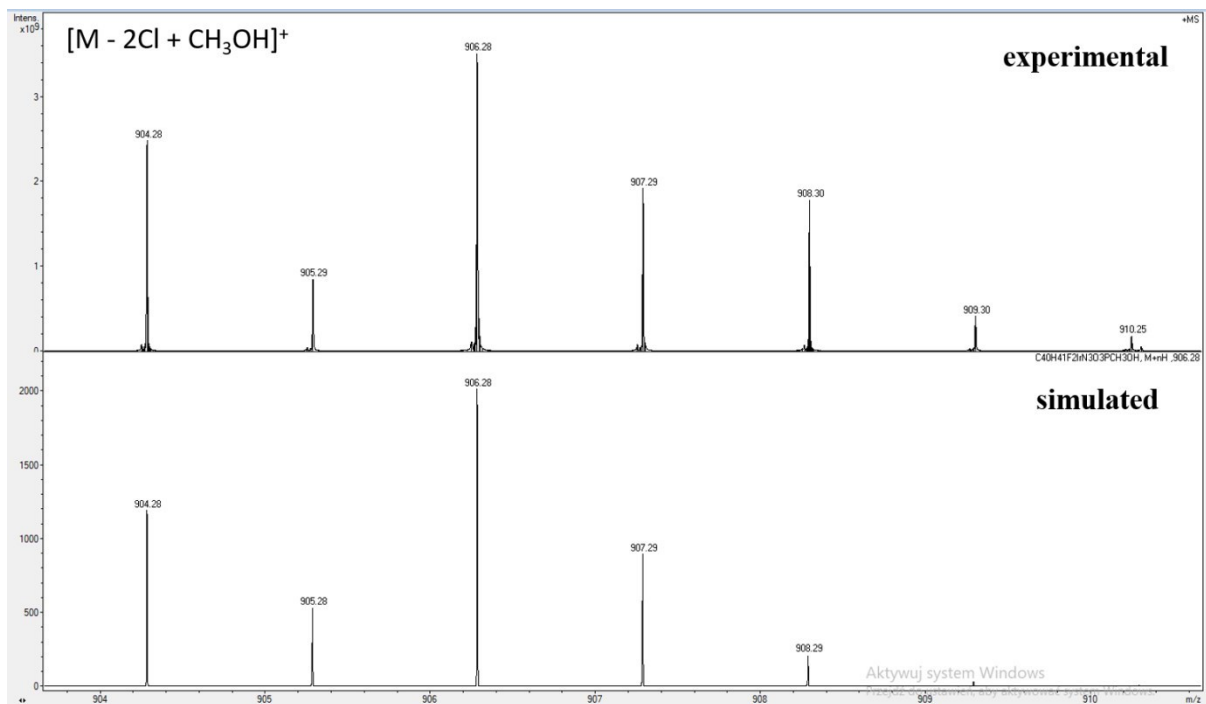


Fig. S21. Experimental and simulated spectra of  $[Ir(\eta^5-Cp^*)PLm + CH_3OH]^+$

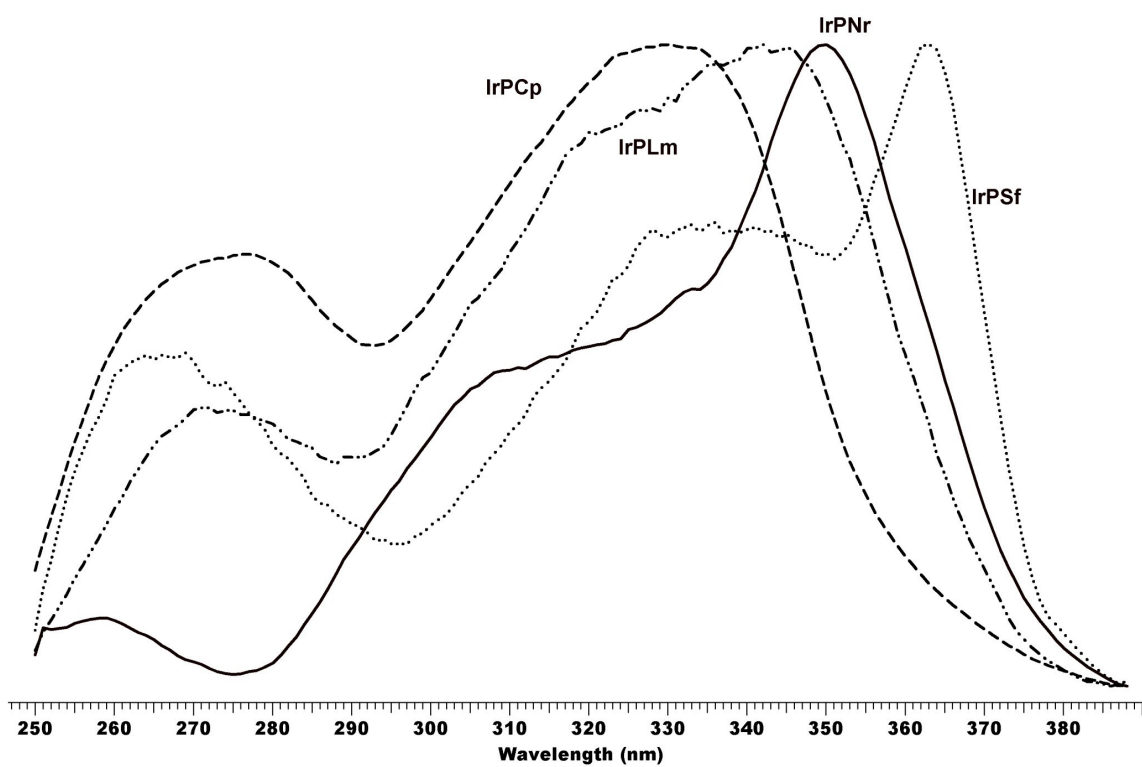


Fig. S22. Excitation spectra of IrPCp, IrPNr, IrPLm and IrPSf



**Table S4.** Values of IC<sub>50</sub> [μM] (concentration of a drug required to inhibit the growth of 50% of the cells) for CT26, A549, MCF7, PANC-1, DU-145, HEK293T cells after 24h and 24h + 48h treatment with the studied compounds and cisplatin as reference.

IC <sub>50</sub> [μM] ± SD;24h						
	CT26	A549	MCF7	PANC-1	DU-145	HEK293T
<b>IrPCp</b>	-*	68.8±1.7	65.7±2.8	43.0±1.3	11.8±1.1	42.1±2.1
<b>IrPSf</b>	-*	64.8±2.8	61.8±4.1	40.3±4.1	9.1±0.5	44.1±1.2
<b>IrPLm</b>	-*	69.7±4.1	64.5±2.2	48.1±4.3	11.3±0.9	46.0±1.6
<b>IrPNr</b>	-*	71.4±1.6	68.8±5.3	42.6±8.1	12.9±2.1	41.8±1.7
<b>cisplatin</b>	>100	>100	51.9±4.6	>100	>100	21.0±1.8
IC <sub>50</sub> [μM] ± SD; 24h + 48h						
<b>IrPCp</b>	6.4±0.3	29.5±0.7	35.0±0.9	8.7±0.3	4.8±0.1	28.5±1.5
<b>IrPSf</b>	4.1±0.7	26.7±1.6	29.3±0.2	7.8±0.6	3.5±0.8	23.0±1.7
<b>IrPLm</b>	5.8±0.2	27.4±1.7	33.7±3.8	8.1±1.1	5.1±0.4	28.0±1.7
<b>IrPNr</b>	5.6±0.4	29.1±1.2	31.7±0.3	8.3±1.3	5.5±0.2	21.4±1.2
<b>cisplatin</b>	80.4± 2.3	71.7±3.7	17.7±8.6	74.5±2.3	65.5±3.6	10.3±2.1

\* no available data

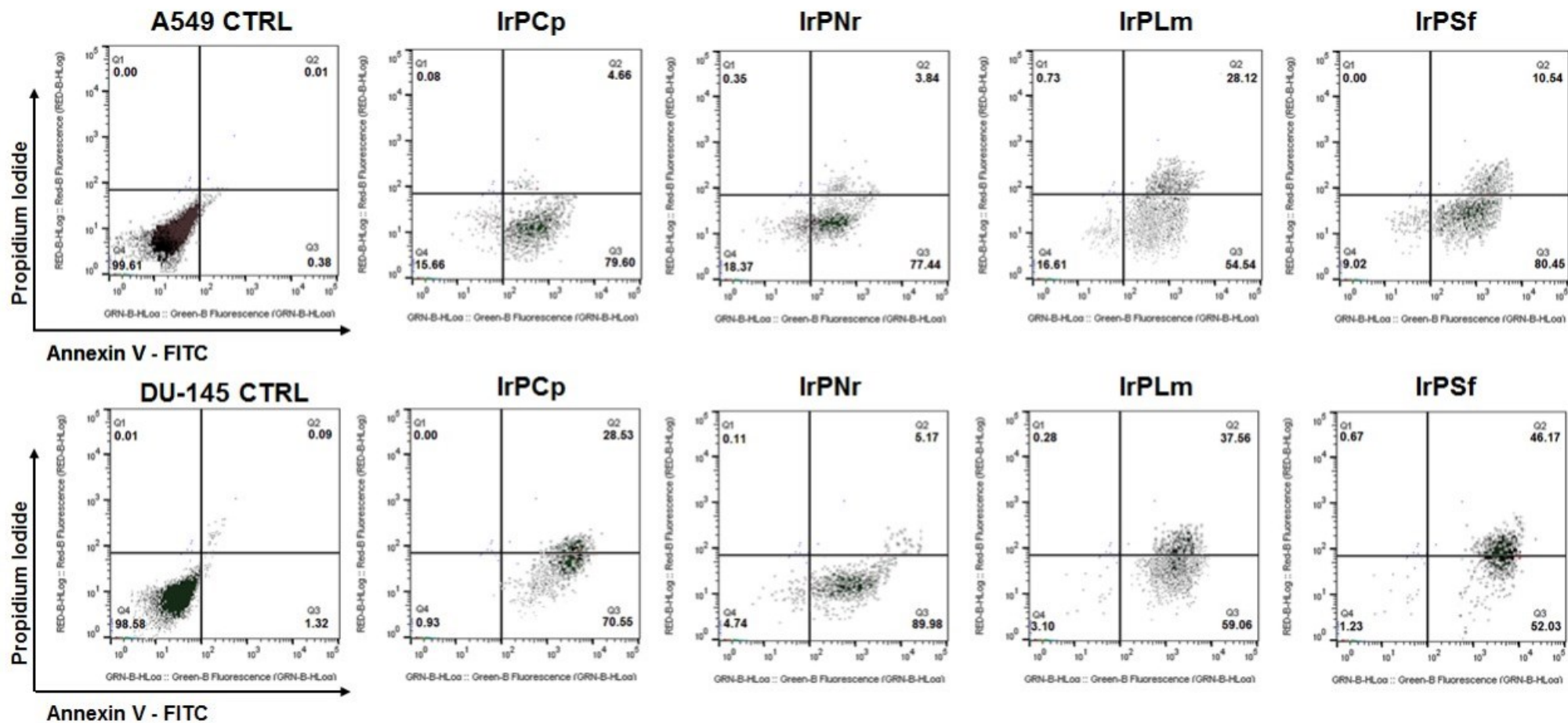


**Fig. S23.** Percentage analysis [%] of the number live, early/late apoptotic and necrotic cells after 24h + 48h of incubation of A549 and Du-145 cell lines with IrPCp, IrPNr, IrPSf, IrPLm in  $c = 100 \mu\text{M}$ . Scatter plots: left bottom – live cells, right bottom – early apoptotic cells, right top – late apoptotic cells, left top – necrotic cells.

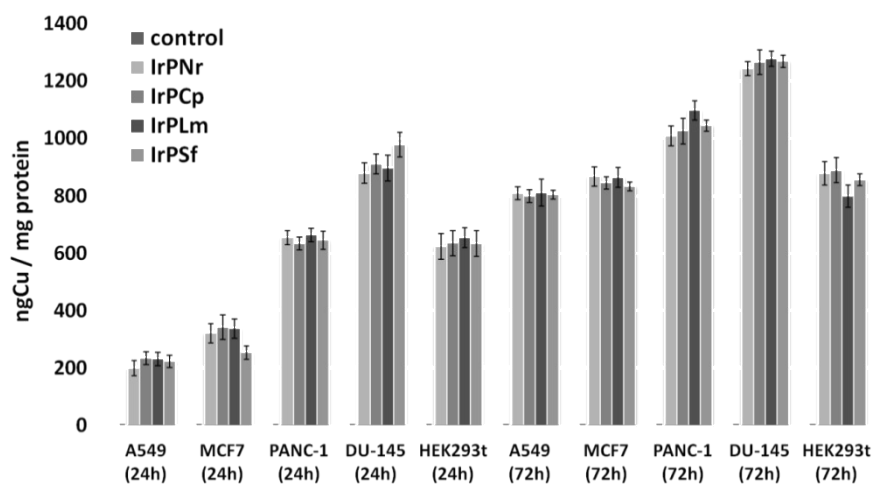


**Fig. S24.** Time-dependency of final intracellular iridium concentration expressed as ng Ir per mg protein after 24h and 24h\* (24h + 48h) of incubation with the A549, MCF7, PANC-1, DU-145 and HEK293T cell lines for IrPCp, IrPNr, IrPSf, IrPLm complexes in  $c = 1 \mu\text{M}$ .

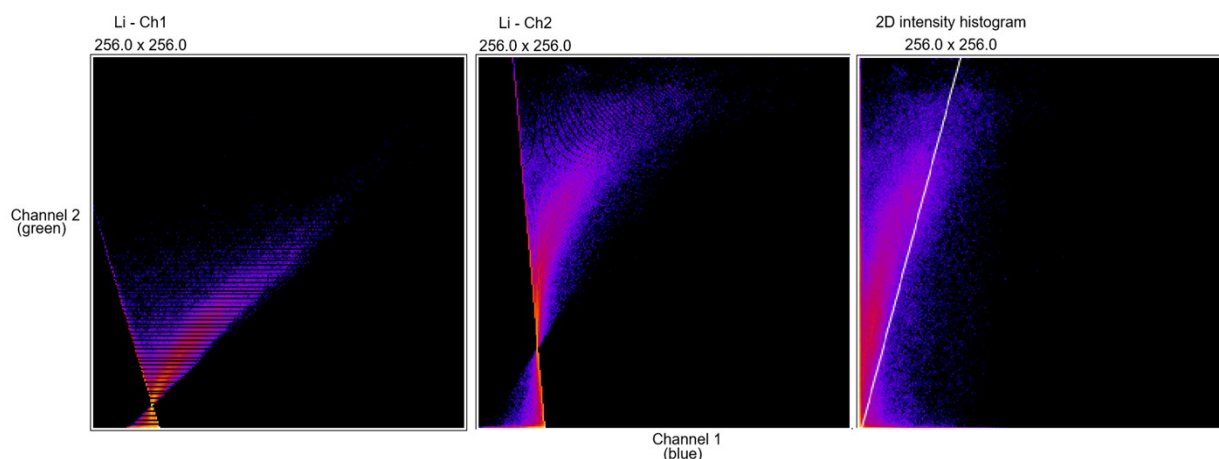


**Fig. S25.** Co-localization analysis performed with ImageJ plugin - Coloc2 which implements and performs the pixel intensity correlation over space.

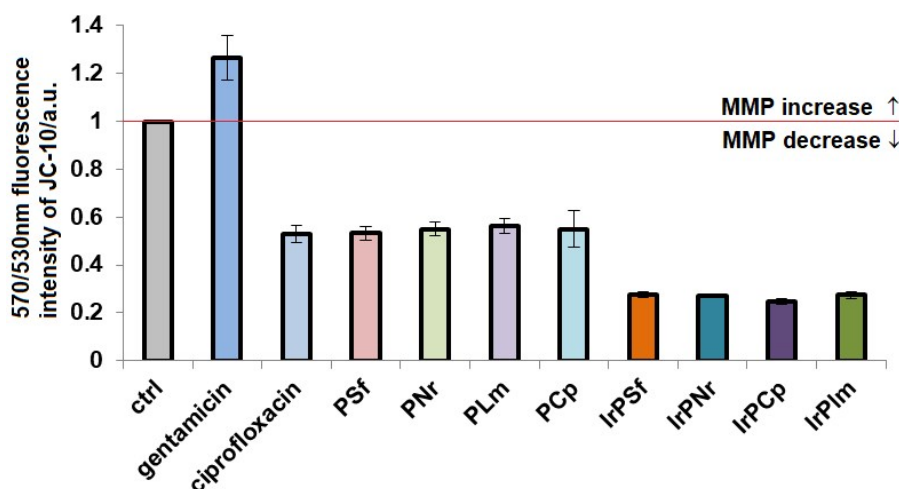


**Fig. S26.** Influence of studied complexes ( $IC_{50}$ ) on intensity of JC-10 fluorescence in treated DU-145 cells. Alteration in MMP is given as an emission ratio 570 nm/530 nm. (ctrl – untreated cells, ciprofloxacin – a negative control, gentamicin – a positive control).

**Table S5.** Hydrodynamic diameter and Zeta potential determined by DLS technique as well as loading content and encapsulation efficiency determined by ICP-MS technique for selected Pluronic P-123 formulations.

Formulation	Hydrodynamic diameter [nm]	Zeta potential [mV]	LC $\pm$ S.D. [%]	EE $\pm$ S.D. [%]
<b>IrPCp_M</b>	$19 \pm 1$ (PDI = $0.5 \pm 0.1$ )	$-1.5 \pm 0.4$	$19.5 \pm 2.9$	$99.5 \pm 1.2$
<b>IrPNr_M</b>	$18 \pm 2$ (PDI = $0.4 \pm 0.1$ )	$-1.6 \pm 0.3$	$29.8 \pm 2.2$	$98.0 \pm 0.5$

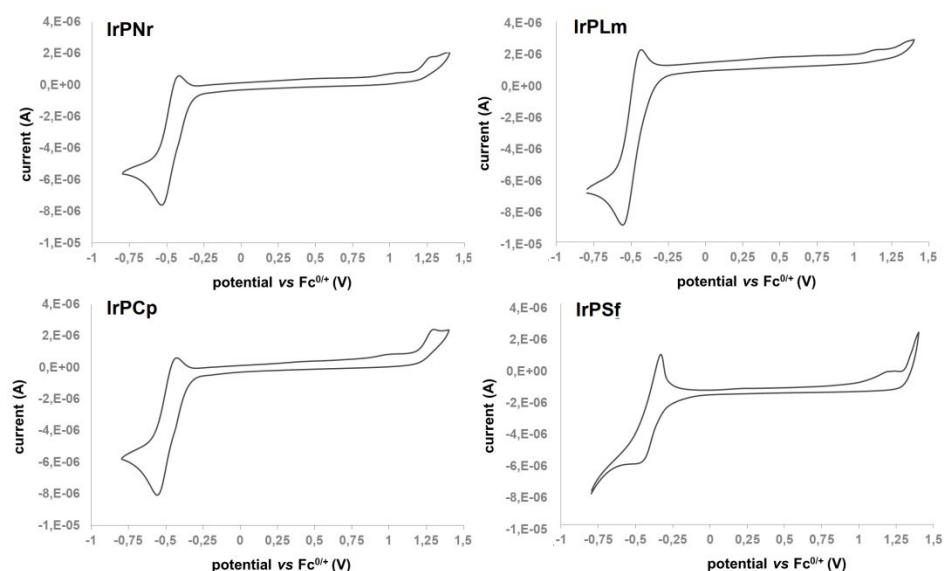


**Fig. S27.** Cyclic voltammograms of iridium(III) complexes (1 mM), recorded with 0.1 M tetrabutyl ammonium perchlorate (TBAP) as supporting electrolyte in DMF solution. Scan rates ( $10 \text{ mVs}^{-1}$ ). The potentials were referenced to the  $\text{Fc}^{0/+}$  redox couple.

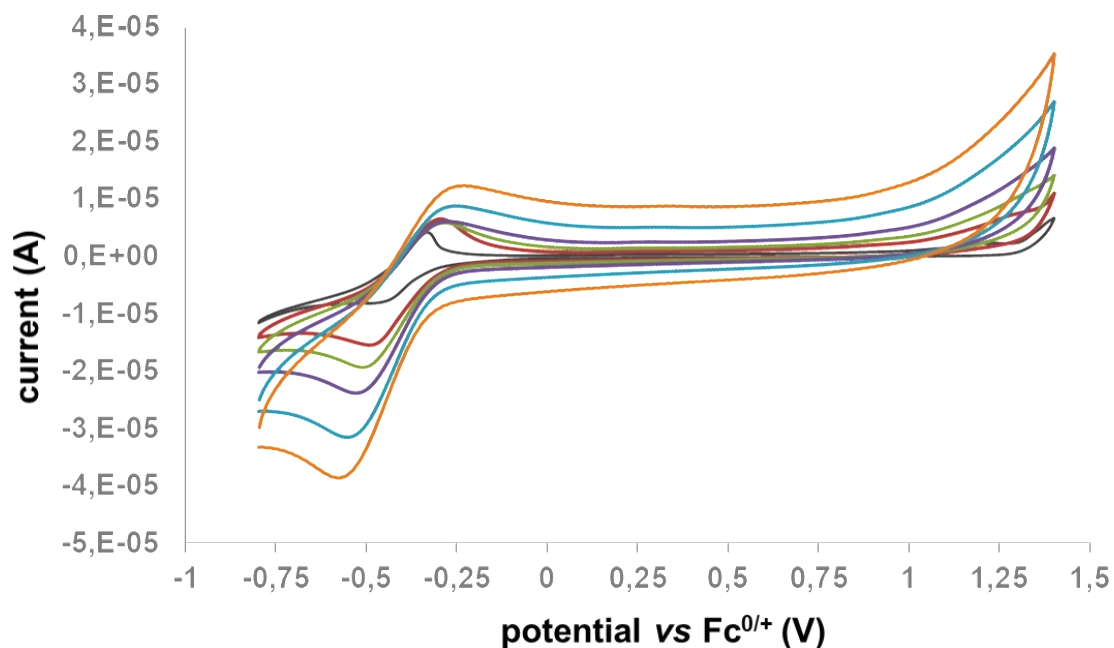


**Fig. S28.** Cyclic voltammetric trace of **IrPSf**(1 mM) as a function of scan rate, recorded with recorded with 0.1 M tetrabutyl ammonium perchlorate (TBAP) as supporting electrolyte in DMF solution. Scan rates 1 – 100 ( $\text{mV s}^{-1}$ ). Potential (V) versus  $\text{Fc}^{0/+}$ .

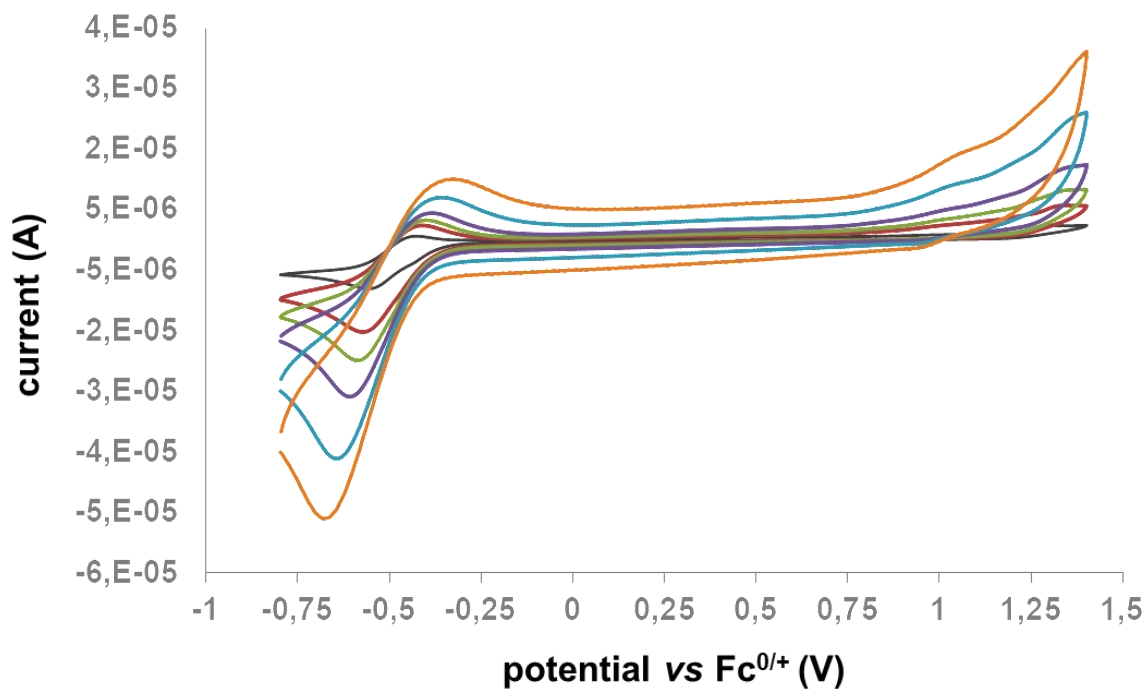


**Fig. S29.** Cyclic voltammetric trace of **IrPCp**(1 mM) as a function of scan rate, recorded with recorded with 0.1 M tetrabutyl ammonium perchlorate (TBAP) as supporting electrolyte in DMF solution. Scan rates 1 – 100 (mV s<sup>-1</sup>). Potential (V) versus Fc<sup>0/+</sup>.

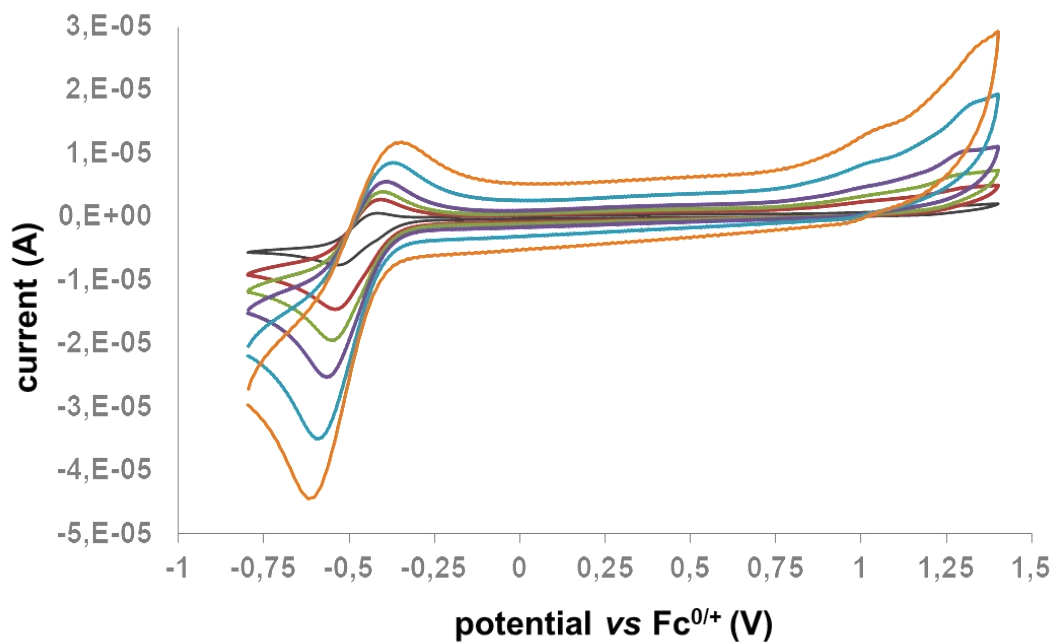


**Fig. S30.** Cyclic voltammetric trace of **IrPCp**(1 mM) as a function of scan rate, recorded with recorded with 0.1 M tetrabutyl ammonium perchlorate (TBAP) as supporting electrolyte in DMF solution. Scan rates 1 – 100 (mV s<sup>-1</sup>). Potential (V) versus Fc<sup>0/+</sup>.

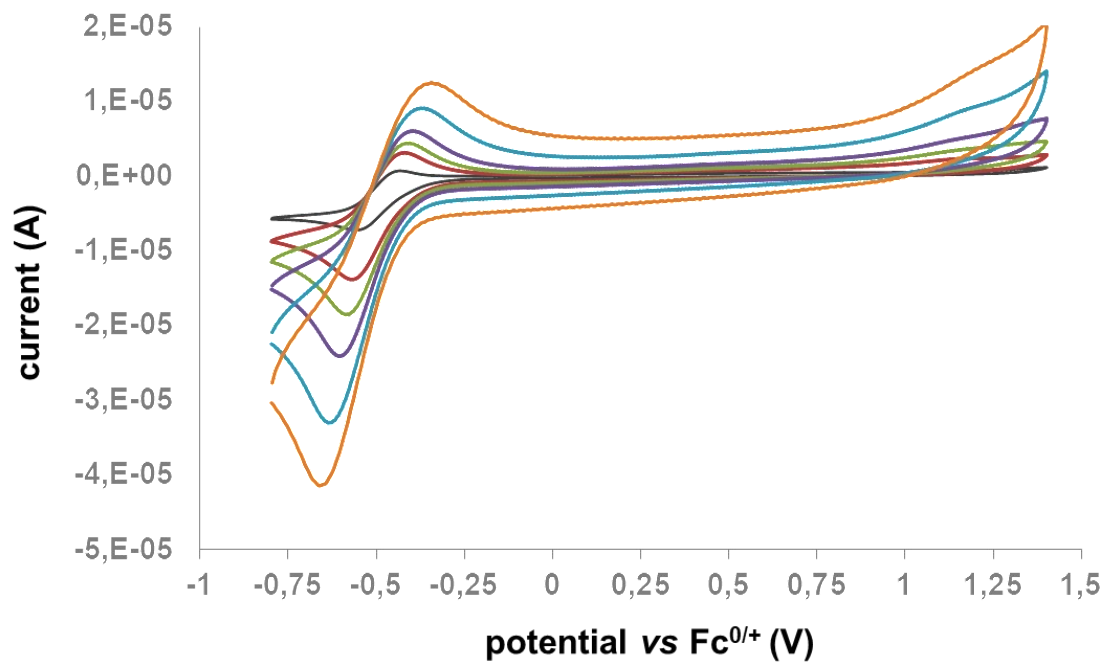


**Fig. S31.** Cyclic voltammetric trace of IrPCp(1 mM) as a function of scan rate, recorded with recorded with 0.1 M tetrabutyl ammonium perchlorate (TBAP) as supporting electrolyte in DMF solution. Scan rates 1 – 100 ( $\text{mV s}^{-1}$ ). Potential (V) versus  $\text{Fc}^{0/+}$ .

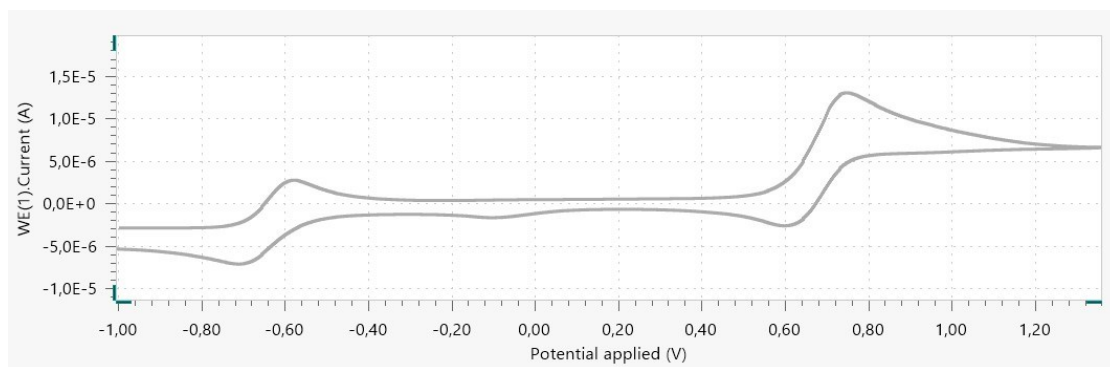


**Fig. S32.** CV voltammograms for ferrocene in DMF in the range of potentials from -01 V to 1.2 V. Scan rate:  $10 \text{ mV s}^{-1}$ .

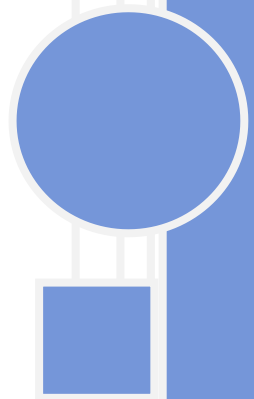
# PUBLICATION S3

Kozieł Sandra, Lesiów Monika Katarzyna, Wojtala Daria, Dyguda-Kazimierowicz Edyta, Bieńko Dariusz, Komarnicka Urszula Katarzyna

*Interaction between DNA, albumin and apo-transferrin and iridium(III) complexes with phosphines derived from fluoroquinolones as a potent anticancer drug.*

Pharmaceuticals, 2021, 14, 685/1-685/25

DOI: [10.3390/ph14070685](https://doi.org/10.3390/ph14070685)







Article

# Interaction between DNA, Albumin and Apo-Transferrin and Iridium(III) Complexes with Phosphines Derived from Fluoroquinolones as a Potent Anticancer Drug

Sandra Amanda Kozieł <sup>1,\*</sup> , Monika Katarzyna Lesiów <sup>1</sup>, Daria Wojtala <sup>1</sup>, Edyta Dyguda-Kazimierowicz <sup>2</sup> ,  
Dariusz Bieńko <sup>2</sup> and Urszula Katarzyna Komarnicka <sup>1,\*</sup>

<sup>1</sup> Faculty of Chemistry, University of Wrocław, Joliot-Curie 14, 50-383 Wrocław, Poland; monika.lesiow@chem.uni.wroc.pl (M.K.L.); daria.wojtala@wp.pl (D.W.)

<sup>2</sup> Faculty of Chemistry, Wrocław University of Science and Technology, Wybrzeże Wyspiańskiego 27, 50-370 Wrocław, Poland; Edyta.Dyguda@pwr.edu.pl (E.D.-K.); dariusz.bienko@pwr.edu.pl (D.B.)

\* Correspondence: sandra.koziel@chem.uni.wroc.pl (S.A.K.); urszula.komarnicka@chem.uni.wroc.pl (U.K.K.)

**Abstract:** A group of cytotoxic half-sandwich iridium(III) complexes with aminomethyl(diphenyl) phosphine derived from fluoroquinolone antibiotics exhibit the ability to (i) accumulate in the nucleus, (ii) induce apoptosis, (iii) activate caspase-3/7 activity, (iv) induce the changes in cell cycle leading to G2/M phase arrest, and (v) radicals generation. Herein, to elucidate the cytotoxic effects, we investigated the interaction of these complexes with DNA and serum proteins by gel electrophoresis, fluorescence spectroscopy, circular dichroism, and molecular docking studies. DNA binding experiments established that the complexes interact with DNA by moderate intercalation and predominance of minor groove binding without the capability to cause a double-strand cleavage. The molecular docking study confirmed two binding modes: minor groove binding and threading intercalation with the fluoroquinolone part of the molecule involved in pi stacking interactions and the Ir(III)-containing region positioned within the major or minor groove. Fluorescence spectroscopic data (HSA and apo-Tf titration), together with molecular docking, provided evidence that Ir(III) complexes can bind to the proteins in order to be transferred. All the compounds considered herein were found to bind to the tryptophan residues of HSA within site I (subdomain II A). Furthermore, Ir(III) complexes were found to dock within the apo-Tf binding site, including nearby tyrosine residues.

**Keywords:** arene iridium(III) complexes; fluoroquinolones; DNA-binding studies; protein-binding studies; drug delivery; reactive oxygen species



**Citation:** Kozieł, S.A.; Lesiów, M.K.; Wojtala, D.; Dyguda-Kazimierowicz, E.; Bieńko, D.; Komarnicka, U.K. Interaction between DNA, Albumin and Apo-Transferrin and Iridium(III) Complexes with Phosphines Derived from Fluoroquinolones as a Potent Anticancer Drug. *Pharmaceuticals* **2021**, *14*, 685. <https://doi.org/10.3390/ph14070685>

Academic Editor: Annie Mayence

Received: 22 June 2021

Accepted: 13 July 2021

Published: 16 July 2021

**Publisher's Note:** MDPI stays neutral with regard to jurisdictional claims in published maps and institutional affiliations.



**Copyright:** © 2021 by the authors. Licensee MDPI, Basel, Switzerland. This article is an open access article distributed under the terms and conditions of the Creative Commons Attribution (CC BY) license (<https://creativecommons.org/licenses/by/4.0/>).

## 1. Introduction

There is a massive development in exploiting the medicinal properties of organometallic compounds in recent years, which have become an alternative to the clinically used anticancer drugs based on platinum (e.g., cisplatin, carboplatin, nedaplatin). These organometallic complexes with novel mechanisms of action have the ability to broaden the spectrum approach to tumors, reduce side effects, and overcome drug resistance [1–3]. The iridium(III) organometallic complexes have been rising stars and possess unique properties such as potential redox features, universal structure, wide range of ligand sub-stitution rates, higher cellular uptake efficiency, large stokes shifts and lower toxicity [4–8]. Moreover, because of the fundamental differences between the chemistry of iridium and platinum complexes, one can also expect diverse mechanisms of action [9]. Furthermore, combining two or even more multifunctional structural elements brings into play different properties of a compound and may result in improving the spectrum of biological activity, novel mechanisms of action, or modification of the pharmacokinetic profile of the drug [4–9]. For example, half-sandwich Ir(III) compounds containing phosphines derived from fluoroquinolones can be outstanding examples of this popular strategy of

combining structural elements currently being used to design new therapeutics. It is worth noting that quinolones are currently undergoing many structural modifications, including the formation of coordination compounds, aimed not only at overcoming the growing antibiotic resistance of microbes but also potential alternatives to established anticancer chemotherapeutic agents [10]. This paper is a continuation of our ongoing projects focused on cytotoxic activity of iridium(III) complexes bearing phosphines derived from fluoroquinolones: ciprofloxacin (HCp) [11], sparfloxacin (HSf) [12], lomefloxacin (HLm) [13], and norfloxacin (HNr) [11].

Since deoxyribonucleic acid plays a significant role in storing and expressing genetic information in a cell [13–15], it is the main target for several anticancer medicines, steroids, and several classes of drug [3]. Many small molecules exert their anticancer activities via binding with DNA, which usually causes damage to DNA in cancerous cells, inhibiting their division, and finally leading to cell death [1,3]. Moreover, most antibiotics and anticancer drugs tend to interact with DNA noncovalently through three selective modes: (i) A groove-bound fashion (minor or major grooves) stabilized by a mixture of hydrophobic, electrostatic, and hydrogen-bonding interactions; (ii) an intercalative association of planar, heteroaromatic moieties between the DNA base pairs and (iii) electrostatic binding [16]. Therefore, DNA-binding studies of Ir(III) complexes performed by us may be valuable in recognizing a specific site of interaction or conformation of deoxyribonucleic acid, which would help to understand the precise mode of their cytotoxic action.

Furthermore, there have been numerous reports on the investigation of interactions between serum proteins with metal complexes such as Cu<sup>II</sup> [17,18], Ru<sup>III</sup>, Ru<sup>II</sup> [19,20], Pt<sup>IV</sup>, or Pt<sup>II</sup> [21,22]. In general, linking proteins with metal complexes can change their biological activity. For example, some *in vitro* and *in vivo* studies have shown that treatment of cancer cells with albumin-NAMI-A or transferrin-NAMI-A adducts (NAMI-A: (ImH)[trans-RuCl<sub>4</sub>(dmsO)(Im)], Im is imidazole), resulting in a significant reduction in biological activity compared with the parent ruthenium complex [23]. On the other hand, the transfer of another ruthenium compound, KP1019 (trans-[tetrachlorobis(1H-indazole)ruthenate(III)]), to the cell was promoted by transferrin. Furthermore, cell fractionation studies showed that after only 2 h of exposure as much as 55% of the intracellular KP1019 was found in the nuclear fraction [24]. In this case, the biological activity increased significantly. Thus, investigating the binding of an anticancer drug with biomacromolecules is the first step to understanding the corresponding mechanism. In addition, the apparent volume of distribution and the rate of drug elimination are influenced by drug interactions at the protein binding level [25]. Biomacromolecules perform several significant functions necessary in normal biological processes that ensure their proper functioning, establishing them as an important field of research in chemistry and medicine.

Human serum albumin (HSA) is one of the most abundant proteins in plasma, accounting for 55–65% of all blood proteins. HSA is involved in the transport of metal ions and metal complexes with drugs through the bloodstream [13,26–28]. Additionally, albumin has shown remarkable promise as a carrier for anticancer agents based on several key characteristics: (1) The ability to extend the half-life of rapidly cleared medicines in the bloodstream; (2) the capability of interacting with different molecules that could be either peptidyl or non-peptidyl in structure; (3) increased uptake and metabolism by fast-growing, nutrient-starved cancer cells; (4) the potential to increase the uptake of the medicine by cancer cells; or, (5) on the other hand, slow down or prevent it from reaching the target tissues. Albumin is a remarkable carrier protein that has the potential to overcome barriers to the delivery of many promising anticancer agents. The report on plasma protein binding is currently accepted as an FDA (The United States Food and Drug Administration) requirement for the early screening of a potential therapeutic agent [21,29,30].

Transferrin (Tf) is responsible for the mobilization of iron by binding two Fe<sup>3+</sup> ions in sites containing two tyrosine residues, a single histidine and asparagine residues, and a carbonate ion, in an overall octahedral environment [31,32]. Transferrin (Tf) transports iron ions to virtually all tissues through the transferrin receptor (TfR, CD71), which is

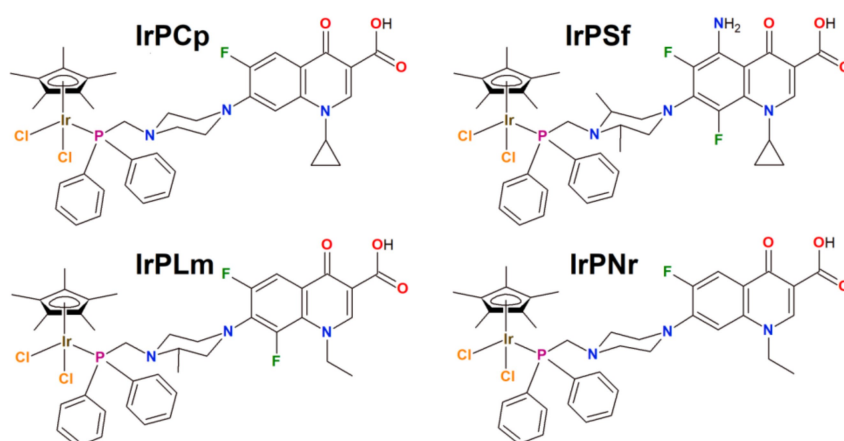
located on cell surfaces. Expression of the TfR is significantly upregulated in a variety of cancer cells, and in many cases, increased expression correlates with tumor stage and is associated with poor prognosis. It is expressed more abundantly in cancer tissues than in normal ones because of the higher iron demand for faster cell growth and division of the cancer cells [33–35]. Based on this fact, transferrin can be an attractive natural carrier for anticancer metal ions [21,36,37] and other chemotherapeutic drugs [38,39]. In blood serum, only 30% of transferrin remains in holo-form while 70% stays in its apo-form (apo-Tf) and can be utilized for binding various ions at the same specific sites as iron [16,34].

The information presented above encouraged our group to explore the interactions of DNA-iridium(III) complexes and protein-iridium(III) complexes in more detail. To realize our goal, we undertook a series of experiments: (i) We tested the ability of iridium(III) complexes to interact with DNA (intercalation, major or minor groove binding) using different methods, e.g., fluorescence spectroscopy, gel electrophoresis, and molecular docking; (ii) to monitor structural changes of DNA, circular dichroism (CD) study was performed; additionally, (iii) to evaluate the ability of studied complexes to HSA and apo-Tf binding, we applied different approaches based on fluorescence spectroscopy, circular dichroism (CD) and molecular docking.

## 2. Results and Discussion

### 2.1. Synthesis, Physicochemical and Biological Characterization

In this paper, we used four half-sandwich Ir(III) complexes (**IrPCp**—Ir(<sup>5</sup>-Cp\*)Cl<sub>2</sub>**PCp**, **IrPSf**—Ir(<sup>5</sup>-Cp\*)Cl<sub>2</sub>**PSf**, **IrPLm**—Ir(<sup>5</sup>-Cp\*)Cl<sub>2</sub>**PLm**, **IrPNr**—Ir(<sup>5</sup>-Cp\*)Cl<sub>2</sub>**PNr**, where Cp\* is pentamethylcyclopentadienyl) with phosphines conjugated with fluoroquinolones as ligands, which were synthesized according to the literature procedure described by our group in previous publications (Scheme 1) [11–14]. All complexes were precisely characterized by selected methods, i.e., absorption and fluorescence spectroscopies, ESI-MS, NMR, and electrochemical techniques.



**Scheme 1.** Organometallic iridium(III) complexes used in this study.

The products of all syntheses were recrystallized in order to obtain pure complexes. Their purity was confirmed using elemental analysis, while the single crystals were colored by the X-ray diffraction technique (Figure 1) [14]. Additionally, long-term stability monitoring was performed using UV-Vis spectroscopy in DMEM (Dulbecco's Modified Eagle's Medium) with 2% DMSO. During 72 h of incubation, no significant changes in the intensity and shape of the characteristic absorption band (MLCT) were observed.

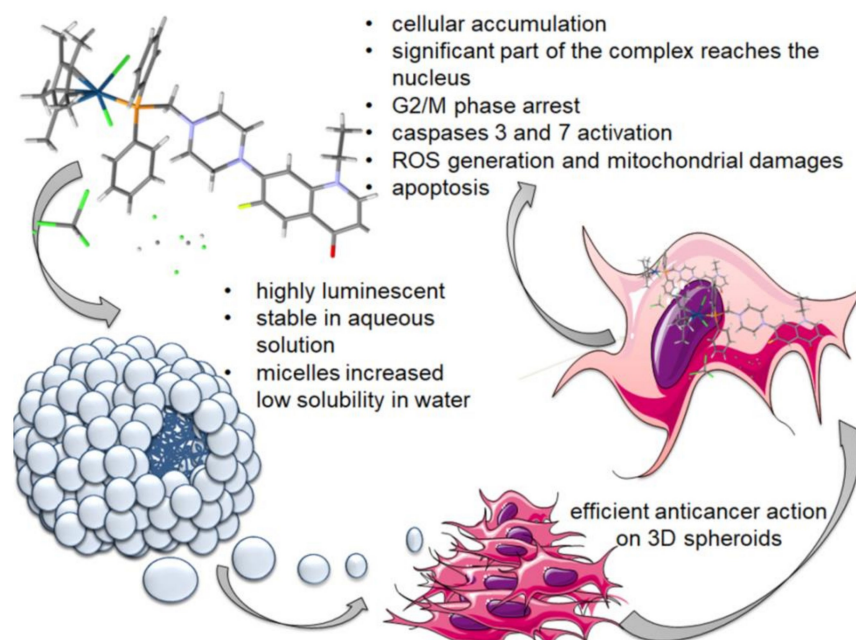


**Figure 1.** Scheme of cytotoxic action mechanism of Ir(III) complexes described by our group in a previous paper (Kozieł, S. et al., *Inorganic Chemistry Frontiers*, 2020, 7, 3386–3401).

It is noteworthy that the analysis of the luminescence spectra showed that **IrPCp**, **IrPNr** and **IrPLm** are characterized by a red luminescence. Only in the case of **IrPSf**, the blue luminescence was noticed. It should be noted that the complexes' fluorescent property provides useful information about the distribution, accumulation, and uptake of the anticancer drugs in living cells or organisms. In addition, we studied their cytotoxic effects in vitro toward selected cancer cell lines: CT26 (mouse colon carcinoma), A549 (human lung adenocarcinoma), MCF7 (human breast adenocarcinoma), PANC-1 (human pancreatic/duct carcinoma), DU-145 (human prostate carcinoma), and normal HEK293T (human embryonic kidney) cell line (Figure 1) [14].

We demonstrated in vitro that the studied complexes are characterized by lower  $IC_{50}$  values than cisplatin, exhibit the ability to induce apoptotic cell death in predominance, and possess a high therapeutic index. Additionally, preliminary investigation on the mode of action in the selected Ir(III) compounds allowed us to formulate the following conclusions: (i) Pearson's co-localization coefficient of 0.63 indicates a uniform distribution of complexes in both the nucleus and cytoplasm; (ii) the tested compounds presumably induce G2/M phase arrest; (iii) both the activation of caspase-3/7 and the decrease of mitochondrial membrane potential confirm the apoptotic pathway of cell death; and (iv) redox potentials enable efficient ROS generation [14]. Many aspects of cancer-inhibiting action displayed by iridium complexes are still unknown. For this reason, in previous [14] and current papers we are trying to understand their mode of action.

## 2.2. Interaction with DNA

### 2.2.1. Competitive Fluorescence Studies and DNA Degeneration

It is well known that the cytotoxic activity of various drugs (e.g., fluoroquinolones) depends on interaction with DNA [1]. Since we proved that investigated Ir(III) complexes can accumulate inside of the cancer nucleus, we decided to study the mode of Ir(III) complex-DNA interactions. Several well-known DNA binding dyes with well-established binding modes were used: ethidium bromide (EB; intercalation), 4<sup>0</sup>,6-diamidino-2-phenylindole (DAPI; binding to a minor groove), and methyl green (MG; binding to a major groove). The compounds that can bind to DNA more strongly than the above-mentioned binding dyes (EB, DAPI, or MG) reduce the DNA-binding dye emission due to the replacement of dye [40,41]. The emission spectra of the CT DNA-binding dye complex were mea-

sured at different concentrations of the investigated compounds, (Figure 2; Supplementary Materials, Figures S1–S4).

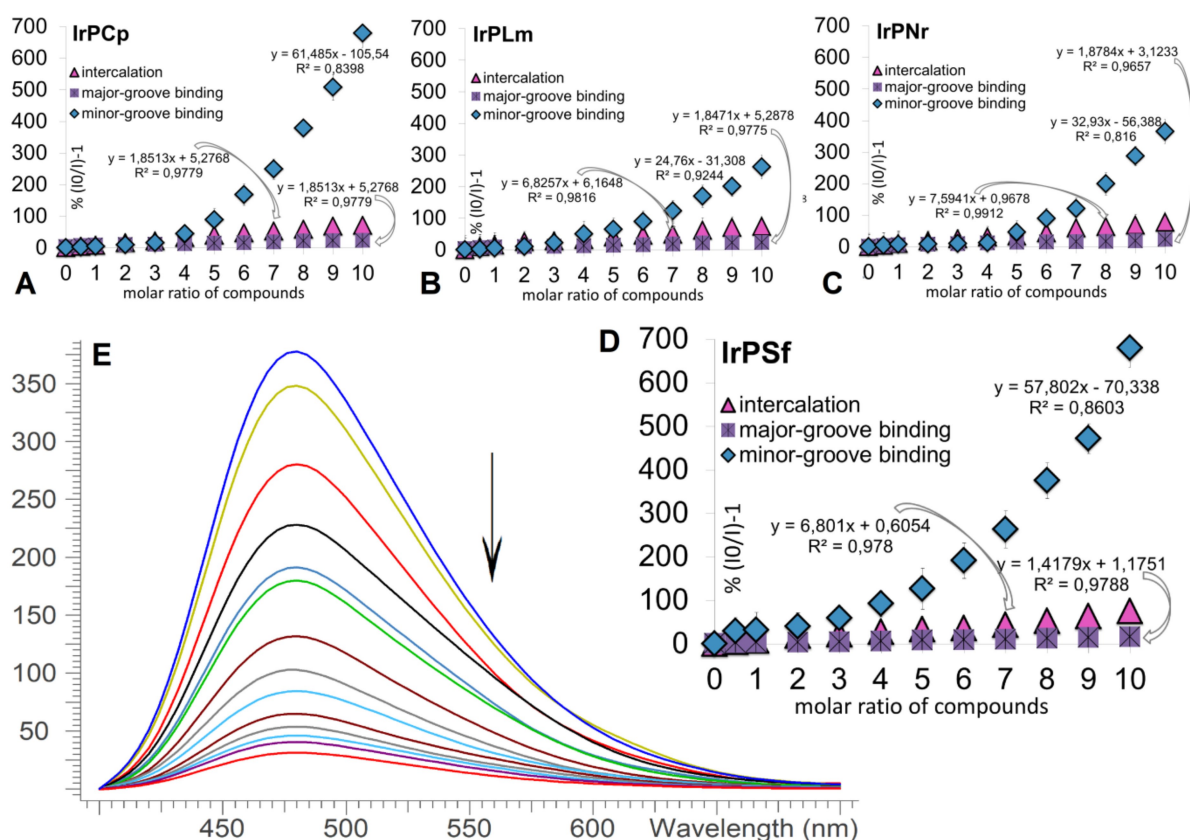


**Figure 2.** Stern–Volmer plots of the CT DNA-EB (intercalation), CT DNA-DAPI (binding to a minor groove) and CT DNA-MG (binding to a major groove), system quenched by (A) IrPCp; (B) IrPLm; (C) IrPNr; (D) IrPSf; ( $I_0$  and  $I$ —intensity of CT DNA-EB or DAPI or MG in the absence and the presence of increasing concentration [mM] of the compounds; (E) Fluorescence quenching of DAPI-DNA ( $C = 5 \cdot 10^{-5}$  M) by IrPSf (molar ratios 0.5–10) in 50 mM pH 7.4 phosphate buffer (axis: y—fluorescence intensity; x—wavelength).

The intensity of the CT DNA-EB, CT DNA-DAPI or CT DNA-MG characteristic emission band significantly decreased with increasing molar ratio (0.5–10) for all discussed compounds (IrPCp, IrPNr, IrPLm, IrPSf, PCp, PNr, PLm, PSf) (Supplementary Materials, Figures S1–S4). This observed fluorescence quenching indicates that studied compounds intercalated between DNA base pairs and are bound in a minor groove of DNA. Due to the negligible binding of the compounds to DNA through the major groove, the corresponding results will not be discussed in detail; however, spectra and  $K_{sv}$  values are presented in Supplementary Figure S4 and Table 1, respectively. Observed spectral changes clearly revealed that complexes exhibited multimodal DNA interaction with the predominance of minor groove binding. In order to confirm the quenching mechanism, the fluorescence quenching was analyzed according to Stern–Volmer equations; determined  $K_{sv}$  values are presented in Table 1.



**Table 1.** Determined  $K_{sv}$  values for the studied phosphines and Ir(III) complexes.

	$K_{sv}$ [M <sup>-1</sup> ]					
	Intercalation		Minor Groove Binding		Major Groove Binding	
	Ligands					
PCp	7.62	101	7.43	103	0.03	101
PNr	5.27	102	1.57	103	0.25	101
PLm	2.59	102	1.91	102	0.14	101
PSf	2.05	102	7.39	103	0.13	101
	Complexes					
IrPCp	1.42	103	1.23	104	3.25	101
IrPNr	1.54	103	8.25	103	0.46	101
IrPLm	1.48	103	6.25	103	2.13	101
IrPSf	1.51	103	1.36	104	0.41	101

Worthy of note is that all noncovalent interactions of iridium(III) complexes with DNA were stronger than the interactions of the corresponding phosphine ligands. Fluorescence quenching plots for CT DNA-EB complex showed that studied Ir(III) complexes tend to interact with negatively charged DNA phosphate chains. The strength of the compounds' interactions with DNA is similar for all complexes discussed (Figure 2; Supplementary Materials, Figure S1, Table 1). Notably, the trend in its ability to displace intercalator EB from CT DNA was different than in the case previously studied by our group regarding ruthenium(II) and copper(I) complexes based on the same phosphine ligands [11,13,41–44]. This trend suggests that the type of metal ions (Cu(I), Ru(II), Ir(III)) have a significant influence on the type and intensity of intercalations with DNA.

Furthermore, we conducted a similar competitive experiment using DAPI (Figure 3, and Figures S2 and S3 in Supplementary Materials). Observed fluorescence quenching of CT DNA-DAPI complex clearly indicates that iridium(III) complexes and their ligands are able to bind in the DNA minor groove. The displacement of bound DAPI from its binding site on CT DNA is much stronger than when EB is used. In order to confirm the quenching mechanism, the fluorescence quenching was analyzed according to Stern–Volmer equations (Figure 3A) and  $K_{DSV}$  (dynamic quenching constant) values, which are presented in Figure 3B. Based on Stern–Volmer plots (Figure 3A), the strength of CT DNA-DAPI fluorescence quenching formed the following order: **IrPSf > IrPCp > IrPNr > IrPLm**. This result suggests that from the perspective of more efficient binding in minor groove DNA, the presence of the cyclopropane substituent in the antibiotic structure plays a crucial role (Figure 3B).

Considering the results presented above, we can expect that the resulting complexes will not exhibit high genotoxicity, as opposed to previously reports of similarly mixed copper(I) or ruthenium(II) complexes bearing phosphines derived from fluoroquinolones [11,41–44] that exert high systemic toxicity related to strong intercalations with DNA.

Circular dichroism (CD) study was conducted to monitor the structural changes after the interaction of studied iridium(III) complexes with CT DNA. The CD spectrum of CT DNA exhibited two bands: a positive band at 276 nm (– base stacking) and a negative band appearing at 248 nm (helicity of B-DNA), Figure 4A–D [45]. The interaction between CT-DNA and complex molecules can be determined by the spectral variation of these two peaks. Upon groove binding or electrostatic binding modes, there will only be a slight spectral change in these two peaks since complex molecules do not exert a strong effect on the aggregation of DNA base pairs and DNA spiral. On the other hand, if complex molecules are inserted into DNA double helix chains, these two peaks will show noticeable spectral change [46,47]. After CT DNA titration by Ir(III) compounds, the bands slightly changed, which is consistent with the binding method suggested above—the predominance of minor groove binding. This slight change means that iridium(III) complexes did not

affect DNA structure. Furthermore, these results are fully consistent with those obtained using gel electrophoresis techniques (Figure 4E1–E3).

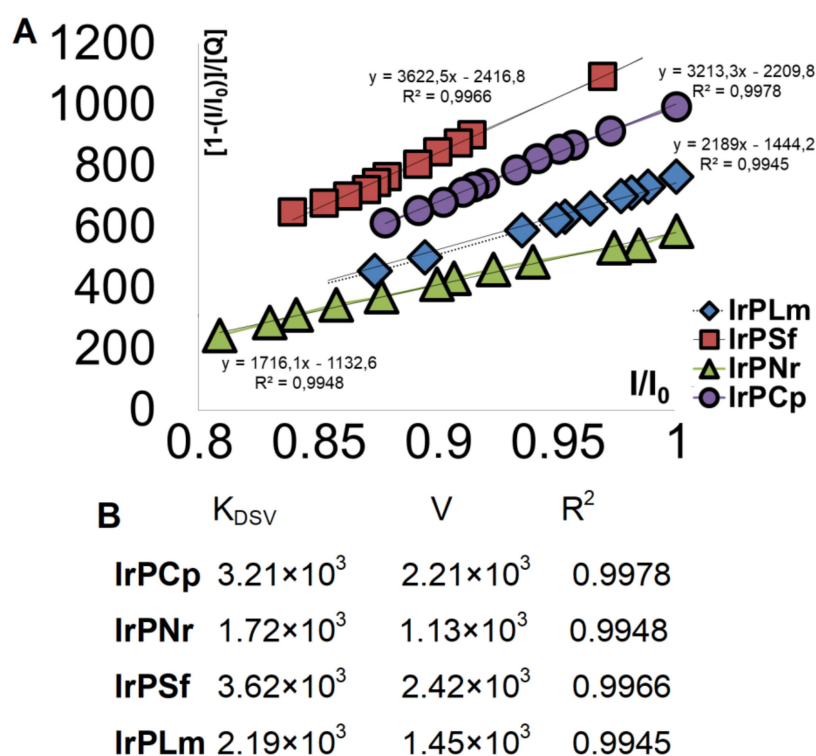


**Figure 3.** (A) Stern–Volmer plots of the CT DNA–DAPI (binding to a minor groove) system quenched by **IrPCp**, **IrPLm**, **IrPNr**, **IrPSf**; (B) determined  $K_{DSV}$  (dynamic quenching constant) values for the studied Ir(III) complexes.

We proved that our complexes exhibited multimodal DNA interaction (minor groove binding and intercalation). Since intercalation usually results in relatively large changes in the double helix structure, we assumed that all iridium(III) complexes cause severe DNA cleavage. The binding ability of iridium(III) complexes with another DNA model—pBR322 plasmid DNA, was studied by gel electrophoresis as a target. The degree of plasmid degradation, which is naturally present in a superhelical form (form I), to determine the ability of the compounds to induce single- and/or double-strand damage of the DNA was checked. This process can lead to the formation of the relaxed/nicked (form II) and linear (form III) forms. The degree of DNA degradation was determined in a wide range of the tested compounds' concentrations (from 10 to 500 M) at three different incubation times: 1 h, 4 h, and 24 h (Figure 4E1–E3).

In reality, iridium(III) complexes, the same as ligands, [11–13] did not cause damage to the double strand of DNA in a short incubation time (Figure 4E1,E2). It is worth noting that after only 24 h of incubation (Figure 4E3), these complexes were able to cause a single-strand plasmid cleavage. Our observation confirmed our previous results *vide supra* that these complexes can probably interact with DNA not only through intercalation but also different ways, e.g., covalent or different noncovalent interactions (electrostatic interactions and groove binding).

It is well-known that hydrogen peroxide is a source of hydroxyl radicals and a strong DNA oxidant in the presence of transition metal ions and their complexes, as we demonstrated in our previous studies focused on copper(I) complexes [48,49].



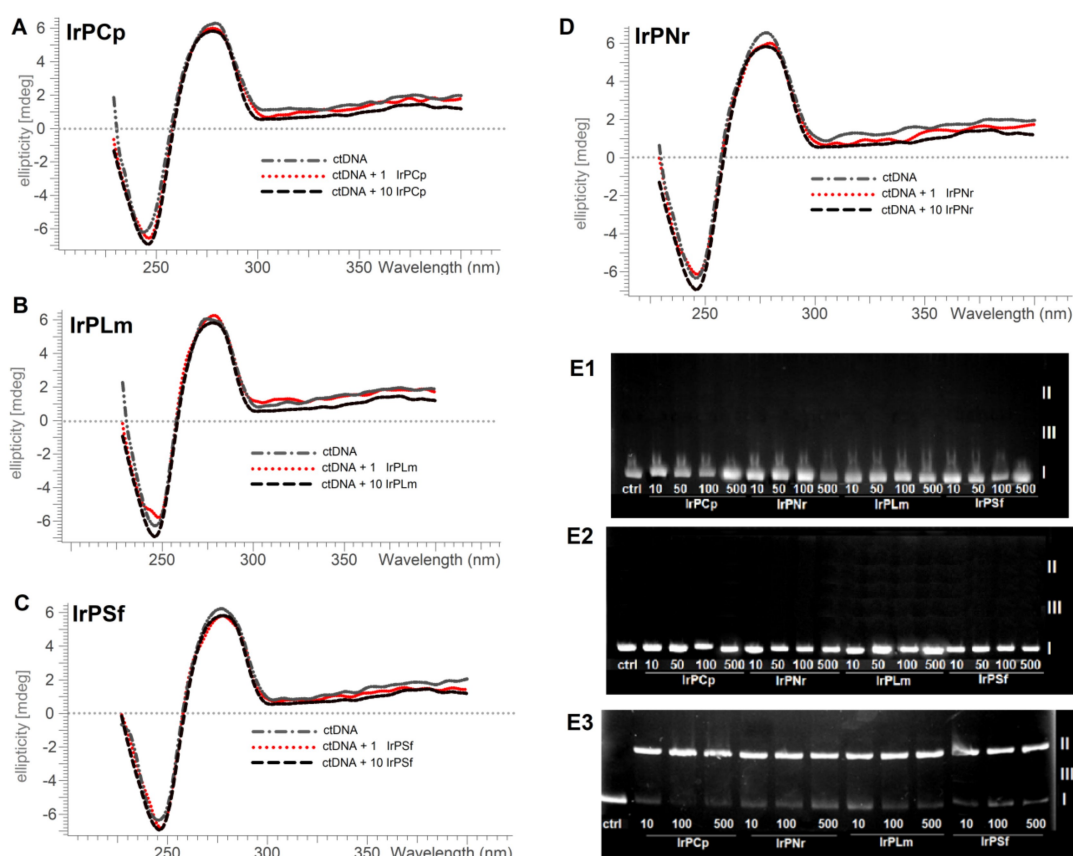


**Figure 4.** Circular dichroism spectra of CT DNA with: (A) IrPCp; (B) IrPLm; (C) IrPSf; (D) IrPNr; (E) agarose gel electrophoresis of pBR322 plasmid cleavage by IrPCp, IrPSf, IrPLm and IrPNr in a DMF (each in the 10% DMF) solution, ctrl: plasmid—control. (E1) 1 h of incubation; (E2) 4 h of incubation; (E3) 24 h of incubation.

It was proven by cyclic voltamperometry, and fluorescence spectroscopy that the studied herein Ir(III) compounds can generate high levels of ROS, therefore the effect of additional  $H_2O_2$  on the overall ROS production and the associated DNA damages caused by this radical pathway [14]. Furthermore, to confirm the generation of particular types of ROS involved in plasmid degradation, the experiment using DMSO (effective scavenger of OH), SOD (effective scavenger of  $O_2^-$ ), [50] and  $NaN_3$  (effective scavenger of  $^1O_2$ ) was performed [51]. In order to exclude the effect of the hydrogen peroxide influence on plasmid DNA degradation, we performed an additional gel electrophoresis for  $H_2O_2$  in different concentrations (Supplementary Materials, Figure S8).

All complexes in presence of hydrogen peroxide caused distinct changes in the plasmid structure, resulting in increased amounts of the nicked form (Figure 5A lines 3, 8, and Figure 5B lines 3, 8). When the hydroxyl radical inhibitor—DMSO—was added to the reaction mixtures, evident inhibition of the DNA damage was observed, suggesting the involvement of hydroxyl radical in the cleavage process (Figure 5A lines 4, 9, and Figure 5B lines 4, 9). Furthermore, slight inhibition of the DNA cleavage was observed in the other cases viz.,  $NaN_3$  (Figure 5A lines 5, 10, and Figure 5B lines 5, 10) and SOD (Figure 5A lines 6, 11, and Figure 5B lines 6, 11) validating the presence of singlet oxygen and superoxide anion radical, respectively.

Overall, the investigated complexes (IrPCp, IrPNr, IrPLm, IrPSf) are not presumably capable of double-strand plasmid damage leading to the formation of a linear form of plasmid (form III). Since it is well-known that cancer cells show obstinately high levels of intracellular ROS that can be involved in iridium-based redox reactions (Ir(III)/(IV) complexes), DNA oxidative damage by radicals cannot be excluded. However, any oxidative DNA damages are not desirable for any new chemotherapeutics, as they may contribute to

overall genotoxicity [48]. The low level of damage of genetic material should be considered a privilege of these new complexes.

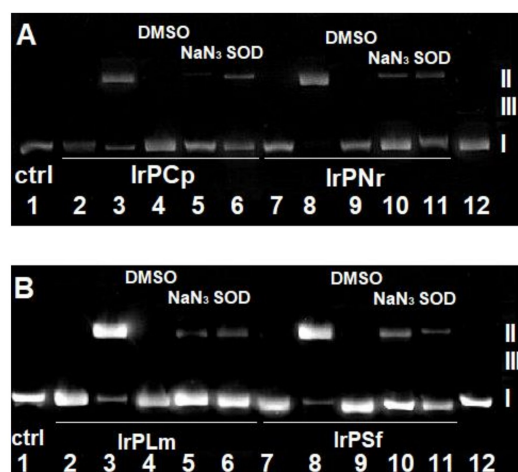


**Figure 5.** Agarose gel electrophoresis of pBR322 plasmid cleavage by: **(A)** IrPCp and IrPNr. Lanes: 1, plasmid control; 2, plasmid + 50 M IrPCp; 3, plasmid + 50 M IrPCp + 50 M H<sub>2</sub>O<sub>2</sub>; 4, plasmid + 50 M IrPCp + 50 M H<sub>2</sub>O<sub>2</sub> + DMSO; 5, plasmid + 50 M IrPCp + 50 M H<sub>2</sub>O<sub>2</sub> + 0.1 M NaN<sub>3</sub>; 6, plasmid + 50 M IrPCp + 50 M H<sub>2</sub>O<sub>2</sub> + 0.62 M SOD; 7, plasmid + 50 M IrPNr; 8, plasmid + 50 M IrPNr + 50 M H<sub>2</sub>O<sub>2</sub>; 9, plasmid + 50 M IrPNr + 50 M H<sub>2</sub>O<sub>2</sub> + DMSO; 10, plasmid + 50 M IrPNr + 50 M H<sub>2</sub>O<sub>2</sub> + 0.1 M NaN<sub>3</sub>; 11, plasmid + 50 M IrPNr + 50 M H<sub>2</sub>O<sub>2</sub> + 0.62 M SOD; 12, plasmid + DMF; **(B)** by IrPLm and IrPSf. Lanes: 1, plasmid control; 2, plasmid + 50 M IrPLm; 3, plasmid + 50 M IrPLm + 50 M H<sub>2</sub>O<sub>2</sub>; 4, plasmid + 50 M IrPLm + 50 M H<sub>2</sub>O<sub>2</sub> + DMSO; 5, plasmid + 50 M IrPLm + 50 M H<sub>2</sub>O<sub>2</sub> + 0.1 M NaN<sub>3</sub>; 6, plasmid + 50 M IrPLm + 50 M H<sub>2</sub>O<sub>2</sub> + 0.62 M SOD; 7, plasmid + 50 M IrPSf; 8, plasmid + 50 M IrPSf + 50 M H<sub>2</sub>O<sub>2</sub>; 9, plasmid + 50 M IrPSf + 50 M H<sub>2</sub>O<sub>2</sub> + DMSO; 10, plasmid + 50 M IrPSf + 50 M H<sub>2</sub>O<sub>2</sub> + 0.1 M NaN<sub>3</sub>; 11, plasmid + 50 M IrPSf + 50 M H<sub>2</sub>O<sub>2</sub> + 0.62 M SOD; 12, plasmid + DMF.

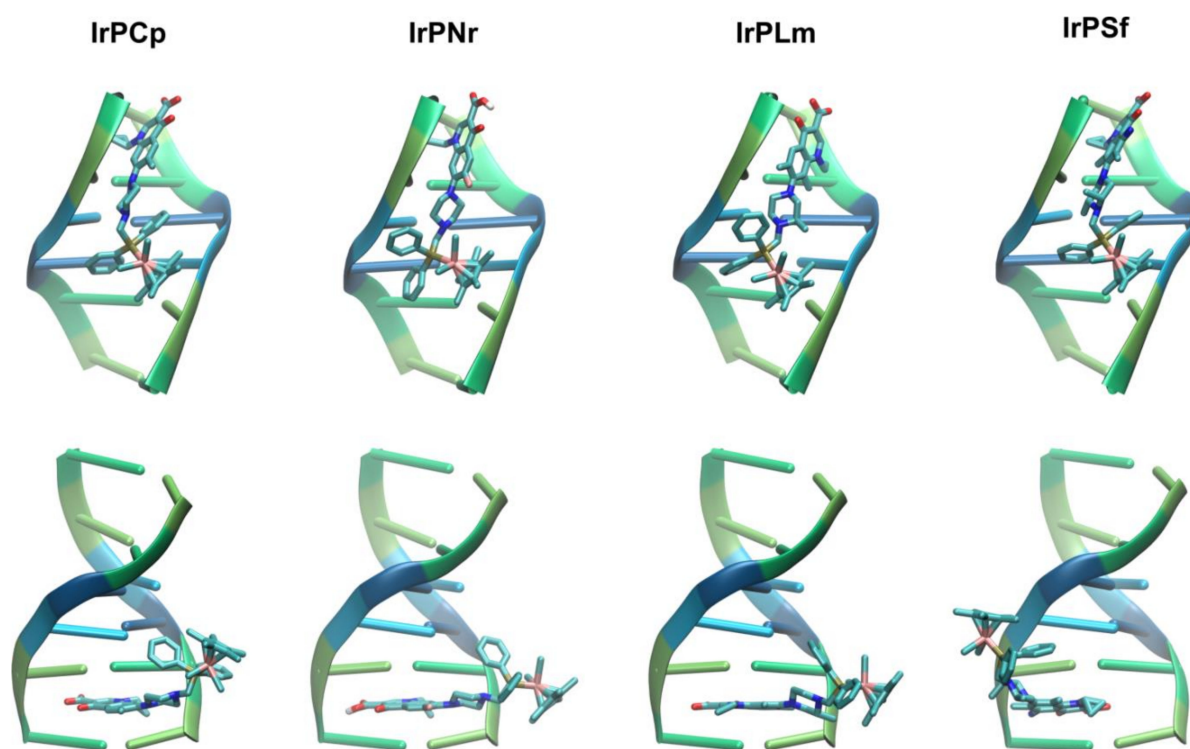
### 2.2.2. Molecular Docking Study of the Interactions between DNA and Ir(III) Complexes

The binding poses obtained from docking simulations performed for each of the metal complexes studied herein were clustered with a 2 Å RMSD threshold. Considering that the absolute value of the difference in the lowest binding energy associated with any pair of clusters is below 2.8 kcal/mol, which is close to the standard deviation of AutoDock force field [52] employed for scoring, analysis of the results was essentially based on the cluster size. About 30 clusters of binding poses were obtained for particular ligands (28, 30, 27, and 31 for IrPCp, IrPNr, IrPLm, and IrPSf, respectively).

Two binding modes were obtained overall, including minor groove binding and threading intercalation with the fluoroquinolone part of the molecule involved in pi stacking interactions and the Ir(III)-containing region positioned within the major or minor groove. The majority of the binding poses correspond to minor groove binding followed by intercalation coupled with major groove binding (Table 2). At most, 17% of the total number of binding poses exhibited threading intercalation accompanied by minor groove binding. The representative structures associated with both of the prevailing binding modes are presented in Figure 6.

**Table 2.** The percentage of binding poses representing the particular binding mode in DNA-phosphino iridium(III) complexes for all the docking results (“All clusters”) or the largest clusters (“Clusters with at least six members”).

	IrPCp		IrPNr		IrPLm		IrPSf	
	All Clusters	Clusters with at Least 6 Members	All Clusters	Clusters with at Least 6 Members	All Clusters	Clusters with at Least 6 Members	All Clusters	Clusters with at Least 6 Members
Minor groove binding	47%	59%	48%	42%	60%	89%	47%	81%
Intercalation ion and major groove binding	41%	41%	44%	58%	34%	11%	36%	19%
Intercalation ion and minor groove binding	12%	-	8%	-	6%	-	17%	-
Number of binding poses	100	61	100	53	100	53	100	37

**Figure 6.** Representative structures of the binding modes of DNA-phosphinoiridium(III) complexes: top, minor groove binding; and bottom, threading intercalation.

Since numerous clusters featured a limited number of members, suggesting that a particular binding mode is significantly less likely, we performed a similar analysis using the clusters encompassing at least six members (Table 2). Focusing on the largest clusters further reinforced the conclusion of dominant minor groove binding and major groove binding-coupled intercalation, as no binding poses were found representing intercalation with the Ir(III) part of the complex positioned within the minor binding groove. Except for DNA-IrPNr complexes, minor groove binding appears to be predominant. In particular, the dual binding mode of intercalation associated with major groove binding might account for as little as 11% in the case of DNA-IrPLm complexes (Table 2). Interestingly, DNA-IrPNr complexes described in the most populated clusters appear to favor intercalation and major groove binding over the minor groove binding, which may be linked to the highest value of Ksv for intercalation of this particular ligand compared with the remaining phosphinoiridium(III) compounds (Table 1). It was concluded from the analysis of Ksv

values that major groove binding is also present in the complexes studied herein, albeit to a modest extent. While no major groove binding was observed in the docking results, the positioning of the Ir(III) part of the intercalated ligands in the major binding groove may explain the experimental findings. Overall, the docking results appear to be in agreement with the K<sub>sv</sub> values, supporting multimodal binding of Ir(III) complexes with the prevalence of minor groove binding.

### 2.3. Possible Reaction with Proteins

#### 2.3.1. Human Serum Albumin Interaction Study

Interest in studying the interaction of metal ions and their compounds with blood plasma proteins, especially with serum albumin (HSA), the most abundant protein in plasma involved in the transport of drugs through the bloodstream, is increasing [27,53]. This molecule has two main binding sites: site I is located in subdomain IIA and site II is located in subdomain IIIA. However, only the first binding site contains tryptophan residue that possesses intrinsic fluorescence—Trp-214 residue (with an excitation wavelength of 295 nm) [54,55]. Changes in the appearance of the Trp-214 residue emission band in HSA, in the presence of the tested compounds, may indicate changes in the protein's conformation, the association of its subunits or denaturation, or the binding of the compound to protein [53,56]. For all the tested compounds (except phosphine ligands) with an increase of concentrations, the intensity of the HSA emission band at 342 nm gradually decreased with the simultaneous appearance of an additional fluorescence band with an emission maximum at 425 nm (Figure 7, Supplementary Figure S5) that can be assigned to the fluorescence from the starting complexes or new system HSA-Ir(III) complex.

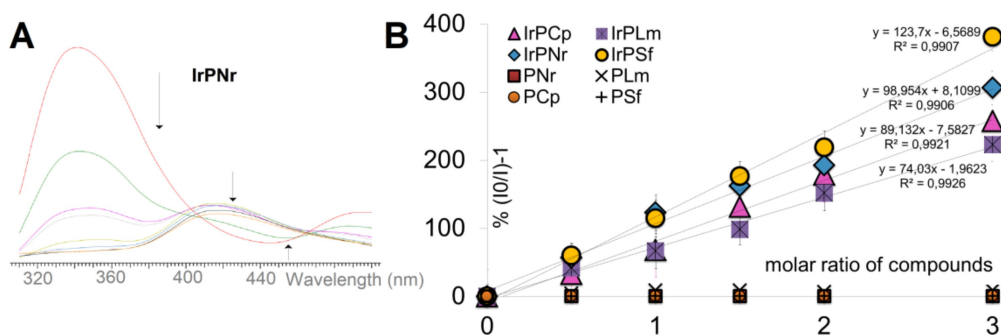


**Figure 7.** (A) Fluorescence quenching of HSA ( $C = 5 \cdot 10^{-5}$  M) by IrPNr, (molar ratios 0.5, 1, 1.5, 2, 3, 4, 5, 6) in 50 mM pH 7.4 phosphate buffer; (B) Stern–Volmer plots of HSA ( $C = 10$  M) quenching by PCp, PNr, PSf, PLm, IrPCp, IrPNr, IrPSf, IrPLm ( $I_0$  and  $I$ —intensity of HSA in the absence and presence of the increasing amounts of the compounds, respectively).

Changes in the intensity and shift of the band maximum toward longer wavelengths indicate the strong interaction of each complex with HSA, increased polarization in the area surrounding the tryptophan residue and/or the energy transfer between the tested compounds and HSA [13]. The strength of albumin quenching can be presented in the following order: IrPSf > IrPLm > IrPCp > IrPNr (Figure 7, K<sub>sv</sub> values, Table 3). This phenomenon can be related to the presence of additional fluorine atoms in the quinolone moiety and methyl group attached to the piperazine ring. Furthermore, the affinity of HSA for all the considered Ir(III) complexes with fluoroquinolone derivatives is much higher than for copper(I) complexes with the same organic derivatives [11,13,41–43]. It is noteworthy that the tendency of the strength of HSA quenching is different from observations for all complexes (Cu(I) and Ru(II)) with the same phosphines derived from fluoroquinolones [11,41–44].

**Table 3.** Determined  $K_{sv}$  values for the studied phosphines and Ir(III) complexes.

$K_{sv}$ [ $M^{-1}$ ]			
PCp	0.21 $10^1$	IrPCp	2.08 $10^6$
PSf	0.11 $10^1$	IrPSf	5.67 $10^6$
PLm	0.53 $10^1$	IrPLm	5.06 $10^6$
PNr	0.19 $10^1$	IrPNr	6.98 $10^5$

### 2.3.2. Molecular Docking Study of the Interactions between Human Albumin and Ir(III) Complexes

The largest clusters obtained from the docking of particular Ir(III) complexes either correspond to the lowest binding energy structures (59 and 33-member clusters for **IrPNr** and **IrPLm**, respectively) or differ by at most 0.5 kcal/mol from the lowest binding energy observed within a given cluster (27 and 37 member clusters for **IrPCp** and **IrPSf**, respectively). Considering the significant difference in the size between the first and remaining clusters for each of the compounds studied herein (i.e., the size of the second largest cluster constituting about 56, 27, 21, and 32% of the number of members in the first largest cluster of **IrPCp**, **IrPNr**, **IrPLm**, and **IrPSf**, respectively), the most probable binding mode was associated with the representative structure of the largest cluster.

The binding mode of particular complexes is presented in Figure 8. All the compounds considered herein were found to bind up to 5 Å of Trp214 residues. In the case of **IrPLm**, **IrPNr**, and **IrPSf**, the shortest distance to Trp214 is equal to 2.91, 3.24, and 3.54 Å, respectively, whereas **IrPCp**-Trp214 separation amounts to 4.94 Å. Presumably, such a distance is short enough to affect the experimentally observed fluorescence quenching of Trp214. Despite the longer distance to Trp214 residue characterizing the **IrPCp** complex, all four complexes appear to occupy the same region of the binding site located in HSA subdomain IIA (see the left side panel in Figure 8).

**IrPCp**, **IrPNr**, and **IrPLm** feature similar binding modes with the Ir(III) core located at the entrance of the binding pocket and fluoroquinolone part buried deeply in the binding site. This binding mode facilitates the formation of at least two hydrogen bonds. In particular, the hydrogen bond between the oxygen atom present in the quinolone moiety and Arg218 residue was observed in all three complexes (see the right-side panel in Figure 8 for a close-up view of interactions). Another hydrogen bond might occur between the compound carboxylate group and His242 (**IrPNr** and **IrPLm**) or Arg257 residue (**IrPCp**). In the case of the **IrPNr** complex, the quinolone oxygen atom could also be hydrogen-bonded to Lys199 residue. Possible hydrophobic interactions may occur between the phenyl ring of phosphine ligand in **IrPCp**, **IrPNr**, **IrPLm** complexes and Pro447, Cys448, and Cys437 residues.

Unlike the three complexes discussed above, **IrPSf** binds in the opposite way, i.e., with the Ir(III) part buried in the binding pocket. Accordingly, the hydrogen-bonding pattern observed in **IrPCp**, **IrPNr**, and **IrPLm** complexes are no longer possible, as the molecule region surrounding Ir(III) core is essentially nonpolar. However, the fluoroquinolone moiety can still be engaged in hydrogen-bonding with Lys444 and Asp451 residues. The nonpolar cyclopentadienyl ligand is surrounded by the hydrophobic patch of Cys200, Cys245, Cys246, and Cys253 residues.

Despite the presumably different binding mode of **IrPSf**, a similar number of interactions characterizing binding of all the iridium complexes analyzed herein appears to be in line with the experimental results demonstrating minor differences in the binding strength of these compounds. Moreover, the distinct binding mode of the **IrPSf** complex might account for the strongest binding of this particular compound, as shown in the fluorescence quenching experiment.



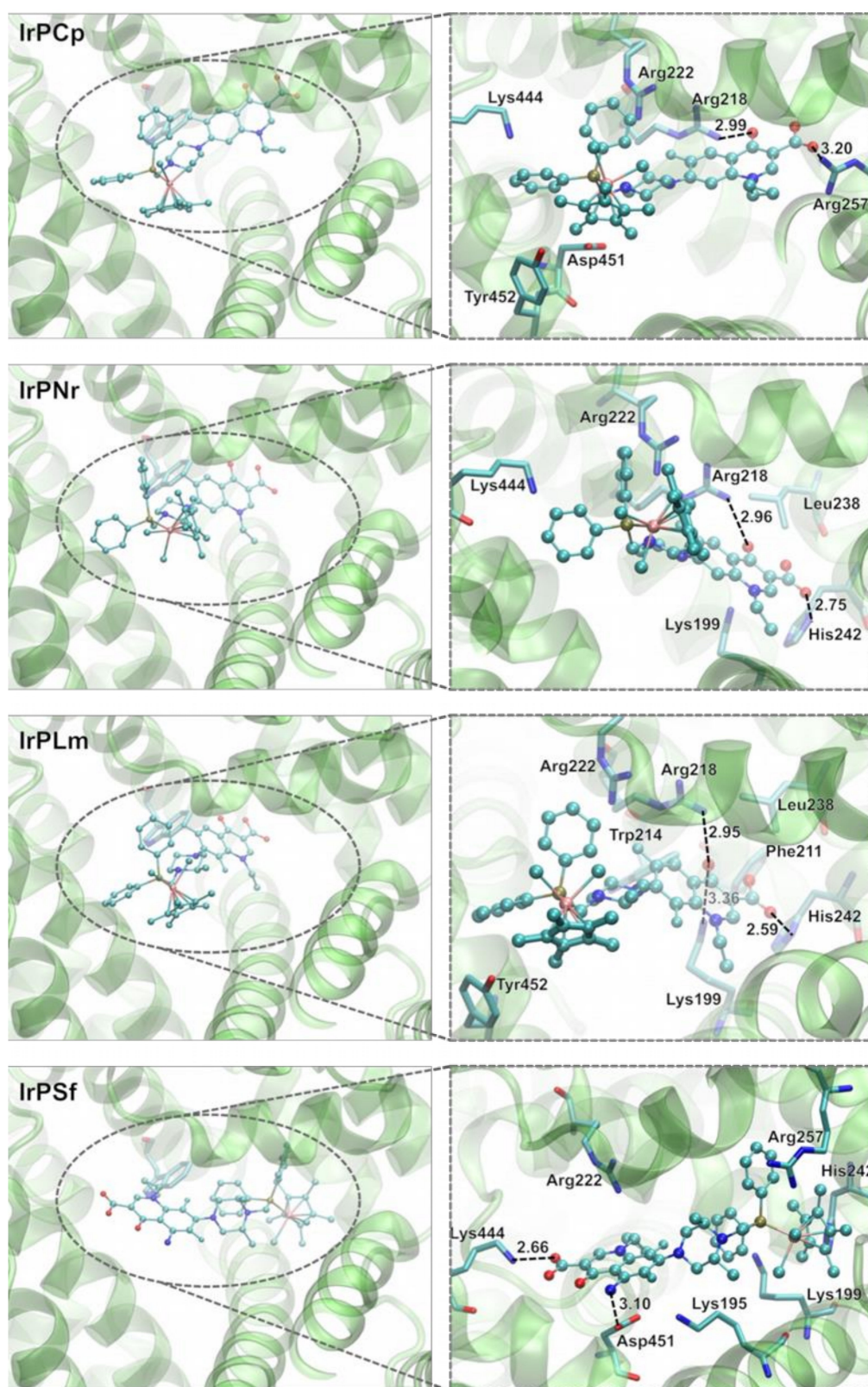


**Figure 8.** Binding mode of HSA-phosphinoiridium(III) complexes. The docked compounds are shown in ball-and-stick representation. Trp214 residue is shown in stick representation in the panels on the left side. In the right side panels are all the HSA residues within 3 Å of the metal complexes. The selected distances are given in Å. Hydrogen atoms are not shown for clarity.

### 2.3.3. Apo-Transferrin Interaction Study

Interactions between Ir(III) complexes and their parent fluoroquinolones-based ligands with the second selected transporter protein, apo-transferrin (apo-Tf), were studied in detail. The protein apo-Tf has been recently considered and investigated as a possible transporter of metal complexes [57].

A solution of apo-Tf was titrated with increasing concentrations of all the tested compounds, and the fluorescence intensity of apo-Tf was monitored spectrophotometrically (Figure 9A; Supplementary Materials, Figures S6 and S7). At the same time, Ksv values were determined from Stern–Volmer plots (Figure 9B, Table 4). The fluorescence intensity of apo-Tf at 343 nm decreased gradually, suggesting that investigated compounds can penetrate the apo-transferrin structure and interrupt the tryptophan's microenvironment.

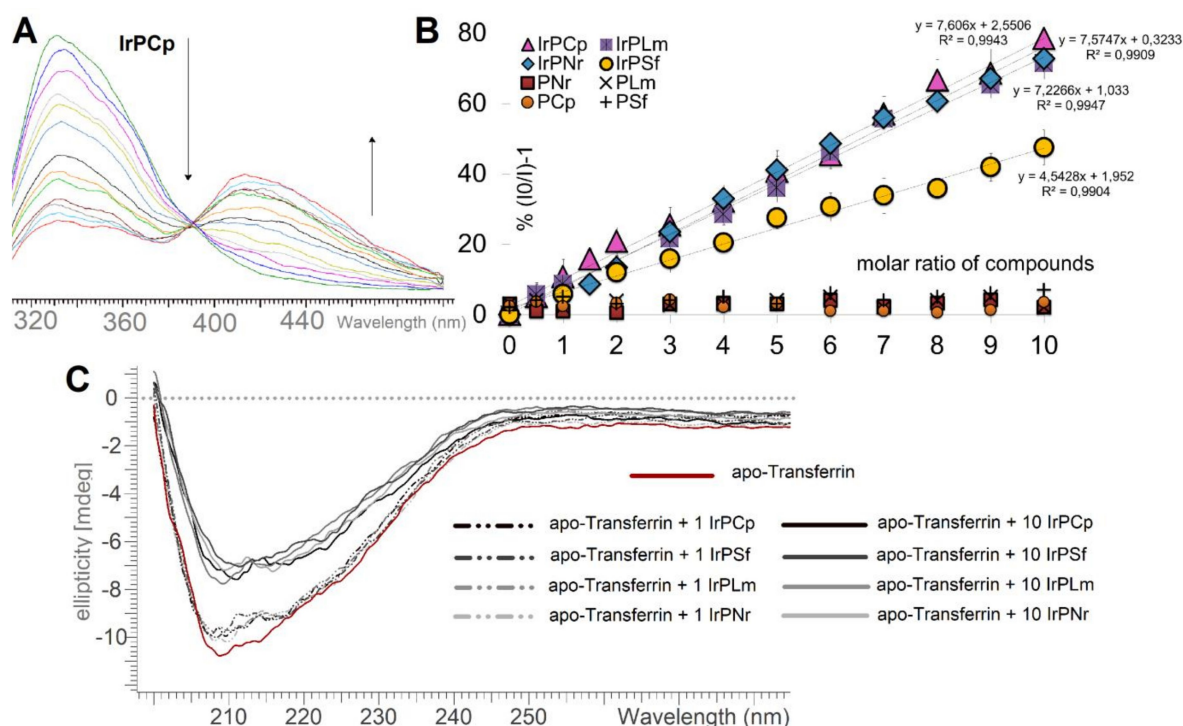


**Figure 9.** (A) Fluorescence quenching of apo-Tf ( $C = 3.6 \cdot 10^{-6}$  M) by IrPCp (molar ratios 0.5, 1, 1.5, 2, 3, 4, 5, 6, 7, 8, 9, 10) in 50 mM pH 7.4 phosphate buffer; (B) Stern–Volmer plots of apo-Tf ( $C = 3.6$  M) quenching by IrPCp, IrPNr, IrPSf, IrPLm, PCp, PNr, PSf, PLm ( $I_0$  and  $I$ —intensity of HSA in the absence and presence of the increasing amounts of the compounds, respectively); (C) Circular dichroism spectra of apo-transferrin with Ir(III) complexes.

**Table 4.** Determined Ksv values for the interactions of studied phosphine and Ir(III) complexes.

	Ksv [ $M^{-1}$ ]		
PCp	$0.45 \cdot 10^1$	IrPCp	$2.18 \cdot 10^4$
PSf	$1.10 \cdot 10^4$	IrPSf	$1.32 \cdot 10^4$
PLm	$1.52 \cdot 10^2$	IrPLm	$1.99 \cdot 10^4$
PNr	$4.56 \cdot 10^1$	IrPNr	$2.02 \cdot 10^4$

Furthermore, as depicted in Table 4, the Ksv for all complexes ranged from  $1.32 \cdot 10^4$  to  $2.18 \cdot 10^4 M^{-1}$ . Thus the interaction between Ir(III) complexes and apo-Tf follows a static quenching mechanism. The strength of apo-Tf fluorescence quenching by complexes can be presented in the following order: IrPCp > IrPNr > IrPLm > IrPSf. Among all studied complexes, IrPSf was the least efficient in interactions with apo-Tf; this can be explained by the most extensively substituted structure of sparfloxacin, which contains the largest number of substituents among all studied antibiotics. In-depth analysis of



Stern–Volmer plots leads to conclusion that from the perspective of more efficient binding to apo-Tf, the absence of the methyl group substituent in the piperazine motif plays a crucial role. Moreover, the complexes interact with apo-transferrin more strongly than organic derivatives.

In order to monitor Ir(III) complex binding, CD spectra of apo-transferrin were recorded (Figure 9C) where three regions—visible (320–600 nm), aromatic (230–320 nm), and intrinsic (180–260 nm)—deliver different information about protein structure [58]. The bands in the CD spectrum of apo-transferrin in the 230–320 nm (aromatic) range are attributed to the optical activity of tyrosine and tryptophan residues. As in HSA, the dichroism in the intrinsic region (180–260 nm) of apo-transferrin is related to secondary structure [59]. Changes in this region of the spectrum when the protein is incubated with metal complexes indicate that the drugs affect the conformation. The presented results (Figure 9C) indicate that a 10-fold excess of the Ir(III) complexes did not alter the helical structure of the protein. These results may be of great importance since transferrin needs to be recognized by specific receptors to be delivered into the cells. Given that two tyrosine residues are directly involved in the binding of iron, and tryptophan residue is in close proximity [31,32], it is reasonable to assume that the studied Ir(III) complexes are binding at the specific binding sites for Fe<sup>3+</sup> ions (see Figure 9C).

Remarkably, the interactions of Ir(III) complexes with studied proteins revealed a diverse mode of the fluorescence quenching, as determined orders of quenching altered differently—HSA: **IrPSf** > **IrPLm** > **IrPCp** > **IrPNr**; apo-Tf: **IrPCp** > **IrPNr** > **IrPLm** > **IrPSf**. This diverse mode suggests that different parts of the complexes and different interactions are probably responsible for the emission quenching of HSA and apo-Tf.

#### 2.3.4. Molecular Docking Study of the Interactions between Apo-Transferrin and Ir(III) Complexes

All the predictions regarding possible apo-Tf binding pockets yielded relatively consistent results encompassing four binding sites presented in Figure 10. In particular, binding pockets #1 and #3 correspond to iron-binding sites located in C- and N-lobes of apo-Tf, and the #2 binding pocket is positioned at the interface between the two lobes, whereas the #4 binding pocket is located in the proximity of the C-lobe iron-binding site. Remarkably, all four binding pockets involve nearby tyrosine or tryptophan residues that can be disturbed by binding of the metal complex.

Ir(III) complexes were found to dock within all four binding sites considered herein. The lowest interaction of energy characterized binding poses was determined for the #2 pocket. All the compounds docked in this particular binding site consistently yielded a lower binding energy value by approximately 3 kcal/mol compared to the binding poses established for the remaining binding pockets. This fact suggests that the binding of iridium(III) complexes is the most favorable in the case of the #2 pocket, but other binding modes are also possible. Considering that the binding energy difference between the #2 pocket and the remaining predicted binding sites exceed the standard deviation of AutoDock force field [52] used for ranking the complexes, #2 pocket binding modes will be discussed in further detail. By pursuing the same reasoning as the HSA docking results, the most plausible binding poses were assumed to be associated with the largest cluster obtained for particular Ir(III) complexes.

Noticeably, the largest clusters were either found to feature the lowest binding energy (27 and 31 member clusters of **IrPNr** and **IrPSf** compounds, respectively) or to differ by 1.7 kcal/mol at most from the lowest energy cluster (which is well within the 2.5 kcal/mol standard deviation of AutoDock force field [52]), as observed in the case of the 34 member cluster of **IrPLm**. The largest cluster obtained of the apo-Tf-**IrPCp** complex consisted of 31 members, closely followed by the second largest cluster at 25 members, featuring a similar binding mode and energy. The difference in the binding energy that characterizes these two clusters and the lowest energy cluster obtained for the apo-Tf-**IrPCp** complex does not exceed 1 kcal/mol, further justifying the choice of this particular binding mode.

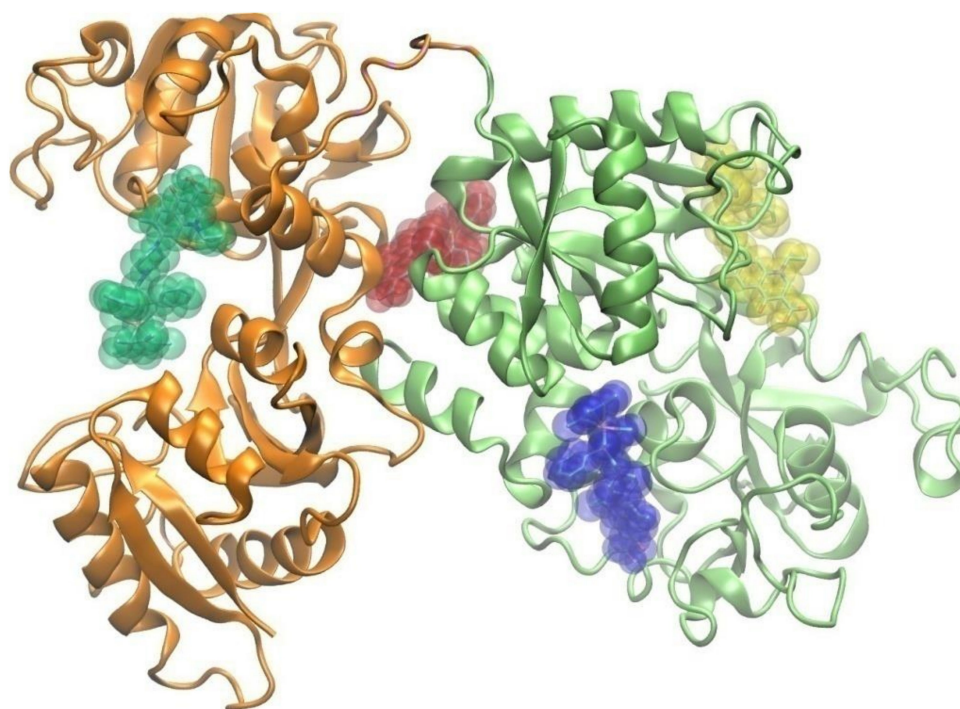


**Figure 10.** The predicted binding pockets within apo-Tf structure. The N- and C-lobes of apo-Tf are shown in orange and light green colors. The location of #1, #2, #3, and #4 binding sites is specified by the docked **IrPCp** shown in blue, red, yellow, and dark green colors, respectively.

The representative structures of the largest clusters obtained for iridium(III) complexes occupying the #2 binding pocket are demonstrated in Figure 11. All the docked compounds are wedged between Tyr317 and Tyr647 residues. In the prevalent binding mode featured by **IrPCp**, **IrPLm**, and **IrPSf** compounds, the shortest distances between fluoroquinolone moiety and Tyr317 residue are equal to 2.11, 2.00, and 1.77 Å, respectively. The shortest separation between the metal core of these complexes and Tyr647 residue is within the 3.2–3.8 Å range. **IrPNr** complex is oppositely positioned to the remaining compounds, with the fluoroquinolone part–Tyr647 distance of 2.00 Å and the metal core separated by 3.46 Å from Tyr317 residue. At least three hydrogen bonds can be formed in the binding mode displayed by **IrPCp**, **IrPLm**, and **IrPSf**. The oxygen atoms present in the fluoroquinolone moiety are prone to hydrogen-bonding interactions with the side chain of Arg677 and the backbone nitrogen atom of Tyr317 residues, whereas Asp240 residue is positioned close enough to certain nitrogen atoms of a piperazine ring, facilitating the formation of another hydrogen bond. The amino group of the **IrPSf** fluoroquinolone part might engage in an additional hydrogen bond with Glu318 residue (see Figure 11). The hydrophobic interactions of **IrPCp**, **IrPLm**, and **IrPSf** compounds may be mediated by Cys402, Leu404, Val405, Met382, and Cys674 residues positioned within 4 Å of particular metal complexes. The distinct binding mode of **IrPNr** features two possible hydrogen-bonding interactions between oxygen-bearing fluoroquinolone moiety and Lys401 residue (Figure 11). Nonpolar residues close enough to participate in hydrophobic interactions with **IrPNr** include Cys227, Leu228, and Cys241 residues.

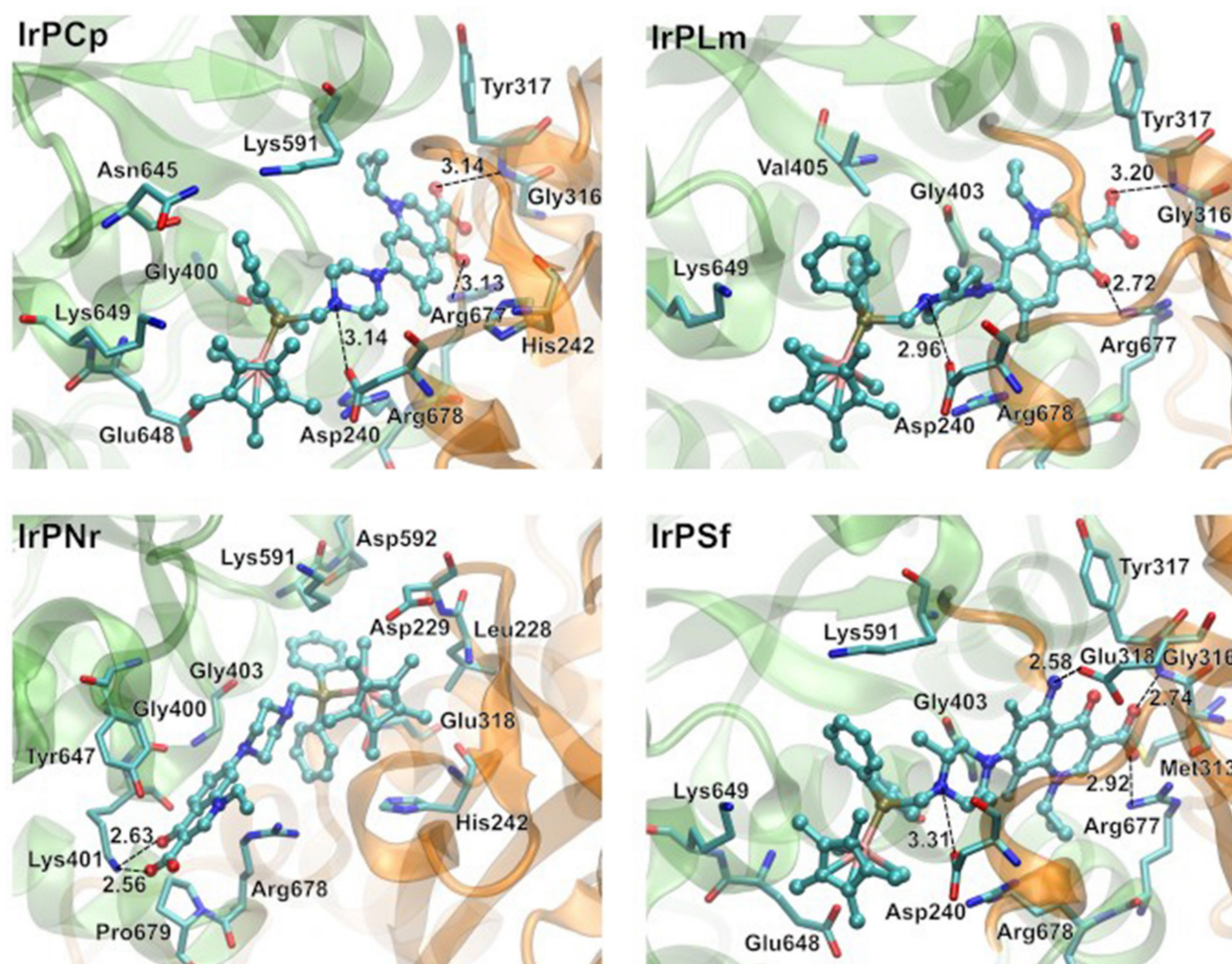


**Figure 11.** Binding mode of apo-Tf-complexes within the #2 binding pocket. The docked compound's molecules are shown in ball-and-stick representation. All the apo-Tf residues within 3 Å of the metal complexes are presented in stick representation. The selected distances are given in Å. Hydrogen atoms are not shown for clarity.

Overall, the binding mode of the representative structures from the largest clusters of the #2 binding pocket might indicate the strongest binding of **IrPSf** featuring an additional hydrogen bond to amino substituent at the fluoroquinolone aromatic rings. Although this conclusion is not exactly supported by the experimental data demonstrating the weakest binding of **IrPSf** by apo-Tf (Table 4), it should be kept in mind that the possible multiple binding mode of iridium(III) complexes (i.e., engaging other binding pockets) cannot be excluded based on the current results and may affect the general binding characteristics.

### 3. Materials and Methods

#### 3.1. Materials

Calf thymus DNA (CT DNA), human serum albumin (HSA), apo-transferrin (apo-Tf), pBR322 DNA, sodium azide ( $\text{NaN}_3$ ), DMSO, superoxide dismutase (SOD), methyl green, DAPI, ethidium bromide (EB), and other chemicals and solvents were purchased from Sigma–Aldrich (Hamburg, Germany). All solvents were deaerated before use.

#### 3.2. Methods

##### 3.2.1. Physical Measurements

Single crystals of **IrPCp** $\text{CHCl}_3$ , **IrPLm** $1.5\text{CHCl}_3$ , and **IrPNr** $2\text{CHCl}_3$  were collected on a SuperNova diffractometer using graphite monochromatic MoK radiation at 293 K, 100 K, or 293 K, respectively. Data processing was undertaken with CrysAlisPRO (Yarnton, England) The structures were solved using direct methods, and for refinement, the



non-H atoms were treated anisotropically. The main calculations were performed with SHELXL. Crystallographic data of the structures was deposited at the Cambridge Crystallographic Data Centre with CCDC reference numbers 1996074 (**IrPCp**CHCl<sub>3</sub>), 1996071 (**IrPLm**1.5CHCl<sub>3</sub>), and 1996073 (**IrPNr**2CHCl<sub>3</sub>).

Elemental analyses (C, H, and N) were conducted with a Vario MICRO Cube (Elementar, Auckland, New Zealand). NMR spectra were recorded using a Bruker Avance II 300 MHz spectrometer in CDCl<sub>3</sub> with traces of CHCl<sub>3</sub> as an internal reference for <sup>1</sup>H and 85% H<sub>3</sub>PO<sub>4</sub> in H<sub>2</sub>O as an external standard for <sup>31</sup>P{<sup>1</sup>H}. Mass spectra were recorded with a Bruker MicrOTOF-Q II spectrometer with an ESI ion source under the following nebulizer pressure conditions: 0.4 bar, dry gas: 4.0 l min<sup>-1</sup> heated to 180 °C. Data were recorded in the positive ion mode, while profile spectra were recorded in the mass range of 50–3000 m/z; end plate offset—500 V; capillary voltage 4500 V; mass resolving power of the instrument—over 18,000. Mass calibration was done using the cluster method with a mixture of 10 mM sodium formate and isopropanol (1:1, v/v) before the run [14].

### 3.2.2. Characterization of Organometallic Iridium(III) Complexes

All iridium(III) complexes (**IrPCp**, **IrPNr**, **IrPLm**, **IrPSf**) were synthesized according to the literature procedure described by our group [14].

Data for [Ir(*h*<sup>5</sup>-Cp\*)Cl<sub>2</sub>**PCp**] (**IrPCp**)

**Yield:** 80%. Anal. found: C, 47.01; H, 4.32; N, 4.00%. Anal. calc. for C<sub>40</sub>H<sub>44</sub>Cl<sub>2</sub>IrN<sub>3</sub>O<sub>3</sub>PCHCl<sub>3</sub> (C<sub>41</sub>H<sub>45</sub>Cl<sub>5</sub>IrN<sub>3</sub>O<sub>3</sub>P): C, 47.02; H, 4.33; N, 4.01%.

**NMR (298 K, CDCl<sub>3</sub>):** <sup>31</sup>P{<sup>1</sup>H}: 1.30 (P<sup>1</sup>, s); <sup>1</sup>H: 1.11–1.33 (H<sup>72,73</sup>, m, 4-H), 1.35 (H<sup>1</sup>, d, 2.2 Hz, 15-H), 2.39 (H<sup>13,14</sup>, bt, 4.8 Hz, 4-H), 2.99 (H<sup>12,15</sup>, bt, 4.8 Hz, 4-H), 3.47 (H<sup>71</sup>, m, 1-H), 4.07 (H<sup>11</sup>, s, 2-H), 7.16 (H<sup>69</sup>, d, 7.1 Hz, 1-H), 7.44–7.53 (H<sup>43,44</sup>, m, 6-H), 7.92 (H<sup>63</sup>, d, 13.3 Hz, 1-H), 8.00–8.11 (H<sup>42</sup>, m, 4-H), 8.72 (H<sup>67</sup>, s, 1-H), 15.02 (H<sup>70</sup>, s, 1-H).

**<sup>+</sup>ESI-MS (CHCl<sub>3</sub>/H<sub>2</sub>O, m/z):** 928.21 [M + H]<sup>+</sup>, 892.23 [M - Cl]<sup>+</sup>, 888.28 [M - 2Cl + CH<sub>3</sub>OH]<sup>+</sup>, 856.26 [M - 2Cl]<sup>+</sup>.

Crystals of **IrPCp**CHCl<sub>3</sub> suitable for X-ray analysis were obtained under refrigeration by slow diffusion of hexane into a solution of the complex in chloroform under normal oxygen conditions. Crystal data: C<sub>41</sub>H<sub>45</sub>Cl<sub>5</sub>IrN<sub>3</sub>O<sub>3</sub>P, M = 1047.22 g mol<sup>-1</sup>, crystal size: 0.20 × 0.20 × 0.02 mm; crystal system: triclinic, space group: P1, a = 9.0544(4) Å, b = 11.8197(5) Å, c = 20.8951(8) Å, α = 85.841(3)°, β = 86.837(3)°, γ = 67.930(4)°, V = 2065.94(16) Å<sup>3</sup>, D<sub>calc</sub> (Z = 2) = 1.683 g cm<sup>-3</sup>, range for data collection: 4.042 to 71.700, Mo K radiation (λ = 1.54184 Å), M<sub>0</sub> = 9.983 mm<sup>-1</sup>, reflections collected/unique: 28 428/7969, [R<sub>int</sub> = 0.0886], completeness to full = 99.9%, final R indices [I > 2(I)]: R<sub>1</sub> = 0.0440, wR<sub>2</sub> = 0.1081, R indices (all data): R<sub>1</sub> = 0.0544, wR<sub>2</sub> = 0.1169, GOF = 1.026, largest diff. peak and hole: 1.919 and -1.931 e Å<sup>-3</sup>, data/restraints/parameters: 7969/0/504, T = 293 K.

Data for [Ir(*h*<sup>5</sup>-Cp\*)Cl<sub>2</sub>**PSf**] (**IrPSf**)

**Yield:** 80%. Anal. found: C, 50.97; H, 4.87; N, 5.65%. Anal. calc. for C<sub>42</sub>H<sub>48</sub>Cl<sub>2</sub>F<sub>2</sub>IrN<sub>4</sub>O<sub>3</sub>P: C, 51.01; H, 4.89; N, 5.67%.

**NMR (298 K, CDCl<sub>3</sub>):** <sup>31</sup>P{<sup>1</sup>H}: 3.06 (P<sup>1</sup>, s); <sup>1</sup>H: 0.72 (H<sup>16,17</sup>, d, 6.4 Hz, 6-H), 1.04–1.20 (H<sup>72,73</sup>, m, 4-H), 1.33 (H<sup>1</sup>, d, 2.2 Hz, 15-H), 2.45 (H<sup>12,15</sup>, m, 2-H), 2.80 (H<sup>13,14</sup>, m, 2-H), 3.07 (H<sup>13,14</sup>, m, 2-H), 3.87 (H<sup>71</sup>, m, 1-H), 4.25 (H<sup>11</sup>, s, 2-H), 6.41 (H<sup>63</sup>, bs, 2-H), 7.43–7.51 (H<sup>43,44</sup>, m, 6-H), 7.98–8.13 (H<sup>42</sup>, m, 4-H), 8.61 (H<sup>67</sup>, s, 1-H), 14.65 (H<sup>70</sup>, bs, 1-H).

**<sup>+</sup>ESI-MS (CHCl<sub>3</sub>/H<sub>2</sub>O, m/z):** 989.25 [M + H]<sup>+</sup>, 949.32 [M - 2Cl + CH<sub>3</sub>OH]<sup>+</sup>, 919.32 [M - 2Cl]<sup>+</sup>.

Data for [Ir(*h*<sup>5</sup>-Cp\*)Cl<sub>2</sub>**PLm**] (**IrPLm**)

**Yield:** 80%. Anal. found: C, 44.20; H, 4.15; N, 3.72%. Anal. calc. for C<sub>40</sub>H<sub>45</sub>Cl<sub>2</sub>F<sub>2</sub>IrN<sub>3</sub>O<sub>3</sub>P1.5CHCl<sub>3</sub> (C<sub>41.5</sub>H<sub>46.5</sub>Cl<sub>6.5</sub>F<sub>2</sub>IrN<sub>3</sub>O<sub>3</sub>P): C, 44.23; H, 4.16; N, 3.73%.

**NMR (298 K, CDCl<sub>3</sub>):** <sup>31</sup>P{<sup>1</sup>H}: 1.82 (P<sup>1</sup>, s); <sup>1</sup>H: 0.62 (H<sup>16</sup>, d, 6.3 Hz, 3-H), 1.34 (H<sup>1</sup>, d, 2.2 Hz, 15-H), 1.50 (H<sup>72</sup>, t, 7.0 Hz, 3-H), 2.14–3.14 (H<sup>12,13,14,15</sup>, m, 7-H), 4.15 (H<sup>11</sup>, dd, J<sub>1</sub> = 40 Hz, J<sub>2</sub> = 16 Hz, 2-H), 4.40 (H<sup>71</sup>, qd, J<sub>1</sub> = 7.2 Hz, J<sub>2</sub> = 3.3 Hz, 2-H), 7.39–7.56 (H<sup>43,44</sup>,

m, 6-H), 7.87 (H<sup>63</sup>, dd, J<sub>1</sub> = 12.0 Hz, J<sub>2</sub> = 1.7 Hz, 1-H), 7.99–8.15 (H<sup>42</sup>, m, 4-H), 8.55 (H<sup>67</sup>, s, 1-H), 14.68 (H<sup>70</sup>, s, 1-H).

<sup>+</sup>ESI-MS (CHCl<sub>3</sub>/H<sub>2</sub>O, m/z): 948.22 [M + H]<sup>+</sup>, 914.26 [M - Cl]<sup>+</sup>, 906.28 [M - 2Cl + CH<sub>3</sub>OH]<sup>+</sup>, 878.28 [M - 2Cl]<sup>+</sup>.

Crystals of IrPLm1.5CHCl<sub>3</sub> suitable for X-ray analysis were obtained under refrigeration by slow evaporation of chloroform/methanol (1:1, v/v) solution under normal oxygen conditions. Crystal data: C<sub>41.5</sub>H<sub>46.5</sub>Cl<sub>6.5</sub>F<sub>2</sub>IrN<sub>3</sub>O<sub>3</sub>P, M = 1126.91 g mol<sup>-1</sup>, crystal size: 0.100 0.100 0.050 mm, crystal system: monoclinic, space group: I2/a, a = 24.6249(3) Å, b = 8.35470(1) Å, c = 44.3459(6) Å, β = 90, γ = 104.3440(10), δ = 90, V = 8839.03(18) Å<sup>3</sup>, D<sub>calc</sub> (Z = 8) = 1.694 g cm<sup>-3</sup>, range for data collection: 2.215 to 31.772, Mo K radiation (λ = 0.71073 Å), Mo = 3.501 mm<sup>-1</sup>, reflections collected/unique: 154 041/13 616, [R<sub>int</sub> = 0.0395], completeness to full = 99.9%, final R indices [I > 2(I)]: R<sub>1</sub> = 0.0321, wR<sub>2</sub> = 0.0716, R indices (all data): R<sub>1</sub> = 0.000394, wR<sub>2</sub> = 0.0734, GOF = 1.059, largest diff. peak and hole: 3.325 and -0.922 e Å<sup>-3</sup>, data/restraints/parameters: 13 616/3/541, T = 100 K.

Data for [Ir(h<sup>5</sup>-Cp\*)Cl<sub>2</sub>PNr] (IrPNr)

**Yield:** 80%. Anal. found: C, 42.60; H, 4.01; N, 3.63%. Anal. calc. for C<sub>39</sub>H<sub>44</sub>Cl<sub>2</sub>FlrN<sub>3</sub>O<sub>3</sub>P2CHCl<sub>3</sub> (C<sub>41</sub>H<sub>46</sub>Cl<sub>8</sub>FlrN<sub>3</sub>O<sub>3</sub>P): C, 42.65; H, 4.02; N, 3.64%.

NMR (298 K, CDCl<sub>3</sub>): <sup>31</sup>P{<sup>1</sup>H}: 1.38 (P<sup>1</sup>, s); <sup>1</sup>H: 1.35 (H<sup>1</sup>, d, 2.2 Hz, 15-H), 1.54 (H<sup>72</sup>, t, 7.3 Hz, 3-H), 2.39 (H<sup>13,14</sup>, bt, 4.6 Hz 4-H), 2.97 (H<sup>12,15</sup>, bt, 4.6 Hz, 4-H), 4.07 (H<sup>11</sup>, s, 2-H), 4.25 (H<sup>71</sup>, q, 7.2 Hz, 2-H), 6.64 (H<sup>69</sup>, d, 6.9 Hz, 1-H), 7.42–7.54 (H<sup>43,44</sup>, m, 6-H), 7.96 (H<sup>63</sup>, d, 13.2 Hz, 1-H), 8.00–8.11 (H<sup>42</sup>, m, 4-H), 8.62 (H<sup>67</sup>, s, 1-H), 15.09 (H<sup>70</sup>, s, 1-H).

<sup>+</sup>ESI-MS (CHCl<sub>3</sub>/H<sub>2</sub>O, m/z): 916.21 [M + H]<sup>+</sup>, 980.24 [M - Cl]<sup>+</sup>, 876.29 [M - 2Cl + CH<sub>3</sub>OH]<sup>+</sup>, 844.27 [M - 2Cl]<sup>+</sup>.

Crystals of IrPNr2CHCl<sub>3</sub> suitable for X-ray analysis were obtained under refrigeration by slow evaporation of chloroform/acetone (1:1, v/v) solution under normal oxygen conditions. Crystal data: C<sub>41</sub>H<sub>46</sub>Cl<sub>8</sub>FlrN<sub>3</sub>O<sub>3</sub>P, M = 1154.58 g mol<sup>-1</sup>, crystal size: 0.300 0.300 0.200 mm, crystal system: monoclinic, space group: P2<sub>1</sub>/n<sub>1</sub>, a = 10.1356(2) Å, b = 17.3727(3) Å, c = 25.6237(4) Å, β = 90, γ = 93.137(1), δ = 90, V = 4505.13(14) Å<sup>3</sup>, D<sub>calc</sub> (Z = 4) = 1.702 g cm<sup>-3</sup>, range for data collection: 3.075 to 71.674, Mo K radiation (λ = 0.71073 Å), Mo = 10.818 mm<sup>-1</sup>, reflections<sup>1</sup>collected/unique: 69 550/8730, [R<sub>int</sub> = 0.1085], completeness to full = 99.8%, final R indices [I > 2(I)]: R<sub>1</sub> = 0.0642, wR<sub>2</sub> = 0.1514, R indices (all data): R<sub>1</sub> = 0.00710, wR<sub>2</sub> = 0.1560, GOF = 1.108, largest diff. peak and hole: 2.658 and -2.947 e Å<sup>-3</sup>, data/restraints/parameters: 8730/0/533, T = 293 K.

### 3.2.3. Interaction with Calf Thymus DNA

The stock solution was prepared by dissolving of the calf thymus (CT DNA) in 50 mM phosphate buffer saline (PBS) (pH = 7.4). The CT DNA concentration (C = 5 × 10<sup>-5</sup> M) was determined by a UV spectrophotometer using the molar absorption coefficient 6600 M<sup>-1</sup>m<sup>-1</sup> at 258 nm [60]. The stock solution was stored at 4 °C and used for > 6 days. The luminescent complexes of CT DNA with EB (ethidium bromide), DAPI (4<sup>0</sup>,6-diamidyno-2-fenyloindol), and MG (methyl green) were prepared by mixing the substrates in the equimolar ratio (C<sub>CT DNA-fluorescent dye</sub> = 5 × 10<sup>-5</sup> M; 50 mM of the phosphate buffer at pH = 7.4). The solution of the CT DNA fluorescent dye system was titrated in different molar ratios (0.5, 1, 2, 3, 4, 5, 6, 7, 8, 9, and 10) with the tested substances (dissolved in DMSO) and incubated for 1 h for each portion of the investigated compounds. The final concentration of DMSO was 2% in each sample. Photoluminescence measurements were recorded at 298 K using a Cary Eclipse Fluorescence Spectrophotometer. The excitation wavelength was 510 nm for the CT DNA-EB complex, 358 nm for the CT DNA-DAPI complex, and 633 nm for the CT DNA-MG complex. The Inner Filter Effect was considered and the corrected intensity of the emission band was calculated using Equation (1) [13], where: Abs—absorbance at analyzed emission wavelength; I<sub>f</sub>—uncorrected emission intensity.

$$I_{\text{cor}} = \frac{I_f \cdot 2.303 \text{ Abs}}{1 - 10^{\text{Abs}}} \quad (1)$$

In order to confirm the quenching mechanism, the fluorescence quenching was analyzed according to Stern–Volmer in Equation (2):

$$\frac{I_0}{I} = 1 + K_{SV}[C] \quad (2)$$

where  $I_0$  and  $I$  are the fluorescence intensities in the absence and presence of the quencher, respectively,  $K_{SV}$  is the Stern–Volmer quenching constant, and  $[C]$  is the concentration of the quencher, respectively.

In same case, it was clearly observed that both static and dynamic quenching occur simultaneously where a nonlinear curve is observed. In such cases, extended Stern–Volmer plots can be used to describe the new situation with the following Equation (3) [61–63].

$$1 - \frac{(I/I_0)}{[C]} = K_{DSV} \left( \frac{I}{I_0} \right) + V \quad (3)$$

where  $I_0$  and  $I$  are the fluorescence intensities in the absence and presence of the quencher, respectively;  $K_{DSV}$  is the dynamic quenching constant;  $[C]$  is the concentration of the quencher, and  $V$  is the volume of the sphere of action. We drew the plots of  $([1 - (I/I_0)]/[C])$  versus  $I/I_0$ .  $K_{DSV}$  is the slope of the plot and the static quenching constant  $V$  is calculated from the intercept of the plot.

The spectra of circular dichroism were recorded using a spectropolarimeter JASCO J-715 (CD and MCD).

### 3.2.4. DNA Strand Break Analysis

The ability of IrPCp, IrPNr, IrPSf, IrPLm, and phosphine ligands to induce single- or double-strand breaks in plasmid DNA was tested with the pBR322 plasmid ( $C = 0.5 \text{ mg/mL}$ ). All compounds were dissolved in DMF; the concentration was kept constant (10% by volume) in the final solution with/without hydrogen peroxide ( $\text{H}_2\text{O}_2$ ,  $C = 50 \text{ M}$ ), superoxide dismutase (SOD,  $C = 0.62 \text{ M}$ ), dimethyl sulfoxide (DMSO,  $C = 1.4 \text{ mM}$ ), or sodium azide ( $\text{NaN}_3$ ,  $C = 40 \text{ mM}$ ) [64]. The reaction was also monitored after the addition of various groove binders: methyl green (MG,  $C \leq 10 \text{ mg/mL}$ ), and 4,6-diamidino-2-phenylindole (DAPI,  $C = 5 \text{ mg/mL}$ ) [48,65,66]. After incubation for 1 h at 37°C, reaction mixtures (20 L) were mixed with 3 L of loading buffer (bromophenol blue in 30% glycerol) and loaded on 1% agarose gels, containing EB, in TBE buffer (90 mM Tris–borate, 20 mM EDTA, pH = 8.0). Gel electrophoresis was performed at a constant voltage of 100V (4 Vcm<sup>-1</sup>) for 60 min. The gel was photographed and processed with a Digital Imaging System (Syngen Biotech, Wrocław, Poland).

### 3.2.5. Interaction with Human Serum Albumin

Human serum albumin (HSA) was dissolved in 50 mM phosphate buffer saline (PBS) (pH = 7.4),  $C(\text{HSA}) = 5 \cdot 10^{-5} \text{ M}$ . The solution of the HSA was titrated at different molar ratios (0.5, 1, 2, 3, 4, 5, 6, 7, 8, 9 and 10) by IrPCp, IrPNr, IrPSf, IrPLm and phosphine ligands (dissolved in DMSO) and incubated for 1 h with any portion from each of the investigated compounds. The final volume of DMSO was 2% in each sample. Afterward, substances were incubated with HSA solution for 1h at room temperature. The excitation wavelength was equal to 295 nm.

### 3.2.6. Interaction with Transferring

Apo-transferrin (apo-Tf) solution was prepared by dissolving the solid protein in 50 mM of phosphate-buffered saline (PBS) (pH = 7.4),  $C(\text{apo-Tf}) = 3.6 \cdot 10^{-6} \text{ M}$ . The solution of the Tf was titrated in different molar ratios (0.5, 1, 2, 3, 4, 5, 6, 7, 8, 9, and 10) by IrPCp, IrPNr, IrPSf, IrPLm with corresponding phosphines (dissolved in DMSO) and incubated for 1h with any portion from each of the investigated compounds. The final volume of DMSO was 2% in each sample. The excitation wavelength was equal to 295 nm.



The spectra of circular dichroism were recorded using a spectropolarimeter JASCO J-715 (CD and MCD).

### 3.2.7. Molecular Docking

Docking of Ir(III) complexes was performed with the program AutoDock4 (4.2.6 Release) [67] using Lamarckian Genetic Algorithm. Preparation of ligands and receptors was conducted with the program AutoDockTools [67] using the default settings unless stated otherwise. Each docking simulation consisted of 100 independent docking runs with the maximum number of energy evaluations set to  $25 \times 10^6$ . The original AutoDock4 parameter file was modified to incorporate iridium parameters obtained from the AutoDock website [68]. The details for particular receptors are outlined in further detail. The binding poses that resulted were clustered with a 2 Å RMSD threshold.

DNA docking was conducted using DNA hexamer d(CGATCG)<sub>2</sub> (PDB code 1Z3F [69]) as the receptor. After removing the intercalating agent present in the crystal structure, two gaps facilitating possible intercalation remained in the structure. The search space described by a three-dimensional grid was set to cover the entire DNA molecule. In particular, the center of the grid was aligned with the geometric center of the receptor. The grid spacing was equal to 0.375 Å. The grid dimensions corresponded to 26.25, 26.25, and 30 Å along the x, y, and z axes, respectively.

A high-resolution crystal structure of human serum albumin (PDB code 1N5U [70]) was employed as the receptor in HSA docking. A cubic grid of 26.25 Å size and 0.375 Å spacing was centered at the side chain nitrogen atoms of Trp214 residue.

The possible binding pockets within apo-Tf structure were determined using the ligand-binding site predictions provided by DeepSite [71], ConCavity [72], and PrankWeb [73,74] tools with default settings. A crystal structure of human serum apo-transferrin (PDB code 2HAV [75]) was used as the receptor for both binding pocket prediction and further docking simulation. The number of ligand binding sites predicted with DeepSite, ConCavity, and PrankWeb was equal to 2, 3, and 6, respectively. When considering the mutual arrangement of these binding pockets, four receptor sites were selected, essentially covering all the predictions obtained with the tools applied herein. Separate docking simulations were conducted for each of the selected binding pockets. The respective four cubic grids with 26.25 Å edge length were centered at the following sets of coordinates:  $x_1 = 42.818$ ,  $y_1 = 7.435$ ,  $z_1 = 21.026$ ,  $x_2 = 36.325$ ,  $y_2 = 1.776$ ,  $z_2 = 3.335$ ,  $x_3 = 23.178$ ,  $y_3 = 4.200$ ,  $z_3 = 12.921$ ,  $x_4 = 55.864$ ,  $y_4 = 3.726$ , and  $z_4 = 18.111$  (in Å units with respect to the original coordinates of 2HAV crystal structure).

## 4. Conclusions

The mode of binding of four Ir(III) complexes (Ir(<sup>5</sup>-Cp\*)Cl<sub>2</sub>Ph<sub>2</sub>PCH<sub>2</sub>Cp; **IrPCp**, Ir(<sup>5</sup>-Cp\*)Cl<sub>2</sub>Ph<sub>2</sub>PCH<sub>2</sub>Sf; **IrPSf**, Ir(<sup>5</sup>-Cp\*)Cl<sub>2</sub>Ph<sub>2</sub>PCH<sub>2</sub>Lm; **IrPLm**, Ir(<sup>5</sup>-Cp\*)Cl<sub>2</sub>Ph<sub>2</sub>PCH<sub>2</sub>Nr; **IrPNr**) with CTDNA and serum proteins human albumin and apo-transferrin was investigated using various techniques (fluorescence spectroscopy, circular dichroism, and gel electrophoresis) and molecular docking studies.

In our investigation, we proved that: (i) Interaction of Ir(III) complexes with DNA is possible by noncovalent modes without a double-strand cleavage; (ii) DNA damage is possible via a ROS-dependent mechanism involving hydroxyl radicals, singlet oxygen, and superoxide anion; (iii) compounds interact with macromolecules such as HSA and apo-Tf; additionally, the molecular docking study indicated that all the compounds considered herein were found to (iv) bind to the tryptophan residues of HSA within site I, and/or (v) to dock within all the four predicted binding sites of apo-Tf, which include nearby tyrosine or tryptophan residues.

This experimental evidence indicates a mechanism of action different from DNA targeting typical of Pt(II) drugs. Its noticeable activity concerns the interaction with DNA with a predominance of groove binding potentially related to negligible genotoxicity, and a high level of ROS generation.

**Supplementary Materials:** The following are available online at <https://www.mdpi.com/article/10.3390/ph14070685/s1>, Figure S1. Fluorescence quenching of EB-CT DNA ( $C = 5 \times 10^{-5}$  M) by IrPCp, IrPNr, IrPLm and IrPSf (molar ratios 0.5, 1, 1.5, 2, 3, 4, 5, 6, 7, 8, 9 and 10) in 50 mM pH 7.4 phosphate buffer (axis: y—fluorescence intensity; x—wavelength), Figure S2. Fluorescence quenching of DAPI-CT DNA ( $C = 5 \times 10^{-5}$  M) by IrPCp, IrPNr, IrPLm and IrPSf (molar ratios 0.5, 1, 1.5, 2, 3, 4, 5, 6, 7, 8, 9, 10) in 50 mM pH 7.4 phosphate buffer (axis: y—fluorescence intensity; x—wavelength), Figure S3. Fluorescence quenching of DAPI-CT DNA ( $C = 5 \times 10^{-5}$  M) by PCp, PNr, PLm and PSf (molar ratios 0.5, 1, 1.5, 2, 3, 4, 5, 6, 7, 8, 9, 10) in 50 mM pH 7.4 phosphate buffer (axis: y—fluorescence intensity; x—wavelength), Figure S4. Fluorescence quenching of DAPI-CT DNA ( $C = 5 \times 10^{-5}$  M) by IrPCp, IrPNr, IrPLm and IrPSf (molar ratios 0.5, 1, 1.5, 2, 3, 4, 5, 6, 7, 8, 9, 10) in 50 mM pH 7.4 phosphate buffer (axis: y—fluorescence intensity; x—wavelength), Figure S5. Fluorescence quenching of HSA ( $C = 5 \times 10^{-5}$  M) by IrPCp, IrPNr, IrPLm and IrPSf (molar ratios 0.5, 1, 1.5, 2) in 50 mM pH 7.4 phosphate buffer (axis: y—fluorescence intensity; x—wavelength), Figure S6. Fluorescence quenching of apo-Tf ( $C = 3.6 \times 10^{-6}$  M) by IrPCp, IrPNr, IrPLm and IrPSf (molar ratios 0.5, 1, 1.5, 2, 3, 4, 5, 6, 7, 8, 9, 10) in 50 mM pH 7.4 phosphate buffer (axis: y—fluorescence intensity; x—wavelength), Figure S7. Fluorescence quenching of apo-Tf ( $C = 3.6 \times 10^{-6}$  M) by PCp, PNr, PLm and PSf (molar ratios 0.5, 1, 1.5, 2, 3, 4, 5, 6, 7, 8, 9, 10) in 50 mM pH 7.4 phosphate buffer (axis: y—fluorescence intensity; x—wavelength). Figure S8. Agarose gel electrophoresis of pBR322 plasmid cleavage by  $H_2O_2$  in different concentrations.

**Author Contributions:** Conceptualization, project administration, methodology, investigation, formal analysis, writing—original draft preparation, writing—review and editing, visualization, validation, funding acquisition, S.A.K. and U.K.K.; partial data analysis, review and editing, M.K.L. and D.W.; molecular docking studies, data analysis, writing—review and editing, D.B. and E.D.-K. All authors have read and agreed to the published version of the manuscript.

**Funding:** This research was funded by the Polish National Science Centre (grant number 2020/37/N/ST4/02698). The UV-Vis measurements were conducted with equipment purchased thanks to the financial support of the Polish National Science Centre (Grant 2016/23/D/ST5/00269).

**Institutional Review Board Statement:** Not applicable.

**Informed Consent Statement:** Not applicable.

**Data Availability Statement:** Data is contained within the article.

**Acknowledgments:** E.D.-K. is thankful to the Department of Chemistry of Wrocław University of Science and Technology for their support. Calculations were conducted using the resources provided by the Wrocław Center for Networking and Supercomputing (WCSS). We thank Rimon Mikhail for language editing on our manuscript. Graphics were prepared based on elements from Servier Medical Art (<https://www.smart.servier.com>, (accessed on 27 February 2021)).

**Conflicts of Interest:** The authors declare no conflict of interest.

## References

1. Fuertes, M.A.; Alonso, A.C.; Pérez, J.M. Biochemical Modulation of Cisplatin Mechanisms of Action: Enhancement of Antitumor Activity and Circumvention of Drug Resistance. *Chem. Rev.* **2003**, *103*, 645–662. [[CrossRef](#)]
2. Uversky, V.N.; Kretsinger, R.H.; Permyakov, E.A. *Encyclopedia of Metalloproteins*. Springer: New York, NY, USA, 2013; Volume 1, pp. 1–89.
3. Dasari, S.; Tchounwou, P.B. Cisplatin in cancer therapy: Molecular mechanisms of action. *Eur. J. Pharmacol.* **2014**, *740*, 364–378. [[CrossRef](#)] [[PubMed](#)]
4. Ruiz, J.; Rodriguez, V.; Cutillas, N.; Samper, K.G.; Capdevila, M.; Palacios, Ò.; Espinosa, A. Novel C,N-chelate rhodium(III) and iridium(III) antitumor complexes incorporating a lipophilic steroidal conjugate and their interaction with DNA. *Dalton Trans.* **2012**, *41*, 12847–12856. [[CrossRef](#)] [[PubMed](#)]
5. Wu, C.; Li, Q.; Zhang, X.; Shi, C.; Li, G.; Wang, M.; Li, K.; Yuan, A. Tuning the Photophysical and Excited State Properties of Phosphorescent Iridium(III) Complexes by Polycyclic Unit Substitution. *Chem. Open* **2019**, *8*, 339–343. [[CrossRef](#)]
6. Štarha, P.; Trávníček, Z. Non-platinum complexes containing releasable biologically active ligands. *Coord. Chem. Rev.* **2019**, *395*, 130–145. [[CrossRef](#)]
7. Millett, A.J.; Habtemariam, A.; Romero-Canelon, I.; Clarkson, G.J.; Sadler, P.J. Contrasting Anticancer Activity of Half-Sandwich Iridium(III) Complexes Bearing Functionally Diverse 2-Phenylpyridine Ligands. *Organometallics* **2015**, *34*, 2683–2694. [[CrossRef](#)]

8. Lapasam, A.; Hussain, O.; Phillips, R.M.; Kaminsky, W.; Kollipara, M.R. Synthesis, characterization and chemosensitivity studies of half-sandwich ruthenium, rhodium and iridium complexes containing  $k^1(S)$  and  $k^2(N,S)$  aroylthiourea ligands. *J. Organomet. Chem.* **2019**, *880*, 272–280. [[CrossRef](#)]
9. Ma, D.-L.; Wu, C.; Wu, K.-J.; Leung, C.-H. Iridium(III) Complexes Targeting Apoptotic Cell Death in Cancer Cells. *Molecules* **2019**, *24*, 2739. [[CrossRef](#)]
10. Yadav, V.; Talwar, P. Repositioning of fluoroquinolones from antibiotic to anti-cancer agents: An underestimated truth. *Biomed. Pharmacother.* **2019**, *111*, 934–946. [[CrossRef](#)]
11. Bykowska, A.; Starosta, R.; Komarnicka, U.; Ciunik, L.; Kyzioł, A.; Guz-Regner, K.; Bugla-Płoskońska, G.; Jeżowska-Bojczuk, M. Phosphine derivatives of ciprofloxacin and norfloxacin, a new class of potential therapeutic agents. *New J. Chem.* **2014**, *38*, 1062. [[CrossRef](#)]
12. Komarnicka, U.; Starosta, R.; Kyzioł, A.; Jeżowska-Bojczuk, M. Copper(i) complexes with phosphine derived from sparfloxacin. Part I—Structures, spectroscopic properties and cytotoxicity. *Dalton Trans.* **2015**, *44*, 12688–12699. [[CrossRef](#)] [[PubMed](#)]
13. Komarnicka, U.; Starosta, R.; Kyzioł, A.; Płotek, M.; Puchalska, M.; Jeżowska-Bojczuk, M. New copper(I) complexes bearing lomefloxacin motif: Spectroscopic properties, in vitro cytotoxicity and interactions with DNA and human serum albumin. *J. Inorg. Biochem.* **2016**, *165*, 25–35. [[CrossRef](#)]
14. Kozieł, S.; Komarnicka, U.K.; Ziólkowska, A.; Skórska-Stania, A.; Pucelik, B.; Płotek, M.; Sebastian, V.; Bieńko, A.; Stochel, G.; Kyzioł, A. Anticancer potency of novel organometallic Ir(III) complexes with phosphine derivatives of fluoroquinolones encapsulated in polymeric micelles. *Inorg. Chem. Front.* **2020**, *7*, 3386–3401. [[CrossRef](#)]
15. Van Holde, K.E.; Zlatanova, J. *The Evolution of Molecular Biology*; Elsevier: Amsterdam, The Netherlands, 2018; pp. 57–63.
16. Płotek, M.; Starosta, R.; Komarnicka, U.; Skórska-Stania, A.; Kołoczek, P.; Kyzioł, A. Ruthenium(II) piano stool coordination compounds with aminomethylphosphanes: Synthesis, characterisation and preliminary biological study in vitro. *J. Inorg. Biochem.* **2017**, *170*, 178–187. [[CrossRef](#)]
17. Kumar, M.; Kumar, G.; Mogha, N.K.; Jain, R.; Hussain, F.; Masram, D.T. Structure, DNA/proteins binding, docking and cytotoxicity studies of copper(II) complexes with the first quinolone drug nalidixic acid and 2,2<sup>0</sup>-dipyridylamine. *Spectrochim. Acta Part A Mol. Biomol. Spectrosc.* **2019**, *212*, 94–104. [[CrossRef](#)]
18. Manna, S.C.; Mistri, S.; Patra, A.; Mahish, M.K.; Saren, D.; Manne, R.K.; Santra, M.K.; Zangrando, E.; Puschmann, H. Synthesis, structure, DNA/protein binding, molecular docking and in vitro anticancer activity of two Schiff base coordinated copper(II) complexes. *Polyhedron* **2019**, *171*, 77–85. [[CrossRef](#)]
19. Kratz, F.; Hartmann, M.; Keppler, B.; Messori, L. The binding properties of two antitumor ruthenium(III) complexes to apotransferrin. *J. Biol. Chem.* **1994**, *269*, 2581–2588. [[CrossRef](#)]
20. Pessoa, J.C.; Tomaz, A.I. Transport of Therapeutic Vanadium and Ruthenium Complexes by Blood Plasma Components. *Curr. Med. Chem.* **2010**, *17*, 3701–3738. [[CrossRef](#)]
21. Yousefi, R.; Kafrani, A.T.; Nabavizadeh, S.M.; Pouryasin, Z.; Shahsavani, M.B.; Khoshaman, K.; Rashidi, M. The binding assessment with human serum albumin of novel six-coordinate Pt(IV) complexes, containing bidentate nitrogen donor/methyl ligands. *Mol. Boil. Res. Commun.* **2015**, *4*, 167–179.
22. Shahraki, S.; Shiri, F.; Mansouri-Torshizi, H.; Shahraki, J. Characterization of the interaction between a platinum(II) complex and human serum albumin: Spectroscopic analysis and molecular docking. *J. Iran. Chem. Soc.* **2016**, *13*, 723–731. [[CrossRef](#)]
23. Bergamo, A.; Messori, L.; Piccioli, F.; Cocchiello, M.; Sava, G. Biological role of adduct formation of the ruthenium(III) complex NAMI-A with serum albumin and serum transferrin. *Investig. New Drugs* **2003**, *21*, 401–411. [[CrossRef](#)]
24. Pongratz, M.; Schluga, P.; Jakupec, M.; Arion, V.B.; Hartinger, C.; Keppler, B.K. Transferrin binding and transferrin-mediated cellular uptake of the ruthenium coordination compound KP1019, studied by means of AAS, ESI-MS and CD spectroscopy. *J. Anal. At. Spectrom.* **2003**, *19*, 46–51. [[CrossRef](#)]
25. Gibaldi, M.; Koup, J.R. Pharmacokinetic concepts ? Drug binding, apparent volume of distribution and clearance. *Eur. J. Clin. Pharmacol.* **1981**, *20*, 299–305. [[CrossRef](#)] [[PubMed](#)]
26. Moghadam, N.H.; Salehzadeh, S.; Tanzadehpanah, H.; Saidijam, M.; Karimi, J.; Khazalpour, S. In vitro cytotoxicity and DNA/HSA interaction study of triamterene using molecular modelling and multi-spectroscopic methods. *J. Biomol. Struct. Dyn.* **2018**, *37*, 2242–2253. [[CrossRef](#)]
27. Kudarha, R.R.; Sawant, K.K. Albumin based versatile multifunctional nanocarriers for cancer therapy: Fabrication, surface modification, multimodal therapeutics and imaging approaches. *Mater. Sci. Eng. C* **2017**, *81*, 607–626. [[CrossRef](#)]
28. Zhao, P.; Wang, Y.; Wu, A.; Rao, Y.; Huang, Y. Roles of Albumin-Binding Proteins in Cancer Progression and Biomimetic Targeted Drug Delivery. *ChemBioChem* **2018**, *19*, 1796–1805. [[CrossRef](#)]
29. Hoogenboezem, E.N.; Duvall, C.L. Harnessing albumin as a carrier for cancer therapies. *Adv. Drug Deliv. Rev.* **2018**, *130*, 73–89. [[CrossRef](#)]
30. Li, C.; Wang, X.; Song, H.; Deng, S.; Li, W.; Li, J.; Sun, J. Current multifunctional albumin-based nanoplatfoms for cancer multi-mode therapy. *Asian J. Pharm. Sci.* **2020**, *15*, 1–12. [[CrossRef](#)]
31. Lambert, L.A.; Perri, H.; Halbrooks, P.J.; Mason, A.B. Evolution of the transferrin family: Conservation of residues associated with iron and anion binding. *Comp. Biochem. Physiol. Part B Biochem. Mol. Biol.* **2005**, *142*, 129–141. [[CrossRef](#)] [[PubMed](#)]
32. Thorstensen, K.; Romslo, I. The role of transferrin in the mechanism of cellular iron uptake. *Biochem. J.* **1990**, *271*, 1–9. [[CrossRef](#)]

33. Guy, J.; Drabek, D.; Antoniou, M. Delivery of drugs, proteins and genes into cells using transferrin as a ligand for receptor-mediated endocytosis. *Mol. Biotechnol.* **1995**, *3*, 237–248. [[CrossRef](#)]
34. Sun, H.; Li, H.; Sadler, P.J. Transferrin as a Metal Ion Mediator. *Chem. Rev.* **1999**, *99*, 2817–2842. [[CrossRef](#)]
35. Wang, J.; Tian, S.; Petros, R.A.; Napier, M.E.; DeSimone, J.M. The Complex Role of Multivalency in Nanoparticles Targeting the Transferrin Receptor for Cancer Therapies. *J. Am. Chem. Soc.* **2010**, *132*, 11306–11313. [[CrossRef](#)] [[PubMed](#)]
36. Li, H.; Qian, Z.M. Transferrin/transferrin receptor-mediated drug delivery. *Med. Res. Rev.* **2002**, *22*, 225–250. [[CrossRef](#)] [[PubMed](#)]
37. Luck, A.N.; Mason, A.B. Structure and dynamics of drug carriers and their interaction with cellular receptors: Focus on serum transferrin. *Adv. Drug Deliv. Rev.* **2013**, *65*, 1012–1019. [[CrossRef](#)] [[PubMed](#)]
38. Wang, D.; Li, Y.; Tian, Z.; Cao, R.; Yang, B. Transferrin-conjugated nanodiamond as an intracellular transporter of chemotherapeutic drug and targeting therapy for cancer cells. *Ther. Deliv.* **2014**, *5*, 511–524. [[CrossRef](#)] [[PubMed](#)]
39. Daniels, T.R.; Bernabeu, E.; Rodríguez, J.A.; Patel, S.; Kozman, M.; Chiappetta, D.A.; Holler, E.; Ljubimova, J.Y.; Helguera, G.; Penichet, M.L. The transferrin receptor and the targeted delivery of therapeutic agents against cancer. *Biochim. et Biophys. Acta (BBA) Gen. Subj.* **2012**, *1820*, 291–317. [[CrossRef](#)]
40. Sparreboom, A.; Verweij, J. Advances in Cancer Therapeutics. *Clin. Pharmacol. Ther.* **2009**, *85*, 113–117. [[CrossRef](#)]
41. Komarnicka, U.K.; Starosta, R.; Płotek, M.; De Almeida, R.F.M.; Jeżowska-Bojczuk, M.; Kyzioł, A. Copper(i) complexes with phosphine derived from sparfloxacin. Part II: A first insight into the cytotoxic action mode. *Dalton Trans.* **2016**, *45*, 5052–5063. [[CrossRef](#)]
42. Bykowska, A.; Starosta, R.; Brzuszkiewicz, A.; Bażanów, B.; Florek, M.; Jackulak, N.; Król, J.; Grzesiak, J.; Kaliński, K.; Jeżowska-Bojczuk, M. Synthesis, properties and biological activity of a novel phosphines ligand derived from ciprofloxacin. *Polyhedron* **2013**, *60*, 23–29. [[CrossRef](#)]
43. Komarnicka, U.K.; Starosta, R.; Guz-Regner, K.; Bugła-Płoskońska, G.; Kyzioł, A.; Jeżowska-Bojczuk, M. Phosphine derivatives of sparfloxacin—Synthesis, structures and in vitro activity. *J. Mol. Struct.* **2015**, *1096*, 55–63. [[CrossRef](#)]
44. Kołoczek, P.; Skórska-Stania, A.; Cierniak, A.; Sebastian, V.; Komarnicka, U.K.; Płotek, M.; Kyzioł, A. Polymeric micelle-mediated delivery of half-sandwich ruthenium(II) complexes with phosphanes derived from fluoroquinolones for lung adenocarcinoma treatment. *Eur. J. Pharm. Biopharm.* **2018**, *128*, 69–81. [[CrossRef](#)]
45. Malik, M.; Bieńko, D.C.; Komarnicka, U.K.; Kyzioł, A.; Dryś, M.; Świtlicka, A.; Dyguda-Kazimierowicz, E.; Jedwabny, W. Synthesis, structural characterization, docking simulation and in vitro antiproliferative activity of the new gold(III) complex with 2-pyridineethanol. *J. Inorg. Biochem.* **2021**, *215*, 111311. [[CrossRef](#)]
46. Subastri, A.; Ramamurthy, C.; Suyavaran, A.; Mareeswaran, R.; Rao, P.L.; Krishna, K.H.; Kumar, M.S.; Sujatha, V.; Thirunavukkarasu, C. Spectroscopic and molecular docking studies on the interaction of troxerutin with DNA. *Int. J. Biol. Macromol.* **2015**, *78*, 122–129. [[CrossRef](#)]
47. Varlan, A.; Ionescu, S.; Hillebrand, M. Study of the interaction between ofloxacin and human serum albumin by spectroscopic methods. *Luminescence* **2011**, *26*, 710–715. [[CrossRef](#)]
48. Komarnicka, U.K.; Koziół, S.; Starosta, R.; Kyzioł, A. Selective Cu(I) complex with phosphine-peptide (SarGly) conjugate contra breast cancer: Synthesis, spectroscopic characterization and insight into cytotoxic action. *J. Inorg. Biochem.* **2018**, *186*, 162–175. [[CrossRef](#)] [[PubMed](#)]
49. Kyzioł, A.; Cierniak, A.; Gubernator, J.; Markowski, A.; Jezowska-Bojczuk, M.; Komarnicka, U.K. Copper(i) complexes with phosphine derived from sparfloxacin. Part III: Multifaceted cell death and preliminary study of liposomal formulation of selected copper(i) complexes. *Dalton Trans.* **2017**, *47*, 1981–1992. [[CrossRef](#)] [[PubMed](#)]
50. Santini, C.; Pellei, M.; Gandin, V.; Porchia, M.; Tisato, F.; Marzano, C. Advances in Copper Complexes as Anticancer Agents. *Chem. Rev.* **2014**, *114*, 815–862. [[CrossRef](#)] [[PubMed](#)]
51. Bancirova, M. Sodium azide as a specific quencher of singlet oxygen during chemiluminescent detection by luminol and Cypridina luciferin analogues. *Luminescence* **2011**, *26*, 685–688. [[CrossRef](#)] [[PubMed](#)]
52. Huey, R.; Morris, G.; Olson, A.J.; Goodsell, D.S. A semiempirical free energy force field with charge-based desolvation. *J. Comput. Chem.* **2007**, *28*, 1145–1152. [[CrossRef](#)] [[PubMed](#)]
53. Živec, P.; Perdih, F.; Turel, I.; Giester, G.; Psomas, G. Different types of copper complexes with the quinolone antimicrobial drugs ofloxacin and norfloxacin: Structure, DNA- and albumin-binding. *J. Inorg. Biochem.* **2012**, *117*, 35–47. [[CrossRef](#)]
54. Sudlow, G.; Birkett, D.J.; Wade, D.N. The characterization of two specific drug binding sites on human serum albumin. *Mol. Pharmacol.* **1975**, *11*, 824–832.
55. Sudlow, G.; Birkett, D.J.; Wade, D.N. Further characterization of specific drug binding sites on human serum albumin. *Mol. Pharmacol.* **1976**, *12*, 1052–1061.
56. Ahmad, B.; Parveen, S.; Khan, R.H. Effect of Albumin Conformation on the Binding of Ciprofloxacin to Human Serum Albumin: A Novel Approach Directly Assigning Binding Site. *Biomacromolecules* **2006**, *7*, 1350–1356. [[CrossRef](#)] [[PubMed](#)]
57. Vincent, J.B.; Love, S. The binding and transport of alternative metals by transferrin. *Biochim. et Biophys. Acta (BBA) Gen. Subj.* **2012**, *1820*, 362–378. [[CrossRef](#)]
58. Martínez, A.; Suárez, J.; Shand, T.; Magliozzo, R.S.; Sánchez-Delgado, R.A. Interactions of arene–Ru(II)–chloroquine complexes of known antimalarial and antitumor activity with human serum albumin (HSA) and transferrin. *J. Inorg. Biochem.* **2011**, *105*, 39–45. [[CrossRef](#)] [[PubMed](#)]

59. Saboury, A.A. Application of a new method for data analysis of isothermal titration calorimetry in the interaction between human serum albumin and Ni<sup>2+</sup>. *J. Chem. Thermodyn.* **2003**, *35*, 1975–1981. [[CrossRef](#)]
60. Sun, Y.; Wang, J.; Jin, L.; Chang, Y.; Duan, J.; Lu, Y. A new conjugated poly(pyridinium salt) derived from phenanthridine diamine: Its synthesis, optical properties and interaction with calf thymus DNA. *Polym. J.* **2015**, *47*, 753–759. [[CrossRef](#)]
61. Kumar, H.M.S.; Kunabenchi, R.S.; Nishti, S.V.; Biradar, J.S.; Kadadevarmath, J.S. Effect of Solvent Polarity on Fluorescence Quenching of New Indole Derivatives by CCl<sub>4</sub>. *Spectrosc. Lett.* **2009**, *42*, 226–234. [[CrossRef](#)]
62. Hanagodimath, S.M.; Manohara, S.R.; Biradar, D.S.; Hadimani, S.K.B. Fluorescence Quenching of 2,2''-dimethyl-p-terphenyl by Carbon Tetrachloride in Binary Mixtures. *Spectrosc. Lett.* **2008**, *41*, 242–250. [[CrossRef](#)]
63. Baslak, C.; Kuş, M.; Cengeloglu, Y.; Ersoz, M. A comparative study on fluorescence quenching of CdTe nanocrystals with a serial of polycyclic aromatic hydrocarbons. *J. Lumin.* **2014**, *153*, 177–181. [[CrossRef](#)]
64. Lesiów, M.K.; Komarnicka, U.K.; Kyzioł, A.; Bieńko, A.; Pietrzyk, P. ROS-mediated lipid peroxidation as a result of Cu(ii) interaction with FomA protein fragments of *F. nucleatum*: Relevance to colorectal carcinogenesis. *Metallomics* **2019**, *11*, 2066–2077. [[CrossRef](#)] [[PubMed](#)]
65. Kim, S.K.; Nordén, B. Methyl green. A DNA major-groove binding drug. *FEBS Lett.* **1993**, *315*, 61–64. [[CrossRef](#)]
66. De Castro, L.F.P.; Zacharias, M. DAPI binding to the DNA minor groove: A continuum solvent analysis. *J. Mol. Recognit.* **2002**, *15*, 209–220. [[CrossRef](#)]
67. Morris, G.M.; Huey, R.; Lindstrom, W.; Sanner, M.F.; Belew, R.K.; Goodsell, D.S.; Olson, A.J. AutoDock4 and AutoDockTools4: Automated docking with selective receptor flexibility. *J. Comput. Chem.* **2009**, *30*, 2785–2791. [[CrossRef](#)] [[PubMed](#)]
68. Autodock. Available online: <http://autodock.1369657.n2.nabble.com/ADL-Parameters-for-docking-with-metal-ions-in-receptor-td2505649.html> (accessed on 30 March 2021).
69. Canals, A.; Purciolas, M.; Aymamí, J.; Coll, M. The anticancer agent ellipticine unwinds DNA by intercalative binding in an orientation parallel to base pairs. *Acta Crystallogr. Sect. D Biol. Crystallogr.* **2005**, *61*, 1009–1012. [[CrossRef](#)] [[PubMed](#)]
70. Wardell, M.; Wang, Z.; Ho, J.X.; Robert, J.; Rueker, F.; Ruble, J.; Carter, D.C. The Atomic Structure of Human Methemalbumin at 1.9 Å. *Biochem. Biophys. Res. Commun.* **2002**, *291*, 813–819. [[CrossRef](#)] [[PubMed](#)]
71. Jiménez, J.; Doerr, S.; Martínez-Rosell, G.; Rose, A.; De Fabritiis, G. DeepSite: Protein-binding site predictor using 3D-convolutional neural networks. *Bioinformatics* **2017**, *33*, 3036–3042. [[CrossRef](#)] [[PubMed](#)]
72. Capra, J.A.; Laskowski, R.; Thornton, J.; Singh, M.; Funkhouser, T.A. Predicting Protein Ligand Binding Sites by Combining Evolutionary Sequence Conservation and 3D Structure. *PLoS Comput. Biol.* **2009**, *5*, e1000585. [[CrossRef](#)]
73. Jendele, L.; Krivák, R.; Skoda, P.; Novotny, M.; Hoksza, D. PrankWeb: A web server for ligand binding site prediction and visualization. *Nucleic Acids Res.* **2019**, *47*, W345–W349. [[CrossRef](#)] [[PubMed](#)]
74. Krivák, R.; Hoksza, D. P2Rank: Machine learning based tool for rapid and accurate prediction of ligand binding sites from protein structure. *J. Chemin.* **2018**, *10*, 39. [[CrossRef](#)] [[PubMed](#)]
75. Wally, J.; Halbrooks, P.J.; Vonrhein, C.; Rould, M.A.; Everse, S.J.; Mason, A.B.; Buchanan, S.K. The Crystal Structure of Iron-free Human Serum Transferrin Provides Insight into Inter-lobe Communication and Receptor Binding. *J. Biol. Chem.* **2006**, *281*, 24934–24944. [[CrossRef](#)] [[PubMed](#)]

# Multi experimental and molecular docking studies on the DNA, albumin and apo-transferrin interaction with phosphino iridium(III) complexes as a potent anticancer drug.

Sandra Kozieł<sup>a\*</sup>, Daria Wojtala,<sup>a</sup> Monika K. Lesiów,<sup>a</sup> Edyta Dyguda-Kazimierowicz,<sup>b</sup> Dariusz C. Bieńko,<sup>b</sup> Urszula K. Komarnicka<sup>a\*</sup>

<sup>a</sup> Faculty of Chemistry, University of Wrocław, Joliot-Curie 14, 50-383 Wrocław, Poland

<sup>b</sup> Faculty of Chemistry, Wrocław University of Science and Technology, Wybrzeże Wyspiańskiego 27, 50-370 Wrocław, Poland

\* Correspondence: authors e-mail address: urszula.komarnicka@chem.uni.wroc.pl, sandra.koziel@chem.uni.wroc.pl

**ABSTRACT:** Group of cytotoxic half-sandwich iridium(III) complexes with aminomethyl(diphenyl)phosphine derived from fluoroquinolone antibiotics exhibits ability to (i) accumulate in nucleus, (ii) induce apoptosis, (iii) activate caspase-3/7 activity, (iv) induce the changes in cell cycle leading to G2/M phase arrest and (v) radicals generation. Herein, to elucidate the cytotoxic effects, we investigated the interaction of these complexes with DNA and serum proteins by gel electrophoresis, fluorescence spectroscopy, circular dichroism, and molecular docking studies. DNA binding experiments established that the complexes interact with DNA by moderate intercalation and predominance of minor groove binding without any capability to cause a double-strand cleavage. Molecular docking study confirmed two binding modes: minor groove binding and threading intercalation with fluoroquinolone part of the molecule involved in pi stacking interactions and the Ir(III)-containing region positioned within the major or minor groove. Fluorescence spectroscopic data (HSA and apo-Tf titration), together with molecular docking provided evidence that Ir(III) complexes are able to bind to the proteins in order to be transferred. All the compounds considered herein were found to bind to the tryptophan residues of HSA within site I (subdomain II A). Furthermore, Ir(III) complexes were found to dock within the apo-Tf binding site, which includes nearby tyrosine residues.

**Keywords:** arene iridium(III) complexes; fluoroquinolones; DNA-binding studies; DNA cleavage; proteins-binding studies; drug delivery; reactive oxygen species; anticancer activity

---



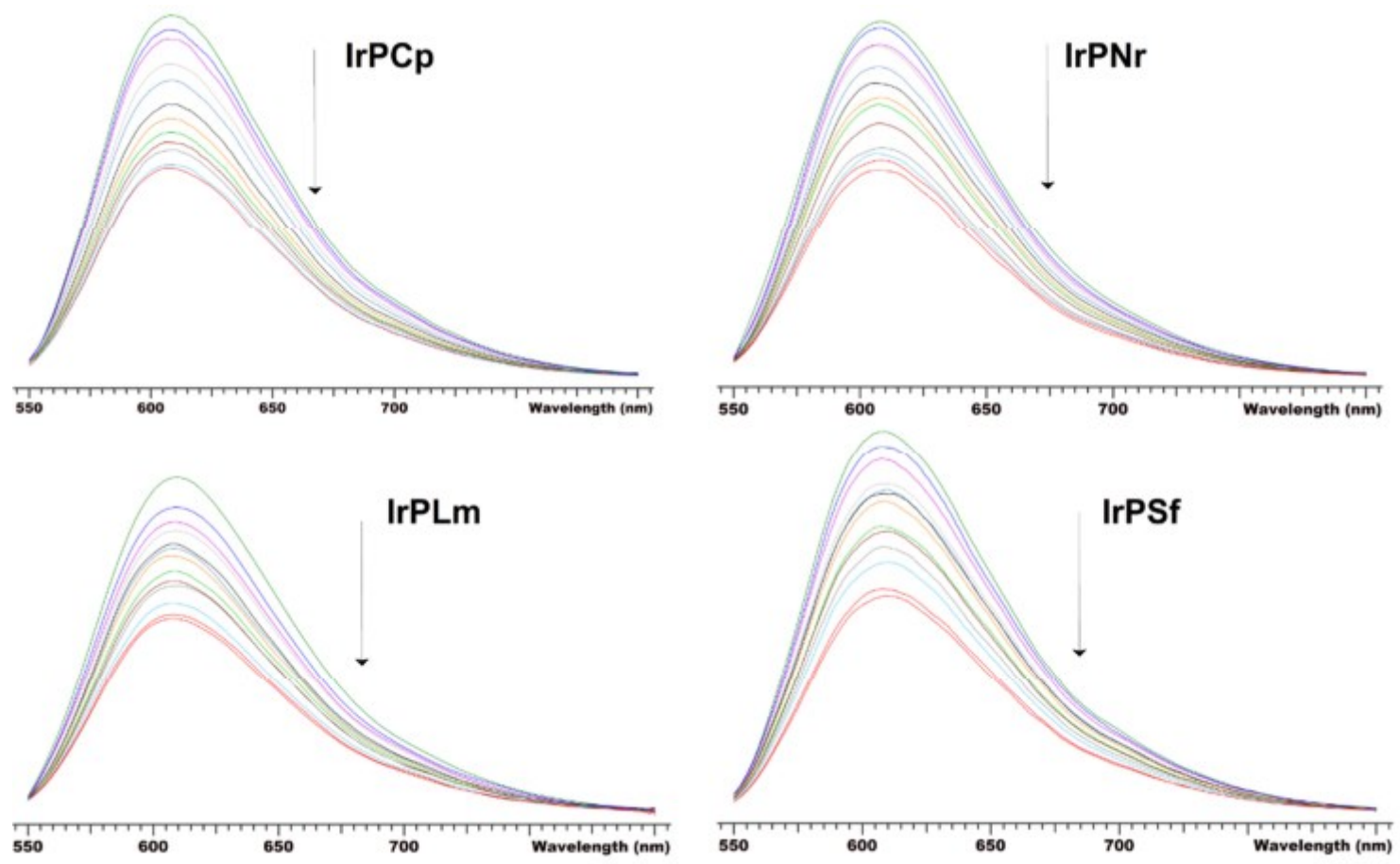


**Figure S1.** Fluorescence quenching of EB-CT DNA ( $C = 5 \times 10^{-5} \text{ M}$ ) by **IrPCp**, **IrPNr**, **IrPLm** and **IrPSf** (molar ratios 0.5, 1, 1.5, 2, 3, 4, 5, 6, 7, 8, 9 and 10) in 50 mM pH 7.4 phosphate buffer (axis: y – fluorescence intensity; x – wavelength).

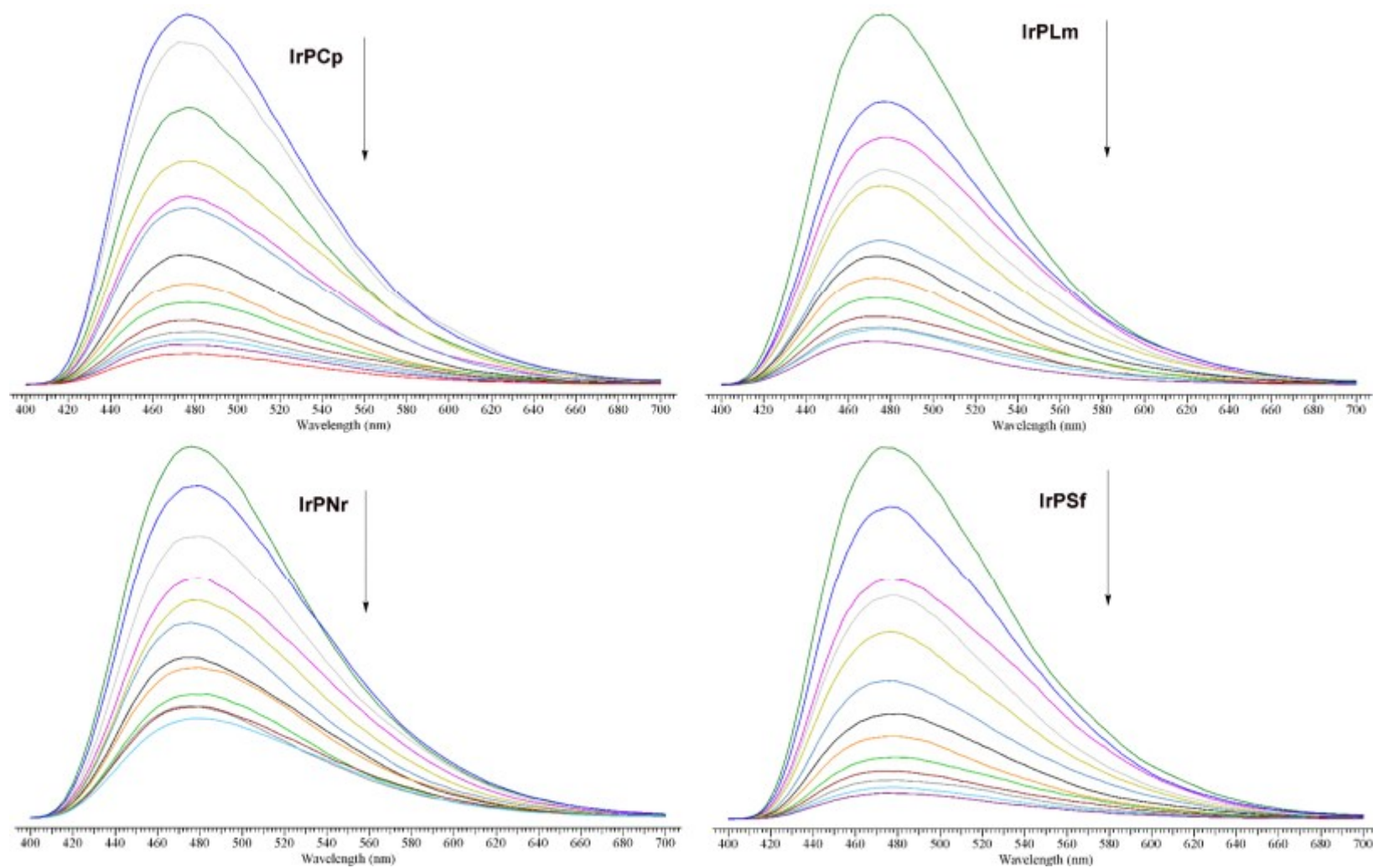


**Figure S2.** Fluorescence quenching of DAPI-CT DNA ( $C = 5 \times 10^{-5}$  M) by **IrPCp**, **IrPNr**, **IrPLm** and **IrPSf** (molar ratios 0.5, 1, 1.5, 2, 3, 4, 5, 6, 7, 8, 9, 10) in 50 mM pH 7.4 phosphate buffer (axis: y – fluorescence intensity; x – wavelength).

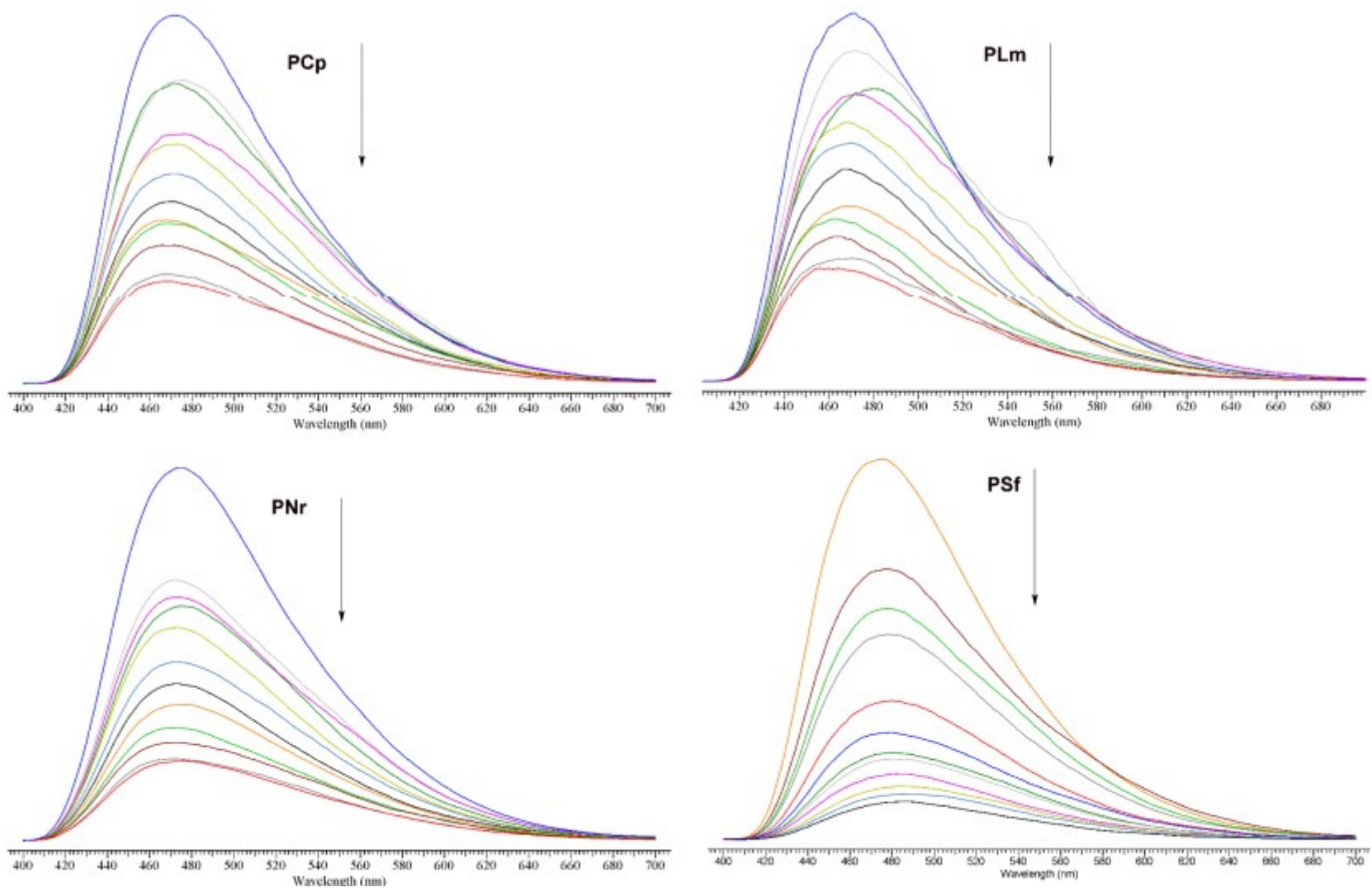


**Figure S3.** Fluorescence quenching of DAPI-CT DNA ( $C = 5 \times 10^{-5}$  M) by **PCp**, **PNr**, **PLm** and **PSf** (molar ratios 0.5, 1, 1.5, 2, 3, 4, 5, 6, 7, 8, 9, 10) in 50 mM pH 7.4 phosphate buffer (axis: y – fluorescence intensity; x – wavelength).

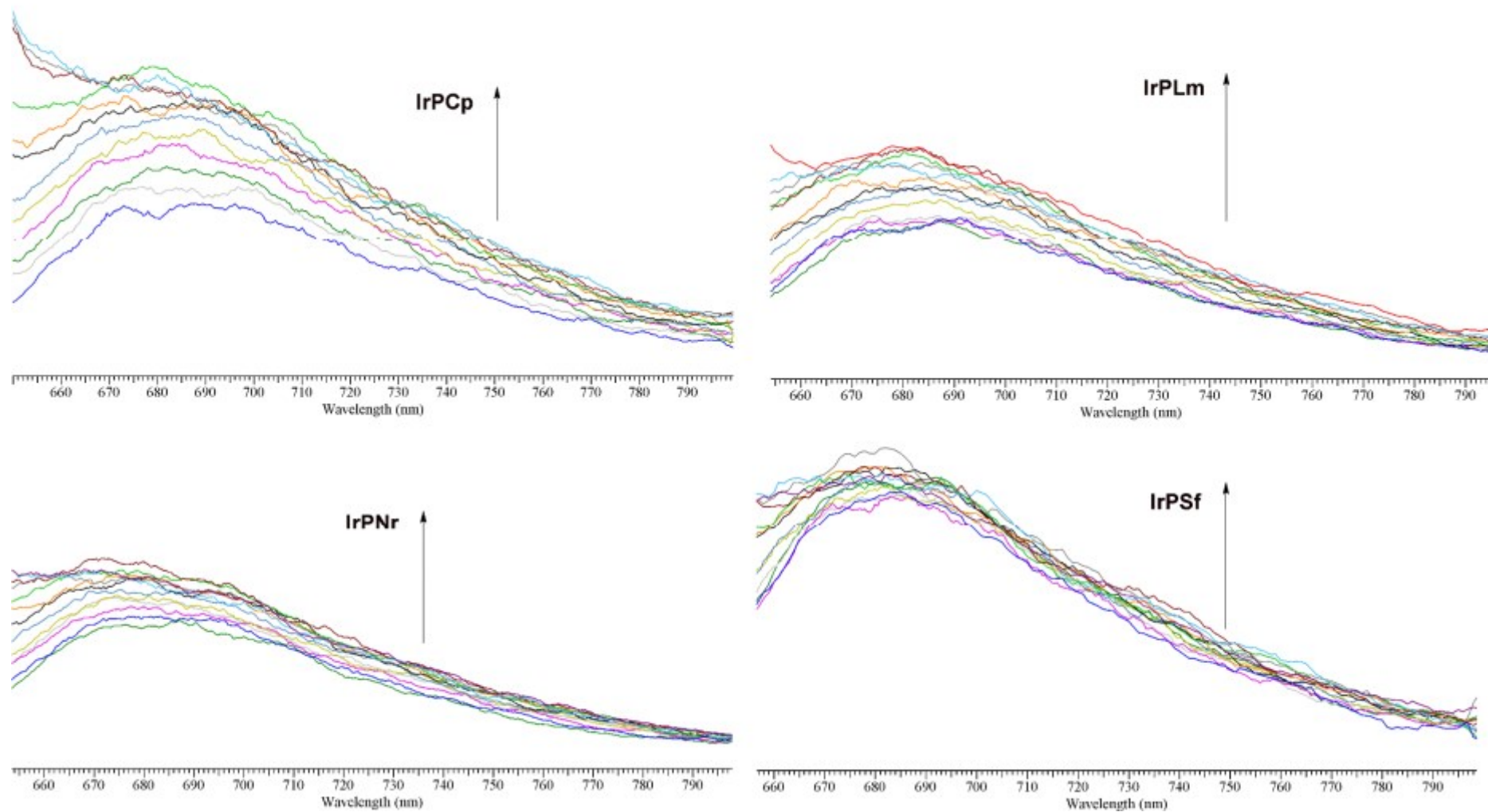


**Figure S4.** Fluorescence quenching of DAPI-CT DNA ( $C = 5 \times 10^{-5}$  M) by **IrPCp**, **IrPNr**, **IrPLm** and **IrPSf** (molar ratios 0.5, 1, 1.5, 2, 3, 4, 5, 6, 7, 8, 9, 10) in 50 mM pH 7.4 phosphate buffer (axis: y – fluorescence intensity; x – wavelength).

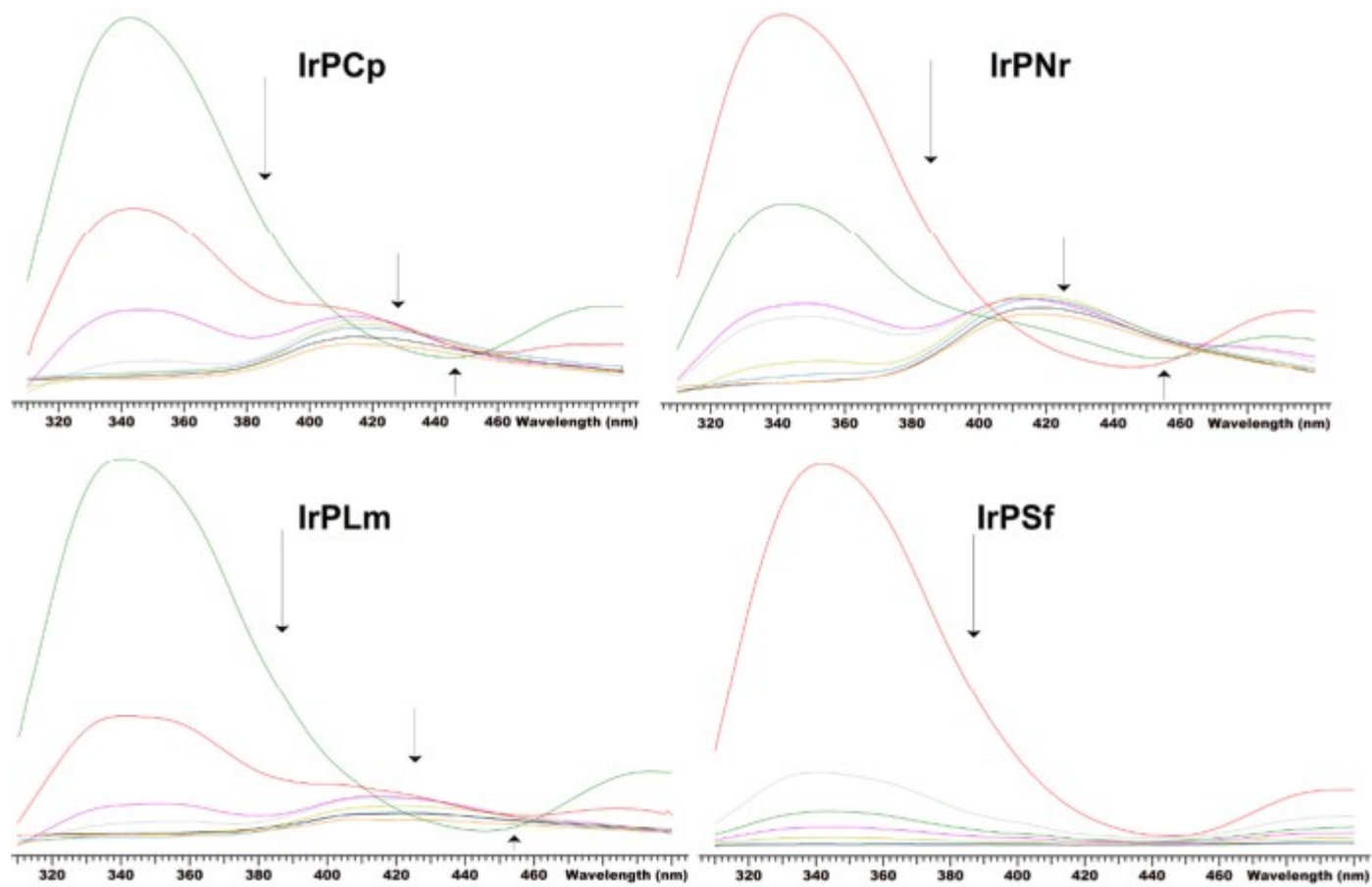


**Figure S5.** Fluorescence quenching of HSA ( $C = 5 \times 10^{-5}$ M) by **IrPCp**, **IrPNr**, **IrPLm** and **IrPSf** (molar ratios 0.5, 1, 1.5, 2) in 50 mM pH 7.4 phosphate buffer (axis: y – fluorescence intensity; x – wavelength).



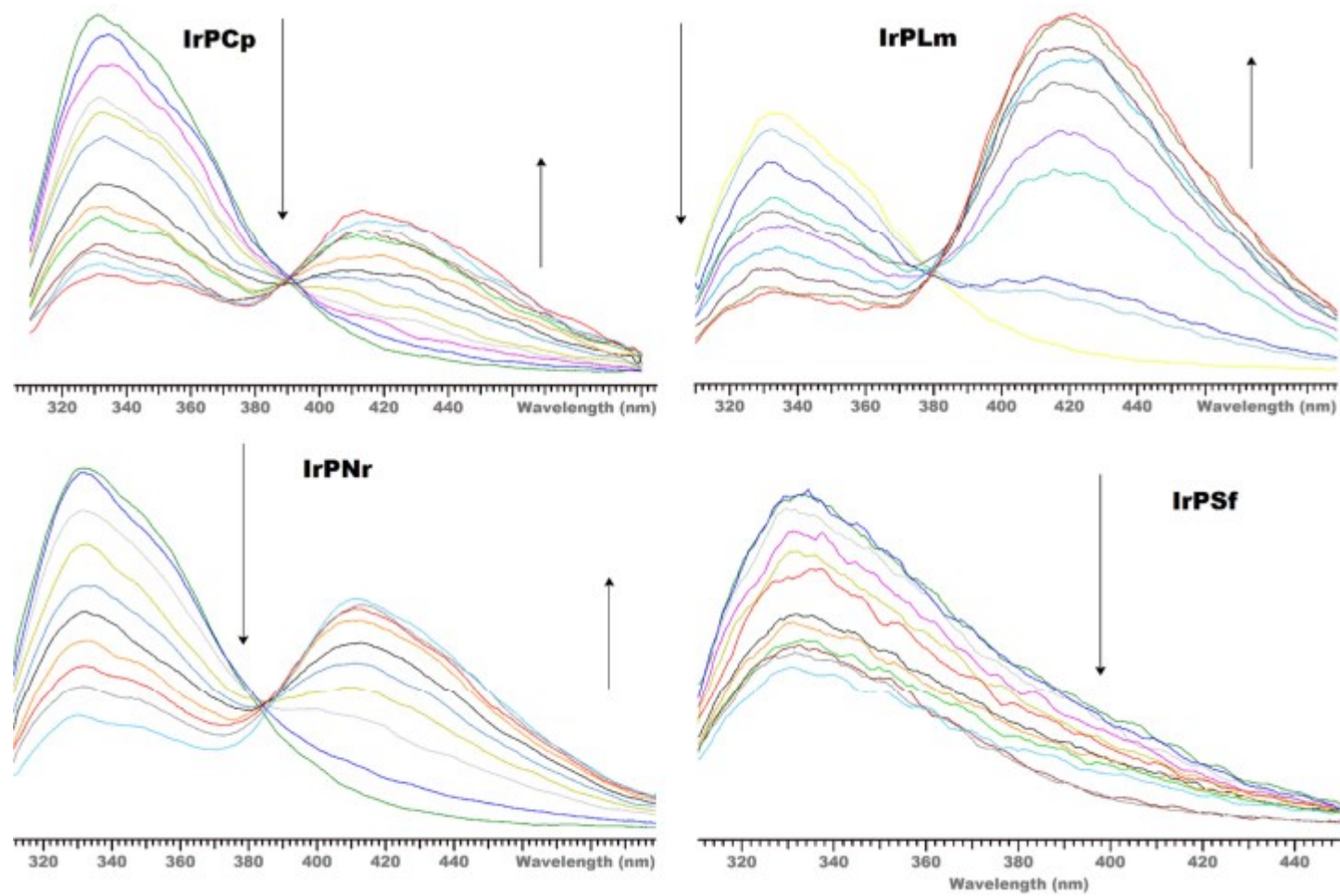


**Figure S6.** Fluorescence quenching of apo-Tf ( $C = 3.6 \times 10^{-6} \text{M}$ ) by **IrPCp**, **IrPNr**, **IrPLm** and **IrPSf** (molar ratios 0.5, 1, 1.5, 2, 3, 4, 5, 6, 7, 8, 9, 10) in 50 mM pH 7.4 phosphate buffer (axis: y – fluorescence intensity; x – wavelength).



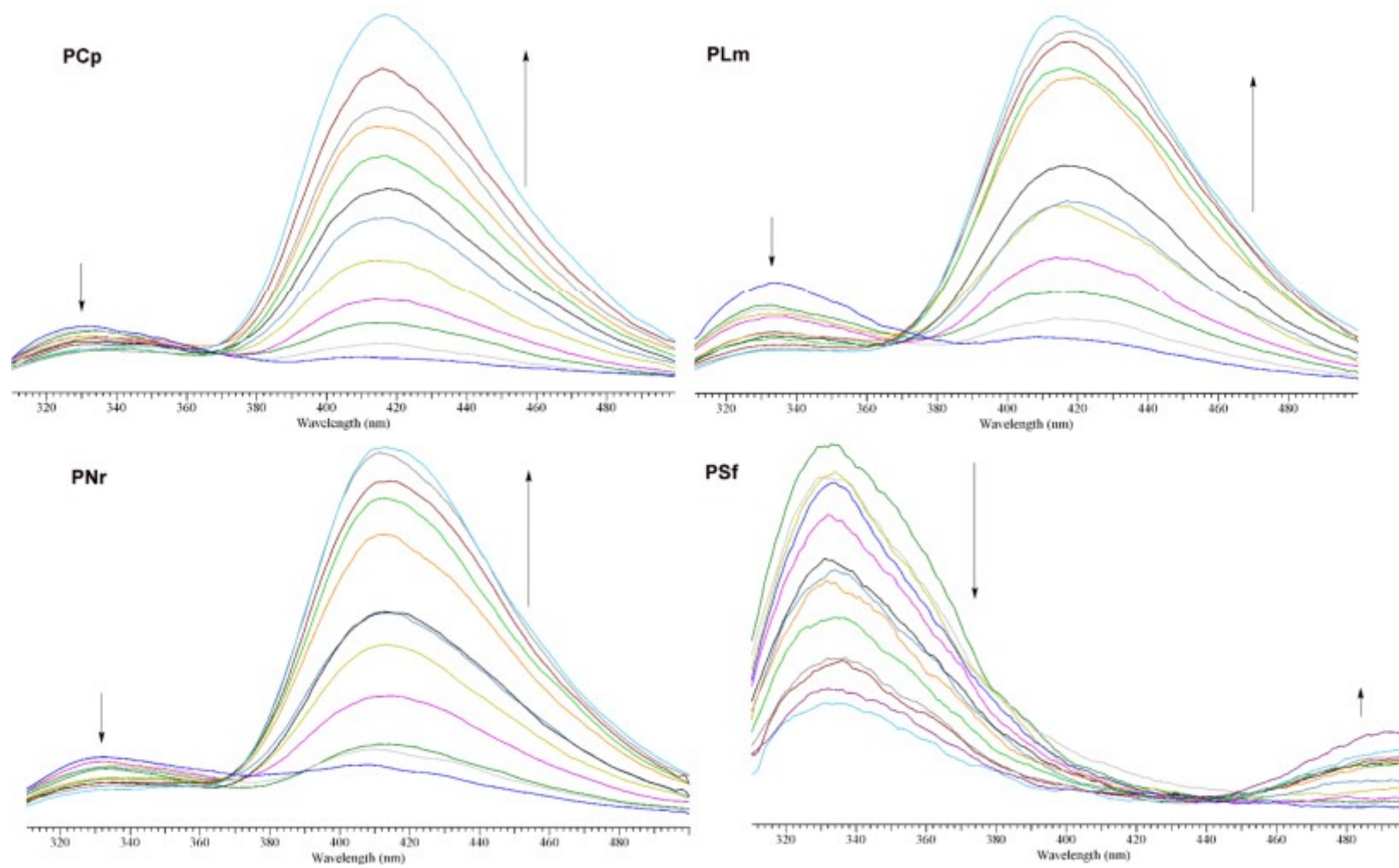


**Figure S7.** Fluorescence quenching of apo-Tf ( $C = 3.6 \times 10^{-6} \text{M}$ ) by **PCp**, **PNr**, **PLm** and **PSf** (molar ratios 0.5, 1, 1.5, 2, 3, 4, 5, 6, 7, 8, 9, 10) in 50 mM pH 7.4 phosphate buffer (axis: y – fluorescence intensity; x – wavelength).

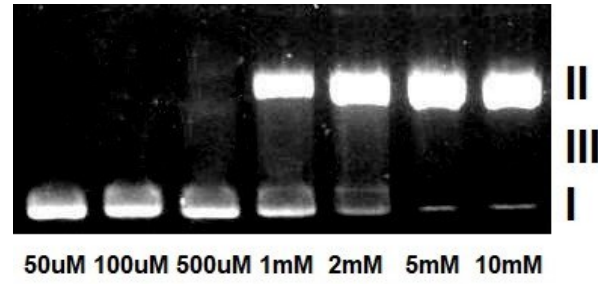


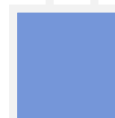
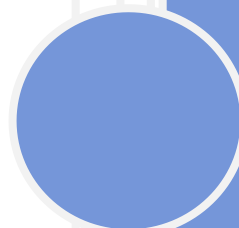
**Figure S8.** Agarose gel electrophoresis of pBR322 plasmid cleavage by H<sub>2</sub>O<sub>2</sub> in different concentrations.

# PUBLICATION S4

Sandra Koziel, Urszula K. Komarnicka, Barbara Pucelik, Agata Barzowska, Miłosz Siczek, Magdalena Malik, Daria Wojtala, Alessandro Niorettini, Agnieszka Kyzioł, Victor Sebastian, Pavel Kopel, Stefano Caramori, Alina Bieńko

*Liposomal formulation of magnetic iridium-copper coordination compounds with phosphine derived from fluoroquinolones for human prostate carcinoma treatment.*

Inorganic Chemistry Frontiers, 2022, 14, submitted



## ARTICLE

# Liposomal formulation of magnetic iridium-copper coordination compounds with phosphine derived from fluoroquinolones for human prostate carcinoma treatment

Received 00th January 20xx,  
Accepted 00th January 20xx

DOI: 10.1039/x0xx00000x

Sandra Koziel,<sup>a</sup> Urszula K. Komarnicka,<sup>a\*</sup> Barbara Pucelik,<sup>b</sup> Agata Barzowska,<sup>b</sup> Miłosz Siczek,<sup>a</sup> Magdalena Malik,<sup>c</sup> Daria Wojtala,<sup>a</sup> Alessandro Nioiretti,<sup>d</sup> Agnieszka Kyzioł,<sup>e</sup> Victor Sebastian,<sup>f,g,h</sup> Pavel Kopel,<sup>i</sup> Stefano Caramori,<sup>d</sup> Alina Bieńko<sup>a</sup>

Novel heteronuclear Ir<sup>III</sup>-Cu<sup>II</sup> coordination compounds ([Ir(η<sup>5</sup>-Cp\*)Cl<sub>2</sub>PCp-Cu(phen)](NO<sub>3</sub>)·1.75(CH<sub>3</sub>OH)·0.75(H<sub>2</sub>O) (**1**), [Ir(η<sup>5</sup>-Cp\*)Cl<sub>2</sub>PNr-Cu(phen)](NO<sub>3</sub>)·1.75(CH<sub>3</sub>OH)·0.75(H<sub>2</sub>O) (**2**), [Ir(η<sup>5</sup>-Cp\*)Cl<sub>2</sub>PLm-Cu(phen)](NO<sub>3</sub>)·1.3(H<sub>2</sub>O)·1.95(CH<sub>3</sub>OH) (**3**), [Ir(η<sup>5</sup>-Cp\*)Cl<sub>2</sub>PSf-Cu(phen)] (**4**) bearing phosphines derived from fluoroquinolones: sparfloxacin (HSf), ciprofloxacin (HCp), lomefloxacin (HLm), and norfloxacin (HNr) have been studied as possible anticancer chemotherapeutics. All compounds were characterized by ESI-MS spectrometry, selected spectroscopic methods (*i.e.*, IR, fluorescence and EPR), cyclic voltammetry, variable-temperature magnetic susceptibility measurements and x-ray diffractometry. Importantly, the crystal structure of [Ir(η<sup>5</sup>-Cp\*)Cl<sub>2</sub>PLm-Cu(phen)] features the 1D metal-organic polymer. It is worth mentioning that all Ir(III)-Cu(II) compounds exhibit weak magnetic interactions. Surprisingly, one of the studied systems [Ir(η<sup>5</sup>-Cp\*)Cl<sub>2</sub>PNr-Cu(phen)] exhibits a slow magnetic relaxation under the moderate DC magnetic field, which is extremely rare in the case of Cu(II) complexes. Investigation of Ir<sup>III</sup>-Cu<sup>II</sup> complexes cytotoxicity *in vitro* reveals their high anticancer potential towards human prostate carcinoma cells simultaneously with low toxicity against healthy cells. Furthermore, liposomes loaded with red-ox active [Ir(η<sup>5</sup>-Cp\*)Cl<sub>2</sub>PCp-Cu(phen)] were prepared to overcome low solubility and minimize serious systemic side effects. Confocal microscopy and an ICP-MS analysis showed that liposomal [Ir(η<sup>5</sup>-Cp\*)Cl<sub>2</sub>PCp-Cu(phen)] effectively accumulates inside human lung adenocarcinoma and human prostate carcinoma cells with colocalization in nuclei. A precise cytometric analysis revealed a predominance of apoptosis over the other types of cell death. Furthermore, the investigated nanoformulation may induce changes in the cell cycle leading to S phase arrest in a dose-dependent manner. *In vitro* cytotoxicity assays were also carried out within multicellular tumour spheroids and efficient anticancer action on these 3D assemblies was demonstrated.

## Introduction

Cancer is a group of diseases that are counted as one of the most life-threatening in the whole world.<sup>1</sup> In accounts of the Global Cancer Observatory is reported that in 2020 there were

over 9 million deaths because of cancer and around 19 million new cases.<sup>2</sup> One of the most used metal-based drugs in chemotherapy is the ones that contain Pt(II) compounds.<sup>3</sup>

The effectiveness of drugs is still hindered by clinical problems, including acquired or intrinsic resistance, a limited spectrum of activity, and high toxicity leading to side effects.<sup>4</sup> One of the strategies adopted to overcome these limitations, scientists to find inspiration in the activity of novel heteronuclear complexes.<sup>5</sup> When we incorporate two different cytotoxic metals into the same molecule, it may improve their activity as antitumor agents, because of the interaction between different metals with multiple biological targets, or through the improved chemophysical properties of the resulting heteronuclear compound. Therefore, in certain cases where a particular type of cancer develops a resistance mechanism that renders one of the metals redundant, the second or third metal might still show some activity. Through the years, several heteronuclear complexes were both synthesized and tested, also with some noticeable results that have been widely described.<sup>5-10</sup> One of the most successful compounds is BBR3464 (novel triplatinum compound), which

<sup>a</sup> Faculty of Chemistry, University of Wrocław, Joliot-Curie 14, 50-383 Wrocław, Poland E-mail: urszula.komarnicka@chem.uni.wroc.pl

<sup>b</sup> Małopolska Centre of Biotechnology, Jagiellonian University, Gronostajowa 7A, 30-387 Krakow, Poland

<sup>c</sup> Faculty of Chemistry, Jagiellonian University, Gronostajowa 2, 30-387 Kraków, Poland

<sup>d</sup> Faculty of Chemistry, Wrocław University of Science and Technology, Wybrzeże Wyspiańskiego 27, 50-370 Wrocław, Poland

<sup>e</sup> Department of Chemical, Pharmaceutical, and Agricultural Sciences, University of Ferrara, Via L. Borsari 46, 44121 Ferrara, Italy

<sup>f</sup> Department of Chemical Engineering, Aragon Institute of Nanoscience (INA), The Aragón Materials Science Institute (ICMA), University of Zaragoza, Campus Río Ebro-Edificio I+D, Mariano Esquillor S/N, 50018 Zaragoza, Spain

<sup>g</sup> Networking Research Center on Bioengineering, Biomaterials and Nanomedicine, CIBER-BBN, 28-029 Madrid, Spain

<sup>h</sup> Instituto de Nanociencia y Materiales de Aragón (INMA), CSIC-Universidad de Zaragoza, Zaragoza 50009, Spain

<sup>i</sup> Department of Inorganic Chemistry, Faculty of Science, Palacký University, 17. listopadu 12, CZ-771 46 Olomouc, Czech Republic

† Footnotes relating to the title and/or authors should appear here.

Electronic Supplementary Information (ESI) available: [details of any

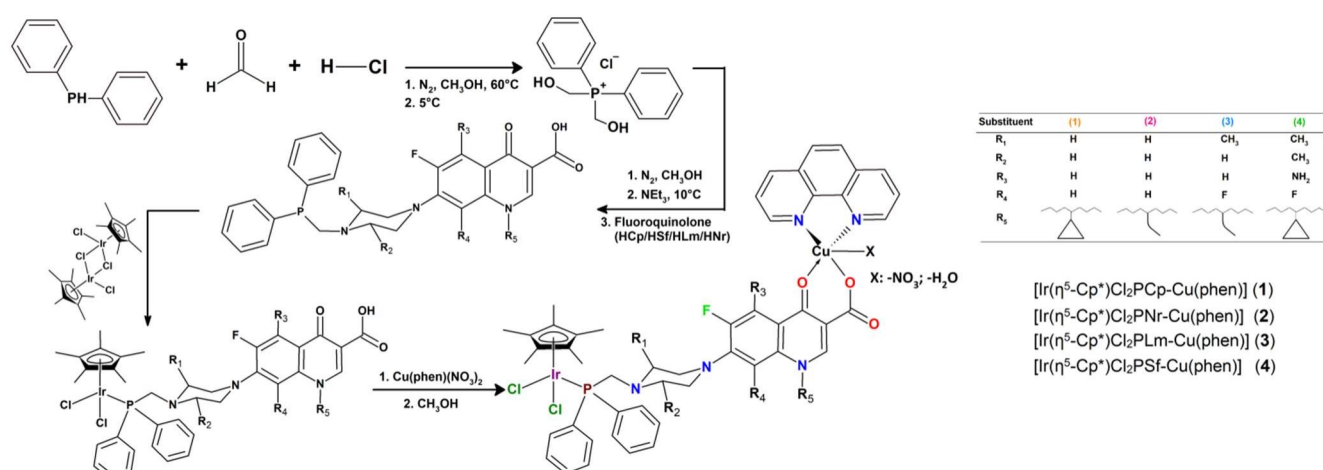
was once in Phase II clinical trials for the treatment of patients with melanoma, pancreatic, lung, ovarian and gastric tumors. It was shown that the complex interacts with the phosphate backbone of DNA and has a larger affinity towards single-strand DNA than cisplatin.<sup>10</sup> G. Zhu and colleagues patented a series of platinum-ruthenium complexes named Ruthplatin with better or comparable activity than cisplatin against a number of cell lines (even towards cisplatin-resistant cell lines). The introduction of the ruthenium centre led to the complexes being less toxic towards healthy MRC-5 lung fibroblast cells compared to the cisplatin control.<sup>11</sup>

Consequently, to this innovative approach, in our research, we decided to incorporate two metal ions in our research: copper(II) and iridium(III). It was proved that through many processes, such as DNA damage or generation of ROS, Cu(II) complexes could effectively induce cancer cells death. In addition, the superiority of these substances is also represented by the fact that Cu(II) ions are already present in the human body limiting the possibility of excessive immunological system response is low.<sup>12</sup> Most importantly, the introduction of a transition metal with unpaired electrons can also give the obtained complexes additional magnetic functionality such as SIM, SMM or superparamagnetic behavior which present slow relaxation of magnetization. After the discovery of first SMM - {Mn12OAc} complex,<sup>13</sup> numerous transition metal complexes<sup>14</sup> flooded the literature with record-breaking ground-state spin ( $S=83/2$  for a Mn19 cluster) reported by Powell and co-workers<sup>15</sup> and effective energy barrier for the magnetization relaxation ( $U_{\text{eff}}=86$  K for a Mn6 cluster) by Brechin and co-workers<sup>16</sup> SMMs can be envisaged for many potential applications such as high-density information storage, spin valves, spintronic, and quantum computing. Whereas superparamagnetic materials can apply in medicine as targeted delivery of drugs or genes, tissue engineering, targeted destruction of tumor tissue through hyperthermia, magnetic transfect ions, chelation therapy and tissue engineering.<sup>17-22</sup> However to the best of our knowledge

there are no studies about SMM based on Cu(II) complexes probably due to the fact that this ion have been overlooked for many years in terms of slow magnetic relaxation (SMR) because of the absence of the barrier to spin reversal: the axial zero-field splitting parameter  $D$  is undefined. In 2017 Boca and co-workers<sup>23</sup> has provided clear evidence that mononuclear Cu(II) complex with  $S = 1/2$  show a field supported SMR of the order of seconds at low temperature. SMR was controlled essentially by the Raman process. Even after this significant discovery, in our opinion, only one other case has been found. In this manuscript, we provide an important continuation of this story.

In the last few years, many researchers around the world have been working on the development of iridium(III) organometallic complexes and have succeeded in proving that iridium(III) complexes are substitutes for platinum-based drugs.<sup>3,24-32</sup> These complexes have unique properties such as potential redox features, universal structure, and wide range of ligand substitution rates, higher cellular uptake efficiency, large Stokes shifts and lower cytotoxicity.<sup>3,24-26,30,31</sup> Various mechanisms are responsible for the antitumor activity of iridium(III) compounds, such as inhibition of protein activity, catalyzing cellular redox reactions and damaging specific subcellular organelles. These amazing properties of iridium(III) complexes make them a rising star for novel curative anticancer agents that can bring and monitor the beneficial response concurrently.<sup>3,24-32</sup>

Additionally, to circumvent the previously mentioned side effects, our potential bioactive molecules will be locked in liposome. Liposomal technology has attracted great interest in the nanomedicine field owing to the liposomal features of low toxicity, biodegradability, and easy cellular uptake.<sup>33-35</sup> This nanocarriers have already been proven to successfully deliver both hydrophilic and hydrophobic molecules to cancer cells and liposomes could also provide protection against complexes speciation in the bloodstream as well as targeting possibilities in solid tumors.<sup>35,36</sup>



Scheme 1 Schematic view of the compounds and synthetic routes. The solvent molecules are omitted for clarity.

The research on anticancer compounds described herein is a continuation of our project in which phosphines ( $\text{Ph}_2\text{P-CH}_2\text{-FQ}$ ,

FQ: fluoroquinolone antibiotic) bearing fluoroquinolones: sparfloxacin (**HSf**), ciprofloxacin (**HCp**), lomefloxacin (**HLm**),

and norfloxacin (**HNr**) were coordinated to various metal centers: Cu(I), Cu(II), Ru(II), Ir(III).<sup>4,37-41</sup> The results described above confirmed that this mononuclear complex with phosphine was a good choice for designing new biological agents. Therefore we decided to extend our studies. Here, we investigate the dual nature of the iridium(III)-copper(II) ( $[\text{Ir}(\eta^5\text{-Cp}^*)\text{Cl}_2\text{PCp-Cu(phen)}](\text{NO}_3)\cdot 1.75(\text{CH}_3\text{OH})\cdot 0.75(\text{H}_2\text{O})$  (**1**),  $[\text{Ir}(\eta^5\text{-Cp}^*)\text{Cl}_2\text{PNr-Cu(phen)}](\text{NO}_3)\cdot 1.75(\text{CH}_3\text{OH})\cdot 0.75(\text{H}_2\text{O})$  (**2**),  $[\text{Ir}(\eta^5\text{-Cp}^*)\text{Cl}_2\text{PLm-Cu(phen)}](\text{NO}_3)\cdot 1.3(\text{H}_2\text{O})\cdot 1.95(\text{CH}_3\text{OH})$  (**3**),  $[\text{Ir}(\eta^5\text{-Cp}^*)\text{Cl}_2\text{PSf-Cu(phen)}]$  (**4**)) merger with phosphine derivatives of fluoroquinolones ( $\text{Ph}_2\text{PCH}_2\text{Cp}$  (**PCp**),  $\text{Ph}_2\text{PCH}_2\text{Nr}$  (**PNr**),  $\text{Ph}_2\text{PCH}_2\text{Lm}$  (**PLm**),  $\text{Ph}_2\text{PCH}_2\text{Sf}$  (**PSf**)) and phenanthroline as an auxiliary ligand. The coordination of two different metal ions would significantly impact the scope of action and could potentially generate interactions with cells through different mechanisms. To take the above issues into account, firstly, their physicochemical properties were determined using X-ray diffraction, elemental analysis, cyclic voltamperometry, mass spectrometry (ESI-MS), spectroscopic techniques and variable-temperature magnetic susceptibility measurements. The cytotoxicity of the compounds was evaluated *in vitro* against lung, breast, melanoma and prostate tumor cell lines and one non-tumor human embryonic kidney cell lines. Based on the findings mentioned above, in this study we carried out a preclinical investigation into the therapeutic potential of complex **IrPCpCu** encapsulated inside liposomes toward 3D lung and prostate cancer cell cultures and proposed an explanation of the working mechanism of this new complex.

## Results and discussion

### Synthesis

The new four heteronuclear complexes  $\text{Ir}^{\text{III}}/\text{Cu}^{\text{II}}$  were synthesized (Scheme 1) by stirring at room temperature  $[\text{Cu}(\text{phen})(\text{NO}_3)_2]$  with 1 equiv. of  $\text{IrFQ}$  ( $[\text{Ir}(\eta^5\text{-Cp}^*)\text{Cl}_2\text{PFQ}]$ ), reported by us in a recent study.<sup>26</sup> Binuclear complexes are soluble in  $\text{CH}_3\text{OH}$ ,  $\text{DMSO}$  and  $\text{CH}_2\text{Cl}_2$  and poorly soluble in water, where as they can be solubilized in water containing 2% of  $\text{DMSO}$ . The syntheses to mononuclear  $\text{IrFQ}$  complexes (incl.) were carried out under a nitrogen environment using Schlenk techniques. Chemical structures of studied  $\text{Ir}(\text{III})/\text{Cu}(\text{II})$  complexes are presented in Scheme 1.

The new compounds were characterized by elemental analysis and by IR and mass spectrometry: Compounds **1**, **2** and **3** were also characterized by single crystal X-ray diffraction techniques. In addition, encapsulation of the resulting heteronuclear  $\text{Ir}(\text{III})/\text{Cu}(\text{II})$  compounds into liposomes drastically increased their water solubility and presumably will improve bioavailability *in vivo*.

### X-ray

The single crystals of  $[\text{Ir}(\eta^5\text{-Cp}^*)\text{Cl}_2\text{PCp-Cu(phen)}](\text{NO}_3)\cdot 1.75(\text{CH}_3\text{OH})\cdot 0.75(\text{H}_2\text{O})$  (**1**),  $[\text{Ir}(\eta^5\text{-Cp}^*)\text{Cl}_2\text{PNr-Cu(phen)}](\text{NO}_3)\cdot 1.75(\text{CH}_3\text{OH})\cdot 0.75(\text{H}_2\text{O})$  (**2**) and  $[\text{Ir}(\eta^5\text{-Cp}^*)\text{Cl}_2\text{PLm-Cu(phen)}](\text{NO}_3)\cdot 1.3(\text{H}_2\text{O})\cdot 1.95(\text{CH}_3\text{OH})$  (**3**) were analysed by the X-ray diffraction technique (Fig. 1, Figs. S1-S4, Tables S1 and S2†). All obtained iridium(III)-copper(II) complexes crystallized in two different space groups (**1** and **2**: crystal system: triclinic, space group: *P1* and **3**: crystal system: orthorhombic, space group: *Pbcn*). Importantly the crystal structure of **3** features the 1D metal-organic polymer assembled from  $\text{Cu}(\text{II})$  centers,  $\text{Ir}(\text{III})$  complex linkers, phen (1,10-phenanthroline) molecule and  $\text{OH}^-$  ligands (Fig. 2). Every structure also contains solvent molecules and anions ( $\text{H}_2\text{O}$ ,  $\text{NO}_3^-$  or  $\text{OH}^-$ ).

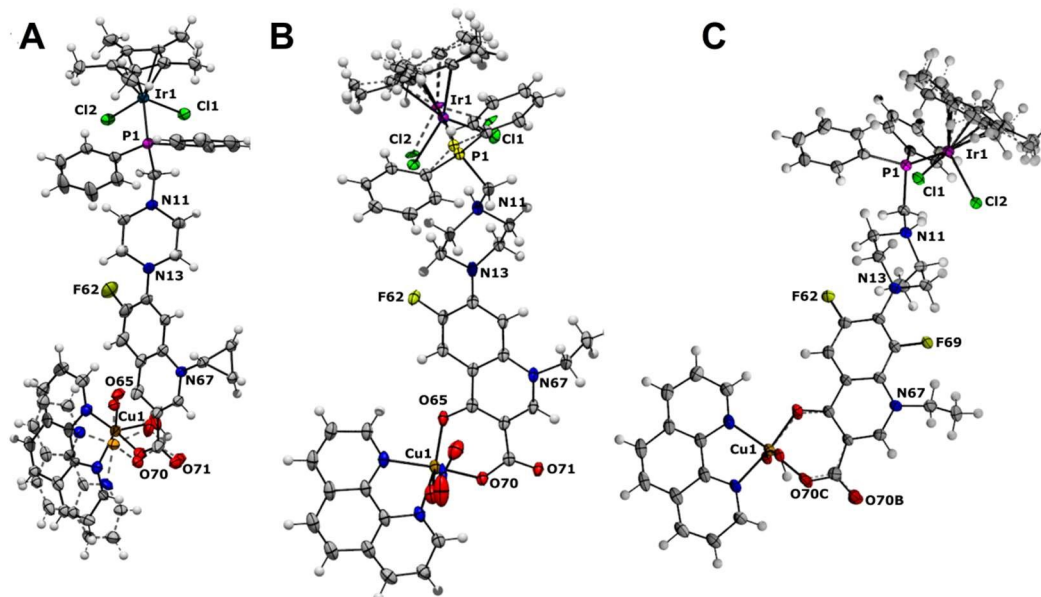


Figure 1. The crystal structures of the complex molecules **IrPCpCu** (**1**), **IrPNrCu** (**2**) and **IrPLmCu** (**3**). The solvent molecules are omitted for clarity.

The coordination geometry of the iridium ion in the all  $\text{Ir}(\text{III})$ - $\text{Cu}(\text{II})$  complexes adopts the expected half-sandwich pseudo-

octahedral “three-leg piano-stool” geometry, where the cyclopentadienyl moiety served as the top of the stool and the



three leg sites were occupied by phosphorous atom from ligand and two terminal chloride anions.<sup>26-29</sup> The bond angle values P–Ir–Cl and Cl–Ir–Cl, suggesting the pseudo-octahedral arrangement of atoms around the metal center, are found to be in the range of 86.73–124.2°. They turned out to be higher than values obtained for previously described by us mononuclear Ir(III) complexes with the same phosphine ligands (the bond angle values P–Ir–Cl and Cl–Ir–Cl are in the range of 86.04–90.45°).<sup>26</sup> The bond distances between iridium atoms and phosphorus atoms of complexes **1**, **2** and **3** were found to be on an average 2.3 Å, whereas the Ir–Cl1 and Ir–Cl2 bond distances of complexes **1**, **2** and **3** were found to be on an average 2.4 Å and are comparable with earlier reported mononuclear Ir(III) complexes.<sup>26-28</sup>

Cu<sup>II</sup> ion in all Ir(III)-Cu(II) complexes is coordinated via nitrogen atoms (from phenanthroline ligand) and IrP(FQ) (where: FQ: fluoroquinolone) complex *via* deprotonated carboxylate and pyridone oxygen atoms forming a distorted square-pyramidal coordination geometry (Fig. 1, Figs. S1-S3†). Average bond lengths for **1** and **2** complexes are as follows: Cu1–N91: 2.002, Cu1–N81: 2.013, Cu1–O65: 1.918 and Cu1–O70: 1.914 Å. Additionally, in the case of **1** bond lengths between Cu1 and O1W (from water molecule) equals 2.232(1) Å, for **2** bond lengths Cu1–N (from NO<sub>3</sub><sup>-</sup> ion) value is equal 2.351(1) Å.

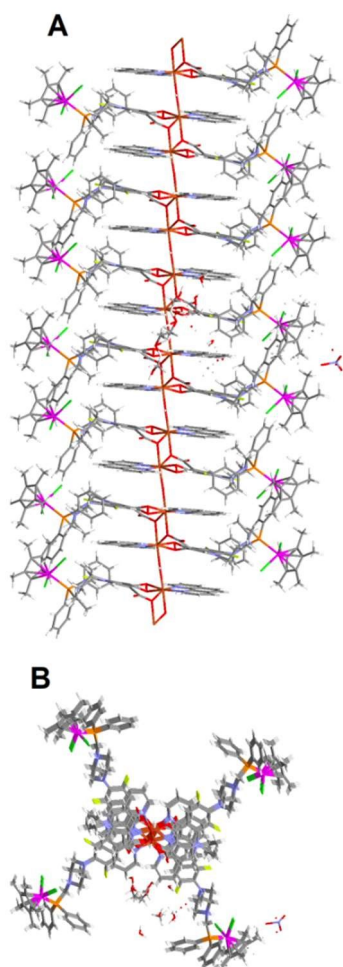


Figure 2 A perspective view (A and B) of the 1D polymer chain in the crystal structure of **3**.

Interestingly, the analysis of the **3** packing reveals that the coordination geometry around Cu<sup>II</sup> ion is distorted octahedral (Fig. 1, Fig. S4†). Cu<sup>II</sup> ion is coordinated by four oxygen atoms (two carboxylate, one pyridine oxygen, and one from OH-group) and two nitrogen atoms from phenanthroline ring leading to **3** polymer formations. This unit with two bridging OW1 and O70 atoms is formed with Cu1–Cu1 distance of 4.193(1) Å, similarly to that observed for Cu<sup>II</sup> complexes with other quinolones and aromatic diimines.<sup>42-45</sup> Additionally, the binuclear unit is stabilized by a pair of  $\pi$ -stacking interactions between phen and lomefloxacin fragments.

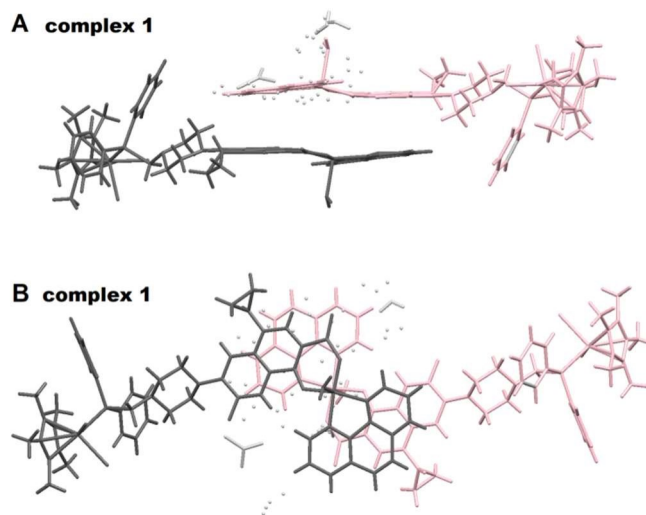


Figure 3 Packing diagram of complex **1** showing (A)  $\pi$ -stacking interaction between the fluoroquinolone rings (B) offset pattern of the  $\pi$ - $\pi$  stacking in complex **1**.

Interactions between two independent fused-ring fragments: the fluoroquinolone rings and the phen ligands can be found as well in cases of **1** and **2**. As it could be expected, this leads to interesting molecular packing of the complexes stabilized by  $\pi$ -stacking interactions (Fig. 3, Figs. S1-S4†ESI). The distances from the two centroids of ciprofloxacin (**1** complex) or norfloxacin (**2** complex) to the phen plane are 3.484 and 3.375 Å. Additionally, the conformation of the antibiotic fragment of complexes can be defined in terms of torsion angle, defining the orientation of the piperazine ring and fluoroquinolone moiety (**1**: C13–N13–C61–C62 –157.56°; **3**: C13–N13–C14–C15–128.45° **2**: C14–N13–C61–C62 –153.29°). Those values differ from torsion angle of piperazine ring and antibiotic motif for analogic monometallic Ir(III) complexes with the same phosphine ligands (Ir( $\eta^5$ -Cp\*)Cl<sub>2</sub>PCp: C13–N13–C61–C62 –165.92°; Ir( $\eta^5$ -Cp\*)Cl<sub>2</sub>PLm: C13–N13–C61–C62 –117.48° Ir( $\eta^5$ -Cp\*)Cl<sub>2</sub>PNr: C14–N13–C61–C62 –165.97°).<sup>26</sup> The value of torsion angle for **3** is significantly lower than values of torsion angle of both complexes **1** and **2**. This phenomenon can be explained by forming dimer by **3** where many various interactions exist.

#### Electrospray ionization mass spectrometry (ESI-MS)

All complexes in this study were also characterized by high-resolution mass spectrometry. In almost every case, a molecular-ion peak was present and consistent with the

expected isotopic distribution for a protonated parent ion,  $[M]^+$  or  $[M + H]^+$ . Only **1** did not show the corresponding  $[M]^+$  molecular ion peaks, but  $[\text{IrPCpCu-2Cl-2H+CH}_3\text{OH}]^+$  ions were detected at  $m/z$  1129.264 (Fig. S5-S8<sup>†</sup>). Less abundant peaks corresponding to  $[M - \text{Cl}]^+$  and  $[M - 2\text{Cl}]^+$  ions were also recorded indicating that chloride groups were easily displaced. Surprisingly, we can also observe adducts with solvent molecules either  $\text{H}_2\text{O}$  or  $\text{CH}_3\text{OH}$ . A solvent molecule, can occupy the coordination site vacated by chloride ions. Additionally, peaks corresponding to the loss of the phosphine ligands and the arena ring are observed, which indicates poor metal-to-ligand and metal-to-arena binding. As illustrated in figure S5-S8<sup>†</sup>, the cluster peaks arising from the experimental traces compared with those calculated for the pertinent species indicate excellent superimposition.

### Infrared spectroscopies

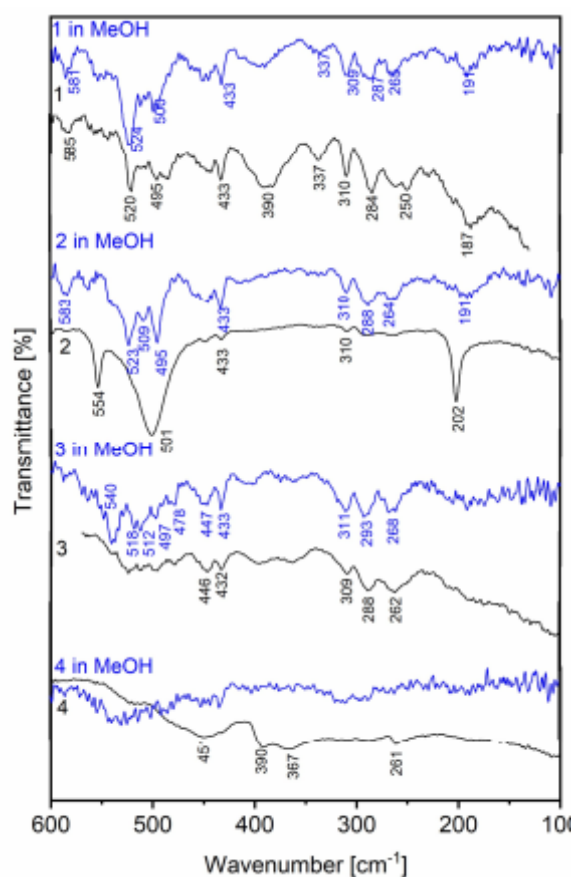


Figure 4 The FT-FIR spectra of complexes **1-4**.

The FT-IR spectra of the four novel iridium(III)-copper(II) complexes in the far infrared region are shown in fig. 4 (and in Fig. S9, ESI for MIR region). The characteristic  $\nu(\text{C-H})$  stretching vibrations generate in the spectral range of 3057-2853  $\text{cm}^{-1}$  the medium peaks in the FT-ATR spectra of discussed complexes. In the free ligands a strong band near 1720  $\text{cm}^{-1}$  is assigned to the  $\nu(\text{C=O})$  stretching vibrations of their carboxylic group ( $-\text{COOH}$ ),<sup>47</sup> which is very weak or not observed in ATR spectra of these complexes. Besides, in the FT-IR spectra of the novel complexes are observed two characteristic bands

attributed to the antisymmetric and symmetric stretching vibrations of  $\nu(\text{COO-})$ , which can be the marker of the coordination model. The bands with medium intensity around 1630  $\text{cm}^{-1}$  and 1335  $\text{cm}^{-1}$  are assigned to the  $\nu_{\text{as}}(\text{COO-})$  and  $\nu_{\text{s}}(\text{COO-})$  stretching vibrations, respectively (Tab. 1). We have determined the model of binding the used ligands to  $\text{Cu}^{2+}$  by showing  $\Delta$  parameter ( $\Delta = (\nu_{\text{as}}(\text{COO-}) - \nu_{\text{s}}(\text{COO-}))$ ). In the studied complexes  $\Delta$  parameters are in the range of 285-339  $\text{cm}^{-1}$ , which indicates the monodentate (unidentate) coordination of the carboxylate group in **1-4**, because  $\Delta$  is larger than in ionic compounds.<sup>46</sup>

Table 1 The characteristic discussed bands in FT-IR spectra of complexes **1-4**

Complex	$\nu_{\text{as}}(\text{COO}^-)$ [ $\text{cm}^{-1}$ ]	$\nu_{\text{s}}(\text{COO}^-)$ [ $\text{cm}^{-1}$ ]	$\Delta \nu$ [ $\text{cm}^{-1}$ ]	$\nu(\text{C=O})$ [ $\text{cm}^{-1}$ ] pyridine group	$\nu(\text{C=N})$ [ $\text{cm}^{-1}$ ]	$\nu(\text{Cu-O})$ [ $\text{cm}^{-1}$ ]	$\nu(\text{Cu-N})$ [ $\text{cm}^{-1}$ ]
1	1618	1333	285	1583	1517	520	543
1*	1630	1334	296	1587	1519	524	548
2	1627	1308	319	1584	1519	501	554
2*	1632	1335	297	1587	1520	523	ov
3	1619	1321	298	1585	1520	512	523
3*	1633	1327	306	1588	1522	512	540
4	1630	1292	338	1576	1519	ov	ov
4*	1632	1293	339	1583	1520	ov	ov

Abbreviations:  $\nu$ - stretching vibrations,  $\nu_{\text{as}}$ - antisymmetric stretching vibrations,  $\nu_{\text{s}}$ -symmetric stretching vibrations, ov- overlapped band; \* in MeOH

Nevertheless, the strong bands observed at 1624  $\text{cm}^{-1}$ , 1628  $\text{cm}^{-1}$ , 1612  $\text{cm}^{-1}$  and at 1645  $\text{cm}^{-1}$  in the FT-IR spectra of  $\text{Ph}_2\text{PCH}_2\text{Cp}$ ,  $\text{Ph}_2\text{PCH}_2\text{Nr}$ ,  $\text{Ph}_2\text{PCH}_2\text{Lm}$ ,  $\text{Ph}_2\text{PCH}_2\text{Sf}$  phosphine ligands are assigned to  $\nu(\text{C=O})\text{py}$  stretching vibrations, respectively. These peaks are shifted to lower frequencies in the range of 1558-1568  $\text{cm}^{-1}$  for the FT-IR spectra of studied iridium-copper complexes indicating decrease in the stretching force constant of the C=O bond as consequence of the coordination of the oxygen atom to the  $\text{Cu}^{2+}$  ions. In the FT-IR spectrum of free phen (1,10-phenanthroline) ligand a characteristic band around 1586  $\text{cm}^{-1}$  is due to  $\nu(\text{C=N})$  stretching vibrations and is shifted to a lower frequency in FT-IR spectra of **1-4** ( $\nu=69-64$   $\text{cm}^{-1}$ ). This shift indicates the coordination of the pyridine nitrogen atoms of phen to the copper ions (from nitrogen atom to the empty d-orbital of the metal ion) in a bidentate model.<sup>46</sup>

Actually, the FT-IR spectroscopy can be used as a good analytical tool to follow the coordination of organic ligands with metal ions,<sup>48</sup> which we confirm by analysis in FIR spectral region of the studied complexes **1-4**. The coordination marker bands:  $\nu(\text{Cu-O})$  and  $\nu(\text{Cu-N})$  are found in the FT-IR spectra of these complexes, *i.e.* at 520, and 543  $\text{cm}^{-1}$  for complex **1**, at 554  $\text{cm}^{-1}$  and 501  $\text{cm}^{-1}$  for complex **2**, respectively. These bands are absent in the spectra of free  $\text{Ph}_2\text{PCH}_2\text{Cp}$ ,  $\text{Ph}_2\text{PCH}_2\text{Nr}$ ,  $\text{Ph}_2\text{PCH}_2\text{Lm}$ ,  $\text{Ph}_2\text{PCH}_2\text{Sf}$  ligands and phen. Nevertheless, dissolving the obtained complexes in methanol hardly changes

their structures, which can be seen in the comparison of the spectra in the solid state with methanol solutions (Fig. 4).

### EPR Spectroscopy

The polycrystalline EPR spectra of the magnetically concentrated samples were recorded at room temperature and liquid nitrogen temperature (Fig. S10, ESI). There is no change in the line shape, line width and resolution as a function of temperature for all complexes. The anisotropic EPR spectral features can be associated to the axial symmetry having  $d_{x^2-y^2}$  ground state, where the geometry can correspond to an elongated octahedral, a square pyramidal or a square planar. At X-band, the EPR spectra for **1**, **2** and **4** showed an asymmetry in the perpendicular region with  $g_x = 2.091$ ;  $g_y = 2.092$ ,  $g_z = 2.21$  ( $g_{av} = 2.13$ ) for **1**,  $g_x = 2.075$ ;  $g_y = 2.151$ ,  $g_z = 2.11$  ( $g_{av} = 2.11$ ) for **2** and  $g_x = 2.091$ ;  $g_y = 2.132$ ,  $g_z = 2.212$  ( $g_{av} = 2.14$ ) for **4**. (see ESI, Figure S10). These values are in the range usually observed in compounds with distorted square-pyramidal geometry. The EPR spectra for **3** are typical of Cu(II) ion coordinated in distorted octahedron with  $g_x = 2.091$ ;  $g_y = 2.131$ ,  $g_z = 2.291$  ( $g_{av} = 2.17$ ) for **3** in agreement with its structure.

The frozen solution EPR spectra of compounds **1** and **2** at 77 K exhibit a well-defined resolution of hyperfine splitting of parallel orientation resulting from the interaction of an unpaired electron with copper nuclei ( $I = 3/2$ ). The spin Hamiltonian parameters are obtained by computer simulation (sim Fig. S11, ESI) of the experimental spectra with  $g_x = g_y = g_{\perp} = 2.065$ ,  $g_z = g_k = 2.211$  and  $A_k = 164$  G for **1**,  $g_x = 2.069$ ,  $g_y = 2.073$ ,  $g_z = g_k = 2.215$  and  $A_k = 113$  G for **2**,  $g_x = g_y = g_{\perp} = 2.098$ ,  $g_z = g_k = 2.289$  and  $A_k = 163$  G for **3** and  $g_x = g_y = g_{\perp} = 2.068$ ,  $g_z = g_k = 2.301$  and  $A_k = 146$  G for **4**. Hence, the EPR parameters of all complexes in frozen solutions are also consistent with the axial symmetry of the Cu(II) coordination sphere. Furthermore, the change of the parameters upon dissolving complexes **1**, **2** and **4** strongly suggest the replacement of the labile water or  $\text{NO}_3^-$  ligands in the binuclear molecule by the solvent molecules in the solutions as was found in many other similar complexes.<sup>49,50</sup>

### Luminescence properties

All heteronuclear  $\text{Ir}^{\text{III}}/\text{Cu}^{\text{II}}$  complexes emit in fluid solution at room temperature upon photoexcitation in the absorption manifold at 340 nm. The emission was structure less, and peaked at 450 nm. A particular case is constituted by complex **4** that manifest an emission peak centered at 540 nm (Fig. 5). Moreover, the emission intensity was stronger in DMF compared to DMSO, probably due to stronger solvation interaction in the case of DMSO, which enhances the non-radiative deactivation of these species (see ESI, Figure S12). So, for this reason we decided to conduct all the spectroscopic measures in DMF. The spectroscopic energy was around 3.2 eV for **1**, **2**, **3** complexes and 2.85 eV for **4** indicating a negligible influence of the solvent in tuning the excited state energetic.

The coordination of Cu(II) to Ir(III) complexes, that were described by us previously, such as  $\text{Ir}(\eta^5\text{-Cp}^*)\text{Cl}_2\text{PCp}$ ,  $\text{Ir}(\eta^5\text{-Cp}^*)\text{Cl}_2\text{PLm}$ ,  $\text{Ir}(\eta^5\text{-Cp}^*)\text{Cl}_2\text{PNr}$  leads to the bathochromic shift of the peak emission maximum wavelength. However, the

incorporation of another metallic centre to  $\text{Ir}(\eta^5\text{-Cp}^*)\text{Cl}_2\text{PSf}$ , causes the red-shift of **4** in comparison to the  $\text{Ph}_2\text{PCH}_2\text{Sf}$ , but blue-shift towards the  $\text{Ir}(\eta^5\text{-Cp}^*)\text{Cl}_2\text{PSf}$ . Therefore, the **1** ( $\lambda_{\text{max}} = 448$  nm), **2** ( $\lambda_{\text{max}} = 442$  nm), as well as **3** ( $\lambda_{\text{max}} = 470$  nm) exhibited a purple emission, whereas **4** ( $\lambda_{\text{max}} = 513$  nm) – green emission (see ESI, Figure S13-S14)

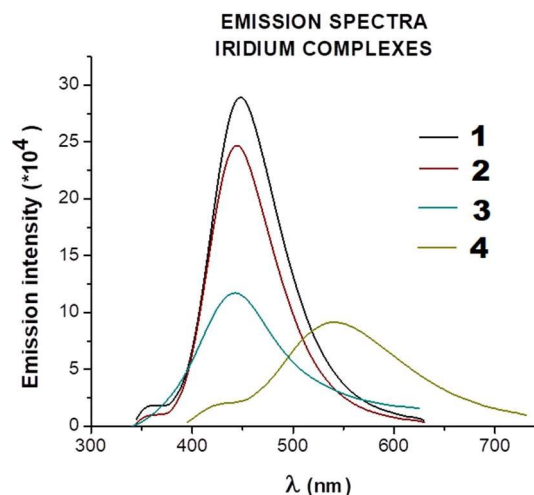


Figure 5 Emission spectra obtained for heteronuclear complexes  $\text{Ir}^{\text{III}}/\text{Cu}^{\text{II}}$  in DMF,  $C$  approx. 0.05M.

It could be concluded that the emission wavelength associated with these bimetallic Ir-Cu complexes is firmly related to the nature of the chosen ligand. While **1**, **2** and **3** seem to be subjected to the same spectroscopic trend only **4** looks to manifest a different emission pattern.<sup>26</sup> The outcome of conducted luminescence experiments corresponds to our previous findings, not only for Ir(III) complexes, but also for Ru(II), as well as Cu(I).<sup>11,25,26</sup>

### Electrochemical characterization

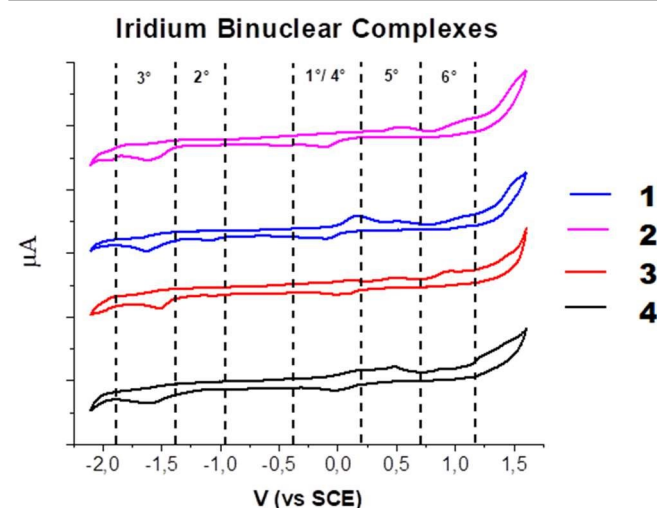


Figure 6 Cyclic voltammetry of binuclear complexes  $\text{Ir}^{\text{III}}/\text{Cu}^{\text{II}}$  in DMF (50mV/s from -2.1 to +1.6 vs SCE, TBAPF<sub>6</sub> 0.1M as supporting electrolyte).

The cyclic voltammetry of iridium binuclear complexes at 50 mV/s in purged DMF is reported in Fig. 6. The scans were recorded by scanning first in the cathodic direction (towards negative voltage) and then moving back to positive values. At negative voltage, we observed two major irreversible reductive waves, the first at ca. -1.1 V vs SCE for all heteronuclear complexes Ir<sup>III</sup>/Cu<sup>II</sup> (wave 2°) followed by another more intense reduction wave centred at ca. -1.6 V vs SCE (wave 3°) that, upon back scanning, results in a first anodic feature at +0.2 V (wave n°4) followed by a convoluted response spanning the voltage range +0.4, +1.3 V (waves n° 5, 6) (see Fig. S15, ESI). On the opposite, the restriction of the voltage scan to -0.3/+0.3 V vs SCE only makes evident the clean quasi reversible process of Cu(II)/(I) with  $E_{1/2}$  of ca. 0 V (peak 1 and

4). The complex appearance of the voltammetric waves in the 0/+1.3 V range of the full scan is mostly originated by the oxidation of decomposition products generated during the cathodic scan at potentials more negative than -0.9 V vs SCE.

#### DC susceptibility

Magnetic data was acquired with the help of the SQUID magnetometer (MPMS, Quantum Design) at the applied field of  $B_0 = 0.5$  T and, after correction to the underlying diamagnetism, transformed to the temperature dependence of the  $\chi_M T$  product (or effective magnetic moment, (Figures 7 – left). The field dependence of the magnetization per formula unit  $M_1 = M_{\text{mol}}/N_A \mu_B$  at the constant temperature is shown in figure 7 – right).

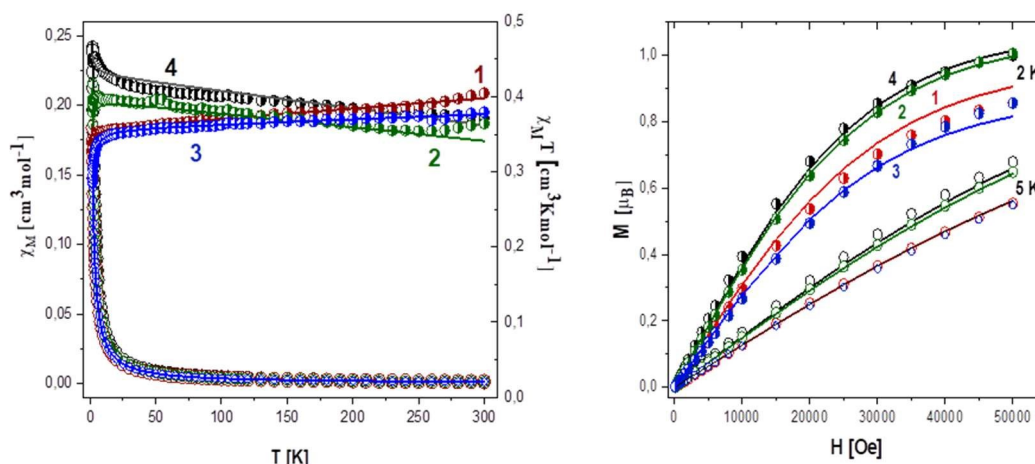


**Figure 7** Left - thermal dependencies of  $\chi_M T$  (half-open circles) and  $\chi_M$  (open circles) for **1** -  $[\text{Ir}(\eta^5\text{-Cp}^*)\text{Cl}_2\text{PCp-Cu}(\text{phen})]$ , **2** -  $[\text{Ir}(\eta^5\text{-Cp}^*)\text{Cl}_2\text{PNr-Cu}(\text{phen})]$ , **3** -  $[\text{Ir}(\eta^5\text{-Cp}^*)\text{Cl}_2\text{PLm-Cu}(\text{phen})]$ , **4** -  $[\text{Ir}(\eta^5\text{-Cp}^*)\text{Cl}_2\text{PSf-Cu}(\text{phen})]$ ; right - magnetization as a function of magnetic field at 2.00 K (half-open circles) and 5.00 K (open circles) for **1** - **IrPCpCu**, **2** - **IrPNrCu**, **3** - **IrPLmCu**, **4** - **IrPSfCu**. The solid lines (on all graphs) are calculated using the HDVV spin Hamiltonian and PHI.<sup>51</sup>

All examined complexes magnetically behave as a mononuclear unit with  $S_{\text{Cu}} = 1/2$  because Ir<sup>III</sup> ions are diamagnetic. Assuming  $g = 2.0$ , the expected high-temperature value for  $S = 1/2$  spin system is  $\mu_{\text{eff}} = g[S(S+1)]^{1/2} = 1.73 \mu_B$ . The experimental data for **1-4** compound show a value of  $\mu_{\text{eff}} = 1.80 \mu_B$  for **1** ( $\chi_M T = 0.41 \text{ cm}^3 \text{ mol}^{-1} \text{ K}$ )  $\mu_{\text{eff}} = 1.75 \mu_B$  for **2** ( $\chi_M T = 0.39 \text{ cm}^3 \text{ mol}^{-1} \text{ K}$ )  $\mu_{\text{eff}} = 1.74 \mu_B$  for **3** ( $\chi_M T = 0.38 \text{ cm}^3 \text{ mol}^{-1} \text{ K}$ )  $\mu_{\text{eff}} = 1.73 \mu_B$  for **4** ( $\chi_M T = 0.38 \text{ cm}^3 \text{ mol}^{-1} \text{ K}$ ) at  $T = 300$  K. The  $\chi_M T$  (and/or the effective magnetic moment) (Fig. 7 left) for **1** and **3** decreases slowly with lowering the temperature down to  $T = 25$  K. Below 50 K, a rapid decrease of the  $\chi_M T$  was registered reaching the value  $\chi_M T = 0.33 \text{ cm}^3 \text{ mol}^{-1} \text{ K}$  ( $1.62 \mu_B$ ) for **1** and  $\chi_M T = 0.29 \text{ cm}^3 \text{ mol}^{-1} \text{ K}$  ( $1.51 \mu_B$ ) for **3** at 1.8 K. This feature indicates antiferromagnetic nature of exchange interaction. Compounds **2** and **4** exhibit weak ferromagnetic coupling (systematic increase of  $\chi_M T$  value with the temperature) with similar strength (Figure 7 - left), which can be seen from the almost the same position of the maximum  $\chi_M T$ . The magnetization data at  $T = 2.0$  and  $BDC = 5.0$  T saturates to  $M_1 = M_{\text{mol}}/(N_A \mu_B) = 0.86 \mu_B$  (**1**, **3**) and  $1.00$  (**2**, **4**) which confirms the presence of some weak antiferromagnetic interaction in the case of **1** and **3**. A significant contribution of the temperature independent paramagnetism (TIP) is reflected in the slopes of the  $\chi_M T$  dependencies at higher temperatures.

To fit and interpret the magnetic susceptibility data of examined complexes, first it is necessary to find all possible magnetic pathways. As mentioned in the structural discussion, complexes **3** can be viewed as a monometallic chain in which the neighboring Cu(II) ions are bridged either by carboxylate groups of phosphino-fluoroquinolone ligands or OH- linkers with Cu...Cu separation of 3.470 Å and 4.193 Å, respectively. Considering above the susceptibility data was analyzed using a Hamiltonian [eq. 1] for an alternating Ising chain shows in scheme S1, ESI<sup>52</sup>:

$$H = \sum_i [-2J_1 S_i S_{i+1} - 2J_2 S_i S_{i+2} - g\beta H(S_i - S_{i+1})], \quad \text{eq. 1}$$

where  $S_i$  denotes the z - component of the 2n-th spin in a linear chain,  $J_1$  and  $J_2$  are.

The zero-field susceptibility of alternating antiferromagnetic Ising chain is:

$$\chi = \frac{1}{k_B T} \left( \frac{1}{1 - K} \right), \quad \text{eq. 2}$$

$$\text{where } K = \frac{J_1}{k_B T}, \quad K = \frac{J_2}{k_B T}.$$



The best agreement with the experimental magnetic data for **3** was obtained with  $J_1 = -0.82 \text{ cm}^{-1}$ ,  $J_2 = -0.29 \text{ cm}^{-1}$ ,  $g_{\text{av}}(\text{Cu}) = 2.09$  and  $\text{TIP} = 66 \cdot 10^{-6} \text{ cm}^3 \text{ mol}^{-1}$ ,  $R = \Sigma[(\chi T)_{\text{exp}} - (\chi T)_{\text{calc}}]^2 / \Sigma[(\chi T)_{\text{exp}}]^2 = 2.42 \cdot 10^{-5}$  (solid blue line in Figure 7A). The calculated curve matches the magnetic data well. The obtained result suggests that the stronger antiferromagnetic exchange interaction is mediated through the doubly oxygen bridge of carboxylate group (the higher  $J$  value, shorter  $\text{Cu} \cdots \text{Cu}$  contact) which correspond to the magneto-structural correlations presented in the literature.<sup>53,54</sup> For dimers with planar or near-planar cores  $[\text{Cu}_2(\mu_2\text{-O})_2]^{2+}$ , the exchange coupling constant ( $J$ ) depends on the value of the  $\text{Cu} - \text{O} - \text{Cu}$  ( $\phi$ ) angle and the  $\text{Cu}-\text{O}$  bridge distance ( $R$ ) especially expressed by the  $\phi / R$  ratio, and from more complicated factors such as geometry around paramagnetic centers.<sup>55-57</sup> Thus for  $\phi > 97.5^\circ$  the interaction is predicted to be antiferromagnetic ( $S = 0$  ground state) and for  $\phi < 97.5^\circ$  the ground state is equal 1 ( $S = 1$ ) and interaction should be ferromagnetic. The small magnitude of this interaction may be due to the asymmetry of the oxide bridge (two different  $R$  values, one much shorter  $2.058 \text{ \AA}$  and the other much longer  $2.220 \text{ \AA}$ ) causing distortion of the OH geometry and an unusually long distance  $\text{Cu} \cdots \text{Cu}$ .

Complexes **1**, **2** and **4** can be considered as mononuclear species which create supramolecular one-dimensional polymeric architecture through  $\pi$ -stacking interactions and system of hydrogen bonds between the water molecule and oxygen atoms from carbonyl groups with shortest  $\text{Cu} \cdots \text{Cu}$  contact  $4.196$  (**1**),  $4.904$  (**2**)  $\text{ \AA}$ .

The intermolecular interactions in all monomeric complexes was calculated using the well-known PHI program<sup>51</sup> which allows the simultaneous fitting of  $\chi T(T)$  and  $M(H)$  dependencies. The TIP was also included into the fitting

procedure. The least squares fit of the experimental data by these expressions leads to the following results:  $g_{\text{av}}(\text{Cu}) = 2.09$ ,  $zJ' = -0.09 \text{ cm}^{-1}$ ,  $\text{TIP} = 138 \times 10^{-6}$  for **1** (red lines in Fig. 7A) and  $g_{\text{av}}(\text{Cu}) = 2.11$ ,  $zJ' = 0.15 \text{ cm}^{-1}$ ,  $\text{TIP} = 192 \times 10^{-6}$  for **2** (green lines in Fig. 7A) and  $g_{\text{av}}(\text{Cu}) = 2.14$ ,  $zJ' = 0.28 \text{ cm}^{-1}$ ,  $\text{TIP} = 226 \times 10^{-6}$  for **4** (black lines in Fig. 7A). The discrepancy factor is  $2.09 \times 10^{-5}$  (**1**),  $6.93 \times 10^{-6}$  (**2**) and  $3.57 \times 10^{-6}$  (**4**). These data indicate that a weak exchange interaction between nearest copper atoms in the crystal lattices can exist of antiferromagnetic in **1** and ferromagnetic in **2** and **4** nature. The temperature-independent paramagnetic term is bigger than usually found. Although the origins of the observed phenomenon are unclear, it was verified by repeated measurements.

#### AC susceptibility

New information was obtained from the AC susceptibility measurements. They were performed first at low temperature  $T = 2.0 \text{ K}$  for a set of representative frequencies of the alternating field ( $f = 1.1, 11, 111, \text{ and } 1111 \text{ Hz}$ ) by ramping the magnetic field from zero to  $B_{\text{DC}} = 1 \text{ T}$  with the working amplitude  $B_{\text{AC}} = 0.3 \text{ \mu T}$ . There was no absorption signal (out-of-phase susceptibility component  $\chi''$ ) at the zero-field owing to a fast magnetic tunneling. With the increasing external field, this component raised, and only for complex **2** passed through a maximum between  $0.1$  and  $0.2 \text{ T}$  at the highest frequencies (Figure 8). This behavior indicates that **2** can exhibit the field induced slow magnetic relaxation. Subsequent experiments were done at a fixed external magnetic field  $B_{\text{DC}} = 0.1 \text{ T}$  (the maximum of the high-frequency signal) changing the frequency between  $f = 0.1$  to  $1500 \text{ Hz}$  for a set of temperatures between  $T = 1.8$  and  $12 \text{ K}$  (Figure S16, ESI).

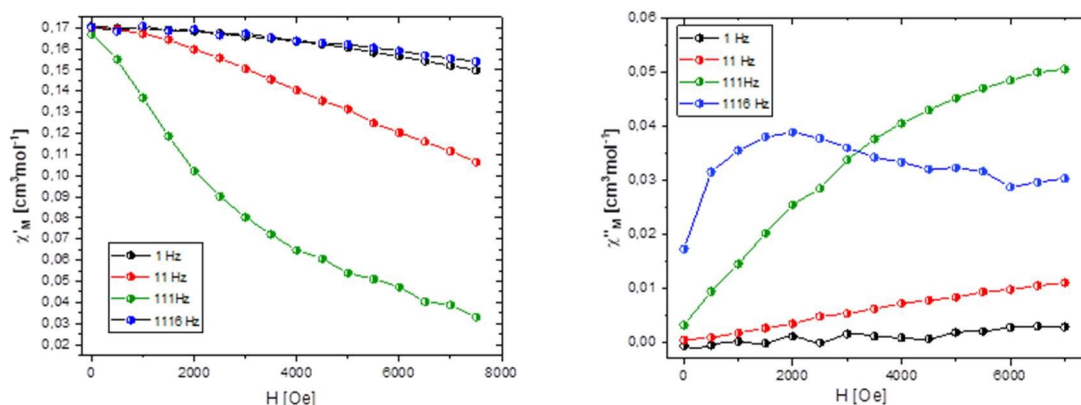


**Figure 8** Field dependencies of the AC susceptibility components for **2** at  $T = 2.0 \text{ K}$  for a set of frequencies of the AC field. Lines are a guide for the eye.

The in-phase ( $\chi M'$ ) and out-of-phase ( $\chi M''$ ) components exhibit small frequency dependences with the application of an external field of  $0.2 \text{ T}$ , indicative the possibility of a slow relaxation of magnetization, although the maxima in  $\chi''$  are missing. Using this data we cannot suggest SMM or SIM behaviour. However, the relaxation process for  $\text{Cu}(\text{II})$  ions is very rare due to the absence of a barrier to spin reversal: the axial zero-field splitting parameter  $D$  is undefined. However, some  $S = 1/2$  spin systems such  $\text{V}(\text{IV})$ , low-spin  $\text{Mn}(\text{IV})$ ,  $\text{Ni}(\text{I})$ ,

$\text{III}$ ), only three example of  $\text{Cu}(\text{II})$ ,  $\text{Os}(\text{V})$ ,  $\text{Ir}(\text{IV})$ ,  $\text{Fe}(\text{III})$  and  $\text{Ru}(\text{III})$  complexes show a slow magnetic relaxation (SMR) that is supported by the external magnetic field.<sup>58-62</sup> The presence of a relaxation process in complex **2** can be a result of geometry around  $\text{Cu}(\text{II})$  ions. Though the  $D$  parameter cannot be assigned to mononuclear copper(II) complexes, these are well-known as anisotropic systems showing at least two distinct  $g_z \neq g_x$  values well seen in the EPR spectra of an axial type. Thus, even in the absence of the zero-field splitting, there exists a

magnetic anisotropy. Additionally, the rest complexes not exhibit a relaxation process. This may be due to the presence of higher square-pyramidal geometry distortion in **2** ( $\tau' = 0.26$ ), which should lead to a greater difference between  $g_x$  and  $g_y$  and thus greater anisotropy of  $g$  tensor than those for **1**, **3** and **4**.

#### Partition Coefficients (log P)

The cytotoxic potency of a drug is generally related to its cellular accumulation, which is in turn related to its lipophilicity. In general, hydrophobicity is considered to play a crucial role in structure–activity correlations and in determining the biological properties of the drug.<sup>26</sup> The octanol–water partition coefficients (log P) for all complexes were determined and are listed in Table S3, ESI.

The complexes containing Cu(phen) ligands show substantially lower lipophilicity than mononuclear complexes, which is in accordance with the hydrophilic nature of the diimine ligands and the enlargement of the planar area.<sup>63</sup>

#### Cytotoxic study *in vitro*

The cytotoxicity of the four novel heteronuclear Ir<sup>III</sup>-Cu<sup>I</sup> complexes was evaluated against five selected cancer cell lines: A549, MCF7, DU-145, WM2664 and one normal HEK293T cell line *in vitro*. IC<sub>50</sub> values (concentration of a drug required to inhibit the growth of 50% of the cells) were assessed in two different approaches – after 24 h or 24 h + 48 h using the 3-(4,5-dimethylthiazole)-2,5-diphenyltetrazolium bromide (MTT) method. Cells were also treated with cisplatin in the same concentration range as complexes and considered as a control. IC<sub>50</sub> values were determined from the plots of cell viability at various concentrations of each compound by matching appropriate dose–response curves and are presented in Table S4, ESI.

Notably, all the heteronuclear Ir<sup>III</sup>/Cu<sup>I</sup> complexes displayed a higher cytotoxicity than cisplatin against all cell lines except from the WM2664 cells after 24 h incubation. Interestingly, lung carcinoma cancer cells (A549) were the most sensitive cell line to heteronuclear Ir<sup>III</sup>-Cu<sup>I</sup> complexes even in the case of both experimental approaches. Among all tested complexes, the **4** complex showed the most significant antitumor activity

*in vitro* with an IC<sub>50</sub> value of 0.6  $\mu$ M against A549, which was more than 100 times more effective than the reference drug cisplatin. This activity against A549 cells was higher after 24 h of incubation with the compound and 48 h of regeneration time (24 h + 48 h), compared to the experimental approach where cytotoxicity was determined after 24 h. This indicates that cytotoxic changes initiated in cells during the 24h incubation, cannot be repaired by the cells, and their repair systems that minimize toxicity are not sufficient, which may result in breaking down the resistance. In addition, compound **4** elicited moderate cytotoxicity against other tumor cell lines (except MCF7 after 72 h). Therefore, this suggests that the introduction of the third-generation fluoroquinolone (Ph<sub>2</sub>PCH<sub>2</sub>Sf) causes a significant increase in cytotoxicity to A549 cells compared to the complexes containing the second-generation fluoroquinolones (Ph<sub>2</sub>PCH<sub>2</sub>Nr, Ph<sub>2</sub>PCH<sub>2</sub>Cp, Ph<sub>2</sub>PCH<sub>2</sub>Lm). This is consistent with our previous observations about cytotoxicity mononuclear Ir<sup>III</sup> complexes with the same phosphine ligands.<sup>26</sup>

The results obtained for the tested complexes show that their activity against WM2664 is in the same range as for cisplatin after 24h. Such good cytotoxicity *in vitro* was accomplished with very low toxicity profiles toward normal cell lines. A comparison of the IC<sub>50</sub> values shown by heteronuclear ([Ir( $\eta^5$ -Cp\*)Cl<sub>2</sub>PSf-Cu(phen)] (**4**), ([Ir( $\eta^5$ -Cp\*)Cl<sub>2</sub>PLm-Cu(phen)] (**3**), ([Ir( $\eta^5$ -Cp\*)Cl<sub>2</sub>PCp-Cu(phen)] (**1**), ([Ir( $\eta^5$ -Cp\*)Cl<sub>2</sub>PNr-Cu(phen)] (**2**) vs mononuclear ([Ir( $\eta^5$ -Cp\*)Cl<sub>2</sub>PSf, ([Ir( $\eta^5$ -Cp\*)Cl<sub>2</sub>PLm, ([Ir( $\eta^5$ -Cp\*)Cl<sub>2</sub>PCp, ([Ir( $\eta^5$ -Cp\*)Cl<sub>2</sub>PNr) indicated that the presence of second metal caused a significant decrease in the toxicity against HEK293T cell line.<sup>26</sup> In line A549 the SI (selectivity index - IC<sub>50</sub> (normal cell line) / IC<sub>50</sub> (cancer cell line)) was found to be approximately 1290 for the **4** complex. Remarkably, such a high value was achieved despite the addition of a second metal with phenanthroline, which is known to be toxic.<sup>64</sup> This suggest that the introduction of a second metal is an effective method of minimizing toxicity to healthy cells and may bring into play different properties of the resulting compound.

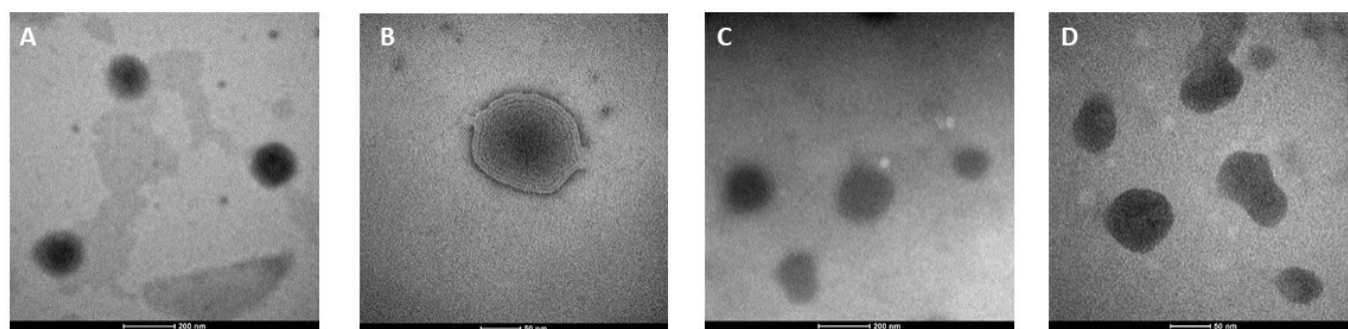


Figure 9 TEM images of empty liposome (A, B) and liposomes loaded with Ir<sup>III</sup>/Cu<sup>I</sup> complex (**1a**; C, D).

#### Characterization of liposomes

Negative staining TEM images revealed spherical shape with smooth surface and laminar character of homogeneous

liposomal dispersion (Fig. 9). Statistical analysis of liposome size resulted from TEM analysis (ImageJ) is in agreement with DLS data (Table S5, ESI). Although the size differences between TEM and DLS can be explained by the technique differences,



where in TEM the nanoparticles are dried and the size should be smaller after shrinking than in DLS.<sup>65</sup> The average size of empty liposomes was ca. 135 nm, while these loaded with Ir<sup>III</sup>/Cu<sup>II</sup> complex ca. 110 nm, both with polydispersity index indicating a quite narrow size distribution. The Zeta potential (the electrostatic repulsion of the particle surface) was examined in PBS (pH = 7.4), resulting in negative values for empty and loaded liposomes (ca. -30 mV and -42 mV, respectively) and indicating a stable dispersion.

#### Cytotoxicity – IC<sub>50</sub> determined by MTT

The anticancer activity of the tested iridium liposomes was evaluated by their cytotoxicity, determined by MTT assay against cancer (A549, Du145) and non-cancer (HaCaT) cells. The IC<sub>50</sub> values (concentration at which 50% of the cells are not able to grow any longer) for the tested compounds after 24h are summarized in Table 2. The cytotoxic activity of the used carriers (liposome, L), the reference compound cisplatin (CDPP) and complex ([Ir(η<sup>5</sup>-Cp\*)Cl<sub>2</sub>PcP-Cu(phen)] (1) encapsulated inside liposomes in two different concentrations (1a: 0.25mg/mL and 1b: 0.5mg/mL) were also determined.

It was observed, that the empty liposome exhibited no cytotoxicity, while IC<sub>50</sub> values for liposomes loaded with the Ir/Cu compounds (1a and 1b) were lower than for CDDP.

**Table 2** IC<sub>50</sub> (μg/ml and μM) values of the investigated compounds toward the selected cancer cell lines for 24 h. (1a: 0.25mg/mL and 1b: 0.5mg/mL)

	HaCaT	A549	Du145
L	180.47±0.108 μg/mL	21,18±0,1430 μg/mL	12,56 ± 0,1746 μg/mL
1a	260,92±0,172μg/mL 200.68±2.081 μM	12,31±0,1302 μg/mL 9.47±0.261 μM	1,744±0,1322 μg/mL 1.34±0.051 μM
1b	200.20±0.118 μg/mL 154.14±1.051 μM	7,257±0,1245 μg/mL 5.58±0.121 μM	1,559 ± 0,1278 μg/mL 1.20±0.071 μM
CDPP	9,694±0,2063 μg/mL 32.20±0.881 μM	17,16±0,1814 μg/mL 56.99±0.481 μM	20,56 ± 0,2189 μg/mL 68.28±2.081 μM

In the case of Du145 line, it can be observed as a 10-fold decrease for complex accumulated inside the liposome. Moreover, the compounds exhibited relatively lower cytotoxic activity against normal cells - human keratinocytes.

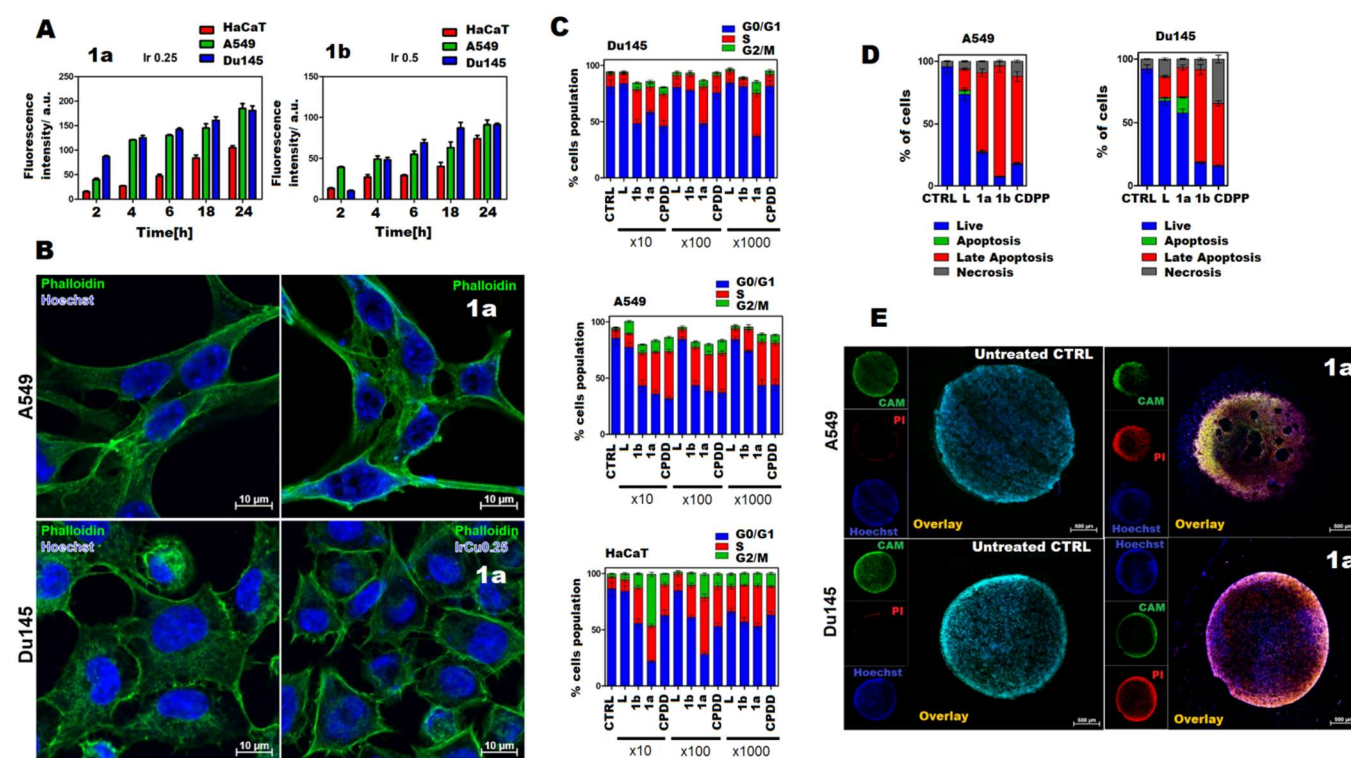


**Figure 10** Cellular Uptake. Accumulation of compounds (1a – IrPCu<sub>L0.25</sub>; 1b - IrPCu<sub>L0.5</sub>) in cells as a function of incubation time. B. Accumulation of 1a in A549 and DU-145 cells. Green fluorescence–phalloidin, blue fluorescence–tested compounds C. Cell cycle analysis. HaCaT, A549 and Du145 cells were treated with investigates compounds for 24 h and then staining by PI. D. Cell death mechanisms. Annexin V-FITC/PI double staining of A549 and DU145 spheroids treated with investigated compounds for 24 h. E. A549 (on top) and Du145 (on bottom) spheroids—representative live/death fluorescence images of spheroids subjected to 1a and corresponding control untreated spheroids grown in the same culturing conditions.

#### Anticancer activities *in vitro*

To investigate the mechanism underlying the activity of liposomes loaded with Ir<sup>III</sup>/Cu<sup>II</sup> complex in selected cell lines

(HaCat, A549 and Du145), and to locate their possible targets in the cell, total cellular uptake and confocal microscopy were first performed. Cellular accumulation of 1 liposomes after treatment of the tested cells was determined by the ICP-MS

technique. Time-dependent cellular uptake of **1a** and **1b** liposomal compounds is given in Fig. 10A. The results obtained confirm that a higher accumulation of liposomes in cells is observed with the increase of time. The highest accumulation of the compound was observed after 24h. The compound **1a** accumulated to a greater extent because a smaller amount of the compound was encapsulated in the liposomes, making them smaller in size. Moreover, we indicated the main accumulation of **1a** in nuclei (Fig. 10B)

It is noteworthy that the accumulation of **1** differed significantly between cancer and normal cells, showing lower accumulation in the non-cancer HaCaT cell line. These results fully corroborate the differences between the cytotoxicity of loaded nanoformulations against the cancer lines and against the normal cell line.

The activity of the tested compounds is certainly associated with cell cycle disruption. Previously published works confirm that cell cycle arrest is a characteristic of many compounds with anticancer properties. The cell cycle is divided into three main phases: the G0/G1 phase, the S phase, and the G2/M phase.<sup>66</sup> DNA content was measured using propidium iodide (PI) and analyzed by flow cytometry (Fig. 10C). Before the experiment, the cells were synchronized and then the test compounds were added at different concentrations. Iridium liposomes strongly inhibit the ability of the cell to further divide regardless of the dose used. Compound **1a**, even at 1000-fold dilution, arrests the cell cycle in the S phase for the A549 line and shows similar effects to CDDP. In studies on the Du145 cell line, an approximately 3-fold increase in S-phase cells was obtained for this compound compared to the reference compound. The cell cycle of normal cells (HaCaT) was not as strongly inhibited as for cancer cells. A similar effect could be observed for empty carriers (**L**). These results indicate that the tested compounds induce cell cycle disruption.

Induction of apoptosis in response to anti-cancer drugs is one of the major mechanisms for cancer cell death. Most tumor cells remain sensitive to certain apoptotic stimuli from chemotherapeutic agents. The apoptosis-inducing ability of drugs appears to be a primary factor in determining their efficacy.<sup>40</sup> The results obtained confirm that the cell death mechanisms are very similar for the iridium liposomes tested. Interestingly, compounds with lower iridium concentrations (**1a**) induce a high percentage of cells in late apoptosis (Fig. 10D). In the case of the Du145 line, less toxicity of the compounds is observed, particularly for the **1b** compound, for which the percentage of apoptotic cells is also the highest. Analyzing the cell death mechanisms induced by iridium liposomes, it can be observed that compounds with lower iridium concentration were more effective and the percentage of living cells was 7% for line A549 and 18% for line Du145, respectively. Compared to cisplatin, a significantly higher percentage of late-apoptotic cells than necrotic cells were observed after treatment with the tested compounds. Apoptosis is a more desirable cell death process because it does not lead to the inflammatory process that occurs with necrosis.

The results obtained on 2D cell culture encouraged us to investigate the antitumor activity of the selected Ir<sup>III</sup>-Cu<sup>II</sup> complex (**1a**) also in 3D A549 and DU-145 spheroidal culture. In addition, compared to classic adherent culture, spheroids can provide a microenvironment that more closely mimics the cellular interactions observed in tumor tissues. The therapeutic potential of synthesized compounds on 3D spheroids was detected by fluorescence staining of live and dead cells (Fig. 10E). For untreated 3D spheroid with normal morphology and structure mostly we observed live cells and a small amount of dead cells mainly in the superficial regions. In contrast, after spheroid treatment by complex, we observed a significant increase in dead cells after spheroid treatment by complex.

## Conclusions

The present work demonstrates the synthesis, physicochemical characterization, and anticancer activity *in vitro* of ([Ir( $\eta^5$ -Cp\*)Cl<sub>2</sub>PCp-Cu(phen))] (**IrPCpCu** (**1**)), [Ir( $\eta^5$ -Cp\*)Cl<sub>2</sub>PNr-Cu(phen))] (**IrPNrCu** (**2**)), [Ir( $\eta^5$ -Cp\*)Cl<sub>2</sub>PLm-Cu(phen))] (**IrPLmCu** (**3**)), Ir( $\eta^5$ -Cp\*)Cl<sub>2</sub>PSf-Cu(phen))] (**IrPSfCu** (**4**)) complexes. All inorganic compounds were characterized by ESI-MS spectrometry, selected spectroscopic methods (*i.e.*, IR, fluorescence and EPR), cyclic voltammetry, and variable-temperature magnetic susceptibility measurements. Three of four complexes were structurally identified by single-crystal X-ray diffraction analysis.

The coordination geometry of the iridium(III) ion in all Ir<sup>III</sup>-Cu<sup>II</sup> complexes adopts the expected half-sandwich pseudo-octahedral “three-leg piano-stool” geometry, where the cyclopentadienyl moiety served as the top of the stool and the three leg sites were occupied by phosphorous atom from ligand and two terminal chloride anions. Cu<sup>II</sup> ion in all Ir<sup>III</sup>-Cu<sup>II</sup> complexes is coordinated *via* nitrogen atoms (from phenanthroline ligand) and IrP(FQ) complex (where: FQ: fluoroquinolone) *via* deprotonated carboxylate and pyridone oxygen atoms forming a distorted square-pyramidal coordination geometry in case of **IrPCpCu** (**1**) and **IrPNrCu** (**3**) complexes. Importantly, the crystal structure of Ir( $\eta^5$ -Cp\*)Cl<sub>2</sub>PLm-Cu(phen))] features the 1D metal-organic polymer and the analysis of **3** packing reveals that the coordination geometry around Cu<sup>II</sup> ion is distorted octahedral.

Furthermore, investigation of the elucidation the behavior of the Ir<sup>III</sup>-Cu<sup>II</sup> compounds allowed us to formulate the following general conclusions: **(i)** All complexes exhibit intense emission in solution; **(ii)** Redox activity of all complexes was confirmed by cyclic voltamperometry; **(iii)** All complexes are characterized by weak magnetic properties. Surprisingly, one of the studied systems [Ir( $\eta^5$ -Cp\*)Cl<sub>2</sub>PNr-Cu(phen))] exhibits a slow magnetic relaxation under the moderate DC magnetic field, that is extremely rare in case of Cu(II) complexes; **(iv)** The heteronuclear Ir<sup>III</sup>/Cu<sup>II</sup> complexes displayed higher cytotoxicity than cisplatin against all cell lines (A549, MCF7, Du-145) except for the WM2664 cell line., **(v)** After encapsulation of complex **1** in liposomal formulation a 10-fold cytotoxicity decrease toward Du145 line was observed., **(vi)** Liposomes loaded with

[Ir( $\eta^5$ -Cp\*)Cl<sub>2</sub>PCp-Cu(phen)] effectively accumulates inside human lung adenocarcinoma and human prostate carcinoma cells with colocalization in nuclei. (vii) A precise cytometric analysis revealed a predominance of apoptosis over the other types of cell death; (viii) Efficient anticancer action in 3D multicellular tumour spheroids Du-145 was demonstrated.

All this data show unique properties of the presented here Ir<sup>III</sup>-Cu<sup>I</sup> complexes and their huge potential in various medical treatments. Redox, luminescence and magnetically active complexes with anticancer effectiveness (preliminarily proved *in vitro*) can be proposed for magnetic resonance imaging (MRI), targeted delivery *via* magnetic field control, targeted destruction of tumor tissue through hyperthermia or reactive oxygen species (phototherapy). We believe that Ir<sup>III</sup>-Cu<sup>I</sup> compounds are promising agents to further more detail investigations as an anticancer drugs.

## Experimental methods

### General procedures

All starting reagents (iridium and ruthenium), 2nd (HCp, HNr, HLm) and 3rd (HSf) generation fluoroquinolones (>98%), phosphanes, [Cu(phen)(NO<sub>3</sub>)<sub>2</sub>], [Ir( $\eta^5$ -Cp\*)Cl<sub>2</sub>]<sub>2</sub> and solvents were purchased from Sigma Aldrich and used without further purifications. All solvents were deaerated prior to use. Anhydrous Dimethylsulphoxide (DMSO) (34869-1L CAS: 67-68-5  $\geq$ 99.7%) and dimethylformamide (227056-1L CAS: 68-12-2  $\geq$ 99.8%) were purchased from Sigma Aldrich. Tetrabutylammoniumhexafluorophosphate (TBAPF<sub>6</sub>) was obtained from Alfa Aesar (CAS: 3109-63-5 98%). Electrodes for cyclic voltammetry were a platinum wire counter electrode (Matech  $\varnothing$ 0.5mm 99.9%) a SCE reference (303/SCG/6) and glassy carbon disk working electrode from Amel Electrochemistry (303/SCG/6). Mononuclear complexes (IrPSf, IrPLm, IrPNr and IrPCp)<sup>26</sup> and aminomethyl(diphenyl)phosphines (PSf,<sup>67</sup> PLm,<sup>38</sup> PNr<sup>37</sup> and PCp<sup>68</sup>) were synthesized as described previously.

### Characterization of organometallic iridium(iii) complexes

X-Ray quality crystals were obtained by slow evaporation mother liquor. SCXRD measurements for **1** and **3**, were performed on a Rigaku Oxford Diffraction XtaLAB Synergy-R DW diffractometer equipped with a HyPix ARC 150° Hybrid Photon Counting (HPC) detector using CuK $\alpha$  ( $\lambda$  = 1.54184 Å). For structure **2** a Xcalibur Gemini Ultra diffractometer equipped with Ruby CCD detector using CuK $\alpha$  ( $\lambda$  = 1.54184 Å) was employed. All measurements were performed at 100 K. Data were processed using the CrystAlisPro software. The structures were solved by intrinsic phasing with SHELXT (2015 release) and refined by full-matrix least-squares methods based F<sup>2</sup> using SHELXL. For all structures, H atoms bound to C atoms were placed in the geometrically idealized positions and treated in riding mode, with C-H = 0.95 Å and U<sub>iso</sub>(H) = 1.2U<sub>eq</sub>(C) for C-H groups, and C-H = 0.98 Å and U<sub>iso</sub>(H) = 1.5U<sub>eq</sub>(C) for CH<sub>3</sub> groups. The N- and O-bonded hydrogen atoms which were at initial stage of refinement located from difference maps and then constrained with AFIX 13 and AFIX 3

command, respectively. Crystallographic data of the structures have been deposited at the Cambridge Crystallographic Data Centre with CCDC reference numbers 2175515: [Ir( $\eta^5$ -Cp\*)Cl<sub>2</sub>PLm-Cu(phen)](NO<sub>3</sub>)·1.3(H<sub>2</sub>O)·1.95(CH<sub>3</sub>OH); 2175516: [Ir( $\eta^5$ -Cp\*)Cl<sub>2</sub>PNr-Cu(phen)](NO<sub>3</sub>)·1.75(CH<sub>3</sub>OH)·0.75(H<sub>2</sub>O) and 2175517: ([Ir( $\eta^5$ -Cp\*)Cl<sub>2</sub>PCp-Cu(phen)](NO<sub>3</sub>)·1.75(CH<sub>3</sub>OH)·0.75(H<sub>2</sub>O).

Elemental analyses (C, H and N) were carried out with a Vario Micro Cube – Elementar. Mass spectra were recorded with a Bruker MicrOTOF-Q II spectrometer with an ESI ion source under the following conditions: nebulizer pressure: 0.4 bar, dry gas: 4.0 l min<sup>-1</sup> heated to 180 °C. Data were recorded in the positive ion mode, while profile spectra were recorded in the mass range 50–3000 m/z; end plate offset –500 V; capillary voltage 4500 V; mass resolving power of the instrument – over 18000. Mass calibration was done using the cluster method with a mixture of 10 mM sodium formate and isopropanol (1 : 1, v/v) before the run. In order to record the spectra the compounds were dissolved in chloroform.

Electronic absorption spectroscopy was carried out with an UV-Vis spectrophotometer (Agilent Technologies, Cary300 UV-Vis).

Steady state luminescence spectra were acquired with an Edinburgh Instruments FS920 spectrofluorimeter equipped with a R928 phototube detector. The spectroscopic energy E<sub>00</sub> was obtained from the crossing of the normalized absorption and emission spectra.

FT-IR spectra of complexes were recorded using a BrukerVertex 70V vacuum spectrometer equipped with a diamond ATR cell with resolution of 2 cm<sup>-1</sup> in the middle-infrared (4000–500 cm<sup>-1</sup>) and far-infrared (600–100 cm<sup>-1</sup>) regions at room temperature as solid state and methanolic solutions (c = 0.80%) as well. The spectral data were collected and further elaborated using Bruker OPUS software.

Direct current (DC) magnetic measurements in the temperature range 1.8–300 K (BDC = 0.1 T) and variable - field (0–5 T) (at low temperature) were performed using a Quantum Design SQUID-based MPMSXL-5-type magnetometer. Corrections were based on subtracting the sample – holder signal and contribution  $\chi$ D estimated from the Pascal constants.<sup>69</sup> Variable-temperature (2–7 K) alternating current (AC) magnetic susceptibility measurements under different applied static fields in the range of BDC = 0–1.0 T were carried out with Quantum Design Physical Property Measurement System (PPMS). Magnetic measurements were carried out by crushing the crystals and restraining the sample in order to prevent any displacement due to its magnetic anisotropy.

### EPR spectroscopy

Electron paramagnetic resonance (EPR) spectra were measured using a Bruker ELEXYS E 500 Spectrometer equipped with NMR teslametr and frequency counter at X-band. The experimental spectra were simulated with use of computer programs (S=1/2) written by Dr. Andrew Ozarowski from NHMFL, University of Florida. The solid compounds dissolved in water and a few drops of DMSO were added to the samples to ensure good glass formation at liquid nitrogen temperature.

### Synthesis of heterometallic iridium-copper complexes

The Ir(III)/Cu(II) complexes **1–4** were prepared according to following general synthetic procedure: a solution of the [Cu(phen)(NO<sub>3</sub>)<sub>2</sub>] (1 equiv) in methanol (5 mL) was slowly added to a stirred solution of mononuclear complexes Ir(III) (1 equiv) in the same solvent (20 mL) and the mixture was stirred at room temperature for 24 h in the dark. Suitable crystals for X-ray diffraction were obtained from slow evaporation of a solution in CH<sub>3</sub>OH.

#### Data for [Ir(η<sup>5</sup>-Cp\*)Cl<sub>2</sub>PCp-Cu(phen)] (1)

**Yield:** 84%, **Molar mass:** 1300.196 g/mol. **Anal. Calcd for** C<sub>52</sub>H<sub>53</sub>Cl<sub>2</sub>CuFIrN<sub>5</sub>O<sub>4</sub>P·(NO<sub>3</sub>)·2.75(H<sub>2</sub>O): C, 48.04; H, 4.54; N, 6.46%. **Found:** C, 48.05; H, 4.55; N, 6.47%.

**ESI(+)**M<sup>S</sup> in CH<sub>3</sub>OH, m/z: 1129.264 (theor.: 1129.274) (100%) [IrPCpCu-HCl-Cl+CH<sub>2</sub>OH]<sup>+</sup>; 1099.260 (theor.: 1099.263) (3%) [IrPCpCu-2Cl]<sup>+</sup>; 858.280 (theor.: 858.281) (6%) [IrPCpCu-2Cl-Cu(phen)+H]<sup>+</sup>; 787.176 (theor.: 787.178) (27%) [IrPCpCu-IrCl<sub>2</sub>+O]<sup>+</sup>; 573.122 (theor.: 573.123) (9%) [IrPCpCu-IrCl<sub>2</sub>-PPh<sub>2</sub>CH<sub>2</sub>]<sup>+</sup>; 564.131 (theor.: 564.133) (5%) [IrPCpCu-2HCl+CH<sub>2</sub>-OH]<sup>2+</sup>; 549.126 (theor.: 549.127) (6%) [IrPCpCu-HCl-Cl]<sup>2+</sup>

#### Data for [Ir(η<sup>5</sup>-Cp\*)Cl<sub>2</sub>PNr-Cu(phen)] (2)

**Yield:** 89%, **Molar mass:** 1353.226 g/mol. **Anal. Calcd for** (C<sub>51</sub>H<sub>52</sub>Cl<sub>2</sub>CuFIrN<sub>6</sub>O<sub>6</sub>P)·(NO<sub>3</sub>)·1.75(CH<sub>4</sub>O)·0.75(H<sub>2</sub>O): C, 46.82; H, 4.51; N, 7.25%. **Found:** C, 46.83; H, 4.52; N, 7.27%.

**ESI(+)**M<sup>S</sup> in CH<sub>3</sub>OH, m/z: 1157.199 (theor.: 1157.201) (100%) [IrPNrCu]<sup>+</sup>; 1123.246 (theor.: 1123.240) (1%) [IrPNrCu-Cl+H]<sup>+</sup>; 916.222 (theor.: 916.218) (4%) [IrPNrCu-Cu+H]<sup>+</sup>; 894.226 (theor.: 894.221) (4%) [IrPNrCu-Cu(phen)-HCl-OH+CH<sub>2</sub>OH]<sup>+</sup>; 759.183 (theor.: 759.183) (17%) [IrPNrCu-IrCl<sub>2</sub>]<sup>+</sup>

#### Data for [Ir(η<sup>5</sup>-Cp\*)Cl<sub>2</sub>PLm-Cu(phen)] (3)

**Yield:** 88%, **Molar mass:** 1357.29 g/mol. **Anal. Calcd for** C<sub>52</sub>H<sub>52</sub>Cl<sub>2</sub>CuF<sub>2</sub>N<sub>5</sub>O<sub>3</sub>PIr·(NO<sub>3</sub>)·1.3(H<sub>2</sub>O)·1.95(CH<sub>4</sub>O): C, 48.26; H, 4.81; N, 6.19%. **Found:** C, 48.28; H, 4.82; N, 6.20%.

**ESI(+)**M<sup>S</sup> in CH<sub>3</sub>OH, m/z: 1191.175 (theor.: 1191.204) (100%) [IrPLmCu]<sup>+</sup>; 1149.285 (theor.: 1149.280) (5%) [IrPLmCu-HCl-Cl+CH<sub>2</sub>OH]<sup>+</sup>; 948.229 (theor.: 948.225) (38%) [IrPLmCu-Cu]<sup>+</sup>; 912.253 (theor.: 912.248) (5%) [IrPLmCu-Cu(phen)-Cl]<sup>+</sup>; 908.303 (theor.: 908.297) (4%) [IrPLmCu-Cu(phen)-2Cl+CH<sub>2</sub>OH]<sup>+</sup>; 878.293 (theor.: 878.287) (3%) [IrPLmCu-Cu(phen)-2Cl+H]<sup>+</sup>; 791.191 (theor.: 791.187) (76%) [IrPLmCu-IrCl<sub>2</sub>]<sup>+</sup>; 593.131 (theor.: 593.129) (43%) [IrPLmCu-IrCl<sub>2</sub>-PPh<sub>2</sub>CH<sub>2</sub>]<sup>+</sup>

#### Data for [Ir(η<sup>5</sup>-Cp\*)Cl<sub>2</sub>PSf-Cu(phen)] (4)

**Yield:** 78%, **Molar mass:** 1231.69 g/mol. **Anal. Calcd for** C<sub>54</sub>H<sub>55</sub>Cl<sub>2</sub>CuF<sub>2</sub>N<sub>6</sub>O<sub>3</sub>PIr: C, 52.66; H, 4.50; N, 6.82%. **Found:** C, 52.65; H, 4.49; N, 6.81%.

**ESI(+)**M<sup>S</sup> in CH<sub>3</sub>OH, m/z: 1230.208 (theor.: 1230.234) (58%) [IrPSfCu]<sup>+</sup>; 989.243 (theor.: 989.251) (4%) [IrPSfCu-Cu(phen)+H]<sup>+</sup>; 947.300 (theor.: 947.308) (52%) [IrPSfCu-Cu(phen)-2HCl+CH<sub>2</sub>OH]<sup>+</sup>; 919.307 (theor.: 919.313) (12%) [IrPSfCu-Cu(phen)-2Cl+H]<sup>+</sup>; 832.210 (theor.: 832.216) (48%) [IrPSfCu-IrCpCl<sub>2</sub>]<sup>+</sup>; 634.158 (theor.: 832.156) (12%) [IrPSfCu-IrCpCl<sub>2</sub>-PPh<sub>2</sub>CH<sub>2</sub>]<sup>+</sup>; 594.651 (theor.: 594.649) (4%) [IrPSfCu-2HCl+CH<sub>2</sub>OH]<sup>2+</sup>

### Electrochemical characterization

Cyclic voltammetry was carried out with an Autolab PGSTAT302N potentiostat-galvanostat. A single compartment cell of the type GC/SCE/Pt containing a deoxygenated supporting electrolyte made of 0.1 M TBAPF<sub>6</sub> in DMF was used. Typically, an analytic concentration of 0.5 mM was adopted. Voltammetric cycles were performed at 50mV/s, scanning from open circuit to negative potentials and backwards.

### Preparation of liposomes

Cholesterol (100 mg) and phosphatidylcholine (200 mg) were dissolved in dichloromethane (4.5 ml). After mixing 150 μl of the solution was transferred to each Eppendorf tube (30 pieces, 1.5 ml). The solvent was blown out by nitrogen during rotating. This way liposome film was formed on the walls of tube. Each Eppendorf tube contained 10 mg of liposome. The complexes (**2**, **1**, **0.5**, **0.25** and **0.125** mg) were dissolved in dichloromethane (300 μl) and added to Eppendorf tube with liposome solution (10 mg in 150 μl of CH<sub>2</sub>Cl<sub>2</sub>). The solutions were homogenized in ultrasonic bath (10 min) and then blown out by nitrogen. Water (1 ml) was poured on the film and Eppendorf tube was homogenized in ultrasonic bath to form light brown or light green liposome suspension. The samples were shaken and heated on Thermomixer comfort for 15 min at 60 °C.

### TEM characterization of liposomes

Liposomes morphology was analyzed by using a FEI™ Tecnai T20 Microscope operated at 200 kV. The size was determined from the enlarged TEM micrographs, using commercially available software ImageJ, counting at least 50 particles in different images.

### DLS characterization of liposomes

The average hydrodynamic diameter and electrokinetic potential were determined by the dynamic light scattering (MADLS; Zetasizer Ultra, Malvern). Measurements were performed in PBS (pH = 7.4) at room temperature.

### Cell cultures

MCF7 cell line (human breast adenocarcinoma, morphology: epithelial-like, ATCC: HTB-22), A549 cell line (human lung adenocarcinoma, morphology: epithelial, ATCC: CCL-185) and HaCaT (human keratinocyte) were cultured in Dulbecco's Modified Eagle's Medium (DMEM, Corning) with phenol red, supplemented with 10% fetal bovine serum (FBS) and with 1% streptomycin/penicillin. WM266-4 cell line (human skin (metastasis), morphology: epithelial, ATCC CRL-1676) were cultured in EMEM (EBSS) + 2mM Glutamine + 1% Non-Essential Amino Acids (NEAA) + 1% Sodium Pyruvate (NaP) + 10% Foetal Bovine Serum (FBS). DU-145 cell line (human prostate carcinoma) and HEK293T cell line (human embryonic kidney) were cultured in minimum essential medium (MEM, Corning) with only 10% fetal bovine serum (FBS). Cultures were incubated at 37°C under a humidified atmosphere containing 5% CO<sub>2</sub>. Cells were passaged using a solution containing 0.05%

trypsin and 0.5 mM EDTA. All media and other ingredients were purchased from ALAB, Poland.

#### Cytotoxic activity

Since most of the studied compounds are insoluble in aqueous media, therefore they needed to be pre-dissolved in DMSO for biological tests. Cytotoxicity was assessed by MTT assay performed according to the protocols described previously.<sup>70</sup> In brief,  $1 \times 10^4$  cells per well, seeded in 96-well flat-bottom microtiter plate, were incubated with the tested complexes (**1**, **2**, **3** and **4**) at various concentrations for 24 h. After that time, solutions of compounds were washed out, cells were washed three times with PBS and fresh medium was applied. Each compound concentration was tested in five replicates and repeated at least three times. Determined values of  $IC_{50}$  (concentration of a drug required to inhibit the growth of 50% of the cells) are given as mean + S.D. (Standard Deviation). Furthermore, post-treatment survival assessment of the treated cells was analyzed under a fluorescence inverted microscope (Olympus IC51, Japan) with an excitation filter 470/20 nm. For this, cells were stained with two versatile fluorescence dyes: fluorescein diacetate (FDA, 5 mg/mL) and propidium iodide (PI, 5 mg/mL) in standard conditions in the dark for 20 min. Before visualization dyes were removed and cells were washed with PBS twice.  $IC_{50}$  values were determined, after 72 h, from the plots of cell viability in the presence of various concentrations of each compound by matching dose–response curves.

#### Cellular uptake

A549 and Du-145 cells at a density of  $2 \times 10^6$  cells per 2 mL were seeded on 6-well plates and were incubated with **1a** and **1b** (2 mL) for 24 h (37 °C, 5% CO<sub>2</sub>). Additional wells were incubated with medium alone as a negative control. Then, compound solutions were removed; the cells were washed twice with PBS buffer, and trypsinized. Measurement of the concentration of iridium ions was carried out using a mass spectrometer (ELAN 6100 PerkinElmer) with inductively coupled plasma (ICP-MS). For analysis, the collected cells were mineralized in 1 mL of 65% HNO<sub>3</sub> at 60 °C for 1 h. The iridium content under each condition is expressed as ng mg<sup>-1</sup> protein. The protein content was assessed with Bradford Protein Assay (Thermo Scientific™).<sup>71</sup> The experiment was repeated at least 3 times and results are presented as mean value + S.D.

#### Confocal laser scanning microscopy

The intracellular uptake of **1a** was studied in the A549 and DU145 cancer cells according to the previously applied protocol.<sup>40</sup> In brief, before imaging, A549 and Du145 cells were seeded on microscopic slides at a density of  $1 \times 10^5$  cells. Cells were kept for 24 h at 37 °C in a 95% atmospheric air and 5% CO<sub>2</sub> humidified atmosphere. After being washed with fresh medium, the cells were incubated in the dark with 1 μM solution of **1a** prepared growth medium for 2 h. Next, cells were stained with phalloidin-atto488 (Sigma Aldrich) to visualize the cytoskeleton and then incubated for 10 min with Hoechst 33342 for nuclear staining. After this incubation, at 37 °C, in the dark, the cells were washed with HBSS two times,

and the slide was transferred to the microscope stage and cells were visualized under a confocal microscope Zeiss LSM 880 (Carl Zeiss, Jena, Germany) with a 63 × oil immersion objective. Images were analyzed by Zeiss ZEN Software.

#### Cell death analysis by flow cytometry

Annexin V Apoptosis Detection Kit FITC (Invitrogen) and Propidium Iodide (Thermo Fischer Scientific, Waltham, Massachusetts, USA) were used to distinguish cell death (apoptotic and necrotic cells) induced by studied compounds quantitatively due to the previously described protocol.<sup>72</sup> In brief, the studied compounds **1a** and **1b** (in a broad range of concentration ranging between 100 and 0.01 μM) were incubated for 24 h with A549 and HaCaT cells (seeded at density  $5 \times 10^5$  cells/mL) in 12-well plates. After this time, the compound solutions were removed, and the cells were washed twice with PBS buffer (phosphate-buffered saline, pH = 7.4). Trypsin was added to the cells and then they were left for 10 min at 37 °C in a humidified atmosphere containing 5% CO<sub>2</sub>. The cells were collected, centrifuged, and separated from the supernatant, then washed twice with 0.5 ml PBS buffer (buffer phosphate saline NaCl, KCl, Na<sub>2</sub>HPO<sub>4</sub>, KH<sub>2</sub>PO<sub>4</sub>) and suspended in Binding Buffer. Fifteen minutes before measuring, cells were stained with Annexin V-FITC and PI and incubated in the dark. Viable and dead (early apoptotic, late apoptotic, and necrotic) cells were detected using the BD Accuri flow cytometer (BD Biosciences). The experiment was repeated at least 3 times.

#### Cell cycle analysis

The A549, Du145 and HaCaT cells ( $3 \times 10^5$ /well) were seeded in 12-well plates and treated with various concentrations of **1a**, **1b** and cisplatin (CDDP) for 24 h. Synchronization of A549, Du145 and HaCaT cell cultures was performed by serum starvation protocol. Serum starvation is widely used for synchronizing donor cells by arresting them in the G<sub>0</sub>/G<sub>1</sub> phase of the cell cycle.<sup>73</sup> Cell cultures were seeded and incubated in a growth medium with 20% FBS overnight to synchronize the cell cultures. Then the cultures were rinsed by PBS and changed to serum-free medium. After serum starvation for 18 h, the cells were passaged and released into the cell cycle by the addition of serum. Then cells were treated with **1a**, **1b** and CDDP for 24 h. For FACS analysis, cell samples were harvested with trypsinization and stained with propidium iodide (20 μg/mL). Cell cycle phase distributions were analyzed by flow cytometry (BD Bioscience). Experiments were repeated at least three times.

#### Three-dimensional culturing *in vitro*

For hanging drop formation, the lid from a tissue culture dish was removed and  $5 \times 10^5$  A549 or DU-145 cells in 10 μl drops were placed on the bottom of the lid. In each case, the cell suspension was homogeneous and did not contain aggregates, since it determines the size and uniformity of spheroids. Then, the lid was inverted onto the PBS-filled bottom chamber and incubated at 37 °C/ 5% CO<sub>2</sub>/ 95% humidity. The sphere growth was monitored daily and incubates until either cell sheets or aggregates were formed. Once sheets were formed, they were

transferred to 96-well plates coated with Geltrex matrix and incubated with a completed growth medium until spheroids were created. Using optimal growth conditions, a period of 4–7 days was found to be optimal for spheroid assembly. The direct effect of drug toxicity was examined on spheroids derived from both A549 and Du-145 cell lines. For cytotoxicity assessment, spheroids were grown and were monitored for 5–7 days. After this time, the spheres were treated with the tested liposomal formulation of **1** (1a) at increasing doses (0.1 × IC<sub>50</sub>, IC<sub>50</sub>, and 10 × IC<sub>50</sub>, IC<sub>50</sub> determined for the corresponding Pluronic P-123 nanoformulations), and the plates were further incubated at 37 °C. Forty-eight hours after treatment, the spheroids were stained with 4',6-diamidino-2-phenylindole (DAPI), calcein AM (CAM), and propidium iodide (PI) to estimate the live/dead cells population for one hour, washed and visualized using a confocal microscope Zeiss LSM 880 (Carl Zeiss, Jena, Germany) with a 10 × oil immersion objective. Images were analyzed by Zeiss ZEN Software.<sup>74</sup>

### Author Contributions

U.K. designed the scientific rationale; U.K. and S.K. performed the synthesis, purification, crystallization and characterization (MS, elemental analysis) of all complexes; U.K., S.K., A.B. analyzed and described EPR and magnetic data; M.S. X-ray measurements and solving crystal structures; U.K. crystallographic data analysis and description; M.M. IR measurements as well as data analysis and description; S.K. U.K., B.P., A.B., A.K. performing biological experiments with cell lines as well as data analysis and description; S.K., D.W. A.N. cyclic voltamperometry and luminescence measurements as well as data analysis and description; P.K. liposome preparation and complexes encapsulation; A.K. liposome characterization; V.S. performing TEM photos; U.K., S.K. A.B., M.M. A.N. wrote manuscript; S.C., M.S., A.K., A.B. text correction. The manuscript was reviewed by all Authors prior to submission.

### Conflicts of interest

There are no conflicts to declare.

### Acknowledgements

This research was funded by the Polish National Science Centre (grant number 2020/37/N/ST4/02698). ICTS and ELECMII- LMA ICTS are gratefully acknowledged.

### Notes and references

- 1 P. C. Sharma, R. Goyal, A. Sharma, D. Sharma, N. Saini, H. Rajak, S. Sharma and V. K. Thakur, Insights on fluoroquinolones in cancer therapy: chemistry and recent developments, *Mater. Today Chem.*, 2020, **17**, 100296
- 2 H. Sung, J. Ferlay, R. L. Siegel, M. Laversanne, I. Soerjomataram, A. Jemal and F. Bray, Global Cancer Statistics 2020: GLOBOCAN Estimates of Incidence and Mortality Worldwide for 36 Cancers in 185 Countries, *CA Cancer J Clin.*, 2021, **71**, 209
- 3 Z. Xu, Y. Yang, X. Jia, L. Guo, X. Ge, G. Zhong, S. Chen and Z. Liu, Novel cyclometalated iridium(III) phosphine-imine (P<sup>^</sup>N) complexes: highly efficient anticancer and anti-lung metastasis agents in vivo, *Inorg. Chem. Front.*, 2020, **7**, 1273
- 4 P. Kofoczek, A. Skórska-Stania, A. Cierniak, V. Sebastian, U.K. Komarnicka, M. Płotek and A. Kyzioł, Polymeric micelle-mediated delivery of half-sandwich ruthenium(II) complexes with phosphanes derived from fluoroquinolones for lung adenocarcinoma treatment, *Eur J Pharm Biopharm.*, 2018, **128**, 69–81
- 5 A. van Niekerk, P. Chellan and S.F. Mapolie, Heterometallic Multinuclear Complexes as Anti-Cancer Agents-An Overview of Recent Developments, *Eur J Inorg Chem.*, 2019, **30**, 3432
- 6 N. Mirzadeh, T. S. Reddy, S. H. Privér and S.K. Bhargava, Synthesis, anti-proliferative and apoptosis-inducing studies of palladacycles containing a diphosphine and a Sn,As-based chelate ligand, *Dalton Trans.*, 2019, **48**, 5183
- 7 M. Wenzel, E. Bigaeva, P. Richard, P. Le Gendre, M. Picquet, A. Casini and E. Bodio, New heteronuclear gold(I)-platinum(II) complexes with cytotoxic properties: are two metals better than one?. *J Inorg Biochem.*, 2014, **141**, 10
- 8 N. P. Farrell, Multi-platinum anti-cancer agents. Substitution-inert compounds for tumor selectivity and new targets, *Chem. Soc. Rev.*, 2015, **44**, 8773
- 9 J. Lopes, D. Alves, T.S. Morais, P. J Costa, M. F. M. Piedade, F. Marques, M. J Villa de Brito and M H. Garcia, New copper(I) and heteronuclear copper(I)-ruthenium(II) complexes: Synthesis, structural characterization and cytotoxicity, *J Inorg Biochem.*, 2017, **169**, 68
- 10 C. Manzotti, G. Pratesi, M. E. R Di Domenico, E. Cavalletti, H. H. Fiebig, L. R. Kelland, N. Farrell, D. Polizzi, R. Supino, G. Pezzoni and F. Zunino, BBR 3464: a novel triplatinum complex, exhibiting a preclinical profile of antitumor efficacy different from cisplatin, *Clin Cancer Res.*, 2000, **6**, 2626
- 11 Zhu G, L. Ma, Preparation Thereof and Therapeutic Use Thereof, 2017, US9650402B2
- 12 M. Wehbe, A. W. Y. Leung, M. J. Abrams, C. Orvig and M. B. Bally, A Perspective – can copper complexes be developed as a novel class of therapeutics?, *Dalton Trans.*, 2017, **46**, 10758
- 13 R. Sessoli, D. Gatteschi, A. Caneschi and M. A. Novak, Magnetic bistability in a metal-ion cluster, *Nature*, 1993, **365**, 141
- 14 A. Nava, L. Rigamonti, E. Zangrando, R. Sessoli, W. Wernsdorfer and A. Cornia, Redox-Controlled Exchange Bias in a Supramolecular Chain of Fe<sub>4</sub> Single-Molecule Magnets, *Angew. Chem. Int. Ed.*, 2015, **54**, 8777
- 15 A. M. Ako, V. Mereacre, Y. Lan, W. Wernsdorfer, R. Clerac, C. E. Anson and A. K. Powell, An Undecanuclear Fe<sup>III</sup> Single-Molecule Magnet, *Inorg. Chem.*, 2010, **49**, 1
- 16 A. M. Ako, I. J. Hewitt, V. Mereacre, R. Clerac, W. Wernsdorfer, C. E. Anson and A. K. Powell, A ferromagnetically coupled mn(II) aggregate with a record S=83/2 ground spin state, *Angew. Chem. Int. Ed.*, 2006, **45**, 4926
- 17 E A Moore, R. Janes, Metal-ligand bonding, Royal Society of Chemistry, ISBN 978-0-85404-979-0
- 18 D. V. Korchagin, E. P. Ivakhnenko, O. P. Demidov, A. V. Akimov, R. B. Morgunov, A. G. Starikov, A. V. Pali, V. I. Minkin and S. M. Aldoshin, Field supported slow magnetic relaxation in a quasi-one-dimensional copper(II) complex with a pentaheterocyclic triphenodioxazine, *New J. Chem.*, 2021, **45**, 21912
- 19 J. Han, L. Xi, X. Huang and L. Li, Magnetic Relaxation in a Dysprosium–Copper Heterometallic Cluster Involving Nitronyl Nitroxide Biradicals, *Cryst. Growth Des.*, 2021, **21**, 7186



- 20 R. Boča, C. Rajnák, J. Titiš, and D. Valigura, Field Supported Slow Magnetic Relaxation in a Mononuclear Cu(II) Complex, *Inorg. Chem.* 2017, **56**, 1478
- 21 K. Hayashi, M. Nakamura, W. Sakamoto, Y. Yogo, H. Miki, S. Ozaki, M. Abe, T. Matsumoto and K. Ishimura, Superparamagnetic Nanoparticle Clusters for Cancer Theranostics Combining Magnetic Resonance Imaging and Hyperthermia Treatment, *Theranostics*, 2013, **3**, 366
- 22 R.M. Patil, N.D. Thorat, P.B. Shete, P.A. Bedge, S. Gavde, M.G. Joshi, S. A M Tofail and R. A Bohara, Comprehensive cytotoxicity studies of superparamagnetic iron oxide nanoparticles, *Biochem Biophys Rep.*, 2018, **13**, 63
- 23 R. A. Bohara, N. D. Thorat, A. K. Chaurasia and Shivaji H. Pawa, Correction: Cancer cell extinction through a magnetic fluid hyperthermia treatment produced by superparamagnetic Co–Zn ferrite nanoparticles, *RSC Adv.*, 2015, **5**, 47225
- 24 X. He, X. Liu, Y. Tang, J. Du, M. Tian, Z. Xu, X. Liu and Z. Liu, Half-sandwich Iridium(III) complexes with triphenylamine-substituted dipyrindine frameworks and bioactivity applications, *Dyes Pigm.*, 2019, **160**, 217
- 25 Q. Du, Y. Yang, L. Guo, M. Tian, X. Ge, Z. Tian, L. Zhao, Z. Xu, J. Li and Z. Liu, Fluorescent half-sandwich phosphine-sulfonate iridium(III) and ruthenium(II) complexes as potential lysosome-targeted anticancer agents, *Dyes Pigm.*, 2019, **162**, 821
- 26 S. Koziel, U.K Komarnicka, A. Ziółkowska, A. Skórska-Stania, B. Pucelik, M. Płotek, V. Sebastian, A. Bieńko, G. Stochel, A. Kyzioł, Anticancer potency of novel organometallic Ir(III) complexes with phosphine derivatives of fluoroquinolones encapsulated in polymeric micelles, *Inorg. Chem. Front.*, 2020, **7**, 3386
- 27 W. Su, X. Wang, X. Lei, Q. Xiao, S. Huang and P. Li, Synthesis, characterization, cytotoxic activity of half-sandwich rhodium(III), and iridium(III) complexes with curcuminoids, *J. Organomet. Chem.*, 2017, **833**, 54
- 28 A. J. Millett, A. Habtemariam, I. Romero-Canelón, G. J. Clarkson and P. J. Sadler, Contrasting Anticancer Activity of Half-Sandwich Iridium(III) Complexes Bearing Functionally Diverse 2-Phenylpyridine Ligands, *Organometallics*, 2015, **34**, 2683
- 29 A. Lapasam, O. Hussain, R. M. Phillips, W. r. Kaminsky and M. R. Kollipara, Synthesis, Characterization and Chemosensitivity Studies of Half-Sandwich Ruthenium, Rhodium and Iridium Complexes Containing  $\kappa^1(S)$  and  $\kappa^2(N,S)$  Aroylthiourea Ligands, *J. Organomet. Chem.*, 2018, **883**, 272
- 30 Z. Liu and P. J. Sadler, Organoiridium Complexes: Anticancer Agents and Catalysts, *Acc. Chem. Res.*, 2014, **47**, 1174
- 31 A. Wilbuer, D.H. Vlecken, D.J. Schmitz, K. Kräling, K. Harms, C.P. Bagowski and E. Meggers, Iridium Complex with Antiangiogenic Properties, *Angew. Chem. Int. Ed.*, 2010, **49**, 3839
- 32 Z. Tian, Y. Yang, L. Guo, G. Zhong, J. Li and Z. Liu, Dual-functional cyclometalated iridium imine NHC complexes: highly potent anticancer and antimetastatic agents, *Inorg. Chem. Front.*, 2018, **5**, 3106
- 33 Qu W, Zuo W, Li N, Y. Hou, Z. Song, G. Gou, J. Yang, Design of multifunctional liposome-quantum dot hybrid nanocarriers and their biomedical application, *J Drug Target.* 2017, **25**, 661
- 34 L. Sercombe, T. Veerati, F. Moheimani, S.Y. Wu, A.K. Sood, S. Hua, Advances and Challenges of Liposome Assisted Drug Delivery, *Front Pharmacol.*, 2015, **6**, 286
- 35 B. S. Pattni, V. V. Chupin and V.r P. Torchilin, New Developments in Liposomal Drug Delivery, *Chem. Rev.*, 2015, **115**, 10938
- 36 A. A. Petrauskas and E. Kolovanov, ACD/Log P methoddescription, *Perspect. Drug Discovery Des.*, 2000, **19**, 99
- 37 A. Bykowska, R. Starosta, U. K. Komarnicka, Z. Ciunik, A. Kyzioł, K. Guz-Regner, G. Bugła-Płoskońska, M. Jeżowska-Bojczuk, Phosphine derivatives of ciprofloxacin and norfloxacin, a new class of potential therapeutic agents, *New J. Chem.*, 2014, **38**, 1062
- 38 U.K. Komarnicka, R. Starosta, A. Kyzioł, M. Płotek, M. Puchalska, M. Jeżowska-Bojczuk, New copper(I) complexes bearing lomefloxacin motif: Spectroscopic properties, in vitro cytotoxicity and interactions with DNA and human serum albumin, *J Inorg. Bio.*, 2016, 165, 25
- 39 U.K. Komarnicka, R. Starosta, A. Kyzioł, M. Jeżowska-Bojczuk, Copper(i) complexes with phosphine derived from sparfloxacin. Part I – structures, spectroscopic properties and cytotoxicity, *Dalton Trans.*, 2015, **44**, 12688
- 40 Kyzioł, A. Cierniak, J. Gubernator, A. Markowski, M. Jeżowska-Bojczuk, U. K. Komarnicka, Copper(i) complexes with phosphine derived from sparfloxacin. Part III: multifaceted cell death and preliminary study of liposomal formulation of selected copper(i) complexes, *Dalton Trans.*, 2018, **47**, 1981
- 41 A. Bykowska, U.K. Komarnicka, M. Jeżowska-Bojczuk, A.Kyzioł, Cu and CuI complexes with phosphine derivatives of fluoroquinolone antibiotics - A comparative study on the cytotoxic mode of action, *J Inorg Biochem.*, 2018, 181, 1-10
- 42 E. K. Efthimiadou, N. Katsaros, A. Karaliota and G. Psomas, Mononuclear copper(II) complexes with quinolones and nitrogen-donor heterocyclic ligands: Synthesis, characterization, biological activity and interaction with DNA, *Inorg. Chim. Acta*, 2007, **360**, 4093
- 43 E. K. Efthimiadou, H. Thomadaki, Y. Sanakis, C. P. Raptopoulou, N. Katsaros, A. Scorilas, A. Karaliota and G. Psomas, Structure and biological activities of metal complexes of flumequine, *J. Inorg. Biochem.*, 2007, **101**, 64
- 44 E. K. Efthimiadou, Y. Sanakis, M. Katsarou, C. P. Raptopoulou, A. Karaliota, N. Katsaros and G. Psomas, Metal Complexes of Quinolone Antibiotics and Their Applications: An Update, *J. Inorg. Biochem.*, 2006, **100**, 1378
- 45 K008 G. Psomas, A. Tarushi, E. K. Efthimiadou, Y. Sanakis, C. P. Raptopoulou and N. Katsaros, Complexes of nalidixic acid with some vital metal ions: Synthesis, chemical structure elucidation, and antimicrobial evaluation, *J. Inorg. Biochem.*, 2006, **100**, 1764
- 46 K. Nakamoto, Infrared and Raman Spectra of Inorganic and Coordination Compounds, Part B, J. Wiley & Sons Inc., New York, 2009. G. Socrates, Infrared and Raman characteristic group frequencies: tables and charts, John Wiley & Sons, 2004
- 47 K. Nakamoto, Infrared and Raman Spectra of Inorganic and Coordination Compounds, Part B, J. Wiley & Sons Inc., New York, 2009
- 48 S. Yadav and R.V. Singh, Ferrocenyl-substituted Schiff base complexes of boron: Synthesis, structural, physico-chemical and biochemical aspects, *Spectrochim. Acta Part A*, 2011, **78**, 298
- 49 J. C. Jeffery, J. P. Mather, C. A. Otter, P. Thornton and M. D. Ward, Synthesis of the potentially pentadentate ligand 6,6''-bis(2-hydroxyphenyl)-2,2' :6',2''-terpyridine (H2L) and the crystal structure and magnetic properties of  $\{[Cu(HL)_2][PF_6]_2 \cdot 5MeCN\}$ , *J. Chem. Soc., Dalton Trans.*, 1995, 5, 819 – 824
- 50 E. Garribba, G. Micera, D. Sanna and L. StrnnaErre, The Cu(II)-2,2'-bipyridine system revisited, *Inorg. Chim. Acta*, 2000, 299, 253 - 261
- 51 N.F. Chilton, R.P. Anderson, L.D. Turner, A. Soncini and K.S. Murray, PHI: A Powerful New Program for the Analysis of

- Anisotropic Monomeric and Exchange-Coupled Polynuclear d- and f-Block Complexes, *J. Comput. Chem.*, 2013, **34**, 1164
- 52 Kahn, O. Molecular Magnetism; Wiley-VCH: New York, 1993
- 53 V.H. Crawford, H.W. Richardson, J.R. Wasson, D.J. Hodgson and W.E. Hatfield, Relation between the singlet-triplet splitting and the copper-oxygen-copper bridge angle in hydroxo-bridged copper dimers, *Inorg. Chem.*, 1976, **15**, 2107
- 54 B. Graham, M.T.W. Hearn, P.C. Junk, C.M. Kepert, F.E. Mabbs, B. Moubaraki, K.S. Murray and L. Spiccia, Syntheses, Crystal Structures, Magnetic Properties, and EPR Spectra of Tetranuclear Copper(II) Complexes Featuring Pairs of "Roof-Shaped" Cu<sub>2</sub>X<sub>2</sub> Dimers with Hydroxide, Methoxide, and Azide Bridges, *Inorg. Chem.*, 2001, **40**, 1536
- 55 K. Skorda, T.C. Stamatatos, A.P. Vafiadis, A.T. Lithoxidou, A. Terzis, S.P. Perlepes, J. Mroziński, C.P. Raptopoulou, J.C. Plakatouras and E.G. Bakalbassis, Copper(II) chloride/1-methylbenzotriazole chemistry: influence of various synthetic parameters on the product identity, structural and magnetic characterization, and quantum-chemical studies, *Inorg. Chim. Acta*, 2005, **358**, 565
- 56 S. Thakurta, P. Roy, G. Rosair, C.J. Gómez-García, E. Garribba and S. Mitra, S. Ferromagnetic exchange coupling in a new bis( $\mu$ -chloro)-bridged copper(II) Schiff base complex: Synthesis, structure, magnetic properties and catalytic oxidation of cycloalkanes, *Polyhedron*, 2009, **28**, 695
- 57 M. Grove, J. Sletten, M. Julve and F. Floret, F. Solid state polymerization causing transition to a ferromagnetic state. Crystal structures and magnetic properties of [Cu<sub>2</sub>(dpp)(H<sub>2</sub>O)(dmsO)Cl<sub>4</sub>].dmsO and [Cu<sub>2</sub>(dpp)Cl<sub>4</sub>]<sub>n</sub> (dpp = 2,3-bis(2-pyridyl)pyrazine), *J. Chem. Soc., Dalton Trans.* 2001, 2487-2493.
- 58 M. Ding, A. K. Hickey, M. Pink, J. Telsler, D. L. Tierney, M. Amoza, M. Rouzières, T. J. Ozumerzifon, W. A. Hoffert, M. P. Shores, E. Ruiz, R. Clérac and J. M. Smith, Magnetization Slow Dynamics in Ferrocenium Complexes, *Eur. J. Chem.*, 2019, **25**, 10625
- 59 B. Buades, V. S. Arderiu, L. Maxwell, M. Amoza, D. Choquesillo-Lazarte, N. Aliaga-Alcalde, C. Viñas, F. Teixidor and E. Ruiz, Slow-spin relaxation of a low-spin S = 1/2 Fe<sup>III</sup> carborane complex, *Chem. Commun.*, 2019, **55**, 3825
- 60 S.-Q. Wu, Y. Miyazaki, M. Nakano, S.-Q. Su, Z.-S. Yao, H.-Z. Kou and O. Sato, Slow Magnetic Relaxation in a Mononuclear Ruthenium(III) Complex, *Chem. – Eur. J.*, 2017, **23**, 10028.
- 61 H.I. Buvailo, V.G. Makhankova, V.N. Kokozay, A.A. Babaryk, I.V. Omelchenko, S.V. Shishkina, D.C. Bieńko, J. Jezierska, A. Bieńko, Hybrid Cu-containing compounds based on lacunary Strandberg anions: synthesis under mild conditions, crystal structure, and magnetic properties, *Inorg. Chem.*, 2022, **61**, 5701
- 62 D. Valigura, C. Rajnákl, J. Titiš, J. Moncol, A. Bieńko, R. Boča, Unusual slow magnetic relaxation in a mononuclear copper(II) complex, *Dalton Trans.*, 2022, **51**, 5612
- 63 M. Mlakar, V. Cuculić, S. Frka and B. Gašparović, Copper-phospholipid interaction at cell membrane model hydrophobic surfaces, *Bioelectrochemistry*, 2018, **120**, 10
- 64 P. Hazarika, B. Bezbaruah, P. Das, O.K. Medhi and C. Medhi, A model study on the stacking interaction of phenanthroline ligand with nucleic acid base pairs: An ab initio, MP2 and DFT studies, *J. Inorg. Biochem.*, 2011, **2**, 152
- 65 Z. Wang, A. Bilegsaikhon, R.T. Jerozal, T.A. Pitt and P.J. Milner, Evaluating the Robustness of Metal-Organic Frameworks for Synthetic Chemistry, *ACS Appl Mater Interfaces.*, 2021, **13**, 17517
- 66 V. W. Yang, Chapter 15 - The Cell Cycle, Physiology of the Gastrointestinal Tract (Fifth Edition), 2012, 451
- 67 U.K. Komarnicka, R. Starosta, K. Guz-Regner, G. Bugla-Płoskońska, A. Kyzioł and M. Jeżowska-Bojczuk, Phosphine derivatives of sparfloxacin- synthesis, structures and in vitro activity, *J. Mol. Struct.*, 2015, **1096**, 55
- 68 A. Bykowska, R. Starosta, A. Brzuszkiewicz, B. Bażanów, M. Florek, N. Jackulak, J. Król, J. Grzesiak, K. Kaliński and M. Jeżowska-Bojczuk, Synthesis, properties and biological activity of a novel phosphines ligand derived from ciprofloxacin, *Polyhedron*, 2013, **60**, 23
- 69 G. A. Bain and J. F. Berry, Diamagnetic Corrections and Pascal's Constants, *J. Chem. Educ.*, 2008, **5**, 532
- 70 M. L. Circu and T. Y. Aw, Reactive oxygen species, cellular redox systems, and apoptosis, *Free Radicals Biol. Med.*, 2010, **48**, 749–762
- 71 S. Tardito, A. Barilli, I. Bassanetti, M. Tegoni, O. Bussolati, R. Franchi-Gazzola, C. Mucchino and L. Marchiò, Copper-dependent, cytotoxicity of 8-hydroxyquinoline derivatives correlates with their hydrophobicity and does not require caspase activation, *J. Med. Chem.*, 2012, **55**, 10448–10459
- 72 U.K. Komarnicka, B. Pucelik, D. Wojtala, M.K. Lesiów, G. Stochel and A. Kyzioł, Evaluation of anticancer activity in vitro of a stable copper(I) complex with phosphine-peptide conjugate, *Sci Rep.*, 2021, **11**, 23943
- 73 M. Chen, J. Huang, X. Yang, B. Liu, W. Zhang, L. Huang, F. Deng, J. Ma, Y. Bai, R. Lu, B. Huang, Q. Gao, Y. Zhuo and Jian Ge, Serum starvation induced cell cycle synchronization facilitates human somatic cells reprogramming, *PLoS One*, 2012, **7**, e28203
- 74 B. Pucelik, L. G. Arnaut, G. Stochel and J. M. Dabrowski, Design of Pluronic-based formulation for enhanced redaporfin-photodynamic therapy against pigmented melanoma, *ACS Appl. Mater. Interfaces*, 2016, **8**, 22039–22055

# Liposomal formulation of magnetic iridium-copper coordination compounds with phosphine derived from fluoroquinolones for human prostate carcinoma treatment

Sandra Koziół,<sup>a</sup> Urszula K. Komarnicka,<sup>a\*</sup> Barbara Pucelik,<sup>b</sup> Agata Barzowska,<sup>b</sup> Miłosz Siczek,<sup>a</sup> Magdalena Malik,<sup>c</sup> Daria Wojtala,<sup>a</sup> Alessandro Nioiretini,<sup>d</sup> Agnieszka Kyzioł,<sup>e</sup> Victor Sebastian,<sup>f,g</sup> Pavel Kopel,<sup>h</sup> Stefano Caramori,<sup>d</sup> Alina Bieńko<sup>a</sup>

<sup>a</sup>Faculty of Chemistry, University of Wrocław, Joliot-Curie 14, 50-383 Wrocław, Poland E-mail: urszula.komarnicka@chem.uni.wroc.pl

<sup>b</sup>Małopolska Centre of Biotechnology, Jagiellonian University, Gronostajowa 7A, 30-387 Krakow, Poland

<sup>c</sup>Faculty of Chemistry, Jagiellonian University, Gronostajowa 2, 30-387 Kraków, Poland

<sup>d</sup>Faculty of Chemistry, Wrocław University of Science and Technology, Wybrzeże Wyspiańskiego 27, 50-370 Wrocław, Poland

<sup>e</sup>Department of Chemical, Pharmaceutical, and Agricultural Sciences, University of Ferrara, Via L. Borsari 46, 44121 Ferrara, Italy

<sup>f</sup>Department of Chemical Engineering, Aragon Institute of Nanoscience (INA), The Aragón Materials Science Institute (ICMA), University of Zaragoza, Campus Río Ebro-Edificio I+D, Mariano Esquillor S/N, 50018 Zaragoza, Spain

<sup>g</sup>Networking Research Center on Bioengineering, Biomaterials and Nanomedicine, CIBER-BBN, 28-029 Madrid, Spain

<sup>h</sup>Department of of Inorganic Chemistry, Faculty of Science, Palacky University, 17. listopadu 12, CZ-771 46 Olomouc, Czech Republic

Novel heteronuclear Ir<sup>III</sup>-Cu<sup>II</sup> complexes ([Ir( $\eta^5$ -Cp\*)Cl<sub>2</sub>PCp-Cu(phen)](NO<sub>3</sub>)·1.75(CH<sub>3</sub>OH)·0.75(H<sub>2</sub>O) (**1**), [Ir( $\eta^5$ -Cp\*)Cl<sub>2</sub>PNr-Cu(phen)](NO<sub>3</sub>)·1.75(CH<sub>3</sub>OH)·0.75(H<sub>2</sub>O) (**2**), [Ir( $\eta^5$ -Cp\*)Cl<sub>2</sub>PLm-Cu(phen)] (**3**), Ir( $\eta^5$ -Cp\*)Cl<sub>2</sub>PSf-Cu(phen)](NO<sub>3</sub>)·1.3(H<sub>2</sub>O)·1.95(CH<sub>3</sub>OH) (**4**) bearing phosphines derived from fluoroquinolones: sparfloxacin (HSf), ciprofloxacin (HCp), lomefloxacin (HLm), and norfloxacin (HNr) have been studied as possible anticancer chemotherapeutics. All compounds were characterized by ESI-MS spectrometry, selected spectroscopic methods (*i.e.*, IR, fluorescence and EPR), cyclic voltammetry, variable-temperature magnetic susceptibility measurements and x-ray diffractometry. Importantly, the crystal structure of [Ir( $\eta^5$ -Cp\*)Cl<sub>2</sub>PLm-Cu(phen)] features the 1D metal-organic polymer. It is worth mentioning that all Ir(III)-Cu(II) inorganic compounds exhibit weak magnetic interactions. Surprisingly, one of the studied systems [Ir( $\eta^5$ -Cp\*)Cl<sub>2</sub>PNr-Cu(phen)] exhibits a slow magnetic relaxation under the moderate DC magnetic field, that is extremely rare in case of Cu(II) complexes. Investigation of Ir<sup>III</sup>-Cu<sup>II</sup> complexes cytotoxicity *in vitro* reveals their high anticancer potential towards human prostate carcinoma cells simultaneously with low toxicity against healthy cells. Furthermore, liposomes loaded with red-ox active [Ir( $\eta^5$ -Cp\*)Cl<sub>2</sub>PCp-Cu(phen)] was prepared to overcome low solubility and minimize serious systemic side effects. Confocal microscopy and an ICP-MS analysis showed that liposomal [Ir( $\eta^5$ -Cp\*)Cl<sub>2</sub>PCp-Cu(phen)] effectively accumulates inside human lung adenocarcinoma and human prostate carcinoma cells with colocalization in nuclei. A precise cytometric analysis revealed a predominance of apoptosis over the other types of cell death. Furthermore, the investigated nanoformulation may induce changes in the cell cycle leading to S phase arrest in a dose-dependent manner. *In vitro* cytotoxicity assays were also carried out within multicellular tumour spheroids and efficient anticancer action on these 3D assemblies was demonstrated.

<b>Table S1.</b> Crystallographic experimental details			
Parameters	<b>IrPNrCu·(NO<sub>3</sub>)·1.75(CH<sub>4</sub>O)·0.75(H<sub>2</sub>O)</b>	<b>IrPCpCu·(NO<sub>3</sub>)·2.75(H<sub>2</sub>O)</b>	<b>IrPLmCu·(NO<sub>3</sub>)·1.3(H<sub>2</sub>O)·1.95(CH<sub>4</sub>O)</b>
Moiety Formula	(C <sub>51</sub> H <sub>52</sub> Cl <sub>2</sub> CuF <sub>2</sub> IrN <sub>6</sub> O <sub>6</sub> P)·(NO <sub>3</sub> )·1.75(CH <sub>4</sub> O)·0.75(H <sub>2</sub> O)	C <sub>52</sub> H <sub>53</sub> Cl <sub>2</sub> CuF <sub>2</sub> IrN <sub>5</sub> O <sub>4</sub> P·(NO <sub>3</sub> )·2.75(H <sub>2</sub> O)	C <sub>52</sub> H <sub>53.5</sub> Cl <sub>2</sub> CuF <sub>2</sub> IrN <sub>5</sub> O <sub>3.5</sub> P·(NO <sub>3</sub> )·1.3(H <sub>2</sub> O)·1.95(CH <sub>4</sub> O)
Formula weight (g·mol <sup>-1</sup> )	1353.19	1300.15	1348.02
Crystal description	blue	pale green	green
Crystal size (mm)	0.26 × 0.12 × 0.04	0.25 × 0.10 × 0.05	0.28 × 0.11 × 0.06
Temperature (K)	293	100	100
Type of radiation	Cu Kα	Cu Kα	Cu Kα
Crystal system	Triclinic	Triclinic	Orthorhombic
Space group	<i>P</i> -1	<i>P</i> -1	<i>Pbcn</i>
a (Å)	10.801 (2)	10.531 (3)	48.765 (5)
b (Å)	13.114 (3)	15.039 (4)	15.889 (2)
c (Å)	20.180 (5)	18.734 (5)	14.660 (3)
α (°)	100.01 (2)	66.38 (3)	
β (°)	99.95 (2)	82.87 (3)	
γ (°)	91.82 (2)	78.35 (2)	
Volume (Å <sup>3</sup> )	2766.9 (11)	2659.4 (14)	11359 (3)
Z	2	8	8
Density calc. (mg/m <sup>3</sup> )	1.624	1.624	1.577
Absorptioncoeff. (mm <sup>-1</sup> )	6.81	7.028	6.63
F(000)	1364	1309	5445
θ <sub>min</sub> – θ <sub>max</sub> (°)	4.2–66.9	3.2–74.2	3.9 – 67.5
hkl ange	12 ← h ← - 12 15 ← k ← - 14 23 ← l ← - 24	13 ← h ← - 13 17 ← k ← - 18 21 ← l ← - 23	58 ← h ← - 58 16 ← k ← - 19 17 ← l ← - 17
Reflections collected	33507	43007	63264
Independent reflections	9814	10849	10196
R <sub>int</sub>	0.037	0.034	0.053
Completeness to θ <sub>full</sub> (%)	99.5	99.7	99.8
Absorptioncorrectiontype	analytical	gaussian	gaussian
T <sub>max</sub> and T <sub>min</sub>	0.773, 0.389	1.000, 0.320	1.000, 0.304
Data/restraints/parameters	9814/6/786	10849/0/877	10196/36/855
Goodness of fit F <sup>2</sup>	1.240	1.039	1.127
R <sub>1</sub> , wR <sub>2</sub> [I>2σ(I)]	0.0442, 0.1082	0.0508, 0.1250	0.0630, 0.1677
R <sub>1</sub> , wR <sub>2</sub> (all data)	0.0455, 0.109	0.0601, 0.132	0.0665,
Largest diff. peak and hole (eÅ <sup>-3</sup> )	0.99, -0.89	2.03, -3.49	2.29, -2.31

<b>Table S2.</b> Selected bond lengths (Å) and angles (°) for crystallized complexes			
	<b>IrPNrCu·(NO<sub>3</sub>)·1.75(CH<sub>4</sub>O)·0.75(H<sub>2</sub>O)</b>	<b>IrPCpCu·(NO<sub>3</sub>)·2.75(H<sub>2</sub>O)</b>	<b>IrPLmCu·(NO<sub>3</sub>)·1.3(H<sub>2</sub>O)·1.95(CH<sub>4</sub>O)</b>
C <sup>6</sup> – C <sup>10</sup>	1.447(10)	1.451(8)	1.44(4)
C <sup>6</sup> – C <sup>7</sup>	1.433(9)	1.412(9)	1.40(4)
C <sup>7</sup> – C <sup>8</sup>	1.454(8)	1.463(9)	1.46(3)
C <sup>8</sup> – C <sup>9</sup>	1.440(9)	1.414(10)	1.51(4)
C <sup>9</sup> – C <sup>10</sup>	1.449(9)	1.447(9)	1.46(3)
C(Cp*ring)-C(Cp*CH <sub>3</sub> )			1.4862
Ir <sup>1</sup> – C <sup>6</sup>	2.235(6)	2.245(6)	2.19(4)
Ir <sup>1</sup> – C <sup>7</sup>	2.224(6)	2.237(6)	2.21(3)
Ir <sup>1</sup> – C <sup>8</sup>	2.198(7)	2.142(6)	2.18(2)
Ir <sup>1</sup> – C <sup>9</sup>	2.195(6)	2.155(6)	2.19(2)
Ir <sup>1</sup> – C <sup>10</sup>	2.203(6)	2.154(6)	2.21(2)
Ir <sup>1</sup> – C <sub>Cp*</sub> (average)	2.211(0)	2.186(6)	2.196
Ir <sup>1</sup> – C <sub>centroid</sub>			1.835
Ir <sup>1</sup> – P <sup>1</sup>	2.312(16)	2.291(15)	2.304(18)
Ir <sup>1</sup> – Cl <sup>1</sup>	2.410(2)	2.411(15)	2.407(18)
Ir <sup>1</sup> – Cl <sup>2</sup>	2.427(4)	2.448(17)	2.413(18)
P <sup>1</sup> – C <sup>11</sup>	1.839(5)	1.846(6)	1.859(7)
P <sup>1</sup> – C <sup>21</sup>	1.815(5)	1.822(6)	1.814(7)
P <sup>1</sup> – C <sup>31</sup>	1.812(5)	1.816(6)	1.819(7)
Cu <sup>1</sup> – O <sup>70A</sup>	1.911(4)	1.917(17)	2.057(12)
Cu <sup>1</sup> – O <sup>70A'</sup>	-	-	2.220(14)
Cu <sup>1</sup> – O <sup>65A</sup>	1.917(4)	1.919(17)	1.923(19)
Cu <sup>1</sup> – O <sup>65B</sup>	-	-	1.959(18)
Cu <sup>1</sup> – N <sup>91</sup>	2.019(5)	1.999(13)	2.004(7)
Cu <sup>1</sup> – N <sup>81</sup>	2.014(5)	2.013(12)	1.991(8)
Cu <sup>1</sup> – O <sup>1N</sup>	2.351(6)	-	-2.298(3)
Cu <sup>1</sup> – O <sup>1W</sup>	-	2.32(2)	3.743
FQ <sub>centroid</sub> – phen <sub>centroid</sub>			87.93(6)
P <sup>1</sup> – Ir <sup>1</sup> – Cl <sup>1</sup>	87.57(1)	86.73(5)	90.19
P <sup>1</sup> – Ir <sup>1</sup> – Cl <sup>2</sup>	124.2(2)	91.14(6)	88.28
Cl <sup>1</sup> – Ir <sup>1</sup> – Cl <sup>2</sup>	86.96(13)	88.39(5)	134.59
C <sub>centroid</sub> – Ir <sup>1</sup> – P <sup>1</sup>			121.28
C <sub>centroid</sub> – Ir <sup>1</sup> – P <sup>1</sup>			121.68
C <sub>centroid</sub> – Ir <sup>1</sup> – P <sup>1</sup>			114.0(2)
Ir <sup>1</sup> – P <sup>1</sup> – C <sup>11</sup>	114.44(18)	112.06(19)	118.6(3)
Ir <sup>1</sup> – P <sup>1</sup> – C <sup>21</sup>	111.4(2)	113.2(2)	116.0(2)
Ir <sup>1</sup> – P <sup>1</sup> – C <sup>31</sup>	118.76(19)	117.1(2)	103.8(3)
C <sup>31</sup> – P <sup>1</sup> – C <sup>21</sup>	105.5(2)	107.1(3)	97.2(3)
C <sup>31</sup> – P <sup>1</sup> – C <sup>11</sup>	104.4(3)	101.2(3)	104.4(3)
C <sup>21</sup> – P <sup>1</sup> – C <sup>11</sup>	100.4(2)	104.8(3)	82.1(3)
N <sup>91</sup> – Cu <sup>1</sup> – N <sup>81</sup>	82.1(2)	81.6(5)	88.2(6)
O <sup>70A</sup> – Cu <sup>1</sup> – O <sup>65A</sup>	94.52(16)	93.7(7)	95.9(6)
O <sup>70A</sup> – Cu <sup>1</sup> – O <sup>65B</sup>	-	-	71.69
O <sup>70A</sup> – Cu <sup>1</sup> – O <sup>70'</sup>			91.0(6)
O <sup>65A</sup> – Cu <sup>1</sup> – N <sup>81</sup>	90.9(2)	88.9(6)	91.1(6)
O <sup>65B</sup> – Cu <sup>1</sup> – N <sup>81</sup>			157.1(5)
O <sup>70A</sup> – Cu <sup>1</sup> – N <sup>81</sup>	172.94(19)	174.5(6)	108.2(3)
O <sup>70'</sup> – Cu <sup>1</sup> – N <sup>81</sup>			167.9(6)
O <sup>65A</sup> – Cu <sup>1</sup> – N <sup>91</sup>	162.68(19)	158.8(7)	167.5(6)
O <sup>65B</sup> – Cu <sup>1</sup> – N <sup>91</sup>			94.4(4)
O <sup>70A</sup> – Cu <sup>1</sup> – N <sup>91</sup>	91.43(18)	94.4(6)	86.2(4)
O <sup>70A'</sup> – Cu <sup>1</sup> – N <sup>91</sup>			
O <sup>1N</sup> – Cu <sup>1</sup> – N <sup>91</sup>	81.7(2)	-	
O <sup>1N</sup> – Cu <sup>1</sup> – N <sup>81</sup>	86.88(19)	-	

$O^{1N} - Cu^1 - O^{65A}$	113.91(18)	-	
$O^{1N} - Cu^1 - O^{70A}$	95.02(18)	-	
$O^{1W} - Cu^1 - N^{91}$	-	102.9(8)	88.6(3)
$O^{1W} - Cu^1 - N^{81}$	-	93.4(10)	108.2(3)
$O^{1W} - Cu^1 - O^{65A}$	-	96.4(9)	103.1(5)
$O^{1W} - Cu^1 - O^{65B}$	-	-	83.6(5)
$O^{1W} - Cu^1 - O^{70A}$	-	-	94.3(4)
$O^{1W} - Cu^1 - O^{70A'}$	-	-	164.5(4)
Ccentroid – centre of gravity			
Ir <sup>1</sup> -CCp* (average) – average calculated from: Ir <sup>1</sup> -C <sup>1</sup> , Ir <sup>1</sup> -C <sup>2</sup> , Ir <sup>1</sup> -C <sup>3</sup> , Ir <sup>1</sup> -C <sup>4</sup> , Ir <sup>1</sup> -C <sup>5</sup>			
C(Cp*ring)-C(Cp*CH <sub>3</sub> ) – average calculated from: C <sup>1</sup> -C <sup>1A</sup> , C <sup>2</sup> -C <sup>2A</sup> , C <sup>3</sup> -C <sup>3A</sup> , C <sup>4</sup> -C <sup>4A</sup> , C <sup>5</sup> -C <sup>5A</sup>			



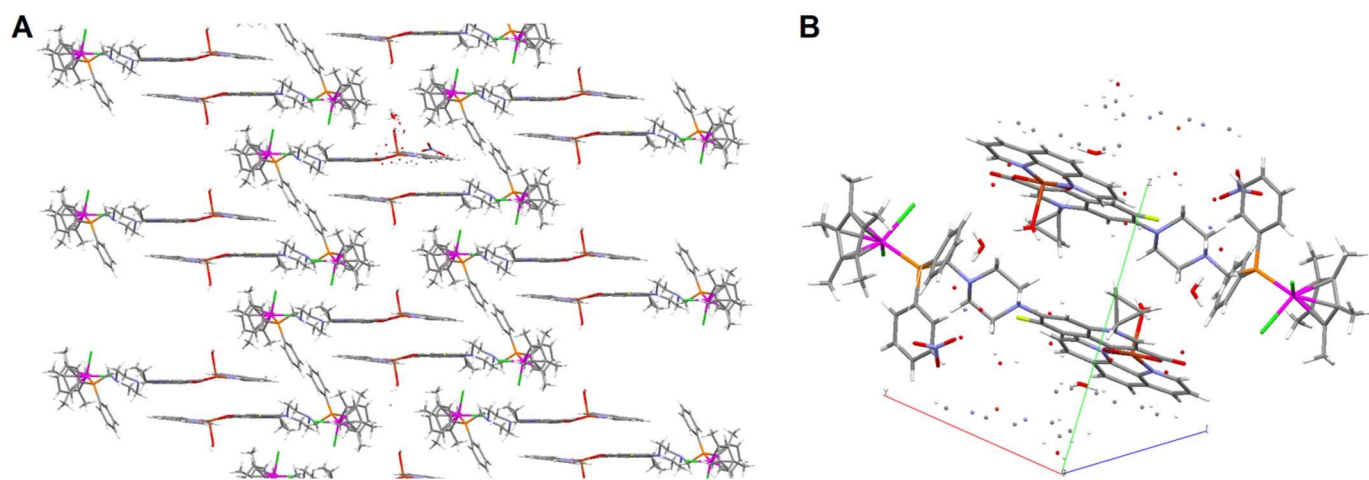


Figure S1 A perspective view of the complex **IrPCpCu** showing (A)  $\pi$ -stacking interaction between the fluoroquinolone rings (B) packing diagram.

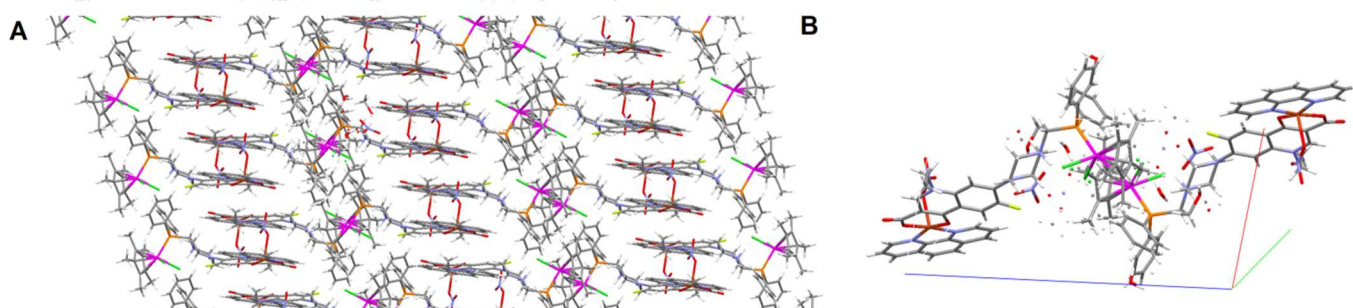


Figure S2 A perspective view of the complex **IrPNrCu** showing (A)  $\pi$ -stacking interaction between the fluoroquinolone rings (B) packing diagram.

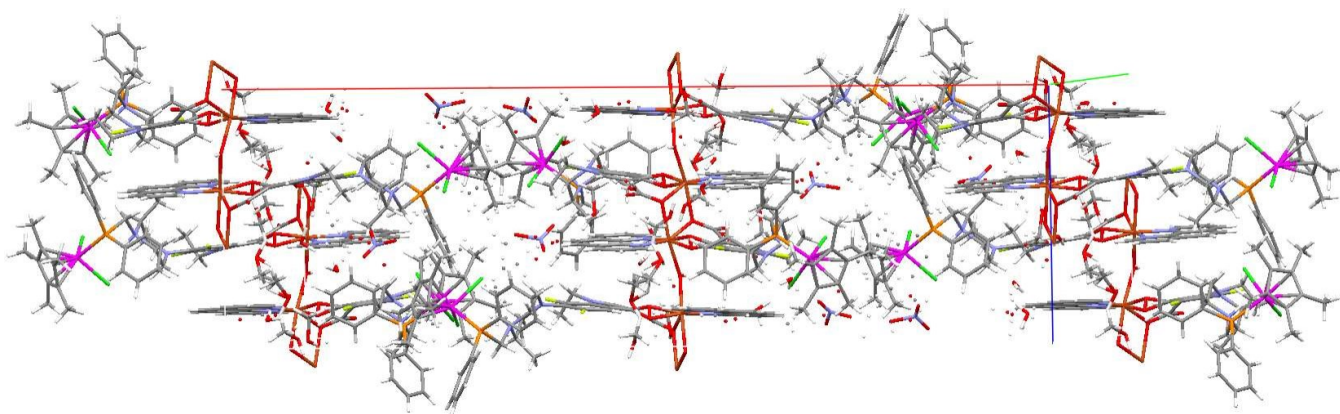


Figure S3 Packing diagram of complex **IrPLmCu**

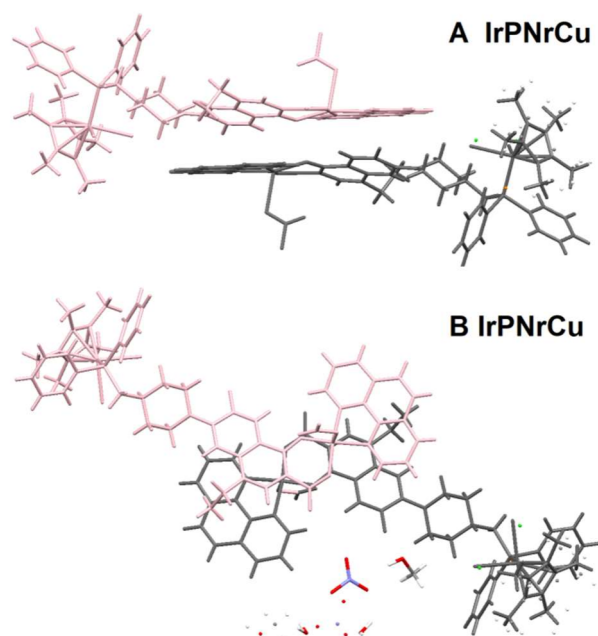


Figure S4 Packing diagram of complex **IrPNrCu** showing (A)  $\pi$ -stacking interaction between the fluoroquinolone rings (B) offset pattern of the  $\pi$ - $\pi$  stacking in complex **IrPNrCu**.

Figure S5 (a)

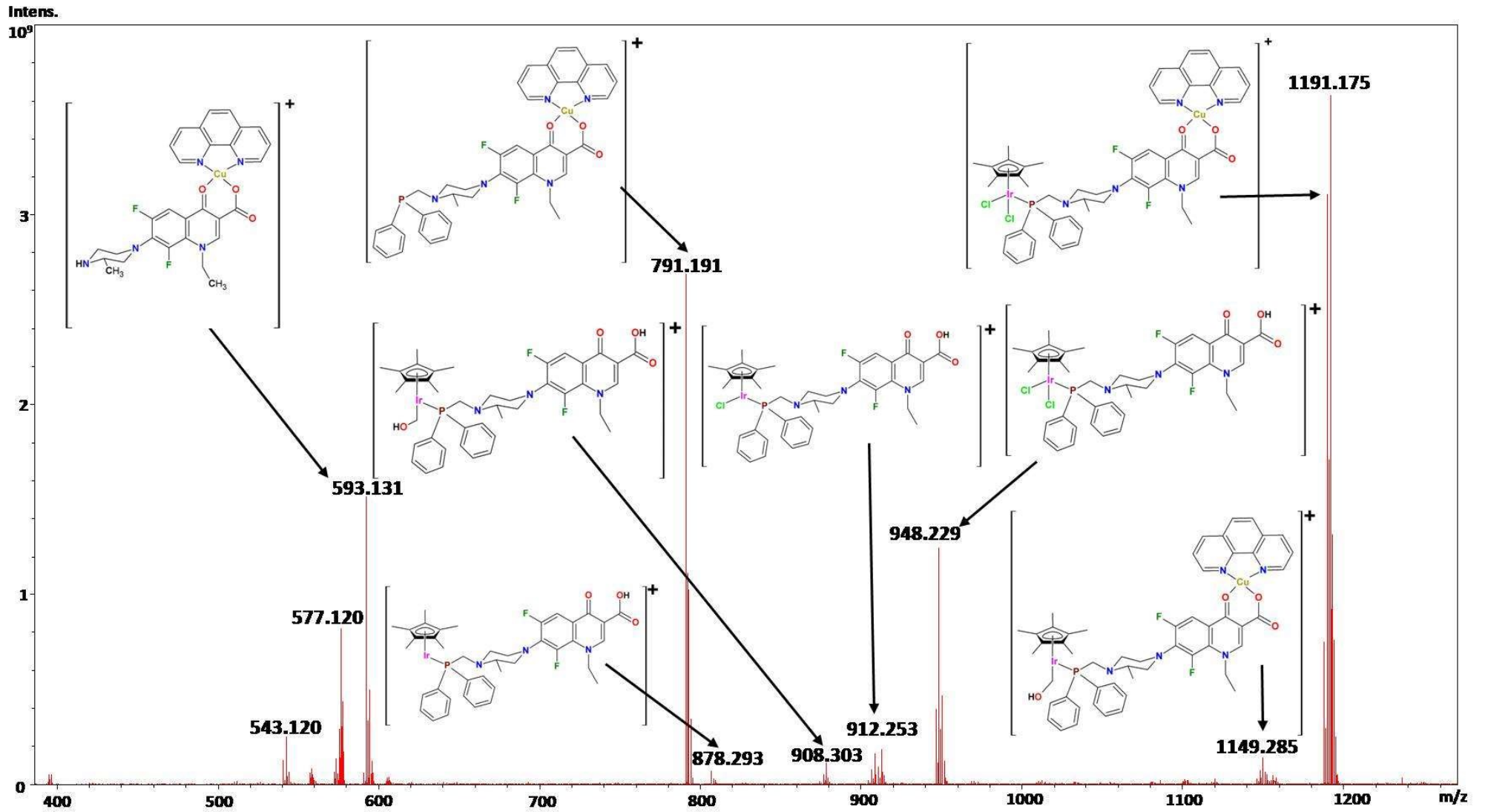


Figure S5 (b)

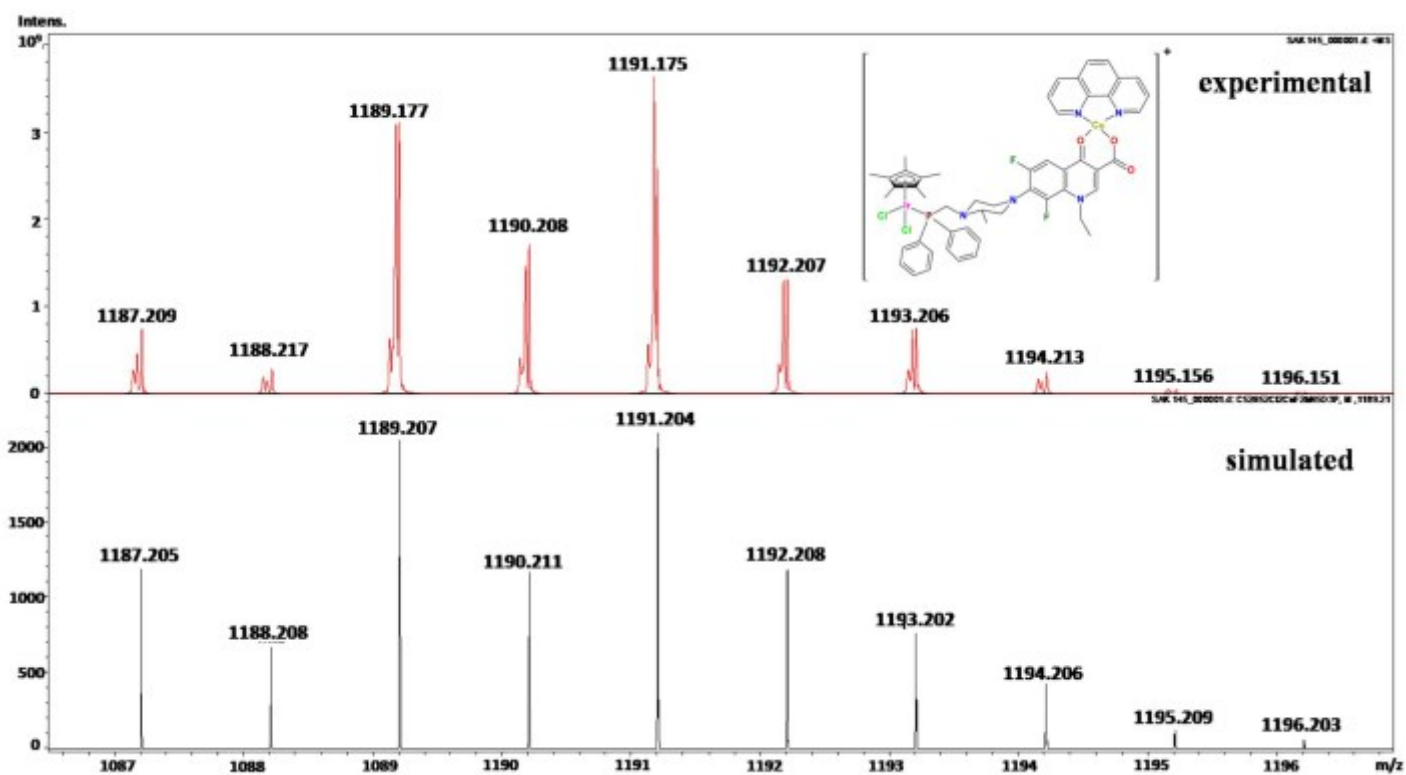


Figure S5 (c)

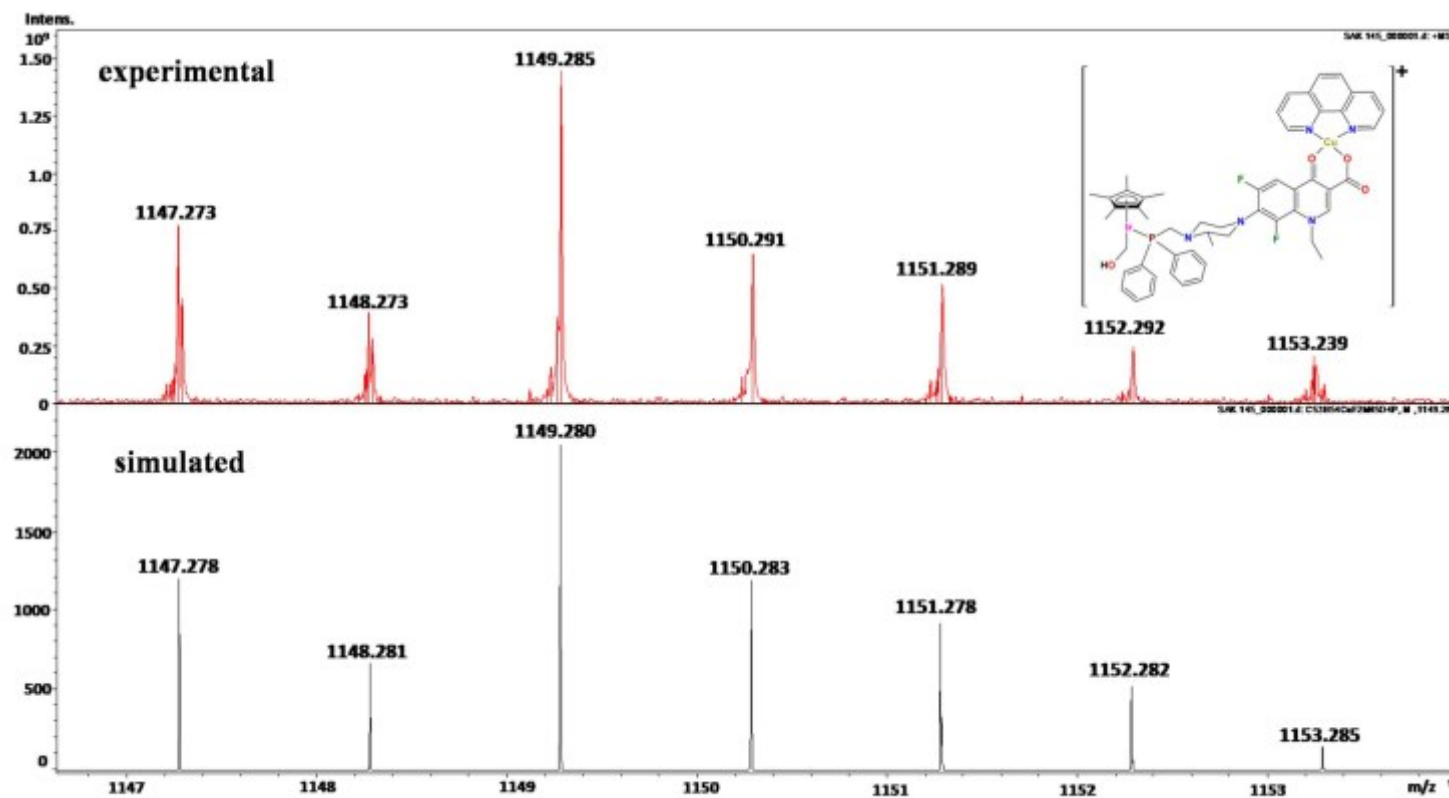


Figure S5 (d)

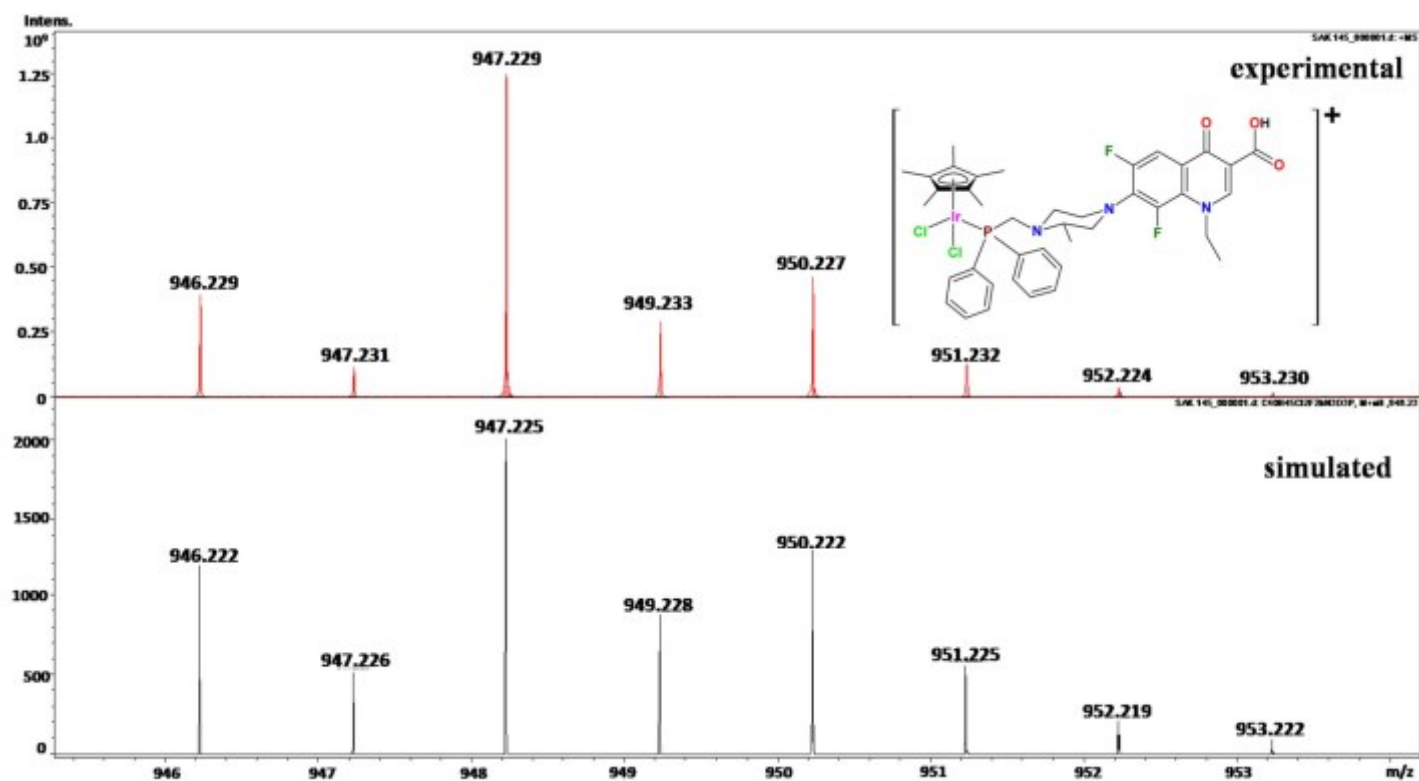


Figure S5 (e)

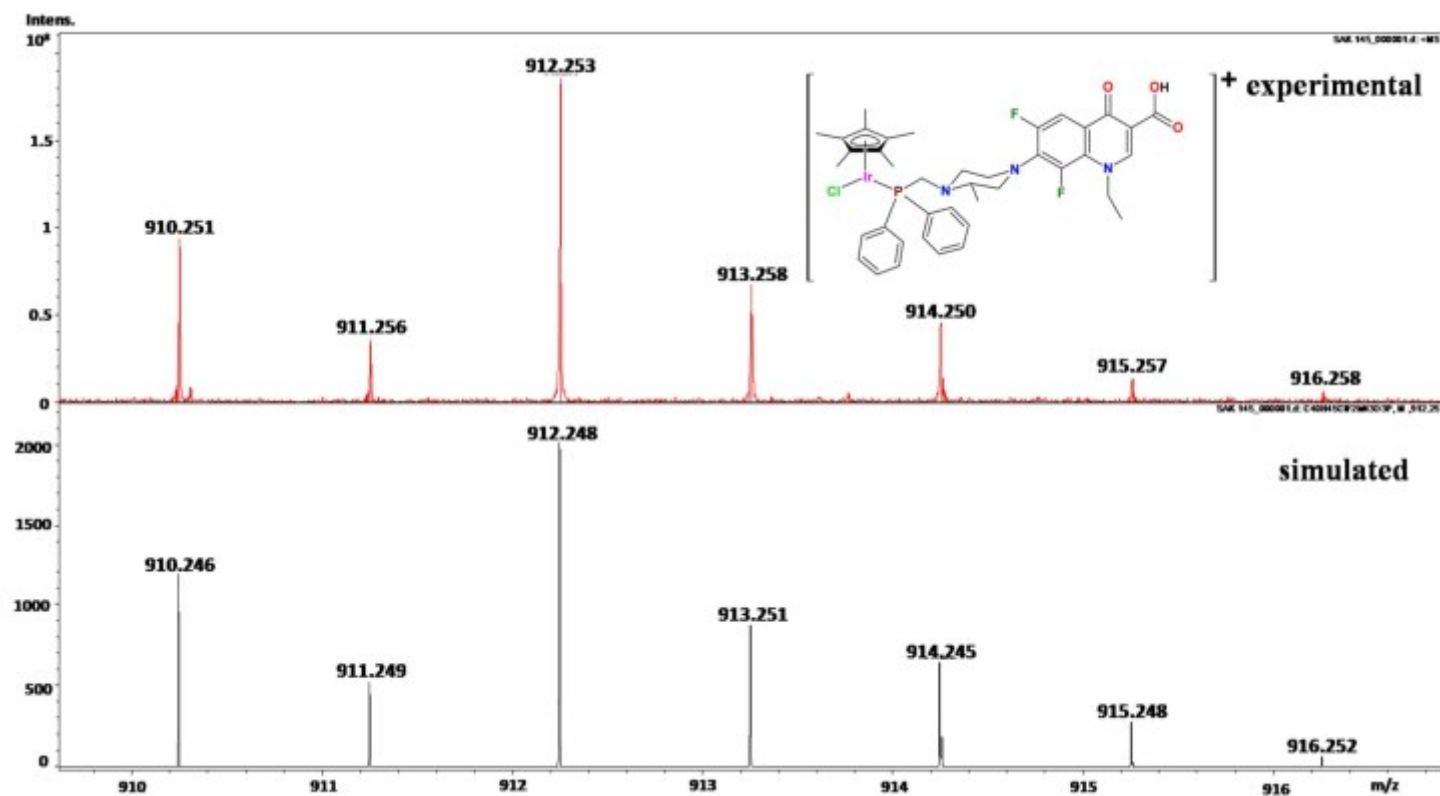


Figure S5 (f)

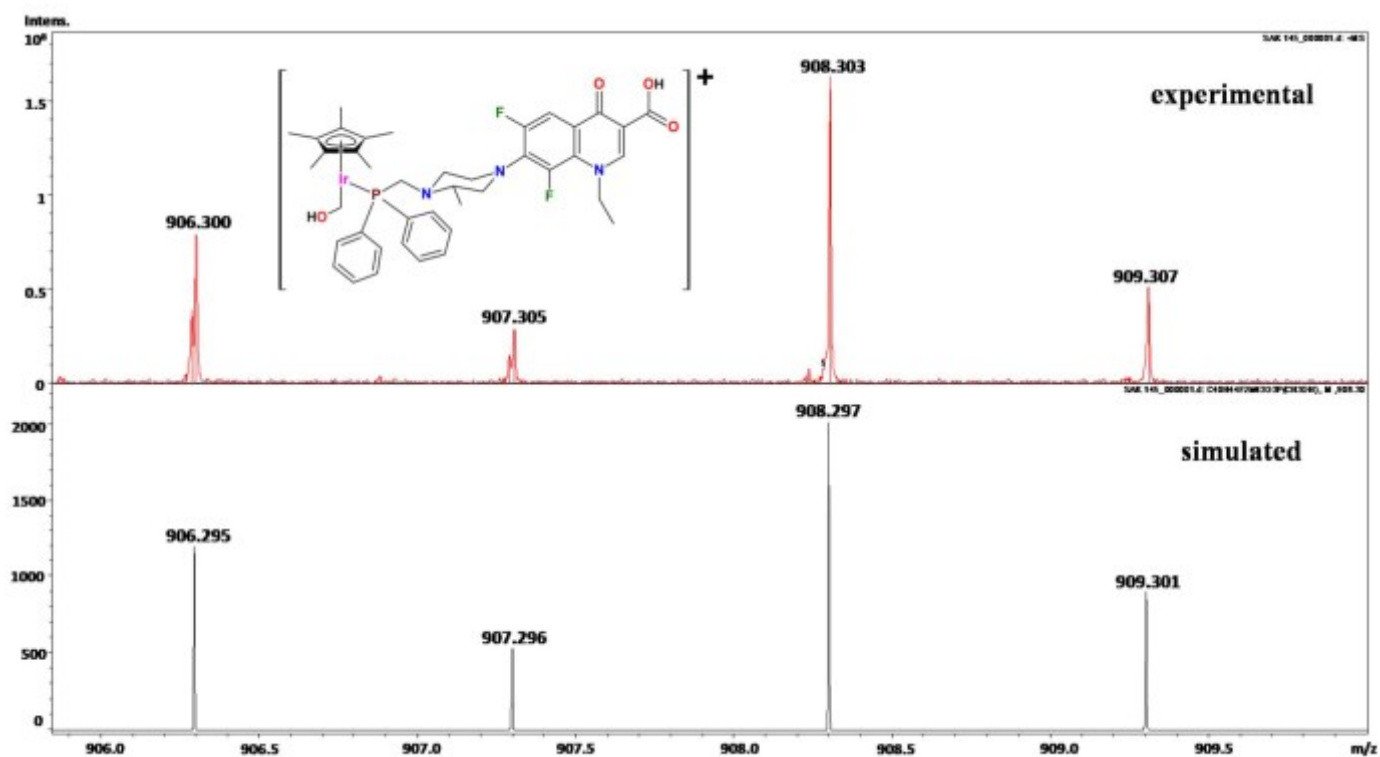


Figure S5 (g)

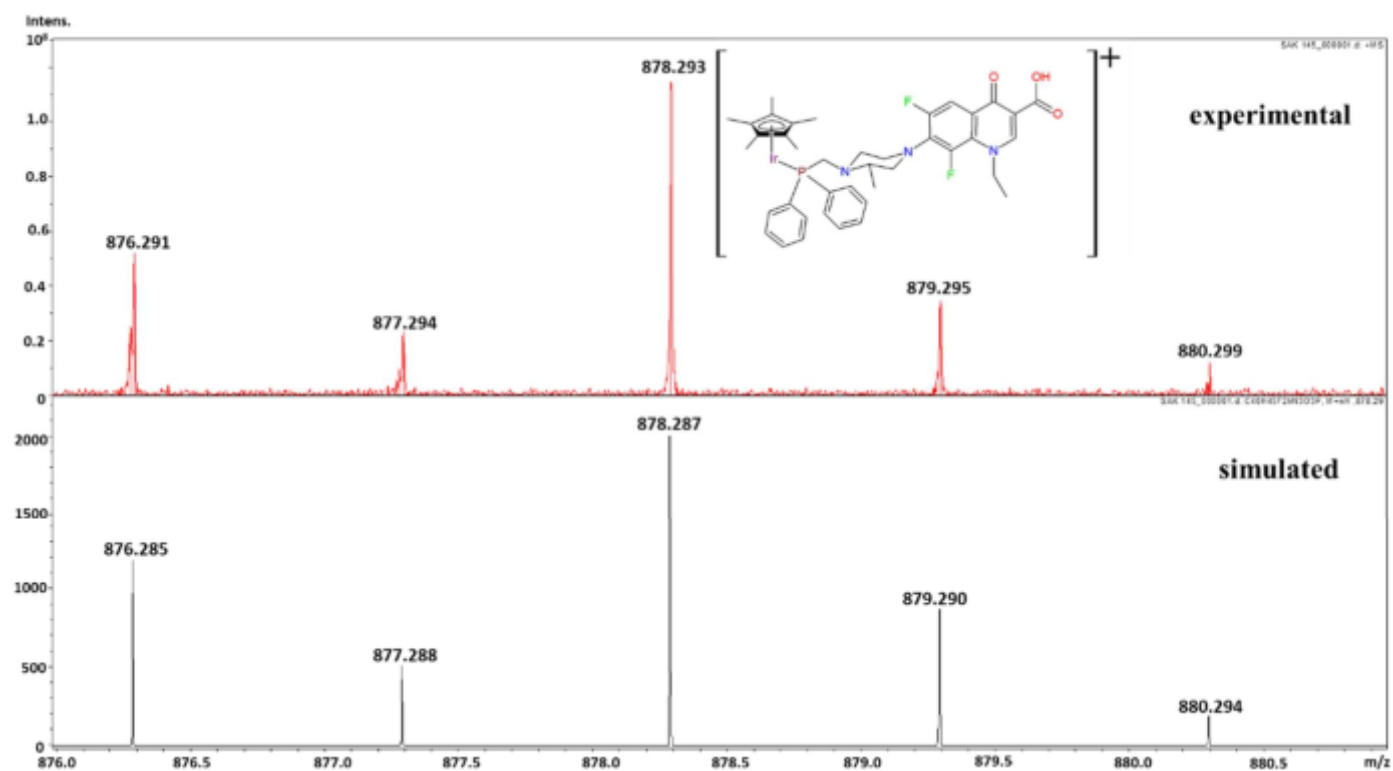




Figure S5 (h)

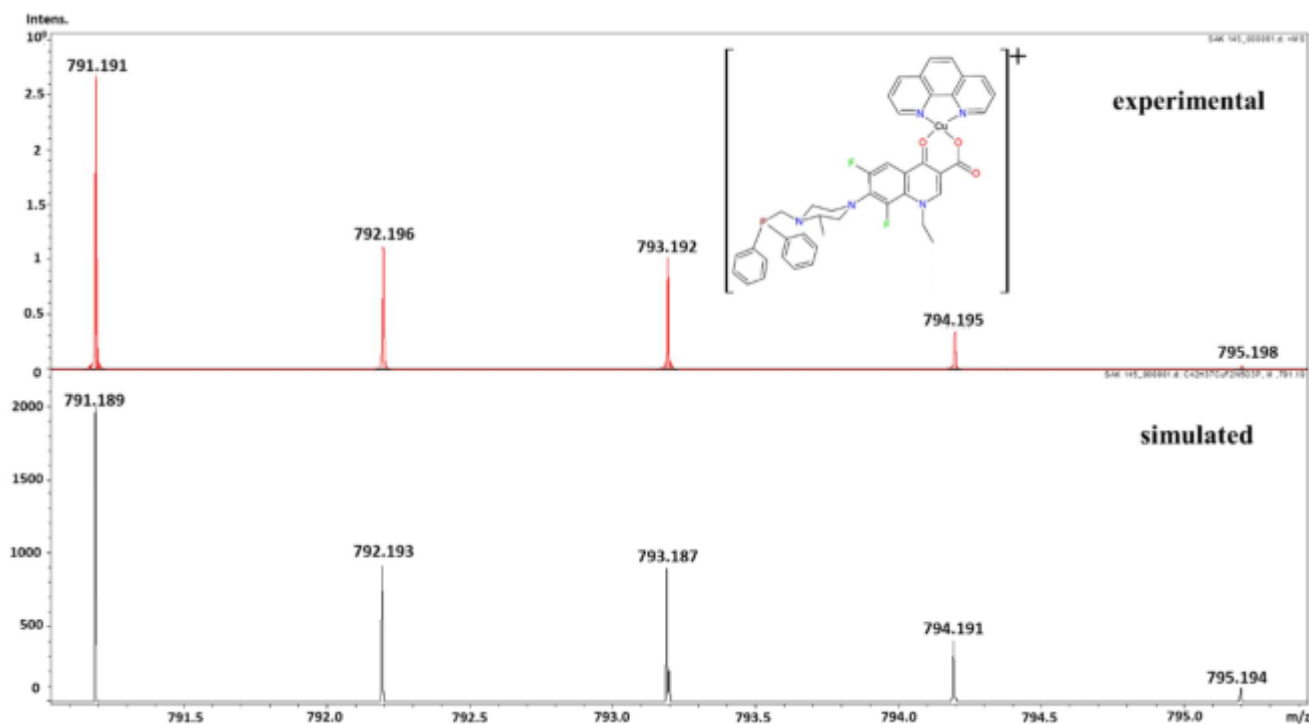
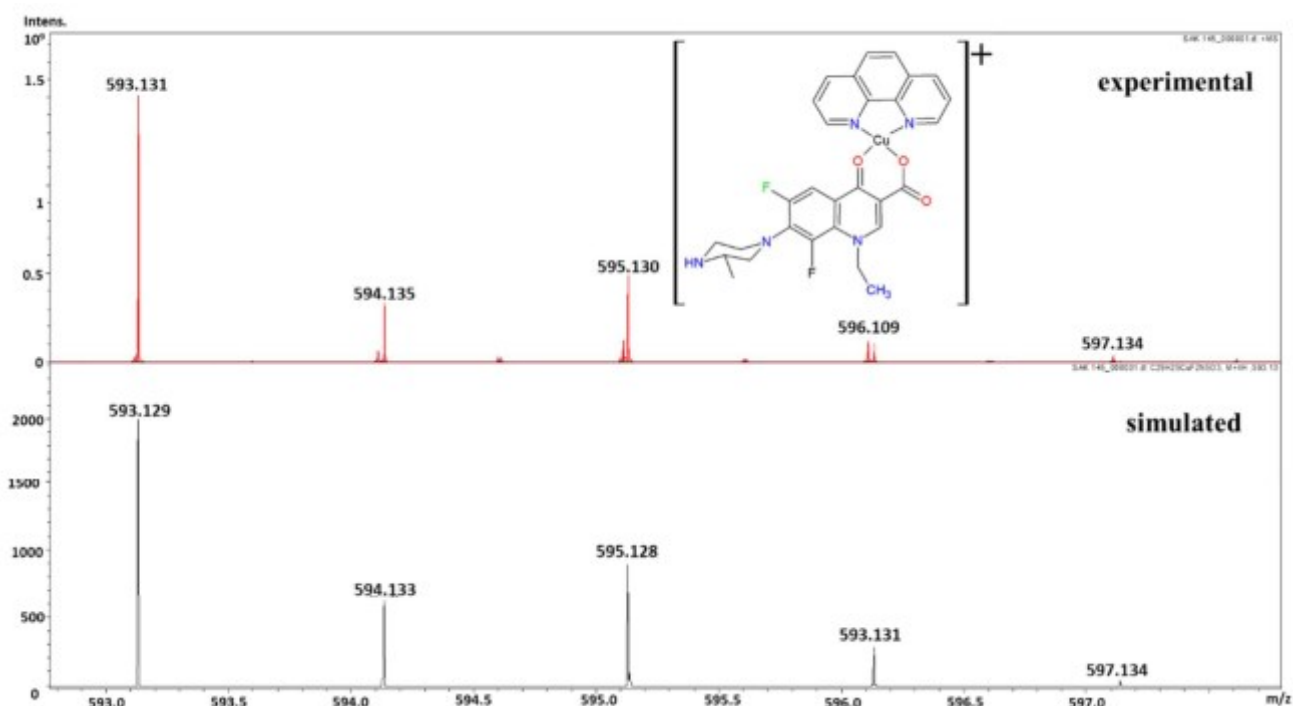


Figure S5 (i)



**Figure S5 (a)** ESI mass spectrum of  $[\text{IrPLmCu(phen)}]^+$ ; 1149.285  $[\text{IrPLmCu(phen)-HCl-Cl+CH}_2\text{OH}]^+$ ; 948.229  $[\text{IrPLmCu(phen)-Cu(phen)+H}]^+$ ; 912.253  $[\text{IrPLmCu(phen)-Cu(phen)-Cl}]^+$ ; 908.303  $[\text{IrPLmCu(phen)-Cu(phen)-2Cl+CH}_2\text{OH}]^+$ ; 878.293  $[\text{IrPLmCu(phen)-Cu(phen)-2Cl+H}]^+$ ; 791.191  $[\text{IrPLmCu(phen)-IrCl}_2]^+$ ; 593.131  $[\text{IrPLmCu(phen)-IrCl}_2\text{-PPh}_2\text{CH}_2]^+$  **(b)** experimental and simulated spectra of  $[\text{IrPLmCu(phen)+H}]^+$  **(c)** experimental and simulated spectra of  $[\text{IrPLmCu(phen)-2Cl-2H+CH}_3\text{OH}]^+$  **(d)** experimental and simulated spectra of  $[\text{IrPLmCu(phen)-Cu(phen)}]^+$  **(e)** experimental and simulated spectra of  $[\text{IrPLmCu(phen)-Cu(phen)-Cl}]^+$  **(f)** experimental and simulated spectra of  $[\text{IrPLmCu(phen)-Cu(phen)-2Cl-H+CH}_3\text{OH}]^+$  **(g)** experimental and simulated spectra of  $[\text{IrPLmCu(phen)-Cu(phen)-2Cl+H}]^+$  **(h)** experimental and simulated spectra of  $[\text{IrPLmCu(phen)-IrCl}_2]^+$  **(i)** experimental and simulated spectra of  $[\text{IrPLmCu(phen)-IrCl}_2\text{-PPh}_2\text{CH}_2]^+$

Fig. S6 (a)

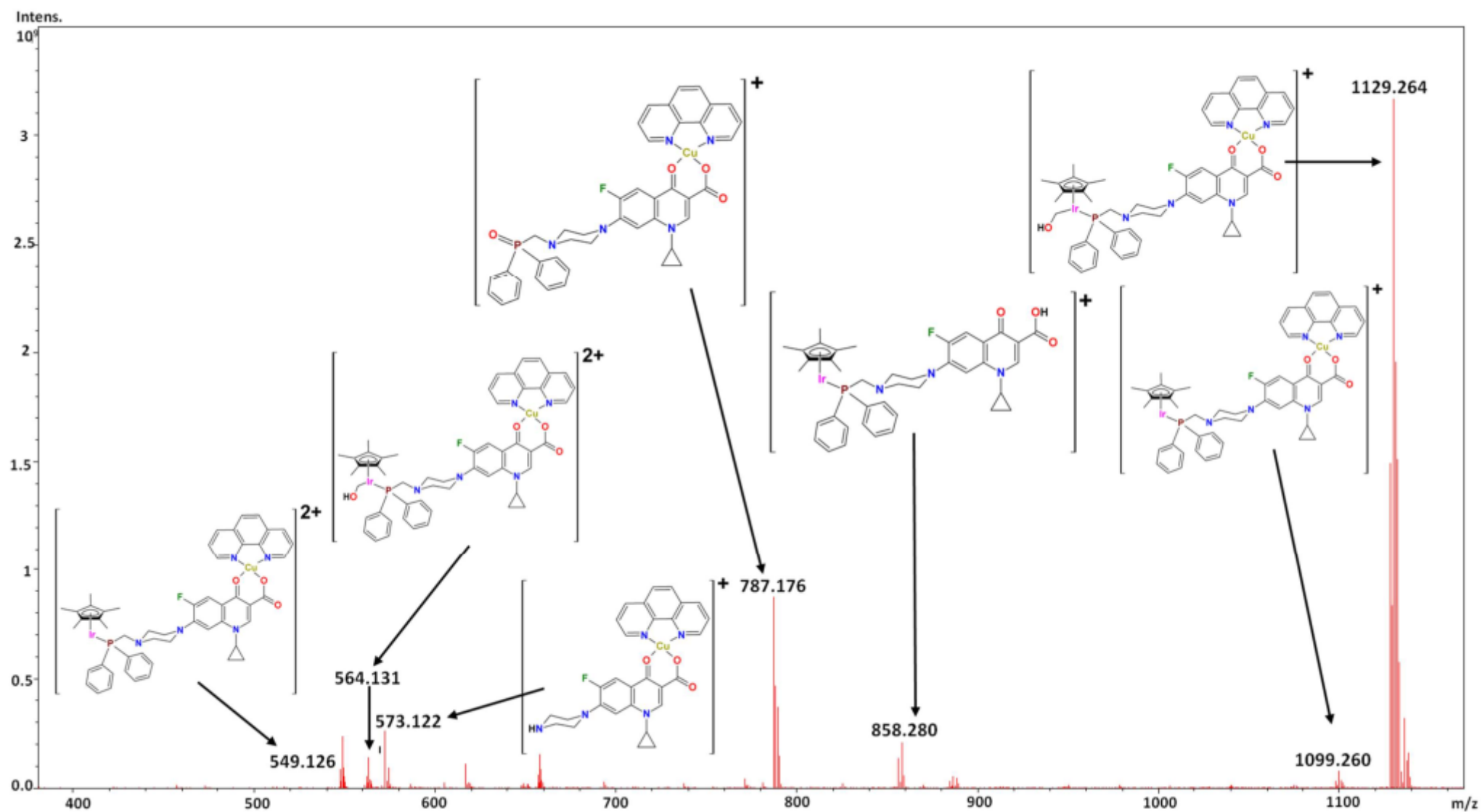


Fig. S6 (b)

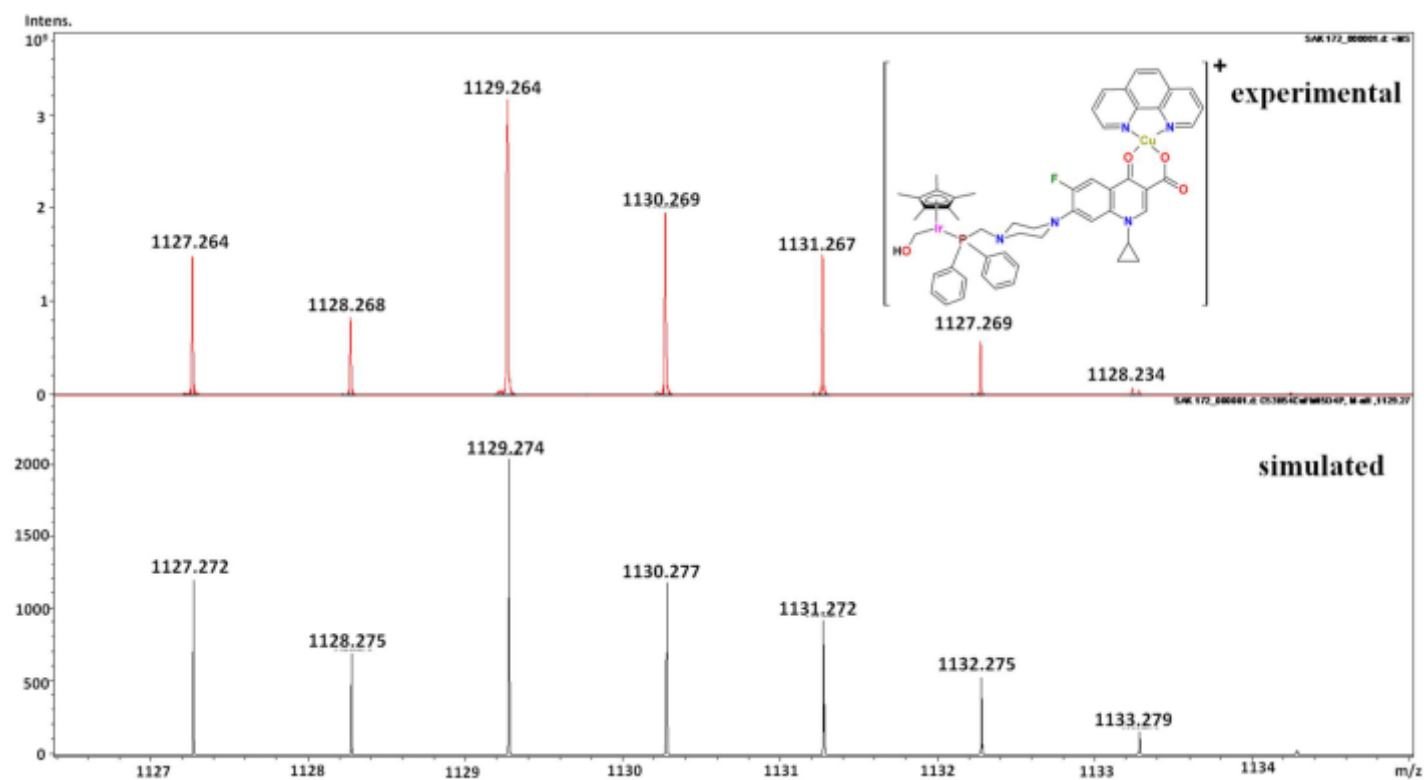


Fig. S6 (c)

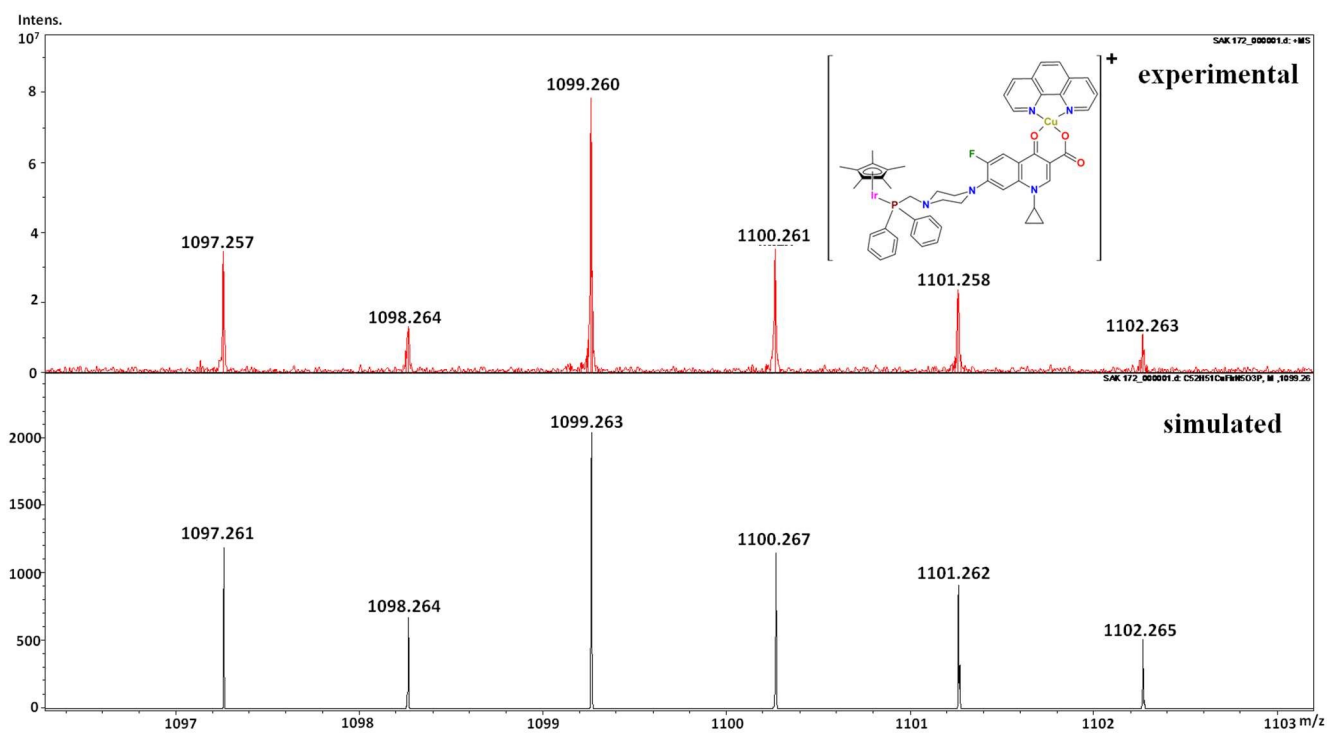


Fig. S6 (d)

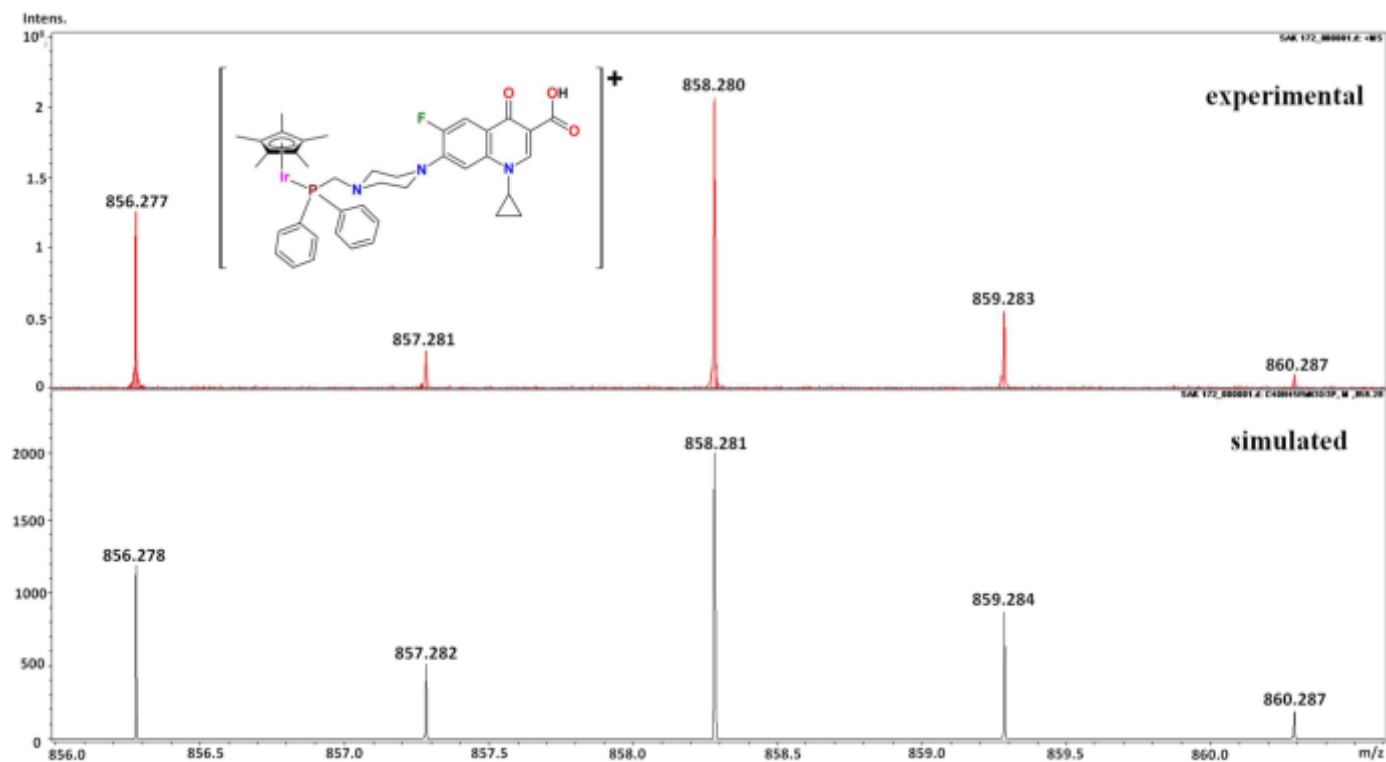


Fig. S6 (e)

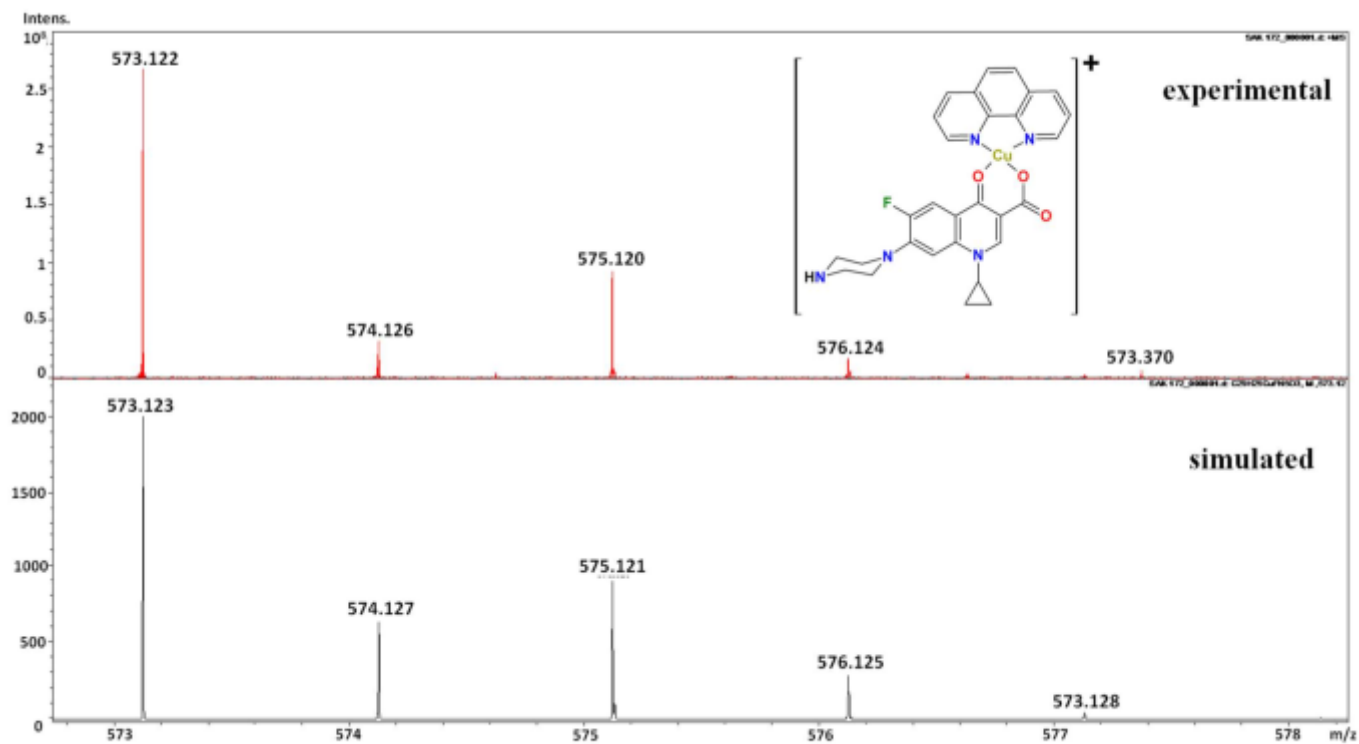


Fig. S6 (f)

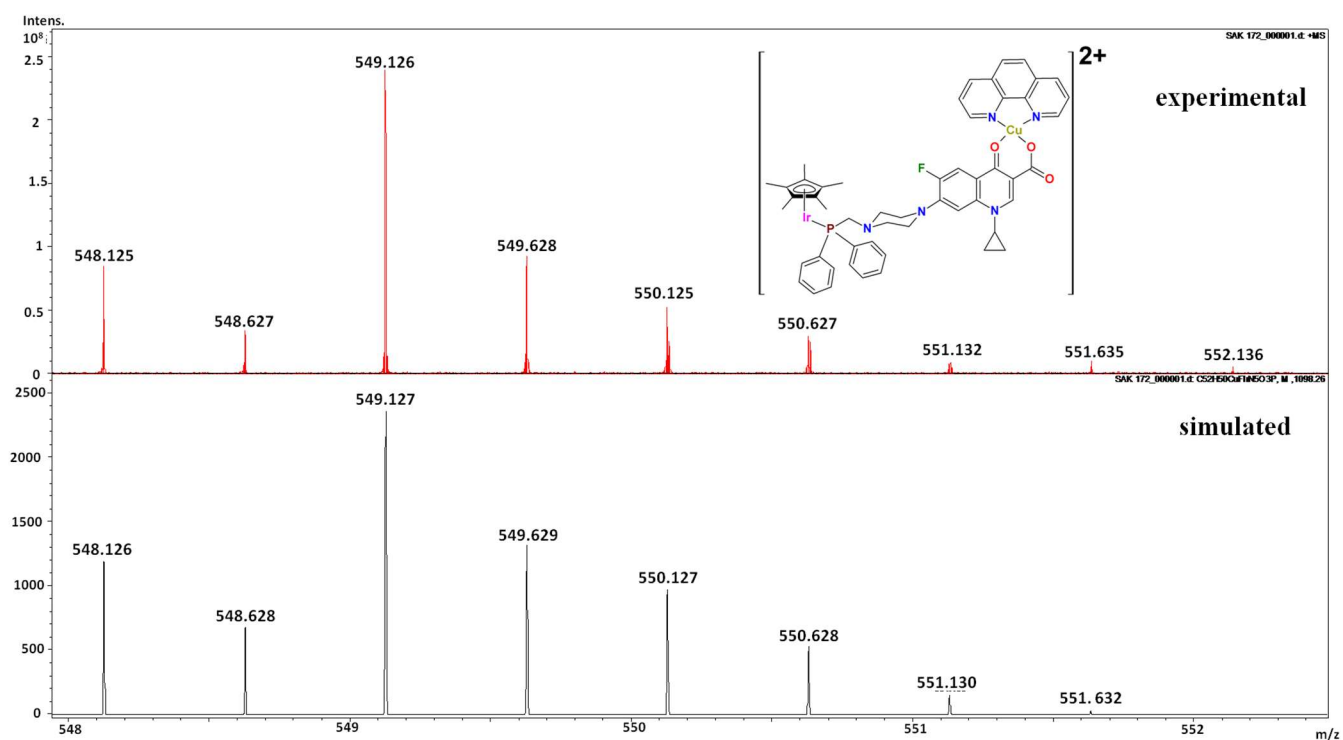


Fig. S6 (g)

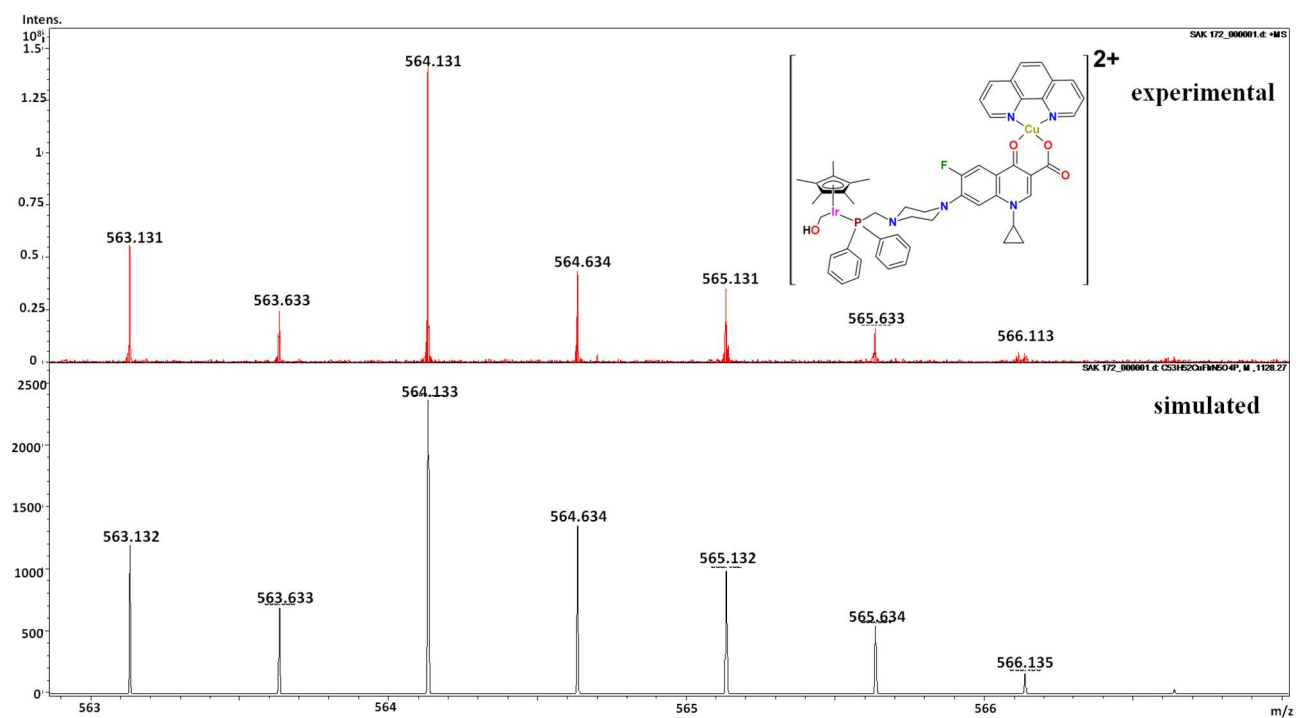
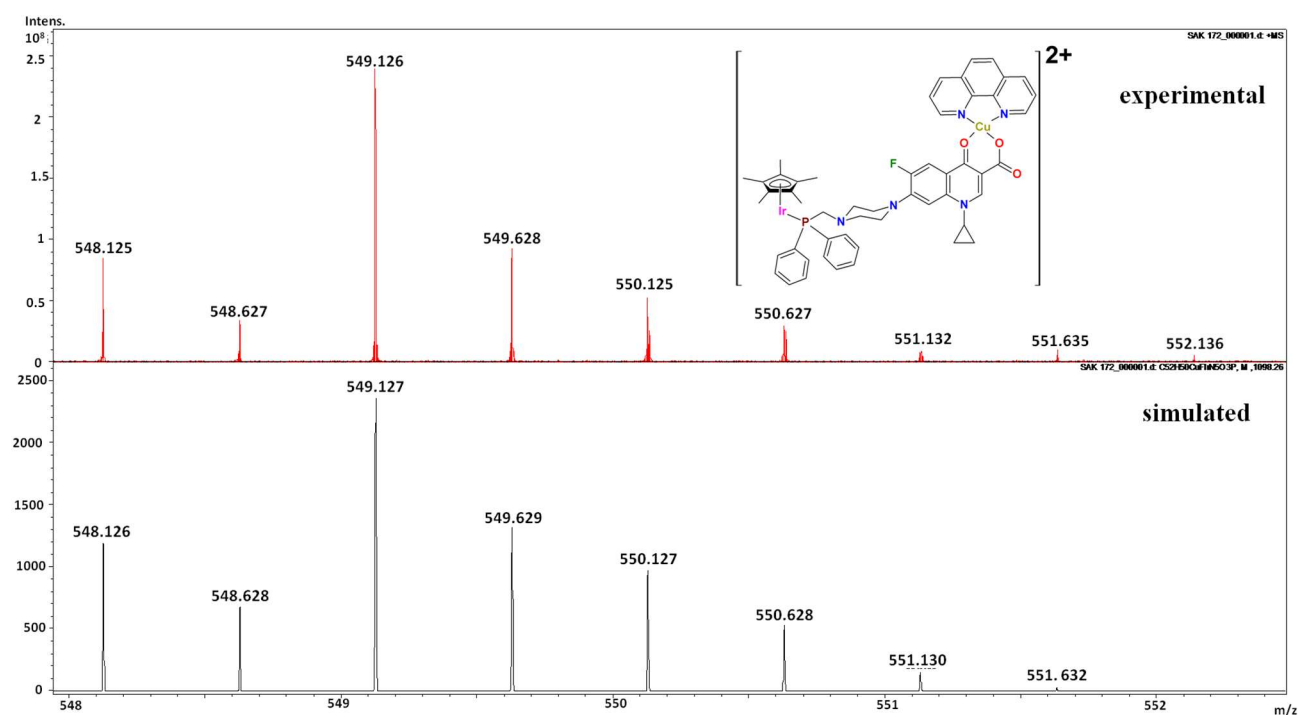


Fig. S6 (h)



**Figure S6 (a)** ESI mass spectrum of IrPCpCu(phen). ESI(+)-MS in CH<sub>3</sub>OH, m/z: 1129.264 [M-HCl-Cl+CH<sub>2</sub>OH]<sup>+</sup>; 1099.260 [M-2Cl]<sup>+</sup>; 858.280 [M-2Cl-Cu(phen)+H]<sup>+</sup>; 787.176 [M-IrCpCl<sub>2</sub>+O]<sup>+</sup>; 573.122 [M-IrCpCl<sub>2</sub>-PPhCH<sub>2</sub>]<sup>+</sup>; 564.131 [M-2HCl+CH<sub>2</sub>OH]<sup>2+</sup>; 549.126 [M-HCl-Cl]<sup>2+</sup> (b) experimental and simulated spectra of [M-HCl-Cl+CH<sub>2</sub>OH]<sup>+</sup> (c) experimental and simulated spectra of [M-2Cl]<sup>+</sup> (d) experimental and simulated spectra of [M-2Cl-Cu(phen)+H]<sup>+</sup> (e) experimental and simulated spectra of [M-IrCpCl<sub>2</sub>+O]<sup>+</sup> (f) experimental and simulated spectra of [M-IrCpCl<sub>2</sub>-PPhCH<sub>2</sub>]<sup>+</sup> (g) experimental and simulated spectra of [M-2HCl+CH<sub>2</sub>OH]<sup>2+</sup> (h) experimental and simulated spectra of [M-HCl-Cl]<sup>2+</sup>



Fig. S7 (a)

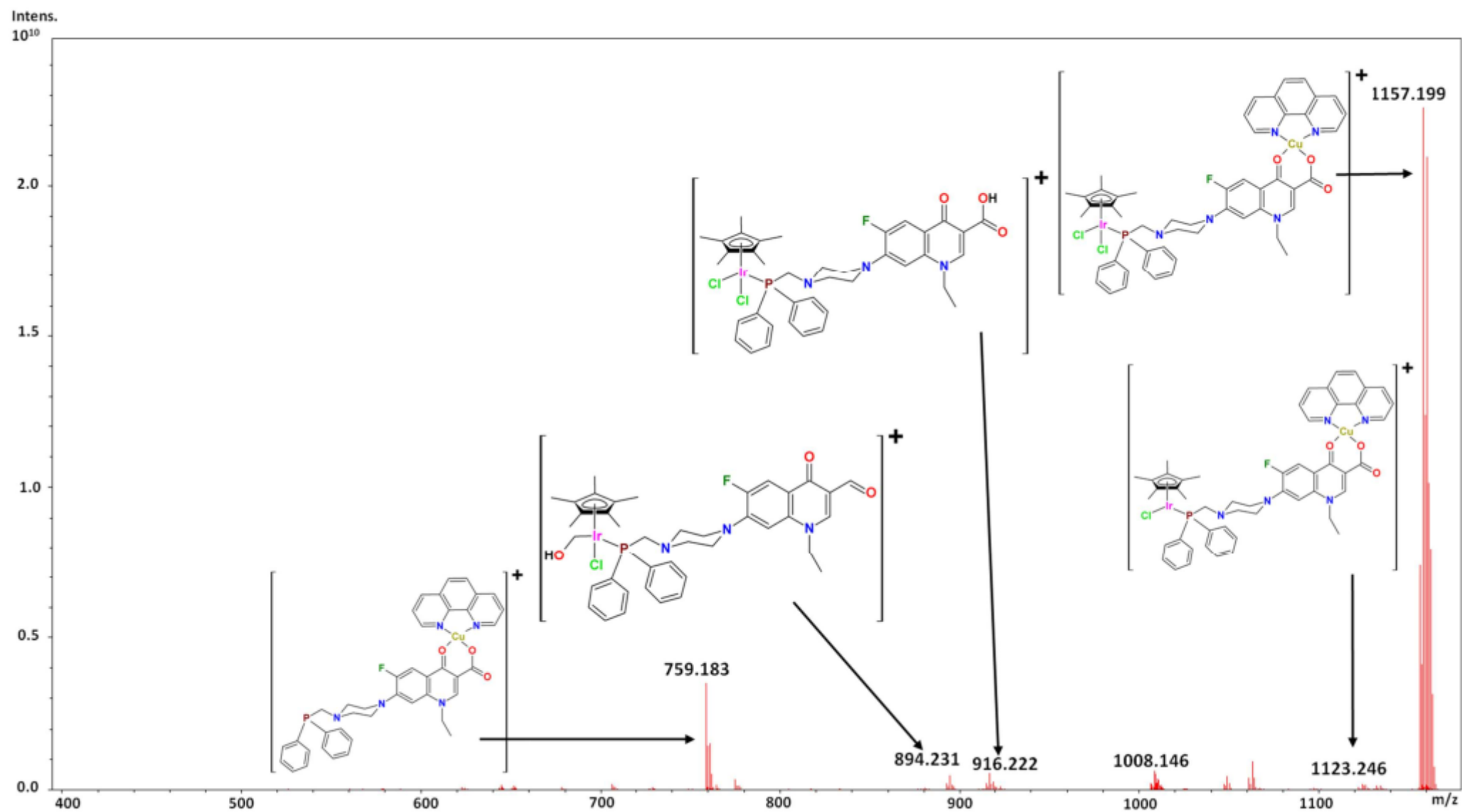


Fig. S7 (b)

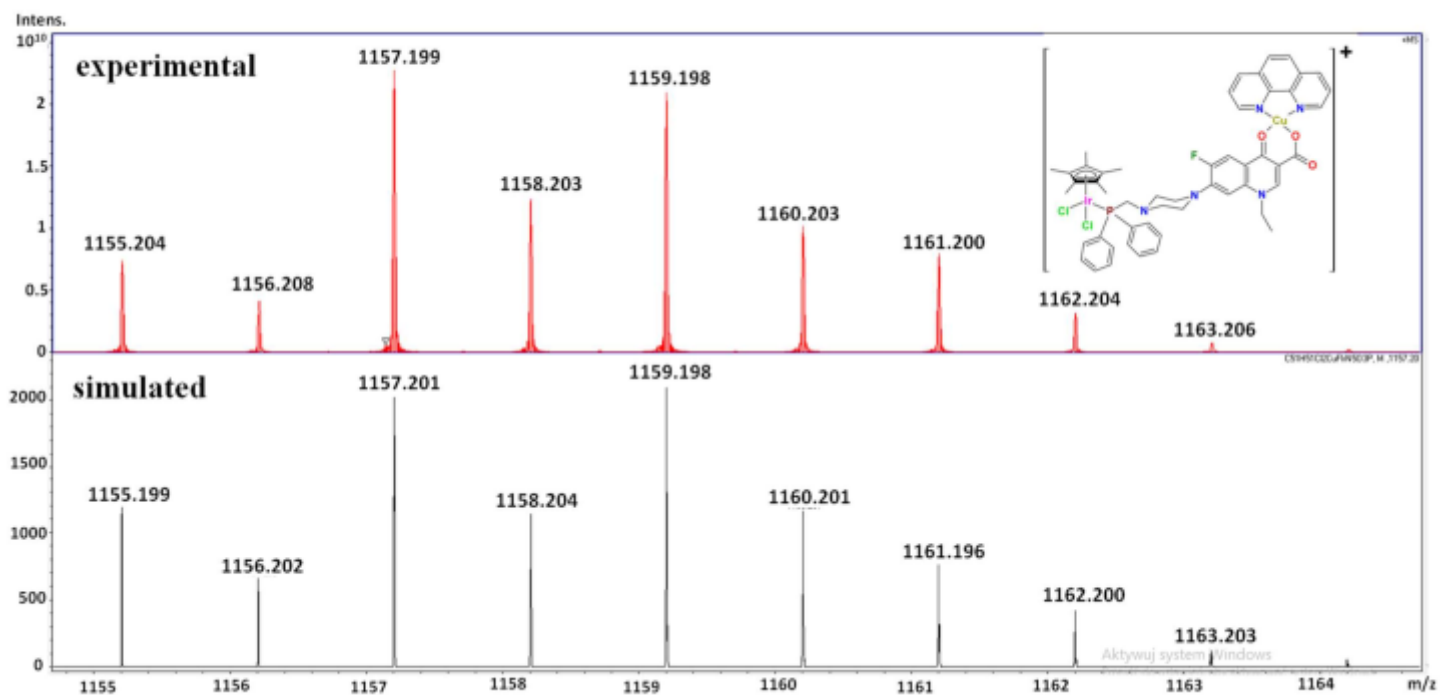


Fig. S7 (c)

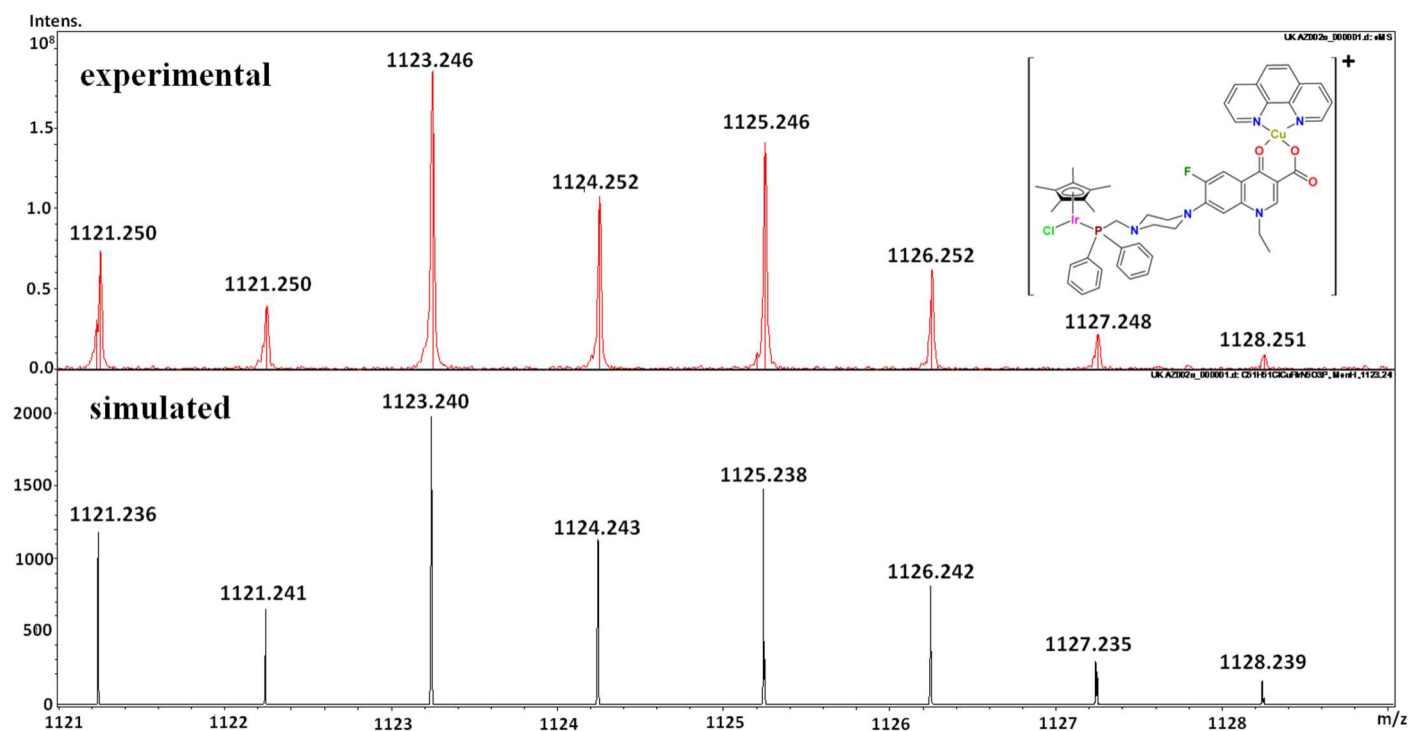


Fig. S7 (d)

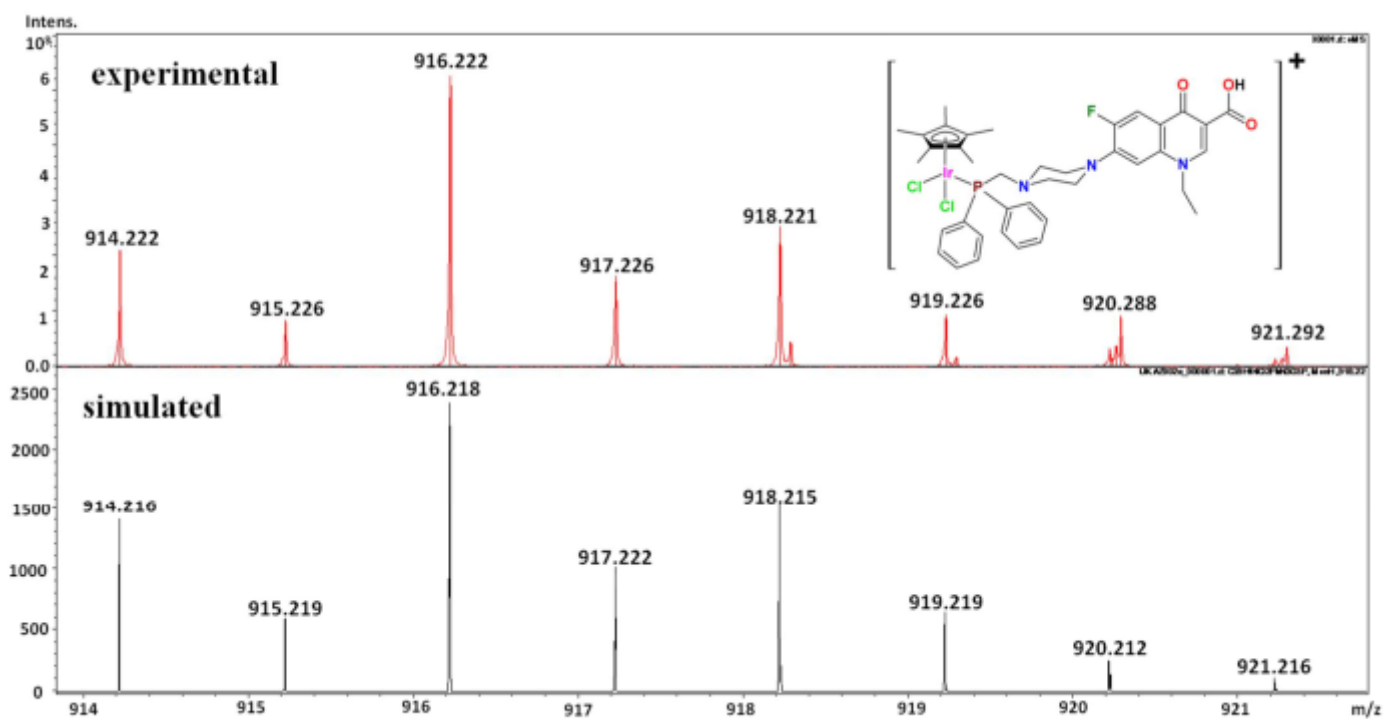


Fig. S7 (e)

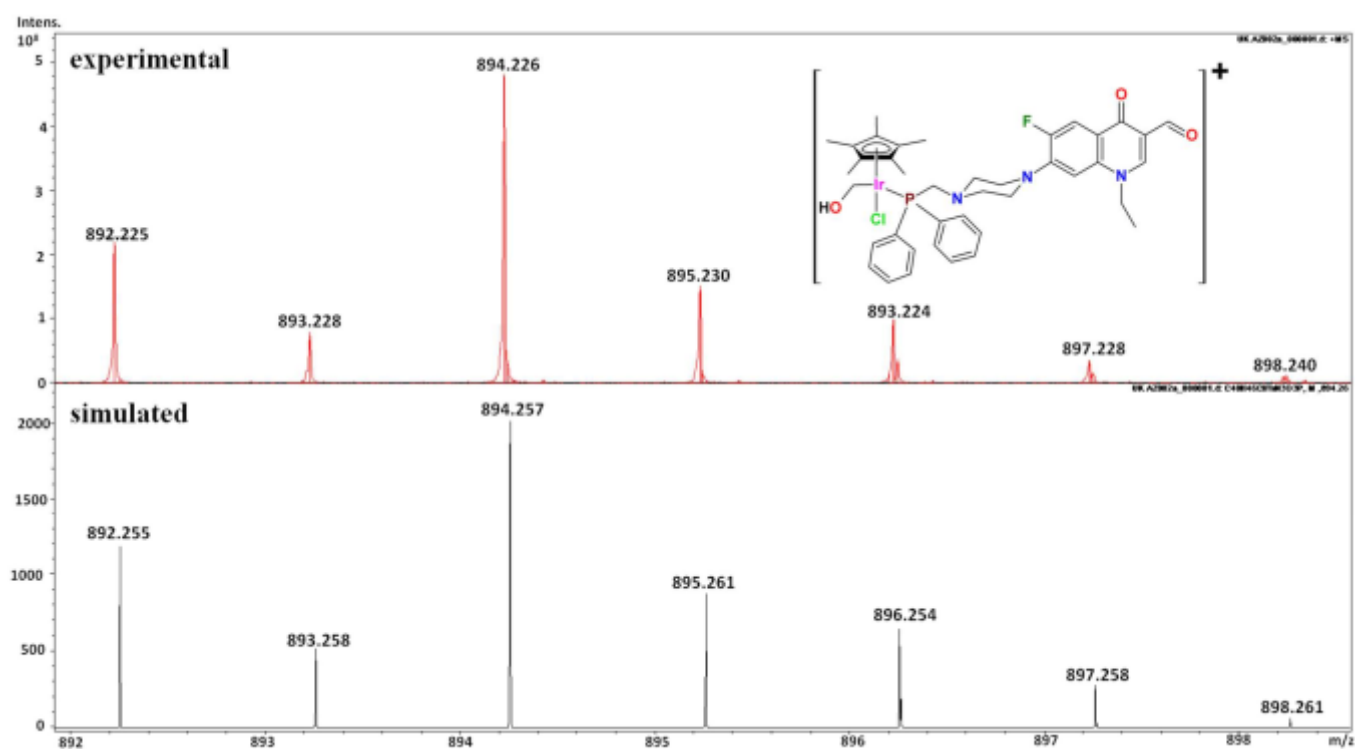
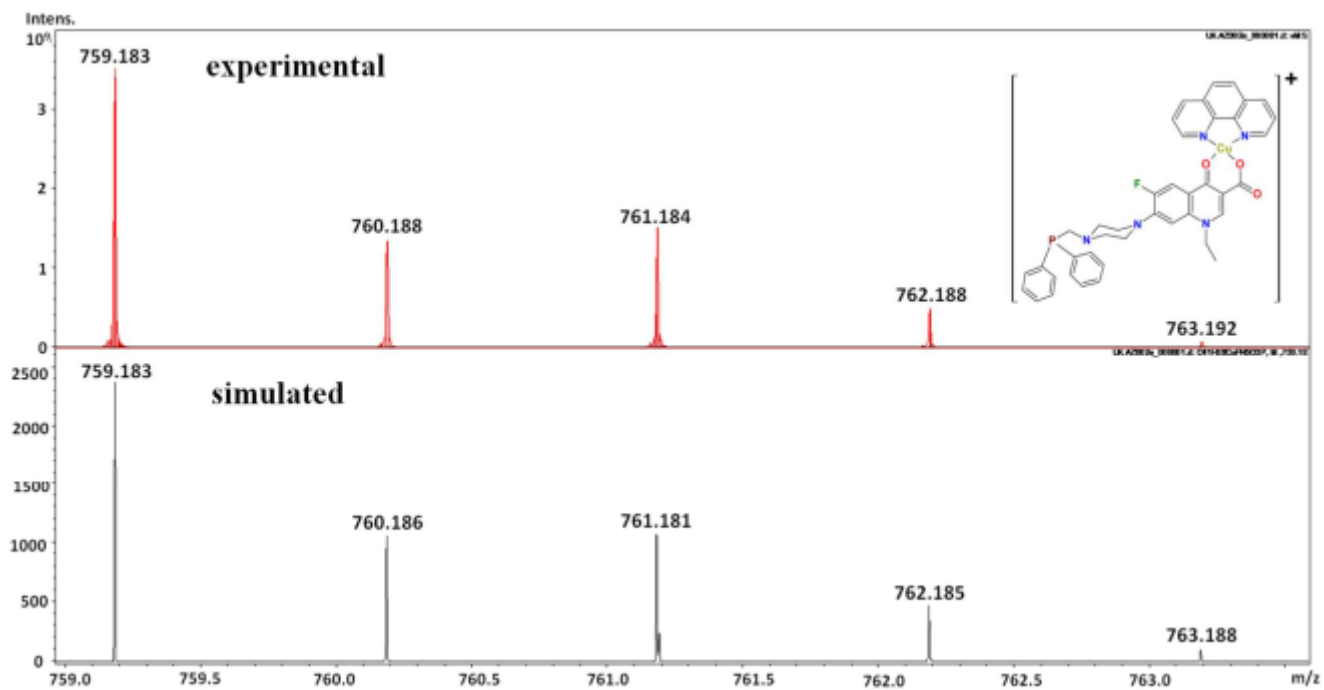


Fig. S7 (f)



**Figure S7 (a)** ESI mass spectrum of IrPNrCu(phen). ESI(+)<sup>MS</sup> in CH<sub>3</sub>OH, m/z: 1157.199 [M]<sup>+</sup>; 1123.246 [M-Cl+H]<sup>+</sup>; 916.222 [M-Cu(phen)+H]<sup>+</sup>; 894.226 [M-HCl-OH+CH<sub>2</sub>OH]<sup>+</sup>; 759.183 [M-IrCpCl<sub>2</sub>]<sup>+</sup>; **(b)** experimental and simulated spectra of [M]<sup>+</sup>; **(c)** experimental and simulated spectra of [M-Cl+H]<sup>+</sup>; **(d)** experimental and simulated spectra of [M-Cu(phen)+H]<sup>+</sup>; **(e)** experimental and simulated spectra of [M-HCl-OH+CH<sub>2</sub>OH]<sup>+</sup>; **(f)** experimental and simulated spectra of [M-IrCpCl<sub>2</sub>]<sup>+</sup>

Fig. S8 (a)

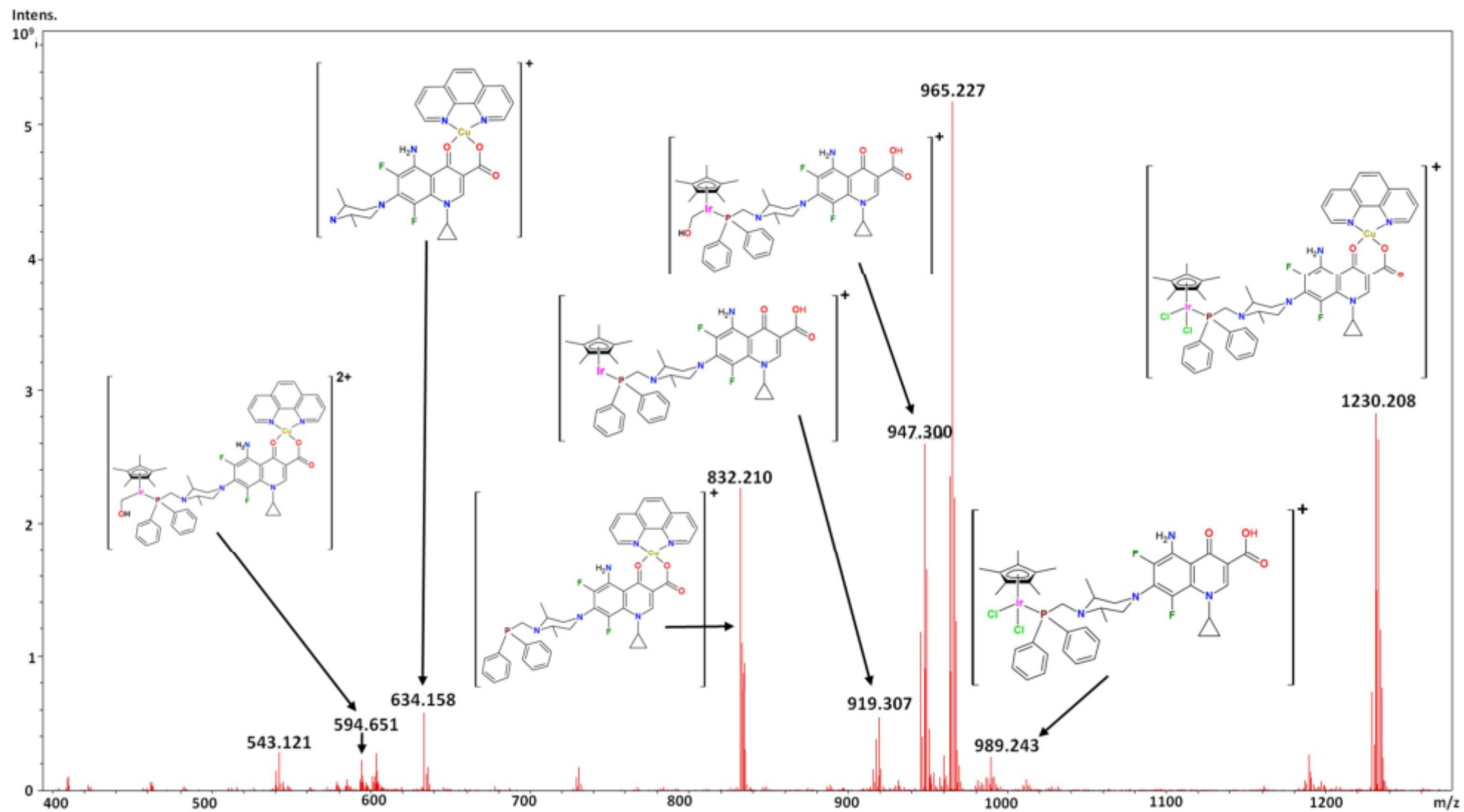


Fig. S8 (b)

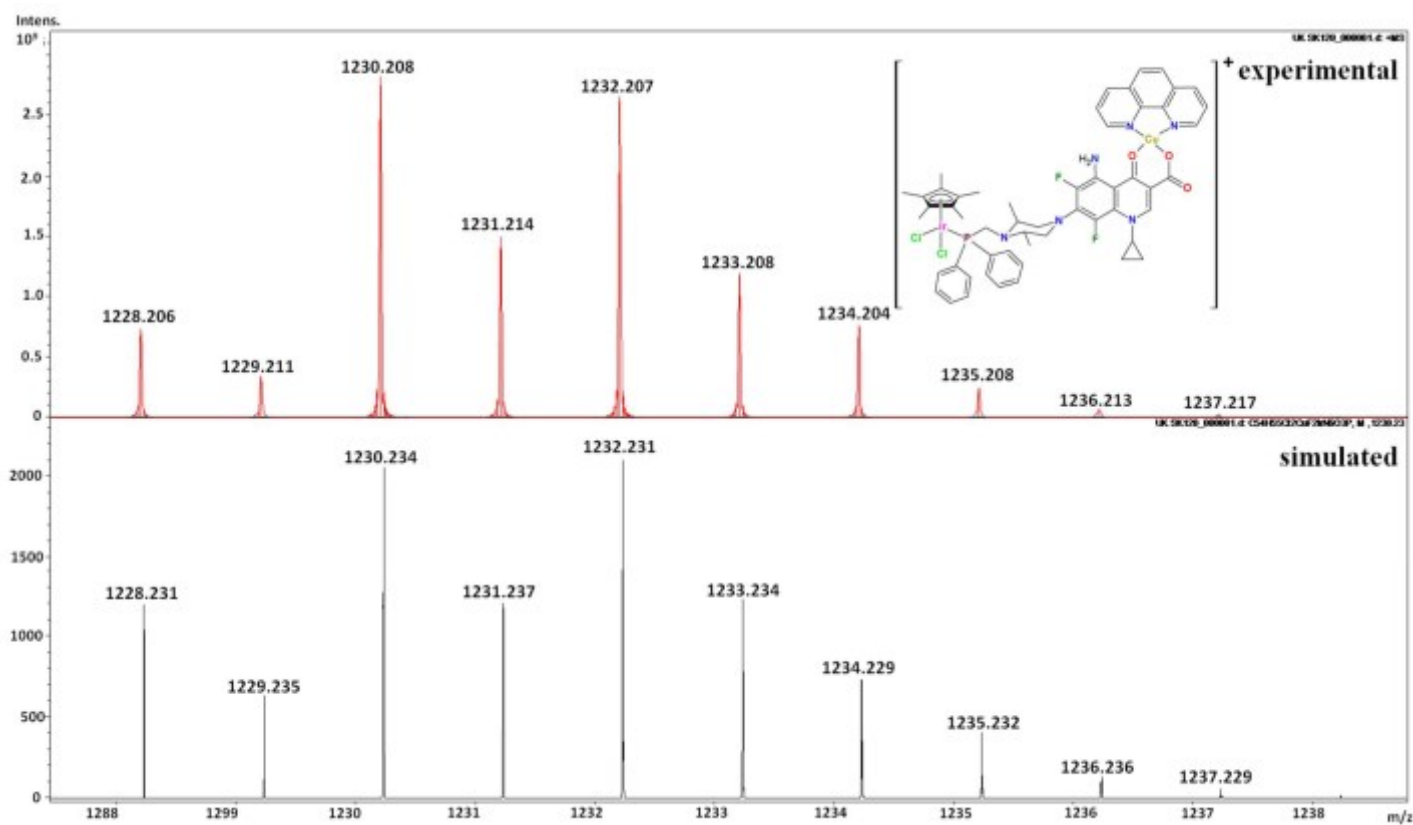


Fig. S8 (c)

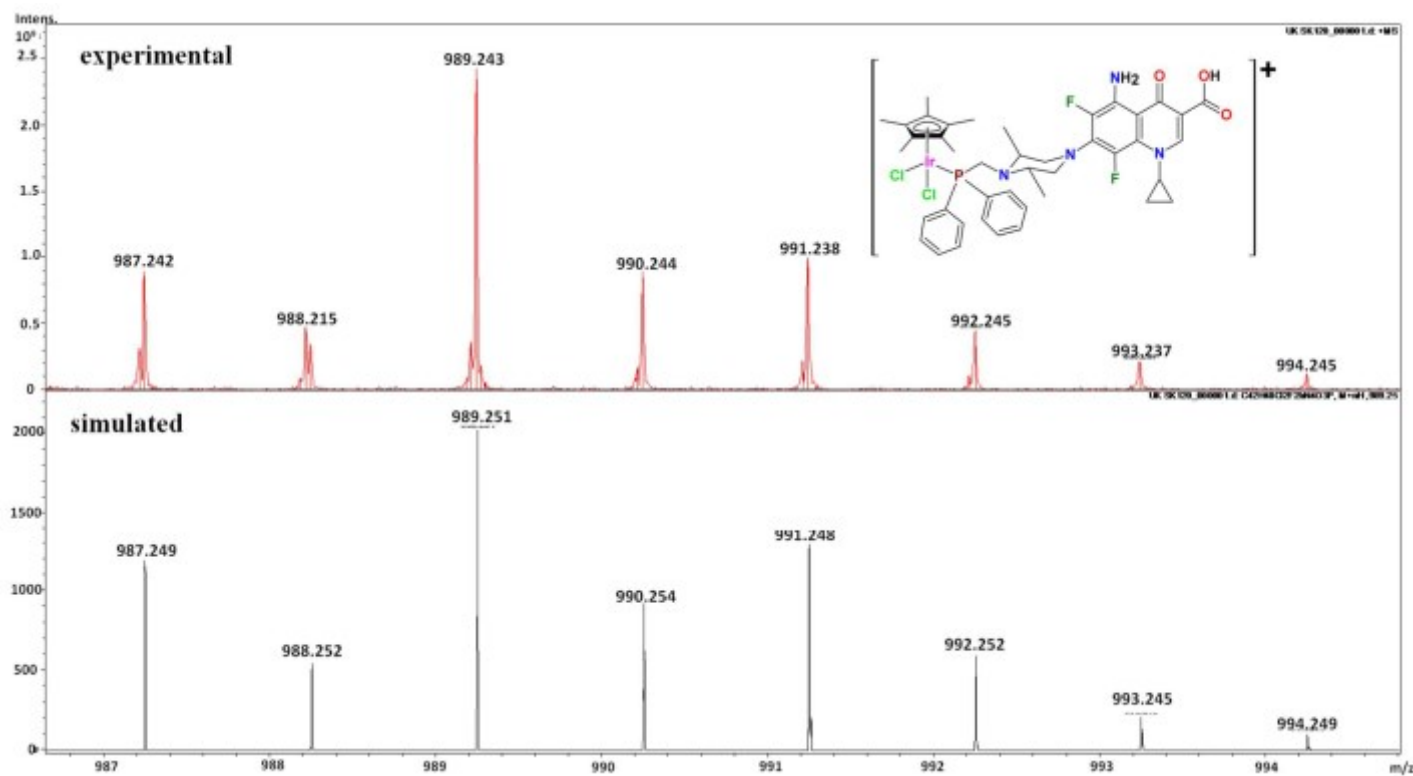




Fig. S8 (d)

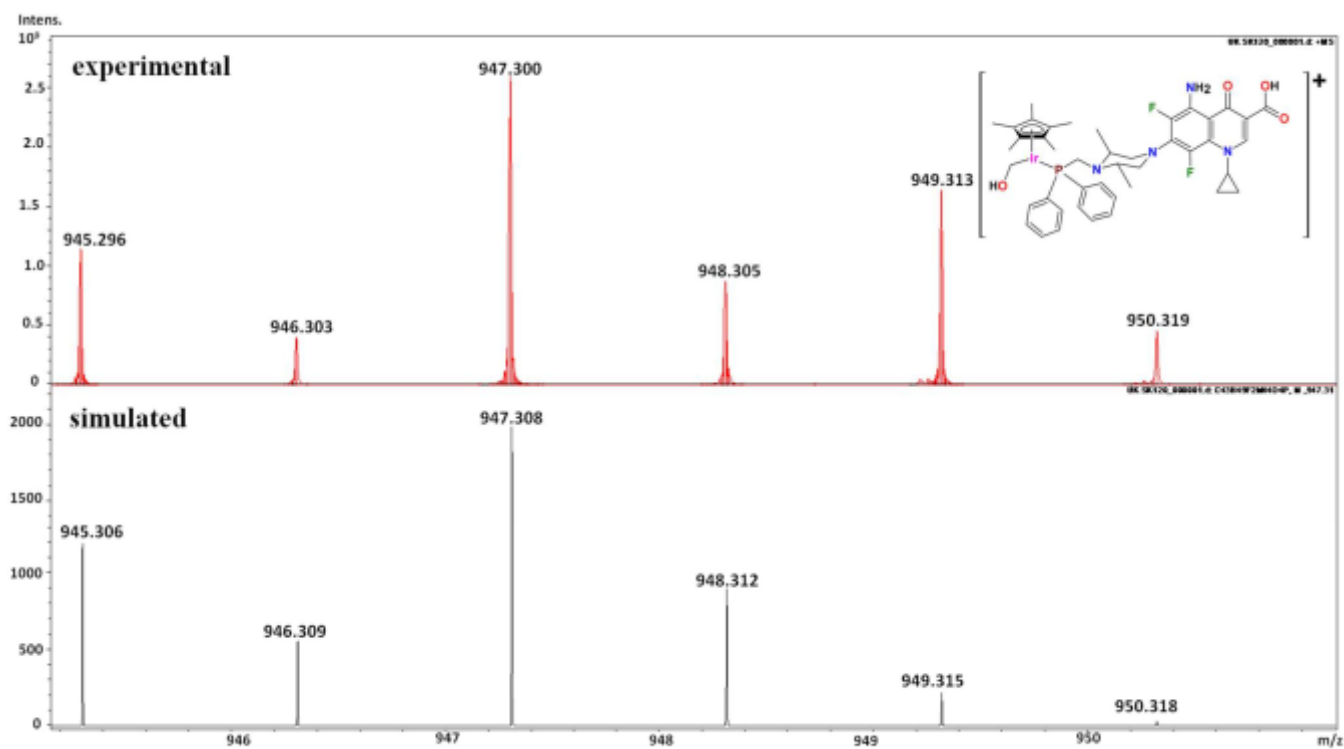


Fig. S8 (e)

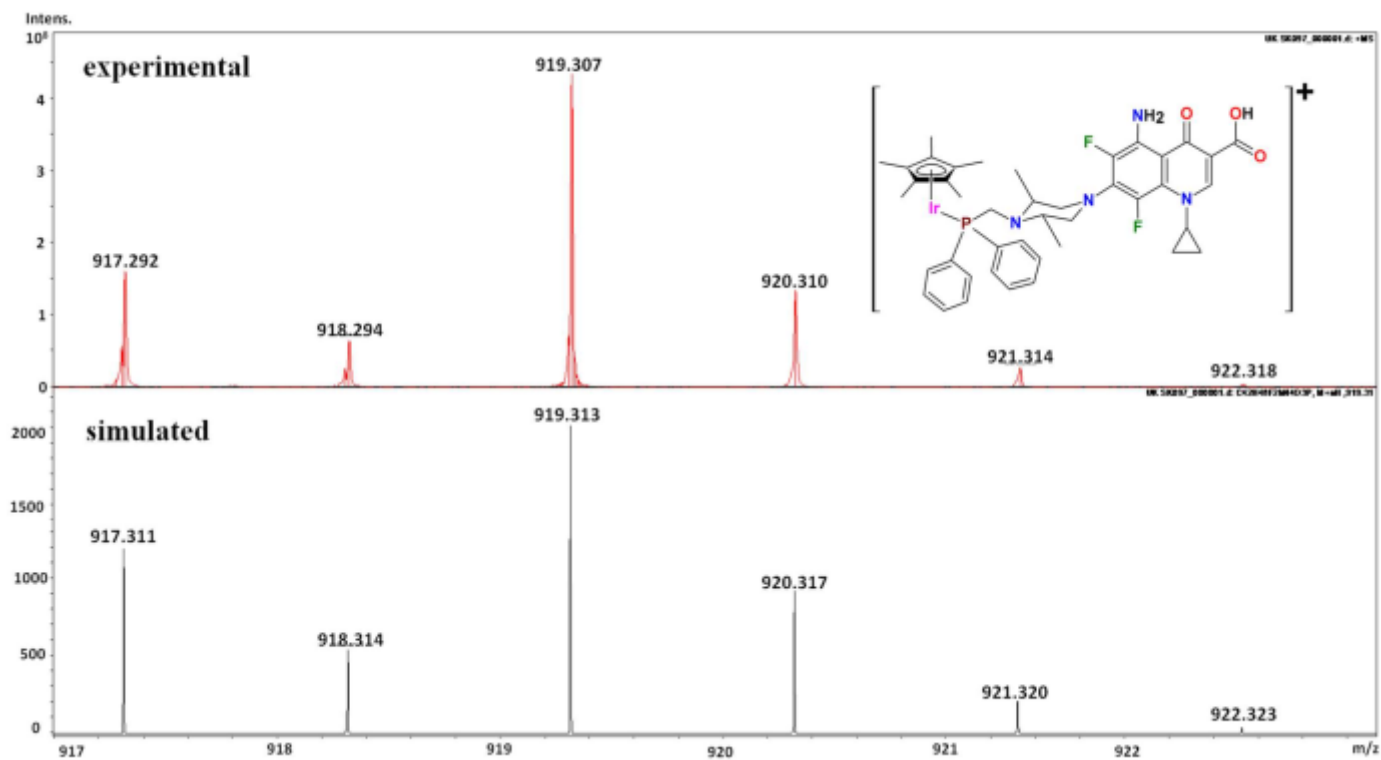


Fig. S8 (f)

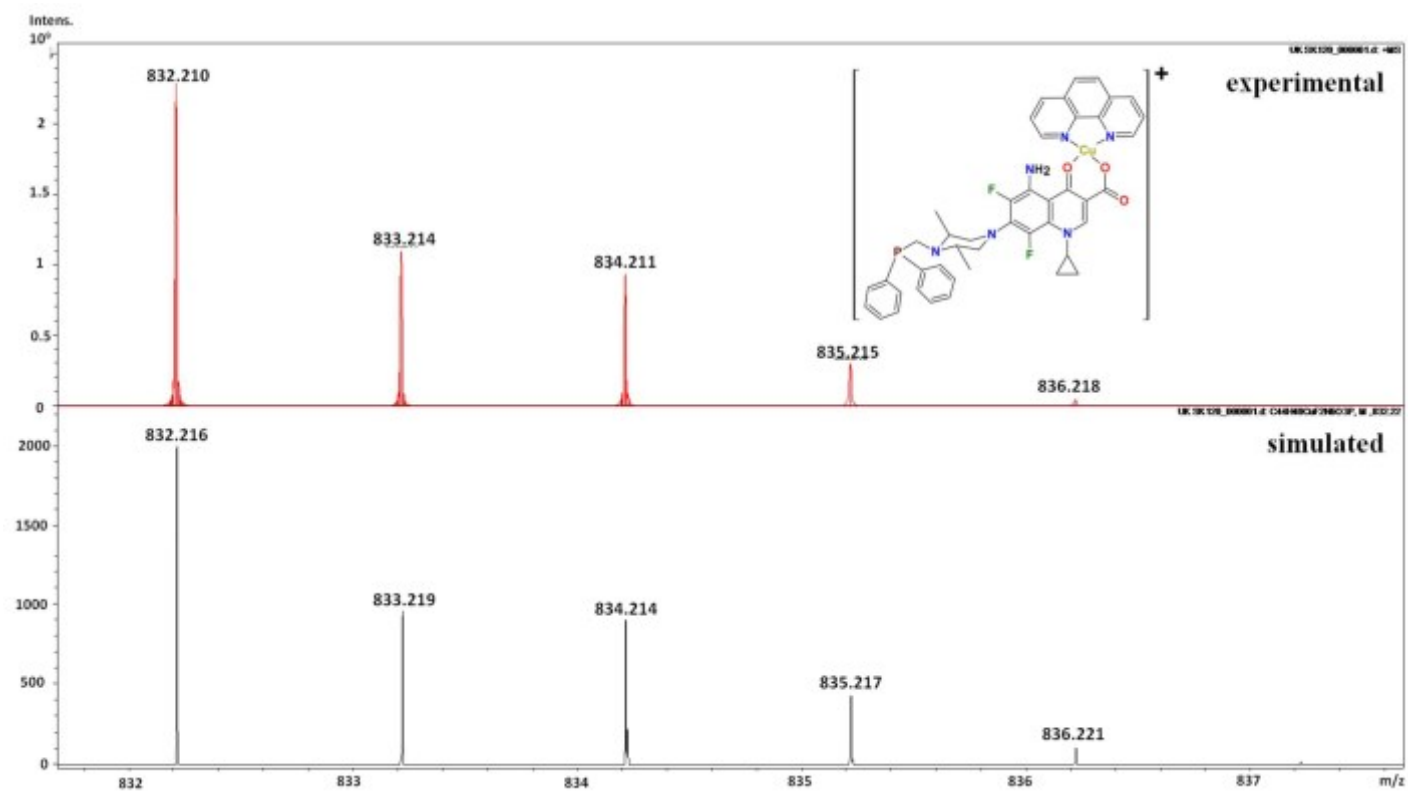


Fig. S8 (g)

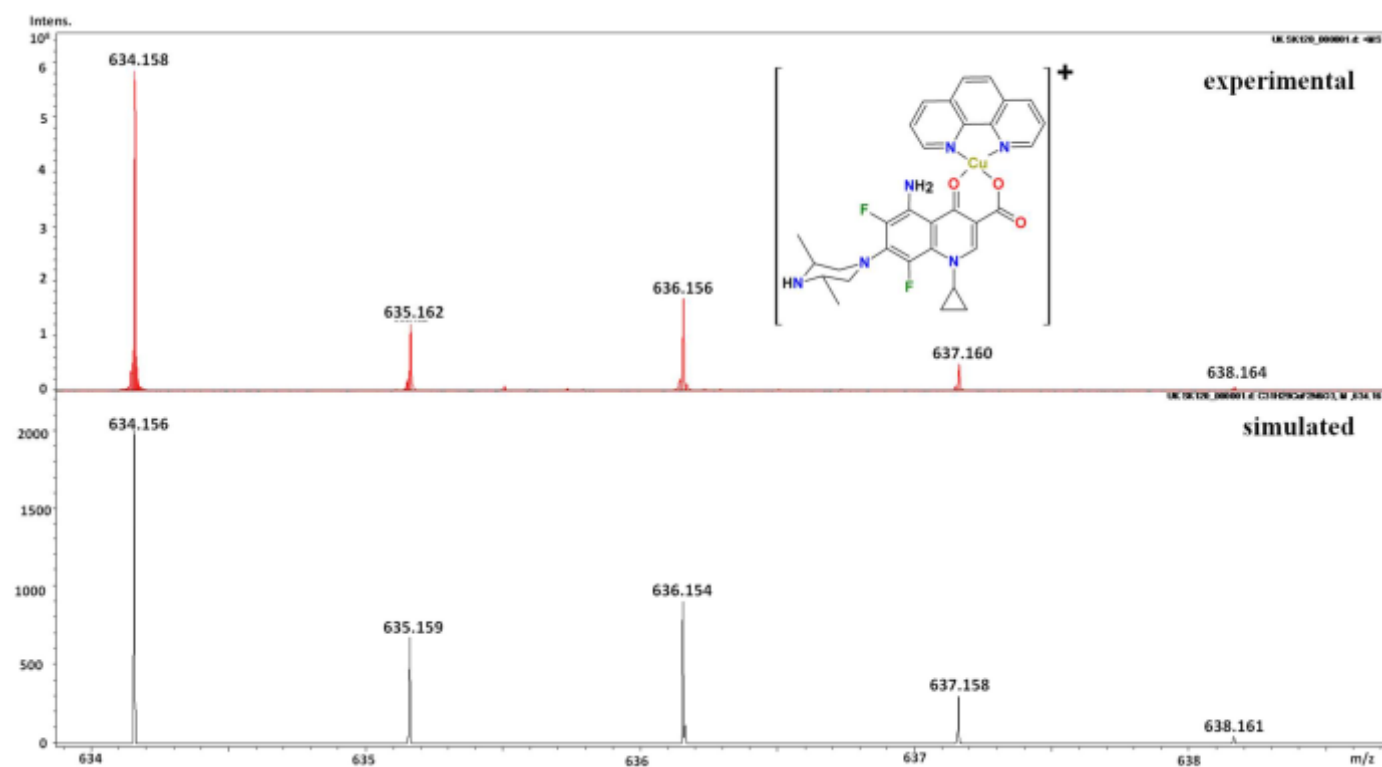
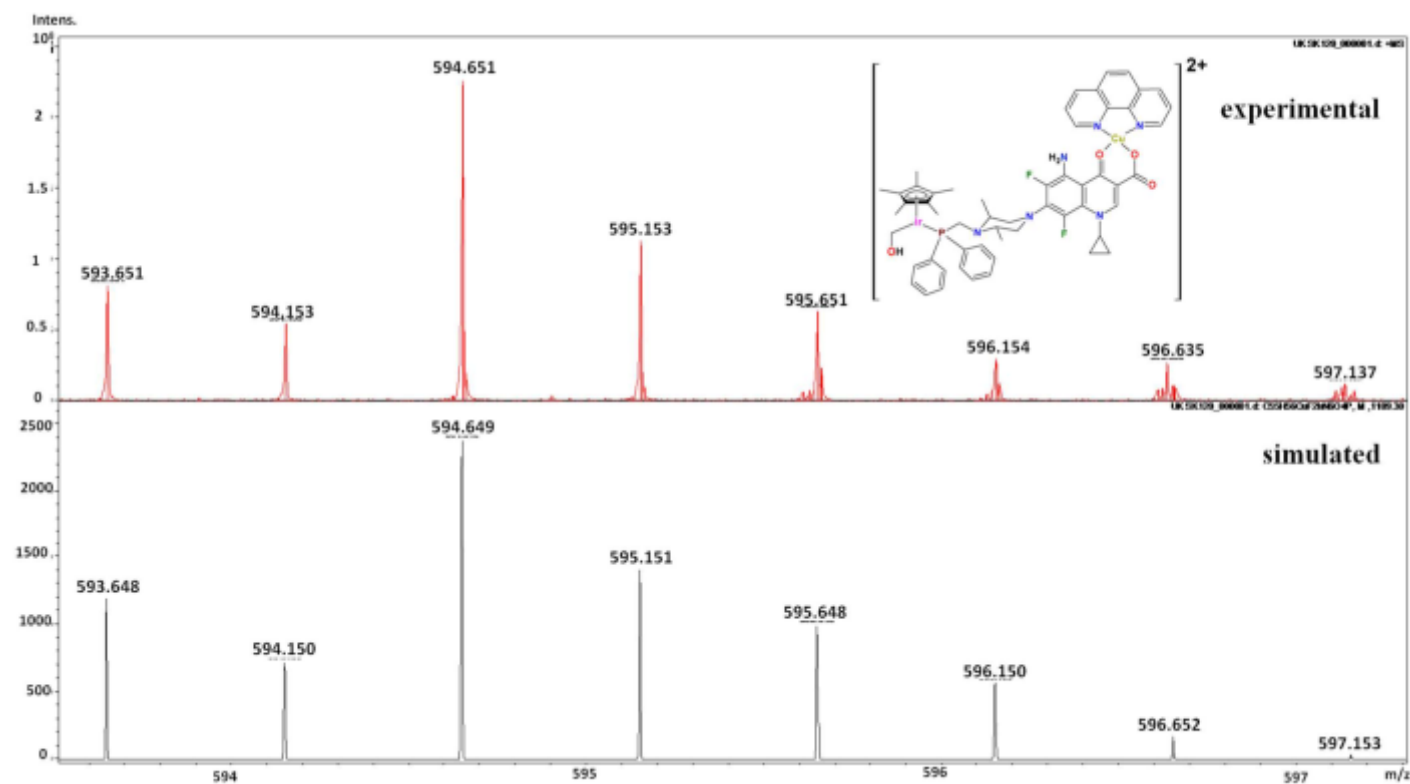


Fig. S8 (h)



**Figure S8** (a) ESI mass spectrum of **IrPSfCu(phen)**. ESI(+)<sup>MS</sup> in CH<sub>3</sub>OH, m/z: 1230.208 [**M**]<sup>+</sup>; 989.243 [**M**-Cu(phen)+H]<sup>+</sup>; 947.300 [**M**-Cu(phen)-2HCl+CH<sub>2</sub>OH]<sup>+</sup>; 919.320 [**M**-Cu(phen)-2Cl+H]<sup>+</sup>; 832.210 [**M**-IrCpCl<sub>2</sub>]<sup>+</sup>; 634.158 [**M**-IrCpCl<sub>2</sub>-PPhCH<sub>2</sub>]<sup>+</sup>; 594.651 [**M**-2HCl+CH<sub>2</sub>OH]<sup>2+</sup> (b) experimental and simulated spectra of [**M**]<sup>+</sup> (c) experimental and simulated spectra of [**M**-Cu(phen)+H]<sup>+</sup> (d) experimental and simulated spectra of [**M**-Cu(phen)-2HCl+CH<sub>2</sub>OH]<sup>+</sup> (e) experimental and simulated spectra of [**M**-Cu(phen)-2Cl+H]<sup>+</sup> (f) experimental and simulated spectra of [**M**-IrCpCl<sub>2</sub>]<sup>+</sup> (g) experimental and simulated spectra of [**M**-IrCpCl<sub>2</sub>-PPhCH<sub>2</sub>]<sup>+</sup> (h) experimental and simulated spectra of [**M**-2HCl+CH<sub>2</sub>OH]<sup>+</sup>

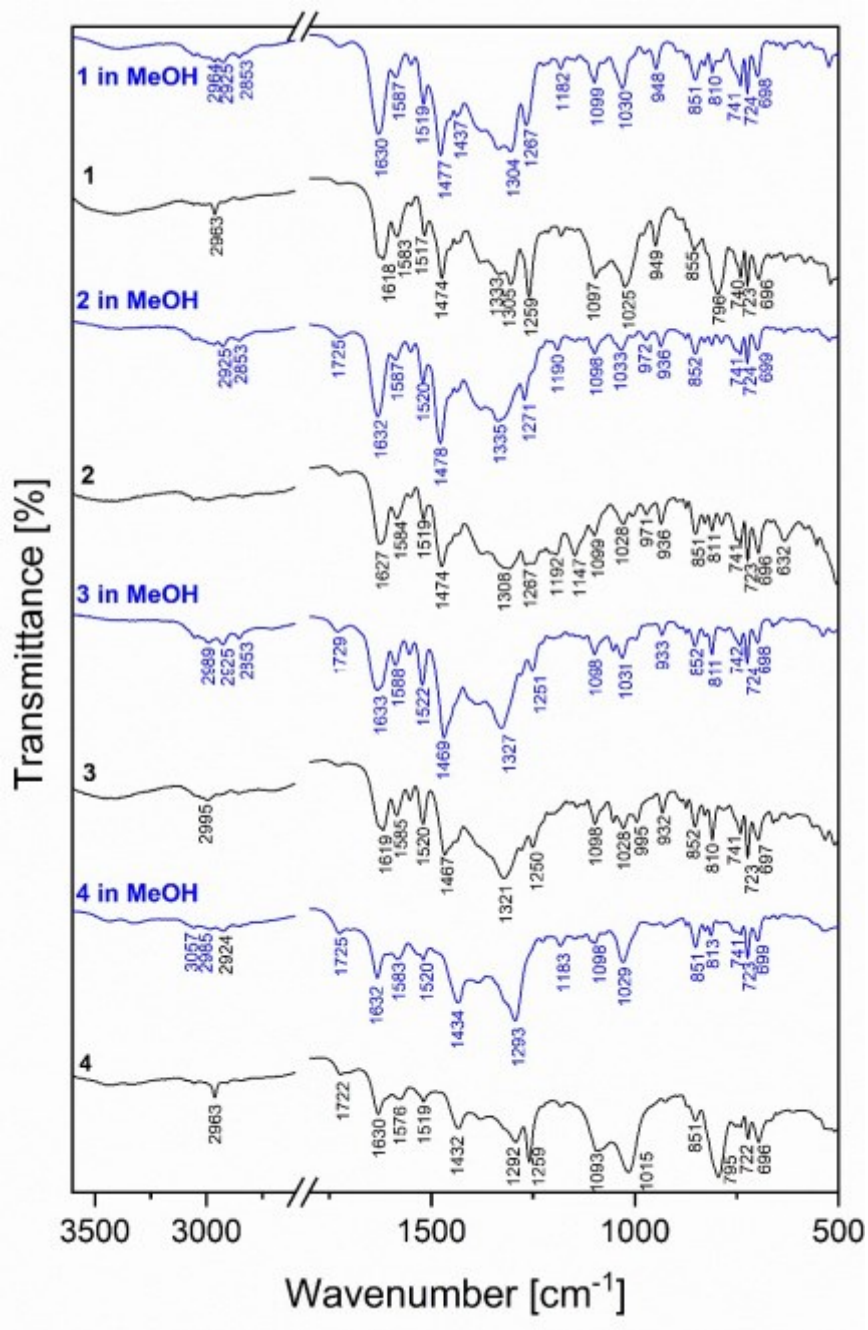
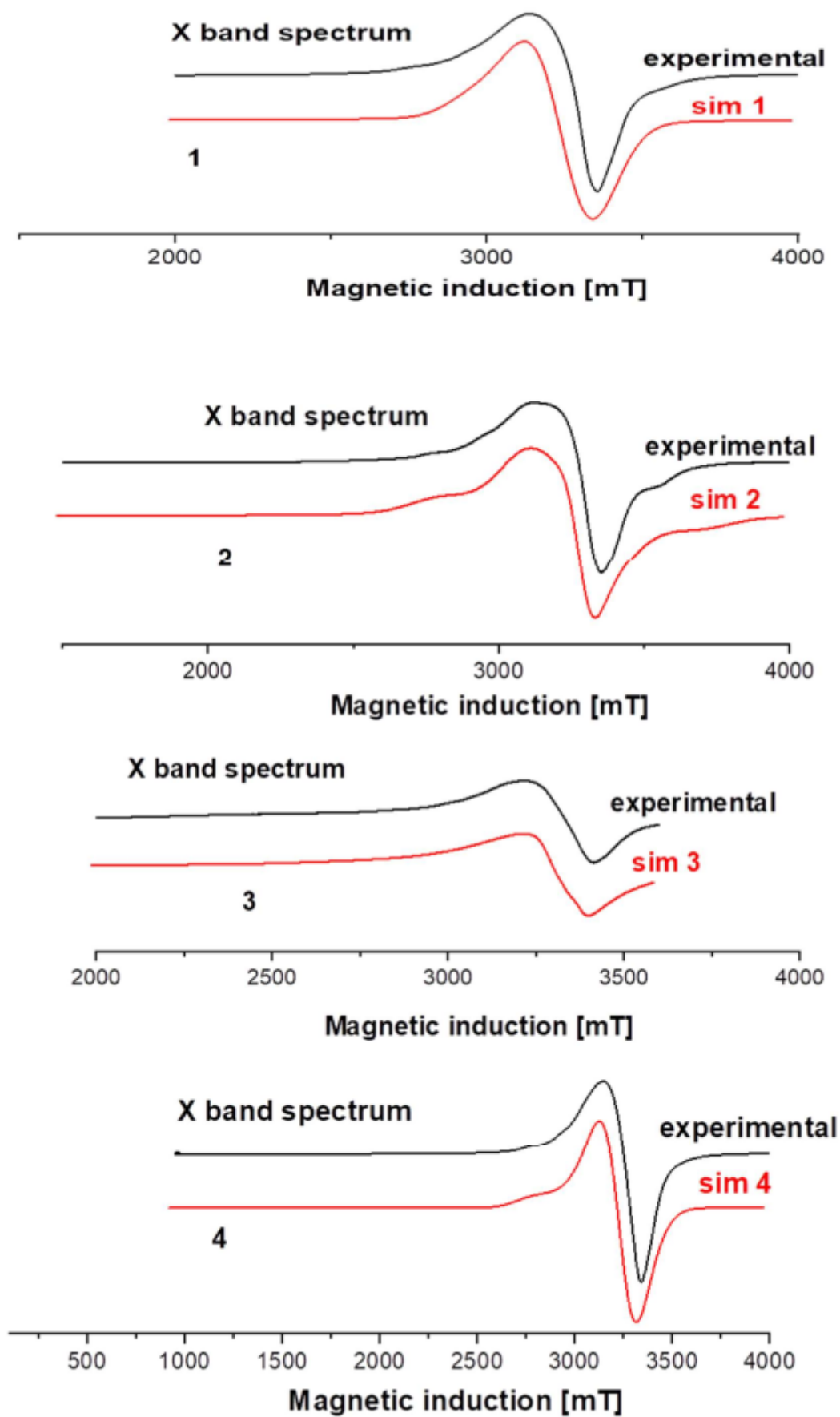
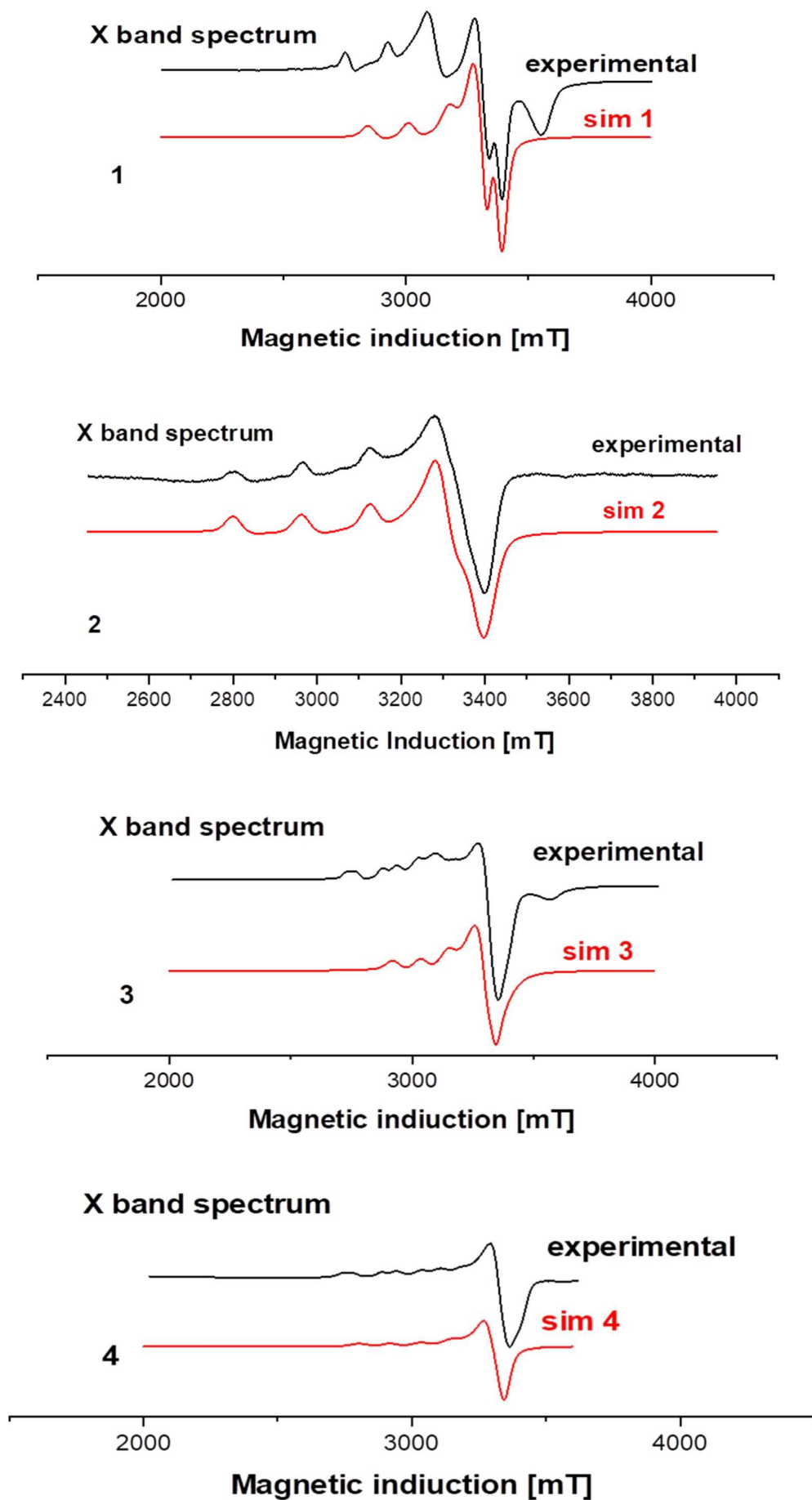


Figure S9 The FT-IR spectra of complexes 1-4 in the MIR spectral region



**Figure S10** The X-band EPR spectra of **1** - **4** at 77 K together with the spectrum calculated by computer simulation of the experimental spectra with spin Hamiltonian parameters given in the text.



**Figure S11** EPR frozen solution spectra (at 77 K) of compounds **1 - 4**; in DMSO solvent together with the theoretical spectrum calculated using the parameters given in the text.



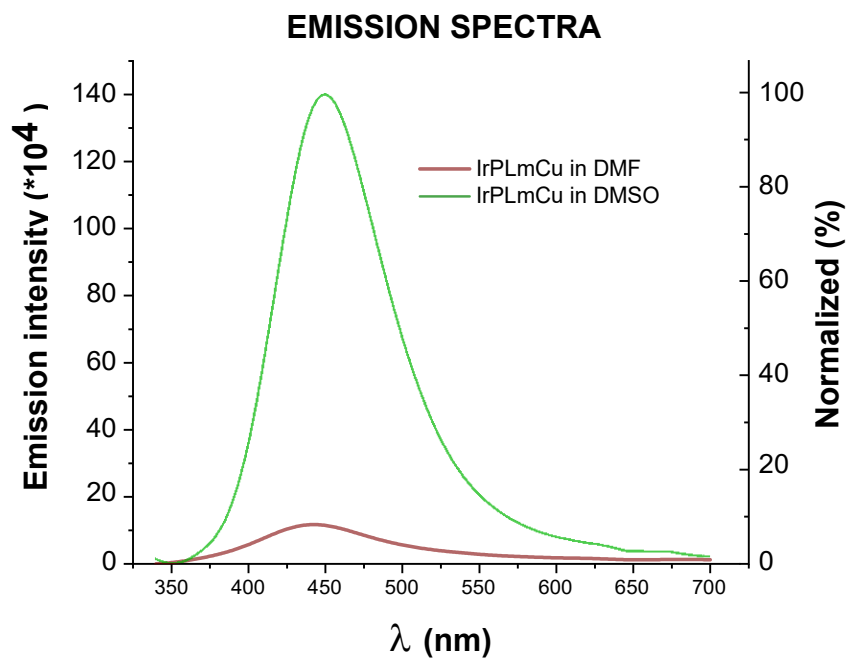


**Figure S12** Emission spectra obtained for IrPLmCu(Phen) and RuPLmCu(Phen) both in DMF and DMSO solution.

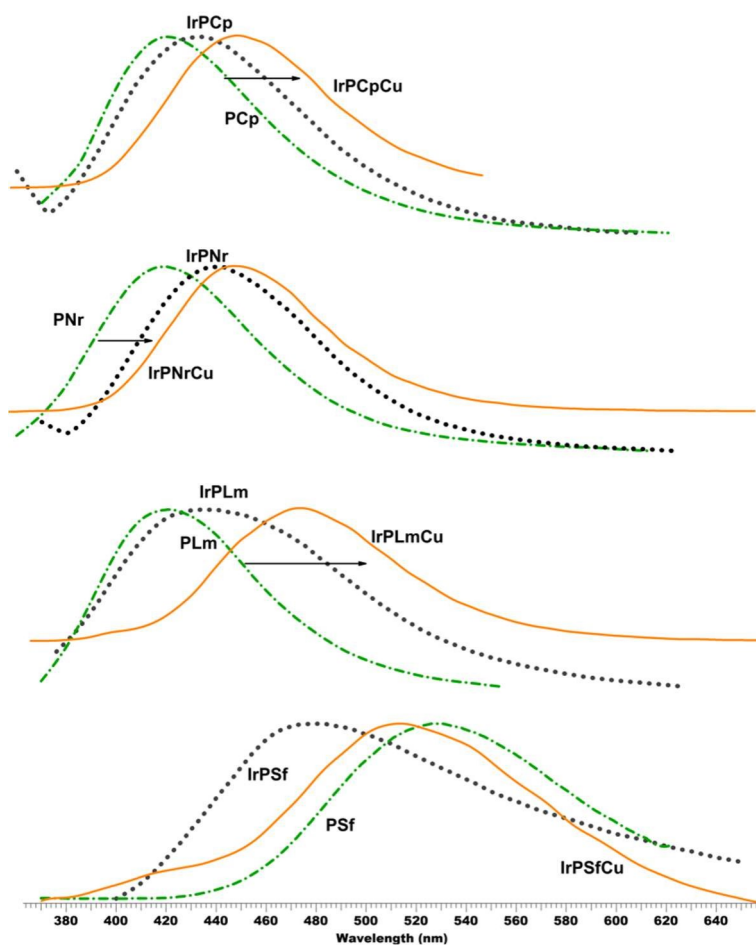


**Figure S13** Normalized emission spectra for heteronuclear Ir(III)/Cu(II) complexes, homonuclear Ir(III) complexes and the corresponding phosphine ligands;  $\lambda_{ex} = 340$  nm, 298 K.

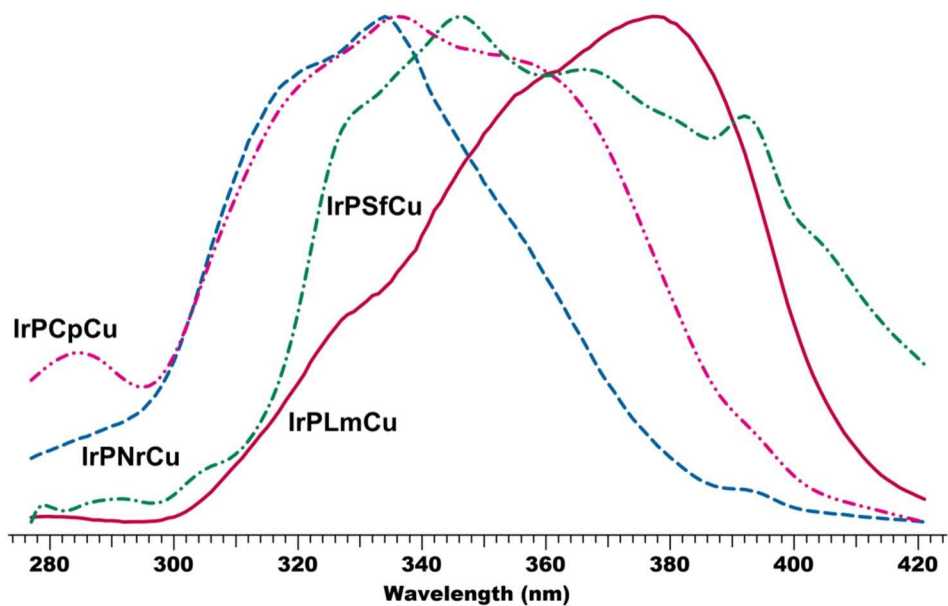


**Figure S14** Excitation spectra of IrPCpCu, IrPNrCu, IrPLmCu and IrPSfCu

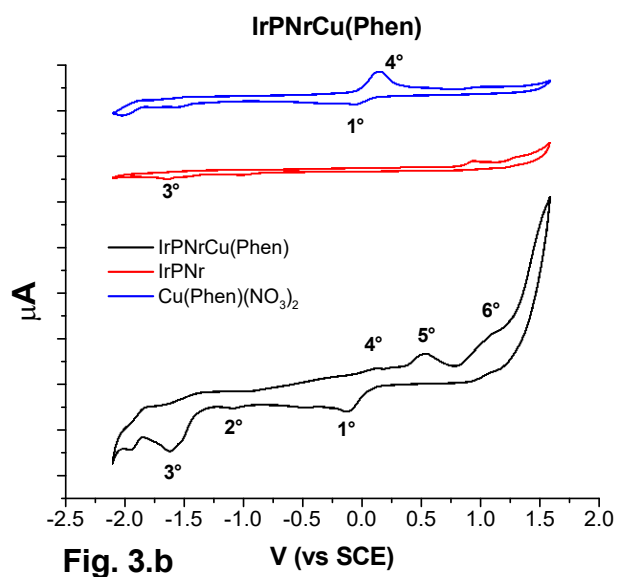
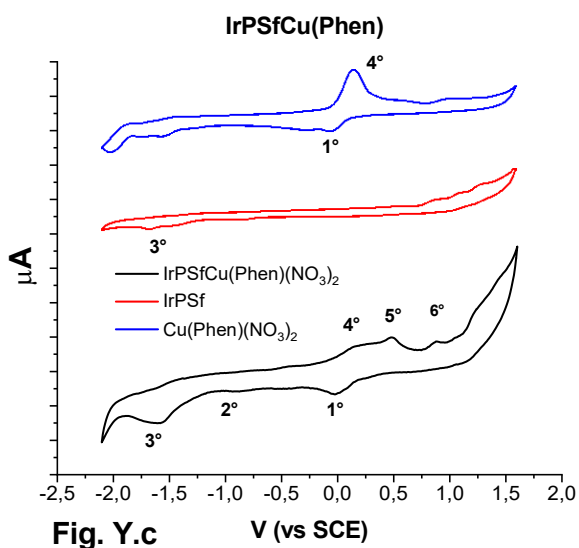
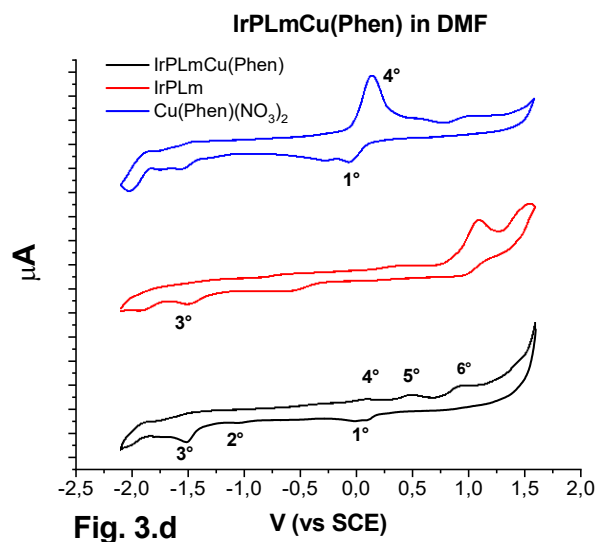
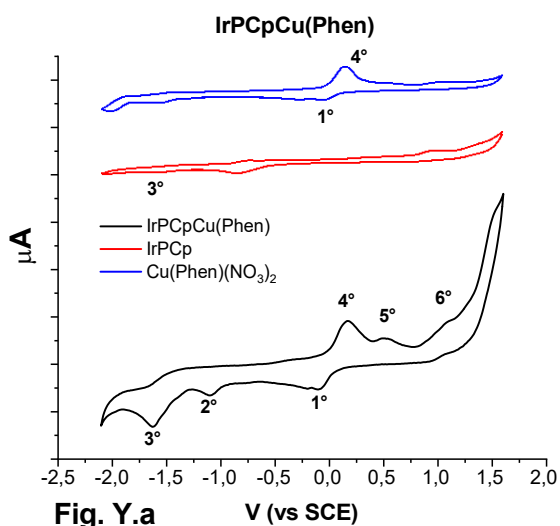
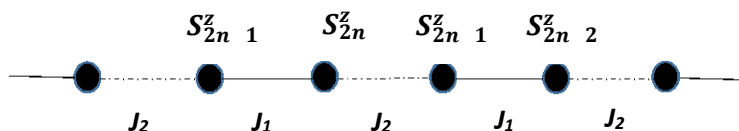


**Figure S15** Cyclic voltammetry of the mononuclear fragments of Iridium complexes in DMF (50mV/s from -2.1 to +1.6 vs SCE, TBAPF<sub>6</sub> 0.1M as supporting electrolyte).



**Scheme S1** Alternating Ising chain.

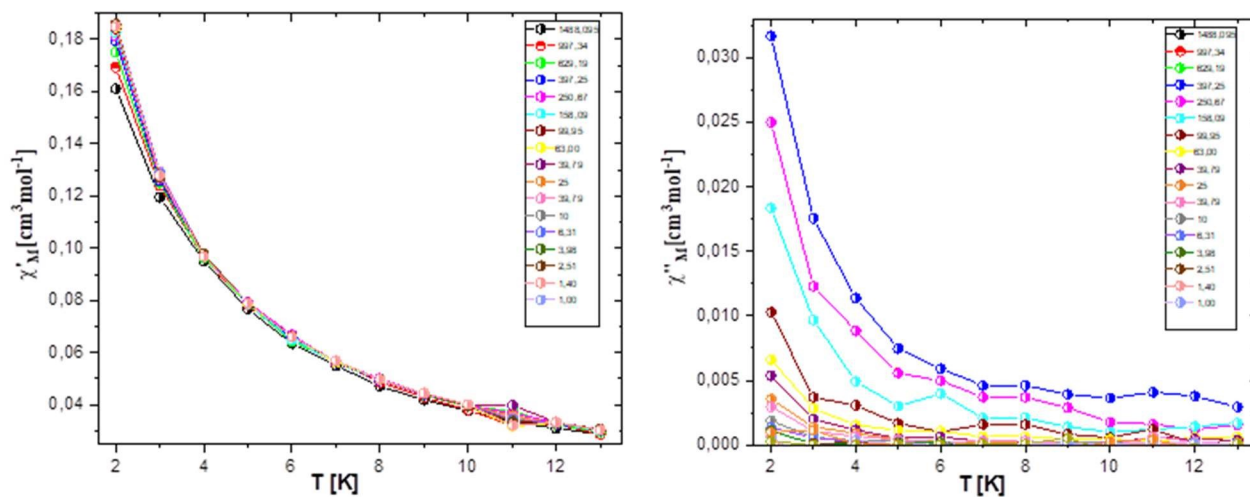


**Figure S16** Temperature dependence of (a) the in-phase and (b) out-of-phase molar susceptibility of **2**.

**Table S3.** Calculated log P values for ligands using program ACD/log P<sup>1</sup> and complexes using program ALOGPS 2.150.<sup>2,3</sup>

Ligands		Homonuclear Ir <sup>III</sup> complexes		Heteronuclear Ir <sup>III</sup> -Cu <sup>II</sup> complexes	
PCp	5.81	IrPCp	7.73	IrPCpCu	3.47
PSf	6.35	IrPSf	7.44	IrPSfCu	3.83
PLm	6.86	IrPLm	7.51	IrPLmCu	3.92
PNr	5.97	IrPNr	7.26	IrPNrCu	3.55

**Table S4** Values of IC<sub>50</sub> [μM] (concentration of a drug required to inhibit the growth of 50% of the cells) for WM2661, A549, MCF7, DU-145, HEK293T cells after 24h and 24h + 48h treatment with the studied compounds and cisplatin as reference

IC <sub>50</sub> [μM] ± SD; 24h					
	A549	MCF7	DU-145	WM2664	HEK293T
<b>IrPCpCu</b>	35.5± 5.6E-03	35.3± 6.5	12.8±2.7E-07	5.15± 4.1E-03	786.8 ± 11.2
<b>IrPLmCu</b>	31.6± 7.6E-03	24.2± 7.2	14.2± 2.4E-03	10.1± 2.2E-03	775.8 ± 15.7
<b>IrPNrCu</b>	11.2± 7.8E-03	30.00± 0.7	10.8± 1.9E-04	9.9± 3.8E-03	756.8 ± 5.7
<b>IrPSfCu</b>	18.1± 1.3E-03	10.5± 0.8	10.1± 2.9E-03	6.2± 2.4E-03	676.8 ± 9.2
<b>Cisplatin (CDDP)</b>	56.99±1.3E-03	51.9±4.6	68.28±1.3E-03	2.6±0.6	21.0±1.8
IC <sub>50</sub> [μM] ± SD; 72h (24h + 48h)					
<b>IrPCpCu</b>	42.4± 7.3E-05	>1000	125.7± 3.4	137.1± 2.2	886.8± 12.7
<b>IrPLmCu</b>	36.0± 2.2E-02	>1000	126.2± 4.4	229.3± 25.9	822.8± 12.3
<b>IrPNrCu</b>	36.6± 2.8E-03	>1000	122.7± 5.4	155.1± 3.2	856.8± 15.9
<b>IrPSfCu</b>	0.6± 2.9E-04	>1000	53.6± 0.40	212.2± 10.5	776.8± 15.3
<b>Cisplatin (CDDP)</b>	71.7±3.7	17.7±8.6	65.5±3.6	8.3±0.4	10.3±2.1

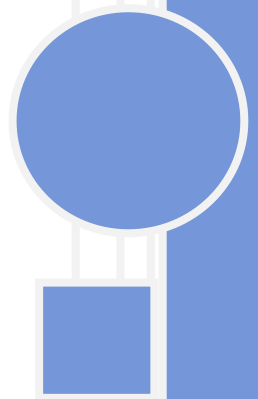
**Table S5** Hydrodynamic diameter and Zeta potential determined by DLS technique as well as loading content and encapsulation efficiency determined by ICP-MS technique for selected liposome formulations

Formulation	Diameter [nm] (TEM, ImageJ)	Hydrodynamic diameter [nm] (DLS)	Zeta potential [mV] (pH =)
<b>L</b>	135.8 ± 21.0 nm	146.8 ± 13.6, PDI = 0.01	-30.2 ± 2.7 mV
<b>1a</b>	83.7 ± 18.4 nm	108.8 ± 24.7, PDI = 0.05	-42.3 ± 6.2 mV

## References

- 1 A. A. Petrauskas and E. Kolovanov, ACD/Log P method description, *Perspect, Drug Discovery Des.*, 2000, **19**, 99–116
- 2 V. Tetko, J. Gasteiger, R. Todeschini, A. Mauri, D. Livingstone, P. Ertl, V. A. Palyulin, E. V. Radchenko, N. S. Zefirov, A. S. Makarenko, V. Y. Tanchuk and V. V. Prokopenko, *J. Comput.-Aided Mol. Des.*, 2005, **19**, 453;
- 3 VCCLAB, Virtual Computational Chemistry Laboratory – Design and Description, Virtual Computational Chemistry Laboratory, <http://www.vcclab.org>, 2005

# AUTHORS STATEMENTS





mgr inż. Sandra Kozieł

Wrocław, dn. 30.05.2022

Zespół Materiałów Magnetycznych

Wydział Chemii

Uniwersytet Wrocławski

## Oświadczenie

Oświadczam, że mój udział w pracy:

1. Urszula K. Komarnicka, Sandra Kozieł, Agnieszka Skórska-Stania, Agnieszka Kyzioł, Francesco Tisato, Synthesis, physicochemical characterization and preliminary in vitro antitumor activity of phosphino Ru(II) and Ir(III) complexes, Dalton Transactions, 2022

stanowiącej podstawę mojej rozprawy doktorskiej polegał na:

- Współtworzeniu merytorycznej koncepcji badań (wspólnie z dr Urszulą Komarnicką);
- Doborze metodyki prowadzącej do rozwiązania problemu naukowego (wspólnie z dr Urszulą Komarnicką);
- Syntezie i oczyszczeniu aminometylofosfiny ( $\text{PPh}_2\text{CH}_2\text{OH}$ ), a także syntezie związków kompleksowych irydu(III) wraz z otrzymaniem monokryształów do pomiarów XRD;
- Charakterystyce fizykochemicznej otrzymanych związków (z wyjątkiem opisu struktur krystalicznych oraz widm masowych);
- Analizie procesu hydrolizy wszystkich związków kompleksowych w roztworze oraz ich właściwości katalitycznych (NMR, UV-Vis);
- Wykonaniu badań biologicznych (wspólnie z dr U. Komarnicką) oraz interpretacji ich wyników,
- Przygotowaniu manuskryptu publikacji.

Oświadczam, że mój udział w pracy:

2. Kozieł Sandra, Komarnicka Urszula K., Ziółkowska Aleksandra, Skórska-Stania Agnieszka, Pucelik Barbara, Płotek Michał, Sebastian Victor, Bieńko Alina, Stochel Grażyna, Kyzioł Agnieszka, Anticancer potency of novel organometallic Ir(III)

complexes with phosphine derivatives of fluoroquinolones encapsulated in polymeric micelles; *Inorganic Chemistry Frontiers*, 2020, 7, 3386-3401

stanowiącej podstawę mojej rozprawy doktorskiej polegał na:

- Współtworzeniu merytorycznej koncepcji badań (wspólnie z dr Urszulą Komarnicką);
- Doborze metodyki prowadzącej do rozwiązania problemu naukowego (wspólnie z dr Urszulą Komarnicką);
- Syntezie i oczyszczeniu aminometylofosfin będących pochodnymi ciprofloksacyny, norfloksacyny oraz lomefloksacyny a także syntezie ich związków kompleksowych irydu(III) (IrPCp, IrPNr, IrPLm) wraz z otrzymaniem monokryształów do pomiarów XRD,
- Charakterystyce fizykochemicznej otrzymanych związków;
- Wykonaniu badań biologicznych (wspólnie z dr U. Komarnicka oraz dr B. Pucelik) oraz interpretacji ich wyników,
- Przygotowaniu manuskryptu publikacji.

Oświadczam, że mój udział w pracy:

3. Kozieł Sandra, Lesiów Monika Katarzyna, Wojtala Daria, Dyguda-Kazimierowicz, Edyta, Bieńko Dariusz, Komarnicka Urszula Katarzyna, Interaction between DNA, albumin and apo-transferrin and iridium(III) complexes with phosphines derived from fluoroquinolones as a potent anticancer drug; *Pharmaceuticals*, 2021, 14, 685/1-685/25;

stanowiącej podstawę mojej rozprawy doktorskiej polegał na:

- Stworzeniu merytorycznej koncepcji badań;
- Doborze metodyki prowadzącej do rozwiązania problemu naukowego;
- Przeprowadzeniu wszystkich prac eksperymentalnych opisanych w publikacji (w jednym przypadku eksperyment wykonywany był przy pomocy mgr Darii Wojtala: pomiar widm fluorescencyjnych układu DNA-bromek etydyny w obecności kompleksu IrPNr);
- Przygotowaniu manuskryptu publikacji.

*Sandra Kozieł*

Dr Urszula Komarnicka  
Zespół Materiałów Magnetycznych  
Wydział Chemii  
Uniwersytet Wrocławski

Wrocław, dn. 30.05.2022

## Oświadczenie

Oświadczam, że mój udział w pracy:

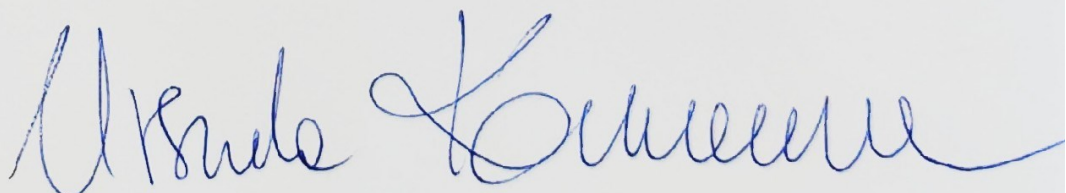
1. Urszula K. Komarnicka, Sandra Kozieł, Agnieszka Skórska-Stania, Agnieszka Kyzioł, Francesco Tisato, Synthesis, physicochemical characterization and preliminary in vitro antitumor activity of phosphino Ru(II) and Ir(III) complexes, Dalton Transactions, 2022 stanowiącej podstawę rozprawy doktorskiej mgr inż. Sandry Kozieł polegał na tworzeniu, razem z Doktorantką, merytorycznej koncepcji badań. Otrzymaniu i czynnym udziale w charakterystyce fizykochemicznej i biologicznej kompleksów Ru(II) a także pomocy w interpretacji wyników i przygotowaniu części publikacji związanej z badaniami biologicznymi.

Oświadczam, że mój udział w pracy:

2. Kozieł Sandra, Komarnicka Urszula K., Ziółkowska Aleksandra, Skórska-Stania Agnieszka, Pucelik Barbara, Płotek Michał, Sebastian Victor, Bieńko Alina, Stochel Grażyna, Kyzioł Agnieszka, Anticancer potency of novel organometallic Ir(III) complexes with phosphine derivatives of fluoroquinolones encapsulated in polymeric micelles; Inorganic Chemistry Frontiers, 2020, 7, 3386-3401 stanowiącej podstawę rozprawy doktorskiej mgr inż. Sandry Kozieł polegał na tworzeniu, razem z Doktorantką, merytorycznej koncepcji badań. Otrzymaniu i czynnym udziale w charakterystyce fizykochemicznej i biologicznej fosfinowej pochodnej sparfloksacyny oraz jej kompleksu IrPSf, czynnym udziale w przeprowadzeniu badań biologicznych razem z Doktorantką oraz dr B. Pucelik, także pomocy w interpretacji wyników i przygotowaniu części publikacji związanej z badaniami biologicznymi.

Oświadczam, że mój udział w pracy:

3. Kozieł Sandra, Lesiów Monika Katarzyna, Wojtala Daria, Dyguda-Kazimierowicz, Edyta, Bieńko Dariusz, Komarnicka Urszula Katarzyna, Interaction between DNA, albumin and apo-transferrin and iridium(III) complexes with phosphines derived from fluoroquinolones as a potent anticancer drug; Pharmaceuticals, 2021, 14, 685/1-685/25; stanowiącej podstawę rozprawy doktorskiej mgr inż. Sandry Kozieł polegał na konsultacji projektu badawczego oraz merytorycznej dyskusji wyników.



**dr Monika Lesiów**

Wrocław, dn. 30.05.2022

Zespół Materiałów Magnetycznych

Wydział Chemiczny

Uniwersytet Wrocławski

### **Oświadczenie**

Oświadczam, że mój udział w niżej wymienionej pracy polegał na merytorycznej dyskusji wyników.

1. Kozieł Sandra, Lesiów Monika Katarzyna, Wojtala Daria, Dyguda-Kazimierowicz Edyta, Bieńko Dariusz, Komarnicka Urszula Katarzyna, Interaction between DNA, albumin and apo-transferrin and iridium(III) complexes with phosphines derived from fluoroquinolones as a potent anticancer drug; *Pharmaceuticals*, 2021, 14, 685/1-685/25; DOI:10.3390/ph14070685

*Lesiów Monika*



mgr Daria Wojtala

Wrocław, dn. 30.05.2022

Zespół Materiałów Magnetycznych

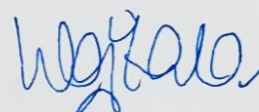
Wydział Chemiczny

Uniwersytet Wrocławski

### Oświadczenie

Oświadczam, że mój udział w niżej wymienionej pracy polegał na pomocy w pomiarze widm fluorescencyjnych układu DNA-bromek etydyny miareczkowanym zwiększającym się stężeniem kompleksu IrPNr.

1. Koziół Sandra, Lesiów Monika Katarzyna, Wojtala Daria, Dyguda-Kazimierowicz Edyta, Bieńko Dariusz, Komarnicka Urszula Katarzyna, Interaction between DNA, albumin and apo-transferrin and iridium(III) complexes with phosphines derived from fluoroquinolones as a potent anticancer drug; Pharmaceuticals, 2021, 14, 685/1-685/25



mgr Aleksandra Ziółkowska  
absolwentka Wydziału Chemii UWr

Wrocław, dn. 30.05.2022

### Oświadczenie

Oświadczam, że mój udział w niżej wymienionej pracy polegał na pomocy przy syntezie i oczyszczaniu kompleksu IrPNr.

1. Koziół Sandra, Komarnicka Urszula K., Ziółkowska Aleksandra, Skórska-Stania Agnieszka, Pucelik Barbara, Płotek Michał, Sebastian Victor, Bieńko Alina, Stochel Grażyna, Kyzioł Agnieszka Anticancer potency of novel organometallic Ir(III) complexes with phosphine derivatives of fluoroquinolones encapsulated in polymeric micelles; Inorganic Chemistry Frontiers, 2020, 7, 3386-3401

Aleksandra Ziółkowska



Dr hab. Agnieszka Skórska-Stania  
Zespół Inżynierii Krystalicznej i Analizy Strukturalnej  
Wydział Chemii  
Uniwersytet Jagielloński

Kraków, dn. 30.05.2022

### Oświadczenie

Oświadczam, że mój udział w publikacji:

Koziół Sandra, Komarnicka Urszula K., Ziółkowska Aleksandra, Skórska-Stania Agnieszka, Pucelik Barbara, Płotek Michał, Sebastian Victor, Bieńko Alina, Stochel Grażyna, Kyziół Agnieszka Anticancer potency of novel organometallic Ir(III) complexes with phosphine derivatives of fluoroquinolones encapsulated in polymeric micelles; *Inorganic Chemistry Frontiers*, 2020, 7, 3386-3401

polegał na wykonaniu pomiarów na monokryształach zsyntezowanych związków metodą dyfrakcji rentgenowskiej oraz na rozwiązaniu i udokładnieniu struktur krystalicznych, a także zdeponowaniu ich w Cambridge Structural Database.

Oświadczam, że mój udział w publikacji:

Urszula K. Komarnicka, Sandra Koziół, Agnieszka Skórska-Stania, Agnieszka Kyziół, Francesco Tisato, *Synthesis*, physicochemical characterization and preliminary in vitro antitumor activity of phosphino Ru(II) and Ir(III) complexes, *Dalton Transactions*, 2022

polegał na wykonaniu pomiarów na monokryształach zsyntezowanych związków metodą dyfrakcji rentgenowskiej oraz na rozwiązaniu i udokładnieniu struktur krystalicznych, a także zdeponowaniu ich w Cambridge Structural Database. Przeanalizowałam również otrzymane związki pod względem strukturalnym, zamieszcłam krótki opis i rysunki tej analizy.

Agnieszka Skórska-Stania  
(podpis)

Dr hab. Alina Bieńko, prof. UWr

Wrocław, dn. 30.05.2022

Kierownik Zespołu Materiałów Magnetycznych

Wydział Chemii

Uniwersytet Wrocławski

### Oświadczenie

Oświadczam, że mój udział w niżej wymienionej pracy polegał na konsultacji projektu badawczego oraz merytorycznej dyskusji wyników.

1. Koziół Sandra, Komarnicka Urszula K., Ziółkowska Aleksandra, Skórska-Stania Agnieszka, Pucelik Barbara, Płotek Michał, Sebastian Victor, Bieńko Alina, Stochel Grażyna, Kyzioł Agnieszka Anticancer potency of novel organometallic Ir(III) complexes with phosphine derivatives of fluoroquinolones encapsulated in polymeric micelles; *Inorganic Chemistry Frontiers*, 2020, 7, 3386-3401

Alina Bieńko



**dr inż. Edyta Dyguda-Kazimierowicz**

Wrocław, dn. 27.05.2022

Instytut Materiałów Zaawansowanych

**dr hab. Dariusz Bieńko**

Katedra Chemii Fizycznej i Kwantowej

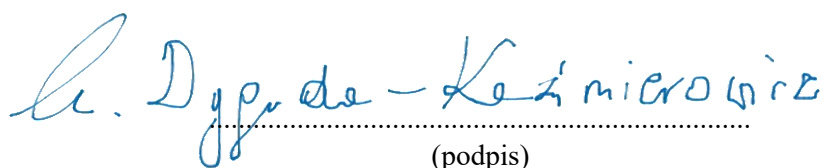
Wydział Chemii


Politechnika Wroclawska

### Oświadczenie

Oświadczam, że nasz udział w niżej wymienionej pracy polegał na wykonaniu, analizie oraz opisie obliczeń kwantowo-mechanicznych.

1. Koziół Sandra, Lesiów Monika Katarzyna, Wojtala Daria, Dyguda-Kazimierowicz Edyta, Bieńko Dariusz, Komarnicka Urszula Katarzyna, Interaction between DNA, albumin and apo-transferrin and iridium(III) complexes with phosphines derived from fluoroquinolones as a potent anticancer drug; Pharmaceuticals, 2021, 14, 685/1-685/25

  
.....  
(podpis)

  
.....  
(podpis)

**Dr. Francesco Tisato**  
ICMATE – CNR  
Corso Stati Uniti, 4  
35127 Padova, Italy  
Francesco.tisato@cnr.it  
Currently retirement

Padova, May 30 2022

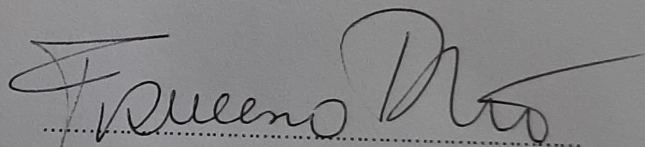
### Declaration

I hereby declare that in the article,

- Urszula K. Komarnicka, Sandra Koziół, Agnieszka Skórska-Stania, Agnieszka Kyzioł, Francesco Tisato, Synthesis, physicochemical characterization and preliminary in vitro antitumor activity of phosphino Ru(II) and Ir(III) complexes, Dalton Transactions, 2022

my own contribution amounted to:

- Mass spectrometry measurements, analysis and description data.



(sign here)

dr Barbara Pucelik

Kraków, dn. 30.05.2022

Grupa Badawcza Krystalografii Białek

Małopolskie Centrum Biotechnologii

Uniwersytet Jagielloński

### Oświadczenie

Oświadczam, że mój udział w niżej wymienionej pracy polegał na pomocy w przeprowadzeniu badań biologicznych wspólnie z mgr inż. Sandrą Kozieł oraz dr Urszulą Komarnicką (aktywacja kaspaz 3/7, badanie faz cyklu komórkowego, lokalizacja związków za pomocą mikroskopu konfokalnego, hodowla sferoidów).

1. Kozieł Sandra, Komarnicka Urszula K., Ziółkowska Aleksandra, Skórska-Stania Agnieszka, Pucelik Barbara, Płotek Michał, Sebastian Victor, Bieńko Alina, Stochel Grażyna, Kyzioł Agnieszka Anticancer potency of novel organometallic Ir(III) complexes with phosphine derivatives of fluoroquinolones encapsulated in polymeric micelles; *Inorganic Chemistry Frontiers*, 2020, 7, 3386-3401



(podpis)

Uniwersytet Jagielloński  
MAŁOPOLSKIE CENTRUM  
BIOTECHNOLOGII  
ul. Gronostajowa 7a, 30-387 Kraków  
tel. 12 664-53-69

dr Michał Płotek

Kraków, dn. 30.05.2022

Biuro Karier i Promocji

Wydział Chemii

Uniwersytet Jagielloński

### Oświadczenie

Oświadczam, że mój udział w niżej wymienionej pracy polegał na merytorycznej dyskusji wyników.

1. Koziół Sandra, Komarnicka Urszula K., Ziółkowska Aleksandra, Skórska-Stania Agnieszka, Pucelik Barbara, Płotek Michał, Sebastian Victor, Bieńko Alina, Stochel Grażyna, Kyzioł Agnieszka Anticancer potency of novel organometallic Ir(III) complexes with phosphine derivatives of fluoroquinolones encapsulated in polymeric micelles; Inorganic Chemistry Frontiers, 2020, 7, 3386-3401

Michał Płotek



prof. dr hab. Grażyna Stochel

Kraków, dn. 30.05.2022

Zespół Fizykochemii Koordynacyjnej i Bionieorganicznej

Wydział Chemii

Uniwersytet Jagielloński

### Oświadczenie

Oświadczam, że mój udział w niżej wymienionej pracy polegał na merytorycznej dyskusji wyników.

1. Kozieł Sandra, Komarnicka Urszula K., Ziółkowska Aleksandra, Skórska-Stania Agnieszka, Pucelik Barbara, Płotek Michał, Sebastian Victor, Bieńko Alina, Stochel Grażyna, Kyzioł Agnieszka Anticancer potency of novel organometallic Ir(III) complexes with phosphine derivatives of fluoroquinolones encapsulated in polymeric micelles; Inorganic Chemistry Frontiers, 2020, 7, 3386-3401



.....  
(podpis)

dr hab. Agnieszka Kyzioł, prof. UJ

Kraków, dn. 30.05.2022

Zespół Fizykochemii Koordynacyjnej i Bionieorganicznej

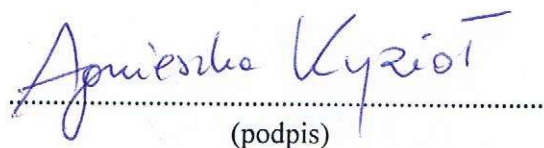
Wydział Chemii

Uniwersytet Jagielloński

### Oświadczenie

Oświadczam, że mój udział w niżej wymienionej pracy polegał na konsultacji projektu badawczego, merytorycznej dyskusji wyników oraz korekcie napisanej publikacji.

1. Koziół Sandra, Komarnicka Urszula K., Ziółkowska Aleksandra, Skórska-Stania Agnieszka, Pucelik Barbara, Płotek Michał, Sebastian Victor, Bieńko Alina, Stochel Grażyna, Kyzioł Agnieszka Anticancer potency of novel organometallic Ir(III) complexes with phosphine derivatives of fluoroquinolones encapsulated in polymeric micelles; *Inorganic Chemistry Frontiers*, 2020, 7, 3386-3401; DOI:10.1039/d0qi00538j
2. Urszula K. Komarnicka, Sandra Koziół, Agnieszka Skórska-Stania, Agnieszka Kyzioł, Francesco Tisato, Synthesis, physicochemical characterization and preliminary in vitro antitumor activity of phosphino Ru(II) and Ir(III) complexes, *Dalton Transactions*, 2022

  
.....  
(podpis)

Prof. Victor Sebastian

Zaragoza, May 30 2022

-Department of Chemical Engineering, Aragon Institute of Material and Nanoscience (INMA), University of Zaragoza.

-Networking Research Center on Bioengineering, Biomaterials and Nanomedicine, CIBER-BBN,

### Declaration

I hereby declare that in the article:

Kozieł Sandra, Komarnicka Urszula K., Ziółkowska Aleksandra, Skórska-Stania Agnieszka, Pucelik Barbara, Płotek Michał, Sebastian Victor, Bieńko Alina, Stochel Grażyna, Kyzioł Agnieszka Anticancer potency of novel organometallic Ir(III) complexes with phosphine derivatives of fluoroquinolones encapsulated in polymeric micelles; Inorganic Chemistry Frontiers, 2020, 7, 3386-3401

my contribution amounted to performance of TEM images of Pluronic P-123 formulation with the encapsulated IrPCp complex (IrPCp\_M).



.....  
(sign here)



Università  
degli Studi  
di Ferrara

Sezioni

## Dottorati di ricerca

Il tuo indirizzo e-mail

sandra.koziel@unife.it

Oggetto:

Dichiarazione di conformità della tesi di dottorato

Io sottoscritto Dott. (Cognome e Nome)

Koziel Sandra Amanda

Nato a:

Sandomierz

Provincia:

Polonia

Il giorno:

02/06/1992

Avendo frequentato il Dottorato di Ricerca in:

Scienze chimiche

Ciclo di Dottorato

34

Titolo della tesi:

Iridium(III) complexes with phosphine-fluoroquinolone conjugates - design, synthesis, bioactivity and nanoformulation as a potential platform for drug delivery

Titolo della tesi (traduzione):

Complessi di Iridio(III) con coniugati fosfina-fluoroquinolone - design, sintesi, bioattività e nanoformulazione come potenziali piattaforme per drug delivery

Tutore: Prof. (Cognome e Nome)

Alina Bienko, Stefano Caramori

Settore Scientifico Disciplinare (S.S.D.)

chim/03

Parole chiave della tesi (max 10):

Drug delivery, Iridium complexes, Heteronuclear complexes, Phosphines, Fluoroquinolone, Anticancer drug, Cancer 3D spheroids, Polymeric micelles, Nanoparticle

Consapevole, dichiara

CONSAPEVOLE: (1) del fatto che in caso di dichiarazioni mendaci, oltre alle sanzioni previste dal codice penale e dalle Leggi speciali per l'ipotesi di falsità in atti ed uso di atti falsi, decade fin dall'inizio e senza necessità di alcuna formalità dai benefici conseguenti al provvedimento emanato sulla base di tali dichiarazioni; (2) dell'obbligo per l'Università di provvedere al deposito di legge delle tesi di dottorato al fine di assicurare la conservazione e la consultabilità da parte di terzi; (3) della

procedura adottata dall'Università di Ferrara ove si richiede che la tesi sia consegnata dal dottorando in 1 originale cartaceo e 1 in formato PDF/A caricata sulla procedura informatica Esse3 secondo le istruzioni pubblicate sul sito: <http://www.unife.it/studenti/dottorato> alla voce ESAME FINALE – disposizioni e modulistica; (4) del fatto che l'Università, sulla base dei dati forniti, archiverà e renderà consultabile in rete il testo completo della tesi di dottorato di cui alla presente dichiarazione attraverso la pubblicazione ad accesso aperto nell'Archivio Istituzionale dei Prodotti della Ricerca IRIS-UNIFE ([www.iris.unife.it](http://www.iris.unife.it)) oltre che attraverso i Cataloghi delle Biblioteche Nazionali Centrali di Roma e Firenze; DICHIARO SOTTO LA MIA RESPONSABILITÀ: (1) che la copia della tesi depositata presso l'Università di Ferrara in formato cartaceo è del tutto identica a quella caricata in formato PDF/A sulla procedura informatica Esse3, a quelle da inviare ai Commissari di esame finale e alla copia che produrrò in seduta d'esame finale. Di conseguenza va esclusa qualsiasi responsabilità dell'Ateneo stesso per quanto riguarda eventuali errori, imprecisioni o omissioni nei contenuti della tesi; (2) di prendere atto che la tesi in formato cartaceo è l'unica alla quale farà riferimento l'Università per rilasciare, a mia richiesta, la dichiarazione di conformità di eventuali copie; (3) che il contenuto e l'organizzazione della tesi è opera originale da me realizzata e non compromette in alcun modo i diritti di terzi, ivi compresi quelli relativi alla sicurezza dei dati personali; che pertanto l'Università è in ogni caso esente da responsabilità di qualsivoglia natura civile, amministrativa o penale e sarà da me tenuta indenne da qualsiasi richiesta o rivendicazione da parte di terzi; (4) che la tesi di dottorato non è il risultato di attività rientranti nella normativa sulla proprietà industriale, non è stata prodotta nell'ambito di progetti finanziati da soggetti pubblici o privati con vincoli alla divulgazione dei risultati, non è oggetto di eventuali registrazioni di tipo brevettale o di tutela. PER ACCETTAZIONE DI QUANTO SOPRA RIPORTATO

Firma del dottorando

Ferrara, li \_\_\_\_\_ (data) Firma del Dottorando \_\_\_\_\_ Sandra Amanda  
Koziel Sandra Koziel

Firma del Tutore

Visto: Il Tutore Si approva Firma del Tutore \_\_\_\_\_ Alina Bienko, Stefano  
Caramori \_\_\_\_\_

Stefano Caramori Alina Bienko